Chapter 8
Technology and Droop Study for High Internal Quantum Efficiency

Bo Shen and Zhizhong Chen

8.1 Introduction

Recently, the highest record of the luminous efficiency of white light-emitting diode (LED) was reported as high as 303 lm/W at the current of 350 mA by Cree Co (http://www.cree.com/News-and-Events/Cree-News/Press-Releases/2014/March/300LPW-LED-barrier). It indicates a lower cost and smaller size for lighting source. The internal quantum efficiency (IQE) has been approached to 90% for blue LED [1]. However, the actual luminous efficiency is about 150 lm/W for white LED in the market at present. There still exist many theoretical and technique problems preventing to reach the ultimate values of the luminous efficiency. The IQE of a LED is defined as the generated photon numbers divided by the number of pairs of injected carriers in the pn junction. Except for the radiative recombination, the non-radiative recombination also occurs in the semiconductor. If the radiative one dominates in the operation, the IQE should be high. The luminous efficiency will be high too upon the same light extraction efficiency (LEE) and serial resistance.

IQE is strongly dependent on the crystalline quality and device structure. Although the IQE of the blue LED is very high at normal injection level, those for green LED and UV LED are still rather low. The well-known "green gap" has become a big issue for some years [2]. One major obscure is the increased quantum-confined Stark effect (QCSE) when the indium content increases in InGaN/GaN multiple quantum wells (MQWs). The other cause is the large number of defects because of the phase separation in InGaN layers and large misfit between GaN barriers and InGaN quantum wells (QWs). The wave function overlapping of electron and hole in QWs reduces, and more non-radiative recombination centers

B. Shen · Z. Chen (✉)
Peking University, Beijing, China
e-mail: bshen@pku.edu.cn; zzchen@pku.edu.cn

© Springer International Publishing AG, part of Springer Nature 2019

J. Li, G. Q. Zhang (eds.), *Light-Emitting Diodes*, Solid State Lighting Technology and Application Series 4, https://doi.org/10.1007/978-3-319-99211-2_8

appear with the indium content increasing. On the other hand, when indium disappeared in QWs, the IQE could also be rather small, especially for the deep ultraviolet LED made by GaN/AlGaN MQWs [3]. Without carrier localization to the indium content fluctuation, the high-density threading dislocations (TDs) will become detrimental for light emission.

The IQE in III-nitride materials is usually estimated from the temperature dependence of the photoluminescence (PL) intensity [4]. The IQE at low temperature (below 10 K) is assumed as unity, and the IQE at room temperature (RT) is estimated as the ratio of the PL intensity at RT to that at low temperature. However, the non-radiative recombination and radiative recombination of the defects are not zero at low temperature. Moreover, the recombination process for optical excitation is different from that for electrical excitation. So the validity of the conventional IQE measurement should be carefully checked.

Efficiency droop (hereafter droop, for brevity) is a phenomenon that the luminous efficiency or IQE will reduce gradually with the current density increasing [5]. Even with good thermal dissipation, the droop exists and takes an important role under high injection level. It is ineffective to reduce the lighting cost by cutting down the chip size or increasing the operation current. The droop may be due to Auger recombination, current leakage, carrier delocalization or defect activated, and so on. The high carrier concentration in the active layer is a serious problem when the TD density is high and polarization field is strong. A lot of efforts have been made to alleviate the droop. These routes include carrier concentration reduction, uniform and symmetry injection for both electron and hole, low TDD GaN substrate, etc. Under high injection level, the many body effect [6] and energy bandgap renormalization (BGR) effect [7] should also be considered. However, droop is still an unresolved problem and required more efforts to dig out its origin and find some alleviation methods.

In this chapter, we will briefly introduce the technique progress for IQE promotion of blue LED. The techniques for high IQE green and UV LEDs will be stressed, respectively. Then the new methods for IQE measurement are given. The main content will be focused on the droop and high injection performance of LED. The high radiative recombination rate and low loss will be demonstrated as a result of alleviating the droop effect.

8.2 Techniques for High Internal Quantum Efficiency

The first blue LED with high brightness of 1 Cd was commercialized in Nichia Co. in 1993. It is amazing that the TDD is about 10^{10} cm^{-2} in the GaN material of the high-brightness blue LED [8]. The defects seem not affecting on the efficiency of the GaN-based LED. However, Tsao et al. reported that the defects may influence the performance significantly at high injection level, high temperature, or with the short wavelength UV emission, as shown in Fig. 5 of the Ref. [9]. It indicates that the IQE can be improved by TDD reduction. Soraa Co. reported their UV LED

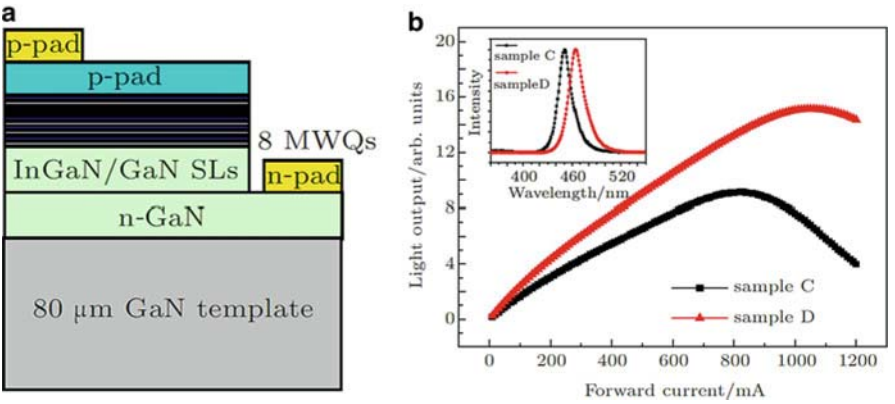

Fig. 8.1 (**a**) Structure of quasi-homoepitaxial LED, (**b**) the L–I curves under cw measurement mode of samples C (conventional) and D (quasi-homoepitaxial). The inset shows the normalized EL spectra [15]

on freestanding GaN substrate with external quantum efficiency (EQE) of 68% at 180 Acm^{-2} [10]. The TDD of GaN substrate is about $10^{5–6}$ cm^{-2}. All performances are maintained at J: 100∼1000 Acm^{-2}, as is device reliability.

The GaN substrate is very expensive compared to the popular sapphire substrate or Si substrate. The laser lift-off (LLO) and quasi-homoepitaxy techniques are developed to enhance the LED efficiency. Thirty-three micrometer freestanding thick film vertical structure LED (VSLED) was made by LLO and hydride vapor phase epitaxy (HVPE) technique [11]. Compared to the thin film (3–4 μm) VSLED on Cu or Si substrate, their electrical and optical performance is high because of less damage on the quantum wells caused by the LLO process. The thick film devices also have a low thermal resistance about 0.15–0.2 K/W. With the current of 500 mA, the 33 μm freestanding thick film VSLEDs obtain over 1.3 times light output power (LOP) than that of the 4 μm thin film VSLEDs on Cu substrates. Speck et al. found that the TDD in the GaN layers is inversely proportional to the film thickness [12]. The TDD of 80-μm-thick GaN template corresponds to 10^7 cm^{-2}, which is two orders lower than that of several-micron-thin GaN film on sapphire substrate. According to Reynolds' results, the surface is strain-free at the thickness [13]. Gorgen et al. proposed that a fully relaxed sample is able to incorporate more indium during its process of growth than a strained sample [14]. We fabricated GaN-based blue LED on 80-μm-thick GaN template with emission wavelength of 464 nm successfully by MOCVD, HVPE, and LLO techniques, as shown in Fig. 8.1 [15]. The light output at 350 mA from the thick GaN template LED is doubled compared to traditional LEDs, and the forward bias is also substantially reduced. The high performance of 80-μm-thick GaN template LED depends on the high crystal quality.

There is no doubt that the sapphire substrate is the most popular substrate for epitaxy of GaN-based material. Two-step growth method on the sapphire substrate opens a new era of nitride [16, 17]. Akasaki, Amano, and Nakamura won the 2014

Nobel Prize for their invention of the first GaN-based blue LED. Using the concept of selective area epitaxy (SAE), an effective method to improve the crystalline quality of GaN epilayer is provided, which is named as epitaxial lateral overgrowth (ELOG) [18]. The 2-μm-thick GaN epilayer was firstly grown on the c-plane sapphire substrate. Then a periodic SiO_2 mask was made along ⟨10–10⟩or⟨11–20⟩of the GaN epilayers. The stripe width, period, and thickness are about 3 μm, 6 μm, and 100 nm. The second growth was performed on the patterned GaN epilayer. Lateral overgrowth wing regions would be coalesced to form a smooth surface of GaN. The TDD reduced about two orders compared to that for convention method. After the basic ELOG technique, many evolutions are provided, such as pendo-epitaxy, air-bridge epitaxy, grooved sapphire substrate, and so on. These techniques solve the problems of the basic ELOG and reduce the TDD further. Among these methods, the grooved sapphire substrate has been gradually developed to patterned sapphire substrate (PSS) [19, 20], which becomes the most popular substrate for commercial GaN epitaxy now. Around 2005, many types of the PSS patterns appeared, including circular hole, truncated circular cone, circular cone, inverted circular cone, pyramid, inverted pyramid, hemisphere, and so on. PSS technology can not only improve the crystalline quality by TDD reduction and modify the strain but also enhance the light extraction efficiency by changing the propagation direction of the total inner reflection (TIR).

PSS technology is a mask-free method and does not require second growth. It is economic and acceptable for commercialization. In 2011, Wang et al. fabricated different period and shape of PSS by photoresist reflow technique [21]. They grew GaN films on these PSS by MOCVD. The TEM results show that the cone-shaped PSS is more effective to reduce the TDD in comparison to the truncated cone-shaped PSS. The short-period PSS makes the GaN epilayer more strain relaxed than the long period one. The epilayer on the cone-shaped PSS also shows more strain relaxation than that on the truncated cone-shaped PSS. Some researchers changed the tilt angle of the cone of PSS. They found that when the angle was about 30°, the crystalline quality was better than those of other tilt angles [22]. Huang et al. found the LEE is also enhanced for the LED grown on the 30° tilt PSS [23].

In 2000 Ashby et al. predicted that the TDD in GaN epilayer would reduce when the pattern size of the PSS decreased to nanoscale. Nano PSS (NPSS) has been applied in LED fabrication since 2007. Wang et al. thought that nanoscale pattern made the number of the pattern in per area increases [24]. The light would be more easily scattered and reflected out from the semiconductor. Su reported their 1.5 times light emission enhancement results by NPSS. They used the nanosphere lithography and ICP dry etching. The size of the sphere is about 450 nm. The spacing is about 50 nm with depth about 150 nm. They reported that the crystalline quality of GaN on NPSS was not improved compared to that on conventional micro-PSS. Moreover, the air gap in their epilayer was thought as the barrier in the thermal path, which led to the reduction of the saturation current of the LED. In 2011 Wetzel et al. fabricated NPSS by nanoimprint technology [25]. The period and depth of the NPSS are about 450 and 125 nm, respectively. Compared to the planar sapphire substrate, the LEDs grown on that NPSS achieved a three times light emission enhancement. The IQE is

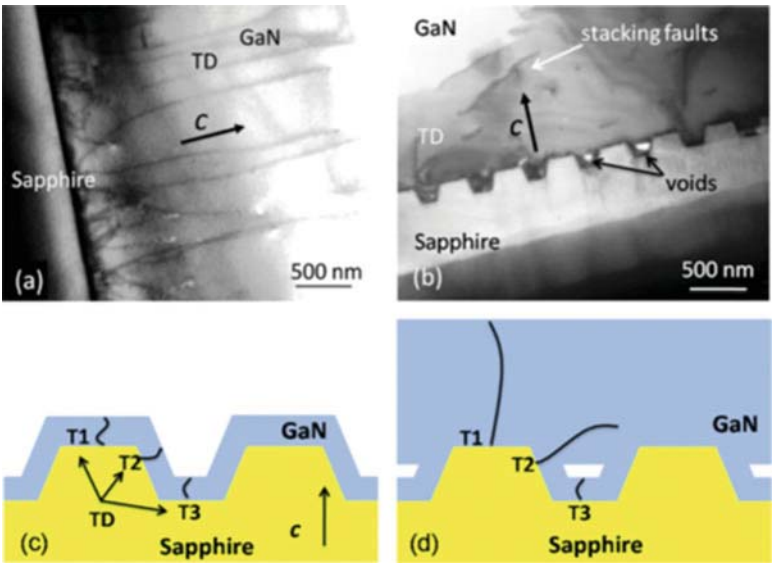

Fig. 8.2 Cross-sectional TEM of the epitaxial GaN/sapphire interface on (**a**) planar and (**b**) nano-patterned sapphire. Schematics showing early (**c**) and late (**d**) phases of the TD (T1, T2, T3) formation on the nano-patterned substrate [25]

enhanced two times, and the LEE is enhanced 58%. They observed 44% reduction of TDD in TEM images, as shown in Fig. 8.2.

Different views for the crystalline quality improvements of GaN on NPSS are reported by different research groups. It is accepted that the size and shape of PSS will determinate the growth route. The species transport processes on the NPSS is quite different to those on conventional PSS or planar substrate. Ee et al. found that the surface energy of the sapphire substrates was altered by nano-patterns [26]. We used silane in the process of the nucleation island growth and coalescence. Silicon, acting as a surfactant, will change the species mobility and surface energy [27]. An extremely smooth surface was achieved with an average roughness of 0.10 nm over $3 \times 3\ \mu m^2$ for a sample with 600 s 3D growth and 2400 s lateral growth on the NPSS. The silane addition causes the effective 3D growth. The size, homogeneity, and faceted sidewalls of islands by the 3D growth lead to a high crystalline quality, much strain relaxation, and a specular surface for the GaN epilayers. The growth time could be shortened more by further reducing the pattern size and optimizing the 3D growth conditions.

Besides the low TDD and strain-controlled substrate, the IQE improvement of LED mostly depends on the structure of the active layer. The first GaN-based LED was fabricated using metal-insulator-semiconductor (MIS) [28]. The first GaN-based pn junction LED was achieved by Amano et al. after p-type GaN was successfully obtained [29]. Both of the two LEDs are not very bright because of the lower carrier confinement in the junction area. S. Nakamura reported the

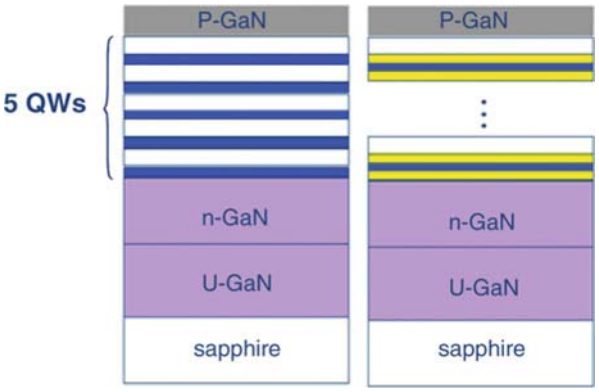

Fig. 8.3 The schematic structures of (**a**) the conventional LED, (**b**) the sandwiched LED

first high-brightness blue LED of 1 Cd using the double hetero-structure (DH) of AlGaN/InGaN/GaN [30]. In order to enhance the carrier confinement further, the single quantum well (SQW) and multiple quantum wells (MQWs) are proposed successively. Moreover, the electron-blocking layer (EBL) is added into the active layer after the MQWs growth because the mobility of electron is much higher than that of holes. Meanwhile, the electron reservoir layer (ERL) is also added before the MQWs growth to improve the carrier capture ability in the active layer [31].

Since the group III cation does not locate at the center of the nitrogen tetrahedron, the group III nitrides show very strong polarization, including spontaneous and piezoelectric ones. The polarization plays an important role on the IQE of almost all nitride LED on c-plane nitride template by bending the energy band. The QCSE makes the separation between the wave functions of electron and hole, which leads to the reduction of the radiative recombination possibility. The trapezoid QW shows better performance than the rectangular one [32]. The trapezoid QW is made by a graded indium content of InGaN QW and GaN barrier. The overlapping of the wave functions in QWs is increasing, and the homogeneous quantum dot-like attributes the high performance of the trapezoid QW [32]. We have developed a sandwiched QW structure to modify the polarization field [33]. The schematic structures are shown in Fig. 8.3. LEDs using InGaN/GaN MQWs with thin low-temperature GaN (LT-GaN) layers bounding each InGaN layer are grown by MOVPE. It is observed that the effect of polarization modification by LT-GaN is more significant. The LT-GaN layers also improve the crystal quality of the sandwiched InGaN. This in turn leads to lower defect-related recombination in the sandwiched QW, accompanied by higher radiative recombination efficiency and smaller FWHM of the emission peak. Doping in the barrier is an effective method to screen the polarization field [34]. With the doping concentration increasing, the Stokes shift becomes small. The Si concentration reaches $1 \times 10^{19}/\text{cm}^3$ so that the piezoelectric field can be fully screened. Furthermore, the interface of GaN/InGaN becomes smoother, and the radiative recombination lifetime reduces.

Kim et al. calculated the band diagram of InGaN/AlInGaN MQW LED structures, as shown in Fig. 8.4 [35]. When the total spontaneous and piezoelectric

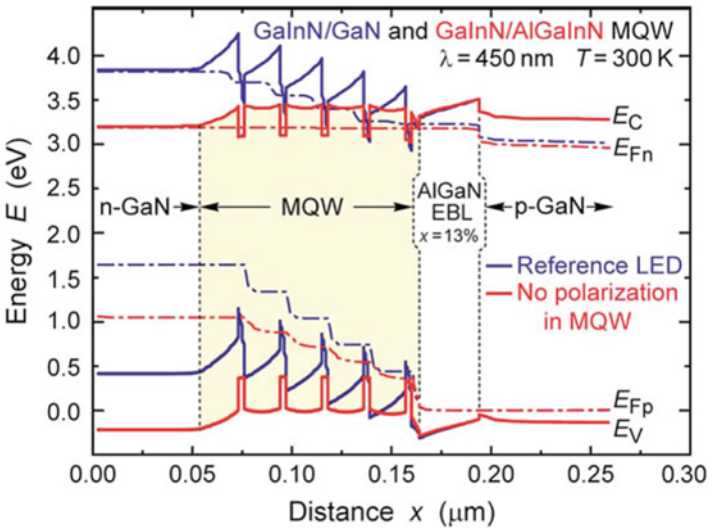

Fig. 8.4 Calculated band diagram of reference GaInN/GaNLED as well as GaInN/AlGaInN LED structure with polarization-matched MQW under a forward bias condition [35]

polarization charges in InGaN QWs are matched by equal polarization charges in AlGaInN quantum barriers, and the remaining polarization charges at the bottom and top of the MQW are respectively compensated by n- and p-type delta doping, the triangular barriers disappear. Besides the barrier, using a certain content of AlInGaN, the EBL can also be polarization matched to GaN. When the polarizations in barriers and EBL are matched to the GaN layer, the band becomes flat and the conduction band on the p-side is now higher than on the n-side making it much more difficult for electrons to reach the p-side. So the light output increases by 138% at 350 mA [35]. Some researchers found that the AlInGaN barriers could lead to interband transition instead of recombination by localization states or quantum dots. It shows high performance in high injection level [36]. In conventional injection level, the IQE is lower than that for GaN barriers.

Due to the direction of the net dipole moment along c-axis, the nonpolar or semipolar plane will show zero or small polarization in the growth direction. The less polarization field in QWs will enhance the light emission of the LEDs. The available substrates include m-, a-, and r-plane GaN; r- and m-plane sapphire; (100) planeγ-$LiAlO_2$; (100) and (110) plane $MgAl_2O_4$; and so on [37–39]. Researchers have achieved many excellent performances for nonpolar or semipolar LEDs, such as higher radiative recombination rate, high mobility, high In incorporation, polarized light, and so on. S. Nakamura reported their hole concentration of a-plane p-GaN as $2 \times 10^{18}/cm^3$. However, the luminous efficiency of the nonpolar or semipolar LEDs is not superior to that of polar ones. The growth of the GaN epilayer is very difficult on nonpolar and semipolar substrates because pure group III or N atom monolayer cannot be formed likely and stack fault densities become

higher. There are still many efforts required on the growth on nonpolar or semipolar substrates.

As mentioned above, it is hard to achieve high IQE for green LED when the indium content becomes high in InGaN QWs [2]. Poor crystalline quality and high polarization field are serious for green LEDs. Moreover, the carrier localization around the In-rich area will become weak in high indium content QWs [40]. Nakamura reported their green LEDs on nonpolar and semipolar GaN substrate [41–43]. Firstly, the TDD of the freestanding GaN substrate approaches 10^5 cm^{-2}, so the crystalline quality of the active layer of green LED is improved. The In incorporation into the QWs is rather easy when the strain on the growth surface become small [14]. What's more, the polarization field is reduced or alleviated by the semipolar or nonpolar GaN substrate. IQE will be enhanced by less QCSE for green LED on these substrates. However, GaN substrate is very expensive. It is difficult to get a 2 in. nonpolar or semipolar GaN substrate. High-quality GaN growth on nonpolar substrate is difficult because there are two types of atoms, both nitrogen and group III atoms on the nonpolar plane, which will influence the mobility and anisotropy on the growth surface. Using semipolar substrate, the crystalline quality of LED wafer will be improved. It is achieved an external quantum efficiency (EQE) of 13.4% with a peak emission wavelength of 563 nm [44]. The EQE of the semipolar LED is much higher than that of AlInGaP LED (Fig. 8.5).

It is obvious that the nonpolar and semipolar substrates are very effective to enhance the IQE of green LED. The GaN substrate is too expensive to use for cheap LED fabrication. Heteroepitaxially grown (11–22) semipolar LED on sapphire substrates are continuously paid attention to due to the lower cost and larger sizes of sapphire substrate [45–47]. High-quality (11–22) GaN templates are grown on (10–12) r-plane PSS by MOCVD [45]. Recently, Wang group reported (11–22) plane InGaN LEDs from green to amber (605) on their overgrown GaN on micro-rod templates [46]. They used m-plane sapphire substrate. They provided many evidences of polarization reduction and obtained a polarization ratio of about 25% for their (11–22) LEDs. Nakamura et al. also obtained efficient semipolar (11–22) 550 nm yellow/green InGaN LEDs on low TDD (11–22) GaN/PSS [47]. It is hopeful to fabricate high efficiency semipolar InGaN LEDs with long emission wavelength on large area sapphire substrate (Fig. 8.6).

Besides the large area growth of (11–22) semipolar LED, the core-shell LEDs were reported to obtain high IQE of green LED. The m-plane of GaN is easy to grow or etched by induced coupling plasma (ICP) etching. The m-plane InGaN LED shell can be grown on the m-plane n-GaN core [48]. The cost is much lower than that using am-plane freestanding GaN substrate. The large surface of the core-shell LED induces new optical and electrical properties. The emission wavelength can be tuned to green or amber by changing the diameter of the nanorods [49]. In May 2012, Samsung Co. reported their core-shell green LED in the XVI International Conference on MOVPE (ICMOVPE-XVI). The IQE is as high as 75% at the wavelength of 550 nm. The value is five times of the highest IQE by other techniques. Glo Co. also reported their green LED based on nanorod array

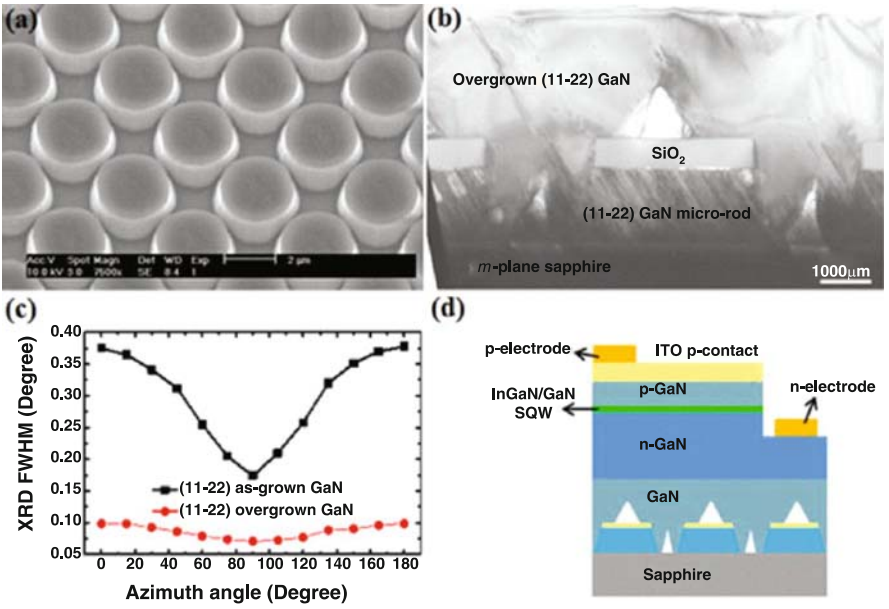

Fig. 8.5 (**a**) SEM image of a micro-rod GaN template; (**b**) TEM image of the (11–22) GaN overgrown on micro-rods; (**c**) XRD FWHMs of the overgrown (11–22) GaN and (11–22) GaN template, measured at azimuth angles ranging from 0° to 180°; (**d**) schematic of (11–22) InGaN SQW LED [46]

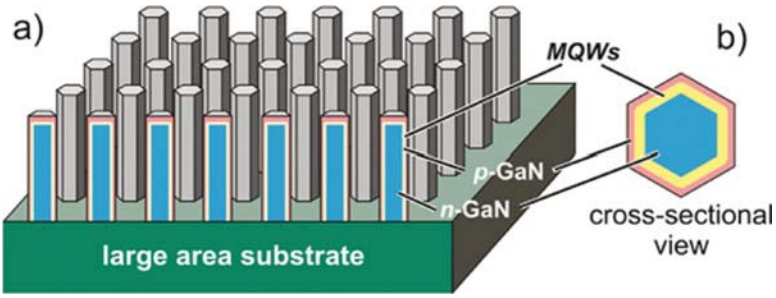

Fig. 8.6 Core-shell strategy for the fabrication of GaN-based nanoLEDs. Sketches of (**a**) core-shell nanoLED ensemble. (**b**) Cross-sectional view of a core-shell nanoLED. The active LED area can be increased approximately by a factor of four times the aspect ratio in comparison to a planar LED [48]

in the 10th International Conference on Nitride Semiconductor (ICNS-10). The SMASH project in the Europe Union organized Osram and Obducat companies and the research institutes in Germany, the UK, France, etc. to study the nanorod LEDs. It is much superior for nanorod LED arrays. The growth of nanorod avoided the effects of lattice and thermal misfit in heteroepitaxy by compliance "bridges" from the mismatched epilayers to the nano-patterned substrates [50]. The TDD even

reduced to zero after the growth condition optimization. The emission area increases several times from the conventional LED [48]. There are no guided wave modes in the nanorod when the diameter is below 170 nm [51].

There is still much room to improve the efficiency of the polar green LEDs. Polarization match can be used to lower down the QCSE in high indium content active layer [35]. The Rensselaer Polytechnic Institute group used AlInGaN layers as polarization-matched barriers and electron-blocking layer (EBL). The IQE was enhanced 1.38 times compared with the conventional LEDs. However, the growth of high-quality AlInGaN is very difficult because of the opposite growth conditions for AlGaN and InGaN. A pulsed-flow growth method is provided to fabricate the AlInGaN barriers [52]. The electron overflow is much suppressed in N-polar GaN green LEDs ($\lambda \sim$ 535–550 nm) [53]. The LEDs were found to operate with a low ($\sim$2.3 V) turn-on voltage. The reversed (N-face) polarization charges benefit the elimination of the potential barriers against carrier injection (outside the QW region) and generation of potential barriers to confine carriers (inside the QW region). O'Donnell et al. provided a nonradiative shunt for electron-hole recombination, particularly at higher excitation densities. Solid-state lighting is redefined by bandgap engineering techniques (SORBET). A novel bandgap engineering strategy based upon quantum well intermixing (QWIM) offers solutions to IQE green gap [2]. All graded SQW show a significant increase in IQE compared to a rectangular SQW for a wide range of current densities. A tapered AlGaN EBL were used in green LED structure, which improved the hole injection and electron overflow [54]. A charge asymmetric resonance tunneling (CART) structure was applied to nitride-based green LEDs to enhance their output efficiency [55]. The structures of barrier and wells can also be optimized, including the thickness, doping, content gradation, and so on. The sandwiched QWs structure is a potential technique because of prevention of the indium diffusion from low-temperature quantum wells [33].

According to the thermodynamics theory, the high In content InGaN is metastable and easy to phase separate [56]. The structure and processing of high In content InGaN QWs should be paid great attentions. InAs quantum dots (QDs) are put forward by Arakawa and Sakaki in 1982. They used QDs to lower the current density threshold and enhance the differential gain [57]. Due to its low defect density and high confinement of carriers, the QDs structures are hopeful to act as the active layer for green LEDs. Generally, the InGaN phase separation is very little when the size of QDs is small. In early works, InGaN QDs are obtained by self-assembling method [58]. In the self-assembling method, it is hard to control the size and density of the InGaN QDs. Arakawa et al. achieved uniform InGaN QDs by selective growth [59]. Mi et al. reported a high efficiency green, yellow, and amber emission from InGaN/GaN dot-in-a-wire hetero-structures [60]. The IQE is about 45% at 570 nm. The value is the highest one in InGaN-based green LED.

Although most green LEDs are grown on sapphire and freestanding GaN substrate, green LEDs on Si substrate is being industrialized [61–64]. Both the lattice mismatch and thermal mismatch between GaN and Si cause the tensile strain generated in GaN epilayer. The tensile strains benefit for In incorporation into InGaN QWs. It indicates that the QW growth temperature of LEDs on Si substrate

can be set 20° higher than that of sapphire, which is helpful for improving the quality of QWs [61]. V-pits is also paid attention to in the green LED on Si substrate. The prestrained layers consisted of a low-temperature (LT)-GaN layer, InGaN/GaN SLs, and blue QWs. LT-GaN is used to generate V-pits. The V-pits can divide the QW plane into small areas, which lead to strain relaxation in QW. The V-pits may also form high potential barrier preventing carriers from recombination at TD. Due to the thin InGaN/GaN layers on the sidewall, the hole tunneling into the planar QWs becomes easier [62, 63]. In the longer wavelength at 566 nm, the EQE of high-power LEDs on Si substrate has been achieved to 9.4% [64].

As an alternative route, the surface plasmon (SP) are paid much attention to obtain high-efficiency green LEDs. SP mode is a collective electron oscillation on the surface by the external excitations [65]. Using Ag, Au, and Al films on the InGaN QW, the PL intensity was enhanced 17 times at the resonant wavelength [66]. The GaN spacer is about 10 nm thick between the InGaN QW and metal film. SP modes include SP polaritons (SPP) and localized SP (LSP). To realize the coupling of photons and SPPs, wave vector matching is essentially required, while LSP coupling does not require the matching. LSP coupled with QWs for green LED emission enhancement is of great interest for many researchers because of zero momentum-matching and adjustable resonance energy [67–70]. The metal material, size, shape, covering dielectric layer, and spacer thickness of the metallic nanoparticles (NPs) are studied to obtain high-efficiency green LED and to study its coupling mechanisms. Compared to that in the randomly distributed metallic NPs, LSP in the periodical ones shows many advantages for light extraction and spontaneous emission enhancement [69, 70]. The NPs with rigid period and the specific size of Ag can diffract and effectively scatter more light from the semiconductor and metal. We successfully fabricate Ag NPs array in photonic crystal (PhCs) holes of p-GaN by soft-stamp nanoimprinting and lift-off techniques [71].

Figure 8.7 shows the scanning electron microscope (SEM) images of Ag NPs array embedded into p-GaN layer of green LEDs. The PL intensity is enhanced to 4.5 times and the PL decay time reduced 3.8 times by the Ag NPs array. We also reveal that Ag NPs, with a diameter over a large range from 90 nm to 200 nm and α larger than 1.5, would help to get a significant emission enhancement on green LEDs.

The improvement of luminous efficiency for green LED is urgently required to promote the quality of semiconductor lighting. In a near future, polarization engineering, strain engineering, and MOCVD processing optimization can be carried out. With the development on nanoscience and technology, LSP, PhC, QDs, and core-shell structures can play important role in the green LED fabrication. The high-efficiency, low-cost green LED will be the key device to promote the development of semiconductor lighting.

Recently, AlGaN-based deep ultraviolet light-emitting diodes (DUV-LEDs) have received considerable attentions due to their promising applications, such as purification, sterilization, biomedicine, UV curing, gas sensing, optical data storage, and non-line-of-sight communication [72]. Compared with the EXE of the visible

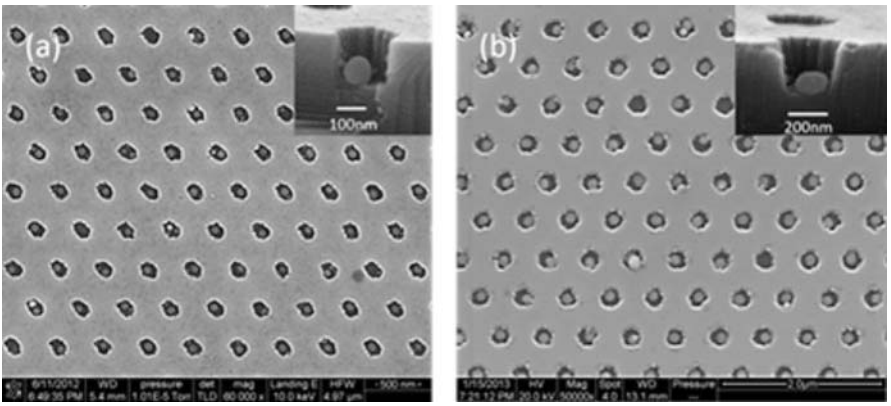

Fig. 8.7 Top view and cross-view (inset) SEM images for the Ag arrayed LED (**a**) sample 1 and (**b**) sample 2 on the green LED epitaxial wafer, for the hexagonal arrayed nanoholes into the p-GaN cladding layer; every hole is filled with single Ag NP [71]

LED usually exceeding 50%, the EXE of AlGaN-based DUV LED is hard to be beyond 10% [73]. There are many problems in substrate, high Al content AlGaN growth, polarization, p-doping, and so on.

I. Akasaki et al. analyzed the IQE of whole-composition-range AlGaN multi-quantum wells (MQWs) on AlGaN with various dislocation densities (DDs) by excitation-density-dependent PL measurement [74]. They found that with an excess carrier density of 1×10^{18} cm^{-3}, the IQE changes from 4 to 64% with the DD changing from $6 \times 10^{9}$to 2×10^{8} cm^{-2} for DUV MQWs with the emission wavelength from 230 to 350 nm. Because aluminum adatoms have a much larger sticking coefficient and much lower surface mobility than gallium adatoms, the UV-transparent low DD AlN and AlGaN is difficult to grow. A low V/III ratio (about 1:4) and high growth temperature in excess of 1200 °C were used to achieve two-dimensional growth mode for AlN on sapphire. A. Khan et al. suggested that a pulsed atomic-layer epitaxy (PALE) approach could be used to grow high-quality AlN and AlGaN films [75]. In PALE the flow rates of group III and group V precursors are sequentially modulated, thus enhancing the surface migration of aluminum and gallium adatoms. In our study the AlN buffer was fabricated by the PALE method, and then AlN epilayer was continuously grown on it [76]. TEM images show that PALE-AlN buffer is a region with high-density TDs, and the subinterface can play an obvious role for blocking TDs. Initially, dislocations are generated at the points of grain boundaries in the PALE buffer. With increase in the lateral growth rate, small islands are incorporated by bigger islands, and they became coalescence. During the coalescence of these islands, the dislocation line will be bended due to their image force. When encountering another dislocation, a dipole half loop will be formed. If the two dislocation lines have opposite Burger vectors, they will be annihilated by each other. Otherwise, the large kinks form and TDs reorient back into approximately [0001] direction [76].

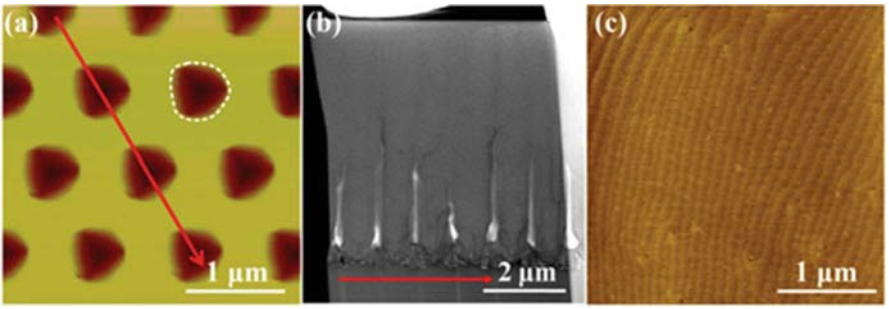

Fig. 8.8 (**a**) AFM image of a typical NPSS ($3 \times 3\ \mu m^2$). (**b**) The cross-sectional STEM image for this chosen sample fabricated by focused ion beam. (**c**) A typical AFM image of the surface morphology of the AlN sample on NPSS with 650 nm hole patterns ($3 \times 3\ \mu m^2$) [79]

PSS used for AlN growth are also paid much attention on. However, large spacing between micro-patterns usually requires a great coalescence thickness close to 10 μm, implying long growth time and high cost. To obtain a thinner coalescence thickness, AlN epitaxy on NPSS and nano-patterned AlN/sapphire template are considered [77, 78]. Although their results are exciting, the growth mechanism and dislocation evolution are not clear for AlN epitaxy on NPSS. We performed a series of AlN/NPSS experiments by changing the size of the pattern and V/III ratio [79]. Figure 8.8 shows the AFM image of the prepared NPSS with hexagonal hole patterns and STEM and AFM images of AlN epilayer on 650 nm hole diameter NPSS. The period is about 1 μm. The crystalline quality can be greatly improved by using optimized 1 μm period, 650 nm diameter NPSS. The XRD ω-scan FWHMs for (0002) and (10–12) reflections are 171 and 205 arcsec, respectively. The optimized NPSS contribute to eliminating almost entirely the threading dislocations (TDs) originating from the AlN/sapphire interface via bending the dislocations by image force from the void sidewalls before coalescence.

In addition, reducing the misorientations of the adjacent regions during coalescence adopting the low lateral growth rate is also essential for decreasing TDs in the upper AlN epilayer.

Stress in the AlGaN growth should be well controlled on the above AlN/sapphire template. Interlayers of AlN and AlGaN and its SLs have been grown at low temperatures to avoid cracking of AlGaN [80–82]. The use of AlN/AlGaN SLs to alleviate the cracking of thick AlGaN films over sapphire substrates has also been reported [82]. X-ray measurements show that these SLs were efficient in enhancing the AlGaN mosaic block dimensions. Development of the AlGaN/AlN SL buffer layers enabled growth of highly doped n-AlGaN to a thickness >2.0 μm [82], enabling development of UV-B and UV-C LED devices first with submilliwatt- and later with milliwatt-level output powers. Further optimization of the AlN buffer layer quality by means of PALE enabled improvements in the material quality of the n-AlGaN bottom-cladding layer, as well as the multiple QW layers, and resulted in the first milliwatt level UV-C LEDs [83]. We studied the influence of growth

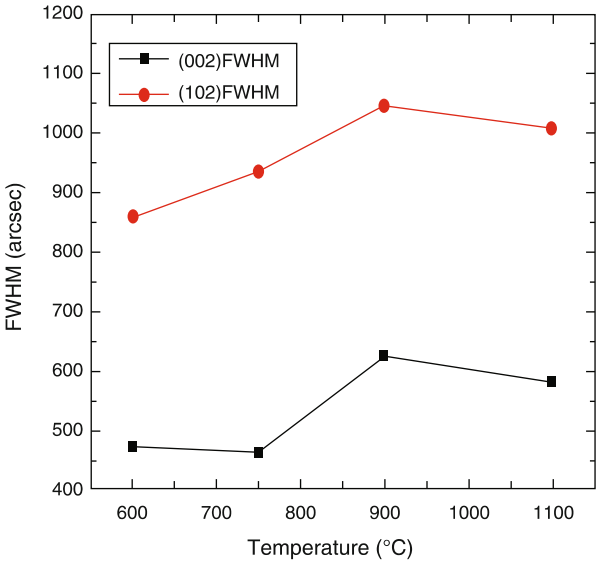

Fig. 8.9 (002)- and (102)-plane FWHMs of ω-scan XRD for $Al_{0.65}Ga_{0.35}N$ epilayers on AlN/sapphire template with GaN interlayer grown at different temperatures [84]

temperature for the low-temperature (LT) GaN interlayer on the crystalline quality of AlGaN. Figure 8.9 shows a suitable temperature as 600 °C for the growth of LT GaN interlayer.

Doping in high Al content AlGaN is difficult for both n- and p-type. The bandgap of the semiconductor increases, and the ionization energies for silicon (n-type dopant) and magnesium (p-type dopant) increase, resulting in a lower ionization efficiency. P-type doping of high-aluminum-content AlGaN is even more challenging. In order to increase the doping efficiency of Mg-doped AlGaN, indium (In) ambient assistant growth was used for Mg doping of AlGaN. It was found that In ambient assistant growth can decrease the acceptor activation energy significantly [84]. The LED device with p-type AlGaN grown under In ambient exhibit better electric properties than that without In ambient assistant growth. Surfactant In-assisted Mg delta doping in AlGaN is successful to obtain high p-type concentration of 4×10^{18} cm^{-3} [85]. A novel multidimensional Mg-doped SLs is proposed to enhance the vertical hole conductivity in conventional Mg-doped AlGaN SL which generally suffers from large potential barrier for holes [86]. The hole concentration reaches up to 3.5×10^{18} cm^{-3}, while the corresponding resistivity reduces to 0.7 Ω cm at room temperature. The hole in 3D SL are likely to be more delocalized rather than concentrated in the well compared with that in the conventional SL. High hole concentration can improve not only the lateral current spreading but also the hole injection efficiency into the active layer [87]. The IQE will be enhanced significantly with the carrier concentration increases in high Al content AlGaN.

For high IQE DUV-LEDs, the polarization effect should be concerned just like that in the GaN-based visible LEDs. Lin et al. show that through the employment of properly designed quaternary AlInGaN materials in the active region of UV LEDs, the polarization mismatch between hetero-layers can be efficiently mitigated [88]. Owing to the reduced built-in polarization field, not only the hole injection efficiency is improved, but also the electron leakage can be suppressed due to the effective potential height for electrons being increased. By tailoring the polarization in the EBL, the light output power of the AlGaN-based DUV-LED is improved significantly [89]. It indicates that the polarization effect contributes to both the suppression of the electron leakage and increase of the hole injection efficiency. The structures of the barrier and well are also designed to obtain better confinement of carriers. Chen et al. used staggered quantum wells to improve the DUV-LEDs performance [90]. It is due to the diminished piezoelectric polarization fields in QWs which can increase the density of electron and hole and the overlap of the electron and hole wave functions and thus enhance the radiative recombination rate. Wang et al. investigated AlGaN-based DUV-LEDs with composition-varying AlGaN multilayer barriers [91]. The better performance is attributed to the markedly reduced polarization-induced electrostatic field within the QWs. We improve the performance of DUV-LEDs by inserting single spike barriers [92]. The IQE and LOP were remarkably improved compared to those with conventional AlGaN MQWs structures. The spike barriers modulate the carrier distribution and increase the overlapping between electron and hole wave functions in MQWs.

8.3 Characterization for Internal Quantum Efficiency

Nowadays, most IQE values of LED or quantum wells are obtained by temperature-dependent PL (TDPL) [4, 93]. As shown in Fig. 8.10, the integrated PL intensity for the InGaN UL is almost constant at 17–150 K, and it falls gradually with further increase of temperature. Even at RT, however, it remains 71% of that at 17 K [93]. The non-radiative recombination centers near the MQW were greatly reduced by incorporating indium atoms into the underlying layer. Martinez et al. reported that IQE changed with the excitation power density [94]. The IQE increases to a maximum, and then droop appears with the injection level increases. They also performed TRPL as a complementary technique to study the effect of free-carrier screening on the radiative and nonradiative processes in the QWs. Schubert et al. reported a similar work and combined the ABC model to give the exact IQE. The IQE is as high as 64% at a carrier concentration of 1×10^{18} cm^{-3} for the sample with the lowest dislocation density (5.3×10^{8} cm^{-2}) [95]. The three main carrier recombination mechanisms in a bulk semiconductor are Shockley-Read-Hall non-radiative recombination, expressed as An, bimolecular radiative recombination Bn^2, and Auger non-radiative recombination Cn^3, where A, B, and C are the respective recombination coefficients, and n is the carrier concentration. Auger recombination affects LED efficiency only at very high excitation; thus, the generation rate G at

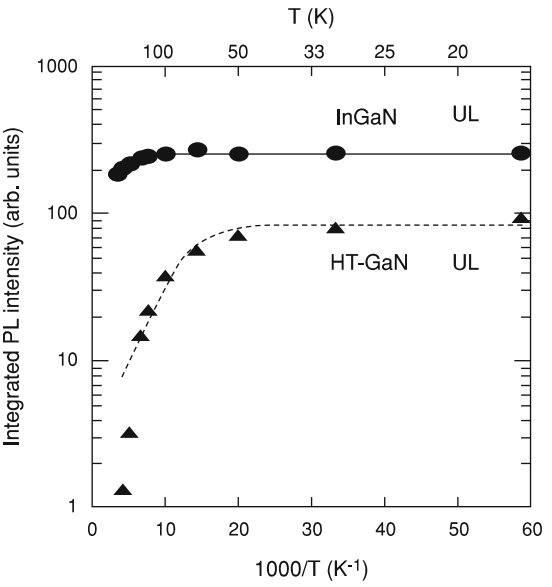

Fig. 8.10 Arrhenius plots of integrated PL intensity for InGaN MQWs prepared by using an InGaN UL (closed circles) and an HT-GaN UL (closed triangles). The solid line and dotted line are the fitting results obtained by thermal quenching equation for integrated PL intensity for InGaN MQWs prepared by using an InGaN UL and an HT-GaN UL, respectively [93]

steady state can be expressed as

$$G = \frac{A}{\sqrt{B\eta}}\sqrt{I_{\mathrm{PL}}} + \frac{1}{\eta} I_{\mathrm{PL}} \tag{8.1}$$

where η is a constant determined by the volume of the excited active region and the total collection efficiency of the luminescence. I_{PL} is the integrated PL intensity. According to the experimental PL integrated intensity, laser spot size, QW thickness, absorption coefficient, and so on, the IQE could be fitted exactly. However, the leakage of carriers from GaInN QWs may occur even when the energy of the optical excitation is much less than the bandgap energy of the GaN quantum barrier [96]. So the IQE results need be further modified by the effect of carrier leakage.

Considering the difference of electrical and optical excitation, we measured electroluminescence (EL) spectra under different injection level [97]. Then we also used ABC model to obtain the IQE. For the GaN-based LEDs, the recombination rate is given by

$$R = An + Bn^2 + Cn^3 + f(n), \tag{8.2}$$

where $f(n)$ denotes the carrier leakage. The light output power (P) is related to Bn^2. By defining

$$x = \sqrt{P} = n\sqrt{B} \tag{8.3}$$

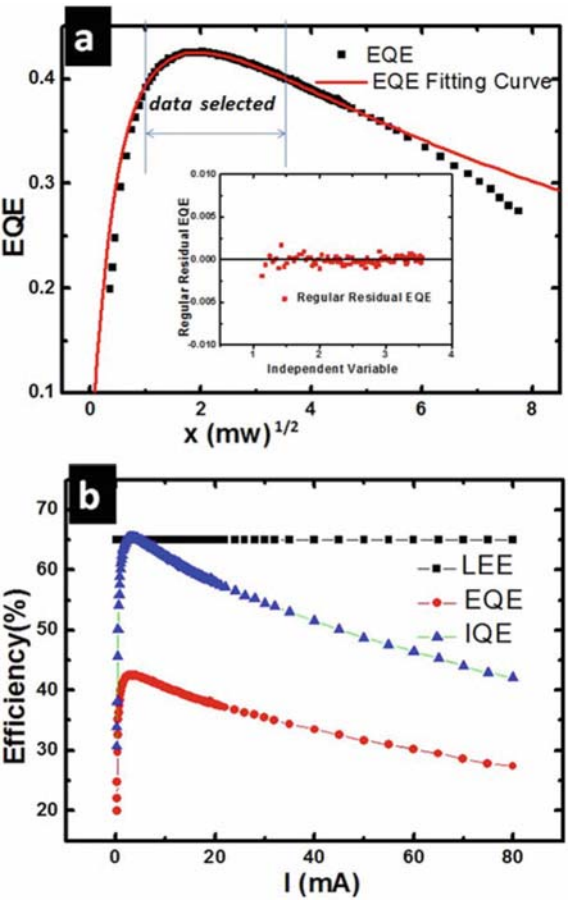

Fig. 8.11 (**a**) Fitting process for EQE to x, (**b**) efficiencies as functions of injection current [97]

At low and moderate current injection levels, carrier leakage is negligible. When the IQE maximum approaches,

$$\mathrm{IQE}\,(n_0) = \frac{Bn_0{}^2}{An_0 + Bn_0{}^2 + Cn_0{}^3} = \frac{a}{a+2} \tag{8.4}$$

where $a = {}^{B}\Big/_{\sqrt{\mathrm{AC}}}$, n_0 is carrier concentration at the IQE maximum.

Normally, the LEE is considered to be constant under varied current injections. With EQE derived from optical power versus injection current curve, IQE can be obtained by dividing EQE by the constant LEE. Figure 8.11 shows atypical fitting analyses process. By fitting the EL spectra under different injection level, IQE and LEE for the blue LED on PSS are 54.6% and 74.0%, respectively.

The assumption for IQE at cryogenic temperature as unity is not reasonable. Kawakami et al. found the evidences from simultaneous measurements of PL

and photo-acoustic (PA) signals [98, 99]. PA signal caused by heat generation in nonradiative processes in the sample was detected as sound wave by a microphone and a signal lock-in amplifier. Although the PL and PA signals are considered to be proportional to radiative and non-radiative recombination rate, respectively, while the intensity of the two signals cannot be compared directly, and thus, the IQE values also cannot be derived. The energy supplied to the sample by optical excitation is emitted either in the form of "light" or "heat" by radiative or non-radiative recombination processes, respectively. Therefore, in case the PL intensity shows a superlinear behavior, the PA intensity should show a sublinear behavior. Conversely, in case PL intensity shows a sublinear behavior, PA intensity should show a superlinear behavior. This complementary relationship enables the comparison of the two signals' intensities to determine the IQE values [98].

They measured the IQE by three types of GaN samples by the PL/PA method and compared with these measured by conventional TDPL [98]. PL/PA measurements show quite reasonable IQE values for the samples.

They also estimate accurate lifetimes from the reliable IQE values estimated by the simultaneous PL/PA measurements. It is found that the radiative recombination lifetime in GaN increases in proportion to the 1.5th power of temperature and that nonradiative lifetime shows little temperature dependence although the nonradiative lifetime itself largely depends on sample quality [99]. It is concluded that decrease in emission efficiency with increasing temperature in GaN is not due to enhancement of nonradiative processes but due to suppression of radiative recombination rate, which is conformed to their early results [100].

Chichibu et al. thought that the IQE measured by the conventional TDPL method is potentially larger than the true IQE in the low-quality samples [101]. They presented the omnidirectional photoluminescence (ODPL) spectroscopy using an integrating sphere, in which both irradiating photons from the excitation source and emitted photons from the sample are omnidirectionally integrated and detected. The IQE in a material can be accurately measured. The ODPL spectra commonly exhibited a characteristic two-peak structure, as shown in Fig. 8.12. They assume the origin of the two-peak structure found in $I_{ODPL}(\omega)$ is the traveling of photons in nearly transparent energy regime below the absorption edge energy (E_{abs}). The other expression is that the traveling photons with the energy higher than E_{abs} of $I_{ODPL}(\omega)$ are completely reabsorbed before escaping from the sample [101]. They also give the expression of IQE:

$$\eta_{int} = \frac{\eta'}{\eta' + \eta_{ext}^{direct} - \eta' \eta_{ext}^{direct}} \tag{8.5}$$

where η_{ext}^{direct} is the direct LEE from surface and η' is the EQE. At last they give a typical IQE as high as 15% for high-quality GaN single crystals grown by HVPE on a GaN seed crystal prepared by the ammonothermal method using acidic mineralizers [101]. They also use ODPL to obtain the absolute quantum efficiency (AQE) and IQE for HVPE growth GaN wafer [102]. The high value of $\eta_{int} = 70.9\%$

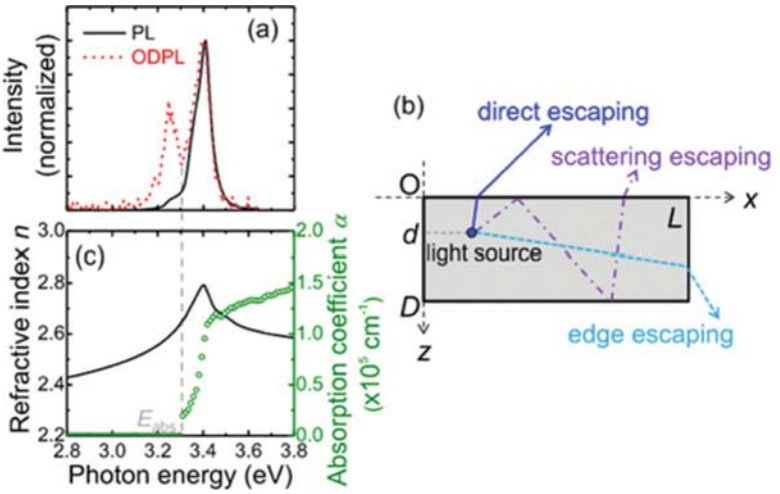

Fig. 8.12 (**a**) PL and ODPL spectra of the HVPE/AT-GaN crystal and (**b**) detectable light-traveling passes considered in the simulation of light extraction: (1) direct escaping from the surface; (2) scattered at the bottom and escaping from the surface; and (3) direct escaping from the edge. (**c**) Refractive index and absorption spectra of HVPE/AT-GaN [101]

may truly represent a considerable decrease in N_{NRC}, which corresponds to the decrease in $[V_{Ga}X]$ of HVPE/AT-GaN in comparison with HVPE/GaN. They note that η_{int} determined in this study is insensitive to the surface quality, because both crystals were prepared using the same polishing process. Therefore, it can be a scale to evaluate the bulk quality.

8.4 Origins of Efficiency Droop

For general lighting, high luminous efficiency and high current density operated LEDs are absolutely the most valuable ones. However, the IQE typically peaks at a few A/cm^2 and then drops at increasing current density, down to values that can be as low as 50% of the peak value for current densities above hundreds of A/cm^2. Even if the measurement is performed under short pulse and low filling factor of current, the efficiency droop (hereafter droop, for brevity) exists too. Verzellesi et al. summarized the possible origins of the droop [103], as shown in Fig. 8.13. There are two types of mechanisms, namely, the internal losses and carrier leakage. Auger recombination is a three-particle process where an electron from the conduction band recombines with a hole in the valence band, and the excess energy resulting from this recombination is transferred to a third electron (eeh) or hole (hhe) by carrier-carrier interaction. The Auger coefficient C determines whether Auger recombination is the major cause for the droop. Previous measurements

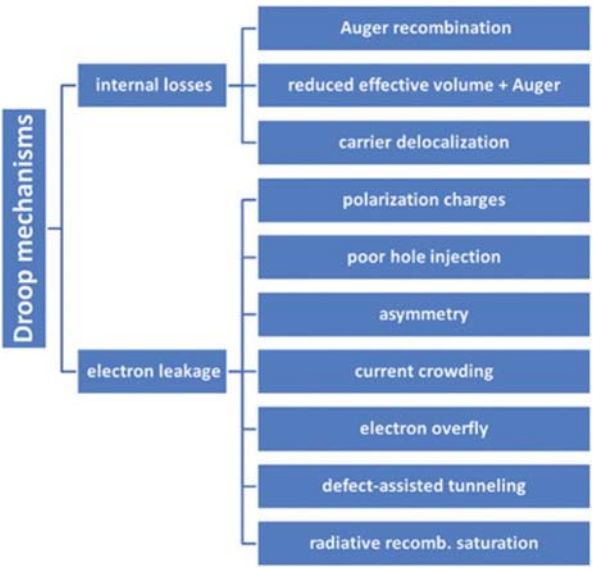

Fig. 8.13 Classification of droop mechanisms [103]

and estimations of the Auger coefficient in nitrides are ranged from 1×10^{-34} to 5.37×10^{-28} cm^6 s^{-1} [104]. One ab initio calculation suggested C values in the order of 10^{-30} cm^6 s^{-1} for a relatively narrow InGaN bandgap range around 2.5 eV, due to resonance between the lowest and the immediately upper conduction bands [105]. The coefficient is associated with indirect Auger processes in bulk InGaN, where the C values are about 3×10^{-31} cm^6 s^{-1}and 10^{-31} cm^6 s^{-1}for phonon-assisted and alloy-disorder-assisted Auger process, respectively [106]. Auger rates may be significantly enhanced in QWs with respect to the bulk case [107]. The direct measurement of the generation of Auger electrons is carried out by electron emission spectra after anode contact Cs [108]. For Auger being the sole cause for large droop effects that are observed in many reported devices, C should exceed 10^{-30} cm^6 s^{-1}.

Another major origin of the droop is the carrier leakage. Kim et al. reported [35] that droop is unrelated to junction temperature; it is not related to MQW efficiency but rather to the recombination of carriers outside the MQW region. Their simulations show that polarization fields in the MQW and electron-blocking layer enable the escape of electrons from the MQW region and thus are the physical origin of the droop. When polarization-matched AlGaInN quantum barriers and EBL are used, the droop at 350 mA decreases from 49.5% to only 5% [35]. The carrier leakage is well proved by Vampola et al. [109]. They grew a QW more with emission wavelength of 405 nm after the 450 nm blue MQWs and EBL. They found that the 405 nm emission did not appear under low injection level. It appeared at high injection level. This means the existence of carrier leakage from MQWs.

Besides the two major origins, there are many other factors causing droop. Carrier delocalization under high injection level is one of the important droop

mechanisms [110]. It is observed a reduction in the localization induced S-shape temperature dependence of the peak photoluminescence energy with increasing excitation power density. This S-shape dependence is a key fingerprint of carrier localization. The onset of efficiency droop occurs at the same carrier density as the onset of the carrier delocalization. It is concluded that the saturation of the localized states is a contributory factor to efficiency droop whereby nonlocalized carriers recombine nonradiatively. Similar to the carrier delocalization under high injection, the extra, defect-related process has been modeled in Ref. [111] and termed density-activated defect recombination (DADR). Experimental droop data have been fitted in Ref. [111], by assuming a recombination rate proportional to the second power of the carrier density. With the carrier concentration increases, the defects become electrically and optically active. They turn out to be non-radiative recombination centers.

Except for the above polarization-induced carrier leakage, there are many other factors for carrier leakage, such as poor hole injection, current crowding, electron overfly, defect-assisted tunneling, radiative recombination saturation, and so on [103]. Both the hole concentration and mobility of Mg doping in p-GaN and AlGaN EBL layers are small [112]. The valence band offset and polarization charges at the EBL/spacer interface prevent the hole injection. Asymmetry in the electron and hole active doping concentration and in carrier transport parameters (mobility and related diffusivities) has been explicitly indicated as a droop cause [113]. Current crowding affects the droop through Auger effect or leakage in high current density area and defect-assisted tunneling in the low current density area. Electron overfly might be exacerbated by nonequilibrium electron transport effects induced by extra kinetic energy gained by electrons as they are injected from GaN into InGaN due to conduction-band discontinuity, since these "hot electrons" are assumed to have an enhanced overfly probability [114, 115]. Bandgap renormalization (BGR) and band-filling should occur when the carrier concentration is higher than mid 10^{18} cm^{-3} [116]. The BGR effect can build an additional potential barrier for carriers to inhibit their transferring from high to low energy state, thus leading to efficiency saturation [117]. Defect-assisted tunneling from the QW into defects in the p-side QB and "under" the QW through deep states in the QBs attributes to the carrier leakage and resulting droop. These defect-assisted tunneling effects have been correlated with the observed decrease in IQE in the low-energy part of the emission spectrum in a single QW LED [118]. The IQE and EL spectra of blue and green LEDs make the researchers conclude that a major role in the enhanced droop observed at low temperatures lies in the electron leakage promoted by the saturation of the radiative recombination rate [119].

There are still other explanations for the droop. Using fully microscopic many-body theory, Hader et al. investigate the droop causing mechanisms in GaN-based LEDs [6]. The most plausible droop model appears to be a combination of carrier delocalization at very low temperatures and pump powers, density-activated defect recombination at low to medium pumping, and injection/escape losses at strong pumping. Some groups found that the radiative recombination rate is saturated while the nonradiative one is increased with current density increases [119–121].

Lu et al. studied the droop by aging experiment on GaN-based LEDs [122]. They found that with increasing stressing time, the overall quantum efficiency of the aged LEDs drops while the peak-efficiency-current shifts toward higher magnitude. They thought that the sample variations were the root cause of the differences in opinions over the origin of efficiency droop. The absolute efficiency of LEDs should be stressed when comparing different device structures and material qualities. Temperature-dependent droops in LEDs are also studied [123]. In the low current density region, the temperature dependence of the EQE is mainly dominated by the Shockley-Read-Hall recombination and hence the dislocation density of the device. In the high current density region, carrier leakage from the quantum wells is the main factor influencing the decrease in the EQE with ambient temperature, and in this region, the LEDs become less temperature sensitive with increasing quantum well barrier height.

8.5 Some Remedies to Alleviate the Efficiency Droop

Nearly all of the reports on droop give their remedies to improve droop characteristics. However, there are no general methods to deal with all the droops effectively. Verzellesi et al. also propose a classification of the droop remedies based on their primary goal, whether it is (a) reducing the QW carrier densities, (b) improving the electron confinement within the active region, or (c) enhancing the hole injection into the active region [103]. Reducing the QW carrier densities is a direct method to resolve many problems that lead to droop, both for Auger recombination and carrier leakages. Lumileds Co. reported their InGaN/GaN double hetero-structure (DH) LED [124] (Fig. 8.14).

By increasing the thickness (∼9–12 nm) of InGaN layer, the EQE reaches to its maximum at the current density of 200 A/cm^2. The spectral width of the DH LED is also sharper than that of the MQW LED. The shift of the peak wavelength is much smaller too. Their epi-structures are not clear but quite different from the DH LED reported in 1994 [30]. The earlier DH LED is GaN/InGaN/AlGaN structure. The thickness of InGaN is much high as about 50 nm. The FWHM of the spectrum is about 70 nm. DH structure reduces the droop significantly. However, with the thickness of InGaN increasing, the difficulties for InGaN growth and its large QCSE should be well dealt with.

QW number increase is also an easy approach to be considered. It can improve the lateral current spreading and lower the peak current densities for the same driving current [125]. With the QW number increases, electron leakage reduces and the droop mitigates. The actual carrier crowding may be due to the carrier density nonuniformity in the lateral and vertical directions. The effective area becomes small when the polarization field exists in QWs. So the polarization match by polarization engineering will increase the effective area of QWs, which causes the carrier density to be reduced. Chang et al. found that thick InGaN wells and polarization-matched AlGaInN barriers could achieve low-droop LEDs

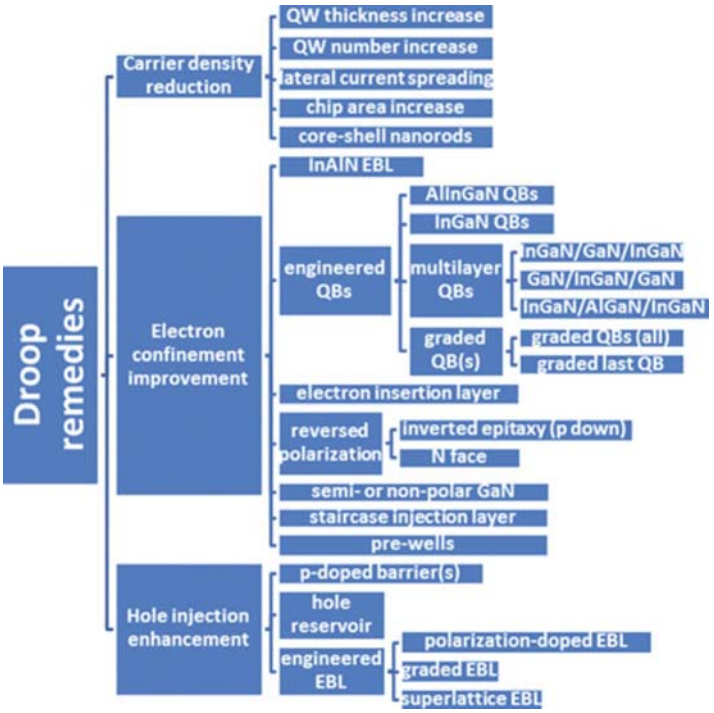

Fig. 8.14 Classification of droop remedies [103]

[126]. However, the number of QWs is reduced for the purpose of mitigating the additional compressive strain in AlGaInN barriers. Due to low activation efficiency of p-type, the current spreading and hole transportation are serious problems for carrier uniformity [112, 113, 127]. The improvement in lateral current uniformity is considered a key droop remedy in Ref. [128] on the basis of a simulation study providing optimized vertical LED structures with interdigital n-region contacts. Rozhansky et al. designed a p-type MQW and npn active structure to improve the asymmetry injection of hole and electron [129]. They found that the EQE did not reduce when the current density was above 60 A/cm^2. Because the radiative recombination occurred at the bottom QWs, their crystalline quality is poor, and the maximum EQE is only 1%. Then ap-doped In 0.05 Ga 0.95 N "hole reservoir" layer was inserted between the MQW and EBL regions [130]. They predicted a droop reduction from >35% to <12%.

The polarization match reduces not only the carrier density in QWs but also the QCSE in the active layer [126]. Another route reducing the QCSE is using nonpolar or semipolar structures [131, 132]. The reduction of the polarization field not only made the band diagram smoother but also restricted electron overflow to the p-GaN layer as shown in the simulations. With increasing the injection current density to 100 A/cm^2, the m-plane LEDs exhibit only 13% efficiency droop, whereas

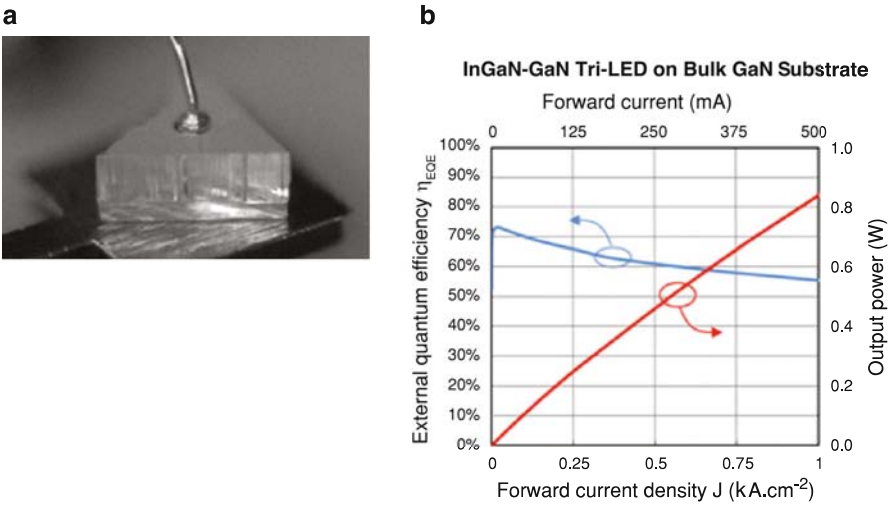

Fig. 8.15 (**a**) Optical microscope image of a finished and assembled III–nitride. (**b**) Pulsed, room temperature EQE versus current density J of a III–nitride tri-LED [10]

conventional c-plane LEDs suffer from efficiency droop at very low injection current density, and the EQE of c-plane LEDs decrease to as little as 50% of its maximum value. The nonpolar, semipolar InGaN-based LEDs can possess a high radiative recombination rate and low efficiency droop at a high injection current.

LED on freestanding GaN substrate shows high performance, especially for droop under high injection [10]. Figure 8.15 shows the InGaN/GaN tri-LED photograph and EQE-J curves. The EQE continues to be high even at current densities up to 1 kA cm^{-2}, at which point EQE = 55.3%, only a 24% drop from the peak value. The high performance in high injection level is due to (1) high LEE, (2) homoepitaxial technology for low current droop structures, and (3) uniform current spreading. We thought that the low TDD and no phonon barriers between the epilayer and substrate should also play important roles in the droop behavior.

Recently, much attention has been paid to specific small LEDs with chip size of tens microns (μ-LEDs), which can effectively reduce the droop phenomenon and endure high current density of even several kA/cm^2 [7, 133–138]. The distinct performances of tens microns μ-LEDs are attributed to uniform current spreading and low junction temperature (Tj) by some groups [136–138]. However, the maximum endured current density still increases as the size of the μ-LEDs reducing down below the current spreading length and operating under low-duty pulse current [7]. BGR and band-filling should occur when the carrier concentration is higher than mid 10^{18} cm^{-3} [116]. The BGR effect can build an additional potential barrier for carriers to inhibit their transferring from high to low energy state, thus leading to efficiency saturation [117]. Figure 8.16 shows the dependence of the light output power (LOP) on the current density (L-I) for μ-LEDs with different diameters. The

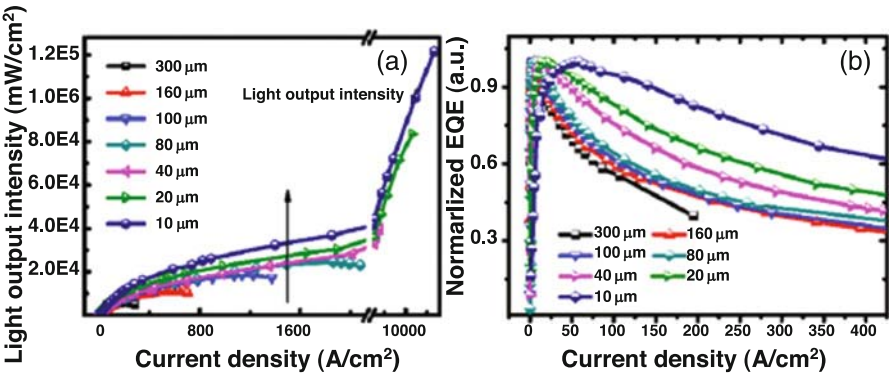

Fig. 8.16 (**a**) The dependence of the light output power in EL spectra on the current density for 10, 20, 40, 80, 160, and 300 μm LEDs. (**b**) The external quantum efficiency (EQE) curves for 10, 20, 40, 80, 160, and 300 μm LEDs with increased current density [7]

10 μm LEDs survive at extremely high current density of 16 kA/cm^2. The droop values of 10 μm and 300 μm LED are 18% and 61%, respectively.

When the size of the LED reduces to nanometer, the droop tends to be zero at the injection level of 640 A/cm^2 [139]. These LEDs operated in the interconnected array. Another work reported that the droop commonly observed in InGaN QW LEDs could also be measured in nanorod devices [140]. They found critical importance of surface recombination on the carrier dynamics and performance of nanorod LEDs. Actually, surface states are very important because of the large ratio of surface area to the volume of nano LEDs. That will be invalid before the current satisfy for emission requirement [141]. It is well known that 3D nano LEDs have the advantages of large emission surface, m-plane growth, and so on [48, 49], which is of potential importance in operation under high injection level. Moreover, we also find the nanocavity effect in these devices [142], which will further improve the droop performance.

At last, SP coupling are also discussed for reduction of the droop. Yang et al. reported that with a current spreading grid pattern on the mesa surface, a smaller grid period leads to more effective carrier transport into the QW regions of Ag deposition for stronger SP–QW coupling such that the droop effect is more significantly reduced, as indicated by the increase in the injection current density of maximum EQE and the decrease in drooping slope [143]. They also get efficiency improvement and low droop of a vertical light-emitting diode through surface plasmon coupling and grating scattering [144]. Based on the reflection measurement from the metal grating structure and numerical simulation result, it is found that the LSP resonance induced around the metal grating crest plays a major role in the SP-QW coupling process. By adding a surface grating structure to the SP-coupled vertical LED on the n-GaN side, the droop effect is further suppressed. By adding a lower-index dielectric interlayer, further reduction of efficiency droop effect is

obtained in SP-coupled LEDs [145]. The SP coupling to QWs should reduce the non-radiative recombination possibility in LEDs, and hence the droop is suppressed.

8.6 Summary

In this chapter, we introduce the definition of IQE and some ideas of how to achieve high IQE for GaN-based LEDs. The effects of defects and polarization are discussed in detail. The IQE of green and DUV-LEDs are particularly concerned. In the IQE measurement, the general TDPL method is analyzed, and some significant developments are introduced to obtain a more accurate value. Droop is a very important issue for high-efficiency, low-cost solid-state lighting. The exact origins are still on debates. We tend to attribute the droop to various origins for different situations. At last, we give some remedies to alleviate the droop. Radiative recombination rate enhancement may be more important for low-droop LEDs. LSP and nanocavity may be the potential candidates for novel low-droop devices.

References

1. Martin Strassburg (OSRAM), Perspectives of III-N optoelectronics, in *International Workshop on Nitride Semiconductors (IWN2016), Orlando, USA*, 2016
2. K.P. O'Donnell, M. Auf der Maur, A. Di Carlo, K. Lorenz, Phys. Status Solidi RRL **6**(2), 49–52 (2012)
3. M. Kneissl, T. Kolbe, C. Chua, V. Kueller, N. Lobo, J. Stellmach, A. Knauer, H. Rodriguez, S. Einfeldt, Z. Yang, N.M. Johnson, M. Weyers, Semicond. Sci. Technol. **26**(1), 014036 (2011)
4. Y. Yamada, K. Iwamura, T. Kuronaka, T. N Shinomura, H. Taguchi, H. Kudo, J. Okagawa, Light Vis. Environ. **32**(2), 191–195 (2008)
5. N.F. Gardner, G.O. Müller, Y.C. Shen, G. Chen, S. Watanabe, W. Götz, M.R. Krames, Appl. Phys. Lett. **91**, 243506 (2007)
6. J. Hader, J.V. Moloney, S.W. Koch, Proc. SPIE **8625**, 86251M (2013)
7. Q.Q. Jiao, Z.Z. Chen, J. Ma, S.Y. Wang, Y. Li, S. Jiang, Y.L. Feng, J.Z. Li, Y.F. Chen, T.J. Yu, S.F. Wang, G.Y. Zhang, P.F. Tian, E.Y. Xie, Z. Gong, E.D. Gu, M.D. Dawson, Opt. Exp. **23**(13), 16565 (2015)
8. S.D. Lester, F.A. Ponce, M.G. Craford, D.A. Steigerwald, Appl. Phys. Lett. **66**, 1249 (1995)
9. J.Y. Tsao, IEEE Circuits Devices Mag. **20**(3), 28–37 (2005)
10. M.J. Cich, R.I. Aldaz, A. Chakraborty, A. David, M.J. Grundmann, A. Tyagi, M. Zhang, F.M. Steranka, M.R. Krames, Appl. Phys. Lett. **101**, 223509 (2012)
11. Y. Sun, S. Qi, Z. Chen, X. Kang, G. Zhu, C. Chen, S. Li, Y. Pan, J. Yan, J. Deng, H. Long, M. Hao, T. Yu, G. Zhang, Phys. Stat. Sol. C **6**(S2), S623 (2009)
12. J.S. Speck, M.A. Brewer, G. Beltz, A.E. Romanov, W. Pompe, J. Appl. Phys. **80**, 3808 (1996)
13. D.C. Reynolds, D.C. Look, B. Jogai, J.E. Hoelscher, J. Appl. Phys. **88**, 1460 (2000)
14. L. Gorgens, O. Ambacher, M. Stutzmann, C. Miskys, Appl. Phys. Lett. **76**, 577 (2000)
15. J.-Z. Li, T. Yue-Bin, C. Zhi-Zhong, J. Xian-Zhe, F. Xing-Xing, J. Shuang, J. Qian-Qian, Y. Tong-Jun, Z. Guo-Yi, Chin. Phys. B **23**(1), 016101 (2014)
16. H. Amano, N. Sawaki, I. Akasaki, et al., Appl. Phys. Lett. **48**, 353 (1986)
17. S. Nakamura, Y. Harada, M. Sehno, Appl. Phys. Lett. **58**, 2021 (1991)

18. O.H. Nam, M.D. Bremser, T. Zheleva, R.F. Davis, Appl. Phys. Lett. **71**, 2638 (1997)
19. C.I.H. Ashby, C.C. Mitchell, J. Han, N.A. Missert, P.P. Provencio, D.M. Follstaedt, G.M. Peake, L. Griego, Appl. Phys. Lett. **77**, 3233 (2000)
20. K. Tadatomo, N. Okada, Proc. SPIE **7954**, 795416 (2005)
21. M.T. Wang, K.Y. Liao, Y. Li, IEEE Photon. Technol. Lett. **23**, 962–964 (2011)
22. J.H. Cheng, Y.S. Wu, W.C. Liao, B.W. Lin, Appl. Phys. Lett. **96**, 051109 (2010)
23. X.H. Huang, J.P. Liu, Y.Y. Fan, J.J. Kong, H. Yang, H.B. Wang, IEEE Photon. Technol. Lett. **23**, 944–946 (2011)
24. J.J. Chen, Y.K. Su, C.L. Lin, S.M. Chen, W.L. Li, C.C. Kao, IEEE Photon. Technol. Lett. **20**, 1193–1195 (2008)
25. Y.F. Li, S. You, M.W. Zhu, L. Zhao, W.T. Hou, T. Detchprohm, Y. Taniguchi, N. Tamura, S. Tanaka, C. Wetzel, Appl. Phys. Lett. **98**, 151102 (2011)
26. Y.-K. Ee, X.-H. Li, et al., J. Cryst. Growth **312**, 1311 (2010)
27. J.Z. Li, Z.Z. Chen, Q.Q. Jiao, Y.L. Feng, S. Jiang, Y.F. Chen, T.J. Yu, S.F. Li, G.Y. Zhang, CrystEngComm **17**, 4469 (2015)
28. J.I. Pankove, J. Lumin. **7**, 114 (1973)
29. H. Amano, M. Kito, K. Hiramatsu, et al., Jpn. J. Appl. Phys. **28**(12), L2112–L2114 (1989)
30. S. Nakamura, T. Mukai, M. Sehno, Appl. Phys. Lett. **64**(13), 1687–1689 (1994)
31. J.-W. Ju, E.-S. Kang, H.-S. Kim, et al., J. Appl. Phys. **102**, 053519 (2007)
32. M.G. Cheong, R.J. Choi, E.-K. Suh, H.J. Lee, Appl. Phys. Lett. **82**, 625–626 (2003)
33. Y.B. Tao, Z.Z. Chen, F.F. Zhang, J. Appl. Phys. **107**, 103529 (2010)
34. G. Franssen, T. Suski, P. Perlin, Appl. Phys. Lett. **87**, 041109 (2005)
35. M.-H. Kim, M.F. Schubert, Q. Dai, J.K. Kim, E. Fred Schuberta, J. Piprek, Y. Park, Appl. Phys. Lett. **91**, 183507 (2007)
36. J. Zhang, J. Yang, G. Simin, M. Shatalov, M. Asif Khan, Appl. Phys. Lett. **77**, 2668–2670 (2000)
37. B.A. Haskell, F. Wu, M.D. Craven, S. Matsuda, P.T. Fini, T. Fujii, K. Fujito, S.P. Den Baars, J.S. Speck, S. Nakamura, Appl. Phys. Lett. **84**, 644 (2003)
38. A. Chakraborty, B.A. Haskell, S. KELLER, J.S. Speck, S.P. Denbaars, S. Nakamura, U.K. Mishra, Jpn. J. Appl. Phys. **44**, L173–L175 (2005)
39. T.J. Baker, B.A. Haskell, F. Wu, P.T. Fini, J.S. Speck, S. Nakamura, Jpn. J. Appl. Phys. **44**, L920–L922 (2005)
40. K. Okamoto, A. Kaneta, Y. Kawakami, S. Fujita, J. Appl. Phys. **98**, 064503 (2005)
41. Y.D. Lin, A. Chakraborty, S. Brinkley, H.C. Kuo, T. Melo, K. Fujito, J.S. Speck, S.P. DenBaars, S. Nakamura, Appl. Phys. Lett. **94**, 261108 (2009)
42. H. Sato, A. Tyagi, H. Zhong, N. Fellows, R.B. Chung, M. Saito, K. Fujito, J.S. Speck, S.P. DenBaars, S. Nakamura, Phys. Stat. Sol. (RRL) **1**(4), 162–164 (2007)
43. S.E. Brinkley, Y.-D. Lin, A. Chakraborty, N. Pfaff, D. Cohen, J.S. Speck, S. Nakamura, S.P. DenBaars, Appl. Phys. Lett. **98**, 011110 (2011)
44. H. Sato, R.B. Chung, H. Hirasawa, N. Fellows, H. Masui, F. Wu, M. Saito, K. Fujito, J.S. Speck, S.P. DenBaars, S. Nakamura, Appl. Phys. Lett. **92**, 221110 (2008)
45. F. Brunner, U. Zeimer, F. Edokam, W. John, D. Prasai, O. Krüger, M. Weyers, Phys. Status Solidi B **252**, 1189 (2015)
46. J. Bai, B. Xu, F.G. Guzman, K. Xing, Y. Gong, Y. Hou, T. Wang, Appl. Phys. Lett. **107**, 261103 (2016)
47. H. Li, M. Khoury, B. Bonef, A.I. Alhassan, A.J. Mughal, E. Azimah, M.E.A. Samsudin, P. De Mierry, S. Nakamura, J.S. Speck, S.P. DenBaars, ACS Appl. Mater. Interfaces **9**(41), 36417–36422 (2017)
48. S. Li, A. Waag, J. Appl. Phys. **111**, 071101 (2012)
49. H. Sekiguchi, K. Kishino, A. Kikuchi, Appl. Phys. Lett. **96**, 231104 (2010)
50. S.D. Hersee, X.Y. Sun, et al., J. Appl. Phys. **97**, 124308 (2005)
51. M.L. Kuo, Y.S. Kim, M.L. Hsieh, et al., Nano Lett. **11**(2), 476–481 (2011)
52. S. Neugebauer, S. Metzner, J. Blasing, F. Bertram, A. Dadgar, J. Christen, A. Strittmatter, Phys. Status Solidi B **253**(1), 118 (2016)

53. F. Akyol, D.N. Nath, S. Krishnamoorthy, P.S. Park, S. Rajan, Appl. Phys. Lett. **100**, 111118 (2012)
54. B.-C. Lin, K.-J. Chen, C.-H. Wang, C.-H. Chiu, Y.-P. Lan, C.-C. Lin, P.-T. Lee, M.-H. Shih, Y.-K. Kuo, H.-C. Kuo, Opt. Express **22**(1), 463 (2014)
55. C.H. Chen, S.J. Chang, Y.K. Su, I.E.E.E. Senior Member, G.C. Chi, J.K. Sheu, J.F. Chen, IEEE J. Sel. Topics Quantum Electron. **8**(2), 284 (2002)
56. I.H. Ho, G.B. Stringfellow, Appl. Phys. Lett. **69**(18), 2701 (1996)
57. Y. Arakawa, H. Sakaki, Appl. Phys. Lett. **40**(11), 939–941 (1982)
58. K. Tachibana, T. Someya, Y. Arakawa, R. Werner, A. Forchel, Appl. Phys. Lett. **75**(17), 2605–2607 (1999)
59. K. Tachibana, T. Someya, S. Ishida, Y. Arakawa, Appl. Phys. Lett. **76**(22), 3212–3214 (2000)
60. Y.L. Chang, J.L. Wang, F. Li, Z. Mi, Appl. Phys. Lett. **96**, 013106 (2010)
61. L. Jun-Lin, Z. Jian-Li, W. Guang-Xu, M. Chun-Lan, X. Long-Quan, D. Jie, Q. Zhi-Jue, W. Xiao-Lan, P. Shuan, Z. Chang-Da, W. Xiao-Ming, F. Wen-Qing, J. Feng-Yi, Chin. Phys. B **24**(6), 067804 (2015)
62. X.M. Wu, J.L. Liu, Z.J. Quan, C.B. Xiong, C.D. Zheng, J.L. Zhang, F.Y. Jiang, Appl. Phys. Lett. **104**, 221101 (2014)
63. Z.J. Quan, L. Wang, C.D. Zheng, J.L. Liu, F.Y. Jiang, J. Appl. Phys. **116**, 183107 (2014)
64. J.L. Zhang, C.B. Xiong, J.L. Liu, Z.J. Quan, L. Wang, F.Y. Jiang, Appl. Phys. A Mater. Sci. Process. **114**, 1049 (2014)
65. J.R. Sambles, G.W. Bradbery, F.Z. Yang, Contemp. Phys. **32**(3), 173–183 (1991)
66. K. Okamoto, I. Niki, A. Shvartser, Y. Narukawa, T. Mukai, A. Scherer, Nat. Mater. **3**, 601 (2004)
67. D.M. Yeh, C.F. Huang, C.Y. Chen, Y.C. Lu, C.C. Yang, Nanotechnology **19**, 345201 (2008)
68. S. Jiang, Z. Hu, Z.Z. Chen, X.X. Fu, X.Z. Jiang, Q.Q. Jiao, T.J. Yu, G.Y. Zhang, Opt. Express **21**(10), 12100–12110 (2013)
69. J. Henson, E. Dimakis, J. DiMaria, R. Li, S. Minissale, L.D. Negro, T.D. Moustakas, R. Paiella, Opt. Express **18**(20), 21322–21329 (2010)
70. C.H. Lu, C.C. Lan, Y.L. Lai, Y.L. Li, C.P. Liu, Adv. Funct. Mater. **21**(24), 4719–4723 (2011)
71. S. Jiang, Z. Chen, F. Xingxing, Q. Jiao, Y. Feng, W. Yang, J. Ma, J. Li, S. Jiang, Y. Tongjun, G. Zhang, IEEE Photon. Technol. Lett. **27**(13), 1363 (2015)
72. M. Kneissl, *A Brief Review of III-Nitride UV Emitter Technologies and Their Applications* (Springer, Cham, 2016), pp. 1–25. https://doi.org/10.1007/978-3-319-24100-5_1
73. M. Kneissl, T. Kolbe, C. Chua, et al., Advances in group III-nitride-based deep UV light-emitting diode technology. Semicond. Sci. Technol. **26**, 014036 (2011)
74. K. Ban, J.-i. Yamamoto, K. Takeda, K. Ide, M. Iwaya, T. Takeuchi, S. Kamiyama, I. Akasaki, H. Amano, Appl. Phys. Express **4**, 052101 (2011)
75. M.A. Khan, J.N. Kuzina, D.T. Olson, T. George, W.T. Pike, GaN/AlN digital alloy short-period superlattices by switched atomic layer metalorganic chemical vapor deposition. Appl. Phys. Lett. **63**, 3470–3472 (1993)
76. L.W. Sang, Z.X. Qin, G.Y. Zhang, et al., Appl. Phys. Lett. **93**, 122104 (2008)
77. P. Dong et al., Appl. Phys. Lett. **102**, 241113 (2013)
78. M. Conroy et al., J. Mater. Chem. C **3**, 431–437 (2015)
79. L. Zhang, F. Xu, J. Wang, C. He, W. Guo, M. Wang, B. Sheng, L. Lu, Z. Qin, X. Wang, B. Shen, Sci. Rep. **6**, 35934 (2016)
80. S. Kamiyama et al., J. Cryst. Growth **223**, 83–91 (2001)
81. J. Han et al., Appl. Phys. Lett. **78**, 67–69 (2001)
82. J.P. Zhang et al., Appl. Phys. Lett. **80**, 3542–3544 (2002)
83. M.A. Khan, M. Shatalov, H.P. Maruska, H.M. Wang, E. Kuokstis, Jpn. J. Appl. Phys. **44**, 7191–7206 (2005)
84. G. Zhang, B. Shen, Z. Chen, et al., Chin. Sci. Bull. **59**(12), 1201–1218 (2014)
85. Y. Yang, J. Liu, L. Liu, A. Anders, Appl. Phys. Lett. **106**, 162102 (2015)
86. T.C. Zheng, W. Lin, R. Liu, Sci. Rep. **6**, 21897 (2016)
87. A. Khan, K. Balakrishnan, T. Katona, Nat. Photonics **2**, 77–84 (2008)

88. Y. Lin, B. Liou, J. Chang, Y. Kuo, Proc. SPIE **8619**, 86191V (2013)
89. G. Yang, J. Chang, J. Wang, Q. Zhang, F. Xie, J. Xue, D. Yan, F. Wang, P. Chen, R. Zhang, Y. Zheng, Superlattice. Microst. **83**, 1–8 (2015)
90. Z. Min, L. Yang, C. Shengchang, T. Wu, X. Jintong, L. Xiangyang, W. Zhihao, F. Yanyan, D. Jiangnan, C. Changqing, Superlattice. Microst. **75**, 63–71 (2014)
91. A.Y. Yi, W. Naiyin, F. Guanghan, Z. Yong, Superlattice. Microst. **76**, 149–155 (2014)
92. W. Guo, F. Xu, Y. Sun, L. Lu, Z. Qin, T. Yu, X. Wang, B. Shen, Superlattice. Microst. **100**, 941–946 (2016)
93. T. Akasaka, H. Gotoh, T. Saito, T. Makimoto, Appl. Phys. Lett. **85**, 3089 (2004)
94. C.E. Martinez, N.M. Stanton, A.J. Kent, J. Appl. Phys. **98**, 053509 (2005)
95. Q. Dai, M.F. Schubert, M.H. Kim, J.K. Kim, E.F. Schubert, D.D. Koleske, M.H. Crawford, S.R. Lee, A.J. Fischer, G. Thaler, M.A. Banas, Appl. Phys. Lett. **94**, 111109 (2009)
96. M.F. Schubert, J. Xu, Q. Dai, F.W. Mont, J.K. Kim, E.F. Schubert, Appl. Phys. Lett. **94**, 081114 (2009)
97. C. Xu, T. Yu, J. Yan, Z. Yang, X. Li, Y. Tao, X. Fu, Z. Chen, G. Zhang, Phys. Status Solidi C **9**(3–4), 757–760 (2012)
98. T. Nakano, K. Kawakami, A.A. Yamaguchi, Proc. SPIE **9748**, 97481W (2016)
99. K. Kawakami, T. Nakano, A.A. Yamaguchi, Proc. SPIE **9748**, 97480S (2016)
100. A.A. Yamaguchi, Y. Mochizuki, M. Mizuta, Jpn. J. Appl. Phys. **39**, 2402 (2000)
101. K. Kojima, T. Ohtomo, K.-i. Ikemura, Y. Yamazaki, M. Saito, H. Ikeda, K. Fujito, S.F. Chichibu, J. Appl. Phys. **120**, 015704 (2016)
102. K. Kojima, H. Ikeda, K. Fujito, S.F. Chichibu, Appl. Phys. Lett. **111**, 032111 (2017)
103. G. Verzellesi, D. Saguatti, M. Meneghini, F. Bertazzi, M. Goano, G. Meneghesso, E. Zanoni, J. Appl. Phys. **114**, 071101 (2013)
104. Y.C. Shen, G.O. Mueller, S. Watanabe, N.F. Gardner, A. Munkholm, M.R. Krames, Appl. Phys. Lett. **91**, 141101 (2007)
105. K.T. Delaney, P. Rinke, C.G. Van de Walle, Appl. Phys. Lett. **94**(19), 191109 (2009)
106. E. Kioupakis, P. Rinke, K.T. Delaney, C.G. Van de Walle, Appl. Phys. Lett. **98**, 161107 (2011)
107. A.S. Polkovnikov, G.G. Zegrya, Phys. Rev. B **58**(7), 4039 (1998)
108. J. Iveland, L. Martinelli, J. Peretti, J.S. Speck, C. Weisbuch, Phys. Rev. Lett. **110**, 177406 (2013)
109. K.J. Vampola, M. Iza, S. Keller, S.P. DenBaars, S. Nakamura, Appl. Phys. Lett. **94**(6), 061116 (2009)
110. S. Hammersley, D. Watson-Parris, P. Dawson, M.J. Godfrey, T.J. Badcock, M.J. Kappers, C. McAleese, R.A. Oliver, C.J. Humphreys, J. Appl. Phys. **111**, 083512 (2012)
111. J. Hader, J.V. Moloney, S.W. Koch, Appl. Phys. Lett. **96**(22), 221106 (2010)
112. J. Xie, X. Ni, Q. Fan, R. Shimada, U. Ozgur, H. Morkoc, Appl. Phys. Lett. **93**(12), 121107 (2008)
113. D.sS. Meyaard, G.-B. Lin, Q. Shan, J. Cho, E.F. Schubert, H. Shim, M.-H. Kim, C. Sone, Appl. Phys. Lett. **99**(25), 251115 (2011)
114. X. Ni, X. Li, J. Lee, S. Liu, V. Avrutin, U. Ozgur, H. Morkoc¸, A. Matulionis, T. Paskova, G. Mulholland, and K. R. Evans, Appl. Phys. Lett. 97(3), 031110 (2010)
115. X. Ni, X. Li, J. Lee, S. Liu, V. Avrutin, U. Ozgur, H. Morkoc¸, and A. Matulionis, J. Appl. Phys. 108, 033112 (2010)
116. M. Feneberg, S. Osterburg, K. Lange, C. Lidig, B. Garke, R. Goldhahn, E. Richter, C. Netzel, M.D. Neumann, N. Esser, S. Fritze, H. Witte, J. Bläsing, A. Dadgar, A. Krost, Phys. Rev. B **90**(7), 075203 (2014)
117. K. Jarašiūnas, S. Nargelas, R. Aleksiejunas, S. Miasojedovas, M. Vengris, S. Okur, H. Morkoç, Ü. Özgür, C. Giesen, Ö. Tuna, M. Heuken, J. Appl. Phys. **113**(10), 103701 (2013)
118. N.I. Bochkareva, V.V. Voronenkov, R.I. Gorbunov, A.S. Zubrilov, Y.S. Lelikov, P.E. Latyshev, Y.T. Rebane, A.I. Tsyuk, Y.G. Shreter, Appl. Phys. Lett. **96**(13), 133502 (2010)
119. D.-S. Shin, D.-P. Han, J.-Y. Oh, J.-I. Shim, Appl. Phys. Lett. **100**(15), 153506 (2012)
120. A. David, M.J. Grundmann, Appl. Phys. Lett. **96**, 103504 (2010)
121. J. Yun, H.-S. Yeom, J.-I. Shim, J. Korean Phys. Soc. **63**(6), 1218–1221 (2013)

122. X. Shao, H. Lu, D. Chen, Z. Xie, R. Zhang, Y. Zheng, Appl. Phys. Lett. **95**, 163504 (2009)
123. N.L. Ploch, S. Einfeldt, M. Frentrup, J. Rass, T. Wernicke, A. Knauer, V. Kueller, M. Weyers, M. Kneissl, Semicond. Sci. Technol. **28**, 125021 (2013)
124. N.F. Gardner, G.O. Müller, Y.C. Shen, et al., Appl. Phys. Lett. **91**, 243506 (2007)
125. C.S. Xia, Z.M. Simon Li, Z.Q. Li, Y. Sheng, Z.H. Zhang, W. Lu, L.W. Cheng, Appl. Phys. Lett. **100**, 263504 (2012)
126. J.-Y. Chang, F.-M. Chen, Y.-K. Kuo, Y.-H. Shih, J.-K. Sheu, W.-C. Lai, H. Liu, Opt. Lett. **38**(16), 3158 (2013)
127. X. Guo, E.F. Schubert, J. Appl. Phys. **90**(8), 4191 (2001)
128. C.-K. Li, Y.-R. Wu, IEEE Trans. Electron Devices **59**(2), 400 (2012)
129. I.V. Rozhansky, D.A. Zakheim, Phys. Status Solidi A **204**(1), 227–230 (2007)
130. T. Lu, S. Li, C. Liu, K. Zhang, Y. Xu, J. Tong, L. Wu, H. Wang, X. Yangs, Y. Yin, G. Xiao, Y. Zhou, Appl. Phys. Lett. **100**(14), 141106 (2012)
131. S.-C. Ling, T.-C. Lu, S.-P. Chang, J.-R. Chen, H.-C. Kuo, S.-C. Wang, Appl. Phys. Lett. **96**, 231101 (2010)
132. C.-H. Chiu, D.-W. Lin, C.-C. Lin, Z.-Y. Li, W.-T. Chang, H.-W. Hsu, H.-C. Kuo, T.-C. Lu, S.-C. Wang, W.-T. Liao, T. Tanikawa, Y. Honda, M. Yamaguchi, N. Sawaki, Appl. Phys. Express **4**, 012105 (2011)
133. A. Castiglia, D. Simeonov, H.J. Buehlmann, J.-F. Carlin, E. Feltin, J. Dorsaz, R. Butté, N. Grandjean, Appl. Phys. Lett. **90**(3), 033514 (2007)
134. Z. Gong, S. Jin, Y. Chen, J. McKendry, D. Massoubre, I.M. Watson, E. Gu, M.D. Dawson, J. Appl. Phys. **107**(1), 013103 (2010)
135. Y.B. Tao, S.Y. Wang, Z.Z. Chen, Z. Gong, E.Y. Xie, Y.J. Chen, Y.F. Zhang, J. McKendry, D. Massoubre, E.D. Gu, B.R. Rae, R.K. Henderson, G.Y. Zhang, Phys. Status Solidi C **9**(3–4), 616–619 (2012)
136. P. Tian, J.J.D. McKendry, Z. Gong, B. Guilhabert, I.M. Watson, E. Gu, Z. Chen, G. Zhang, M.D. Dawson, Appl. Phys. Lett. **101**(23), 231110 (2012)
137. T.I. Kim, Y.H. Jung, J. Song, D. Kim, Y. Li, H.S. Kim, I.-S. Song, J.J. Wierer, H.A. Pao, Y. Huang, J.A. Rogers, Small **8**(11), 1643–1649 (2012)
138. N. Lobo Ploch, H. Rodriguez, C. Stölmacker, M. Hoppe, M. Lapeyrade, J. Stellmach, F. Mehnke, T. Wernicke, A. Knauer, V. Kueller, M. Weyers, S. Einfeldt, M. Kneissl, IEEE Trans. Electron Devices **60**(2), 782–786 (2013)
139. H.P.T. Nguyen, S. Zhang, K. Cui, X. Han, S. Fathololoumi, M. Couillard, G.A. Botton, Z. Mi, Nano Lett. **11**, 1919 (2011)
140. S. Zhang, Y. Li, S. Fathololoumi, H.P.T. Nguyen, Q. Wang, Z. Mi, Q. Li, G.T. Wang, AIP Adv. **3**, 082103 (2013)
141. Q. Li, K.R. Westlake, M.H. Crawford, S.R. Lee, D.D. Koleske, J.J. Figiel, K.C. Cross, Opt. Express **19**(25), 25528 (2011)
142. Q. Jiao, Z. Chen, Y. Feng, S. Li, S. Jiang, J. Li, Y. Chen, T. Yu, X. Kang, B. Shen, G. Zhang, Nanoscale Res. Lett. **11**, 340 (2016)
143. C.-F. Lu, C.-H. Liao, C.-Y. Chen, C. Hsieh, Y.-W. Kiang, C.C. Yang, Appl. Phys. Lett. **96**, 261104 (2010)
144. C.-H. Lin, C. Hsieh, C.C. Yang, et al., Opt. Express **23**(S2), A842 (2014)
145. C.-H. Lin, C.-Y. Su, Y. Kuo, C.-H. Chen, Y.-F. Yao, P.-Y. Shih, H.-S. Chen, C. Hsieh, Y.-W. Kiang, C.C. Yang, Appl. Phys. Lett. **105**, 101106 (2014)

Chapter 9
On the Light Extraction Efficiency for III-Nitride-Based Light-Emitting Diodes

Zi-Hui Zhang, Yonghui Zhang, Sung-Wen Huang Chen, Wengang Bi, and Hao-Chung Kuo

9.1 Introduction

III-nitride semiconductor has the direct bandgap, the family of which comprises GaN, InN, and AlN, and the ternary/quaternary materials can be made by alloying any of the binary ones. The material alloy for III-nitride semiconductor can tune the energy bandgap from 0.70 to 6.2 eV, which makes III-nitride semiconductor material very promising for optoelectronic devices [1]. One of the important applications for III-nitride semiconductor lies on light-emitting diodes (LEDs), the emission wavelength for which can cover the spectral range between the deep ultraviolet and the infrared region. A very important index for evaluating the excellence of III-nitride-based LEDs is the external quantum efficiency (EQE), which is to measure the ratio of the number of photos emitted into the free space per second and the number of the electrons injected into the device per second. The EQE is the product of the internal quantum efficiency (IQE) and the light extraction efficiency (LEE). The IQE is defined as the ratio of the number of photos emitted from the active region per second and the number of the electrons injected into the device. The LEE is defined as the ratio of the number of the photons emitted into the free space per second and the number of the photons emitted from the active region per second [2, 3]. An improved EQE requires a better IQE and LEE. The IQE is strongly

Z.-H. Zhang · Y. Zhang · W. Bi
Institute of Micro-Nano Photoelectron and Electromagnetic Technology Innovation, School of Electronics and Information Engineering, Hebei University of Technology, Key Laboratory of Electronic Materials and Devices of Tianjin, Tianjin, P. R. China

S.-W. Huang Chen · H.-C. Kuo (✉)
Department of Photonics and Institute of Electro-optical Engineering, National Chiao Tung University, Hsinchu, Taiwan
e-mail: hckuo@faculty.nctu.edu.tw

© Springer International Publishing AG, part of Springer Nature 2019

J. Li, G. Q. Zhang (eds.), *Light-Emitting Diodes*, Solid State Lighting Technology and Application Series 4, https://doi.org/10.1007/978-3-319-99211-2_9

affected by quite a few factors including the dislocation/defect density, the carrier injection efficiency, the current spreading effect, the polarization-induced electric field within the quantum wells, Auger recombination, etc. [3]. There have been several reports that have extensively discussed the IQE for III-nitride-based LEDs [2, 4–7]. Hence this chapter is concentrated on the LEE enhancement.

The large contrast between the refractive indices for the air and the III-nitride film results in a low LEE for III-nitride-based LEDs, and the LEE for the bare nitride film is low and further decreases if the emission wavelength becomes even shorter [8, 9]. For [0001] oriented III-nitride LEDs emitting visible light, the emitted photons are dominated by transverse electric (TE) mode. Numerically simulated results indicate that no more than 30% of the visible photons are able to escape out of the planar LEDs [10]. In the case of deep ultraviolet (DUV) LED, the portion of the TM mode increases as the Al composition increases or the emission wavelength decreases; the LEE can be even lower than 10% if the DUV photonics are not specifically treated [11]. There are a number of approaches aiming to increase the LEE for LED chips, e.g., chip structure engineering, reflection engineering, surface engineering, substrate engineering, photonics crystal, surface plasmon engineering, etc. Details will be addressed subsequently.

9.2 Chip Structure Engineering

The chip structure and the chip package have essentially important impact on the LEE. At the current stage, III-nitride-based LEDs are normally grown on foreign insulating sapphire substrates. Therefore, a conventional lateral LED (CC) structure is adopted (see Fig. 9.1a), which comprises the mesa, the current spreading layer,

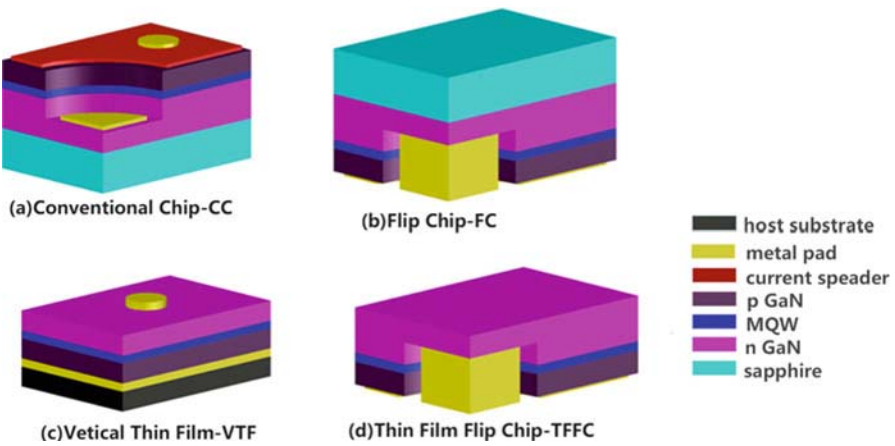

Fig. 9.1 Different chip configurations for sapphire-based InGaN/GaN LEDs: (**a**) conventional lateral chip (CC), (**b**) flip-chip (FC), (**c**) vertical-injection thin-film (VTF), (**d**) thin-film flip-chip (TFFC)

the p-pad, and the n-pad. The conventional lateral LED device is designed to have the photons emitted from the p-type material. This can inevitably cause the optical absorption by the p-type current spreading layer and the p-type bonding metal, leading to the unsatisfied LEE. Fortunately, the previously mentioned concerns can be solved by utilizing a flip-chip (FC) design, the device structure of which is shown in Fig. 9.1b. A reflective mirror is deposited on the p-type layer surface, and by doing so, the light beams can escape from the LED from the sapphire side. The sapphire has the energy bandgap of ∼10 eV, leading to a negligible optical absorption. In addition, the distance between the reflective mirror and the quantum wells is in the order of the optical wavelength, and the optical cavity effects can occur that helps to tune the radiation pattern and results in more light into escape cone [12, 13]. Another strategy to improve the LEE can be realized by using the vertical thin-film (VTF) chip, which adopts the substrate removal process and has the N-face GaN layer upward, serving as the out-light plane. More importantly, the random-textured N-face GaN layer can be obtained by the low-cost wet etching technology and can result in the LEE as high as 75%. Besides the high LEE, such design also enables the benefit of almost 100% top-surface emission and a near-Lambertian radiation pattern [13]. However, similar to the CC design, the typical VTF design suffers from the light blocking and the optical absorption effects by the n-type metal electrode as is illustrated in Fig. 9.1c. An alternative design that combines the advantage of the CC chip and the VTF chip is the thin-film flip-chip (TFFC) structure, which enables the 1.3-fold LEE enhancement [13].

9.3 Engineering the Optical Reflections

As has been mentioned in the last section, both the flip-chip and vertical LED structures have to utilize the reflective mirror to tune the light propagation. Therefore, the LEE can be improved by engineering the optical reflections through different types of reflective mirrors. If the effect of the side facet is neglected, ideal reflective mirrors can approximately double the intensity of the light compared with the LED without the reflective mirror. The reflector mainly includes distributed Bragg reflectors (DBRs), metal reflectors, and omnidirectional reflectors (ODRs) as depicted in Fig. 9.2a–c, respectively [14].

A distributed Bragg reflector is a multilayer structure consisting of N pairs of dielectric layers. The periodic dielectric layers possess the high and low refractive indices (n_h and n_l, respectively) which require the respective layer thickness of the "quarter-wave" at a certain wavelength λ, i.e., $n_l d_l = n_n d_n = \frac{1}{4}\lambda$. In an ideal condition, the DBR structure shall feature a large refractive index contrast (Δn), small mismatches for the lattice constant and the thermal expansion coefficient with the underlying epi-layer, a large bandgap, and a high electrical conductivity [15]. The large refractive index contrast can fulfill the better reflectivity; the small mismatches for the lattice constant and the thermal expansion coefficient with the underlying epi-layer can maintain excellent crystal quality for the subsequently

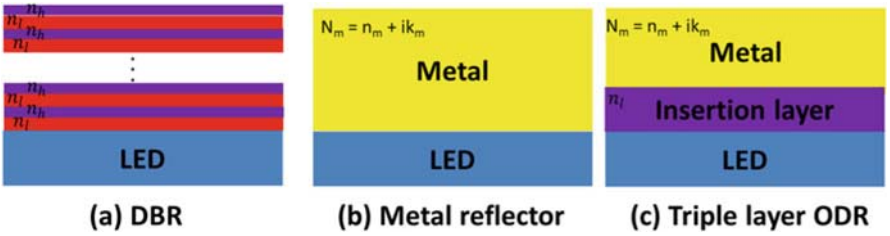

Fig. 9.2 Schematic cross-sectional views for (**a**) distributed Bragg reflector (DBR), the periodic dielectric layers with high and low refractive indices of n_h and n_l, respectively; (**b**) a metal reflector; and (**c**) a triple-layer omnidirectional reflector (ODR). The semiconductor has the refractive index of n_s; the coated material with a low refractive index layer of n_{li}; the metal with a complex refractive index $N_m = n_m + ik_m$, where k_m is the extinction coefficient

grown epi-layer; a reduced optical absorption caused by the DBR can be obtained by using DBR materials with large energy bandgap; the DBR has to be electrically conductive to allow the current flow and reduce the fabrication complexity.

For the purpose of cost saving, it is more advised to in situ grow GaN/AlNDBRs in the metal-organic chemical vapor deposition (MOCVD) system for III-nitride-based LEDs. Nevertheless, the main difficulty in fabricating AlN/GaN DBRs lies on the fact that there is a huge lattice mismatch (2.4%) between the GaN layer and the AlN layer. The very large lattice mismatch may cause cracks for the films [15]. Besides the in situ DBRs, the DBRs can also be obtained by depositing TiO_2/SiO_2 periodic structures by using electron beam evaporator system [16], and the reflectance for the fully optimized TiO_2/SiO_2 DBR can be as high as 99% [17]. Unfortunately, the small bandgap of 3.3 eV for the TiO_2 thin layer limits the application for the TiO_2/SiO_2 DBR in the UV LEDs. Instead, HfO_2/SiO_2 DBRs [18] and Ta_2O_5/SiO_2 DBRs [17] can be excellent candidates for UV LEDs. Moreover, DBRs can be patterned into three-dimensional (3D) photonic crystal reflector to enhance the scattering ability for the incoming light [16, 19]. Huang et al. report to use the self-assembled polystyrene nano-spheres and fabricate the 3D colloidal-photonic-crystal (CPC) bottom reflector for blue GaN-based LEDs [20].

DBRs can serve as excellent reflective mirrors with very high reflectivity if they are fully optimized. Nevertheless, the reflectivity is strongly subject to the incident angle and the wavelength [14]. Therefore, metal reflectors that can be insensitive to the incident angle and the emission wavelength over a wide wavelength range are proposed. However, the disadvantage for the metal reflectors is not competitive when compared with DBRs, e.g., Al and Ag reflective mirrors yield the reflectivity of ~95% for visible spectral range [21]. Their report shows that only Al metal is of high reflectivity even if the wavelength is shorter than 400 nm, and Ag metal can be an excellent reflective mirror for visible wavelength regime. Significant optical absorption can be found for Au metal when the emission falls into the blue spectral range.

The next optical device is called omnidirectional reflector (ODR) which is less affected by the incidence angle, and the ODR can also maintain a very high

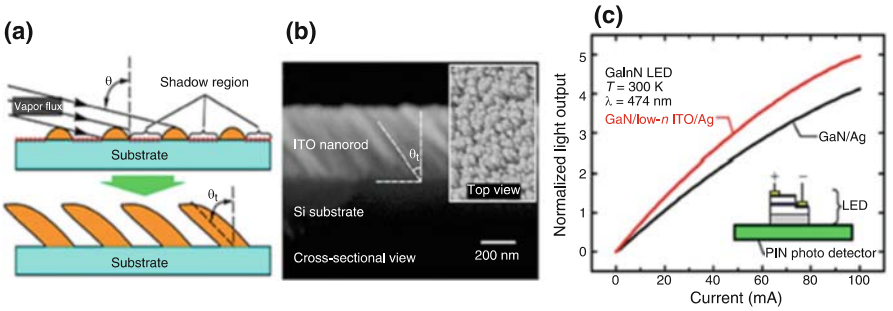

Fig. 9.3 (**a**) Schematic diagram for the oblique-angle deposition, (**b**) SEM images for ITO nanorods deposited by oblique-angle e-beam evaporation on a Si substrate, (**c**) light output power in terms of the injection current for LEDs with Ag reflective mirror and with the proposed ODR structure, respectively. Reproduced from Ref. [24], with the permission of AIP Publishing

reflectivity. The ODR structure is illustrated in Fig. 9.2c that comprises a low refractive indexed insertion layer and the metal. The reflectivity can be further enhanced if the refractive index contrast between the insertion layer and the semiconductor becomes large. To meet that goal, quite a few designs have been demonstrated. It is proved that low refractive indexed nanoporous SiO_2 with the average pore size of ~2 nm can be fabricated by using the sol–gel process [14]. An even lower refractive index of $n = 1.05$ can be obtained by adopting SiO_2 nanorods that are grown by oblique-angle deposition [22]. Alternatively, indium–tin oxide (ITO) nanorods with the refractive index as low as 1.34 at 461 nm via oblique-angle deposition approach (see Fig. 9.3a) also help to form excellent ODR structure as shown in Fig. 9.3b [23, 24]. Compared to the LEDs with merely the Ag reflector, the light output power for the InGaN/GaN-based blue LED with the proposed ODR structure is enhanced by 31.6%, which is well ascribed to the enhanced reflectivity of the ODR and the lower losses of the wave-guided modes [24]. However, during the process for fabrication of the ODR with nanostructures, more care shall be paid to the rough nanostructures that may cause the textured metal mirror and then decrease the reflectivity [25].

Besides III-nitride-based visible LEDs, the reflective mirror is also particularly important for AlGaN-based DUV LEDs. Current DUV LEDs adopt the p-GaN layer to form the good ohmic contact and provide sufficient holes. However, the p-GaN layer can significantly absorb the DUV photons. Therefore, the combination of a transparent contact layer and a highly reflective p-type electrode is desirable to realize a decent LEE. According to Ref. [21], we can get that the reflectance of a conventional Ni/Au p-electrode is low (<30%) and cannot function as a highly reflective mirror for DUV photons. Although the Al mirror can possess a high reflectivity of 92% in DUV spectral range, the ohmic contact is difficult to achieve. As a result, Lobo et al. propose to grow the nanopixel Pd ohmic contacts on the p-AlGaN layer to realize excellent current–voltage characteristics. The Pd nanopixels are then covered by the Al reflective mirror. The better ohmic contact and the Al

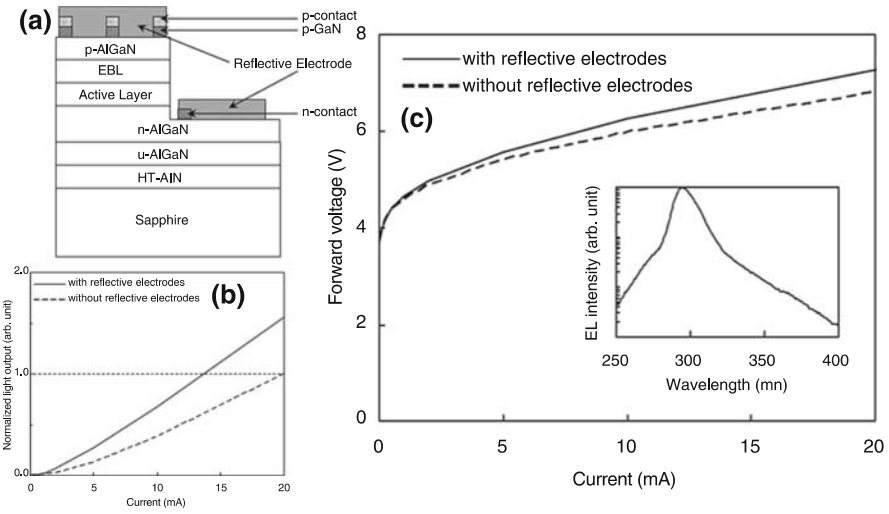

Fig. 9.4 (**a**) Schematic device architecture for the LED structure with the proposed reflective electrode, (**b**) optical power as the function of the injection current, and (**c**) current–voltage characteristics for the two LEDs with and without reflective electrodes, respectively. The inset in (**c**) shows the emission spectra for the two LEDs. Reproduced from Ref. [27], with the permission of IOP Publishing

reflective mirror enhance the light output power by 90% [26]. Inazu et al. partially remove the p-GaN layer so that the Al windows can be directly obtained on the p-AlGaN layer [27]. Ni is deposited on the rest p-GaN layer, and finally the Al/Ni/p-GaN structure is formed (see Fig. 9.4a). By doing so, a 1.55-fold increase in the LEE has been demonstrated which has been depicted in Fig. 9.4b. Nevertheless, these mesh ohmic contacts result in an increase in the forward voltage due to the reduced contact area according to Fig. 9.4c. Takano et al. grow the DUV LED films on the pattern sapphire substrate, which have the Rh mirror electrode, and the chips are finally encapsulated by resin to improve the light extraction. The EQE of 20% at the peak emission wavelength of 275 nm is achieved [28].

Besides the optically absorptive p-GaN layer, another bottleneck limiting the LEE for the Al-rich AlGaN-based DUV LEDs arises from the strong anisotropic light emission from the active region, such that the TM-polarized light propagates in parallel with the growth plane [7]. To address that issue, Wierer et al. report to use the inclined sidewall reflectors which can favor the extraction for the anisotropic light, and especially, the LEE for the TM-polarized light is enhanced up to four times [29]. Zhang et al. also numerically confirm that inclined sidewall reflectors are more beneficial to scatter TM-polarized light than TE-polarized light [30]. Kim et al. utilize the micro-reflectors that are deposited on the sidewalls for the selectively grown n-GaN micro-mesa to improve the LEE. The micro-reflectors are able to

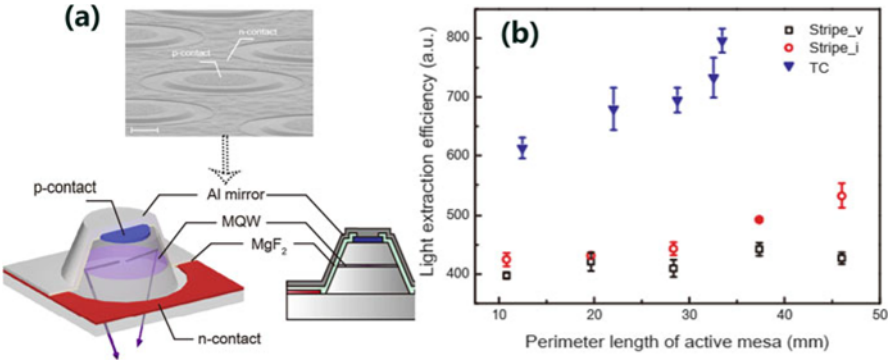

Fig. 9.5 (**a**) Scanning electron microscopic images, 3D and cross-sectional schematic illustrations for truncated cone (TC) AlGaN structure, along which we also schematically draw the MgF_2/Al ODR, (**b**) light extract efficiency for the three device structures with different perimeter length of the active mesa. Reproduced from Ref. [32] with the permission of ACS Publishing

tune the propagation for both the TE- and TM-polarized DUV photons [31]. Kim et al. further demonstrate coating low refraction indexed MgF_2/Al ODR mirror on the inclined sidewalls for the truncated cone (TC)-shaped mesa [32, 33], and the truncated cone-shaped mesa is shown in Fig. 9.5a. They also study another two device architectures, i.e., Strip_v and Strip_i, for comparison. Here, Strip_v means the strip-type DUV LED with vertical sidewalls, and Strip_i means the strip-type DUV LED with inclined sidewalls. The sidewalls for both Strip_v and Strip_i DUV LEDs possess MgF_2/Al ODR mirror. Figure 9.5b reflects that the TC configuration shows the highest LEE.

9.4 Micro-/Nanostructure Engineering

It has been shown that the large refractive index difference at the GaN/air interface results in a small critical angle of 23°. Therefore, a considerable amount of light emitted from the MQWs is trapped by the total internal reflection (TIR) at the GaN/air interface. The trapped light is reabsorbed by MQWs and is eventually converted into heat [34]. This process significantly deteriorates the LEE and reliability for LEDs. Therefore, it is a key step to break the TIR process to enhance the LEE. Various microscale surface roughness approaches have been adopted to enhance LEE of LED due to increased probability of light escaping from LEDs through multiple scattering in the microscale structure [1]. In this section, the progress of surface engineering to enhance photon extraction of GaN-based LEDs is reviewed and investigated.

9.4.1 Surface Texturing

Dry etching is often used to texture the surface of GaN material. However, the preparation for the photomask tends to make the cost high and the process complicated. Moreover, the surface defects that are induced during the dry etching process can sacrifice the electronic characteristics of LEDs. The degraded electronic properties often lead to high leakage current, thus decreasing the device reliability [1]. An alternate strategy of avoiding the etching-induced surface is to wet etch the GaN material. However, the [0001] oriented Ga-polar GaN film is hardly wet etched, whereas the [000-1] oriented N-face GaN plane can be more easily wet etched by using hot KOH solution. This is because the dangling bond density (DBD) for the N-face facet or other planes is larger than that for the Ga-polar facet [35]. Fortunately, the N-face of the GaN layer for the [0001] oriented LED can be obtained by using the laser-liftoff technology.

Nakamura et al. report an n-side-up GaN-based LED with a hexagonal "cone-like" surface [36]. The N-face surface for the GaN layer is exposed by using the laser-liftoff technique. The exposed N-face GaN surface is treated with an anisotropic wet etching process to roughen the surface, which improves the LEE and doubles the light output power. The LEE can be further improved if the periodical corrugated surfaces of the N-face n-GaN surface are fabricated before wet etched [37]. By doing so, integrated surface textures can be generated. Compared to the LED for which the surface is treated by using the conventional wet etching technique, the proposed LED structure increases the light output power by 32%. It is worth noting that the formation of hexagonal pyramid-like structures by the photochemical etching may generate threading dislocations (TDs), which serve as diffusion pathways for metals and act as leakage current pathways. The electrical properties for LEDs will be correspondingly degraded [38]. In addition, the randomly textured patterns on the N-face GaN evolve into the hexagonal pyramid structures with a fixed sidewall angle of about 31.6 ° due to the lower etching rate of the r-surface GaN when compared to the N-face GaN surface [38]. However, the inclination angle is believed to be essentially important in deciding the LEE. Therefore, cone-shaped nanostructures with optimized inclination angle of 23.4° for the sidewalls are further developed by using the SiO_2 nanosphere lithography technique. Experimental and numerically calculated results show that V-LEDs with the proposed design are effective to eliminate TIR and the optical power enhancement of 6% is obtained compared to those using the photochemical etching technique [38]. On the other hand, N-polar wet etching technique can be used to fabricate high-efficiency pyramids LED and bendable LED [39, 40]. Ma et al. report the fabrication for nitride-based hexagonal pyramids array (HPA) vertical-injection light-emitting diodes (V-LEDs) by N-polar wet etching technique [39]. The wet etching process penetrates through the active region, and hence the quantum wells in each pyramid are isolated from the ones in the adjacent pyramids (see Fig. 9.6a–c for the schematic process flow). The deep wet etching eliminates the TDs in hexagonal pyramids. As a result, the performance of HPA V-LEDs devices is

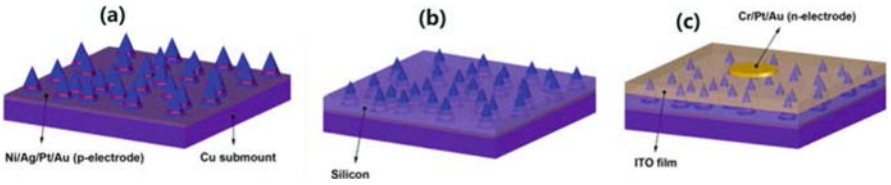

Fig. 9.6 Schematic fabrication processes for obtaining the nitride-based hexagonal pyramids array (HPA) vertical-injection light-emitting diodes: (**a**) pyramids with isolated quantum wells are formed by wet etching the N-face GaN surface, (**b**) silicon gel is spin coated to protect the quantum wells, and (**c**) deposition of ITO film and the Cr/Pt/Au n-electrode. Reproduced from Ref. [39], with the permission of OSA publishing

significantly improved with 30% higher internal quantum efficiency and 20% higher LEE compared with conventional roughened broad area V-LEDs.

Despite the difficulty in wet etching the Ga-polar GaN, the c-plane GaN layer can still be wet etched into pits at defect sites. Ha et al. report that the selectively chemical etching of the p-GaN surface enables the improved LEE and better device reliability [41]. The improved LEE is ascribed to the textured p-GaN surface, and the decrease in the number of defects in the p-GaN interprets the better device reliability. In addition, the p-GaN surface can also be in situ textured by reducing the growth temperature. To in-depth investigate the impact of the growth temperature for the p-GaN layer on the LEE, Liu et al. grew Mg-doped p-GaN epitaxial layers at different temperatures [42]. They find that, compared to the p-GaN layer grown at the temperature of 1000 °C, the p-GaN layer grown at the temperature of 800 °C can most enhance light output power for the LED partially because of the rough p-GaN surface. However, the rough p-GaN surface also aggravates the leakage current and device reliability. Moreover, Si or Mg treatment after high-temperature p-GaN layer also can achieve an in situ textured p-GaN surface [43, 44]. Nevertheless, the formation of the highly resistive thin MgN or SiN layers results in the slightly high forward voltage. A more advanced strategy that can considerably increase the LEE involves the hierarchical structures, which comprise in situ textured p-GaN microdomes and the post-grown SiO_2 nanorods on LED surface [45]. The SEM image for hierarchical structures is depicted in Fig. 9.7b. For better comparison, the SEM image with only in situ textured p-GaN microdomes is shown in Fig. 9.7a. Figure 9.7c shows that the suggested two structures have negligible effects on the current–voltage characteristics. Insightful investigations into Fig. 9.7d–f illustrate that the hierarchical micro-/nanoscale architecture can best enhance the LEE and the corresponding light output for blue LEDs is enhanced by up to 36.8%. The mechanism of enhanced LEE is attributed to the multiple reflections in the microdomes and additional graded refractive index profile provided by SiO_2 nanorods [45].

The surface texturing technology either by wet etching or by in situ epitaxial technique is most economical and convenient. However it is difficult to completely avoid the damages to the epi-layer and the resulting degradation for the electrical

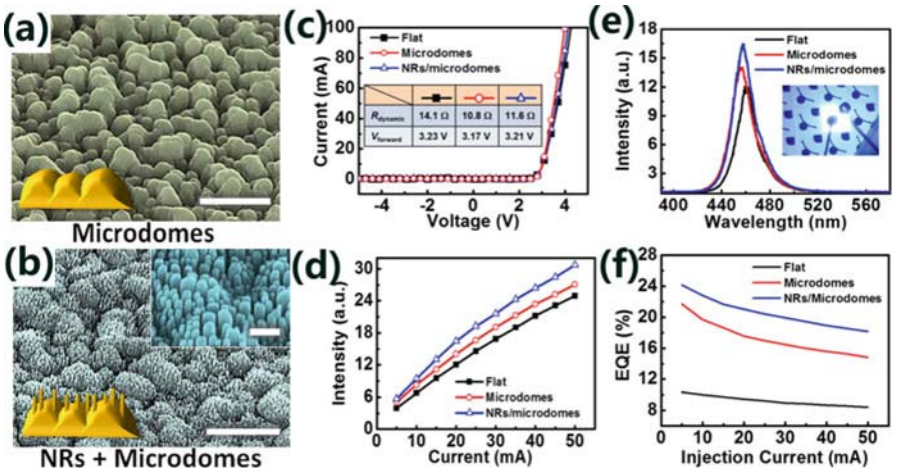

Fig. 9.7 SEM images of the p-GaN surface with (**a**) p-GaN microdomes and (**b**) SiO_2nanorods/p-GaN microdomes, (**c**) current–voltage characteristics, (**d**) measured light output power at different current levels, (**e**) measured electroluminescence spectra at the injection current of 20 mA, and (**f**) EQEs as a function of driving current for the three types of LEDs. Reproduced from Ref. [45], with the permission of AIP publishing

properties. Therefore, it is a good choice to texture the ITO current spreading layer through the wet etching technique. Oh et al. suggest the dual-layer ITO electrode to increase the LEE for InGaN/GaN blue LEDs. The proposed method lies on the fact that the etching selectivity for the as-deposited top ITO layer and the annealed bottom ITO layer varies, and this can produce textured the top ITO layer by rinsing the samples in the BOE solution [46]. Compared to the reference LED, the proposed textured dual-layer ITO configurations can double the optical output power. More importantly, the proposed structure does not degrade the electrical property. Oh et al. further fabricate the ITO nanoballs by using the wet etching technique to increase the LEE of UV LED (see Fig. 9.8a–c) [47]. The ITO nanoballs are finally coated by the Al film to form the nanoball ODR (NODR). The high reflection can be realized by the proposed ODR structure, and in the meantime, the increase of diffuse reflection is enabled by the interfaces between the ITO nanoball layer and Al film. Moreover, the nanovoids in the ITO layer further contribute to the diffuse reflection. Therefore, the enhanced LEE can be obtained for the UV LED, and this simultaneously increases optical power as demonstrated in Fig. 9.8d. Figure 9.8e depicts that the proposed ODR structures have less impact on the electrical properties.

To enhance the LEE for DUV LEDs, the sidewall texture technology is even more important due to the anisotropic light emission from the AlGaN-based active region [48]. Guo et al. roughen the sidewall of the sapphire substrate by using picosecond laser dicing technique [49]. Their results show thatthe LEE does not monotonically

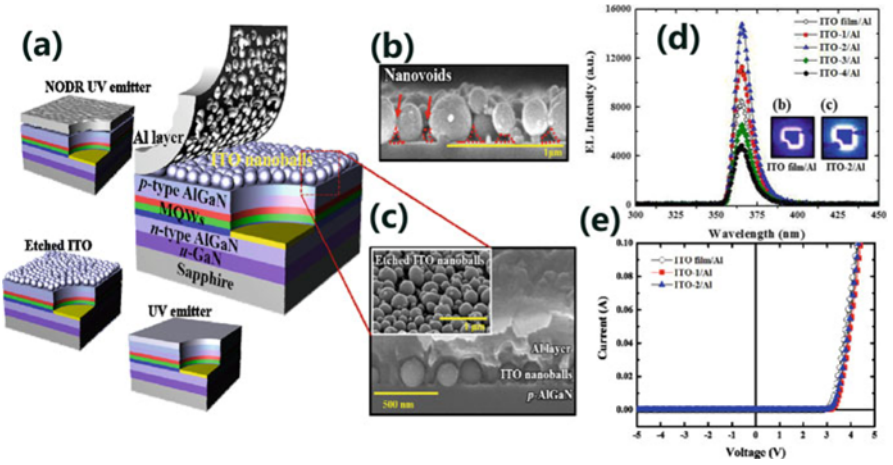

Fig. 9.8 (**a**) Schematic diagrams for the UV LED with the proposed ITO nanoballs/Al film NODR structure; (**b**) cross-sectional SEM image for ITO nanoballs, along with which the nanovoids are also shown; (**c**) ITO nanoballs/Al film NODR structure on a p-type AlGaN layer; (**d**) electroluminescence spectra for UV LEDs with the ITO film/Al ODR and different NODRs; and (**e**) injection current at different applied biases for UV LED with the ITO film/Al ODR and different NODRs. Reproduced from Ref. [47], with the permission of The Royal Society of Chemistry

improve as the number of the diced layer increases as can be indicated from Fig. 9.9. The electrical properties are also not significantly impacted by the dicing process, since the sapphire serves as the insulating layer and provides no current paths. Guo et al. later also suggest fabricating oblique sidewalls for AlGaN-based DUV LEDs by using the picosecond laser multiple-scribing technique [50]. According to their report, the oblique sidewalls help to improve the LEE and increase the power by 13.8% when the inclination angle is set to 60°.

9.4.2 Photonic Crystal

Photonic crystal (PhC) is well known as a periodic configuration of the optical medium with a photonic bandgap. The photonic bandgap is able to prevent the light falling into a certain wavelength range from propagating in certain directions [51]. The most popular occurrence of one-dimensional (1D) PhC is DBR, which is a multiple-layer dielectric stack with periodic refractive index and allows the photons to possess very high reflectivity/transmittance with an angular cone around normal incidence. Two-dimensional (2D) PhCs can increase the angular range of the bandgap and limit the propagation of light in plane. In spite that three-dimensional (3D) PhCs are able to support an omnidirectional bandgap, practical implementation for 3D PhCs is more challenged at the current stage. Therefore, significant research effort has been invested to 2D PhCs for III-nitride-based LEDs.

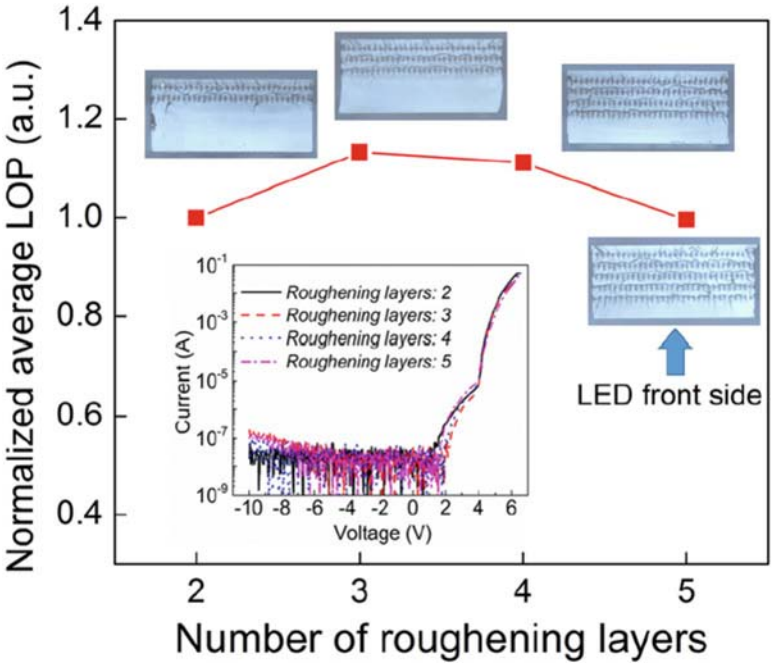

Fig. 9.9 Normalized average light optical power (LOP) for 275 nm DUV LEDs. Inset micrographs show the cross section of the sidewalls for the sapphire substrate sidewalls. Current–voltage characteristics are also presented in the inset. Reproduced from Ref. [49], with the permission from AIP publishing

In the ideal case of a full in-plane bandgap for the 2D PhC, no guided modes exist, and all of the guided light emission is then inhibited. Therefore, the light can only propagate in the out-of-plane modes, and this gives rise to the ideal LEE of 100%. As a matter of fact, the bandgap for the realistic 2D PhC only extends up to a maximum off-plane propagation angle. As a result, it is difficult to design 2D PhC with a bandgap that can cover the whole range of angles to suppress all guided modes especially for very thick LED films [51]. In spite of that, the PhCs that are located very close to the active area can lead to the direct light out-coupling process and the strong light scattering results in a high LEE [52]. However, the 2D PhCs etched through the active region directly are inevitable to reduce the active region area and create new surface defects. Therefore the reduced radiative recombination rate results in the poor internal quantum efficiency. Recently, the bottom-up nanorod LEDs and core-shell LEDs offer good solutions to fabricate 2D PhCs. The active area can be self-assembled embodied into 2D PhCs. The proposed structures are also featured with the advantages of strain relaxation and no dislocations. Djavid et al. demonstrate that the LEE for TM-polarized light can be significantly enhanced

if AlGaN-based nanowired DUV LED structures are adopted because the nanorod PhCs inhibit the emission of guided modes and redirect the trapped light into the radiated modes [53]. Core-shell LEDs possess unique features of three-dimensional MQWs and the PhC-effect-caused LEE enhancement, and therefore the photon generation rate can be even more [1].

Although the embedded PhCs can increase the LEE and avoid the dislocations, nevertheless, the LEDs with embedded PhCs demand complicated process, e.g., how to keep excellent electrical properties? Think about above these challenges: 2D PhCs as the diffraction gate is more practical in improving the overall performance for LEDs. For the LEDs with properly designed photonic crystals, the light that is trapped by total internal reflection can be redirected into the radiated modes, which can greatly enhance the LEE [51]. 2D PhCs as the diffraction gate can also be induced onto the surface for the p-GaN layer, the n-GaN layer, and the dielectric material for LEDs. In 2004, Oder et al. fabricate triangular arrays of the PhCs in p-GaN of blue and UV LED using electron-beam lithography and inductively coupled plasma dry etching. The enhancement of optical output power reveals an increase by 63% and 95% for the blue and UV LEDs, respectively. The enhancement for LEDs is attributed to refractive index periodicity creating a cutoff frequency for the guided modes. Modes above the cutoff frequency couple with PhC resulting in leaky mode. Compared with random scattering from a randomly textured surface, the PhCs offer a short escaped length for light, thus avoiding parasitic absorption [54]. The PhC that serves as the diffraction gate only has a high overlap with high-order modes. Unfortunately, low-order modes also carry a large portion of 30% for the rest optical energy [55]. A lower-index $Al_xGa_{1-x}N$ layer can be used to modify low-order modes as proposed by David et al. [55].

The large electrical resistivity for the p-GaN window layer gives rise to the poor current spreading for LEDs. Although the resistance can be reduced with a thicker p-GaN layer, the increased thickness can result in excessive optical absorption. The issue can be partially solved by inserting dielectric material, embedded photonic crystals which can be obtained by secondary epitaxy [56], thin-film fabrication with periodic nanostructures in the less resistive n-GaN layer [57]. Ee et al. report the InGaN/GaN MQW LED structure utilizing a SiO_2/polystyrene lens array on p-GaN layer to significantly enhance the LEE [58]. As a result, the 249% improvement of the light output power is obtained due to the increase in effective photon escape cone and the reduced Fresnel reflection. Liu et al. incorporate air-voided PhCs into the n-GaN layer to enhance the light extraction efficiency by ~32.7% [56]. Wierer et al. fabricate a 700-nm-thick flip-chip thin-film LED with 2D PhCs in the n-GaN layer. The record-breaking LEE is as high as 73% for the unencapsulated device at that time [57]. In addition to the enhanced LEE, PhCs also yield the benefits for increasing the controllability of the optical emission directionality [59] and preserving the excellent light polarization [60], which are strongly desired in the applications of display, projectors, etc.

9.4.3 *Patterned Substrate*

Patterned sapphire substrates (PSSs) have been widely used in commercial GaN-based LEDs, because the epitaxial layers grown on the PSS possess the decreased TDs and the increased light scattering. At present, the specification of commercial PSSs is the cone shape with 3 μm period, 1.7 μm height, and 0.3 μm space. To further improve the performance for LEDs grown on the PSS, the effective C-plane area that supports the subsequent epi-growth in microscale PSS continues to be reduced in the past few decades. However, more difficulty will be made to grow GaN layer on PSS with too small effective C-plane area. In addition, LEE is substantially affected by the pattern geometries for the PSS [61]. Therefore different pattern geometries for the PSS are continued to be developed by adopting various fabrication processes. Lin et al. transfer the patterns of a cone-shaped patterned sapphire substrate (CPSS) into SiO_2 layer through using nano-imprint lithography (NIL). By doing so, a cone-shaped SiO_2 patterned template is obtained [62]. Compared with the LED grown on CPSS, the LEE of the LED grown on cone-shaped SiO_2 patterned template can be enhanced due to the smaller refractive index for SiO_2 than sapphire. A volcano-shaped patterned sapphire substrate (VPSS in Fig. 9.10a) can be fabricated to improve the LEE of LEDs [63, 64]. The VPSS LED show a top optical flux is 2.8 times higher than that for LEDs grown on planar

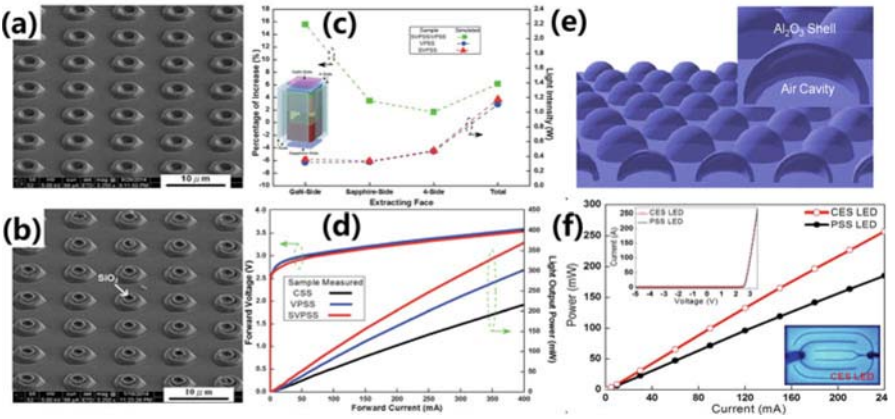

Fig. 9.10 (**a**) SEM images of VPSS and (**b**) SVPSS structures, (**c**) percentage increase in the light intensity of InGaN-based LEDs grown on the VPSS and SVPSS. Inset: schematic representation of different receiver positions considered in the simulation, (**d**) measured light output power and the required voltage at different injection current, (**e**) schematic structures of a hemispherical CES template. Inset: schematically magnifying an inner air cavity covered with a thin alumina shell. (**f**) Light output power in terms of the injection current for CES and PSS LED devices, respectively. Top inset: SEM image magnifying an inner air cavity covered with a thin alumina shell; bottom inset: optical microscopy image for the working LED device. Figures (**a–d**) are reproduced from Ref. [65], with the permission of RSC publishing. Figures (**e**) and (**f**) are reproduced from Ref. [66], with the permission of ACS publishing

substrate and is 1.6 times higher than that for LEDs grown on hemispherical PSS [64]. If a layer of SiO_2 is embodied into the VPSS (i.e., SVPSS in Fig. 9.10b), the LEE and the crystal quality for the LEDs can be further enhanced. Therefore the light output power for LEDs grown on the SVPSS is the strongest as can be seen in Fig. 9.10c, d [65]. Furthermore, Fig. 9.10d also depicts that the electrical properties for different LEDs are not strongly influenced by the substrate. Moon et al. report a novel high-index contrast cavity engineered substrates (CESs) in which hexagonally arranged hemispherical air cavities are covered with a 80-nm-thick crystallized Al_2O_3 shell (see Fig. 9.10e). According to Fig. 9.10f, InGaN/GaN blue LEDs fabricated on the 3 μm pitch CES exhibit ~39% enhancement in the optical power compared to state-of-the-art PSS LEDs [66].

With the development of nanotechnology, the nanoscaled PSS (NPSS) can be fabricated through nano-imprint, e-beam lithography, holographic lithography, metal annealing, and nanosphere lithography. The nanoscaled PSS (NPSS) can provide higher pattern densities than microscaled PSS, leading to the increased possibility of photon scattering and the higher LEE. In the year of 2000, the NPSS is first proposed to tune the strain and to improve the crystal quality for heteroepitaxy films [67]. Later on, Chen et al. report that, due to the efficient optical scattering by NPSS, the output power for LEDs grown on NPSS is 1.11 times higher than that for LEDs grown on micro-patterned sapphire substrates (MPSS) [68]. Kao et al. reveal the further enhancement for the LEE can be achieved by properly increasing the aspect ratio for the NPSS [69]. Note that a too high aspect ratio may result in the decreased LEE and the decrease of the C-plane area, which then also limits the LED epitaxial window [70]. The other advantage for the NPSS is to suppress the quantum-confined Stark effect (QCSE) within the multiple quantum wells [71]. Thus far, various reports show that the NPSS with different designs can increase the LEE. However, a commonly accepted consent implies that a too small pattern size for NPSS cannot promote the LEE [72, 73]. Recently, a hybrid PSS that is obtained by embedding nanopatterns into commercial MPSS has been proposed [74, 75]. Ke et al. fabricate the hybrid PSS with high-density concave nanopattern structures on a PSS (see Fig. 9.11a, b). Comparison between Fig. 9.11c and d depicts that the hybrid PSS can even better support the diffuse reflection. As a result, when comparing conventional PSS LED, the hybrid PSS LED generates a ~22.3% enhancement for the light output power as is shown in Fig. 9.11e, f [75].

Another strategy to further improve the LEE of NPSS is to fill lower refractive index material such as SiO_2 or air voids into the GaN/substrate interface (see Fig. 9.12a). If the material is air void, it can also block or laterally bend TDs. Chiu et al. demonstrate LEDs grown on the SiO_2 nanorod-array patterned sapphire substrate [76]. Compared to conventional LEDs, NPSS LEDs enhance the light output power by 52%. Low cost self-assembled SiO_2 microspheres can be integrated with substrate to relax strain and improve LEE [77, 78]. Ueda et al. demonstrate the high performance of blue LED grown on sapphire substrates coated with a silica-submicron-sphere monolayer film, as shown in Fig. 9.12b [77]. It can be seen from Fig. 9.12a that compared with the LED without silica spheres, the LED output power is increased by 2.5-fold due to the reduced threading dislocation and the enhanced

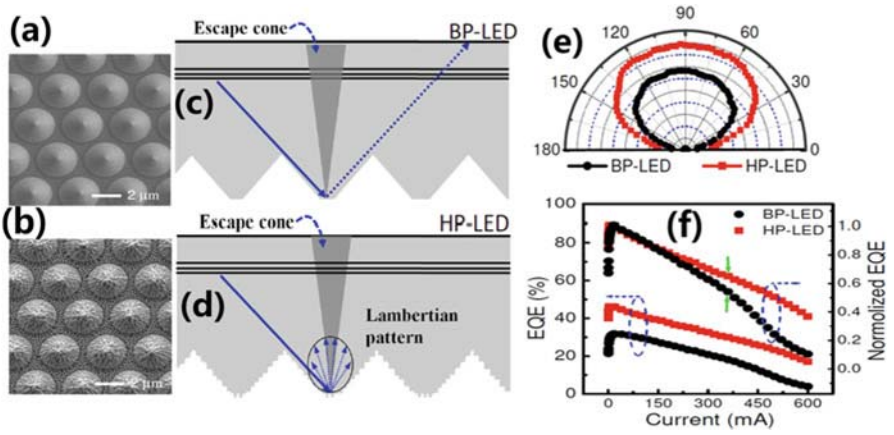

Fig. 9.11 Top-view SEM images of (**a**) bare-PSS (BP) and (**b**) hybrid-PSS (HP), (**c**) light racing schematic diagrams for BP-LED, (**d**) light racing schematic diagrams for HP-LED, (**e**) far-field radiation patterns of the BP-LED and HP-LED, (**f**) EQE and normalized EQE of BP-LED and HP-LED at various injection currents. Reproduced from Ref. [75], with the permission of ACS publishing

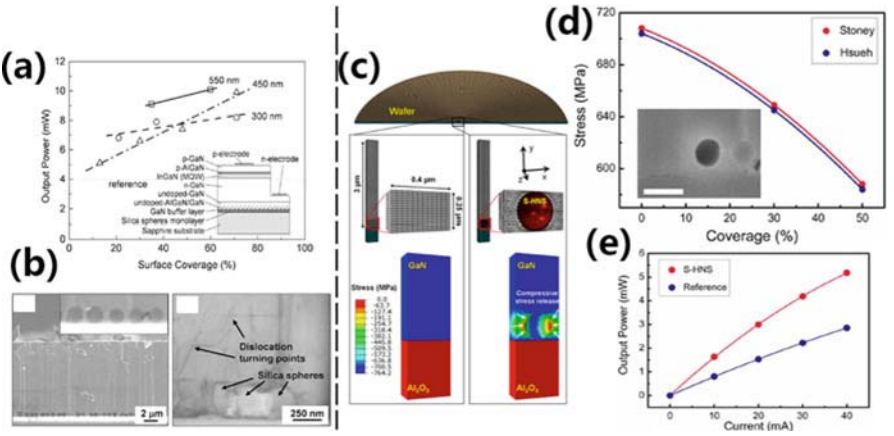

Fig. 9.12 (**a**) LED output power at various silica-sphere surface coverages on substrates. Inset: the GaN-based LED device structure. (**b**) SEM and TEM images of GaN films deposited on silica-coated substrates, (**c**) the stress analysis of GaN without S-HNS (left) and with a S-HNS monolayer with 30% surface coverage (right) obtained by FE simulations. Reduction in compressive stress as well as a strong stress gradient is notable around the S-HNS, (**d**) compressive stress in the GaN epitaxial layer at various S-HNS surface coverages. The stress values for 3 μm thick GaN layers on sapphire substrates were estimated from the measured wafer bowing and radius of curvature by an optical means. Inset: SEM image of ellipsoidal S-HNS taken after GaN epitaxial growth. The deformation of S-HNS from spherical to ellipsoidal shape by compressive stress in GaN is clearly observed (scale bar 200 nm), (**e**) output power of LEDs fabricated with and without S-HNS monolayers at various input currents. Figures (**a**) and (**b**) are reproduced from Ref. [77], with the permission of AIP publishing. Figures (**c–e**) are reproduced from Ref. [79], with the permission of Nature Group

light extraction. Pan et al. introduce a monolayer silica hollow nanosphere on the sapphire substrate (S-HNS) (see the insert in Fig. 9.12d). A four times enhancement of output power is attained by well-defined voids embedded at the GaN/sapphire interface (see Fig. 9.12e). The wafer bowing is reduced due to partial alleviation of compressive stress in GaN through the deformation of hollow nanospheres during growth, as depicted in Fig. 9.12c, d [79].

In addition to the enhanced LEE, a thinner coalescence thickness on NPSS can be realized, which reduces the growth time and is especially important for DUV LEDs. Epitaxial lateral overgrowth (ELO) technique on micro-stripe patterned sapphires usually requires a great coalescence thickness close to 10 μm because of the low mobility of Al atom, yielding a long growth time and a high cost. Dong et al. demonstrate 282 nm AlGaN-based DUV LEDs are grown on the novel NPSS fabricated through the nanosphere lithography technique [80]. Full coalescence is achieved at the 3-μm thick AlN layer (see Fig. 9.13a), and dislocation density also

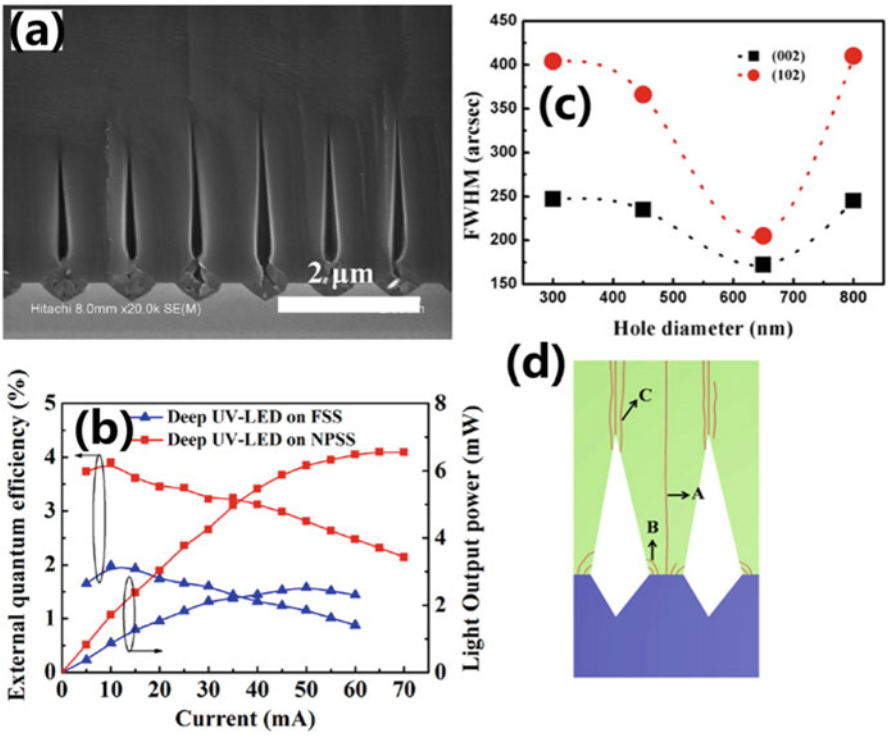

Fig. 9.13 (**a**) A cross-sectional SEM image of AlN grown on NPSS. (**b**) LOP-I-EQE curves of the deep UV LEDs grown on NPSS and flat sapphire substrate (FSS), (**c**) dependence of the XRCFWHM of AlN epi-layers on hole diameter of the NPSS, (**d**) three main competitive processes influencing TDD of AlN epi-layers on NPSS. Figures (**a**) and (**b**) are reproduced from Ref. [80], with the permission of AIP publishing. Figures (**c**) and (**d**) are reproduced from Ref. [81], with the permission of Nature Group

decreases. The EQE is enhanced by 98% (see Fig. 9.13b), which is attributed to the improved IQE and the better LEE [80]. Zhang et al. also declare that, by optimizing NPSS and the growth process, the threading dislocations (TDs) originating from the AlN/sapphire interface are bent because of the image force from the void sidewalls before coalescence. Hence, agreeing well with the findings by Dong et al. in Ref. [80], the dislocation density can be reduced as depicted in Fig. 9.13c, d [81].

9.5 Surface Plasmon-Enhanced LEDs

In the year of 2004, Okamoto et al. first report the possibility of increasing the IQE for blue LEDs by the surface plasmon (SP) [82]. The mechanism of the enhanced IQE by the SP effect can be explained that, when the resonant frequency of the surface plasmon polaritons (SPPs) of rough Ag film overlaps the emission frequency for the quantum well emission, the energy coupled to the mode is significantly increased [82]. Then, an additional channel of energy transfer from the QW-SP coupling can occur, and thus the IQE is enhanced [1, 83]. Since then, surface plasmon (SP)-enhanced LEDs have drawn intensive research efforts. It should be noted that, in order to maintain efficient QW-SP coupling, the distance between QW and metal is no more than 100 nm and the optimum distance is 20 nm due to the exponential decay of SP evanescent waves [84]. Therefore, metal nanoparticles are often embedded into the epi-layer or assembled into the partially etched p-GaN [85, 86]. Besides improving IQE, the SP effect can also modify polarized emission for DUV LEDs (DUV structure is shown in Fig. 9.14a) according to the report by Zhang et al., such that partial TM emission turns into TE emission [86]. The localized surface plasmon (LSP) effect is achieved by using Al nanoparticles, of which the surface roughness of the Al nanoparticles measured by AFM is presented in Fig. 9.14b. LSPs are generated at the interface between the AlGaN cap layer and Al nanoparticles. The in-plane (TE) polarization is improved from 13.7% to 19.7% as depicted in Fig. 9.14e.

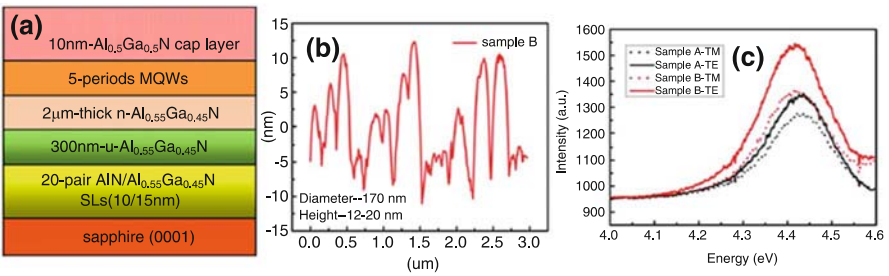

Fig. 9.14 (**a**) Schematic illustration of the structure for sample A, (**b**) AFM depth profile of Al particles on AlGaN surface of sample B, (**c**) wavelength dependent Purcell enhancement ratios of TE mode and TM mode, which are calculated to describe the enhancement ratio of the radiative recombination rate. Reproduced from Ref. [87], with the permission of Nature Group

Recently, it has been found that the SP also can be used to increase LEE by means of out-coupling of the generated photons through both scattering and localized surface plasmon resonance (LSPR) effects [88]. When distance between the metal and QW is more than 100 nm, surface plasmon (SP)-enhanced LEDs can only stem from the improved LEE by the metal SP. Sung et al. fabricate gold NPs on the ITO current spreading layer and lead to an electroluminescence (EL) increase by 1.8-fold [88]. Then, Sung et al. further confirm that the origin for the improved light emission arises from the combined action of the LSPR modes and the light scattering modes [89]. Chuang et al. find that the Ag nanoparticles on the p-GaN layer can be embedded into the subsequent growth ITO layer, and this can result in the three-dimensional distribution of Ag-based nanoparticles (see Fig. 9.15a, b)

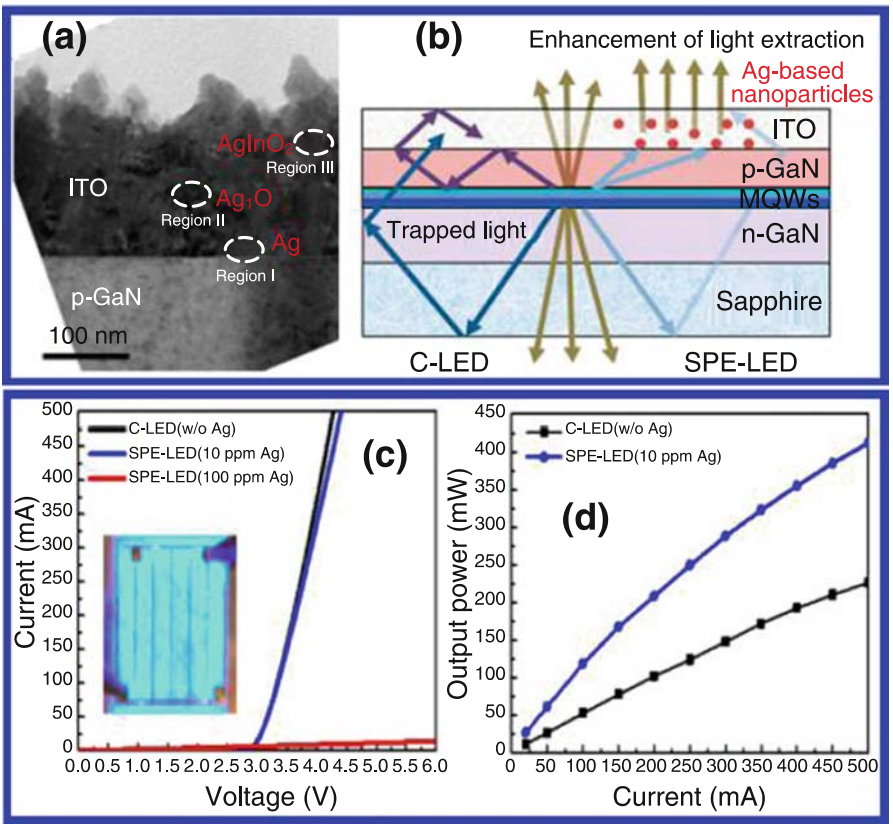

Fig. 9.15 (**a**) Cross-sectional TEM images of ITO film embedded with Ag-based nanoparticles on the p-GaN top layer (using the nano-Ag solution with 10 ppm concentration), (**b**) schematic diagram of light output enhanced mechanisms of surface plasmon-enhanced LED (SPE-LED) in comparison with the conventional LED (C-LED), (**c**) typical current−voltage characteristics of SPE-LED samples fabricated with different concentrations of a nano-Ag solution, (**d**) light output power as a function of injection current for SPE-LED and C-LED. Reproduced from Ref. [90], with the permission of ACS publishing

[90]. Then, an 88.10% enhancement in the light output power is achieved (see Fig. 9.15d). Since the Ag nanoparticles are 200 nm away from the active region, then the enhancement is well attributed to the enhanced LEE. Note, Fig. 9.15c shows that the forward voltage for the LED will become dramatically high if the nano-Ag solution is 100 ppm. The very large forward voltage originates from the resistive $AgInO_2$, and therefore Chuang et al. optimize the nano-Ag solution to 10 ppm in their experiment.

Enhancing the LEE through LSP–TM light coupling becomes increasingly useful in the case of DUV LEDs which mainly have TM-polarized light emission. By means of using the metal Al thin layer for SP coupling, Gao et al. demonstrate the 217% enhancement in the photoluminescence intensity for the 294 nm AlGaN-based DUV LEDs [91]. However, the thin Al layer can only couple the TM-polarized light parallel to the surface of the device. For a TE-polarized light propagating in the direction parallel to the device surface, SP coupling does not occur. Worse still, when the thickness of the Al layer is 6 nm, the photon energy will be reduced to approximately 40% of its initial energy [92]. Then, Huang et al. further use the oblique-angle deposition method (see Fig. 9.16a) to deposit polygonal Al nanoparticles (see Fig. 9.16b–d) on the top surfaces of the DUV LEDs. The localized surface plasmon-enhanced AlGaN-based LEDs showed a maximum 5.1-fold bottom-emission EL enhancement at the wavelength of 287 nm (see Fig. 9.16e, f). Even more importantly, the proposed technique enables both the TM-polarized and the TE-polarized light to be effectively coupled with the LSP in the Al nanoparticles [92].

9.6 Summary

The technologies presented for extracting photons from III-nitride-based LED chips have been reviewed and summarized in this chapter. Various LEE-enhancing techniques, such as anti-reflective coating, surface roughening, photonic crystals, patterned substrate, surface plasmonics, and omnidirectional reflector, have been compared. Insightful physical interpretations for different LEE-enhancing approaches have also been revealed.

The highest LEE of InGaN/GaN-based blue LEDs has been up to 80% at the current stage [13]. Therefore the LEE is not a bottleneck that limits the EQE for blue LEDs, and as a result a 303 lm/W white LED lamp has ever been announced by Cree Company [93]. We believe that the most important issue for blue LED now lies on the efficiency droop and fabrication cost, to which we suggested more efforts have to be devoted.

Techniques that are effective to improve the LEE for InGaN/GaN-based blue LED are not always applicable for AlGaN-based DUV LEDs. One of the essentially critical strategies is to find the alternative material to remove the p-GaN layer, so that

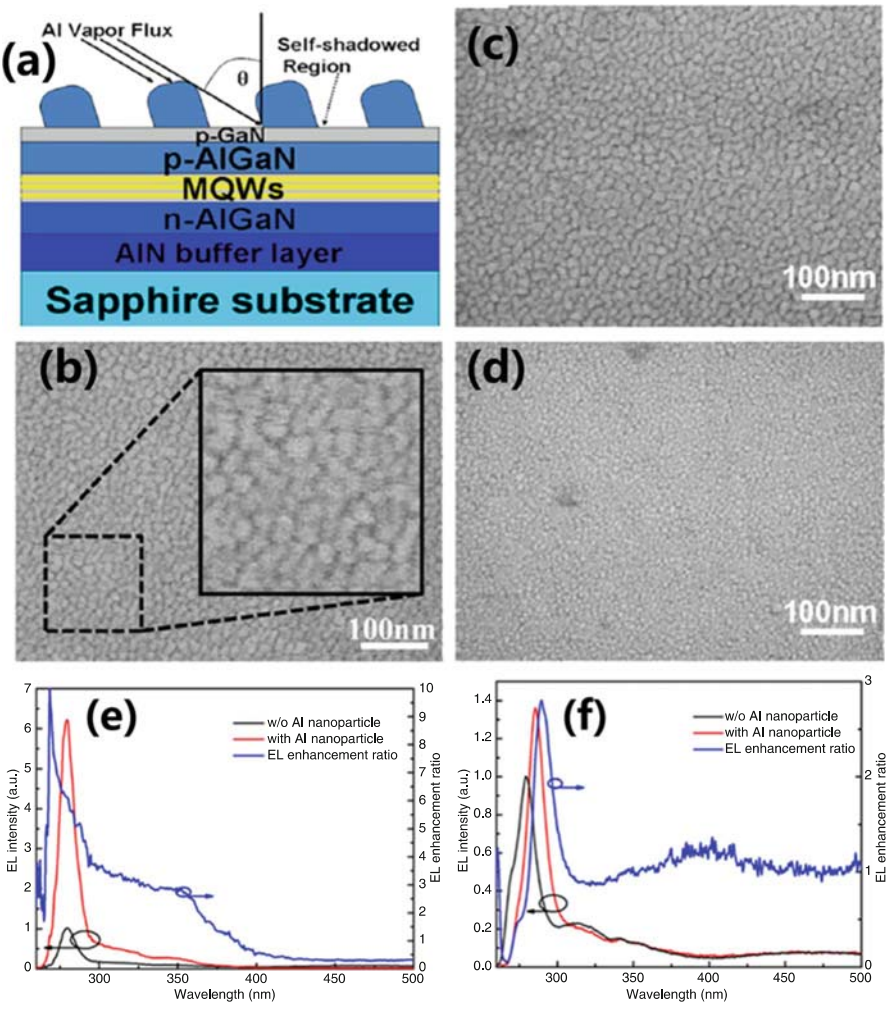

Fig. 9.16 Schematic illustration and top-view SEM images of the oblique-angle deposition of Al NPs. (**a**) Schematic illustration of oblique-angle deposition on complete structural deep UV LEDs; (**b–d**) top-view SEM images of Al NPs deposited on LEDs with deposition angles of 45°, 60°, and 75°, respectively; (**e**) top-emission EL spectra of DUV LED samples without Al NPs (black line) and with Al NPs deposited on the top surface at 60° (red line) as well as the enhancement ratio between them (blue line); (**f**) bottom-emission EL spectra of DUV LED samples without Al NPs (black line) and with Al NPs deposited on the top surface at 60 ° (red line) as well as the enhancement ratio between them (blue line). Reproduced from Ref. [92], with the permission of Nature Group

the optical absorption can be reduced and the excellent p-type ohmic contact can also be obtained simultaneously. At present, flip-chip configuration has been widely employed for DUV LEDs so that DUV photons can escape from the transparent sapphire. In addition, because of the anisotropic emission nature of the high Al-rich AlGaN quantum wells for DUV LEDs, the sidewall scattering engineering such as sapphire sidewall texturing and inclined sidewall reflectors are also important methods for the better TE and TM light extraction. By combining the advanced epitaxial growth technique on PSS with the current photon management designs, the EQE for DUV LED can reach 20% [28], which number is, however, still far below the EQE for the state-of-the-art InGaN/GaN blue LEDs. Hence, more efforts shall be invested to further increase the LEE for DUV LEDs, e.g., reducing the TM portion by managing the stress for the Al-rich AlGaN quantum wells.

Acknowledgments This work is supported by the National Natural Science Foundation of China (Nos. 61604051, 51502074), Natural Science Foundation of Tianjin City (No. 16JCQNJC01000), and Natural Science Foundation of Hebei Province (No. F2017202026).

References

1. Y.-L. Tsai, K.-Y. Lai, M.-J. Lee, Y.-K. Liao, B.S. Ooi, H.-C. Kuo, J.-H. He, Prog. Quantum Electron. **49**, 1 (2016)
2. Z.-H. Zhang, Y. Zhang, W. Bi, H.V. Demir, X.W. Sun, Phys. Status Solidi A **213**, 3078 (2016)
3. E.F. Schubert, *Light-Emitting Diodes*, 2nd edn. (Cambridge University Press, Cambridge, 2006)
4. L. Li, Y. Zhang, S. Xu, W. Bi, Z.-H. Zhang, H.-C. Kuo, Materials **10**, 1221 (2017)
5. J. Cho, E.F. Schubert, J.K. Kim, Laser Photonics Rev. **7**, 408 (2013)
6. G. Verzellesi, D. Saguatti, M. Meneghini, F. Bertazzi, M. Goano, G. Meneghesso, E. Zanoni, J. Appl. Phys. **114**, 071101 (2013)
7. J.-S. Park, J.K. Kim, J. Cho, T.-Y. Seong, ECS J. Solid State Sci. **6**, 42 (2017)
8. A. Khan, K. Balakrishnan, T. Katona, Nat. Photonics **2**, 77–84 (2008)
9. H. Hirayama, N. Maeda, S. Fujikawa, S. Toyoda, N. Kamata, Jpn. J. Appl. Phys. **53**, 100209 (2014)
10. S. Dang, C. Li, T. Li, W. Jia, P. Han, B. Xu, Optik **125**, 3623 (2014)
11. H.-Y. Ryu, I.-G. Choi, H.-S. Choi, J.-I. Shim, Appl. Phys. Express **6**, 062101 (2013)
12. Y.C. Shen, J.J. Wierer, M.R. Krames, M.J. Ludowise, M.S. Misra, F. Ahmed, A.Y. Kim, G.O. Mueller, J.C. Bhat, S.A. Stockman, P.S. Martin, Appl. Phys. Lett. **82**, 2221 (2003)
13. M.R. Krames, O.B. Shchekin, R. Mueller-Mach, G.O. Mueller, L. Zhou, G. Harbers, M.G. Craford, J. Disp. Technol. **3**, 160 (2007)
14. K.P. Streubel, J.K. Kim, H.W. Yao, J.Q. Xi, E.F. Schubert, E.F. Schubert, Proc. SPIE **6134**, 61340D (2006)
15. A.I. Zhmakin, Phys. Rep. **498**, 189 (2011)
16. J.-K. Liou, P.-C. Chou, C.-C. Chen, Y.-C. Chang, W.-C. Hsu, S.-Y. Cheng, J.-H. Tsai, W.-C. Liu, IEEE Trans. Electron Devices **61**, 831 (2014)
17. Y. Ma, B. Fan, Z. Chen, Y. Lao, L. Yan, X. Ma, Y. Zhuo, Y.L. Pei, G. Wang, IEEE Photon. Technol. Lett. **29**, 1564 (2017)
18. Y.K. Song, H. Zhou, M. Diagne, A.V. Nurmikko, R.P. Schneider, C.P. Kuo, M.R. Krames, R.S. Kern, C. Carter-Coman, F.A. Kish, Appl. Phys. Lett. **76**, 1662 (2000)
19. Y.-C. Chang, J.-K. Liou, W.-C. Liu, IEEE Electron Device Lett. **34**, 777 (2013)

20. K.-M. Huang, H.-J. Chang, C.-L. Ho, M.-C. Wu, IEEE Photon. Technol. Lett. **24**, 1298 (2012)
21. M. Kneissl, J. Rass, *III-Nitride Ultraviolet Emitters* (Springer, Berlin, 2016)
22. J.Q. Xi, M.F. Schubert, J.K. Kim, E.F. Schubert, M.F. Chen, S.Y. Lin, W. Liu, J.A. Smart, Nat. Photonics **1**, 176 (2007)
23. J.K. Kim, S. Chhajed, M.F. Schubert, E.F. Schubert, A.J. Fischer, M.H. Crawford, J. Cho, H. Kim, C. Sone, Adv. Mater. **20**, 801 (2008)
24. J.K. Kim, T. Gessmann, E.F. Schubert, J.Q. Xi, H. Luo, J. Cho, C. Sone, Y. Park, Appl. Phys. Lett. **88**, 013501 (2006)
25. A. Zhen, P. Ma, Y. Zhang, E. Guo, Y. Tian, B. Liu, S. Guo, L. Shan, J. Wang, J. Li, Appl. Phys. Lett. **105**, 251103 (2014)
26. N. Lobo, H. Rodriguez, A. Knauer, M. Hoppe, S. Einfeldt, P. Vogt, M. Weyers, M. Kneissl, Appl. Phys. Lett. **96**, 081109 (2010)
27. T. Inazu, S. Fukahori, C. Pernot, M.H. Kim, T. Fujita, Y. Nagasawa, A. Hirano, M. Ippommatsu, M. Iwaya, T. Takeuchi, S. Kamiyama, M. Yamaguchi, Y. Honda, H. Amano, I. Akasaki, Jpn. J. Appl. Phys. **50**, 122101 (2011)
28. T. Takano, T. Mino, J. Sakai, N. Noguchi, K. Tsubaki, H. Hirayama, Appl. Phys. Express **10**, 031002 (2017)
29. J.J. Wierer, A.A. Allerman, I. Montaño, M.W. Moseley, Appl. Phys. Lett. **105**, 061106 (2014)
30. Y. Zhang, R. Meng, Z.-H. Zhang, Q. Shi, L. Li, G. Liu, W. Bi, IEEE Photon. J. **9**, 2736642 (2017)
31. D.Y. Kim, J.H. Park, J.W. Lee, S. Hwang, S.J. Oh, J. Kim, C. Sone, E.F. Schubert, J.K. Kim, Light-Sci. Appl. **4**, e263 (2015)
32. J.W. Lee, J.H. Park, D.Y. Kim, E.F. Schubert, J. Kim, J. Lee, Y. Kim, Y. Park, J.K. Kim, ACS Photon. **3**, 2030 (2016)
33. J.W. Lee, D.Y. Kim, J.H. Park, E.F. Schubert, J. Kim, J. Lee, Y.-I. Kim, Y. Park, J.K. Kim, Sci. Rep. **6**, 22537 (2016)
34. P.-H. Fu, G.-J. Lin, H.-P. Wang, K.-Y. Lai, J.-H. He, Nano Energy **8**, 78 (2014)
35. K.-S. Im, C.-H. Won, S. Vodapally, D.-H. Son, Y.-W. Jo, Y. Park, J.-H. Lee, J. Cryst. Growth **441**, 41 (2016)
36. T. Fujii, Y. Gao, R. Sharma, E.L. Hu, S.P. Den Baars, S. Nakamura, Appl. Phys. Lett. **84**, 855 (2004)
37. H. Kim, K.K. Choi, K.K. Kim, J. Cho, S.N. Lee, Y. Park, J.S. Kwak, T.-Y. Seong, Opt. Lett. **33**, 1273 (2008)
38. J.H. Son, J.U. Kim, Y.H. Song, B.J. Kim, C.J. Ryu, J.L. Lee, Adv. Mater. **24**, 2259 (2012)
39. J. Ma, L. Wang, Z. Liu, G. Yuan, X. Ji, P. Ma, J. Wang, X. Yi, G. Wang, J. Li, Opt. Express **21**, 3547 (2013)
40. L.C. Wang, J. Ma, Z.Q. Liu, X.Y. Yi, H.W. Zhu, G.H. Wang, ACS Photon. **1**, 42 (2014)
41. G.-Y. Ha, T.-Y. Park, J.-Y. Kim, D.-J. Kim, K.-I. Min, S.-J. Park, IEEE Photon. Technol. Lett. **19**, 813 (2007)
42. C.H. Liu, R.W. Chuang, S.J. Chang, Y.K. Su, L.W. Wu, C.C. Lin, Mat. Sci. Eng. B **112**, 10 (2004)
43. Y.P. Hsu, S.J. Chang, Y.K. Su, S.C. Chen, J.M. Tsai, W.C. Lai, C.H. Kuo, C.S. Chang, IEEE Photon. Technol. Lett. **17**, 1620 (2005)
44. C.M. Tsai, J.K. Sheu, W.C. Lai, Y.P. Hsu, P.T. Wang, C.T. Kuo, C.W. Kuo, S.J. Chang, Y.K. Su, IEEE Electron Device Lett. **26**, 464 (2005)
45. C.-H. Ho, Y.-H. Hsiao, D.-H. Lien, M.S. Tsai, D. Chang, K.-Y. Lai, C.-C. Sun, J.-H. He, Appl. Phys. Lett. **103**, 161104 (2013)
46. S. Oh, P.-C. Su, Y.-J. Yoon, S. Cho, J.-H. Oh, T.-Y. Seong, K.-K. Kim, Opt. Express **21**, A970 (2013)
47. S. Oh, K.J. Lee, S.J. Kim, K. Ha, J. Jeong, D. Kim, K.-K. Kimb, S.-J. Park, Nanoscale **9**, 7625 (2017)
48. K.H. Lee, H.J. Park, S.H. Kim, M. Asadirad, Y.T. Moon, J.S. Kwak, J.-H. Ryou, Opt. Express **23**, 20340 (2015)

49. Y. Guo, Y. Zhang, J. Yan, H. Xie, L. Liu, X. Chen, M. Hou, Z. Qin, J. Wang, J. Li, Appl. Phys. Lett. **111**, 011102 (2017)
50. Y. Guo, Y. Zhang, J. Yan, X. Chen, S. Zhang, H. Xie, P. Liu, H. Zhu, J. Wang, J. Li, Appl. Phys. Express **10**, 062101 (2017)
51. A. David, H. Benisty, C. Weisbuch, Rep. Prog. Phys. **75**, 126501 (2012)
52. Y.C. Shin, D.H. Kim, E.H. Kim, J.-M. Park, K.-M. Ho, K. Constant, J.H. Choe, Q.H. Park, H.-Y. Ryu, J.H. Baek, T. Jung, T.G. Kim, IEEE J. Quantum Electron. **46**, 116 (2010)
53. M. Djavid, Z. Mi, Appl. Phys. Lett. **108**, 051102 (2016)
54. T.N. Oder, K.H. Kim, J.Y. Lin, H.X. Jiang, Appl. Phys. Lett. **84**, 466 (2004)
55. A. David, T. Fujii, R. Sharma, K. McGroddy, S. Nakamura, S.P. DenBaars, E.L. Hu, C. Weisbuch, H. Benisty, Appl. Phys. Lett. **88**, 061124 (2006)
56. C.-Y. Liu, C.-Y. Huang, P.-Y. Wu, J.-K. Huang, T.S. Kao, A.-J. Zhou, D.-W. Lin, Y.S. Wu, C.-Y. Chang, IEEE Electron Device Lett. **37**, 452 (2016)
57. J.J. Wierer, A. David, M.M. Megens, Nat. Photonics **3**, 163 (2009)
58. E. Yik-Khoon, P. Kumnorkaew, R.A. Arif, T. Hua, H. Zhao, J.F. Gilchrist, N. Tansu, IEEE J. Sel. Topics Quant. Electron. **15**, 1218 (2009)
59. D. Qing-an, L. Kang, K. Fanmin, C. Xinlian, Z. Jia, J. Disp. Technol. **10**, 909 (2014)
60. Q. Zhang, K.H. Li, H.W. Choi, IEEE Photon. Technol. Lett. **24**, 1642 (2012)
61. C.T. Kuo, L.H. Hsu, B.H. Huang, H.C. Kuo, C.C. Lin, Y.J. Cheng, Appl. Opt. **55**, 7387 (2016)
62. D.-W. Lin, J.-K. Huang, C.-Y. Lee, R.-W. Chang, Y.-P. Lan, C.-C. Lin, K.-Y. Lee, C.-H. Lin, P.-T. Lee, G.-C. Chi, H.-C. Kuo, J. Disp. Technol. **9**, 285 (2013)
63. S.X. Jiang, Z.Z. Chen, X.Z. Jiang, X.X. Fu, S. Jiang, Q.Q. Jiao, T.J. Yu, G.Y. Zhang, CrystEngComm **17**, 3070 (2015)
64. J.B. Kim, S.M. Kim, Y.W. Kim, S.K. Kang, S.R. Jeon, N. Hwang, Y.-J. Choi, C.S. Chung, Jpn. J. Appl. Phys. **49**, 042102 (2010)
65. Y.H. You, F.C. Chu, H.C. Hsieh, W.H. Wu, M.L. Lee, C.H. Kuan, R.-M. Lin, RSC Adv. **5**, 67809 (2015)
66. Y.J. Moon, D. Moon, J. Jang, J.Y. Na, J.H. Song, M.K. Seo, S. Kim, D. Bae, E.H. Park, Y. Park, S.-K. Kim, E. Yoon, Nano Lett. **16**, 3301 (2016)
67. D. Zubia, S.H. Zaidi, S.R.J. Brueck, S.D. Hersee, Appl. Phys. Lett. **76**, 858 (2000)
68. J.J. Chen, Y.K. Su, C.L. Lin, S.M. Chen, W.L. Li, C.C. Kao, IEEE Photon. Technol. Lett. **20**, 1193 (2008)
69. C.-C. Kao, Y.-K. Su, C.-L. Lin, J.-J. Chen, Appl. Phys. Lett. **97**, 023111 (2010)
70. Y. Zhang, T. Wei, J. Wang, D. Lan, Y. Chen, Q. Hu, H. Lu, J. Li, AIP Adv. **4**, 027123 (2014)
71. V.C. Su, P.H. Chen, R.M. Lin, M.L. Lee, Y.H. You, C.I. Ho, Y.-C. Chen, W.-F. Chen, C.-H. Kuan, Opt. Express **21**, 30065 (2013)
72. J.W. Pan, P.J. Tsai, K.D. Chang, Y.Y. Chang, Appl. Opt. **52**, 1358 (2013)
73. Z. Lin, H. Yang, S. Zhou, H. Wang, X. Hong, G. Li, Cryst. Growth Des. **12**, 2836 (2012)
74. Y. Cheng, L. Wang, Y. Zhang, H. Zheng, J. Ma, X. Yi, G. Wang, J. Li, ECS Solid State Lett. **2**, Q93 (2013)
75. W.C. Ke, F.W. Lee, C.Y. Chiang, Z.Y. Liang, W.K. Chen, T.Y. Seong, ACS Appl. Mater. Interfaces **8**, 34520 (2016)
76. C.H. Chiu, H.H. Yen, C.L. Chao, Z.Y. Li, P. Yu, H.C. Kuo, T.C. Lu, S.C. Wang, Appl. Phys. Lett. **93**, 081108 (2008)
77. K. Ueda, Y. Tsuchida, N. Hagura, F. Iskandar, K. Okuyama, Y. Endo, Appl. Phys. Lett. **92**, 101101 (2008)
78. S.J. An, Y.J. Hong, G.C. Yi, Y.J. Kim, D.K. Lee, Adv. Mater. **18**, 2833 (2006)
79. J. Kim, H. Woo, K. Joo, S. Tae, J. Park, D. Moon, et al., Sci. Rep. **3**, 3201 (2013)
80. P. Dong, J. Yan, J. Wang, Y. Zhang, C. Geng, T. Wei, P. Cong, Y. Zhang, J. Zeng, Y. Tian, L. Sun, Q. Yan, J. Li, S. Fan, Z. Qin, Appl. Phys. Lett. **102**, 241113 (2013)
81. L. Zhang, F. Xu, J. Wang, C. He, W. Guo, M. Wang, B. Sheng, L. Lu, Z. Qin, X. Wang, B. Shen, Sci. Rep. **6**, 35934 (2016)
82. K. Okamoto, I. Niki, A. Shvartser, Y. Narukawa, T. Mukai, A. Scherer, Nat. Mater. **3**, 601 (2004)

83. X. Gu, T. Qiu, W. Zhang, P.K. Chu, Nanoscale Res. Lett. **6**, 199 (2011)
84. A. Fujiki, T. Uemura, N. Zettsu, M. Akai-Kasaya, A. Saito, Y. Kuwahara, Appl. Phys. Lett. **96**, 043307 (2010)
85. M.-K. Kwon, J.-Y. Kim, B.-H. Kim, I.-K. Park, C.-Y. Cho, C.C. Byeon, S.-J. Park, Adv. Mater. **20**, 1253 (2008)
86. C.-H. Lu, C.-C. Lan, Y.-L. Lai, Y.-L. Li, C.-P. Liu, Adv. Funct. Mater. **21**, 4719 (2011)
87. C. Zhang, N. Tang, L. Shang, L. Fu, W. Wang, F. Xu, X. Wang, W. Ge, B. Shen, Sci. Rep. **7**, 2358 (2017)
88. J.-H. Sung, B.-S. Kim, C.-H. Choi, M.-W. Lee, S.-G. Lee, S.-G. Park, E.-H. Lee, O. Beom-Hoan, Microelectron. Eng. **86**, 1120 (2009)
89. J.-H. Sung, J.S. Yang, B.-S. Kim, C.-H. Choi, M.-W. Lee, S.-G. Lee, S.-G. Park, E.-H. Lee, B.-H. O, Appl. Phys. Lett. **96**, 261105 (2010)
90. S.H. Chuang, C.S. Tsung, C.H. Chen, S.L. Ou, R.H. Horng, C.Y. Lin, D.-S. Wuu, ACS Appl. Mater. Interfaces **7**, 2546 (2015)
91. N. Gao, K. Huang, J. Li, S. Li, X. Yang, J. Kang, Sci. Rep. **2**, 816 (2012)
92. K. Huang, N. Gao, C. Wang, X. Chen, J. Li, S. Li, X. Yang, J. Kang, Sci. Rep. **4**, 4380 (2014)
93. J. Cho, J.H. Park, J.K. Kim, E.F. Schubert, Laser Photonics Rev. **11**, 1600147 (2017)

Chapter 10
Enhancing Wall-Plug Efficiency for Deep-UV Light-Emitting Diodes: From Crystal Growth to Devices

SM Islam, Vladimir Protasenko, Shyam Bharadwaj, Jai Verma, Kevin Lee, Huili (Grace) Xing, and Debdeep Jena

10.1 Introduction

Sub-280-nm deep ultraviolet (DUV) photonic devices (Light-Emitting Diodes and Lasers) are in strong demand due to their applications in several areas including water disinfection, medical diagnostics, and security. Replacing mercury-based DUV lamps by semiconductor LEDs is environmentally friendly, enables miniaturization, and can ensure higher energy efficiency and portability. The family of high Al-containing $Al_xGa_{1-x}N$ alloy ($x > 0.5$) semiconductors is well suited for such LEDs. DUV emission from LEDs using AlGaN multi-quantum well light-emitting active region has been demonstrated in many reports [1–7]. Though AlGaN UV-C LEDs spanning the 210–280-nm spectral window have been demonstrated, they suffer from low external quantum efficiency (EQE) [7], which drops dramatically for wavelengths shorter than 240 nm.

The reasons for this efficiency drop are manifold. The LEDs are typically grown on nonnative substrates such as sapphire with a large lattice mismatch, leading to dislocation densities $\sim 1 \times 10^{10}$ cm^{-2}. Non-radiative recombination in the quantum well active regions causes a significant decrease in the internal quantum efficiency (IQE). Spontaneous and piezoelectric polarization-induced internal electric fields in the polar AlGaN crystal spatially separate the electron and hole wavefunctions, reducing the overlap integral and the oscillator strength for interband radiative transitions [8]. This quantum-confined Stark effect (QCSE) reduces the IQE by lowering the radiative recombination rate.

SM Islam (✉) · V. Protasenko · S. Bharadwaj · K. Lee · H. (Grace) Xing · D. Jena
Cornell University, Ithaca, NY, USA
e-mail: smi29@cornell.edu; vvp7@cornell.edu

J. Verma
University of Notre Dame, Notre Dame, IN, USA

© Springer International Publishing AG, part of Springer Nature 2019

J. Li, G. Q. Zhang (eds.), *Light-Emitting Diodes*, Solid State Lighting Technology and Application Series 4, https://doi.org/10.1007/978-3-319-99211-2_10

Poor doping efficiency especially for p-AlGaN causes ohmic losses at the LED contact regions. Unlike the visible light emitters, the activation energy of acceptor-type dopants for Al-rich AlGaN alloys is $\gg$kT, inhibiting activation of dopants at 300K. Lack of suitable metal for ensuring ohmic contact further reduces the wall-plug efficiency. Low density of holes in the p-region requires higher operating voltages for the UV-LEDs, which further causes overflow of electrons in the p-region and therefore reduction of injection efficiency.

The extraction of generated photons from the LEDs causes further challenge in achieving high efficiency. The light extraction is limited by total internal reflection due to refractive index mismatch. Polarization property of the emitted light from the active region is also an important factor that decides the light extraction efficiency. Use of p-GaN on top of UV-LEDs to reduce the contact resistance to metal further reduces the light extraction by absorption.

In the subsequent sections, an organized approach to achieve efficient deep-UV emission with novel heterostructure design methods is presented. Section 10.2 gives an introduction to various loss mechanisms that limit the overall efficiency of deep-UV LEDs. This motivates the need of new heterostructure design to overcome the losses. Section 10.3 discusses the use of ultrathin GaN/AlN quantum heterostructures to enhance the internal quantum efficiency and the light extraction efficiency components from theoretical perspective. The crystal growth using plasma-assisted molecular beam epitaxy of ultrathin GaN/AlN quantum structures is presented in Sect. 10.4. The experimentally measured IQE enhancement of GaN/AlN compared to commonly used AlGaN-based design is presented. The use of polarization-induced doping to enhance injection and wall-plug efficiency is discussed in Sect. 10.5. The effectiveness of polarization-induced doping over conventional doping is manifested by cryogenic operation of a deep-UV LED. Finally, the enhancement of light extraction efficiency by the use of GaN/AlN quantum structures is discussed in Sect. 10.6.

10.2 UV-LED Efficiency Components

The efficiency of the best reported UV LEDs so far is ~20% for ~280-nm emission [9], which lags far behind their visible counterparts. The efficiency decreases dramatically at shorter wavelengths [10]. A summary of the reasons behind low efficiency of UV LEDs is presented here. The performance metric of UV LEDs is the external quantum efficiency (EQE) which is composed of three components:

$$\eta_{\mathrm{EQE}} = \eta_{\mathrm{IQE}} \times \eta_{\mathrm{INJ}} \times \eta_{\mathrm{EXTR/LEE}} \tag{10.1}$$

where

$$\eta_{\mathrm{EQE}} = \frac{rate\ of\ emitted\ photons}{rate\ of\ carriers\ injected\ into\ LED}$$

$$\eta_{\mathrm{IQE}} = \frac{rate\ of\ generated\ photons}{rate\ of\ carriers\ injected\ into\ active\ region}$$

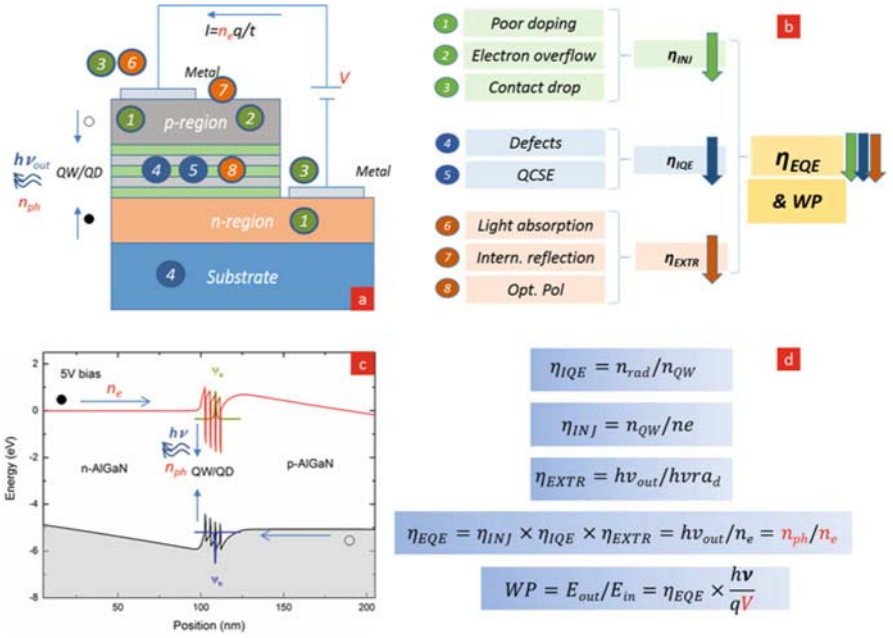

Fig. 10.1 Summary of loss mechanisms in DUV LEDs: (**a**) schematic showing locations where losses occur (V: applied bias, I: current, n_e =number of injected electrons, n_{ph} =number of emitted photons, (**b**) description of losses, (**c**) energy band diagram for a forward-biased LED to visualize the loss mechanisms, (**d**) efficiency equations, n_{rad} =No. of electrons recombining radiatively, n_{QW} =electrons captured in the QW, $h\nu_{\text{out}}$ =released photon energy, $h\nu_{\text{rad}}$ =generated photon energy, WP=Wall-plug efficiency (Output power/Input power)

$$\eta_{\text{INJ}} = \frac{rate\ of\ carriers\ injected\ into\ active\ region}{rate\ of\ carriers\ injected\ into\ LED}$$

$$\eta_{\text{EXTR/LEE}} = \frac{rate\ of\ emitted\ photons}{rate\ of\ generated\ photons}.$$

Each of these efficiency components is briefly discussed in the following in context to DUV photonic devices (Fig. 10.1).

10.2.1 Internal Quantum Efficiency (IQE)

The internal quantum efficiency (IQE) is defined as the ratio of rates of radiative recombination to total recombination:

$$\eta_{\text{IQE}} = \frac{R_r}{R_r + R_{nr}}\ . \tag{10.2}$$

The recombination rates can be expressed in terms of lifetimes as:

$$R_r = \frac{1}{\tau_r} , \tag{10.3}$$

and similarly,

$$R_{nr} = \frac{1}{\tau_{nr}} . \tag{10.4}$$

Therefore, Eq. (10.4) reduces to:

$$\eta_{\text{IQE}} = \frac{R_r}{R_r + R_{nr}} = \frac{\frac{1}{\tau_r}}{\frac{1}{\tau_r} + \frac{1}{\tau_{nr}}} = \frac{1}{1 + \frac{\tau_r}{\tau_{nr}}} \tag{10.5}$$

where R_r (R_{nr}) and τ_r (τ_{nr}) represent radiative (non-radiative) rate and lifetime. Radiative lifetime depends on material constants, oscillator strength, and operating wavelength:

$$\tau_r \propto \frac{\lambda^2}{f_{\text{osc}}} . \tag{10.6}$$

Non-radiative recombination through defects is often an Arrhenius function of temperature. This is expressed as:

$$\tau_{nr} = \tau_{nr0} e^{\frac{E_a}{kT}} . \tag{10.7}$$

Using this, IQE is expressed as:

$$\eta_{\text{IQE}} = \frac{1}{1 + ae^{-\frac{E_a}{kT}}} \tag{10.8}$$

where a = $\frac{\tau_r}{\tau_{nr0}}$ and E_a is the activation energy for non-radiative recombination centers.

The lifetime represents the average time carriers spend before they recombine either radiatively or non-radiatively. If the radiative lifetime is much shorter, that means an electron radiatively recombines with a hole before it recombines through a defect non-radiatively. In order to have a high $\eta_{\text{IQE}} \sim 1$, the necessary condition is $\tau_r \ll \tau_{nr}$ (Fig. 10.2).

The IQE is also explained with the ABC model [12] by the following equation:

$$\eta_{\text{IQE}} = \frac{Bn}{A + Bn + Cn^2} \tag{10.9}$$

where A is the monomolecular non-radiative recombination coefficient, B is the bimolecular radiative recombination coefficient, C is the Auger recombination coefficient, and n is the electron concentration. SRH recombination process is usually caused by defects or dislocations in the crystal. Auger recombination is

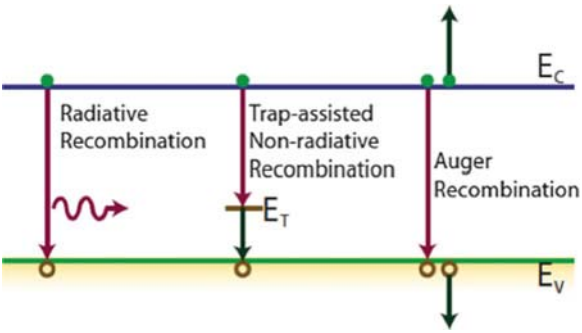

Fig. 10.2 Schematic energy band diagram showing various recombination mechanisms in an LED [11]

only considered at high carrier densities ($>1\times10^{19}$ cm^{-3}). Plenty of studies have been performed on elimination of the efficiency droop in visible LEDs [13–15]. Chichibu et al. have shown that dislocations act as non-radiative centers (NRCs) [16]. However, InGaN-based active region's localization effect reduces trapping of carriers into threading dislocations causing efficient photon emission. Dai et al. have also used photoluminescence to extract the IQE dependence on the dislocation density in the epi-layer [17]. They concluded that the threading dislocations reduce the IQE of the InGaN-based visible light emitters. Similar techniques have been applied to AlGaN-based active region for IQE estimation.

For deep-UV LEDs, the choice of the substrate is limited to AlN due to favorable bandgap. At present, AlN is available both as templates on a foreign substrate or as bulk single crystals. AlN on sapphire (Al_2O_3) is the most commonly used templates for deep-UV LEDs. Due to large lattice mismatch of 13.3% [18] between AlN and sapphire, the templates have threading dislocation density (TDD) of $\sim10^{10}$cm^{-2}. There are several techniques to further reduce the dislocation in the AlN film. For example, Hirayama et al. have used epitaxial lateral overgrowth (ELO) method to reduce the TDD down to 3×10^{8}cm^{-2} [19, 20]. Jmerik et al. have employed AlGaN/AlN superlattice and insertion of ultrathin GaN layers in the AlN to reduce the TDD to $\sim6\times10^{9}$cm^{-2} [21]. To achieve low TDD, single crystal bulk AlN is the most desired substrate. Using physical vapor transport (PVT) crystal growth technique, single crystal bulk AlN substrate with a TDD as low as 10^{4}cm^{-2} has been achieved [22].

10.2.1.1 Threading Dislocations

Internal quantum efficiency (IQE) decreases due to high densities of threading dislocations (TDs, τ_{nr} is shortened) and due to the quantum-confined stark effect (QCSE, τ_r becomes large). In the presence of high ($>10^9$ cm^{-2}) dislocation densities, the IQE decreases rapidly. The effect of TDs on the reduction of IQE is discussed in Speck et al. [23] and Kneissl et al. [10]. Because dislocations act as non-radiative recombination centers, they increase the rate of the non-radiative SRH process in LEDs (increase the A coefficient value).

Increasing IQE with low TDD motivates the use of high-quality bulk AlN substrates for UV applications. Unfortunately, such substrates are extremely expensive compared to AlN templates and currently have significant absorption in the deep-UV range because of carbon-based defects which absorb emission shorter than 265 nm [24]. Continuous improvement of bulk crystal growth techniques is helping to reduce this sub-bandgap absorption, and bulk crystals will eventually replace AlN templates on sapphire for deep-UV applications specifically for lasers. Recently, the growth of thick (~100s of nm) AlGaN with Al composition of 65% has been realized on bulk AlN substrates with small relaxation (<10%) [25]. These promising results motivate the use of bulk AlN for LED structures with low dislocation densities.

10.2.1.2 Quantum-Confined Stark Effect (QCSE)

The other factor leading to low IQE is the reduction of the oscillator strength by QCSE (Fig. 10.3). III-nitride heterostructures are commonly grown on polar c-plane AlN surface. This results in built-in polarization charges at the hetero-interfaces due to both spontaneous and piezoelectric components. The polarization charges result in electric fields in the active region (i.e., quantum wells), causing the spatial separation of the electron and hole wavefunctions and reduction of their wavefunction overlap. This also reduces the oscillator strength which is expressed as:

$$f_{\text{osc}} \propto \lambda \times \left| \int \psi_e \psi_h \right|; \tag{10.10}$$

The integral in this equation represents wavefunction overlap. Since the IQE is proportional to the oscillator strength, it is reduced because of QCSE.

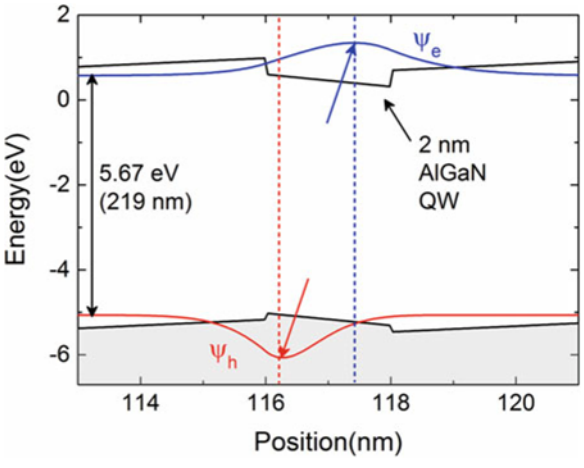

Fig. 10.3 QCSE in thick AlGaN QWs. Separation of electron and hole wavefunction is shown explicitly using energy band diagram

This undesirable reduction in the oscillator strength due to QCSE can be avoided by using nonpolar/semipolar-oriented substrates, where the polarization charges are low, or simply absent. Alternatively, for growth on polar substrates, the use of very thin quantum structures can also be very effective in solving this problem. The ultrathin quantum structures enhance the overlap significantly and therefore can boost the IQE even in heterostructures on polar substrates.

10.2.2 Injection Efficiency (INJ) and Wall-Plug Efficiency (WPE)

Wall-plug efficiency (WPE) is a measure of useful light output power to input electrical power and is limited by ohmic losses in injection regions of the LED. Optimal injection regions are transparent to light emission, requiring an aluminum content greater than 65% for ~250-nm emitters, and leads to high dopant activation energies [4]. Difficulty in incorporating dopants especially acceptor type into these wide-bandgap AlGaN cladding regions compounded with low activation of dopant impurities leads to high sheet resistances and contact resistances and hence large ohmic losses. For high-aluminum composition, n-cladding regions transparent to ~260-nm emission, sheet resistances as low as 0.0075 Ωcm, and contact resistances of $\sim 1 \times 10^{-6}$ Ωcm^2 have been reported [26, 27] as measured by the transmission line method (TLM) and Hall effect. However, p-cladding regions exhibit conductivities that are at best two orders of magnitude lower [28–36], reducing the WPE for 270-nm emitters to ~6% [37].

A strategy widely used to enhance dopant activation and thus WPE is polarization-induced doping. Polarization-induced doping utilizes the inherent spontaneous and piezoelectric polarization properties of the wurtzite crystal structure to ionize dopants more effectively [38]. As shown in Fig. 10.4, polarization-induced doping can enhance conductivity greatly over impurity doping alone. With proper tuning of well and barrier thickness in superlattices, enhanced vertical and lateral transport in p-type layers can be achieved.

Simply enhancing carrier transport is not enough to enhance EQE for LEDs. Equally necessary is capturing the carriers in the active region so that radiative recombination may occur. Injection efficiency (INJ) is a measure of the proportion of carriers in the active region versus total carriers generated. Use of quantum structures such as quantum dots/disks and wells provides carrier confinement, though carriers may still escape beyond the active region into the opposite cladding region. Generally, due to their lower effective mass, electrons are most likely to escape beyond the active region. Use of an abrupt heterojunction electron blocking layer or compositionally graded p-type cladding region can help eliminate carrier escape and enhance the injection efficiency [39].

Another consequence of using Al-rich AlGaN for the p/n regions is the formation of Schottky contact between metal and the doped region. Due to wide bandgap of

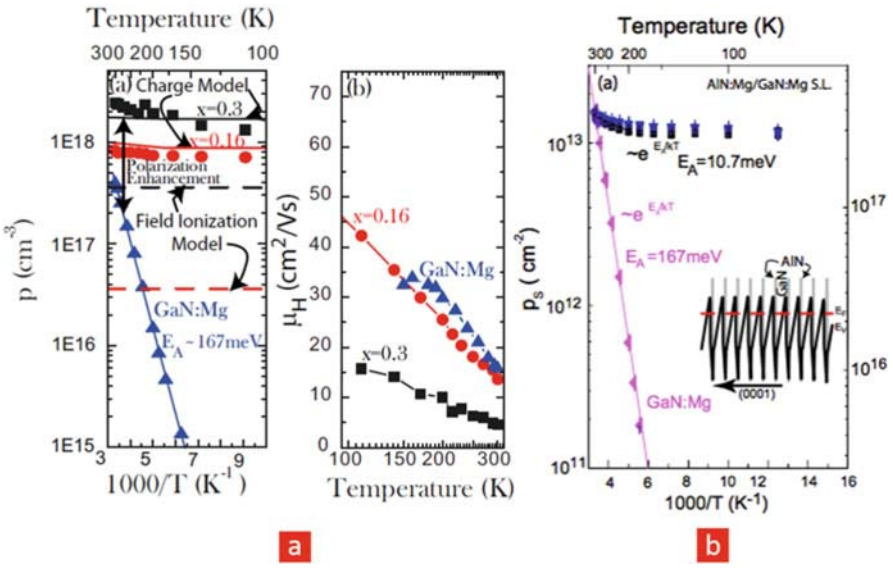

Fig. 10.4 (**a**) Temperature-dependent Hall data for a polarization-doped compositionally graded p-GaN sample on N-polar substrate, (**b**) sheet charge measured by Hall effect for one constant composition GaN sample (pink dots) and two superlattice samples (blue and black dots) showing the lack of freeze-out due to polarization-induced 2DEGs [38]

these AlGaN alloys, metals with desired work functions that can form low-resistance ohmic contacts to either n- or p-type AlGaN are not available. This introduces further increase in undesirable voltage drop at the contacts.

As a solution to these problems, polarization-induced doping is proposed for the n and p regions of deep-UV LEDs. It will be demonstrated next that this technique is very effective in boosting the carrier densities, even at cryogenic temperature. Since the polarization is a very weak function of temperature, the use of polarization-induced doping in deep-UV LED structures has made it possible to observe the operation of the devices at cryogenic temperatures. The heterostructures used for polarization-induced doping also reduce the electron overflow without introducing additional potential barriers for hole injection into the active region. Consequently, the voltage drop and loss outside the active region are reduced and both the INJ and WPE are enhanced.

10.2.3 Light Extraction Efficiency (LEE)

Once light is generated within the active region of an LED, it must escape in order to be collected for any useful application. Light extraction for deep-UV LEDs poses a challenge due to the high refractive index differences between the semiconductor–air interfaces and absorbing contact layers. Such a large difference promotes total internal reflection and reduces the escape cone down to $\sin^{-1}(n_0/n_s) = 23°$ for a

GaN/air interface. The photons emitted from the Al-rich AlGaN alloy are mostly TM polarized. The TE component of emitted light decreases, as the Al composition increases. Above ~70% AlGaN composition, the emission is predominantly TM polarized. This means that the light is emitted perpendicular to the growth direction towards the side of the wafer which poses an added challenge for efficient light extraction. Clever active region design can promote out-of-plane (TE) emission over TM emission [6], though total internal reflection and absorption still limit LEE in conventional devices to ~9% [9]. Light that is total-internally reflected may escape after several round trips, but absorbing defects, metal contact pads, and p-GaN contact layers make such a process unlikely. Light extraction efficiency (LEE) for 260-nm LEDs is a bottleneck for LED EQE, remaining around 10% [9] prior to specific preparations for enhancing light extraction.

Several methods are available for enhancing light extraction. Surface roughening promotes light extraction by changing the angle at which photons reach the semiconductor–air interface. Roughening can be achieved through dry or wet etching or polishing, and can enhance LEE by >40% (demonstrated at 326 nm by Zhang et al. [40]). For flip-chipped LEDs, light extraction can be enhanced through the use of reflective contacts (such as Rh or Al for 275-nm diodes) [9] or dielectric mirror stacks which serve to reflect light that travels up towards the p-layers back to the substrate (or opposite if not flip-chipped). Such a method can be combined with patterning of contact layers to reduce absorbance [4].

Use of p-AlGaN contact layers in place of commonly used p-GaN can reduce absorbance and enhance LEE [41]. Modifying the shape of the LED itself through truncated inverted pyramid (TIP) design has been shown to improve LEE by redirecting light towards the surface more effectively (demonstrated at visible wavelengths by Krames et al. [42]).

In addition to these methods, LED packaging serves to further improve light extraction. Encapsulation with refractive index matched to the semiconductor will allow all emitted light to be coupled into it, and if a spherical shape is chosen, all light will have normal incidence to the surface preventing total internal reflection. The best results to date for wavelengths of 275 nm use a combination of flip-chip packaging with resin, a reflective Rh p-electrode, patterned sapphire substrates, and p-AlGaN contact layers to achieve LEE of ~50%, with device structure shown in Fig. 10.5 [9].

LEE can be improved by using ultrathin GaN quantum structures as the deep-UV emitting active region instead of Al-rich AlGaN. Since GaN has TE polarized emission property, it is expected to be more effective in enhancing the light extraction compared to Al-rich AlGaN alloy active regions.

Based on the discussion on different efficiency components, ultrathin GaN/AlN superlattice is a promising candidate to replace the AlGaN-based active regions to enhance the IQE (by reduction of QCSE) and the LEE (by enhanced TE emission). The following sections of the chapter discuss such efficiency enhancement with ultrathin GaN/AlN quantum structures.

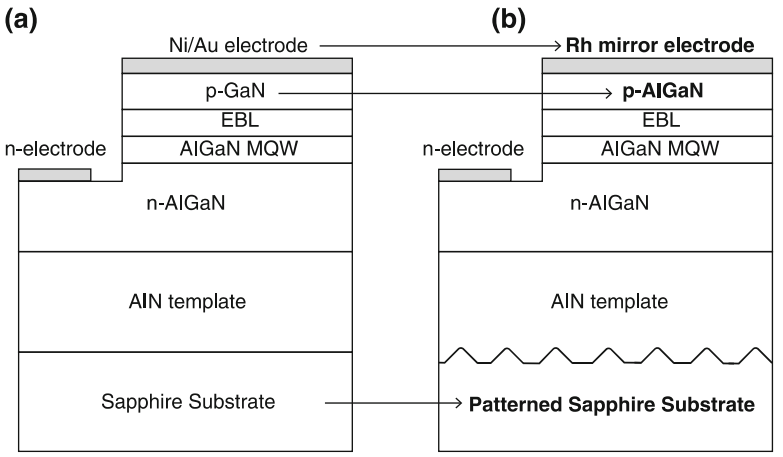

Fig. 10.5 (**a**) Conventional LED structure, (**b**) UV LED structure with patterned sapphire substrate, p-AlGaN contact layer, and Rh mirror electrode using flip-chip geometry and encapsulant resin (not shown) for improved light extraction [9]

10.3 Deep-UV Photon Emission from Extreme Quantum-Confined GaN/AlN Heterostructures

The conventional design of DUV photonic devices (LEDs and LASERs) employs high Al-containing $Al_xGa_{1-x}N$ alloys as the light-emitting active region material. The benefit of using $Al_xGa_{1-x}N$ is the tunability of the emission wavelength over a wide range from 200 nm (x:1.0, 6.2 eV) to 360 nm (x:0.0, 3.4 eV) encompassing the UV-A (400-320 nm), UV-B (320-280 nm), and the UV-C (280-200 nm) spectral regimes. But as the shorter wavelengths (<250 nm) are approached, the AlGaN-active region-based design suffers from several challenges. This section discusses a plausible alternative: use of ultrathin GaN as the active region material to overcome these challenges.

10.3.1 Motivation of Using GaN Instead of AlGaN

To date, sub-280-nm LEDs suffer from very low external quantum efficiency (<10%) [7] due in part to material-based challenges as well as physical challenges. Material-based challenges include high dislocation densities (10^{10} cm^{-2} in AlN and AlGaN layers) [43, 44] which lower EQE by diverting electrons from the active region, and high resistivities in the n- and p-AlGaN cladding regions [11, 40, 45–47] which incur large ohmic losses. Physical challenges for conventional AlGaN QW structures include severe valence band-mixing [48–52] and quantum-confined Stark effect (QCSE) mediated lowering of wavefunction overlap [8, 53, 54].

Specifically, studies have shown that transverse-magnetic (TM)-polarized emission dominates for high Al-containing (> 68%, $\lambda \sim$ 220–230 nm) AlGaN QWs due to a dominant crystal-field split-off (CH) sub-band [48]. TE-polarized spontaneous emission is favored over TM-polarized when Al composition is decreased, as the heavy hole (HH) sub-band gradually moves towards the higher energy light hole (LH) and CH sub-bands, causing conduction band to heavy hole (C-HH) transitions to occur with similar probability as C-LH and C-CH transitions around $\lambda \sim$ 250–300 nm. In this manner, a TE-polarized spontaneous emission rate (TE-R_{sp}) greater than TM-R_{sp} can be obtained, though both are still low at these wavelengths for two reasons: (1) the three valence sub-bands HH, LH, and CH are nearly degenerate leading to low populations in all sub-bands, and (2) QCSE causes a significant spatial separation between electron and HH sub-bands, leading to low wavefunction overlap and low recombination rates. It is therefore apparent that conventional AlGaN QW structures are not sufficient for realizing high-efficiency high-power mid-UV emitters.

Zhang et al. [55] have proposed a novel active region design of AlN-delta-GaN QW to replace the conventional AlGaN QW structures, so as to enhance TE-polarized emission at mid-UV wavelengths. Insertion of a delta-GaN layer in the active region provides two advantages: (1) strong valence band mixing is introduced, restoring the HH sub-band as the highest energy sub-band, leading to high TE-R_{sp} at $\lambda \sim$ 250–300 nm, and (2) QCSE is mitigated due to strong electron and hole wavefunction localization and overlap in the delta-GaN QW.

10.3.2 Evolution of Band Structure of Ultrathin AlN/GaN/AlN Heterostructures

To provide further insight, the band structure of ultrathin GaN/AlN superlattices is analyzed in this section followed by a comparison between GaN/AlN and AlGaN/AlN valence band structure. Basic 8×8 k.p theory fails to provide accurate estimates of the bandgap of GaN QWs/AlN barriers due to non-parabolicity of GaN's band structure and extreme quantum confinement. For this reason, many-body perturbation theory is employed to predict both electronic and optical bandgaps, including excitonic effects. The analysis proceeds as follows: first, the band structure of bulk GaN is calculated, followed by a calculation of the quantum confinement effect through inserting ultrathin layers (1 and 2 monolayers, or MLs) of GaN into an AlN matrix. Figure 10.6 summarizes the three calculations. The band structure of bulk GaN (Fig. 10.6a) follows expectations with a direct gap of 3.37 eV. The 2-ML GaN/AlN heterostructure is calculated to have a gap of 4.65 eV (266 nm), which increases to 5.45 eV for the 1-ML GaN/AlN heterostructure. Both gaps remain direct which is encouraging for use as DUV light emitters [56].

Valence band (VB) structure renormalization in GaN versus in AlGaN is looked at in more detail here. As previously mentioned, low Al-containing (<30% Al)

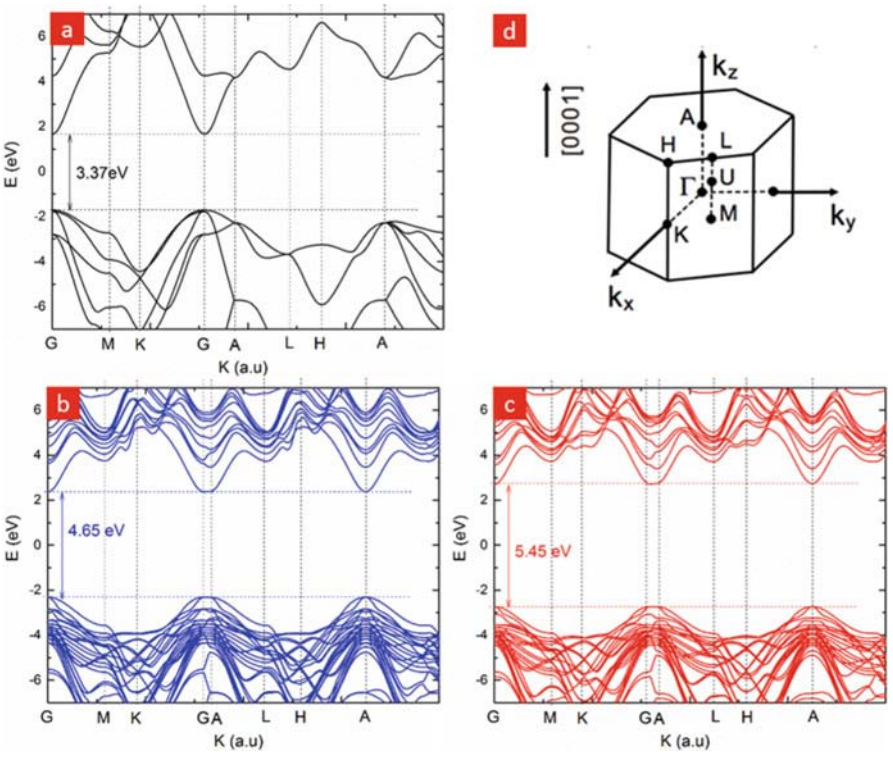

Fig. 10.6 First principle band structure calculation for (**a**) bulk GaN, (**b**) 2-ML GaN/AlN, and (**c**) 1-ML GaN/AlN superlattices. (**d**) The conventional high symmetry points of the band structure. Provided by Dr. Dylan Bayerl and Prof. Emmanouil Kioupakis

AlGaN heterostructures are used for UV-A and UV-B emitters. The VB structure for an AlN/$Al_{0.2}Ga_{0.8}N$ QW for such UV-A and UV-B emitters is shown in Fig. 10.7a. The HH, LH, and CH sub-bands that comprise the VB are indicated. Optical transitions occur between the conduction band (CB) minimum and VB maximum, which in the case of an AlN/$Al_{0.2}Ga_{0.8}N$ QW is the HH1 sub-band. Characteristics of the HH band necessitate TE-polarized emission from this transition. In contrast, Fig. 10.7b describes VB structure for an AlN/$Al_{0.8}Ga_{0.2}N$ QW, in which the CH sub-band is now the VB maximum. The optical transition occurring here is TM-polarized instead of TE-polarized. These high compositions of AlGaN are required for UV-C emission of <280 nm, which at the moment, constitutes the most demanding practical application.

Figure 10.7c shows the VB structure of an AlN/GaN heterostructure to compare to AlN/AlGaN heterostructures. GaN well thickness is held at 0.5 nm (2 monolayers) for this calculation, corresponding to a bandgap of 4.65 eV. In this scenario, the HH1 sub-band is the VB maximum, meaning that TE-polarized emission will be preferred. Such an emission polarization is advantageous for light extraction, and will further be discussed in Sect. 10.6.

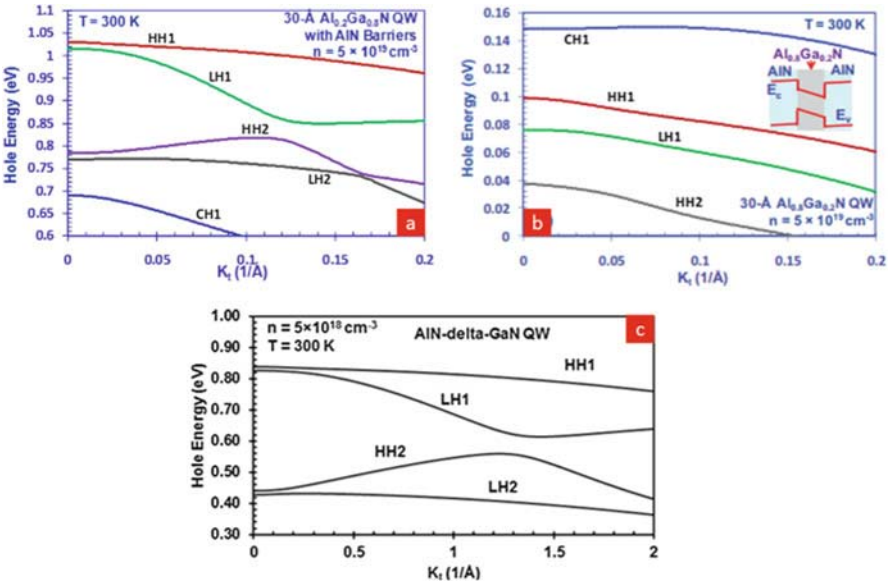

Fig. 10.7 Valence band structure renormalization using first principle band structure calculation for: (**a**) 3 nm $Al_{0.2}Ga_{0.8}N$/AlN QW, (**b**) $Al_{0.8}Ga_{0.2}N$/AlN, and (**c**) 0.5 nm GaN/AlN QW [55]. Reproduced from Appl. Phys. Lett. 98, 171111 (2011), with the permission of AIP Publishing

10.3.3 Achievable Wavelengths and Inhomogeneous Broadening: Theory vs Experiment

A combined approach of theoretical analysis along with experimental work is presented in this section that explores the range of wavelengths GaN/AlN quantum structures are capable of realizing in the DUV spectral region. The effect of change of GaN quantum well thickness and AlN barrier thickness is explored by both theory and experiments. First principle methods based on density functional and many-body perturbation theory were used to calculate the optical and electronic properties [56]; the GW method was used to find electronic gaps for 1- and 2-ML GaN/AlN heterostructures with varying AlN thickness, and the Bethe–Salpeter equation (BSE) method using Quantum ESPRESSO [57], BerkeleyGW [58], and Wannier90 [59] codes were used to find optical gaps. Experimental analysis was carried out through growing a series of samples via plasma-assisted molecular beam epitaxy (MBE). Samples were structurally characterized using high-resolution X-ray diffraction (HR-XRD) along with scanning transmission electron microscopic (STEM) analysis. Photoluminescence (PL) measurements were then performed for optical characterization.

The theoretical analysis is summarized in Fig. 10.8. A structural schematic, energy band diagram, and calculated electronic and optical bandgap is shown for 2 different GaN QW thicknesses (1 and 2 MLs) and AlN barrier thickness ranging

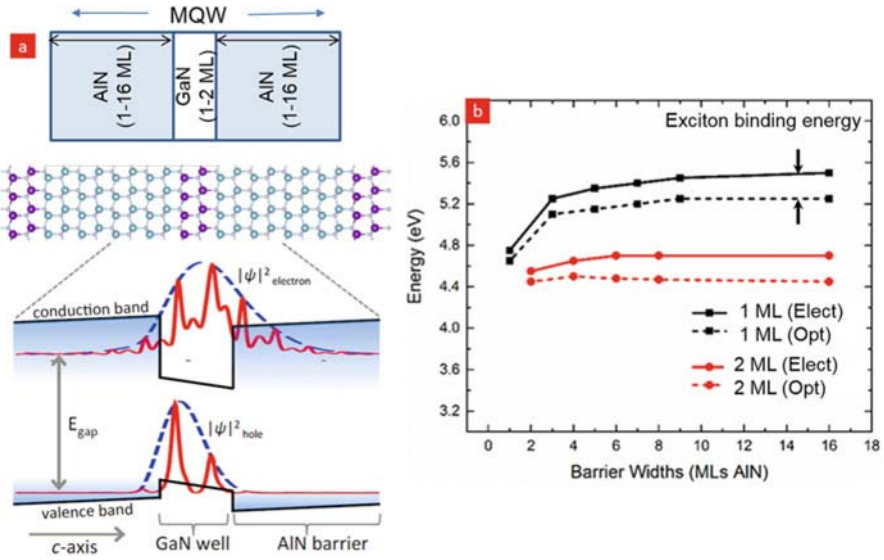

Fig. 10.8 First principle calculation of optical and electronic gap for ultrathin GaN/AlN superlattices: (**a**) simulated structure and the envelope function, (**b**) summary of calculated gap [56]. Reproduced from Appl. Phys. Lett. 109, 241102 (2016), with the permission of AIP Publishing

from 1–9 MLs. Data from 10–16 MLs AlN thickness have been extrapolated. Based on the theoretical prediction, it can be seen that deep-UV emission at ~5.2 eV and ~4.5 eV can be attained with 1-ML and 2-ML GaN QWs, respectively. Beyond 8-ML AlN barrier thickness, the effective bandgap is relatively constant.

Experimental data is summarized in Fig. 10.9 which includes the schematic structure of the MBE-grown samples, structural characterization by HR-XRD and STEM, and optical characterization by PL. The XRD in Fig. 10.9b shows a secondary GaN peak, which is a signature of GaN/AlN superlattice formation. Simulated XRD data agrees with the measured data suggesting that the targeted thicknesses were achieved. STEM analysis in Fig. 10.9c further confirms that ultrathin GaN layers with the desired thicknesses were present within the AlN matrix. From PL data measured at 300K and 77K, the sample with 1-ML GaN QWs had an optical gap around 5.5 eV, while the 2-ML GaN QW sample had a gap around 4.8 eV. Slight blue shift consistent with Varshni's law could be observed at the lower temperature.

Figures 10.8 and 10.10 compare and contrast the experimental data with theoretical simulation. Measured PL results agreed well with theory, especially for 1-ML GaN QWs, with discrepancy below 150 meV (Fig. 10.10). A slightly larger deviation was observed for the 2-ML GaN structures, potentially due to nonuniformity in the well thickness in the plane of the sample.

PL spectra in Fig. 10.11 show significant broadening (0.3–0.4 eV) due to carrier occupation and structural disorder. The occupational structural broadening

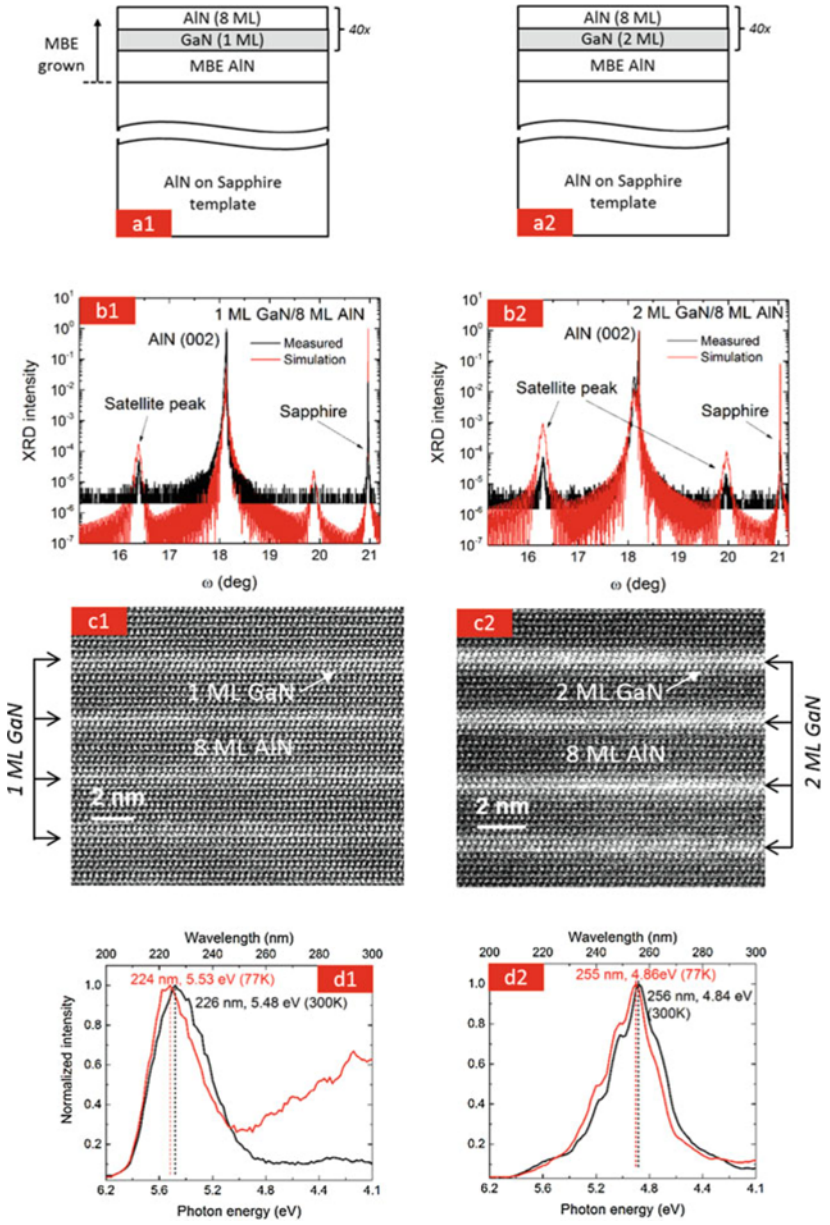

Fig. 10.9 Experimental verification for the simulated data: (**a**) structural layout, (**b**) XRD, (**c**) TEM characterization, and (**d**) PL measurements for some representative samples [56]. Reproduced from Appl. Phys. Lett. 109, 241102 (2016), with the permission of AIP Publishing

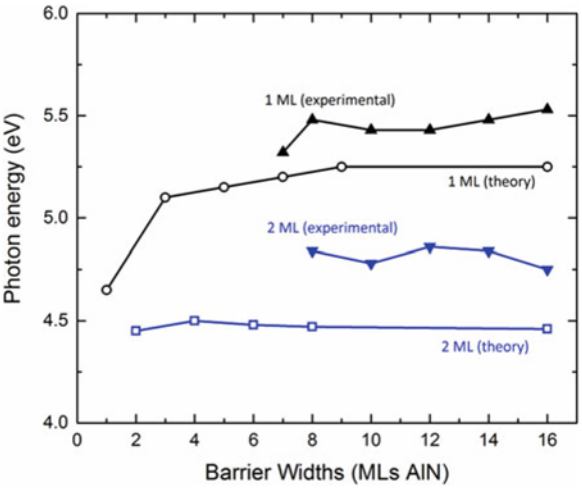

Fig. 10.10 Experimental data added to the simulated data of Fig. 10.8b for comparison [56]. Reproduced from Appl. Phys. Lett. 109, 241102 (2016), with the permission of AIP Publishing

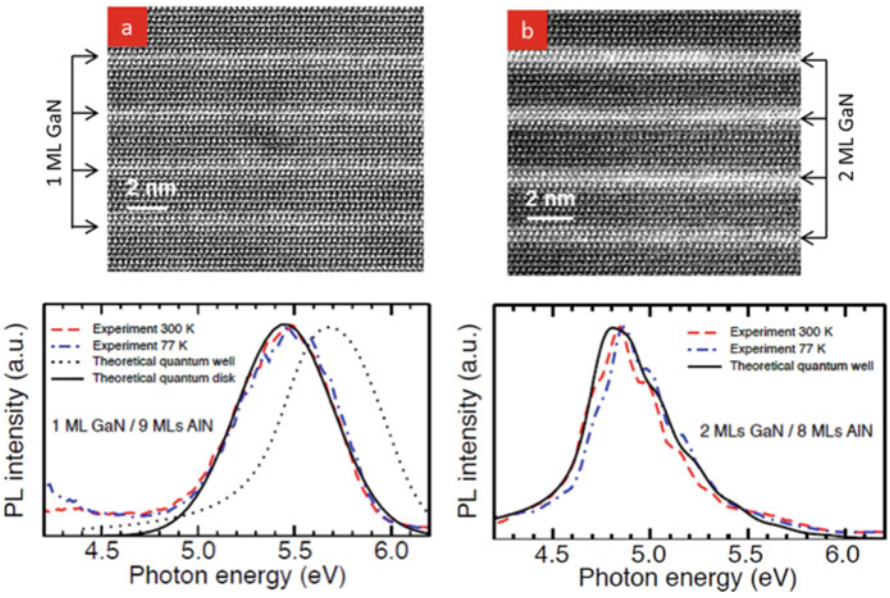

Fig. 10.11 Inhomogeneous broadening of the PL spectra: for (**a**) 2-ML GaN, (**b**) 1-ML GaN [56]. Reproduced from Appl. Phys. Lett. 109, 241102 (2016), with the permission of AIP Publishing

parameter has been estimated for 2-ML GaN QWs to be 0.22–0.32 eV from the slope of the logarithm of the high-energy PL tail, but estimation could not be carried out for 1-ML GaN structures as there was no well-defined linear region in the PL spectra.

Additionally, modeled spectra were compared with the experimental spectra for structures with 8–9-ML AlN barriers. Modeling was carried out with the Shockley

van Roosbroeck (SvR) equation. With proper choice of fitting parameters, excellent agreement for the 2-ML GaN structure between the SvR model and experiment was obtained both for lineshapes and peak positions. In contrast, regardless of choice of fitting parameters, the SvR model incorrectly predicted peak position (much higher emission energy than experiment) for 1-ML GaN structures, though the lineshape was accurate. The poor fit suggested that 1-ML GaN quantum structures did not exhibit well-like character, but rather luminesced as quantum disks with homogenously broadened emission at the electronic gap energy [60]. A very accurate fit was obtained by altering the 1 ML GaN structures as disks.

The peak position and lineshape predicted by the quantum disk model are governed by the electronic gap and broadening parameter. Broadening can be attributed to fractional GaN ML formation [61]. Any deviation from ideal monolayer formation leads to fractional ML formation, as observed in InN/GaN heterostructures [62], explaining the different PL characteristics of 1-ML and 2-ML GaN structures. Growth kinetics of ultrathin GaN lead to fractional instead of full coverage for 1-ML GaN, and lead to 1-ML plus 1 fractional ML when 2-ML GaN is intended. Thus, 1-ML GaN layers acted as isolated quantum disks, while 2-ML GaN layers still had well-like behavior as coverage was continuous. Another signature of fractional monolayer formation was broadening of the PL spectrum. Monolayer thickness fluctuations over 5–10-nm lateral distance could cause the observed broadening.

The first principle calculations and experimental data obtained by MBE grown samples suggest that ultrathin GaN/AlN superlattices can achieve DUV emission as short as 224 nm. The following section of the chapter discusses a brief introduction of the MBE system and the growth process of ultrathin GaN/AlN heterostructures using MBE.

10.4 MBE Growth of GaN/AlN Quantum Structures (Wells and Dots) for Enhanced IQE

10.4.1 MBE System in Brief

All samples discussed in the experimental part of this chapter were grown with plasma-assisted MBE system. MBE provides precise control over the thickness and composition of the grown epitaxial layer and therefore is best suited for ultrathin heterostructure epitaxy. The high purity sources (99.99999%) and the high vacuum (1×10^{-11} Torr) condition also ensure high quality of the material. In the following subsections, a short overview of the system itself, in situ RHEED-based characterization, and various MBE growth modes are presented showing how these are relevant to realize the desired GaN/AlN heterostructure.

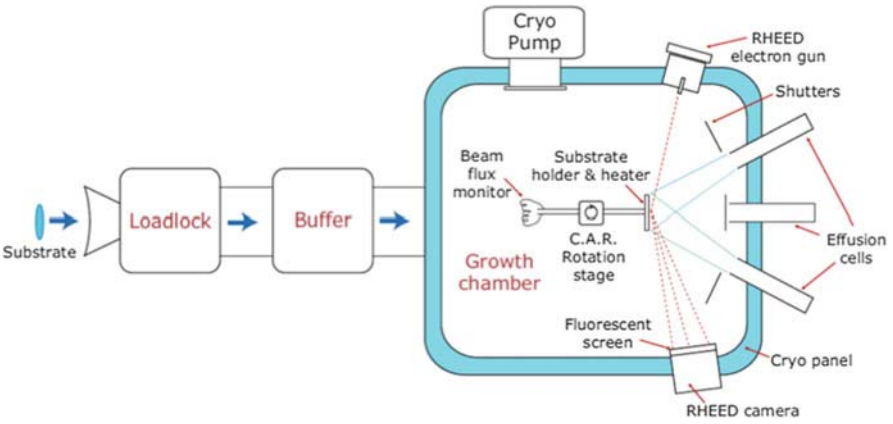

Fig. 10.12 Schematic for a typical MBE system [11]

10.4.1.1 Basic MBE Structure

The main features of an MBE system (Fig. 10.12) for epitaxial growth of crystals are ultrahigh vacuum (UHV) in the growth chamber and the use of ultrahigh purity (UHP) source materials for growth. In the UHV environment, the mean free path for molecules is longer than the physical MBE chamber dimensions. Thus, the molecular beam does not scatter and moves ballistically from the source to the surface of the desired substrate. This ensures a precision in the growth of pure crystals and heterostructures. A combination of cryogenic, turbo-molecular, and ion pumps are used to maintain the high level of vacuum in different sections of the system. The high purity source materials (i.e., group III: B, Al, Ga, and In) are loaded in effusion cells and heated to high temperatures ($\sim$1200°C) using resistive heaters to generate molecular beams. As shown in Fig. 10.12, shutters operated by pneumatic control block/allow the molecular beams from the effusion cells to be deposited on the substrate during growth. The flux of the beam from metal sources is controlled by varying the corresponding cell temperatures with an accuracy of $\sim$1°C. The resulting beam flux is measured with an ion gauge called the beam flux monitor (BFM).

The beam-equivalent pressure (BEP) measured by the BFM helps to control the specific growth conditions, and to reproduce a growth recipe that has been found optimum. During the growth of III-nitride semiconductors using a plasma-assisted MBE, chemically active group V elemental nitrogen is generated using an RF-based plasma source. The stable state of nitrogen gas is the molecular form N_2, which is inert and does not incorporate into the crystal during growth. To make the nitrogen species reactive and available for incorporation in the crystal, it is ionized to form atomic nitrogen using the RF plasma source. Ultrahigh purity nitrogen gas

is supplied through a mass flow controller (MFC) into the plasma unit at a controlled flow rate that determines the growth chamber pressure and the growth rate. A typical chamber pressure during growth is $\sim 2\times10^{-5}$ Torr.

The growth chamber is surrounded by an LN_2 cryo-panel that maintains the wall at a very low temperature. Unwanted molecular species condense on the wall and therefore do not incorporate in the crystal during growth. The substrate holder can be resistively heated by W-Re coils embedded in a PBN disk up to ~1000°C. Typical growth temperatures of III-nitride semiconductor layers are in the 600–900°C range.

The substrate holder and heater are connected to a continuous azimuthal rotation (CAR) stage that is rotated during growth at typically ~20 rpm to ensure uniformity. The CAR also enables the transfer of the samples in and out of the growth chamber. The two other chambers are the buffer chamber and the loadlock chamber. Samples are introduced into the UHV environment of the MBE system from the atmospheric condition through the loadlock chamber, where it is heated at 200°C for a few hours for degassing and primarily the removal of adsorbed surface water. The buffer chamber is placed between the growth and the loadlock chamber and is used for sample preparation prior to growth. This process involves heating the sample to ~450°C for ~1–2 h for surface cleaning and degassing. The standby pressure for buffer chamber is $<5\times10^{-9}$ Torr. This pressure level can be maintained by an ion pump.

Proper surface cleaning of samples and carrier wafers is essential prior to loading. A typical process involves ultrasonication in organic solvents (acetone, methanol, and iso-propanol). Small (~1×1 cm) substrates are mounted on lapped 3" silicon carrier wafers by melting and resolidifying metallic indium paste. Larger wafers may be mounted directly without using the indium paste. These wafers are then loaded into the UHP N2 vented loadlock chamber and baked at 200°C for at least 5 h till the background chamber pressure reaches $<5\times10^{-9}$ Torr. This baking expels water molecules from the wafer surface. The samples are then transferred into the buffer chamber where they are baked at 450°C for 1.5 h. The samples from the buffer chamber are transferred into the growth chamber once the pressure difference between these chambers is a minimum. A residual gas analyzer (RGA) is used to detect leaks in the UHV system, or the presence of unwanted elements or gases inside the growth chamber.

10.4.1.2 In Situ Characterization of Growth: Use of RHEED

For in situ characterization during MBE growth, reflection high-energy electron diffraction (RHEED) technique is used. The RHEED electron gun emits an electron beam that is incident on the sample surface at grazing incidence (<5°) at a voltage of ~14 kV (λ ~10pm). The electron beam penetrates only a few nm from the sample surface because of the grazing incidence. The resulting diffraction pattern formed due to Bragg scattering of the incident electrons from the crystal surface is captured on a fluorescent screen. This RHEED diffraction pattern allows real-time

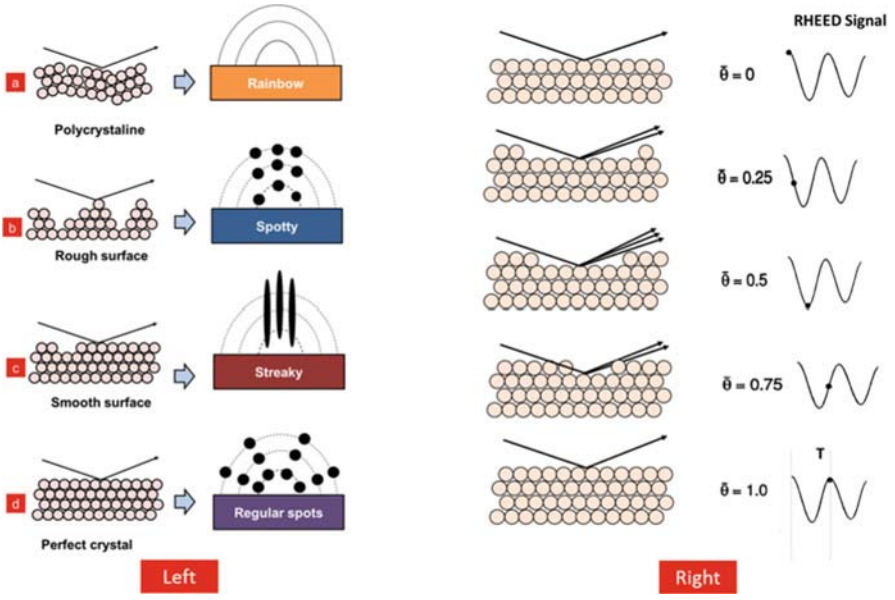

Fig. 10.13 (Left) RHEED pattern from different surfaces (**a**) arc from poly-crystalline, (**b**) spots from rough, (**c**) streaks from smooth, and (**d**) spots on arc from perfect crystals [63]. (Right) Formation of RHEED intensity oscillations with respect to surface layer orientation. T is the time period for one full cycle [63]

tracking of the smoothness and lattice structure of the epitaxial surface. The growth conditions can be adjusted dynamically based on the observed RHEED pattern. As shown in Fig. 10.13 (left), different diffraction patterns are generated based on the surface orientation of the crystal. For example, a polycrystalline surface produces rings/arcs which are Laue circles formed by the merger of specific diffraction spots of randomly oriented crystalline grains. A spotty pattern is produced from a rough surface. The spots overlap and become long steaks in case of a smooth surface. For atomically smooth crystal surfaces, the RHEED pattern consists of bright spots.

Another important application of the RHEED is to measure the growth rate and to track the growth conditions by following the time dynamics of the diffraction pattern, for example using intensity oscillations.

Figure 10.13 (right) shows the time evolution of RHEED intensity with the growth of monolayers of a semiconductor crystal. A bright spot is obtained due to constructive interference of diffracted electrons from a smooth surface, whereas a rough surface causes partial destructive interference, which leads to a lowering of the diffraction beam intensity. The time period for one complete intensity oscillation therefore corresponds to the formation of one monolayer of the crystal. The growth rate is then estimated in nm/hr from this information. For example, if the time period for one RHEED intensity oscillation is 4s during the growth of AlN (1 monolayer of AlN= 0.25 nm), then the corresponding growth rate is 225 nm/hr.

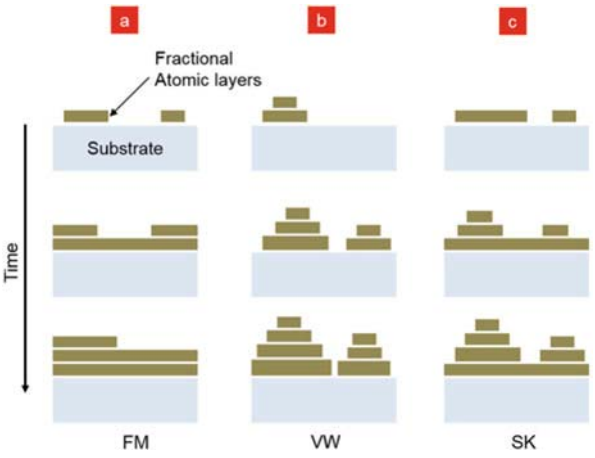

Fig. 10.14 MBE growth modes, (**a**) FM: layer by layer (**b**) VW, and (**c**) SK [63]

10.4.1.3 MBE Growth Modes

The growth mode in MBE is determined by the interaction and forces between the substrate and the adatoms that are deposited on it. There are three growth modes as depicted in Fig. 10.14. These are the Frank–van der Merwe (FM), Volmer–Weber (VW), and Stranski–Krastanov (SK) modes. In the FM mode, the interaction between the crystal surface and the adatom is stronger than between the adatoms themselves, making it energetically favorable for the adatoms to completely "wet" the surface. Thus, a layer-by-layer growth is possible; the second layer does not form till the first layer is completely formed. This mode typically occurs for homoepitaxial growth at high substrate temperatures that provides high kinetic energy for adatoms.

The second growth mode is VW, which occurs at low substrate temperatures when the interaction between adatoms is stronger than the adatom-interface interaction. Consequently, the adatoms do not wet and form 3D islands on the substrate surface. These can coalesce and form films over time.

The third one (SK) is a combination of the FM and VW growth modes. In the SK growth mode, layer-by-layer (2D) growth occurs in the initial phase, and after a few monolayers, the growth mode switches to the formation of 3D islands. The typical driving force for the formation of islands is strain due to lattice mismatch.

10.4.1.4 MBE Growth Condition Markers

To grow GaN/AlN heterostructures with thin (few monolayers) GaN layers, the MBE growth conditions need to be precisely controlled. The growth conditions can be monitored by observing a) RHEED oscillations and b) RHEED side streaks. The growth rate can be precisely determined from RHEED intensity oscillations [46, 64].

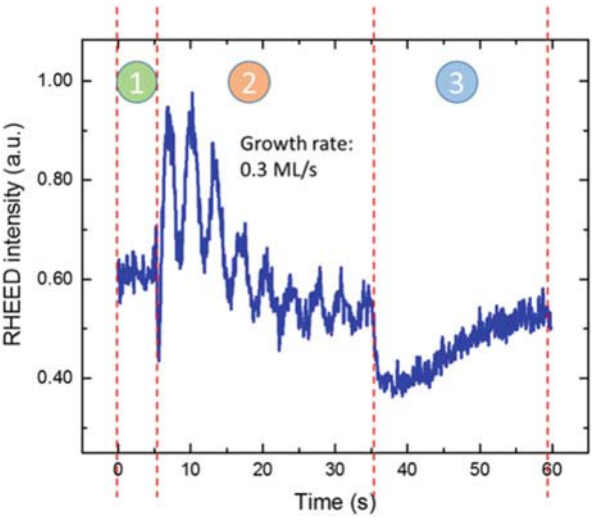

Fig. 10.15 Observation of RHEED intensity oscillations for GaN homo-epitaxial growth with plasma power of 275W and substrate temperature of 730°C. (1) Scan for background intensity, (2) GaN growth in layer-by-layer mode, and (3) excess Ga desorption. The inset highlights the area over which the RHEED beam intensity is tracked [63]

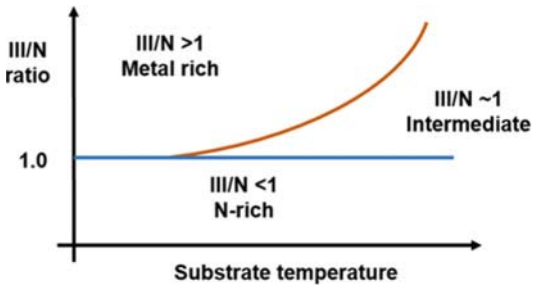

Fig. 10.16 Growth diagram for III-Ns showing three growth regimes based on III/N ratio and the substrate temperature

To calibrate growth rates by RHEED oscillations, epitaxial GaN layers were grown on GaN substrates in a slightly metal-rich condition ensuring smooth surface morphology (2-ML excess Ga) [65]. The substrate temperature was set at 730°C with a plasma RF power of 275W. As shown in Fig. 10.15, both the shutters for Ga and nitrogen were kept open from 5s to 35s within which layer-by-layer growth of GaN takes place, and 9 oscillations were observed. Since 9 monolayers of GaN were deposited over 30s, the growth rate was 0.3 ML/s (equivalent to 4.5 nm/min or 270 nm/hr). As the shutters for Ga and nitrogen were closed at 35s, the RHEED intensity started to increase and approach the initial value of t = 0 s. This happened due to the desorption of accumulated Ga from the surface at the growth temperature. Metal-rich growth condition for GaN was the reason for such Ga accumulation. The growth rate is controlled by plasma RF power. A higher growth rate can be achieved with higher plasma power.

For the GaN/AlN superlattice, it is essential to grow the AlN layer with smooth hetero-interfaces. An Al/N ratio of ∼1 is maintained to achieve this, which is called the intermediate growth window as depicted in Fig. 10.16. Metal-rich growth provides a smooth growth surface. On the contrary, nitrogen-rich growth makes

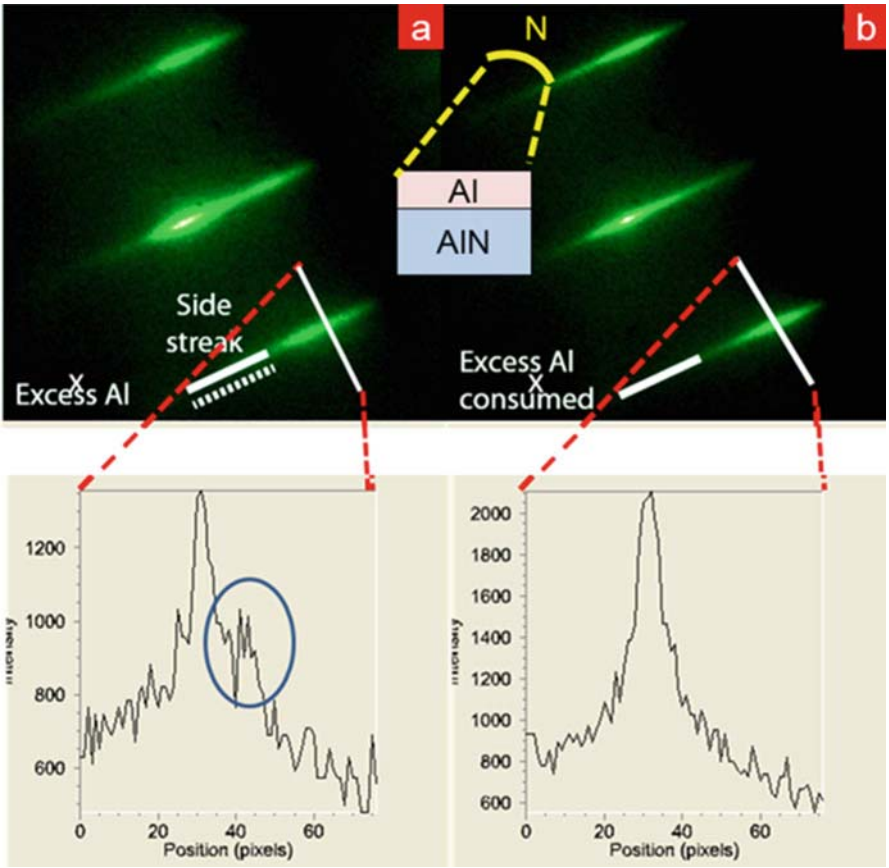

Fig. 10.17 Side streak observation to check AlN growth condition. (**a**) AlN side streak becomes diffused with additional shoulder peak due to accumulation of metal on the surface, (**b**) side streak becomes bright once excess metal is consumed by N and forms AlN. The shoulder peak is no longer present

the surface rough. Excessive supply of metal flux during the MBE growth can cause accumulation on the surface and initiate generation of dislocations and therefore deteriorate crystal quality. This is why growth in the intermediate regime is best-suited to obtain metal-free smooth surfaces. To ensure intermediate growth condition for AlN, RHEED side streak observation was employed. This was done by growing homo-epitaxial AlN. For this growth, the substrate was kept at 730°C with plasma RF power of 275W. First, only the Al shutter is kept open for 30s to deposit Al on the AlN substrate. During this process, RHEED side streak becomes diffused as shown in Fig. 10.17a, and an additional shoulder peak is observed. This peak most likely corresponds to a different lattice parameter of Al metal compared to the underlying AlN layer. To consume this excess metal, Al shutter was closed, and N2-shutter was kept open. Once all the excess metal was consumed and converted to AlN, the side streak became bright and streaky (Fig. 10.17b). The shoulder peak also

disappeared. This bright and streaky RHEED pattern is a signature for metal-free surfaces. The intermediate growth condition is achieved when the Al-consumption time is almost as equal as the Al-deposition time.

10.4.2 MBE Growth of GaN/AlN Quantum Heterostructures

The following subsections describe realization of ultrathin GaN/AlN quantum heterostructures with MBE using the RHEED-based growth markers.

10.4.2.1 Quantum Wells/Quantum Dots/Disks

The optimum MBE growth temperature for AlN is ~200–300°C [25] higher than that for GaN. For example, GaN starts to decompose >800°C [66] and therefore is generally grown at <750°C in plasma MBE. On the contrary, optimum AlN growth temperatures are >900°C. To grow GaN/AlN heterostructures, first an optimum growth temperature of 730°C was chosen which prevents GaN decomposition. Since Al adatom mobility is not too high at this temperature, migration-enhanced epitaxy (MEE) [67] technique was used to grow the AlN layers. This means that the opening of the Al and N shutters were alternated for 30s each to obtain a given thickness of the AlN layer.

The quantum heterostructures were realized by inserting a thin layer of a lower bandgap material (Material 2, i.e., GaN) in between a higher bandgap material (Material 1, i.e., AlN). Material 1 is the barrier. Figure 10.18 shows schematics for quantum wells (QWs) and quantum dots (QDs). In this work, material 1 is AlN and material 2 is GaN.

For GaN QWs, the growth condition was set as close as possible to stoichiometry (Ga/N ratio of ~1) to ensure the formation of a smooth 2D layer. Although

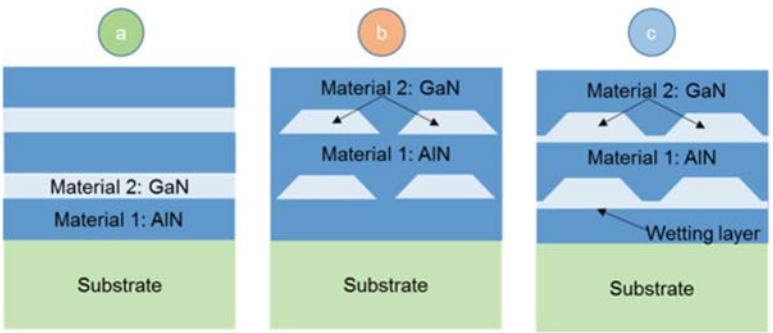

Fig. 10.18 Schematics for (**a**) quantum wells, (**b**) quantum dots/disks, and (**c**) quantum dots/disks with wetting layers

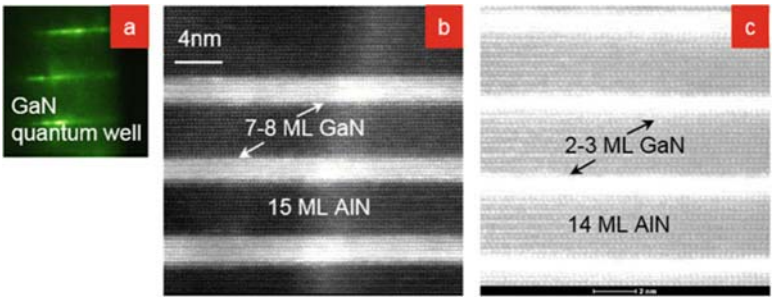

Fig. 10.19 MBE growth of GaN QWs in AlN barriers: (**a**) streaky RHEED during GaN QW growth suggesting a smooth surface, (**b**) STEM for 7–8-ML-thick GaN QWs in AlN, and (**c**) 2–3 MLs GaN QWs in AlN

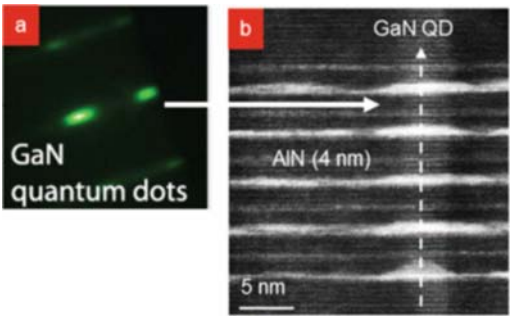

Fig. 10.20 MBE growth of GaN QDs in AlN barriers: (**a**) spotty RHEED during GaN QD growth suggesting surface roughening, and (**b**) STEM image of self-organized GaN QD growth in AlN matrix

smooth layers can be grown with metal-rich growth condition, it poses the risk of accumulation of excess metal and consequently result thicker QWs than expected. Such thickness variations are not desired because they can cause multi-peak emission during luminescence. Figure 10.19a shows the streaky RHEED during growth of a GaN QW. The streaky RHEED confirms formation of a smooth 2-D surface. Some typical thick and thin GaN QW STEM images are shown as examples in Fig. 10.19b–c.

For quantum dots/disks (QDs), material 2 is grown as a 3D structure (Fig. 10.18b). The 3D growth mode can be achieved in either of the two ways:

(a) SK mode
(b) Modified SK mode

To ensure SK (Stranski–Krastanov) growth mode for QDs, the growth condition for GaN needs to be nitrogen rich (Ga/N <1). 3D islands of GaN are formed due to compressive strain from AlN [68, 69]. Self-aligned QD formation occurs due to the existence of underlying thin strained spacer layers of AlN in between GaN QDs (Fig. 10.20b). Besides growing in nitrogen-rich condition, the 3D GaN islands are left in vacuum for a given amount of time (annealed) at the growth temperature before capping with the barrier material (AlN). This process is termed as "ripening" in this chapter. Ripening helps the QDs to rearrange themselves due to the strain

from the underlying AlN layer. Thus, QDs can be reshaped by both the ripening process and the Ga/N ratio. The spotty RHEED (Fig. 10.20a) indicates formation of a rough surface, which is also a signature of formation of 3D islands or QDs.

The second method to grow QDs is called the modified SK mode [65]. In this method, the GaN layer is deposited under metal-rich conditions to ensure a smooth 2D film growth. Then, it is ripened for a given amount of time so that the excess Ga can desorb from the surface due to high substrate temperature. If the ripening is done for longer time (>30s), the GaN film can start to decompose and become rough. This roughened 2D layer works as a 3D GaN island or QD. Therefore for this method, the shape of the QDs can be controlled by the duration of ripening time.

For the modified SK mode, the most crucial parameter is the ripening time since it decides whether 3D island formation can take place. On the other hand for SK mode, the nitrogen-rich growth condition decides if dots/disks can form. Therefore, the Ga/N flux ratio is crucial for QD growth by the SK mode.

Schematic structure for an idealistic QD is shown in Fig. 10.18b. But due to SK mode of growth, a thin continuous wetting layer of 1–2-ML thickness is formed below the QDs (Fig. 10.18c). This may lead to some detrimental effects like reduction in quantum efficiency due to extended dislocations in the wetting layer, broadening of the emission spectra, etc.

10.4.2.2 MBE Growth Parameter Optimization

Prior to growing the desired GaN/AlN quantum heterostructures for deep-UV emission, it was essential to investigate the impact of different growth parameters on the emitted light such as the AlN barrier thickness, growth rate, ripening time, etc. The summary of such optimization experiments is presented here.

(a) AlN barrier thickness:

The quantum confinement effect is increased with thicker barriers by reduction of carrier wavefunction penetration into them. The downside of using a thick barrier is the reduction of tunneling probability through the barriers. This has a negative impact on the carrier transport properties needed for LEDs and Lasers. 3 GaN/AlN test structures were grown with different barrier thicknesses to investigate their effect on photoluminescence. 2-ML SK-GaN QD was grown in 2-, 3-, and 4-nm AlN barriers. HR-XRD measurement showed a strong peak from AlN substrate but no satellite peaks were observed due to incoherent reflection from GaN QDs, as shown in Fig. 10.21a. Photoluminescence (PL) measurement was performed at 300K with excitation from a 157-nm excimer laser. The emission energy was found to increase with the thickness of the AlN barrier layers due to higher quantum confinement (2 nm→234 nm, 3 nm→227 nm).

Above 3-nm AlN barrier thickness, the quantum confinement effect was saturated, and the emission energy did not increase further. Based on this observation, a barrier thickness of 2–2.5 nm was used as an optimum value for most of the subsequent experiments to provide quantum confinement with a decent tunneling probability for efficient carrier injection.

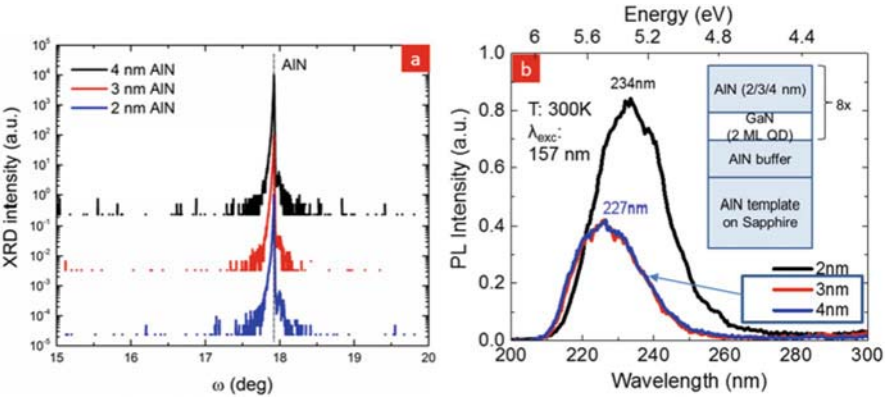

Fig. 10.21 Optimization of AlN barrier thickness: (**a**) (002) ω-2θ HR-XRD showing the absence of secondary peaks due to incoherent reflection from GaN, and (**b**) RTPL spectra for various AlN barriers

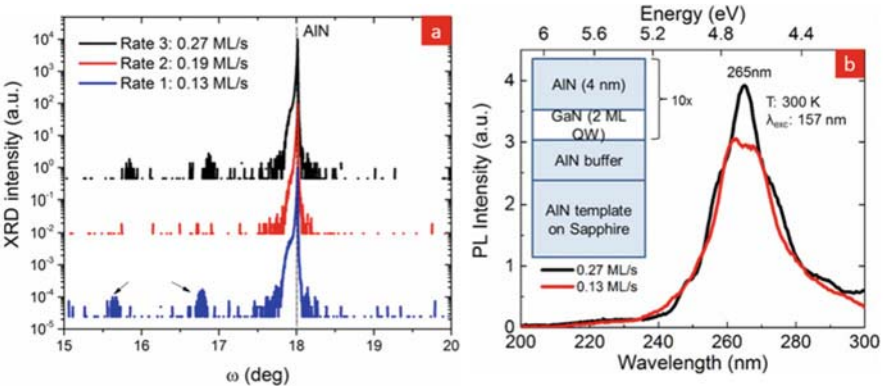

Fig. 10.22 Optimization of growth rate: (**a**) GaN QW reflections are seen from the HRXRD spectra, and (**b**) PL spectra for various growth rates

(b) Growth rate:

For this experiment, test structures containing 2-ML GaN QWs between 4 nm AlN barriers were grown using 3 different growth rates, i.e., 0.13 ML/s, 0.17 ML/s, and 0.27 ML/s. The HR-XRD spectra for the QW samples showed secondary satellite peaks from the GaN layers (Fig. 10.22a). From the PL spectra (Fig. 10.22b), it was found that the sample grown with 0.17 ML/s showed a blue shifted emission compared to the other two (not shown here), most likely because of QD formation instead of QWs.

This claim was further confirmed from the absence of the secondary satellite peaks from the XRD measurement for that sample. The highest PL intensity was achieved from the sample grown with the highest growth rate. Higher growth rates than 0.27 ML/s were not investigated since the ML deposition time reduces below a few seconds, which may cause reduced control over the thickness of a grown layer.

Since the PL intensity dependence was not significant over the investigated range of growth rates, for the rest of the growths, a low growth rate was used for accurate thickness control.

10.4.2.3 Single and Double Monolayer δ-GaN Quantum Wells

Few research groups have realized 1-ML δ-GaN QW/AlN heterostructures, and DUV emission have been reported by Taniyasu et al. [70] and Kamiya et al. [71]. The crystal growth was performed by MOCVD in these reports. 224-nm emission was reported by Kamiya et al. [71] and 237-nm by Taniyasu et al. [70] from the 1-ML GaN quantum structures with a thinner AlN barrier (1.75 nm).

In the current experiment, the structure shown in Fig. 10.23a was grown with MBE. The AlN barrier thickness was 4 nm for both 1- and 2-ML GaN samples. GaN/AlN QW heterostructures were repeated for 10 times.

After the MBE growth, the samples were characterized by XRD triple axis ω-2θ measurements. Figure 10.23b shows the data including the substrate as a control sample. 1-μm-thick AlN template on sapphire was used as the substrate. Satellite fringes in the XRD scans for the QW samples indicates superlattice formation. As a comparison to the control sample, the XRD spectra for the AlN template substrate did not show any satellite fringes. STEM images were taken for both the QW samples to investigate the layer structures. Figure 10.23c–e shows the images indicating that the desired thicknesses for the GaN QWs and AlN barriers were achieved. Figure 10.23e confirms that the GaN QWs were continuous and uniform over the entire plane of the sample.

The optical properties for the QW samples were investigated through PL and absorption measurements. A 157-nm excimer laser source was used to excite all samples. The data is shown in Fig. 10.24a–b. The emission peak at room temperature (RT) is 261 nm for 2-ML QW, which blue shifted to 256 nm at 5K. This is explained due to bandgap increase with temperature by Varshni's law. Similarly, the 1-ML QW showed an emission peak of 224 nm at 300K which also blue shifted to 222 nm at 5K. The absorption data was measured at room temperature and compared with the PL peak emission wavelength to find out the effective bandgap. PL and absorption data showed good agreement.

IQE was estimated from temperature-dependent PL measurement for these samples with the assumption that the non-radiative recombination process ceases out completely at 5K. The IQE was 49% for 2-ML and 17% for the 1-ML GaN QW samples. The high IQE for 2-ML QW is expected because of high overlap integral between the electron and hole wavefunctions, as depicted in Fig. 10.25. The efficiency value is limited by the threading dislocation density of the substrate, which is 1×10^{10} cm^{-2} for this case. A sharp decrease in the measured IQE for the 1-ML QW was observed although the theoretical overlap integral of $>80\%$ from Fig. 10.25 predicts high IQE for such thin QWs.

In summary, 1–2-ML GaN QWs can produce deep-UV emission as short as 224 nm at 300K, but lowering of IQE was observed at shorter wavelengths, most likely due to reduced effective band offsets in the δ-QW structures.

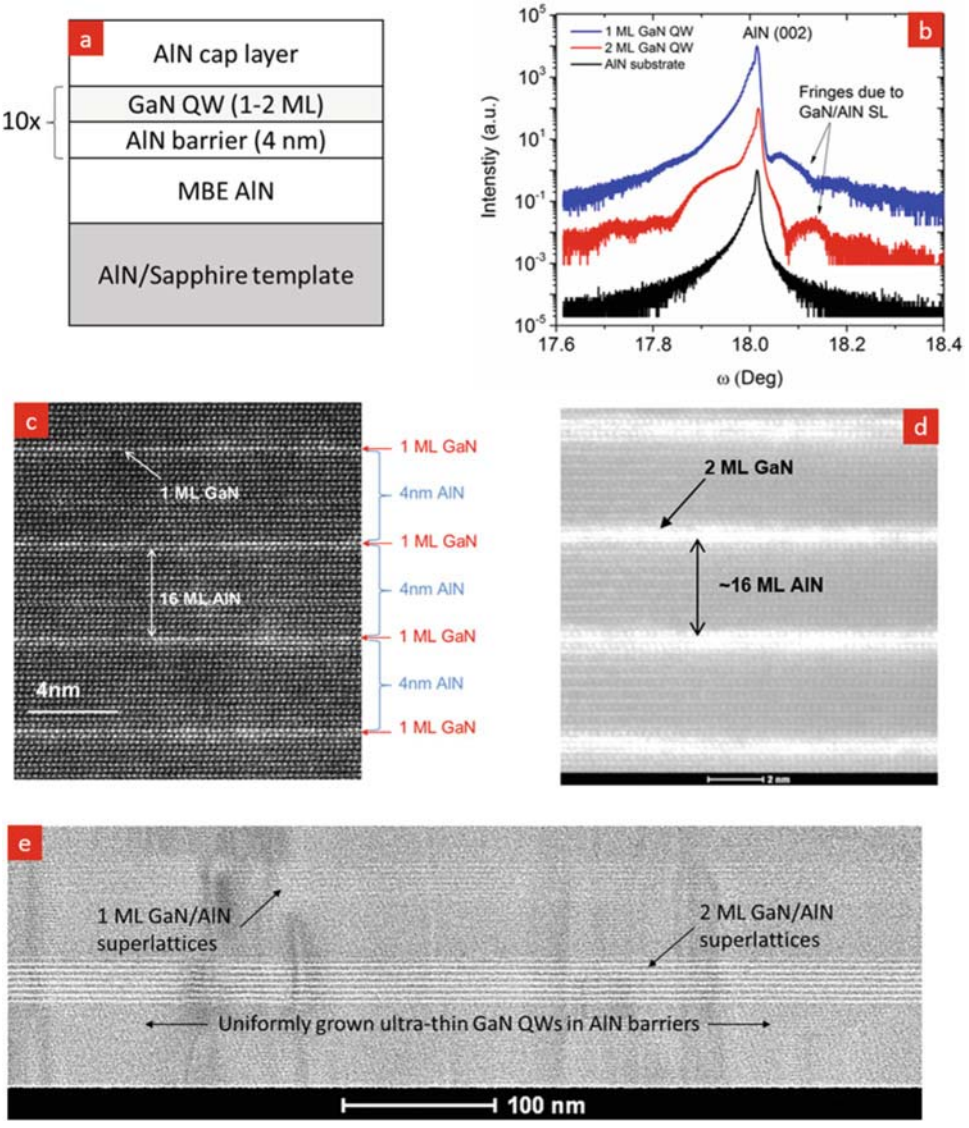

Fig. 10.23 (**a**) Schematic structure for the 1–2-ML GaN/AlN heterostructures, (**b**) measured XRD spectra confirming the presence of GaN/AlN superlattices, STEM images of (**c**) 1-ML GaN and (**d**) 2-ML GaN in AlN matrix, and (**e**) uniformity of the 1- and 2-ML GaN layers over long range [63]

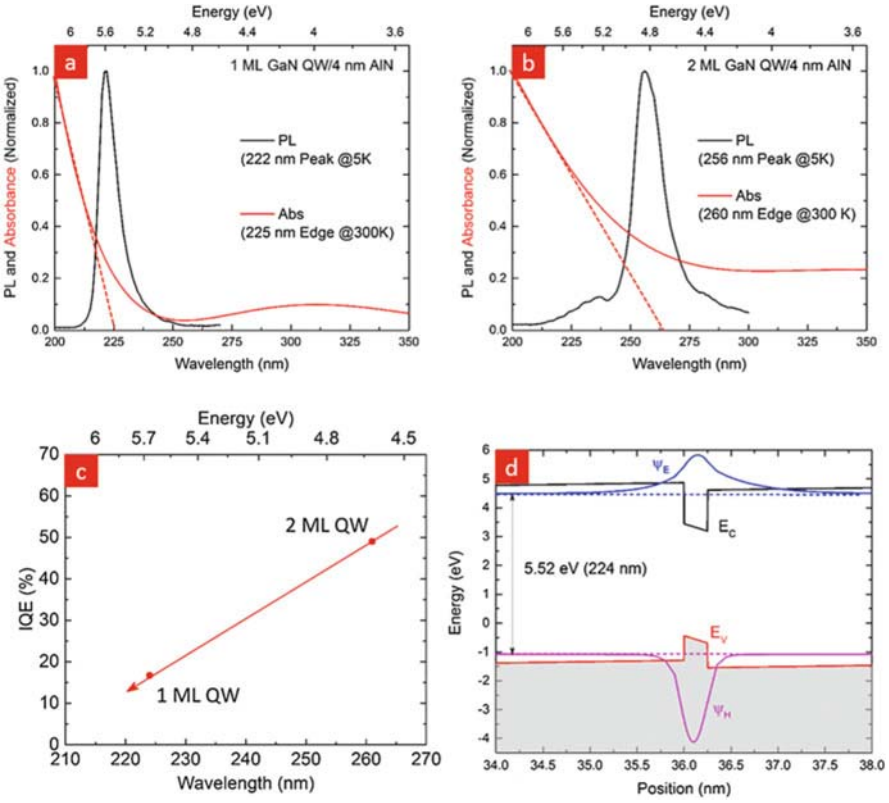

Fig. 10.24 PL and absorption spectra from the (**a**) 1-ML and (**b**) 2-ML GaN/AlN heterostructures, (**c**) IQE measured using temperature-dependent PL, (**d**) simulated energy band diagram to explain the low IQE for 1-ML GaN/AlN heterostructure [63]

10.4.2.4 IQE Improvement with δ-GaN Quantum Disks

Quantum dots/disks (QDs) are confined heterostructures in 3-dimensions (3-D) unlike QWs where the confinement is only along 1 dimension. The additional degree of confinement can help in capturing the carriers in a defect-free region and therefore produce efficient radiative recombination process. The use of QDs to enhance IQE is well known for the InAs/GaAs material system for photonic devices [72]. Also, the state-of-the-art InGaN/GaN heterostructure-based visible photonic devices have reached high EQE [73] owing to the QD-like active regions of InGaN in GaN matrix. In the following sections, an experimental effort to use ultrathin δ-GaN quantum disks to enhance the IQE is presented.

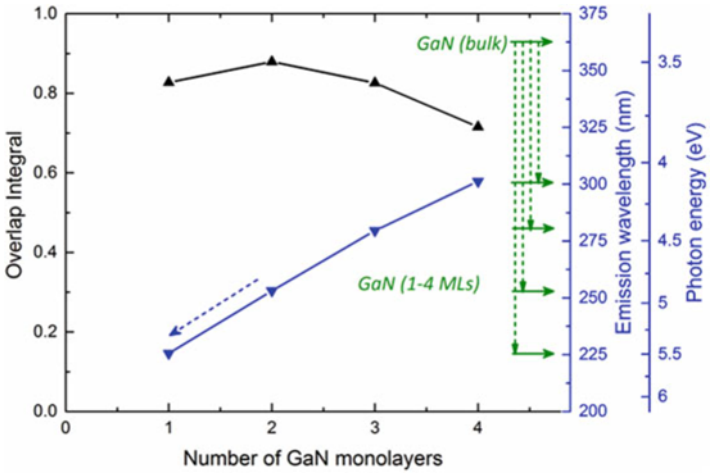

Fig. 10.25 Evolution of simulated overlap integral and emission wavelength as a function of GaN thickness for a GaN/AlN multi-QW heterostructure [63]

10.4.2.4.1 SK Quantum Dots/Disks

For this experiment, the MBE growth and characterization of 1–2-ML GaN QDs in AlN barriers was explored. As it was mentioned earlier (refer to Sect. 10.4.2.1), Ga/N ratio is a very important parameter for growth of QDs in SK mode. Three samples were grown using MBE with different Ga/N ratios for the 2-ML GaN QDs in 4-nm AlN barriers. 10 repeats of the heterostructure were used for enhancing the light emission. All structures were grown on AlN templates on sapphire with threading dislocation densities of 1×10^{10} cm^{-2}.

The schematic of the structure and the growth flow diagram is depicted in Fig. 10.26a–b. The Ga/N ratio was varied over 0.88 (A)-0.75 (B)-0.6 (C) for the three samples. After the MBE growth, structural characterization was done first by HR-XRD measurements. All samples showed a strong AlN peak originating from the substrate. Unlike the XRD spectra of the substrate, the QD samples showed satellite peaks suggesting formation of GaN/AlN superlattices. From the trend of the satellite peak intensities, it was observed that as the Ga/N ratio is reduced, the GaN QD geometry turns more into QW-like producing intense fringes from coherent reflections by the smooth GaN layers [74]. The satellite peak intensities are the strongest for sample C with a Ga/N ratio of 0.6 clearly suggesting QW-like phenomena.

For further structural characterization, TEM imaging was performed. A representative HAADF-STEM image for the sample A is shown in Fig. 10.27. Desired thicknesses of GaN and AlN layers with sharp hetero-interfaces were confirmed from the images. For the GaN layers, a 2-ML QD-like structure was seen with a 1-ML GaN wetting layer. The 1-ML and 2-ML GaN regions are explicitly shown in Fig. 10.27b.

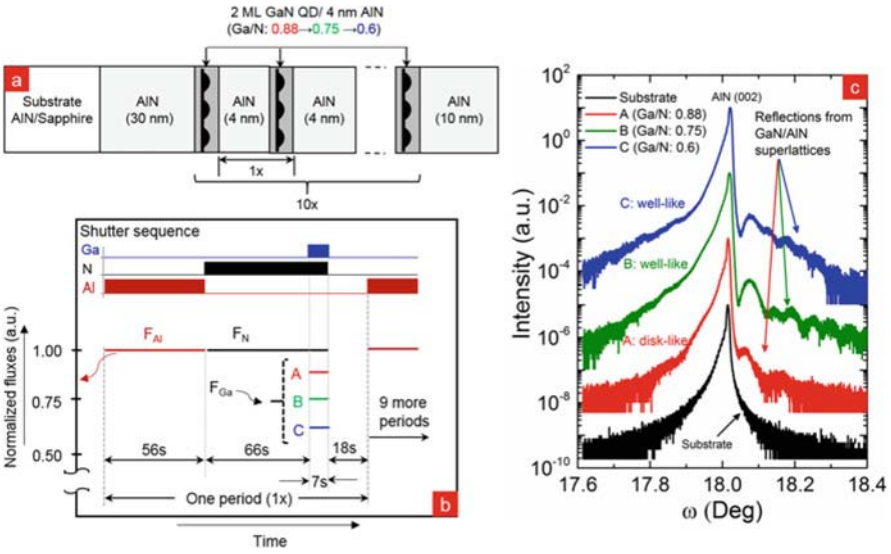

Fig. 10.26 SK-GaN QDs: (**a**) schematic structure, (**b**) MBE growth flow diagram, and (**c**) XRD spectra showing signature of superlattices [47]. Reproduced from Appl. Phys. Lett. 111, 091104 (2017), with the permission of AIP Publishing

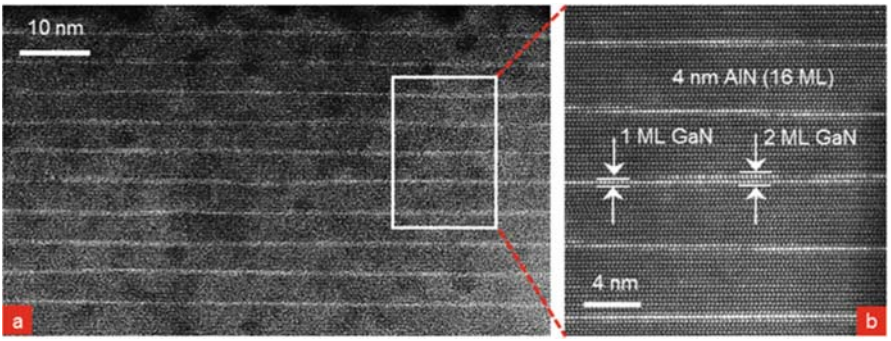

Fig. 10.27 STEM images showing 1–2-ML SK-GaN QDs: (**a**) zoomed-out, and (**b**) zoomed-in [47]. Reproduced from Appl. Phys. Lett. 111, 091104 (2017), with the permission of AIP Publishing

To examine the optical properties, PL measurements were performed for all the samples using a 157-nm excimer laser as a function of temperature. The absorption spectra were measured as well with a standard UV-Vis system at 300K. The measured optical characteristics are shown in Fig. 10.28.

As the Ga/N ratio was reduced from 0.88→0.75→0.6, a monotonic blue shift in the emission wavelengths was observed from 235 nm→222 nm→219 nm. This is the first demonstration of 219-nm emission from GaN-based quantum structures in AlN matrix. The absorption spectra measured at 300K show a similar trend as the PL. But, the absorption edge did not exactly coincide with the PL peak emission

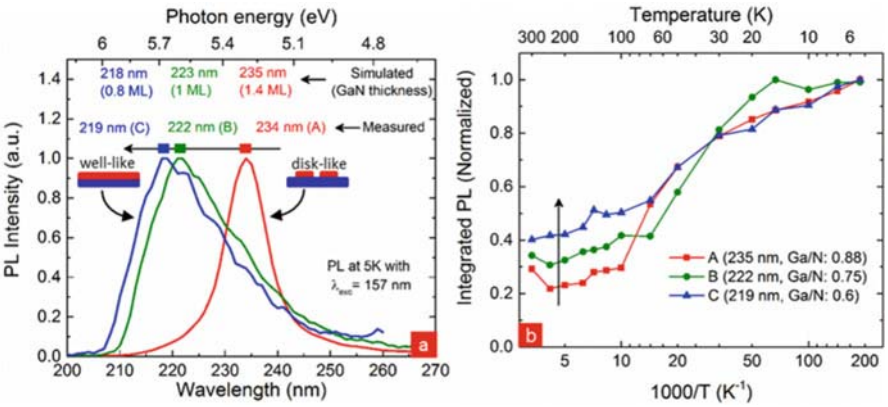

Fig. 10.28 Optical properties of the SK-GaN QDs: (**a**) PL and absorption, and (**b**) IQE [47]. Reproduced from Appl. Phys. Lett. 111, 091104 (2017), with the permission of AIP Publishing

wavelengths. The absorption band edges were also not very sharp most likely because of the small absorption volume of GaN in the whole structure (10 x 2 ML∼5 nm of effective GaN in a sample). The measured PL peak positions were fitted with SiLENSe simulations of GaN QWs to extract the effective GaN thicknesses. The extracted GaN thicknesses are shown in Fig. 10.28a. The simulation suggested that the effective GaN thicknesses can be controlled by tuning the Ga/N ratio during the MBE growth, and therefore the emission wavelength could also be changed accordingly.

Internal quantum efficiency (IQE) was measured for these samples using temperature-dependent integrated PL data. Assuming the non-radiative recombination processes ceases at 5K, the IQE can be measured from the ratio of integrated PL taken at 300K and 5K. It was observed that, as the Ga/N ratio was reduced from sample A→B→C, the IQE increased from 29%→34%→40%. The increase of IQE with a reduction in emission wavelength is explained by enhanced quantum confinement effect by the reduction of QD sizes. The size of the QDs was made smaller by lowering the Ga/N ratio. The smaller QDs were also most likely isolated from the non-radiative recombination centers and thus became more efficient. The 40% IQE at 219-nm emission wavelength is the highest reported number for such a short wavelength with any AlGaN composition.

In summary, ultrathin (1–2ML) GaN/AlN SK-QDs were grown by MBE to achieve emission in the DUV regime. With 1-ML QWs, emission as short as 224 nm can be achieved at 300K, but the IQE was only 17%. For SK-QDs, the shortest emission wavelength achieved was 219 nm with an IQE of 40% which is >2× higher than the IQE of the QW emitting at 222 nm at 5K.

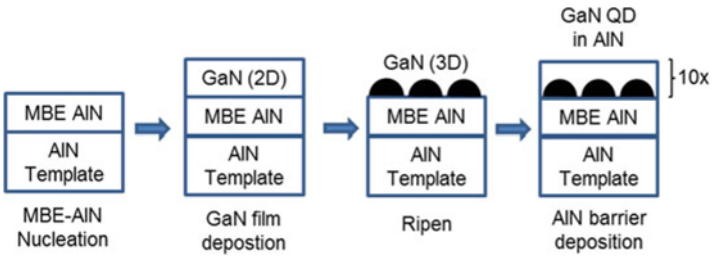

Fig. 10.29 Schematic flow diagram for modified SK growth method [63]

10.4.2.4.2 Modified SK Quantum Dots/Disks

The other method of growing QDs namely the modified SK was examined for deep-UV emission. Previously, Verma et al. [11] demonstrated that QDs grown in modified SK can produce better light emission property with a narrower FWHM for the PL spectra compared to the SK mode.

As explained earlier (refer to Sect. 10.4.2.1), the GaN layers are grown in metal-rich condition first for this modified SK method and then ripened at the growth temperature before capping with AlN. Therefore, the ripening time is a very important parameter to determine the QD formation. To illustrate the process better, the growth flow diagram for modified SK QD is shown in Fig. 10.29.

Based on this modified SK growth scheme, a series of three samples (F/G/H) were grown. 2-ML GaN layers were deposited in 3-nm AlN barriers for each sample, and this GaN/AlN heterostructure was repeated for 10 periods. The ripening time "t" was varied for the three samples: F (30s)→G (45s)→H (60s). As control samples, the two 1-ML and 2-ML GaN QW samples from Sect. 10.4.2.3 were used. Figure 10.30 shows the high-resolution X-ray diffraction (HR-XRD) triple axis (002) ω-2θ scans for the QD samples (F/G/H) and the 2-ML QW control sample. All samples showed a strong AlN substrate peak. The QW sample showed satellite secondary peaks originating from coherent reflection from the smooth GaN layers. QD sample F did not show any such satellite peaks, possibly due to incoherently scattered X-ray reflections from the GaN QDs. QD sample G and H showed satellite peaks like the QW sample suggesting that the GaN layers were more like QWs instead of QDs. This observation is similar to the SK GaN QDs discussed in Sect. 10.4.2.4.1.

To investigate further the structural details, HAADF-STEM images were acquired for the QD samples F, G, and H as shown in Fig. 10.31. Sharp hetero-interfaces were observed for all samples suggesting no intermixing between AlN and GaN. The AlN barrier thicknesses were 3 nm, and GaN QDs were 1–2 MLs for all samples. No clear distinction was observed in the images for the GaN layers grown with different ripening times.

The optical properties were studied through photoluminescence using a 157-nm pulsed excimer laser excitation source. Temperature-dependent PL data was taken down to 5K, as shown in Fig. 10.32. Figure 10.32a is the spectra from the QD

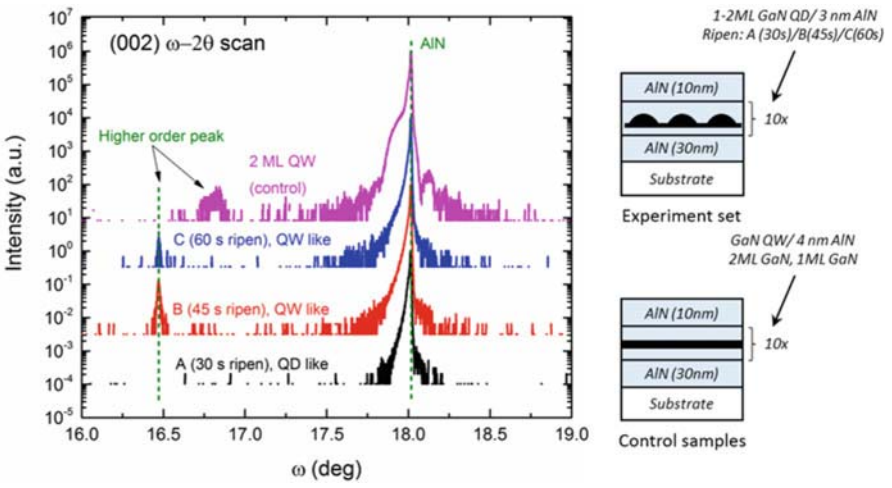

Fig. 10.30 (002) ω-2θ triple axis HR-XRD analysis for QD samples (F/G/H) and the 2-ML QW control sample [63]

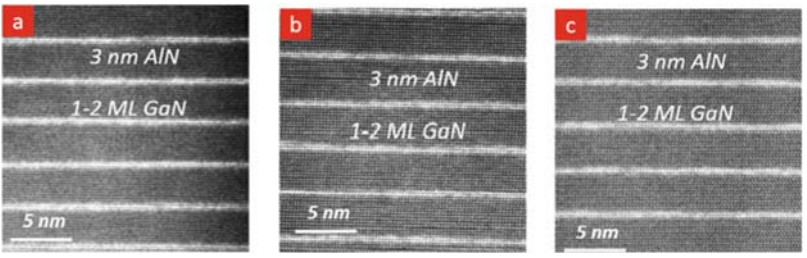

Fig. 10.31 HAADF-STEM images for the samples (**a**) F, (**b**) G, and (**c**) H showing the 1–2-ML GaN layers in 3-nm AlN matrix [63]

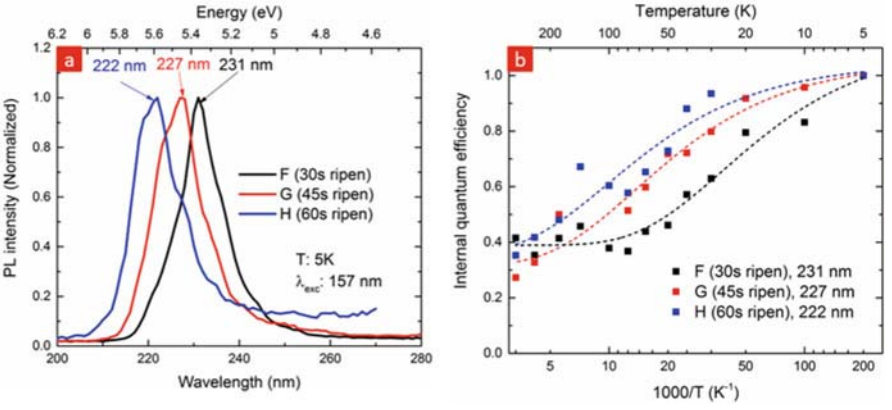

Fig. 10.32 Optical properties of the SK-GaN QDs: (**a**) PL and absorption, and (**b**) IQE [63]

samples measured at 5K. 3 distinct single-peaked emissions were observed for the QD samples F/G/H. As the QD ripening time was increased from 30s→45s→60s, the emission wavelength showed a monotonous blue shift from 231 nm→227 nm→222 nm at 5K. This blue shift is described as a consequence of the quantum confinement effect. As the ripening time was increased, the size of the QDs became smaller due to increased desorption of GaN, causing the lateral quantum confinement. The measured PL full width at half maximum (FWHM) values was small (∼10 nm) for all samples. For the 1-ML (2-ML) QW samples, the widths were 9 nm (16 nm) at 5K.

The relatively wider emission for 2-ML QW might suggest some nonuniformity in the GaN layer thicknesses among the different periods. For the QD samples, the FWHM increased slightly from 11nm→12nm→13nm among F→G→H. These widths suggest relatively uniform distribution of the QD sizes and slight increase in the randomness for the smaller QDs.

To estimate the internal quantum efficiency (IQE), temperature-dependent integrated PL measurements were performed. Figure 10.32b shows the trend of the temperature-dependent IQE for the QD samples. From the integrated PL intensity ratio (IPL(300K)/IPL(5K)), the highest IQE was measured for sample F (37%), and the lowest was for sample G (24%). Sample H showed an IQE of 36%. The activation energy for non-radiative processes was the highest for sample H (222 nm) and was the lowest for sample F (231 nm), meaning that the smaller QDs were thermally more robust. The quantum confinement served two purposes: it shortened the emission wavelength by increasing the effective bandgap, and it also most likely isolated the QDs from the non-radiative recombination centers through an energy barrier, increasing the IQE. The IQE between QDs (mod-SK) and the QW control samples were compared. For QWs, the IQE decreased from 49% (2 ML) to 17% (1 ML) at shorter wavelengths as shown earlier in Fig. 10.24c. For the modified SK QD samples, the IQE stayed around 35% for the whole range of 222–231 nm emission, which is ∼200% higher than 1-ML GaN QWs at 222 nm. This comparative efficiency boost suggests enhanced 3D quantum confinement in QDs.

In summary, tunable deep-UV emission below 230 nm has been obtained from 1–2-ML GaN QDs in AlN barriers grown by MBE in modified SK mode. The emission wavelength could be tuned by controlling the annealing time of the GaN QDs. The FWHM was narrow (11–13 nm) over the entire range of emission of 222–231 nm. IQE from temperature-dependent PL measurements for GaN QDs showed a ∼200% increase compared to quantum wells emitting at similar wavelengths.

Based on the IQE measured for the MBE grown GaN/AlN quantum structures and the experimentally reported IQE for AlGaN-based active regions, a combined IQE plot has been generated as shown in Fig. 10.33 over the entire UV range (200–400 nm). The plot shows a dramatic decrease of IQE for wavelengths shorter than 250 nm with AlGaN-based heterostructures. This drastic decrease in the IQE is explained by reduced overlap of the carrier wavefunctions due to the QCSE effect depicted in Fig. 10.34a.

On the contrary, the GaN-based active regions show markedly enhanced IQE for ∼220-nm emission. For example, the IQE of 40% at 219 nm [47], and 36%

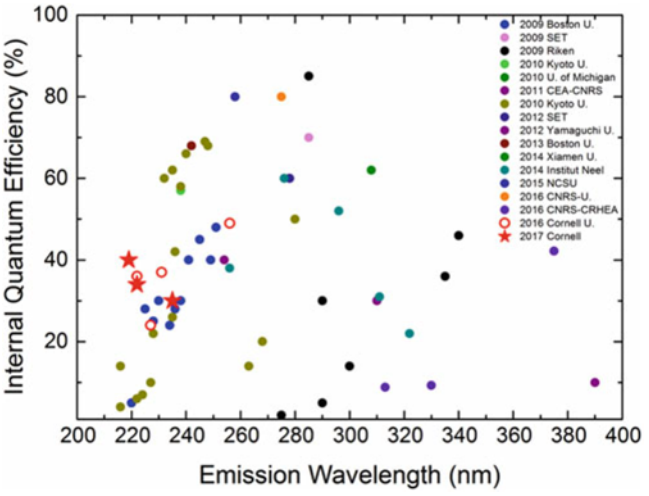

Fig. 10.33 A comparative IQE plot between AlGaN- and GaN-based deep-UV emitters over the entire UV spectral region [7, 19, 57]

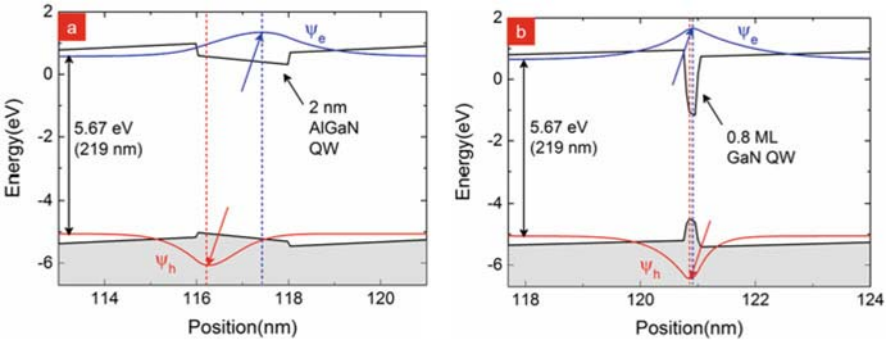

Fig. 10.34 Improvement of wavefunction overlap by using ultrathin GaN quantum structures: (**a**) 2 nm AlGaN QW, and (**b**) 0.25 nm GaN QW [47]. Reproduced from Appl. Phys. Lett. 111, 091104 (2017), with the permission of AIP Publishing

at 222 nm [63] using GaN QDs are almost 8 times higher compared to the 5% at 220 nm using AlGaN QWs (Bhattacharyya et al. 2009). Such enhancement of the IQE is explained by reduction of the QCSE effect by use of very thin "δ" active region. The enhanced overlap of the wavefunctions is illustrated in Fig. 10.34b. This clearly shows the superiority of the GaN-based heterostructures over the AlGaN counterpart to achieve high IQE for sub-250-nm deep-UV emission as was predicted in Sect. 10.3.1.

10.5 Polarization Doping-Assisted Deep-UV LEDs with GaN/AlN Quantum Structures: Enhanced Carrier Injection

Deep-UV light-emitting diodes fabricated using the AlN/GaN heterostructures discussed in the previous sections as the light-emitting active region are presented here. Electrically injected deep-UV LEDs with electroluminescence (EL) emission wavelength as short as 232 nm (5.34 eV) have been achieved [47], which is the shortest EL wavelength with GaN-based active region till now. Polarization-induced doping has been used for the p and n regions for improving carrier injection. The carriers are injected into the light-emitting active region by tunneling mechanism through thin AlN (∼2 nm) barriers. Cryogenic operation of a ∼260-nm (4.77eV) LED has also been realized with a low turn-on voltage of <6V [75]. Repeatable negative differential resistance (NDR) behavior has been observed for the first time in such light-emitting devices. The following subsections discuss the details of such achievements.

10.5.1 Polarization-Induced Doping to Enhance Vertical Electrical Conductivity for LEDs

Si and Mg are the commonly used dopants for III-nitride semiconductors. Doping in Al-rich AlGaN is challenging due to high activation energy for both Si (n-type donor) and Mg (p-type acceptor). As shown in Fig. 10.35, the activation energy for Si increases from 25 meV for GaN to 250 meV for AlN. Unfortunately, the situation is even worse for Mg where it increases from 200 meV for GaN to 600 meV for AlN. Thus, the thermal activation of dopants at room temperature specifically for Mg is very difficult in Al-rich AlGaN.

This problem can be solved to a great extent by exploiting internal polarization fields of III-nitride semiconductors. As discussed in Simon et al. [76] and Jena et al.

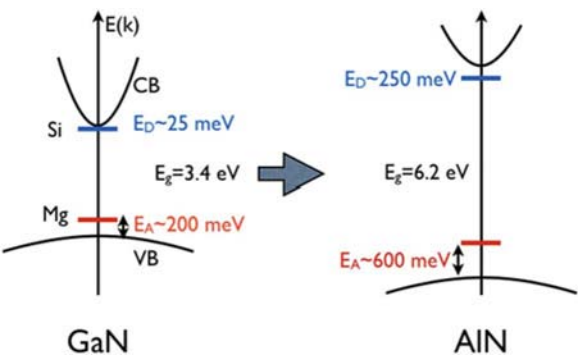

Fig. 10.35 Activation energy of dopants in GaN and AlN [76]

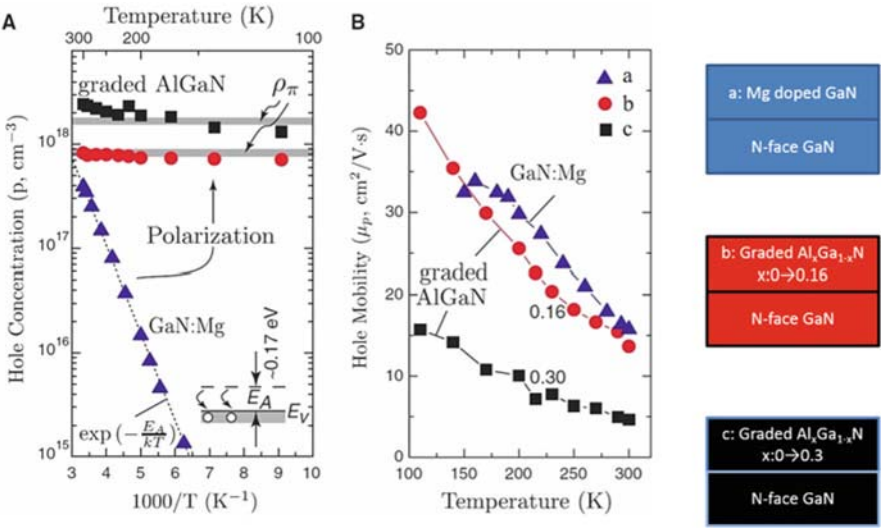

Fig. 10.36 Temperature-dependent hole concentration and mobility comparison between conventional and polarization-induced doping [76]

[77], compositionally graded AlGaN can induce 3-dimensional electron or hole gases (3DEGs or 3DHG). This technique has the potential advantage of reduced ionized impurity scattering, which results in high mobility for carriers even at low temperatures. Dopants are ionized by polarization-induced electric field, and this effect is independent of temperature. Therefore, ionized carriers do not freeze out at low temperatures. This can lead to realization of temperature-independent operation for devices. In Fig. 10.36 (Jena et al. [77]), it is shown that by using a compositionally graded-down $Al_xGa_{1-x}N$ alloy (x: 0.3→0) along the N-polar direction, a hole concentration of $\sim 3\times 10^{18}$ cm^{-3} could be achieved with high mobility. Both the mobility and the carrier concentrations were weakly dependent on temperature. On the contrary, at lower temperature there was complete carrier freeze-out for a conventional Mg-doped p-GaN layer.

This scheme of polarization-induced doping has been used by several research groups [11, 62, 78–81] to improve the carrier injection for deep-UV photonic devices. Besides graded alloys, the other form of using polarization-induced doping is the short period superlattice (SPSL) of $Al_xGa_{1-x}N/Al_yGa_{1-y}N$. The electric field induced by polarization charges at the sharp hetero-interfaces ionizes the dopants. The SPSL method improves the transport of carriers in the plane of the quantum wells, but the vertical transport needs to occur in minibands encountering potential barriers due to the band offsets, leading to a higher vertical resistance than lateral. The SPSL technique has been used widely in device applications [82–85]. The design of SPSLs becomes challenging if one requires these layers to remain optically transparent at shorter wavelengths (<250 nm). To maintain optical transparency, the thickness of AlN layers in the GaN/AlN SPSL needs to

be increased, which negatively impacts the vertical carrier transport. On the other hand, graded alloy-based polarization-induced doping has superior vertical transport without sacrificing optical transparency.

10.5.2 Structural Design of Deep-UV LEDs with Polarization-Induced Doping

To determine the necessary AlGaN compositions for polarization-induced doping, energy band diagram simulations were performed using SiLENSe. A linearly graded composition metal polar $Al_xGa_{1-x}N$ p-n junction without any chemical dopants was investigated. $Al_xGa_{1-x}N$ with 50% Al content has a bandgap of ~4.6 eV which corresponds to ~270-nm bandedge emission. Therefore, the structure containing a 100-nm linearly graded 100% to 50% $Al_xGa_{1-x}N$ will be transparent to all wavelength >270 nm. Due to the compositional grading gradient, polarization-induced electrons and holes will be $\sim 2.5\times10^{18}$ cm^{-3} based on the direction of grading (graded-up: electrons; graded-down: holes, with metal polar growth direction). This charge is solely due to the grading gradient. Additional impurity doping (e.g., Si or Mg) can increase the mobile charge densities. In addition to the composition control, the polarization-induced charge density can also be controlled by changing the thickness of the graded layer. For example, if the thickness of the graded region is reduced to 50 nm, the charge density will double to 5×10^{18} cm^{-3}. The polarization-induced (pi-) doped UV LED structures discussed in the later part of this section make use of these design freedoms.

The effectiveness of pi-doping with deep-UV LEDs especially for the p-AlGaN layer has been demonstrated by Verma et al. [46]. As shown in Fig. 10.37, by replacing the nongraded p-AlGaN layer with pi-doped graded p-AlGaN, the light intensity of the deep-UV LED can be enhanced by 23 times. This experiment clearly demonstrates the benefits of pi-doping over the conventional p-AlGaN doping scheme.

Besides pi-doping, a tunnel injection into the active region scheme was used in the device design for the deep-UV LEDs mentioned in this section. The conventional over-the-barrier carrier injection processes into the active region quantum wells lead to the relaxation of hot carriers. The excess energy equal to the band offset minus the ground state energy of the well is dissipated by optical phonon emission. This leads to heat generation, which translates to loss. To overcome this loss, carriers can be cold-injected by tunneling through the thin barriers. In this technique, the heterostructure is designed in a way that the conduction band states of the doped p and n regions are aligned with the electronic ground states of the active region. The barriers are kept thin to enable tunneling.

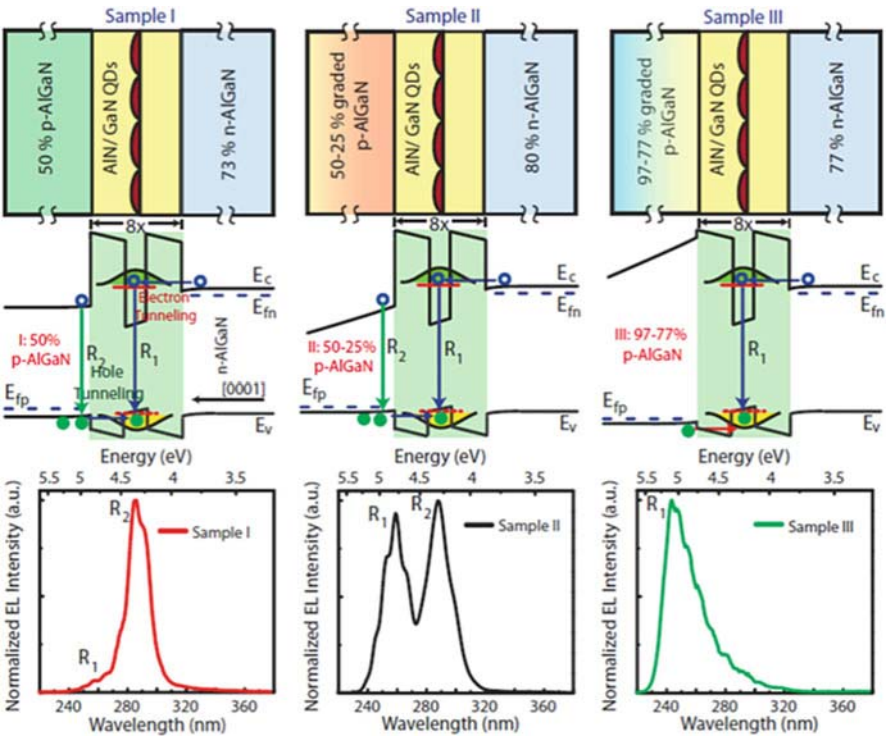

Fig. 10.37 Schematics and corresponding EL data demonstrating enhancement of emission from the active region of a DUV LED due to usage of a polarization-induced graded p-AlGaN cladding layer [11]

10.5.3 Tunable Deep-UV Emission over 232–270 nm

Deep-UV LEDs using ultrathin GaN QDs in the active region are discussed in this section. The emission wavelength has been tuned over 232–270 nm by changing the GaN layer thicknesses with monolayer (ML) precision. The pi-doping scheme is employed for both n and p contact regions to enhance the electrical injection of the carriers into the devices. As outlined in [77], a linearly graded-up metal polar AlGaN layer is used as the pi-doped n region. Similarly, a graded-down layer is used for the p-type doping layer.

The epitaxial structures for the UV-LEDs were grown on commercially available ~1 μm-thick AlN templates on ~430 μm-thick sapphire. These AlN templates have a typical threading dislocation density of 1×10^{10} cm^{-2}. Epilayers were grown by plasma-MBE. A substrate temperature of 700°C (thermocouple reading) was maintained for the crystal growth of the entire LED structure except the Mg-doped region as shown in Fig. 10.38a.

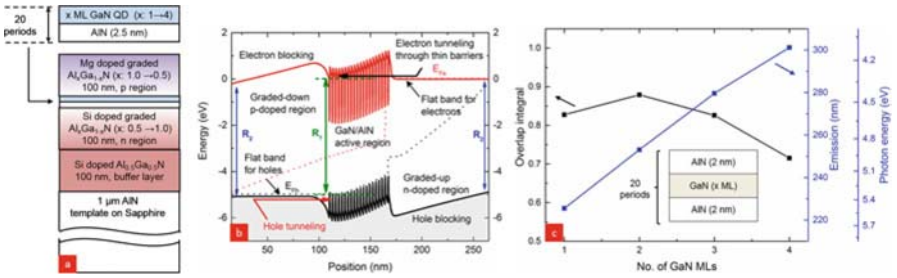

Fig. 10.38 (**a**) Heterostructure layer design of the UV LED devices showing the buffer, pi+Si-doped n layer, the active region, and pi+Mg-doped p layer, (**b**) simulated energy band diagram at 5V forward bias, and (**c**) simulation for evolution of emission wavelength/energy and overlap integral with GaN ML thickness for GaN/AlN heterostructures [47]. Reproduced from Appl. Phys. Lett. 111, 041108 (2017), with the permission of AIP Publishing

First, a 100-nm-thick Si-doped 50% AlGaN layer was grown followed by another 100 nm of linearly graded-up Si-doped AlGaN layer. Si doping concentration of $\sim 1 \times 10^{20}$ cm^{-3} was used. This graded-up layer served to produce pi-doping for enhanced n-conductivity. The composition of this layer was varied from 50% to 100% $Al_xGa_{1-x}N$. For the graded layer, both the Al and Ga fluxes were adjusted simultaneously to keep the surface free from excessive Ga accumulation.

After the n-type graded layer, 20 periods of GaN/AlN active regions were grown at 700°C substrate temperature. The growth rate was adjusted to 0.28 ML/s throughout at 400W of nitrogen plasma power. The GaN QDs were grown using SK growth method. To ensure 3D GaN island formation, a Ga/N$<$1 flux ratio was maintained. The thicknesses of the GaN QDs were adjusted over 1–4 MLs by growth time and Ga/N ratio. Three samples were grown with varying GaN ML thicknesses (D1 (1–2 MLs); D2 (2–3 MLs); D3 (3–4 MLs)). The AlN barrier layer thickness was kept constant at 2 nm to enable tunneling transport through it. The AlN layers were grown using migration-enhanced epitaxy (MEE). Finally, the active region was capped with Mg-doped downgraded AlGaN as a pi-doped p-layer. The composition of the 100-nm p-AlGaN was varied from 100% to 50%. Mg doping concentration of 10^{19} cm^{-3} was used. To incorporate Mg into the crystal, the substrate temperature was reduced to 630°C during the growth of the p-region.

Figure 10.38b shows the simulated energy band diagram at 5V forward bias using SiLENSe. The usefulness of pi-doping is manifested here clearly. Besides ensuring high electron/hole concentrations in the doped regions, there are also built-in electron and hole blocking layers that prevent carriers injected into the active region from spilling over to the p and n regions. The flat bands for holes (p-side) and electrons (n-side) ensure smooth carrier transport into the active region. As only 2-nm-thick AlN barriers were used in the GaN/AlN superlattices, the carriers were injected by tunneling. This mechanism helps reducing the voltage drop across the active region and improves the overall efficiency of the device.

The evolution of the wavelength of emitted photons and the corresponding electron–hole overlap integrals for GaN quantum well (QW)/AlN heterostructures

simulated using SiLENSe are shown in Fig. 10.38c. Based on the simulation, as the GaN thickness is reduced from 4ML→3ML→2ML→1ML the emission wavelength evolves as 290 nm→272 nm→250 nm→222 nm.

After growing the epitaxial layers, LED devices were fabricated. Mesa etch was performed to reach the n-type graded AlGaN region. A Cl_2-based reactive-ion etch was used to realize 200-nm-deep mesas. By using e-beam evaporation technique, Ti (20 nm)/Al (100 nm)/Ni (40 nm)/Au (50 nm) contact stacks were deposited as the n-contact metal. For the p-metal contact, first an Ni (5 nm)/Au (5 nm) current spreading layer was used. On top of this layer, a 50-μm diameter circular Ti (20 nm)/Au (100 nm) metal pad was deposited. The typical size of the UV LEDs investigated in this work was 200×200μm. Figure 10.39a shows the schematic of the processed device from the side. The SEM image taken from top of the device is shown in Fig. 10.39b.

Structural analysis using cross-sectional TEM was performed on the processed devices to investigate the layer structures, contacts, mesa, etc. Figure 10.39c shows a typical cross-sectional view of the device D2 (2–3-ML GaN QD). The grown layers matched the targeted thickness values. Grading in the Al composition was observed for both n and p layers by the change in the image contrast. The zoomed-in HAADF-STEM images are shown for devices D1–D3 in Fig. 10.39d–f. The thickness of the AlN barrier was ∼2 nm for all the three samples. The GaN layer thicknesses match the target value of 1–2 ML (D1), 2–3 ML (D2), and 3–4 ML (D3).

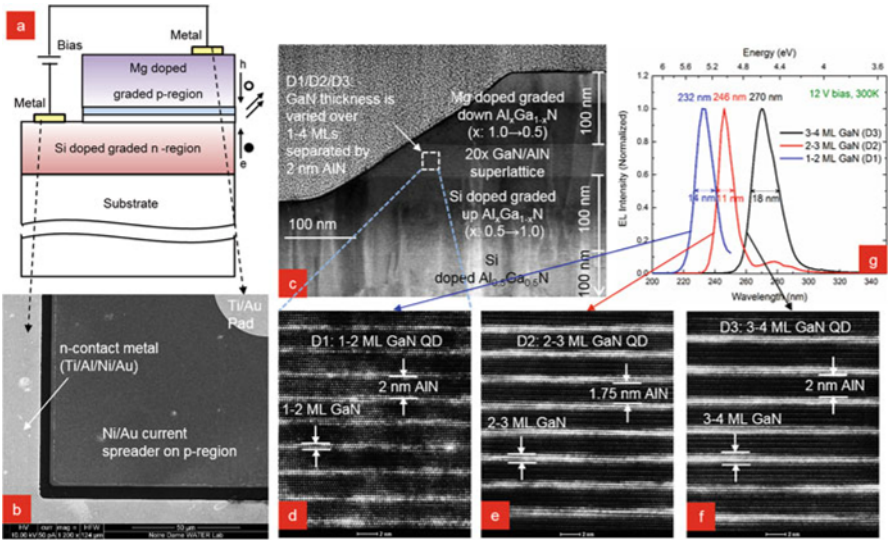

Fig. 10.39 (**a**) Schematic of the processed device, (**b**) SEM (top view) of a processed device showing n and p metal contacts. This is one quadrant view of the whole device, (**c**) cross-section HAADF-STEM image of a processed device showing different layers for a typical sample (D1/D2/D3), zoomed-in active region for (**d**) D1, (**e**) D2, (**f**) D3, and (**g**) EL spectra showing 232–270 nm tunable emission from 1–4-ML GaN active region [47]. Reproduced from Appl. Phys. Lett. 111, 041108 (2017), with the permission of AIP Publishing

For electrical characterization, room temperature electroluminescence (EL) measurements were performed on the samples. To avoid excessive heating, pulsed excitation under 10 kHz, 5% duty cycle was used for the characterization. All LEDs showed strong single peak emission at 300 K (Fig. 10.39g). A blue shift was observed in the EL emission peak wavelength from 270 nm→246 nm→232 nm as the thickness of the GaN layer was reduced. This trend was in good agreement with the simulation shown in Fig. 10.38c. The full width at half maximum (FWHM) was measured to be less than 20 nm (~325 meV) for all devices. Using GaN/AlN active region, the shortest EL wavelength reported before this was 239 nm [70]. This work demonstrates that by changing the thickness of GaN layer with an ML precision, it is possible to achieve tunable deep-UV LEDs emitting as short as 232 nm.

The EL data shown in Fig. 10.39g were measured with a 12-V forward bias. The turn-on voltages for the devices were ~7.5 V, larger than the bandgap and the peak emission wavelength energy. The undesired presence of AlN layers on either side of the active region was observed which can cause an increase in the turn-on voltage because of thicker tunneling barriers for the carriers. This can be avoided by further optimization of the graded layer growth conditions.

Figure 10.40a shows the comparison between the measured and the simulated EL spectra using SiLENSe. The simulation was performed with 1–2–3-ML GaN QW active region. The discrepancy in the peak wavelength between the simulation and measurement was due to the geometry of the GaN region in the experimental devices (QDs instead of uniform QWs). Also in Fig. 10.40b, besides the EL emission peak R1 from the active region, the presence of a secondary EL peak R_2 was seen around ~4.6 eV. The origin of this peak is explained in Fig. 10.38b.

The EL spectra were collected from the top of the devices through the graded-down p-region. This p-AlGaN region was designed to have a minimum Al composition of 50% to boost the polarization doping with a 0.5%/nm grading gradient

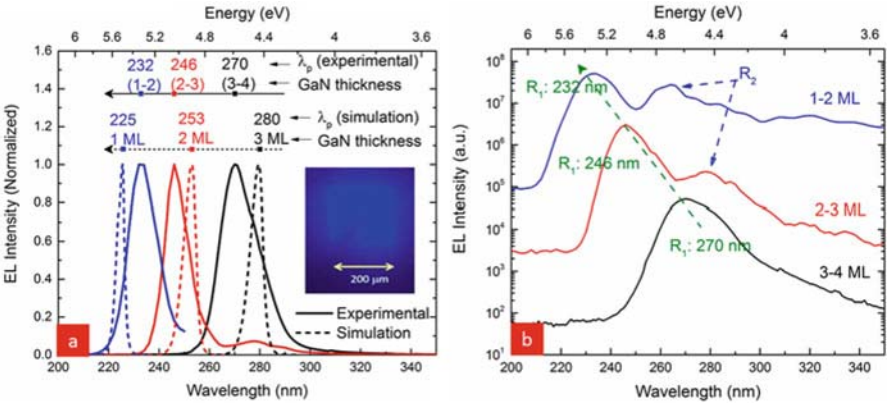

Fig. 10.40 (**a**) Measured and simulated EL spectra, inset shows good current spreading, (**b**) EL spectra plotted in log scale to show the peak due to reabsorption [47]. Reproduced from Appl. Phys. Lett. 111, 041108 (2017), with the permission of AIP Publishing

(graded down from 100% to 50% $Al_xGa_{1-x}N$ over 100 nm). The graded n-AlGaN was designed similarly with a 50% AlGaN as the minimum Al content to boost the polarization-induced doping and also to form a decent contact with the external Ti/Al/Ni/Au metal stack. The 100-nm-thick buffer n-AlGaN therefore had a 50% Al composition as well. $Al_{0.5}Ga_{0.5}N$ has a bandgap of 4.6 eV (~270 nm) and therefore, the 232-nm (246-nm) emission from D1 (D2) active regions was susceptible to absorption in $Al_{0.5}Ga_{0.5}N$. The photons emitted in the active region could get reabsorbed in the 100-nm n-type buffer region and partially in the graded p/n layers. The photons were therefore down converted to generate the secondary R_2 peaks. The secondary emission was relatively stronger for D1 compared to D2, which is explained by a thicker reabsorption volume in the graded layers for D1 due to higher energy R_1 peak (5.34 eV for D1 vs 5.04 eV for D2). On the contrary, D3 showed a single peak (R_1) dominated EL spectra since $Al_{0.5}Ga_{0.5}N$ is transparent to 270 nm. Transparency of the R1 peak can be achieved for D1 and D2 devices by choosing the appropriate minimum composition of p and n-AlGaN, i.e., $Al_{0.7}Ga_{0.3}N$. This will ensure transparency though with a compromise in the boost in polarization doping.

In summary, tunable deep-UV electroluminescence over 232–270 nm has been demonstrated using few monolayers thick GaN quantum structures with AlN barriers on AlN-on-sapphire templates. Emission wavelength as short as 232 nm has been achieved using 1–2-ML GaN quantum structures with a spectral linewidth of 14 nm at 300K. Plasma-assisted molecular beam epitaxy was used to maintain precise control on the thickness of the grown epitaxial layers. Tunneling transport through the barriers and pi-doping was used to enhance electroluminescence in the deep-UV.

10.5.4 Cryogenic Operation of a Deep-UV LED

In this section, a pi-doped and tunneling-injection-assisted deep-UV LED device is discussed that can emit light at cryogenic temperature. The device also showed negative-differential-resistance (NDR) phenomena which is unheard of with regard to a DUV photonic device [75].

The LED structure was grown on a commercially available metal polar 1-μm-thick AlN template on sapphire with a threading dislocation density of $\sim 1 \times 10^{10}$ cm^{-2}. For deep-UV light-emitting region, 1–2 monolayers (MLs)-thick GaN layers were inserted in between 10-ML (2.5-nm)-thick AlN barriers. A linearly graded-down buffer $Al_xGa_{1-x}N$ region was introduced between the AlN substrate and the pi-doped upgraded n-region to eliminate any abrupt change in composition and reduce formation of threading dislocations due to lattice mismatch between AlGaN and AlN substrate.

For the MBE growth of the structure, a 5-nm AlN nucleation layer was first grown at 700°C substrate temperature (T_{sub}) using migration-enhanced epitaxy (MEE). Next, as shown in Fig. 10.41a, there were three ~100-nm linearly graded AlGaN layers in the LED structure:

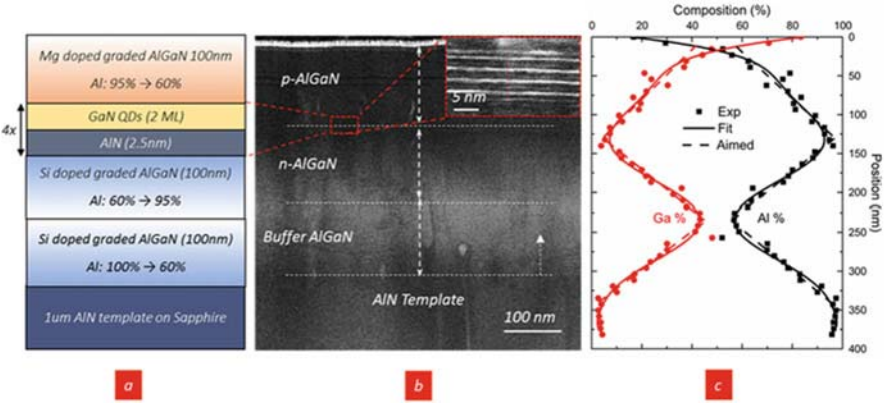

Fig. 10.41 (**a**) Schematic of the deep-UV LED, (**b**) Z-contrast STEM micrograph shows smooth contrast variation for linearly graded AlGaN regions, ML-thick GaN/AlN active region can be observed in the inset, and (**c**) EDX scan across the device showing linear grading of the AlGaN composition with desired compositions [75]

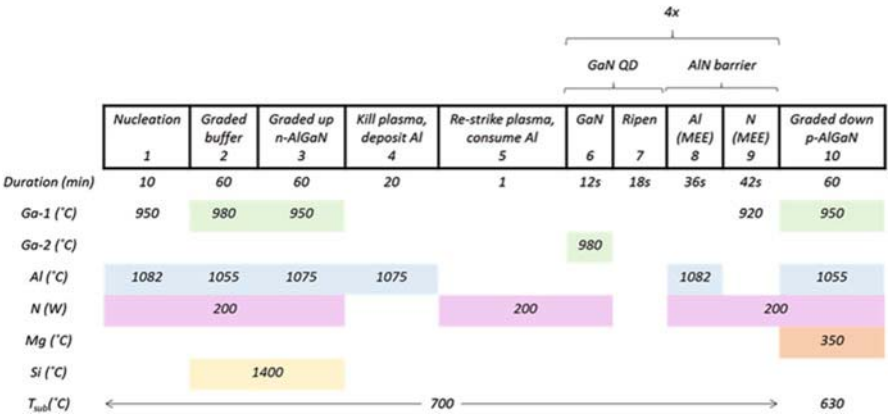

Fig. 10.42 Flux-time diagram showing detailed MBE growth parameters for the LED shown in Fig. 10.41 [63]

(i) Graded-down Si-doped buffer layer (T_{sub} = 700°C),
(ii) Graded-up pi-induced Si-doped n-type layer (T_{sub} = 700°C), and
(iii) Graded-down pi-induced Mg-doped p-type layer (T_{sub} = 630°C).

The substrate temperature was reduced to 630°C for the growth of the p-region to promote the incorporation of Mg into the crystal.

A typical growth flux-time diagram is shown in Fig. 10.42. The duration for growth of each layer, shutter position of effusion cells, cell temperatures, substrate temperature, dopant cell temperature, etc. are mentioned in this diagram. The Al and Ga cell temperatures were controlled by a computer program to obtain a linear

variation of fluxes with growth time. After the n-graded-up layer, the plasma was turned-off, and sample was annealed at 700°C for 20 min to desorb any excess Ga from the surface which accumulates due to metal-rich AlGaN layer growth.

The doping concentrations were 5×10^{19} cm^{-3} (Si) and 1×10^{19} cm^{-3} (Mg) as determined by SIMS calibration growths performed separately. For the graded layer growths, both Al and Ga metal fluxes were varied to avoid significant accumulation of metal on the growth surface. This was confirmed by the observation of streaky RHEED pattern throughout the crystal growth. The growth rate for the whole structure was 0.17 ML/sec. This was accurately estimated from RHEED intensity oscillations and TEM analysis. A precise knowledge of growth rate was essential to grow the ultrathin GaN-/AlN-based active region.

Four periods of ultrathin GaN quantum disk (QD)/AlN barrier heterostructure were inserted between the doped regions as the deep-UV light-emitting active region. The 2 MLs GaN QDs were grown in the SK mode. To ensure such a growth mode, Ga/N ratio was kept <1 for the GaN QDs. MEE method was used to grow 10 MLs (2.5 nm) of AlN barriers.

The AlN barriers were kept thin (2.5 nm) to allow sub-barrier tunneling of carriers into GaN QDs. The active region was designed for an emission wavelength around 250 nm. A minimum Al content for the graded p- and n-type AlGaN layers was designed to be 60% to guarantee optical transparency to 250-nm emission because $Al_{0.6}Ga_{0.4}N$ has an absorption edge <250 nm.

STEM micrographs shown in Fig. 10.41b and the EDX profile in Fig. 10.41c show gradual changes in the image contrast associated with Al and Ga compositional grading. The experimentally measured concentration profile matched closely with the values that were targeted. The zoomed-in image for the active region is shown in the inset of Fig. 10.41b. It confirmed 4 layers of GaN QDs inserted in $\sim$2-nm AlN barriers.

After the MBE growth, a mesa etch was performed using Cl_2-based ICP-RIE to reach the graded n-AlGaN region to form the n-type contacts. Ti (20 nm)/Al (100 nm)/Ni (40 nm)/Au (50 nm) metal stacks were deposited as n-type contacts using e-beam evaporation. For the p-contact, first an Ni (5 nm)/Au (5 nm) current spreading layer was deposited followed by deposition of a smaller area Ti (20 nm)/Au (100 nm) metal pads for probing.

The simulated energy band diagram using SiLENSe for the LED device at 5V forward bias is shown in Fig. 10.43a,b. The graded pi-doped regions provide a flat band profile for smooth carrier transport for both holes on the p-side and electrons on the n-side. The tunnel injection mechanism is schematically shown in Fig. 10.43b. At a forward bias voltage of $\sim$5 V, the energy of electrons in conduction band lines up with carrier eigenstates in 2-ML QDs. The AlN barriers in the active region being thin, the carriers can tunnel through the barriers into the GaN QD eigenstates.

As a part of the device characterization, current density vs. voltage (J-V) and electroluminescence (EL) vs. current/voltage measurements were performed. All examined devices had sizes larger than 100 μm $\times$100 μm. The J-V characteristics revealed a very interesting phenomenon not often observed in bipolar optical

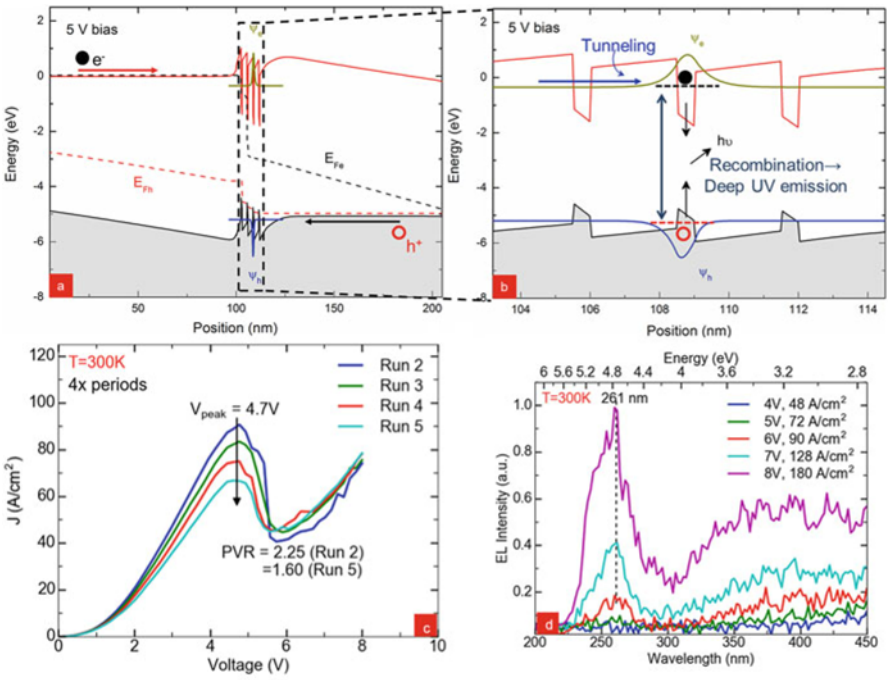

Fig. 10.43 (**a**) Energy band diagram for the active region at 5 V forward bias showing tunnel injection of carriers and (**b**) light emission process due to recombination. (**c**) Tunneling is evidenced by NDR in J-V. (**d**) Light emission turns-ON at NDR voltage [63]

devices, namely negative differential resistance (NDR). Figure 10.43c exhibits J-V sweeps on the UV LED device. Starting from the second sweep, clear NDR is observed at ~4.8 V.

On some devices, the NDR sustained for more than 20 scans, but the peak-to-valley ratio (PVR) degraded over subsequent sweeps. The highest PVR measured was 2.25 for the second scan. The diminishing NDR could be due to charge trapping at defect levels in the AlN barriers. NDR is a signature of tunneling through the barriers into well-defined electronic eigenstates of QDs as often seen in resonant tunnel diodes (RTDs) [86]. For the LEDs, a turn-on voltage around ~5V was expected but the current started to flow at a low bias (<0.5 V). This was probably the leakage current due to the growth on AlN/sapphire templates with high $\sim 1 \times 10^{10}$ cm^{-2} density of threading dislocations (TDs). Each 100 μm×100 μm LED device therefore should contain $\sim 10^6$ TDs and thus might be leaky. Since the tunneling mechanism and the electroluminescence should proceed through the same electronic levels in the GaN regions, a correlation between the NDR and the EL on-set was expected. Indeed, the EL turn-on took place at the same voltage range where the NDR was detected. This was further confirmed from the L-I characteristics plotted in Fig. 10.44b.

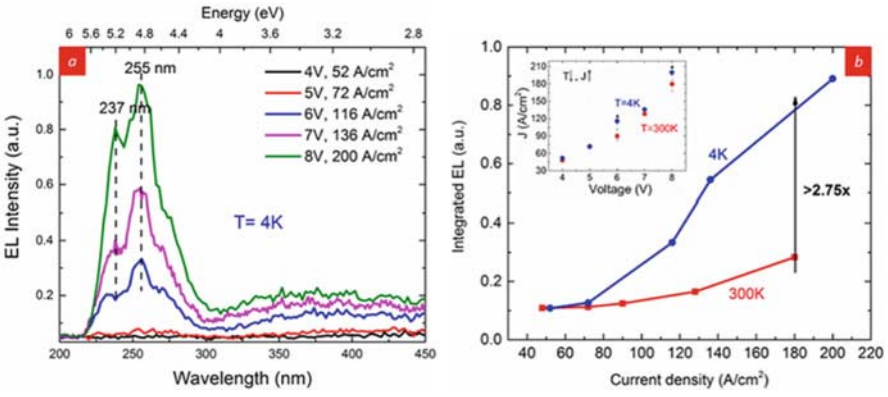

Fig. 10.44 (**a**) Normalized electroluminescence at 4K, and (**b**) comparison of integrated EL between 300K and 4K. Inset shows increase of conductivity of device at low temperature [63]

Figure 10.43d shows the corresponding EL spectra taken at 300K under various injection currents. To avoid excessive heating, pulsed current injection at 10 kHz, 5% duty cycle was used. The 261-nm peak emission with a shoulder around 240 nm appeared first between 5V and 6V biases, in the NDR region. This indicated that the EL and the tunneling mechanisms were closely related, due to tunneling injection of carriers into the GaN active area. A monotonic increase of EL intensity vs. applied bias was observed over 5V→8V range. Above 8V forward bias, the top metal contact started to degrade due to heat dissipation in the p-contact layer. Therefore, for longer measurements the LEDs were limited to biases less than 8V.

Because of the pi-induced doping and the tunneling mechanism for carrier injection both of which are temperature-independent processes, the LEDs examined here were supposed to operate at cryogenic temperatures. To confirm this, the J-V and EL vs. J measurements were performed at temperatures down to 4K. The results are shown in Fig. 10.44a. The low-temperature measurements provided strong evidence that the devices were functional even at 4K. Strong EL was detected and the peak position blue-shifted from 261 nm to 255 nm according to Varshni's law as the temperature was lowered from 300K to 4K. A secondary peak at 237 nm became clearly visible at low temperatures. This is described by the bimodal distribution of GaN QD thicknesses. A prominent 237-nm peak at low temperature indicated suppressed carrier transport between QDs at cryo-temperatures. In contrast, at room temperature the carriers were free to find the lowest energy levels for recombination which were the thicker 2-ML QDs and therefore the ~260-nm emission dominated as seen in Fig. 10.43d. The LED turn-on voltage stayed still between 5–6V at 4K, which coincided with the NDR region. Higher current densities at 4K seen in the inset of Fig. 10.44b indicated that the conductivity of the graded layers increased at lower temperatures. Measurement of EL at 4K with higher contact conductivity than 300K confirmed the effectiveness of polarization doping.

The integrated EL intensity at 4K exhibited more than 275% enhancement of light emission vs. 300K measurements as indicated in Fig. 10.44b. This enhancement of EL emission is explained by the suppression of carrier migration to non-radiative recombination centers such as threading dislocations. A similar ratio was detected for PL of such GaN/AlN heterostructures under 157-nm excitation as explained in Sect. 10.4.2.4.

As a control sample, an LED was fabricated with the conventional nongraded AlGaN layers for contacts but with a similar GaN/AlN light-emitting active region. For such a device, conventional temperature-assisted doping is expected to lead to more resistive contacts at low temperatures due to carrier freeze-out. This should dramatically reduce the electroluminescence intensity at low temperature. The control sample had a 200-nm-thick Si-doped $Al_{0.77}Ga_{0.23}N$ layer as the n-type contact and a 100-nm-thick Mg-doped $Al_{0.5}Ga_{0.5}N$ as the p-type contact. The active region GaN/AlN QD/barrier structure was designed to emit around 300 nm. The EL spectra for the control sample showed strong room temperature EL emission with an emission peak at 298 nm. Temperature-dependent EL measurements showed more than 20 times reduction in the intensity as the device temperature was cooled down to 80K, as shown in Fig. 10.45b.

This reduction is explained by the carrier freeze-out at cryogenic temperatures in the nongraded AlGaN layers. Figure 10.45a on the other hand shows more than 2.75 times enhancement in light emission at 4K. The control sample investigated here had an emission at 298 nm. Carrier injection for $<$260-nm LEDs using conventional doping becomes even more challenging due to more resistive contacts with higher Al-containing AlGaN layers. Therefore, the carrier freeze-out effect for $<$260-nm LED with conventional doping can be more severe. Putting this together, it is concluded that the pi-doping enhances the light emission at least 55 times ($>2.75\times20$) at cryogenic temperature compared to the conventional doping scheme.

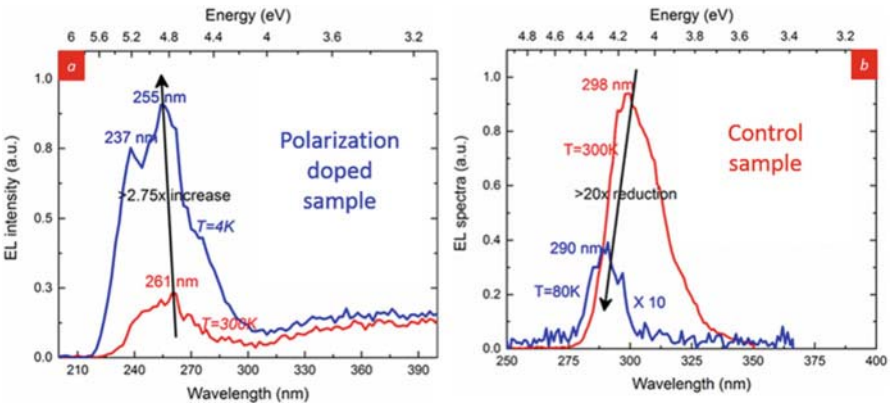

Fig. 10.45 Comparative temperature-dependent EL spectra for (**a**) pi-doped and (**b**) conventionally doped (control sample)

In summary, by exploiting the polarization-induced doping, improved operation of deep-UV LEDs has been achieved at cryogenic temperatures. The LED devices were operated at ~237–260 nm over the temperature range of 4K–300K. 1–2-monolayer-thick GaN quantum disks sandwiched between 10-ML (2.5-nm) AlN barriers were used to generate the deep-UV emission. Carriers were injected into the GaN active layers by tunneling through the AlN barriers. Tunneling was confirmed by the presence of NDR in forward bias J-V characteristics. Improvement in conductivity of the devices due to pi-doping at low temperature was observed. Enhancement in light emission of more than 275% was observed at cryogenic temperature. Also, the effectiveness of pi-doping at lower temperatures was confirmed by comparing the EL with a conventional impurity-doped UV LED device. This demonstration of cryogenic operation of deep-UV LEDs will be attractive in design of light emitters/sensors for low-temperature deep-space applications.

10.6 Enhancement of Light Extraction with Ultrathin GaN/AlN Quantum Heterostructure Deep-UV LEDs

The challenge of light extraction for deep-UV LEDs has been discussed earlier in Sects. 10.2.3 and 10.3.2. For the conventional AlGaN alloy-based active region design, as the Al content is increased to achieve <250-nm deep-UV emission, the valence band structure changes in a way that favors transverse-magnetic (TM) polarized light emission over transverse electric (TE) [51, 52, 70, 87]. For a typical surface-emitting LED, TM polarized light extraction is challenging due to total internal reflection. On the contrary, the valence band structure of GaN allows for isotropic distribution of light emission. The AlN distribution is strongly towards the edge and thus not suitable for a surface-emitting LED.

The ultrathin GaN/AlN quantum heterostructure-based surface-emitting LEDs are therefore promising from the light extraction perspective due to isotropic radiation pattern. Liu et al. [87] performed a careful study of theoretical analysis and experimental measurement of polarization of emitted light for a 298-nm GaN/AlN quantum structure-based UV-LED.

The LED investigated in this study was grown by plasma-assisted MBE on standard metal-polar AlN template on sapphire substrate. First, an MBE AlN nucleation layer is grown followed by Si-doped 200-nm n-AlGaN layer with 77% Al content. The active region of the LED was formed with 3–4-monolayer GaN QDs sandwiched in 2.5-nm AlN tunneling barriers. 8 repeats of the heterostructures were used to enhance the light emission intensity. The AlN barrier layers were formed using migration-enhanced epitaxy technique. The 3–4 monolayers GaN were grown in SK mode aiming for an emission wavelength of 300 nm. The p-AlGaN layer was grown as a 100-nm Mg-doped AlGaN with 50% Al content. The composition of the layers was confirmed based on HR-XRD and HR-TEM analysis. For device processing, standard mesa etch was performed to form n-contact to the

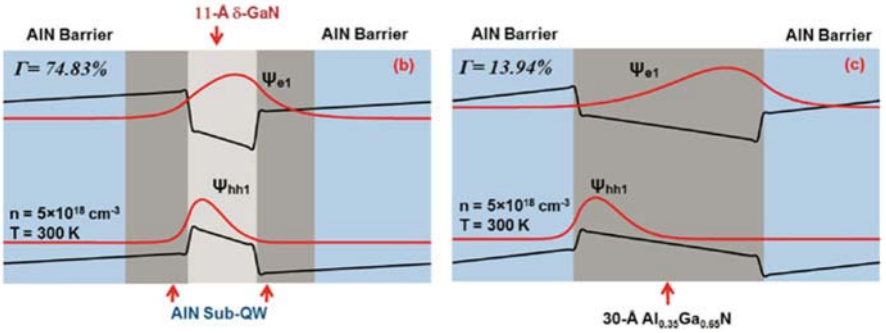

Fig. 10.46 Simulated energy band diagrams and electron–hole wavefunctions comparing ultrathin GaN/AlN and AlGaN/AlN heterostructures for 298-nm emission [87]. Reproduced from Appl. Phys. Lett. 110, 071103 (2017), with the permission of AIP Publishing

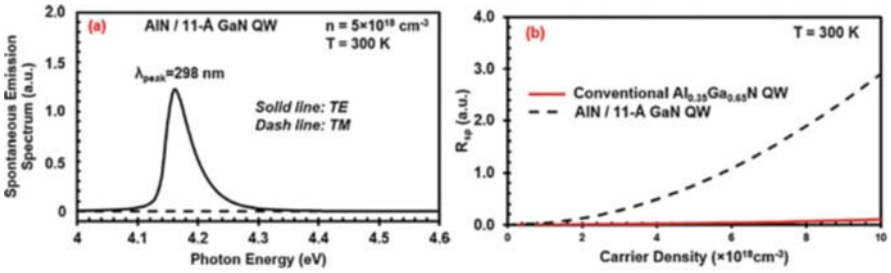

Fig. 10.47 (**a**) Simulated spontaneous emission spectra for the GaN/AlN structure showing strong TE emission with a 298-nm peak wavelength, and (**b**) enhanced spontaneous emission rate is expected for GaN/AlN compared to AlGaN/AlN design [87]. Reproduced from Appl. Phys. Lett. 110, 071103 (2017), with the permission of AIP Publishing

bottom n-AlGaN region. Ti/Al/Ni/Au metal stacks were used for the n-contact. Semitransparent Ni/Au metal stacks were put for contact to the p-AlGaN followed by Ti/Au contact pad. None of the contacts were annealed.

Two different heterostructure designs were simulated for comparison, one containing the GaN/AlN active region and the other having AlGaN/AlN aiming for ~300-nm emission wavelengths. The simulated energy band diagrams and the corresponding electron–hole wavefunctions are depicted in Fig. 10.46. The significantly higher overlap of 74.83% for the GaN/AlN structure compared to 13.94% for the 3-nm AlGaN/AlN quantum well design is a consequence of QCSE effect as discussed in Sect. 10.2.1.2.

This large overlap integral further predicts higher spontaneous emission rate for the GaN/AlN structure compared to AlGaN/AlN. Figure 10.47a shows the simulated spontaneous emission spectra for the GaN/AlN design. A 298-nm peak emission wavelength is calculated for 1.1-nm GaN QW/AlN barrier design. The light emission pattern is calculated to be strongly TE polarized.

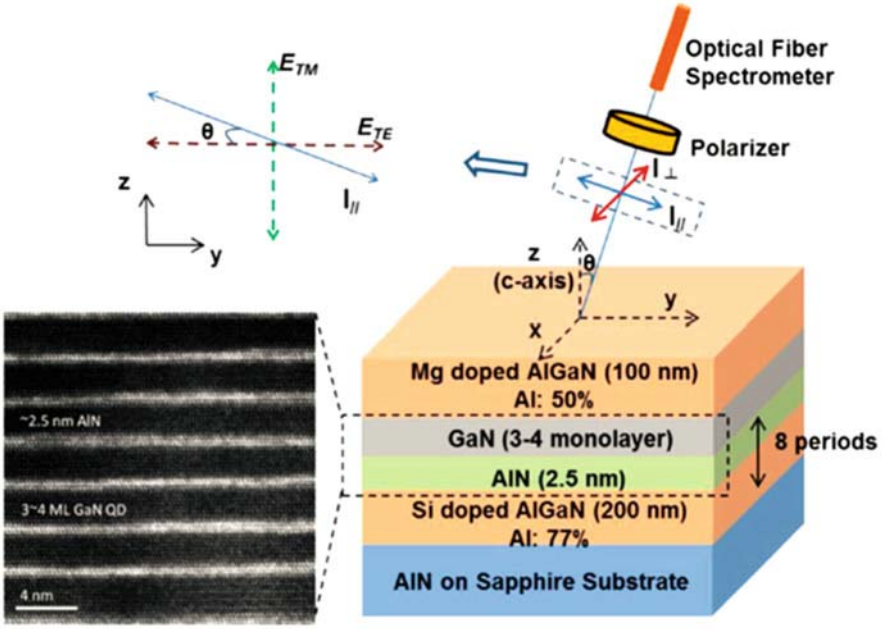

Fig. 10.48 Schematic diagram of the polarization-dependent EL measurement setup and cross-sectional TEM image of the AlN/GaN QW-like structure, the θ stands for the angle between c-axis and collecting fiber. The polarizer is held on a rotational stage to achieve the intensity in y-z plane and the intensity along x direction [87]. Reproduced from Appl. Phys. Lett. 110, 071103 (2017), with the permission of AIP Publishing

Figure 10.47b compares the spontaneous emission rate between GaN/AlN and AlGaN/AlN designs over a wide range of injected carried densities. Figure 10.47a shows the simulated spontaneous emission spectra for the GaN/AlN design. The enhanced spontaneous rate from GaN/AlN confirms what was predicted from the overlap integral simulation from Fig. 10.46.

Angle-resolved electroluminescence measurement was performed on the processed GaN/AlN quantum structure-based LED devices, and polarization of the emitted light was extracted. The schematic setup of such measurement is shown in Fig. 10.48. Strong electroluminescence around 300 nm was measured. The extracted TE/TM ratio at 30° respective to the surface normal to LED was found to be 15.3 as shown in Fig. 10.49. At another collection angle of 45°, the extracted TE/TM ratio of 4.05 still showed TE-dominant emission from the device.

In summary, ultrathin GaN/AlN quantum heterostructure-based LEDs were fabricated as a 298-nm UV-LED, and the polarization property of the emitted light was simulated and measured experimentally. The simulation suggested significantly enhanced TE/TM ratio of emitted light for the GaN/AlN design. The measurement confirmed such prediction over a wide range of angular range. This specific distribution of emitted light pattern will enhance the light extraction efficiency and therefore further boost the overall external quantum efficiency of UV-LEDs.

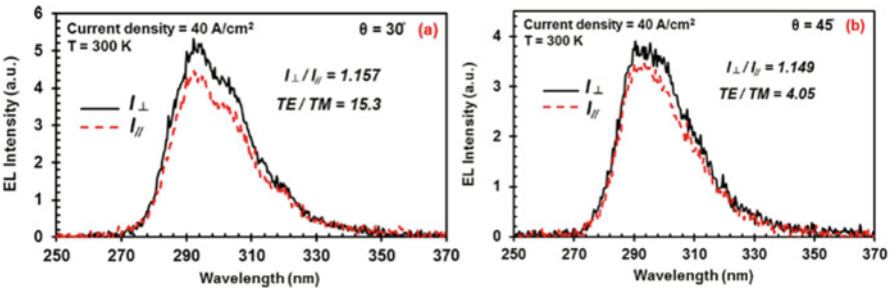

Fig. 10.49 Polarization-dependent EL spectra measured at two different angles, (**a**) 30° and (**b**) 45° [87]. Reproduced from Appl. Phys. Lett. 110, 071103 (2017), with the permission of AIP Publishing

10.7 Conclusion

In this chapter, we have discussed few specific heterostructure design methods to overcome the fundamental bottlenecks that limit external quantum efficiency (EQE) for deep-UV light-emitting diodes. The EQE is composed of internal quantum efficiency (IQE), injection efficiency (INJ), and light extraction efficiency (LEE). Ultrathin GaN/AlN quantum heterostructure can be used to enhance the IQE by improving the electron–hole wavefunction overlap. The use of quantum disks instead of conventional quantum wells can further boost the IQE with additional carrier confinement that prevents non-radiative recombination through defects. Use of compositionally graded AlGaN heterostructures for field-assisted polarization-induced doping can lead to the pathway of enhanced injection efficiency. The doping efficiency for such temperature-independent design is enhanced compared to the conventional thermally assisted dopant activation in AlGaN films, and thus deep-UV LEDs operating at 4K can be realized. Finally, the light emission property of GaN being TE dominated compared to strongly TM-dominated AlGaN in the deep-UV range, the light extraction efficiency can be significantly enhanced with GaN/AlN quantum heterostructures. The enhancement of each of the IQE, INJ, and LEE has been discussed with simulation and experimental data. The experimental analysis consisted of few details of the crystal growth, device processing, and measurement. The combination of all the design rules presented here will help to enhance the current state-of-the-art low external quantum efficiency of deep-UV light-emitting diodes.

References

1. T. Mukai, D. Morita, S. Nakamura, High-power UV InGaN/AlGaN double-heterostructure LEDs. J. Cryst. Growth **189–190**, 778–781 (1998)
2. J.P. Theodore Moustakas, Gallium-Nitride (GaN) II, Vol. 57 (Academic Press, 1998)
3. Y. Taniyasu, M. Kasu, T. Makimoto, An aluminium nitride light-emitting diode with a wavelength of 210 nanometres. Nature **441**(7091), 325–328 (2006)

4. A. Khan, K. Balakrishnan, T. Katona, Ultraviolet light-emitting diodes based on group three nitrides. Nat. Photonics **2**(2), 77–84 (2008)
5. C. Pernot, M. Kim, S. Fukahori, T. Inazu, T. Fujita, Y. Nagasawa, A. Hirano, M. Ippommatsu, M. Iwaya, S. Kamiyama, I. Akasaki, H. Amano, Improved efficiency of 255–280 nm AlGaN-based light-emitting diodes. Appl. Phys. Express **3**(6) (2010)
6. H. Hirayama, Y. Tsukada, T. Maeda, N. Kamata, Marked enhancement in the efficiency of deep-ultraviolet AlGaN light-emitting diodes by using a multiquantum-barrier electron blocking layer. Appl. Phys. Express **3**(3) (2010)
7. M. Shatalov, W. Sun, A. Lunev, X. Hu, A. Dobrinsky, Y. Bilenko, J. Yang, M. Shur, R. Gaska, C. Moe, G. Garrett, M. Wraback, AlGaN deep-ultraviolet light-emitting diodes with external quantum efficiency above 10%. Appl. Phys. Express **5**(8) (2012)
8. F. Bernardini, V. Fiorentini, Nonlinear behavior of spontaneous and piezoelectric polarization in III-V nitride alloys. Phys. Status Solidi (a) **190**(1), 65–73 (2002)
9. T. Takano, T. Mino, J. Sakai, N. Noguchi, K. Tsubaki, H. Hirayama, Deep-ultraviolet light-emitting diodes with external quantum efficiency higher than 20% at 275 nm achieved by improving light-extraction efficiency. Appl. Phys. Express **10**(3) (2017)
10. M. Kneissl, T. Kolbe, C. Chua, V. Kueller, N. Lobo, J. Stellmach, A. Knauer, H. Rodriguez, S. Einfeldt, Z. Yang, N.M. Johnson, M. Weyers, Advances in group III-nitride-based deep UV light-emitting diode technology. Semicond. Sci. Technol. **26**(1) (2011)
11. J.K. Verma, Polarization and band gap engineered III-nitride optoelectronic device structures. Doctoral Dissertation, University of Notre Dame, 2013
12. S. Karpov, ABC-model for interpretation of internal quantum efficiency and its droop in III-nitride LEDs: a review. Opt. Quant. Electron. **47**(6), 1293–1303 (2015)
13. J. Piprek, Efficiency droop in nitride-based light-emitting diodes. Phys. Status Solidi (a) **207**(10), 2217–2225 (2010)
14. M.-H. Kim, M.F. Schubert, Q. Dai, J.K. Kim, E.F. Schubert, J. Piprek, Y. Park, Origin of efficiency droop in GaN-based light-emitting diodes. Appl. Phys. Lett. **91**(18) (2007)
15. G. Verzellesi, D. Saguatti, M. Meneghini, F. Bertazzi, M. Goano, G. Meneghesso, E. Zanoni, Efficiency droop in InGaN/GaN blue light-emitting diodes: Physical mechanisms and remedies. J. Appl. Phys. **114**(7) (2013)
16. S.F. Chichibu, H. Marchand, M.S. Minsky, S. Keller, P.T. Fini, J.P. Ibbetson, S.B. Fleischer, J.S. Speck, J.E. Bowers, E. Hu, U.K. Mishra, S.P. DenBaars, T. Deguchi, T. Sota, S. Nakamura, Emission mechanisms of bulk GaN and InGaN quantum wells prepared by lateral epitaxial overgrowth. Appl. Phys. Lett. **74**(10), 1460–1462 (1999)
17. Q. Dai, M.F. Schubert, M.H. Kim, J.K. Kim, E.F. Schubert, D.D. Koleske, M.H. Crawford, S.R. Lee, A.J. Fischer, G. Thaler, M.A. Banas, Internal quantum efficiency and nonradiative recombination coefficient of GaInN/GaN multiple quantum wells with different dislocation densities. Appl. Phys. Lett. **94**(11) (2009)
18. M. Soltani, R. Soref, T. Palacios, D. Englund, AlGaN/AlN integrated photonics platform for the ultraviolet and visible spectral range. Opt Express **24**(22), 25415–25423 (2016)
19. H. Hirayama, S. Fujikawa, J. Norimatsu, T. Takano, K. Tsubaki, N. Kamata, Fabrication of a low threading dislocation density ELO-AlN template for application to deep-UV LEDs. Phys. Status Solidi (c) **6**(S2), S356–S359 (2009)
20. M. Conroy, V.Z. Zubialevich, H. Li, N. Petkov, J.D. Holmes, P.J. Parbrook, Epitaxial lateral overgrowth of AlN on self-assembled patterned nanorods. J. Mater. Chem. C **3**(2), 431–437 (2015)
21. V.N. Jmerik, E.V. Lutsenko, S.V. Ivanov, Plasma-assisted molecular beam epitaxy of AlGaN heterostructures for deep-ultraviolet optically pumped lasers. Phys. Status Solidi (a) **210**(3), 439–450 (2013)
22. R. Dalmau, Z. Sitar, AlN bulk crystal growth by physical vapor transport, in *Springer Handbook of Crystal Growth*, ed. by G. Dhanaraj, K. Byrappa, V. Prasad, M. Dudley (Springer, Berlin, Heidelberg, 2010), pp. 821–843
23. J.S. Speck, S.J. Rosner, The role of threading dislocations in the physical properties of GaN and its alloys. Phys. B Condens. Matter **273–274**, 24–32 (1999)

24. R. Collazo, J. Xie, B.E. Gaddy, Z. Bryan, R. Kirste, M. Hoffmann, R. Dalmau, B. Moody, Y. Kumagai, T. Nagashima, Y. Kubota, T. Kinoshita, A. Koukitu, D.L. Irving, Z. Sitar, On the origin of the 265 nm absorption band in AlN bulk crystals. Appl. Phys. Lett. **100**(19) (2012)
25. R. Dalmau, B. Moody, R. Schlesser, S. Mita, J. Xie, M. Feneberg, B. Neuschl, K. Thonke, R. Collazo, A. Rice, J. Tweedie, Z. Sitar, Growth and characterization of AlN and AlGaN epitaxial films on AlN single crystal substrates. J. Electrochem. Soc. **158**(5) (2011)
26. K. Zhu, M.L. Nakarmi, K.H. Kim, J.Y. Lin, H.X. Jiang, Silicon doping dependence of highly conductive n-type Al0.7Ga0.3N. Appl. Phys. Lett. **85**(20), 4669–4671 (2004)
27. R. France, T. Xu, P. Chen, R. Chandrasekaran, T.D. Moustakas, Vanadium-based Ohmic contacts to n-AlGaN in the entire alloy composition. Appl. Phys. Lett. **90**(6) (2007)
28. J.P. Zhang, A. Chitnis, V. Adivarahan, S. Wu, V. Mandavilli, R. Pachipulusu, M. Shatalov, G. Simin, J.W. Yang, M.A. Khan, Milliwatt power deep ultraviolet light-emitting diodes over sapphire with emission at 278 nm. Appl. Phys. Lett. **81**(26), 4910–4912 (2002)
29. M.L. Nakarmi, K.H. Kim, M. Khizar, Z.Y. Fan, J.Y. Lin, H.X. Jiang, Electrical and optical properties of Mg-doped Al0.7Ga0.3N alloys. Appl. Phys. Lett. **86**(9) (2005)
30. Y. Bilenko, A. Lunev, X. Hu, J. Deng, T.M. Katona, J. Zhang, R. Gaska, M.S. Shur, W. Sun, V. Adivarahan, M. Shatalov, A. Khan, 10 Milliwatt pulse operation of 265 nm AlGaN light emitting diodes. Jpn. J. Appl. Phys. **44**(3), L98–L100 (2005)
31. H. Yu, E. Ulker, E. Ozbay, MOCVD growth and electrical studies of p-type AlGaN with Al fraction 0.35. J. Cryst. Growth **289**(2), 419–422 (2006)
32. T. Kinoshita, T. Obata, H. Yanagi, S.-i. Inoue, High p-type conduction in high-Al content Mg-doped AlGaN. Appl. Phys. Lett. **102**(1) (2013)
33. T. Mori, K. Nagamatsu, K. Nonaka, K. Takeda, M. Iwaya, S. Kamiyama, H. Amano, I. Akasaki, Crystal growth and p-type conductivity control of AlGaN for high-efficiency nitride-based UV emitters. Phys. Status Solidi (c) **6**(12), 2621–2625 (2009)
34. K.P. Streubel, T. Passow, H. Jeon, R. Gutt, M. Maier, L.-W. Tu, N. Linder, W. Pletschen, M. Kunzer, R. Schmidt, J. Wiegert, D. Luick, S. Liu, K. Köhler, J. Wagner, Ni/Ag as low resistive ohmic contact to p-type AlGaN for UV LEDs, in *Light-Emitting Diodes: Materials, Devices, and Applications for Solid State Lighting* XIV, 2010
35. B.A. Hull, S.E. Mohney, U. Chowdhury, R.D. Dupuis, Ohmic contacts to p-type Al0.45Ga0.55N. J. Appl. Phys. **96**(12), 7325–7331 (2004)
36. H.-K. Kim, T.-Y. Seong, I. Adesida, C.W. Tang, K.M. Lau, Low-resistance Pt/Pd/Au ohmic contacts to p-type AlGaN. Appl. Phys. Lett. **84**(10), 1710–1712 (2004)
37. M. Shatalov, W. Sun, R. Jain, A. Lunev, X. Hu, A. Dobrinsky, Y. Bilenko, J. Yang, G.A. Garrett, L.E. Rodak, M. Wraback, M. Shur, R. Gaska, High power AlGaN ultraviolet light emitters. Semicond. Sci. Technol. **29**(8) (2014)
38. J. Simon, V. Protasenko, C. Lian, H. Xing, D. Jena, Polarization-induced hole doping in wide-band-gap uniaxial semiconductor heterostructures. Science **327**(5961), 60–64 (2010)
39. J. Verma, P.K. Kandaswamy, V. Protasenko, A. Verma, H. Grace Xing, D. Jena, Tunnel-injection GaN quantum dot ultraviolet light-emitting diodes. Appl. Phys. Lett. **102**(4) (2013)
40. Y. Zhang, A.A. Allerman, S. Krishnamoorthy, F. Akyol, M.W. Moseley, A.M. Armstrong, S. Rajan, Enhanced light extraction in tunnel junction-enabled top emitting UV LEDs. Appl. Phys. Express **9**(5) (2016)
41. N. Maeda, H. Hirayama, Realization of high-efficiency deep-UV LEDs using transparent p-AlGaN contact layer. Phys. Status Solidi (c) **10**(11), 1521–1524 (2013)
42. M.R. Krames, M. Ochiai-Holcomb, G.E. Höfler, C. Carter-Coman, E.I. Chen, I.H. Tan, P. Grillot, N.F. Gardner, H.C. Chui, J.W. Huang, S.A. Stockman, F.A. Kish, M.G. Craford, T.S. Tan, C.P. Kocot, M. Hueschen, J. Posselt, B. Loh, G. Sasser, D. Collins, High-power truncated-inverted-pyramid $(Al_xGa_{1-x})_{0.5}In_{0.5}P/GaP$ light-emitting diodes exhibiting >50% external quantum efficiency. Appl. Phys. Lett. **75**(16), 2365–2367 (1999)
43. T. Kolbe, F. Mehnke, M. Guttmann, C. Kuhn, J. Rass, T. Wernicke, M. Kneissl, Improved injection efficiency in 290 nm light emitting diodes with Al(Ga)N electron blocking heterostructure. Appl. Phys. Lett. **103**(3) (2013)

44. Z. Ren, Q. Sun, S.Y. Kwon, J. Han, K. Davitt, Y.K. Song, A.V. Nurmikko, H.K. Cho, W. Liu, J.A. Smart, L.J. Schowalter, Heteroepitaxy of AlGaN on bulk AlN substrates for deep ultraviolet light emitting diodes. Appl. Phys. Lett. **91**(5) (2007)
45. M. Jo, N. Maeda, H. Hirayama, Enhanced light extraction in 260 nm light-emitting diode with a highly transparent p-AlGaN layer. Appl. Phys. Express **9**(1) (2016)
46. J. Verma, S.M. Islam, V. Protasenko, P. Kumar Kandaswamy, H. Xing, D. Jena, Tunnel-injection quantum dot deep-ultraviolet light-emitting diodes with polarization-induced doping in III-nitride heterostructures. Appl. Phys. Lett. **104**(2) (2014)
47. S.M. Islam, K. Lee, J. Verma, V. Protasenko, S. Rouvimov, S. Bharadwaj, H. Xing, D. Jena, MBE-grown 232–270 nm deep-UV LEDs using monolayer thin binary GaN/AlN quantum heterostructures. Appl. Phys. Lett. **110**(4) (2017)
48. J. Zhang, H. Zhao, N. Tansu, Effect of crystal-field split-off hole and heavy-hole bands crossover on gain characteristics of high Al-content AlGaN quantum well lasers. Appl. Phys. Lett. **97**(11) (2010)
49. T. Kolbe, A. Knauer, C. Chua, Z. Yang, S. Einfeldt, P. Vogt, N.M. Johnson, M. Weyers, M. Kneissl, Optical polarization characteristics of ultraviolet (In)(Al)GaN multiple quantum well light emitting diodes. Appl. Phys. Lett. **97**(17) (2010)
50. X.-H. Li, T.-T. Kao, M.M. Satter, Y.O. Wei, S. Wang, H. Xie, S.-C. Shen, P.D. Yoder, A.M. Fischer, F.A. Ponce, T. Detchprohm, R.D. Dupuis, Demonstration of transverse-magnetic deep-ultraviolet stimulated emission from AlGaN multiple-quantum-well lasers grown on a sapphire substrate. Appl. Phys. Lett. **106**(4) (2015)
51. C. Reich, M. Guttmann, M. Feneberg, T. Wernicke, F. Mehnke, C. Kuhn, J. Rass, M. Lapeyrade, S. Einfeldt, A. Knauer, V. Kueller, M. Weyers, R. Goldhahn, M. Kneissl, Strongly transverse-electric-polarized emission from deep ultraviolet AlGaN quantum well light emitting diodes. Appl. Phys. Lett. **107**(14) (2015)
52. J.E. Northrup, C.L. Chua, Z. Yang, T. Wunderer, M. Kneissl, N.M. Johnson, T. Kolbe, Effect of strain and barrier composition on the polarization of light emission from AlGaN/AlN quantum wells. Appl. Phys. Lett. **100**(2) (2012)
53. D.A.B. Miller, D.S. Chemla, T.C. Damen, A.C. Gossard, W. Wiegmann, T.H. Wood, C.A. Burrus, Band-edge electroabsorption in quantum well structures: the quantum-confined Stark effect. Phys. Rev. Lett. **53**(22), 2173–2176 (1984)
54. T. Tetsuya, S. Shigetoshi, K. Maki, K. Miho, T. Hideo, A. Hiroshi, A. Isamu, Quantum-confined Stark effect due to piezoelectric fields in GaInN strained quantum wells. Jpn. J. Appl. Phys. **36**(4A), L382 (1997)
55. J. Zhang, H. Zhao, N. Tansu, Large optical gain AlGaN-delta-GaN quantum wells laser active regions in mid- and deep-ultraviolet spectral regimes. Appl. Phys. Lett. **98**(17) (2011)
56. D. Bayerl, S.M. Islam, C.M. Jones, V. Protasenko, D. Jena, E. Kioupakis, Deep ultraviolet emission from ultra-thin GaN/AlN heterostructures. Appl. Phys. Lett. **109**(24) (2016)
57. J. Selles, C. Brimont, G. Cassabois, P. Valvin, T. Guillet, I. Roland, Y. Zeng, X. Checoury, P. Boucaud, M. Mexis, F. Semond, B. Gayral, Deep-UV nitride-on-silicon microdisk lasers. Sci. Rep. **6**(21650) (2016)
58. E. Kioupakis, Q. Yan, C.G. Van de Walle, Interplay of polarization fields and Auger recombination in the efficiency droop of nitride light-emitting diodes. Appl. Phys. Lett. **101**(23) (2012)
59. J.M. Rondinelli, E. Kioupakis, Predicting and designing optical properties of inorganic materials. Annu. Rev. Mater. Res. **45**(1), 491–518 (2015)
60. J.A. Ferrer-Pérez, B. Claflin, D. Jena, M. Sen, R. Vetury, D. Dorsey, Photoluminescence-based electron and lattice temperature measurements in GaN-based HEMTs. J. Electron. Mater. **43**(2), 341–347 (2014)
61. R. Bhattacharya, B. Pal, B. Bansal, On conversion of luminescence into absorption and the van Roosbroeck-Shockley relation. Appl. Phys. Lett. **100**(22) (2012)
62. L.K. Lee, L. Zhang, H. Deng, P.C. Ku, Room-temperature quantum-dot-like luminescence from site-controlled InGaN quantum disks. Appl. Phys. Lett. **99**(26) (2011)

63. S.M. Islam, V. Protasenko, S. Rouvimov, H. Xing, D. Jena, Sub-230 nm deep-UV emission from GaN quantum disks in AlN grown by a modified Stranski–Krastanov mode. Jpn. J. Appl. Phys. **55**(5S) (2016)
64. C.T. Foxon, C.S. Davis, S.V. Novikov, O.H. Hughes, T.S. Cheng, D. Korakakis, N.J. Jeffs, I. Grzegory, S. Porowski, RHEED studies of group III-Nitrides grown by MBE. Phys. Status Solidi (a) **176**(1), 723–726 (1999)
65. N. Gogneau, D. Jalabert, E. Monroy, E. Sarigiannidou, J.L. Rouvière, T. Shibata, M. Tanaka, J.M. Gerard, B. Daudin, Influence of AlN overgrowth on structural properties of GaN quantum wells and quantum dots grown by plasma-assisted molecular beam epitaxy. J. Appl. Phys. **96**(2), 1104–1110 (2004)
66. D. Doppalapudi, E. Iliopoulos, S.N. Basu, T.D. Moustakas, Epitaxial growth of gallium nitride thin films on A-Plane sapphire by molecular beam epitaxy. J. Appl. Phys. **85**(7), 3582–3589 (1999)
67. Y. Horikoshi, Migration-enhanced epitaxy of GaAs and AlGaAs. Semicond. Sci. Technol. **8**(6), 1032 (1993)
68. C. Adelmann, B. Daudin, R.A. Oliver, G.A.D. Briggs, R.E. Rudd, Nucleation and growth of GaN/AlN quantum dots. Phys. Rev. B **70**(12) (2004)
69. B. Daudin, F. Widmann, G. Feuillet, Y. Samson, M. Arlery, J.L. Rouvière, Stranski-Krastanov growth mode during the molecular beam epitaxy of highly strained GaN. Phys. Rev. B **56**(12), R7069–R7072 (1997)
70. Y. Taniyasu, M. Kasu, Polarization property of deep-ultraviolet light emission from C-plane AlN/GaN short-period superlattices. Appl. Phys. Lett. **99**(25) (2011)
71. K. Kamiya, Y. Ebihara, K. Shiraishi, M. Kasu, Structural design of AlN/GaN superlattices for deep-ultraviolet light-emitting diodes with high emission efficiency. Appl. Phys. Lett. **99**(15) (2011)
72. Z. Zheng, H. Ji, P. Yu, Z. Wang, Recent progress towards quantum dot solar cells with enhanced optical absorption. Nanoscale Res. Lett. **11**(1), 266 (2016)
73. Y.-K. Kuo, T.-H. Wang, J.-Y. Chang, Advantages of blue InGaN light-emitting diodes with InGaN-AlGaN-InGaN barriers. Appl. Phys. Lett. **100**(3) (2012)
74. T. Passow, K. Leonardi, A. Stockmann, H. Selke, H. Heinke, D. Hommel, High-resolution x-ray diffraction investigations of highly mismatched II-VI quantum wells. J. Phys. D Appl. Phys. **32**(10A), A42 (1999)
75. S. Islam, V. Protasenko, S. Rouvimov, J. Verma, H. Xing, D. Jena, Deep-UV LEDs using polarization-induced doping: Electroluminescence at cryogenic temperatures, in *2015 73rd Annual Device Research Conference (DRC)*, 21–24 June 2015; 2015; pp 67–68
76. J. Simon, Y. Cao, D. Jena, Short-period AlN/GaN p-type superlattices: hole transport use in p-n junctions. Phys. Status Solidi (c) **7**(10), 2386–2389 (2010)
77. D. Jena, S. Heikman, D. Green, D. Buttari, R. Coffie, H. Xing, S. Keller, S. DenBaars, J.S. Speck, U.K. Mishra, I. Smorchkova, Realization of wide electron slabs by polarization bulk doping in graded III–V nitride semiconductor alloys. Appl. Phys. Lett. **81**(23), 4395–4397 (2002)
78. J. Yan, J. Wang, P. Cong, L. Sun, N. Liu, Z. Liu, C. Zhao, J. Li, Improved performance of UV-LED by p-AlGaN with graded composition. Phys. Status Solidi (c) **8**(2), 461–463 (2011)
79. S. Li, M.E. Ware, V.P. Kunets, M. Hawkridge, P. Minor, J. Wu, G.J. Salamo, Polarization induced doping in graded AlGaN films. Phys. Status Solidi (c) **8**(7–8), 2182–2184 (2011)
80. S.D. Carnevale, T.F. Kent, P.J. Phillips, M.J. Mills, S. Rajan, R.C. Myers, Polarization-induced pn diodes in wide-band-gap nanowires with ultraviolet electroluminescence. Nano Lett. **12**(2), 915–20 (2012)
81. L. Zhang, X.C. Wei, N.X. Liu, H.X. Lu, J.P. Zeng, J.X. Wang, Y.P. Zeng, J.M. Li, Improvement of efficiency of GaN-based polarization-doped light-emitting diodes grown by metalorganic chemical vapor deposition. Appl. Phys. Lett. **98**(24) (2011)
82. A. Yasan, R. McClintock, K. Mayes, S.R. Darvish, P. Kung, M. Razeghi, Top-emission ultraviolet light-emitting diodes with peak emission at 280 nm. Appl. Phys. Lett. **81**(5), 801–802 (2002)

83. A. Yasan, R. McClintock, K. Mayes, D.H. Kim, P. Kung, M. Razeghi, Photoluminescence study of AlGaN-based 280 nm ultraviolet light-emitting diodes. Appl. Phys. Lett. **83**(20), 4083–4085 (2003)
84. A. Chitnis, V. Adivarahan, M. Shatalov, J. Zhang, M. Gaevski, W. Shuai, R. Pachipulusu, J. Sun, K. Simin, G. Simin, J. Yang, M.A. Khan, Submilliwatt operation of AlInGaN based multifinger-design 315 nm Light Emitting Diode (LED) over sapphire substrate. Jpn. J. Appl. Phys. **41**(Part 2, No. 3B), L320–L322 (2002)
85. B. Cheng, S. Choi, J.E. Northrup, Z. Yang, C. Knollenberg, M. Teepe, T. Wunderer, C.L. Chua, N.M. Johnson, Enhanced vertical and lateral hole transport in high aluminum-containing AlGaN for deep ultraviolet light emitters. Appl. Phys. Lett. **102**(23) (2013)
86. F.A.F. Jimy Encomendero, S.M. Islam, V. Protasenko, S. Rouvimov, P. Fay, D. Jena, H.G. Xing, Repeatable room temperature negative differential conductance in GaN/AlN resonant tunneling diodes. arXiv:1606.08100 [cond-mat.mes-hall] (2016)
87. C. Liu, Y.K. Ooi, S.M. Islam, J. Verma, H. Xing, D. Jena, J. Zhang, Physics and polarization characteristics of 298 nm AlN-delta-GaN quantum well ultraviolet light-emitting diodes. Appl. Phys. Lett. **110**(7), 071103 (2017)

Chapter 11
Reliability of Ultraviolet Light-Emitting Diodes

Carlo De Santi, Desiree Monti, Pradip Dalapati, Matteo Meneghini, Gaudenzio Meneghesso, and Enrico Zanoni

11.1 AlGaN-Based Ultraviolet Light-Emitting Diodes

Operating current and temperature are two important parameters that can influence the degradation of UV LEDs. In this last decade, many research groups studied the impact of current and/or temperature on the optical and electrical characteristics during the aging of the devices, trying to identify the physical mechanisms responsible for the reduction in the efficiency and, in some cases, to propose some solutions in order to optimize it.

In 2004, Allerman et al. reported their progress in the development of deep-ultraviolet (DUV) LEDs with emission between 237 and 297 nm [1]. For a 300-μm square device, the observed operating voltage was 6.7 V at 20 mA and 8.2 V at 50 mA, respectively, whereas the wall-plug efficiency and external quantum efficiency were 0.1% and 0.19%, respectively, at 50 mA. An output power of 0.4 mW has been achieved at this current density (~60 A/cm^2). Stress tests at 20 mA were carried out on the 300 μm × 300 μm devices: analyzing the optical power during the stress for two 295 nm devices, with initial output powers of 92 and 95 μW at 20 mA, a drop of 26–34% was seen.

In 2006, Asif Khan et al. [2, 3] analyzed a group of unpackaged AlGaN-based LEDs with a nominal emission wavelength around 280 nm (at 20 mA), an optical output power of 0.35 mW, and an external quantum efficiency (EQE) of about 0.4%. The use of unpackaged devices had the aim to eliminate the contribution of bonding interfaces and solder from the analysis of the LED degradation process. These samples were mounted on a temperature-controlled chuck in order to carry out stress

C. De Santi (✉) · D. Monti · P. Dalapati · M. Meneghini · G. Meneghesso · E. Zanoni
Department of Information Engineering, University of Padova, Padova, Italy
e-mail: carlo.desanti@dei.unipd.it; matteo.meneghini@dei.unipd.it; gaudenzio.meneghesso@dei.unipd.it

© Springer International Publishing AG, part of Springer Nature 2019

J. Li, G. Q. Zhang (eds.), *Light-Emitting Diodes*, Solid State Lighting Technology and Application Series 4, https://doi.org/10.1007/978-3-319-99211-2_11

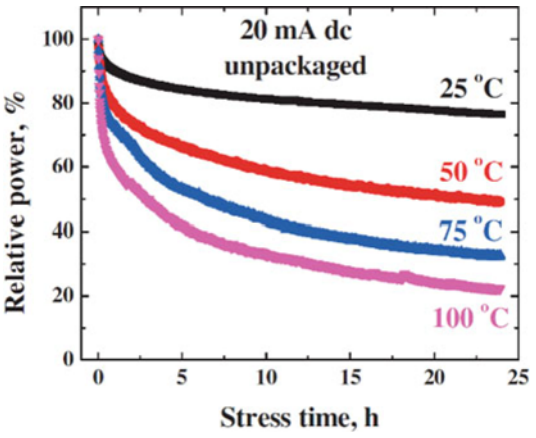

Fig. 11.1 Optical power during the stress at different stress temperatures for 280-nm unpackaged deep UV LED. Reprinted from [2], with the permission of John Wiley & Sons, Inc.

at a fixed current of 20 mA and at different temperatures. Figure 11.1 reports the decrease of the optical power during a 24-h stress at various temperatures, noticing a variation in the degradation rate with the stress temperature. Shatalov et al. [4] analyzed the same samples and observed both catastrophic and gradual output power degradation under DC bias. The catastrophic degradation was found to be caused mostly by the rough surface morphology of the p-GaN contact layer. AFM scans of the 100 μm × 100 μm emission area showed islands morphology, and these islands were attributed to the formation of V-defects in n-AlGaN layers due to the gas phase pre-reaction followed by the overgrowth of these defects with p-AlGaN and p-GaN layers [5]. The open cores of these V-defects work as leakage paths and the high current density will cause a local overheating followed by the alloying of the p-metal, where the EL intensity distribution and the CCD image after catastrophic failure were taken. The propagation of the alloyed region damages the active layer, leading to the shortening of the p–n junction.

Gong et al. continued the work in [6, 7] analyzing the degradation of the optical power also in the case of stress carried out a different pulse current. Current pulses were 1 μs long and of the duty cycle was 5%, in order to provide quasi-steady-state pumping conditions and to minimize device self-heating. Despite self-heating was minimized, the output power degradation was still more prominent for higher pump currents.

The two groups analyzed the stress results and supposed that there are two characteristic time constants discernible in this optical power degradation, associated with the junction temperature and the pump current. The curves were fitted with a double-exponential decay function:

$$P(t) = P_1 \exp(-\beta_1 t) + P_2 \exp(\beta_2 t) \tag{11.1}$$

where P_1 and β_1 are temperature-dependent parameters, whereas P_2 and β_2 are bias-dependent parameters. Parameter β_1 decays exponentially with the junction

temperature T_j as:

$$\beta_1 = \beta_0 \exp\left(-E_a/kT_j\right). \tag{11.2}$$

Asif Khan et al. [3] extrapolated, from the Arrhenius plot of the aging test at 20 mA, an activation energy E_a of 0.27 eV, and a decay parameter β_0 of 97.5 h^{-1}, estimating in this way a value of 5.93 $\times$ 10^{-3} h^{-1} for the parameter β_1. Instead, the parameter β_2 does not have a clear dependence from temperature, and they estimated a value of 0.44 h^{-1}.

Their data suggested them that the degradation of the analyzed deep UV LEDs was mostly related to the device temperature.

By using, instead of a device structure with an area of 100 μm $\times$ 100 μm, a 10 $\times$ 10 micro-pixel UV LEDs, always with a peak emission of 280 nm, the performances improved due to a lower current density, having a larger device area. Additionally, they report a lower operating voltage related to a lower series resistance, and as a consequence also a lower junction temperature, helped also by a lower thermal impedance. Figure 11.2 reports the optical power degradation during the stress for two standard 100 μm $\times$ 100 μm and 200 μm $\times$ 200 μm square devices and for a 10 $\times$ 10 micro-pixel LED. The increase in the junction area increased the reliability of the micro-pixel LED, reducing the optical power degradation during the operation of the device.

In [8], Reed et al. analyzed a group of 280 nm LEDs, studying the impact of self-heating by measuring the output power as function of pulse current for various duty cycles at a fixed pulse width of 1 and 100 μs (Fig. 11.3). In both cases, the output power at 50% approached that of the CW conditions, indicating that heating had a significant impact on the device performance, causing also a small red-shift in wavelength. Stress performed at 100 mA (300 A/cm^2) and room temperature under CW and pulsed conditions of 100 μs and 1% duty cycle have shown that the

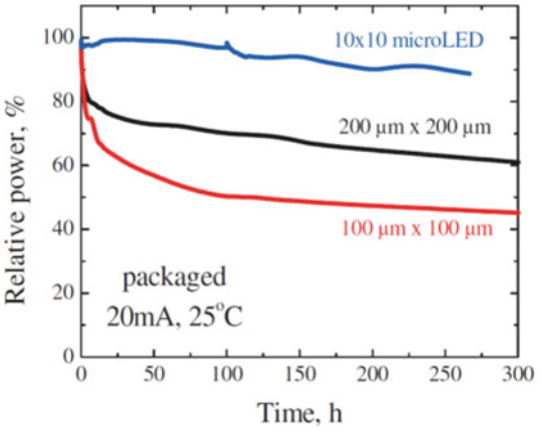

Fig. 11.2 Degradation of the optical power during stress for different type of packaged LEDs stressed at 20 mA and 25 °C. Reprinted from [2], with the permission of John Wiley & Sons, Inc.

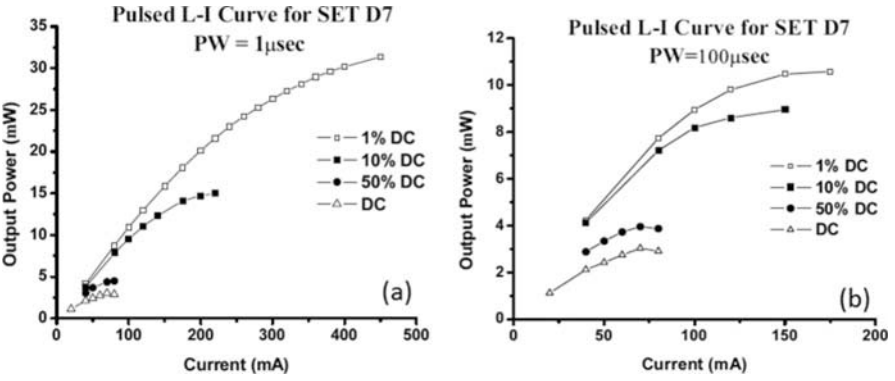

Fig. 11.3 Output power as function of current for (**a**) 1 μs and (**b**) 100 μs pulse at currents from 40 to 450 mA. Reprinted from [8], with the permission of John Wiley & Sons, Inc.

pulsed device presents a half-life of 1400 h, longer than that observed under CW conditions, which produced a half-life of 20 h.

Lifetime measurements on single-chip, packaged 285-nm LEDs were performed by Moe et al. in [9]. In particular, these tests were performed under constant current injection at 20 and 75 mA and were compared to the performance of unbiased LEDs heated in the oven at the equivalent operating junction temperatures. Devices that were thermally stressed showed a lower degradation than those electrically stressed, as reported in Fig. 11.4, and no parasitic peak at longer emission wavelengths (i.e., lower energy) was observed in the EL spectra, indicating that the increased degradation is not due to changes in the active region [10]. Capacitance as function of voltage measurements were carried out for the electrically stressed samples, and allowed to extrapolate the apparent charge profile before and after stress (Fig. 11.5). The results suggested that the depletion region extended further into the p-type layer after electrical degradation, due to the compensation of p-type carriers in the barrier region near the heterojunction.

In another work [11], Asif Khan et al. highlighted the fact that two of the main problems in DUV LEDs are the low efficiency and the long-term reliability. In particular, the low efficiency problem is related to the large amount of threading dislocations that increases with the Al mole fraction in the active layer. The optical power decreases as the emission wavelength decreases from 280 to 250 nm, which means an increase in the Al-mole fraction of the active layer. AlGaN LEDs with a nominal emission wavelength around 280 nm were stressed at two different pump current densities of 100 and 200 A/cm^2. A fast degradation of the output power in the first 1–5 h was detected; this is then followed by a slower degradation. The device lifetime was found to be a strong function of the pump current density and the number of dislocations in the active region.

Since a high threading dislocation density is present in the LED structures due to heteroepitaxial growth on foreign substrates, different groups tried to use different techniques in order to reduce it. Jain et al. report in [12] the growth of low-

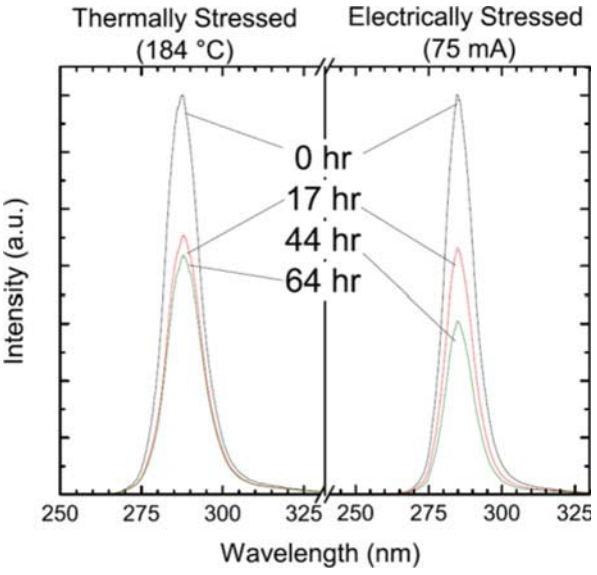

Fig. 11.4 EL spectra of LEDs thermally (left) and electrically (right) stressed over time. Reprinted from "Current-induced degradation of high performance deep ultraviolet light emitting diodes", Craig G. Moe, Meredith L. Reed, Gregory A. Garrett, Anand V. Sampath, Troy Alexander, Hongen Shen, Michael Wraback, Yuriy Bilenko, Maxim Shatalov, Jinwei Yang, Wenhong Sun, Jianyu Deng, and Remis Gaska, Applied Physics Letters 2010 96:21, with the permission of AIP Publishing

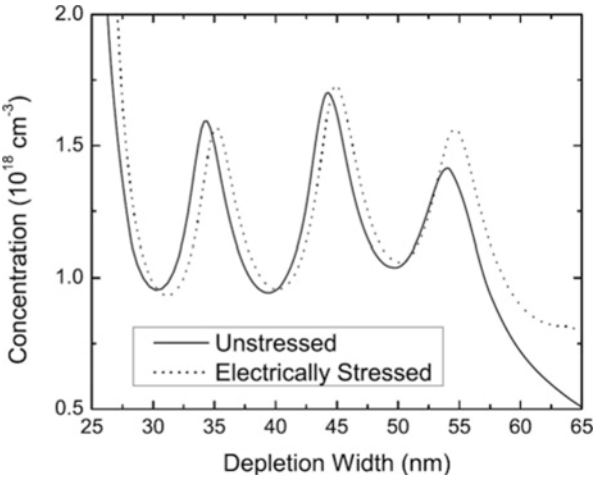

Fig. 11.5 Apparent charge profile as function of depletion width before and after stress. Reprinted from "Current-induced degradation of high performance deep ultraviolet light emitting diodes", C. G. Moe, M. L. Reed, G. A. Garrett, A. V. Sampath, T. Alexander, H. Shen, M. Wraback, Y. Bilenko, M. Shatalov, J. Yang, W. Sun, J. Deng, and R. Gaska, Applied Physics Letters 2010 96:21, with the permission of AIP Publishing

defect thick films of AlN and AlGaN on trenched AlGaN/sapphire templates using migration-enhanced lateral epitaxial overgrowth (MELEO) technique. They were able to realize a DUV LED with a nominal emission wavelength around 310 nm with a CW output power of 1.6 mW at 50 mA. The extrapolated lifetime was estimated to be about 5000 h, with a five times improvement in device reliability, validating the high quality of MELEO grown thick AlN films.

Monitoring common parameters, such as output power, peak wavelength, and current–voltage characteristics, together with additional parameters like the low-frequency current noise at low and high currents, Sawyer et al. [13] characterized a group of AlGaN/AlInGaN LEDs with a nominal emission wavelength of 280 nm.

Devices were aged at 20 mA forward current and showed: (1) no changes in the peak wavelength and full width at half magnitude (FWHM), indicating that the properties of the quantum wells did not change during the stress; (2) a decrease in the power with the square root of time, suggesting the presence of a diffusion process, in this case diffusion of contact metal to the device structure or diffusion of dopant atoms [14]. Low-frequency noise is a sensitive indicator of the semiconductor devices degradation, in particular, at low bias it is sensitive to degradation of the barrier layer, whereas at high bias, it reflects the degradation of the contacts and/or semiconductor layers contributing to the series resistance [15, 16]. Sawyer et al. observed a strong increase in the noise related to the series resistance. Figure 11.6 reports the noise as function of the aging time at two different currents and $f = 10$ Hz. At low current ($I < 10$–50 μA), the noise spectra were close to the $1/f$ noise, and spectral noise density of the short circuit current fluctuations, S_I, was proportional to the first power of the current. At intermediate current (100 μA $< I <$ 1–3 mA), the generation-recombination noise was found in many devices. At higher current, the $1/f$ noise again dominated the spectra and $S_I - I^2$. In general, no correlation between noise, the optical power, and the degradation rate of the optical power was observed.

Pinos et al. investigated the impact of the AlN molar fraction on the AlGaN-based UV LEDs performances [10, 17, 18]. In [10], a 285-nm LED with

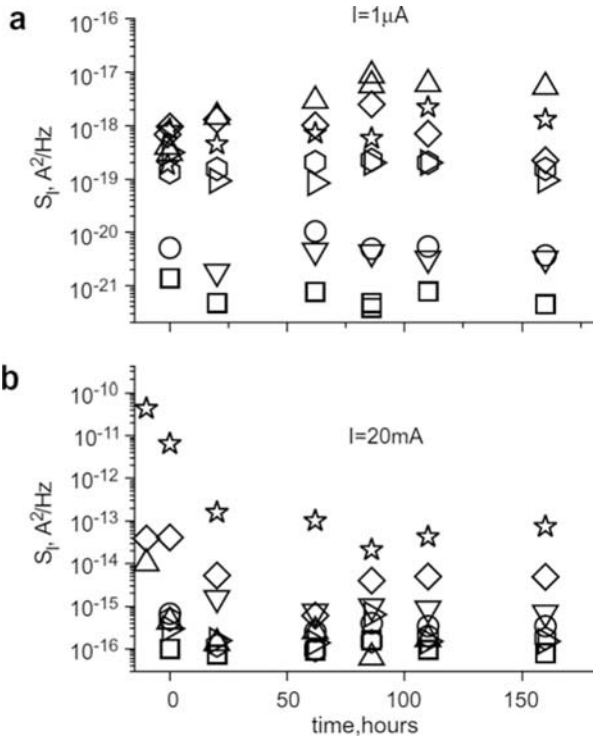

Fig. 11.6 Spectral noise density as function of the stress time measured at (**a**) 1 μA and (**b**) 20 mA. Different symbols correspond to different LEDs, $f = 10$ Hz. Reprinted from Solid-State Electronics, 52, S. Sawyer, S.L. Rumyantsev, M.S. Shur, "Degradation of AlGaN-based ultraviolet light emitting diodes", 968–972, Copyright (2008), with permission from Elsevier

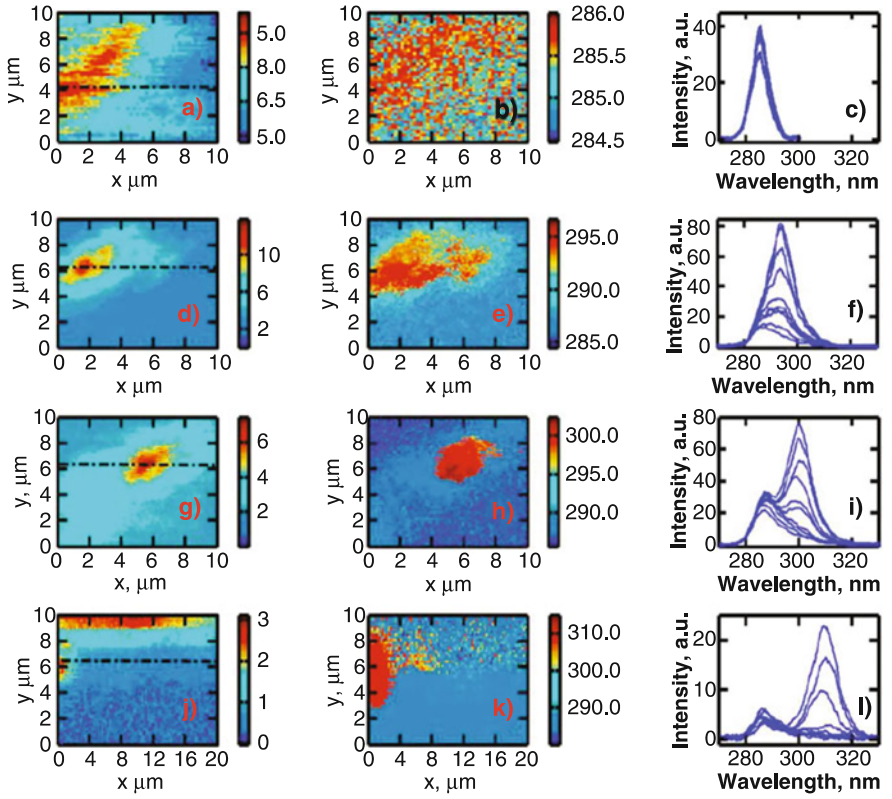

Fig. 11.7 In the first column, the emission intensity of the near-field scan is reported, whereas the second column reports the peak wavelength maps. The third column reports selected spectra taken along the lines shown in the intensity maps. Reprinted from "Aging of AlGaN quantum well light-emitting diode studied by scanning near-field optical spectroscopy", A. Pinos, S. Marcinkevičius, J. Yang, Y. Bilenko, M. Shatalov, R. Gaska, and M. S. Shur, Applied Physics Letters 2010 95:181914, with the permission of AIP Publishing

$Al_{0.35}Ga_{0.65}N/Al_{0.50}Ga_{0.50}N$ multiple QWs in the active region was stressed, and near-field electroluminescence (EL) measurements were performed using a scanning near-field optical microscope (SNOM). From the measurements, they observed that the EL intensity experienced some variation in the scan area, as Fig. 11.7 shows. The emission intensity from the "hot" spots increases, and the wavelength presents a red-shift. This red-shift of the emission wavelength in the domain-like areas was ascribed to an increase in the Ga concentration in the QWs, with a reduction of the AlN molar fraction in the domain due to a vertical diffusion of Al atoms. Since the current crowding occurs only in the "hot" spots, this causes a strong local heating that will cause a change in the atoms diffusion coefficient. This temperature gradient-induced diffusion might overcome diffusion due to Al composition gradient, assuring the net outflow of Al atoms from the domain-like

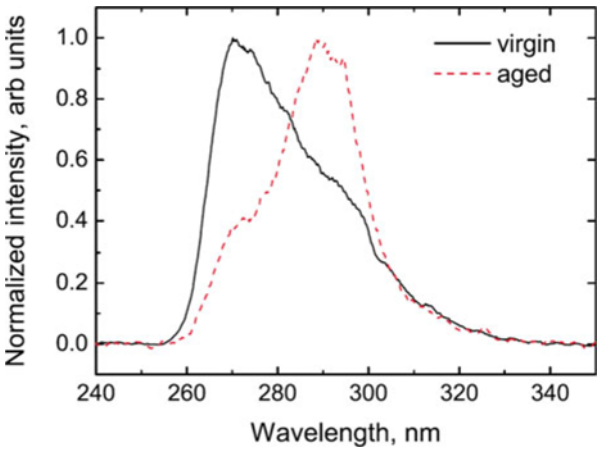

Fig. 11.8 Near-field spectra of the 270-nm device before and after the stress. An increase in the long wavelength component after aging is observed. Reprinted from "Optical studies of degradation of AlGaN quantum well based deep ultraviolet light emitting diodes", A. Pinos, S. Marcinkevičius, J. Yang, R. Gaska, M. Shatalov, and M. S. Shur, Journal of Applied Physics 2010 108:093113, with the permission of AIP Publishing

areas of the QWs. Moreover, dislocations may play an important role in the diffusion process, especially since Al atoms are smaller than Ga and are more likely to diffuse through the dislocations.

In [17], Pinos et al. revealed that, in devices with high Al content, the deterioration of the cladding layers is one important factor in device degradation. In [17], two LEDs with a nominal emission wavelength of 270 and 335 nm were stressed, and, again, near-field optical spectroscopy was performed. The structure of these two LEDs consisted of an AlN buffer, AlN/AlGaN superlattice, a few micrometer-thick n- and p-AlGaN cladding layers and an active region with three to five 2.5–3-nm-wide QWs and 11.5–12 nm barriers. From these measurements, they observed that for 335 nm LED the EL intensity variation did not show any clear tendency with aging and was attributed to nonuniform current injection. Instead, for 270-nm LED permanent changes occurred in the spectra during the aging, as reported in Fig. 11.8: after the stress, the emission peak at longer wavelength becomes dominant. The position of this peak suggested that its origin may be due to either transitions between the conduction band (shallow donor) and Mg acceptor or transitions between ionized nitrogen vacancies and the valence band. The observed increase in the amplitude of this parasitic peak highlighted the fact that the number of states participating in this transition increases. This means that this peak should be ascribed to transition involving the defects in the p-side cladding layer that are most probably nitrogen vacancies.

Other groups analyzed the presence of non-radiative recombination processes carrying out stress tests. Meneghini et al. in [19] analyzed the reliability of a group of DUV LEDs with an AlGaN multiple quantum well (MQW) layer, an n-

AlGaN:Si cladding layer, a p-AlGaN cladding layer, and a p-AlInGaN contact layer [20]. The stress was carried out at the nominal current of 20 mA, by continuously monitoring electrical and optical parameters and carrying out capacitance–voltage measurements in order to extrapolate information on the apparent charge profile. Analyzing the L-I characteristics measured before and after the stress, it was possible to observe that stress induces a decrease in the optical power in the whole current range. Moreover, this degradation took place mostly during the initial hour of stress (first 200 h); instead, the optical power remains quite stable in the remaining stress time. They found that the optical power degradation was more prominent at low measuring current levels, suggesting that the degradation is related to the generation of non-radiative recombination centers.

By analyzing the electrical characteristics, they observed an increase in the reverse leakage current and in the current below the turn-on voltage, indicating that stress induces an increase in the tunneling and generation/recombination processes; effect that was usually attributed to the generation of defects [21, 22]. This hypothesis was better confirmed by the comparison between the optical power degradation and the variation of the forward bias, as reported in [23]. The C–V measurements allowed to analyze the effect of stress on the properties of the active region. In fact, stress induced an increase in the apparent charge profile, probably ascribed to the modification of charge distribution in the active region, which in turn can be related to the worsening in the properties of the active layer that consists in the generation of defective states [24]. The change in the charge took place mostly in the first 250 h of stress, just like the optical power decrease, suggesting a correlation between the optical power degradation and the modification in the charge profile.

In other papers [25, 26], Meneghini et al. analyzed a group of DUV-LEDs with emission wavelength at 310 nm, carrying out several stress at different conditions, in order to evaluate the role of current and temperature in the device degradation. Figure 11.9a reports the electroluminescence spectra carried out during a stress at 17 A/cm^2 and room temperature. It was possible to observe two emission bands: one related to the QW emission, centered around 310 nm, and the second one, a broad green-yellow peak, centered around 520 nm. This parasitic emission is usually attributed to deep-level transitions [27, 28] originating in the AlGaN quantum wells or barrier layers [29]. As the figure shows, stress causes a decrease in the main peak and an increase in the parasitic one. Moreover, the variations in these two peaks are well correlated: Figure 11.9b reports the intensity of the main peak and the intensity of the green-yellow peak during the stress; both of them present very similar kinetics, suggesting that stress induces an increase in the concentration of the defects responsible for the parasitic emission band.

Stress at different current levels and at different junction temperatures allowed to understand if the degradation observed was activated by the temperature or by the flow of carriers through the active region. Figure 11.10 shows the results that they obtained from these measurements. In particular, Fig. 11.10a shows that for these devices, the dependence on the junction temperature is very weak. Instead, by analyzing Fig. 11.10b, it is possible to observe that with increasing stress current, the optical power presents a stronger degradation. With these results, they concluded

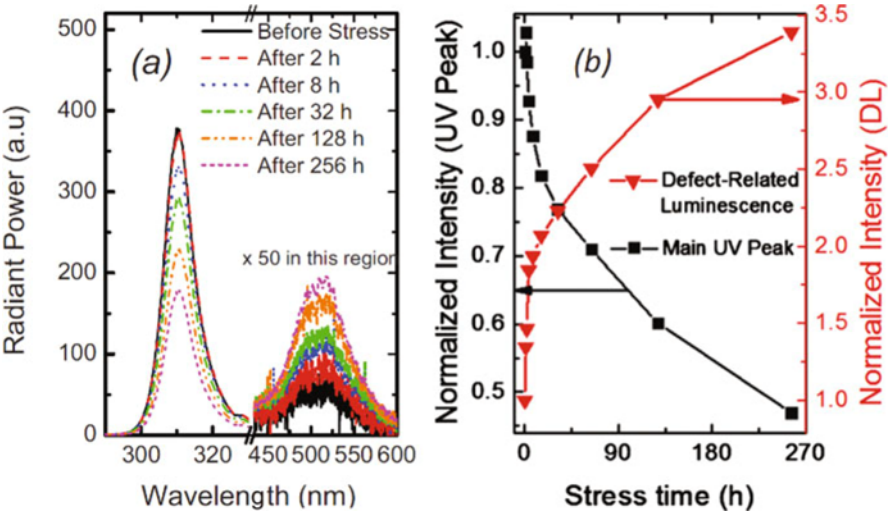

Fig. 11.9 (**a**) EL spectra of one of the analyzed samples during stress. (**b**) Correlation between the intensity of the main peak and of the parasitic one during the stress. Reprinted from "Analysis of the physical processes responsible for the degradation of deep-ultraviolet light emitting diodes", M. Meneghini, D. Barbisan, L. Rodighiero, G. Meneghesso, and E. Zanoni, Applied Physics Letters 2010 97:143506, with the permission of AIP Publishing

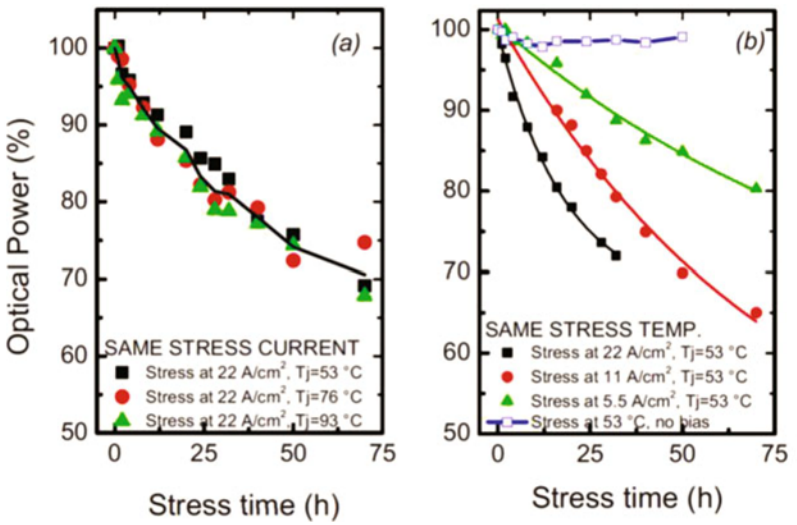

Fig. 11.10 Optical power degradation during stress (**a**) at different junction temperatures and (**b**) at different current levels. Reprinted from "Analysis of the physical processes responsible for the degradation of deep-ultraviolet light emitting diodes", M. Meneghini, D. Barbisan, L. Rodighiero, G. Meneghesso, and E. Zanoni, Applied Physics Letters 2010 97:143506, with the permission of AIP Publishing

in [25] that degradation was not ascribed to a purely thermal effect, but that the flow of the current through the active region may activate this process.

Other performance and reliability measurements were carried out by Grandusky et al. in [30], where they analyzed a group of UV-C LEDs with a 5-period multiple quantum well and with an AlN substrate. Currently, devices are fabricated on sapphire substrate, which cause an increase in dislocation density, lowering the efficiency and lifetime. AlN substrates allow to reduce lattice and thermal mismatch between the substrate and the device layer. Stress at different current levels, 20, 100, and 150 mA, was carried out on these devices. The measurements showed three different mechanisms for power decay. The first mechanism was related to the temperature; this mechanism was reversible; that is, if the device was turned off and allowed to cool, the power would initially recover, followed by a rapid drop until thermal equilibrium was reached. The second mechanism was burn-in: it could be related to impurity diffusion in the material or alloying of the contacts. The third and last mechanism was a slow decay in the optical power. Again, it is possible to observe that the optical power decay is stronger at higher stress current levels. In this case, it was not clear if the degradation was thermally related or current density related. They fitted the data with several functions: the best fit was obtained for a fit with a two-channel exponential decay, even if fitting the first 100 h in order to predict the power after 1000 h, the value was overestimated. In order to predict the correct value, the best function was a log transformation of the x-axis. Grandusky's group expected that these devices had a time to half the initial power greater than 3000 h.

A similar study on UV-C LEDs, with emission wavelength in the range of 250 and 280 nm, grown on AlN substrates by MOCVD, was proposed by Kitamura et al. in [31], where they performed stress tests at various temperatures and currents. For these devices, the degradation in the optical power increased with increasing case temperature above 25 °C, with an acceleration factor of ∼0.25% per °C. $I-V$ characteristics measured before and after a stress of 300 mA at room temperature present an increase in the reverse and forward leakage currents after 1000 h of stress. Moreover, in the range between −5 and 5 V after stress, the shape of the $I-V$ curve maintains asymmetry, suggesting that this variation was not caused by metal migration from the electrodes, which may create a connection between electrodes. As explained in [25], the high current stress induces the increase in the leakage current, reducing the radiative recombination. TEM images were able to clarify the correlation between the position of the leakage path and the presence of structural defects. Specifically, they show the cross sectional image at the point of the emission response related to the leakage current: defects in the MQW and n-AlGaN together with a crystal defect in the AlN substrate under the emission point were observed. This suggested that the crystal defect in the substrate may lead to the generation of the other defects in n-AlGaN and MQW during the epitaxial growth. Therefore, stress induced the diffusion of doping/impurities, such as Mg and Si, towards the active region [32, 33] and non-radiative recombination components arranged along these defects.

In 2014, Fujioka et al. realized 1-mm sized DUV LEDs emitting at 255, 280, and 310 nm suitable for high-current operation and tested the lifetime for the 280-nm LEDs, by means of aging tests varying the junction temperature [34]. Tests were performed first under 350 mA DC condition. After an increase in the first hours of stress, the optical power started to decrease with time. The first behavior was related to an enhanced Mg activation in the p-type AlGaN layer within the first hours of stress that causes an improvement in the internal quantum efficiency of the LED. With increasing junction temperature, they observed a faster decay in the optical power: after 1000 h, the optical power dropped to 73, 50, and 16% of its initial value for the junction temperatures of 35, 98, and 152 °C, respectively. Keeping the junction temperature constant at 85 °C, they performed other reliability tests changing the current density: when both the drive and measurement current are equal to 20 or 150 mA, the rate of power decay was comparable to that of the 350 mA current case and maintained 70% of its initial value after 1000 h. In contrast, when measured at 350 mA, the power decay seemed smaller and kept 99 and 72% for a bias current of 20 and 150 mA, respectively. This means that power has a strong decrease for small measurement current levels. The estimated 50% lifetime (L_{50}) was 3000 h at a junction temperature of 30 °C.

In [35], Rass et al. analyzed a group of high-power UV-B LEDs grown by MOCVD on (0001) c-plane sapphire substrate. They discussed the different parameters responsible for achieving a high EQE, i.e., the internal quantum efficiency (IQE), the injection efficiency (η_{inj}), and the extraction efficiency (η_{ext}), trying to improve these parameters in order to improve the device performances. By growing the LEDs on templates with a thick relaxed n-$Al_{0.50}Ga_{0.50}N$ buffer, they reduced the number of threading dislocations (TDD) from about 2×10^{10} cm^{-2} to 9×10^{9} cm^{-2}. Thanks to this improvement, the IQE, that is related to the defect density, achieved a value of 26% at room temperature. Regarding η_{inj}, varying the Al content of the EBL or by employing an electron blocking heterostructure (EBH), that consist in a conventional EBL and a thin high aluminum content interlayer, they obtained an increase in this figure of merit and reduced the parasitic emission from the p-side. An efficient heat extraction and an improvement in the η_{ext} was gained by flip-chip mounting the LED chips on AlN submounts. The final devices were submitted to a stress at high current densities of 140 A/cm^2 ($I = 100$ mA) at a heatsink of 20 °C. They showed a decrease of about 5–10% of the initial output power in the first 100 h. The degradation kinetic up to 3300 h can be described by a square root time behavior with a low degradation rate. The total output power decrease was about 30% of its initial value and by extrapolating the square root time dependence an L_{50} lifetime (time when the optical power reaches 50% of its initial value) of more than 10,000 h was estimated. Analyzing the electro-optical characteristics after different operation times, they observed that both the leakage current in reverse and at voltages below the band-gap energies (<4 V) have shown an inverse trend compared to the optical power over time; that is, the leakage current at −2.5 V increases, especially in the first 100 h of stress. Moreover, the drive voltage at 100 mA decreased slightly within the first 50–100 h and increased gradually within the rest of the stress. No changes in the position of the main peak emission

were observed, indicating that no changes in the material composition in the active region are happening. What Rass's group assumed was that during operation, a temperature-assisted diffusion of point defects into the active region, that leads to an increase of the non-radiative recombination rate, could be the main degradation mechanism in their devices. In particular, Mg-dopant atom may be the involved diffusion species, explaining in this way the increase in the drive voltage.

Glaab et al. in [36, 37] presented further results on a group of (InAlGa)N-based LEDs with a nominal emission wavelength around 308 with the same structure reported in [35], reporting the strong dependence of the degradation on the current density and the presence of non-recombination centers in the active region. They carried out stress at different conditions in order to characterize the effect of current, current density, and temperature. Analyzing the decrease of the optical power of a sample stressed at 100 mA ($J = 140$ mA/cm^2) and 20 °C, they observed that the degradation kinetics over the time presents two different modes. The first degradation mode takes place within the first 25–100 h of operation, where the optical power presents a fast decrease. The second degradation mode takes place for longer operation time (>100 h), and the optical power has a slower decay; moreover, it shows a square root time dependence.

These two different behaviors were observed also for stress carried out at different temperatures (Fig. 11.11). Regarding degradation mode 1, they subtracted from the optical power the background attributed to mode 2, as reported in [36], and observed that $\Delta P_{opt,1}$ increases with the temperature, indicating that this parameter has a strong influence on mode 1. From the $I-V$ characteristics, it is possible to observe an increase in the reverse leakage current and in the current below the turn-on voltage, with a stronger effect in reverse bias. The increase in the current in this last region may be ascribed to point defects and/or threading dislocations in the active region that form parasitic current paths and short the active region [38, 39].

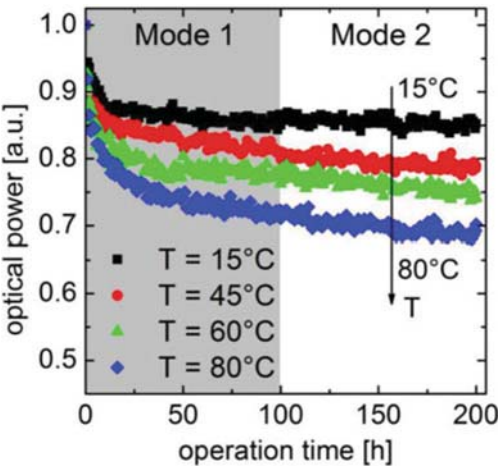

Fig. 11.11 Optical power degradation for different stress carried out at 100 mA (67 A/cm^2) and at different heat sink temperatures between 15 and 80 °C. Reprinted from [37], with the permission of Cambridge University Press

Considering degradation mode 2, they attributed this behavior to the involvement of a diffusion process, due to the square root time dependence of this degradation. The diffusing species are supposed to diffuse towards the active region, increasing the defectiveness within. This species may act as non-radiative recombination centers, causing the reduction of the optical power, and may create parasitic current paths, inducing an increase in the reverse leakage current, as the $I-V$ characteristics reports. In the literature, different diffusing species are proposed: Mg-atoms may diffuse from the p-doped layers [40], hydrogen atoms from the SiN passivation [41], or metal atoms from the contacts [13]. In order to better investigate the dependence of the degradation on the temperature, Glaab's group stressed another group of samples at constant current and different heat sink temperatures, in the range between 15 and 80 °C. The activation energies for the two degradation modes were found to be $E_{a,1} = 0.13$ eV for degradation mode 1, and $E_{a,2} = 0.21$ eV for degradation mode 2, indicating that both the two models have a strong dependence on temperature. However, the degradation rate of mode 2 was found to be more dependent on the current density. In conclusion, degradation mode 2 is probably ascribed to the diffusion of point defects associated with threading dislocations and/or recombination enhanced defect reactions. Since the activation energy of mode 1 cannot be readily attributed to other activation energies in the literature, and since this degradation occurs in a relatively short period of time, this process could be not related to the movement and increase of point defects, but rather could be ascribed to an activation process of fixed non-radiative recombination centers, that saturate in the second phase of the degradation.

The variation of the emission spectra during the degradation was studied in a following work [42], where two InAlGaN-based UV-B LEDs with different emission wavelengths, one at 290 nm and one at 310 nm, were stressed at a nominal current of 100 mA ($J = 140$ A/cm^2). Another difference between the two LED heterostructures can be found in the layers next to the pn-junction. In order to improve the carrier injection in the active region of the 290 nm LEDs, a 4-nm-thick highly Mg-doped AlN interlayer was introduced between the active region and the EBL. The two LEDs present a QW emission peak that decreases during the aging of the device, and a broad parasitic band at wavelength between 310 and 450 nm. This parasitic peak does not show the strong decrease detected for the main peak during the stress. In particular, the parasitic band in 290-nm LED shows an increase stronger than the parasitic peak in the 310-nm LED. The parasitic peak between 310 and 350 nm was associated with transition between the conduction band and Mg-related deep acceptor levels in the p-type superlattice (SL) [43, 44]. Regarding the parasitic emission at wavelength longer than 350 nm, this could be related to transitions involving Mg acceptors and V_N [45]. They report the evolution of the main peak intensity and the ratio of the peak intensities of the parasitic and main peak luminescence of the (a) 290 nm and (b) 310 nm during a stress of 1000 h. The main peak decreases rapidly in the first hours of stress for both LEDs, but stronger and more rapidly for the 290-nm LED. In the following hours, the degradation becomes slower. Again, two degradation modes were proposed as in the previous paper. In particular, QW peak and parasitic peak have opposite trend:

the fast initial reduction of the QW luminescence results from an increased non-radiative recombination within the QWs. The leakage current across the EBL is reduced, but since it is not affected by the non-radiative recombination in the QWs, the parasitic luminescence does not change over time or can slightly increase if the EBL does not block the carriers in an efficient way.

The high III/V molar ratio during growth and the high Mg-concentration in the AlN interlayer present in 290-nm LED could produce additional point defects, such V_N and Mg cluster close to the active region. Moreover, the thickness of the last quantum barrier before the p-region is only 2.5 nm in the 290-nm LED instead of 5.0 nm in the 310-nm LED. This could explain the difference in the parasitic emission band and its change during operation. Mg-dopant atoms may diffuse through the active region due to the temperature and mat act as non-radiative recombination centers or promote optical transition to V_N. For this reason, the lower overall intensity and the higher relative intensity of the parasitic band for wavelength higher than 350 nm in the 290-nm LED compared to the 310-nm LED could be explained by a larger Mg-atom concentration in the active region.

Monti et al. in [46, 47] and De Santi et al. in [48] worked on similar UV-B LEDs, with emission wavelength around 308 nm, grown on a sapphire substrate and with (In)AlGaN multi-quantum wells [35]. In order to study the correlation between the degradation and the generation of defects in the analyzed samples, they carried out a stress at a current of 100 mA and room temperature, performing also deep-level transient spectroscopy (DLTS) analysis and photocurrent (PC) spectroscopy. From the DLTS analysis, the group observed the presence of different peaks associated to different defects. In particular, during the stress, the activation energy of the trap h1 is in the range 0.11–0.24 eV, and one possible origin of this deep level is Mg-related acceptor traps, already proposed as the major gradual degradation mechanism in InAlGaN-based LEDs in [33]. Instead, the PC spectroscopy (Fig. 11.12) allowed to detect the presence of mid-gap states, between 2 and 3.5 eV, that may act as non-radiative recombination centers and increase the trap-assisted tunneling components, detected also by the increase in the current below the turn-on voltage.

An in-depth study on the dependence on temperature of the optical power degradation (thermal droop [49]) was performed in [48], where also an analysis of the origins of the different EL peaks was reported. From the analysis of the QW peak as function of temperature, three different trends were investigated: (1) at low temperature and high currents, where the optical power increases due to an enhanced hole injection from the p side to the n side; (2) at high temperature, where the optical power decreases due to an increase in the SRH recombination rate; and (3) at low temperature and low currents, where, instead, the optical power decay is probably caused by exciton delocalization from potential minima inside the QWs. The emission peak 3 was ascribed to parasitic intra-bandgap radiative transitions beyond the p side and is influenced by the increase in the injection of holes with increasing temperature at higher current levels. The last peak (peak 4) was attributed to a parasitic radiative transition, possibly in the p-AlGaN superlattice, assisted by a mechanism that causes a transfer in the charge.

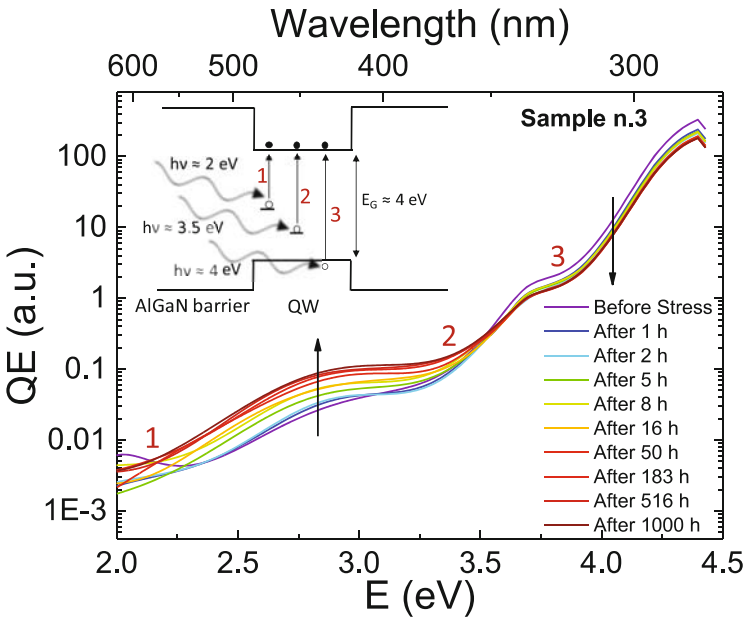

Fig. 11.12 PC spectra of the analyzed samples during the stress. The inset shows the different mechanisms responsible for the changes in the slope of the PC signal. © 2017 IEEE. Reprinted, with permission, from D. Monti et al., "Defect-Related Degradation of AlGaN-Based UV-B LEDs," in IEEE Transactions on Electron Devices, vol. 64, no. 1, pp. 200–205, Jan. 2017

11.2 InGaN-Based Ultraviolet Light-Emitting Diodes

The UV LEDs in the wavelength range 365–420 nm are commonly manufactured with InGaN/GaN quantum wells. A high degree of effort has been put into the development of high-reliability InGaN-based UV LEDs, but these devices still have open issues, such as the smaller height of the confinement potential barriers (in the range 0.1–0.15 eV or even lower), carrier escape and overflow processes, and high density of the threading dislocations (TDs) during GaN layer growth [50, 51].

In order to increase the long-term reliability, Wang et al. used a patterned sapphire substrate (PSS) to fabricate UV LEDs [50]. During the 1000 h test, they measured the variation of EL intensity of the PSS and conventional UV LEDs under a forward current of 20 mA at room temperature. The EL intensity of PSS and conventional LEDs showed a decay of 18% and 23%, respectively. They suggest that this result indicates a positive effect of the decreased trap density and non-radiative recombination centers (induced by TD) due to the growth on PSS.

Similar long-term reliability test was carried out by Mukai et al. with two different UV LEDs, grown on epitaxial lateral overgrown (ELO) GaN (TDD: $1 \times 10^7/\text{cm}^2$) and standard GaN template (TDD: $1 \times 10^8/\text{cm}^2$) [51]. After 4000 h aging test, the ELO-GaN showed almost no degradation of the output power,

whereas a stronger degradation was reported for the standard GaN template. This result further supports the negative effect of the dislocation density on the device reliability.

Liu et al. employed the vertical LED design to fabricate high-power UV LEDs, with wavelengths from 365 to 410 nm [52]. These LEDs were attached to a metal base with silicon submount package and showed very good reliability, thanks to the high-thermal conductivity from the junction to the board and heat sink.

Lin et al. tested the effect on the reliability of an un-doped $Al_{0.23}Ga_{0.77}N$ EBL inserted between the p-type doped $Al_{0.23}Ga_{0.77}N$ EBL and the last barrier [53]. As the un-doped EBL was inserted, the output power (at 19 A/cm^2) of the UV-LED with 365-nm wavelength showed a 400% enhancement. The degradation of EL peak intensity after 1032 h of stress was 17% and 33% for 365-nm UV-LEDs, fabricated with and without inserting an un-doped EBL, respectively. Moreover, the leakage current densities were increased to 4.5×10^{-4} and 4.7×10^{-3} A/cm^2 for 365-nm UV-LEDs, confirming the improvement in the device reliability with the insertion of the un-doped AlGaN EBL. The authors attribute this effect to the lower defect generation rate in the active region caused by the reduced Mg back-diffusion.

Reliability accelerated tests in continuous mode and cycled working mode for two types of commercial UV-LEDs (type A and B) were carried out in [54]. After 1500 h of test at three different temperatures (60, 75, and 90 °C), they found that the degradation is stronger for LEDs working at continuous current mode in all tests. This degradation is related to the worsening of the properties of the chip and of the encapsulation. The cracking of the silicone encapsulation was observed in both types during CW operation, and also during high-temperature test (90 °C) in cycled mode. They relate the faster degradation to a thermos-mechanical stress of silicone lens in contact with the semiconductor chip.

The effect of reverse-bias stress in water vapor on near UV LEDs was investigated in [55]. No reverse-bias luminescence was observed on a device stressed up to 60 min, whereas an increase in reverse-bias EL was detected in devices stressed up to 75 min and more. The result of spatially resolved EL maps revealed that the luminescence was distributed near the chip edge. They attributed the EL to hot electron-induced emission at high-electric field. By means of SEM, EDX, and SIMS analysis on cross-sectioned devices, they detected the down diffusion of Au towards the active region, and attributed to this process a role in the final device degradation.

Monti et al. analyzed extensively the degradation of UV-A LEDs with nominal peak wavelengths from 385 to 420 nm submitted to constant current stress ranging from 1 to 1.3 A at various temperatures (25, 50, and 75 °C) [56]. The time-to-failure (defined as the time to reach a 30% optical power reduction) showed an almost linear dependence on stress current, confirming that the stress current acts as a relevant driving force for the degradation process. The reliability is negatively affected by the temperature, leading to an activation energy of 0.36 eV, confirming that the degradation, ascribed to the generation of defects inside the active region, is a current-driven and thermally activated process.

11.3 Reliability of Packages for Ultraviolet Light-Emitting Diodes

LED chips are usually placed in suitable packages in order to make them compatible with the surface-mounted device (SMD) technology. The empty parts of the package are covered with filler materials, whose goal is to protect the device from air and moisture and to improve the extraction efficiency, lowering the refractive index mismatch with air. Given the high energy of the photons and the high temperature reached during operation, the materials composing the package may be affected by degradation themselves.

A comprehensive study on the properties and reliability of encapsulant materials was presented by Li et al. [57]. They incorporated into the epoxy five different filler materials, namely quartz, fused silica, cristobalite, spherical silica, and spherical silicone and tested their stability under various test conditions.

The first aging was purely thermal at 150 °C, and its results are presented in Fig. 11.13 for the representative cases of epoxy without any filler and with quartz. A decrease of the transmittance is clearly visible in the UV region, and it is more intense in the filled epoxies, leading to a higher yellowing and to a lower optical power. A similar test was carried out under illumination with a 365-nm UV light, and Fig. 11.14 reports the increase in yellowing over time for the various materials. Quartz and cristobalite were the systems with the lowest change in both tests, pure epoxy aside, and the difference was assumed to be related to variations in the reflection, caused by the different refractive index of the various materials.

Yazdan Mehr et al. tested the degradation of thermoplastic Bisphenol A Polycarbonate (BPA-PC) submitted to thermal storage at temperatures comparable with nominal operating conditions [58]. They detected a significant thermally activated increase in absorbance below 400 nm and the presence of a peak at 290 nm, attributed to the formation of phenolic end groups in the polymer. By means of infrared spectra in attenuated total reflection (ATR) mode, they report an increase in the absorption bands of aromatic ketones and cyclic anhydrides in the carbonyl region, resulting from thermal oxidation, and no change in the hydroxyl region, pointing out no major contribution of the Fries rearrangement reaction to the yellowing. Additionally, they detect no band in the ATR spectra caused by carboxylic acids. The proposed reaction pathway for the thermal oxidation causing the yellowing is sketched in Fig. 11.15.

Bae et al. proposed a new oligosiloxane resin as encapsulant, obtained by hydrosilylation of hydrogen-methyl oligosiloxane resin and vinyl-methyl siloxane resin, and compared it to polydimethylsiloxane (PDMS) [59]. The transmittance spectrum of the two materials is similar in a wide wavelength range (see Fig. 11.16a), and the largest benefit is an improved reliability. As can be seen from comparing Fig. 11.16b, c, the degradation resulting from illumination with UVB light at 10 mW/cm^2 is lower for the methyl hybrimer, especially in the UV-A and UV-B spectral range. The comparison between the two materials is reported in Fig. 11.16d, which includes also the result of a thermal stress test at 200 °C, confirming

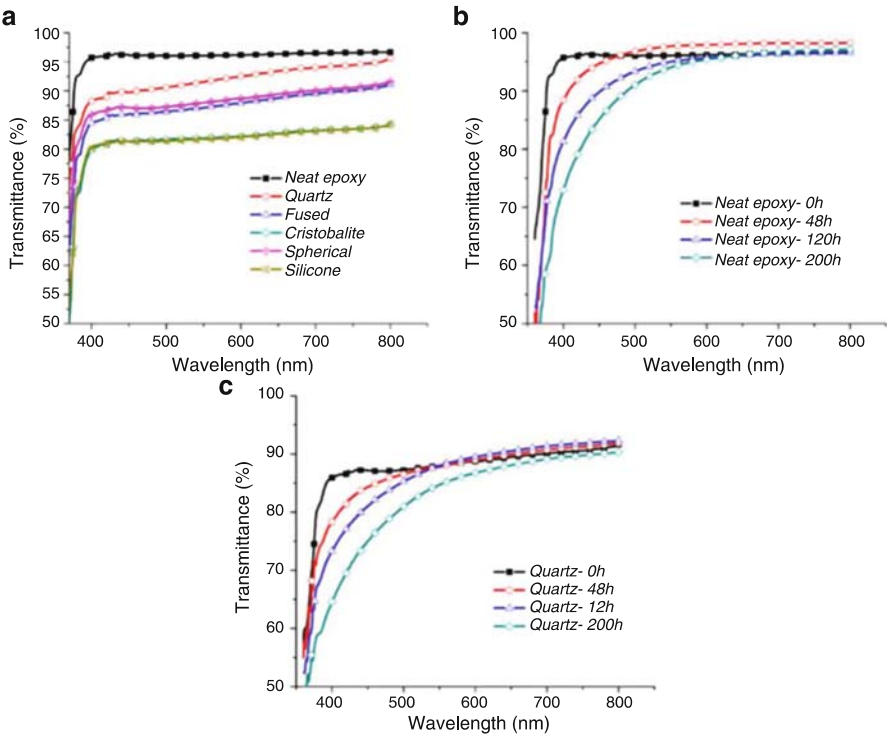

Fig. 11.13 (**a**) Transmittance spectra of various filler materials before stress and corresponding spectra during thermal stress for (**b**) pure epoxy and (**c**) quartz. Reprinted with permission from "High-Performance Light-Emitting Diodes Encapsulated with Silica-Filled Epoxy Materials", T. Li, J. Zhang, H. Wang, Z. Hu, and Y. Yu, ACS Applied Materials & Interfaces 2013 5 (18), 8968–8981. Copyright (2013) American Chemical Society

the stability of the new material. No visible formation of cracks or shrinkage was detected during the stresses, indicating no major light-induced scission of organic groups. The authors relate the higher stability to several factors, such as lower radical sources (such as Pt catalyst and unreacted organic phases), the robust siloxane network, the hyper-branched cross-linking, and the high cross-link density of vinyl and hydrogen groups.

In a following study, the same research group further improved the material creating a fluoro-siloxane hybrid, with superior performance and higher reliability in the UV-C range [60]. Even though the methyl hybrimer has a higher initial transmittance, due to its large free volume and long and homogeneous siloxane backbone, during UV-B aging the transparency decreases due to the formation of methyl radicals and to the radical-activated oxidative degradation of the organic pendants in the siloxane backbone. The fluoro hybrimer showed almost no degradation under the same condition, and the authors suggest that it is related to the high number of vinyl and fluoro groups, low amount of methyl groups, and hydrosilylation-derived short

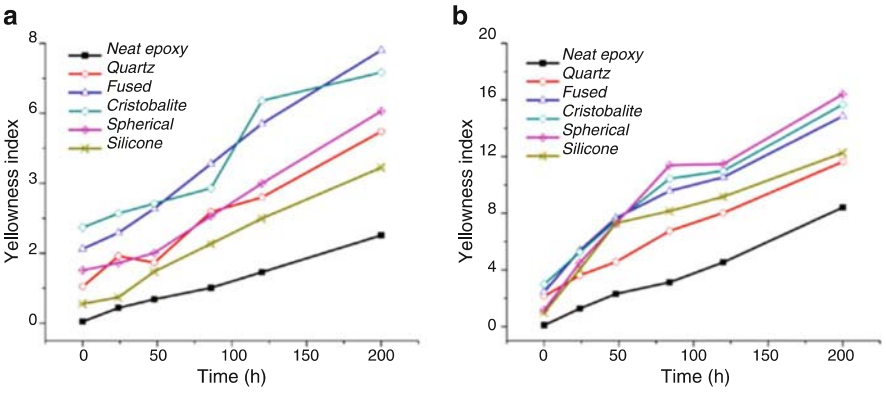

Fig. 11.14 Yellowing of various filler materials as a consequence of (**a**) thermal aging and (**b**) UV aging. Reprinted with permission from "High-Performance Light-Emitting Diodes Encapsulated with Silica-Filled Epoxy Materials", T. Li, J. Zhang, H. Wang, Z. Hu, and Y. Yu, ACS Applied Materials & Interfaces 2013 5 (18), 8968–8981. Copyright (2013) American Chemical Society

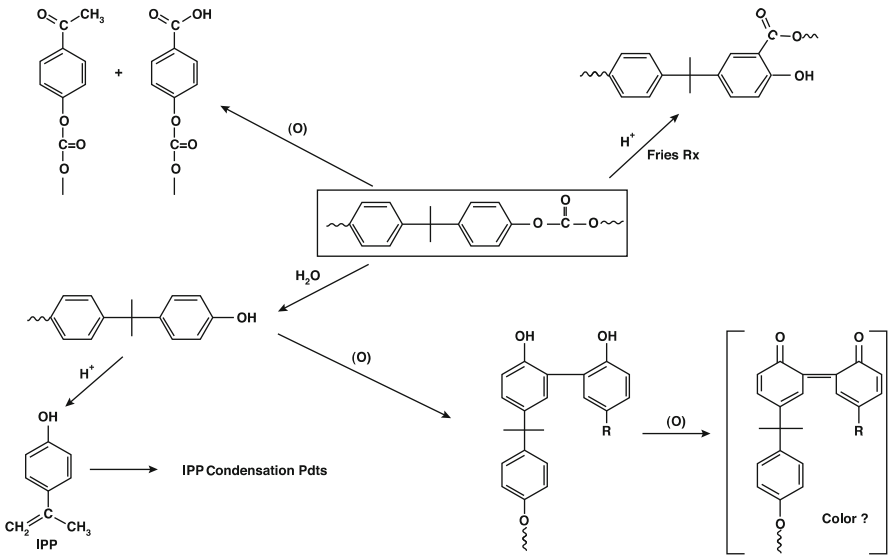

Fig. 11.15 Thermal oxidation reaction causing the yellowing of BPA-PC during thermal aging [58]. Reprinted from Microelectronics Reliability, 54, M. Yazdan Mehr, W.D. van Driel, S. Koh, G.Q. Zhang, "Reliability and optical properties of LED lens plates under high temperature stress", 2440–2447, Copyright (2004), with permission from Elsevier

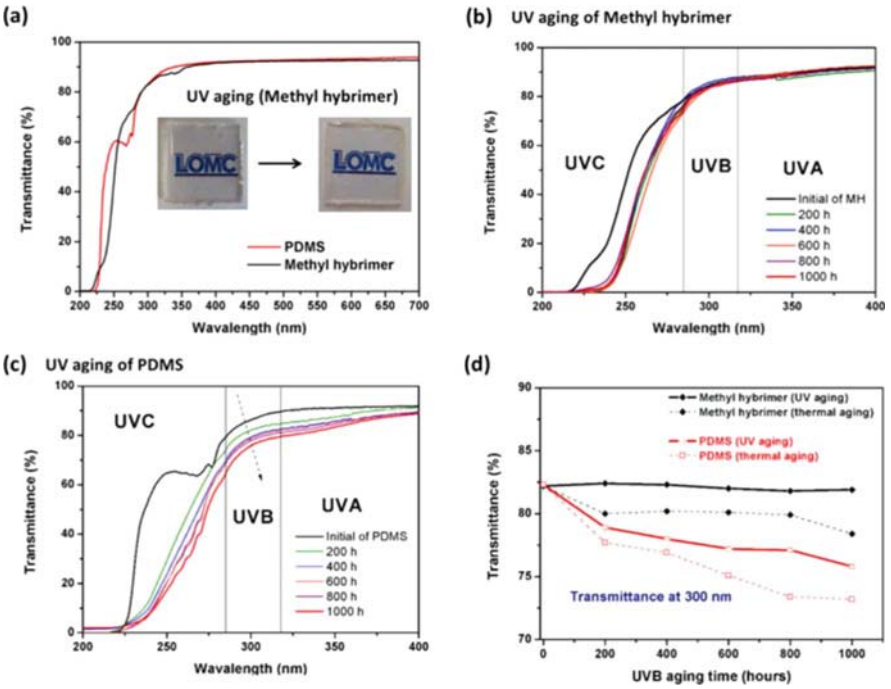

Fig. 11.16 (**a**) Transmittance of common PDMS compared to the proposed methyl hybrimer. (**b**) and (**c**) show its variation during UV-B stress for the two materials, summarized in (**d**) along with the results of a thermal stress at 200 °C [59]. Reprinted with permission from "Ultraviolet Light Stable and Transparent Sol–Gel Methyl Siloxane Hybrid Material for UV Light-Emitting Diode (UV LED) Encapsulant", J., YongHo Kim, H. Kim, Y. Kim, J. Jin, and B. Bae, ACS Applied Materials & Interfaces 2015 7 (2), 1035–1039. Copyright (2015) American Chemical Society

cross-links. The two hybrimers were compared also during UV-C stress, leading to the transmittance changes highlighted in Fig. 11.17a, b for fluoro and methyl hybrimer, respectively. The new material showed an increase in its transmittance as a consequence of irradiation in a wide spectral range (see Fig. 11.17c), attributed to a vinyl radical stabilization induced by the UV light.

The effect of the chain flexibility of the encapsulant was analyzed by Chen et al. [61]. They tested cycloaliphatic epoxy resin (3–4-epoxycy-clohexane) methyl 3–4-epoxycyclohexyl-carboxylate (ECC), both pure and with addition of various quantities of diglycidyl ether (HBADGE). They found that, even though the pure ECC showed the best reliability under thermal and UV stress, up to 30% HBADGE still led to comparable stability (see Fig. 11.18). The 30% HBADGE inclusion proved effective in lowering the water sorption and in maximizing the pass rate during various reliability tests according to the JEDEC J-STD-020 standard, attributed to the lower thermal expansion coefficient and storage modulus at reflow temperature.

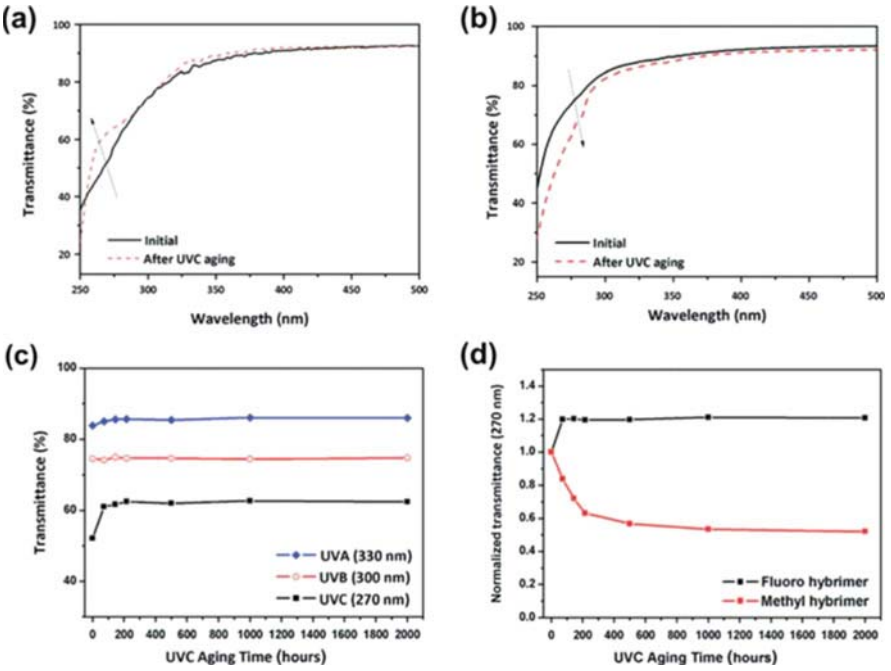

Fig. 11.17 Transmittance of (**a**) fluoro hybrimer and (**b**) methyl hybrimer before and after UV-C aging. The improvement in a wider spectral range is shown in (**c**) as a function of stress time, and the UV-C transmittance of the two materials is compared in (**d**). Reproduced from Ref. [60] with permission of The Royal Society of Chemistry

A similar set of tests was carried out by Wen et al., incorporating silicone instead of HBADGE into ECC [62]. They found better thermal and UV stability with increasing silicone content, due to the higher bond energy of Si–O with respect to C–O and C–C. The added silicone has a beneficial effect on delamination issues, thanks to the lower internal stress of the epoxy matrix, and on water sorption, given the hydrophobic nature of Si–O–Si compounds.

Transparent materials for filling make up most of the reports on package-related issues in the literature. An analysis of the reflectance of the materials for the package substrate was reported by Qiu et al., who tested epoxy molding compounds (EMC) and silicone molding compounds (SMC) during stress at high temperature (150 °C) and under a mercury UV lamp [63]. The SMC reflectance was unaffected by the thermal stress, whereas EMC showed an increase in the 365–375-nm range. SEM analysis of EMC plates highlighted the removal of the epoxy resin from the surface, leaving the filler particles exposed. No change was detected in the surface morphology of SMC plates. During the UV stress, the reflectance of SMC did not change, and the increase in the EMC reflectance was stronger. The surface of the SMC plate became rougher after the stress, and in the EMC case this phenomenon

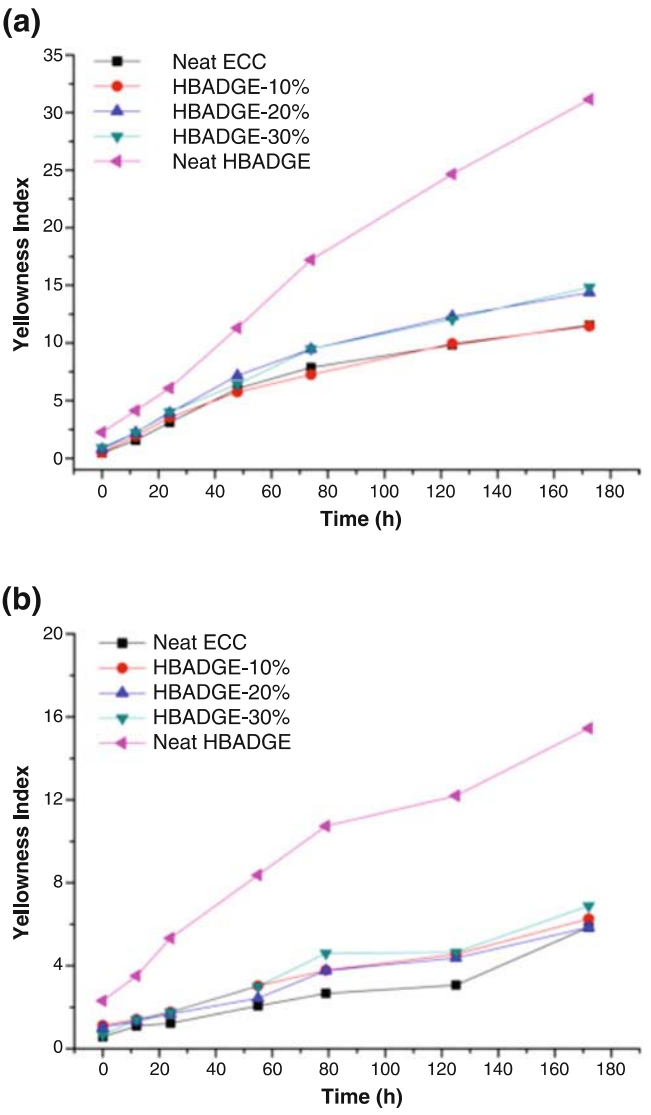

Fig. 11.18 Variation in yellowness index during (**a**) thermal and (**b**) UV aging of various epoxy encapsulants [61]. Reprinted with permission from "Effect of Chain Flexibility of Epoxy Encapsulants on the Performance and Reliability of Light-Emitting Diodes", Z. Chen, Z. Liu, G. Shen, R. Wen, J. Lv, J. Huo, and Y. Yu, Industrial & Engineering Chemistry Research 2016 55 (28), 7635–7645. Copyright (2016) American Chemical Society

was more intense. This effect could be caused by the chalking effect, i.e., the erosion of the top layer of organic molecules caused by the UV light.

11.4 Summary

Ultraviolet GaN-based LEDs are promising candidates for replacing traditional UV light sources, lowering their environmental impact. The adoption is still limited by the nonoptimal reliability, caused by the stronger generation of defects inside the devices containing aluminum alloys, leading to an increase in SRH recombination. The degradation is accelerated by the significant self-heating originated by the high turn-on voltage of the higher bandgap devices. The stability of the package and encapsulant materials against high-energy photons is an additional open issue that must be solved in order to maximize device lifetime.

References

1. A.A. Allerman, M.H. Crawford, A.J. Fischer, K.H.A. Bogart, S.R. Lee, D.M. Follstaedt, P.P. Provencio, D.D. Koleske, Growth and design of deep-UV (240-290 nm) light emitting diodes using AlGaN alloys. J. Cryst. Growth **272**(1–4), 227–241 (2004). https://doi.org/10.1016/j.jcrysgro.2004.08.035
2. M. Asif Khan, AlGaN multiple quantum well based deep UV LEDs and their applications. Phys. Status Solidi Appl. Mater. Sci. **203**(7), 1764–1770 (2006). https://doi.org/10.1002/pssa.200565427
3. M. Asif Khan, Deep ultraviolet light emitting diodes with emission below 300 nm. MRS Proc. **892** (2005). https://doi.org/10.1557/PROC-0892-FF01-01
4. M. Shatalov, Z. Gong, M. Gaevski, S. Wu, W. Sun, V. Adivarahan, M. Asif Khan, Reliability of AlGaN-based deep UV LEDs on sapphire. SPIE **6134**, 61340P (2006). https://doi.org/10.1117/12.647204
5. J.P. Zhang, H.M. Wang, W.H. Sun, V. Adivarahan, S. Wu, A. Chitnis, C.Q. Chen, M. Shatalov, E. Kuokstis, J.W. Yang, M. Asif Khan, High-quality AlGaN layers over pulsed atomic-layer epitaxially grown AlN templates for deep ultraviolet light-emitting diodes. J. Electron. Mater. **32**(5), 364–370 (2003). https://doi.org/10.1007/s11664-003-0159-2
6. Z. Gong, M. Gaevski, V. Adivarahan, W. Sun, M. Shatalov, M. Asif Khan, Optical power degradation mechanisms in AlGaN-based 280 nm deep ultraviolet light-emitting diodes on sapphire. Appl. Phys. Lett. **88**(12), 1–4 (2006). https://doi.org/10.1063/1.2187429
7. Z. Gong, S. Chhajed, M.E. Gaevski, W.H. Sun, V. Adivarahan, M. Shatalov, M. Asif Khan, Reliability and degradation modes of 280 nm deep UV LEDs on sapphire. Mater. Res. Soc. Symp. Proc. **892**, 169–174 (2006)
8. M.L. Reed, M. Wraback, A. Lunev, Y. Bilenko, X. Hu, A. Sattu, J. Deng, M. Shatalov, R. Gaska, Device self-heating effects in deep UV LEDs studied by systematic variation in pulsed current injection. Phys. Status Solidi Curr. Top. Solid State Phys. **5**(6), 2053–2055 (2008). https://doi.org/10.1002/pssc.200778402
9. C.G. Moe, M.L. Reed, G.A. Garrett, A.V. Sampath, T. Alexander, H. Shen, M. Wraback, Y. Bilenko, M. Shatalov, J. Yang, W. Sun, J. Deng, R. Gaska, Current-induced degradation of high performance deep ultraviolet light emitting diodes. Appl. Phys. Lett. **96**(21), 213512 (2010). https://doi.org/10.1063/1.3435485
10. A. Pinos, S. Marcinkevičius, J. Yang, Y. Bilenko, M. Shatalov, R. Gaska, M.S. Shur, Aging of AlGaN quantum well light emitting diode studied by scanning near-field optical spectroscopy. Appl. Phys. Lett. **95**(18), 181914 (2009). https://doi.org/10.1063/1.3262964
11. M. Asif Khan, S. Hwang, J. Lowder, V. Adivarahan, Q. Fareed, Reliability issues in AlGaN based deep ultraviolet light emitting diodes. 2009 IEEE Int. Reliab. Phys. Symp. 89–93. https://doi.org/10.1109/IRPS.2009.5173229

12. R. Jain, W. Sun, J. Yang, M. Shatalov, X. Hu, A. Sattu, A. Lunev, J. Deng, I. Shturm, Y. Bilenko, R. Gaska, M.S. Shur, Migration enhanced lateral epitaxial overgrowth of AlN and AlGaN for high reliability deep ultraviolet light emitting diodes. Appl. Phys. Lett. **93**(5), 110–113 (2008). https://doi.org/10.1063/1.2969402
13. S. Sawyer, S.L. Rumyantsev, M.S. Shur, Degradation of AlGaN-based ultraviolet light emitting diodes. Solid State Electron. **52**(6), 968–972 (2008). https://doi.org/10.1016/j.sse.2008.01.027
14. G. Meneghesso, S. Levada, E. Zanoni, S. Podda, G. Mura, M. Vanzi, A. Cavallini, A. Castaldini, S. Du, I. Eliashevich, Failure modes and mechanisms of DC-aged GaN LEDs. Phys. Status Solidi **194**(2), 389–392 (2002). https://doi.org/10.1002/1521-396X(200212)194:2<389::AID-PSSA389>3.0.CO;2-O
15. S. Bychikhin, D. Pogany, L.K.J. Vandamme, G. Meneghesso, E. Zanoni, Low-frequency noise sources in as-prepared and aged GaN-based light-emitting diodes. J. Appl. Phys. **97**(12), 123714 (2005). https://doi.org/10.1063/1.1942628
16. X. Chen, A. Pedersen, A.D. van Rheenen, Effect of electrical and thermal stress on low-frequency noise characteristics of laser diodes. Microelectron. Reliab. **41**(1), 105–110 (2001). https://doi.org/10.1016/S0026-2714(00)00201-8
17. A. Pinos, S. Marcinkevičius, J. Yang, R. Gaska, M. Shatalov, M.S. Shur, Optical studies of degradation of AlGaN quantum well based deep ultraviolet light emitting diodes. J. Appl. Phys. **108**(9), 93113 (2010). https://doi.org/10.1063/1.3506697
18. A. Pinos, S. Marcinkevičius, M.S. Shur, High current-induced degradation of AlGaN ultraviolet light emitting diodes. J. Appl. Phys. **109**(10) (2011). https://doi.org/10.1063/1.3590149
19. M. Meneghini, M. Pavesi, N. Trivellin, R. Gaska, E. Zanoni, G. Meneghesso, Reliability of deep-UV light-emitting diodes. IEEE Trans. Device Mater. Reliab. **8**(2), 248–254 (2008). https://doi.org/10.1109/TDMR.2008.919570
20. J.P. Zhang, X. Hu, Y. Bilenko, J. Deng, A. Lunev, M.S. Shur, R. Gaska, M. Shatalov, J.W. Yang, M. Asif Khan, AlGaN-based 280 nm light-emitting diodes with continuous-wave power exceeding 1 mW at 25 mA. Appl. Phys. Lett. **85**(23), 5532–5534 (2004). https://doi.org/10.1063/1.1831557
21. O. Pursiainen, N. Linder, A. Jaeger, R. Oberschmid, K. Streubel, Identification of aging mechanisms in the optical and electrical characteristics of light-emitting diodes. Appl. Phys. Lett. **79**(18), 2895–2897 (2001). https://doi.org/10.1063/1.1413721
22. T. Yanagisawa, T. Kojima, Degradation of InGaN blue light-emitting diodes under continuous and low-speed pulse operations. Microelectron. Reliab. **43**(6), 977–980 (2003). https://doi.org/10.1016/S0026-2714(03)00093-3
23. M. Meneghini, N. Trivellin, L. Trevisanello, A. Lunev, J. Yang, Y. Bilenko, W. Sun, M. Shatalov, R. Gaska, E. Zanoni, G. Meneghesso, Combined optical and electrical analysis of AlGaN-based deep-UV LEDs reliability. IEEE Int. Reliab. Phys. Symp. Proc. 441–445 (2008). https://doi.org/10.1109/RELPHY.2008.4558925
24. F. Rossi, M. Pavesi, M. Meneghini, G. Salviati, M. Manfredi, G. Meneghesso, A. Castaldini, A. Cavallini, L. Rigutti, U. Strass, U. Zehnder, E. Zanoni, Influence of short-term low current dc aging on the electrical and optical properties of InGaN blue light-emitting diodes. J. Appl. Phys. **99**(5), 10–17 (2006). https://doi.org/10.1063/1.2178856
25. M. Meneghini, D. Barbisan, L. Rodighiero, G. Meneghesso, E. Zanoni, Analysis of the physical processes responsible for the degradation of deep-ultraviolet light emitting diodes. Appl. Phys. Lett. **97**(14), 143506 (2010). https://doi.org/10.1063/1.3497082
26. M. Meneghini, D. Barbisan, Y. Bilenko, M. Shatalov, J. Yang, R. Gaska, G. Meneghesso, E. Zanoni, Defect-related degradation of deep-UV-LEDs. Microelectron. Reliab. **50**(9–11), 1538–1542 (2010). https://doi.org/10.1016/j.microrel.2010.07.089
27. V. Adivarahan, W. Sun, A. Chitnis, M. Shatalov, S. Wu, H. Maruska, M. Asif Khan, 250 nm AlGaN light-emitting diodes. Appl. Phys. Lett. **85**(12), 2175 (2004). https://doi.org/10.1063/1.1796525
28. N. Otsuka, A. Tsujimura, Y. Hasegawa, G. Sugahara, M. Kume, Y. Ban, Room temperature 339 nm emission from Al0.13Ga0.87N/Al0.10Ga0.90N double heterostructure light-emitting diode on sapphire substrate. Jpn. J. Appl. Phys. **39**(Part 2, No. 5B), L445–L448 (2000). https://doi.org/10.1143/JJAP.39.L445

29. J.S. Park, D.W. Fothergill, P. Wellenius, S.M. Bishop, J.F. Muth, R.F. Davis, Origins of parasitic emissions from 353 nm AlGaN-based ultraviolet light emitting diodes over SiC substrates. Jpn J. Appl. Physics, Part 1 Regul. Pap. Short Notes Rev. Pap. **45**(5 A), 4083–4086 (2006). https://doi.org/10.1143/JJAP.45.4083
30. J. Grandusky, Y. Cui, S. Gibb, M. Mendrick, L. Schowalter, Performance and reliability of ultraviolet-C pseudomorphic light emitting diodes on bulk AlN substrates. Phys. Status Solidi Curr. Top. Solid State Phys. **7**(7–8), 2199–2201 (2010). https://doi.org/10.1002/pssc.200983635
31. K. Kitamura, J.R. Grandusky, C.G. Moe, J. Chen, M.C. Mendrick, Y. Li, M. Toita, K. Nagase, T. Morishita, H. Ishii, S. Yamada, L.J. Schowalter, S3-P1: reliability and lifetime of pseudomorphic UVC leds on AlN substrate under various stress condition. Lester Eastman Conference 2014—High Performance Devices, LEC (2014), pp. 2–6. https://doi.org/10.1109/LEC.2014.6951561
32. S. Tomiya, T. Hino, S. Goto, M. Takeya, M. Ikeda, Dislocation related issues in the degradation of GaN-based laser diodes. IEEE J. Sel. Top. Quantum Electron. **10**(6), 1277–1286 (2004). https://doi.org/10.1109/JSTQE.2004.837735
33. S.N. Lee, H.S. Paek, J.K. Son, H. Kim, K.K. Kim, K.H. Ha, O.H. Nam, Y. Park, Effects of Mg dopant on the degradation of InGaN multiple quantum wells in AlInGaN-based light emitting devices. J. Electroceram. **23**(2–4), 406–409 (2009). https://doi.org/10.1007/s10832-008-9478-2
34. A. Fujioka, K. Asada, H. Yamada, T. Ohtsuka, T. Ogawa, T. Kosugi, D. Kishikawa, T. Mukai, High-output-power 255/280/310 nm deep ultraviolet light-emitting diodes and their lifetime characteristics. Semicond. Sci. Technol. **29**(8), 84005 (2014). https://doi.org/10.1088/0268-1242/29/8/084005
35. J. Rass, T. Kolbe, N. Lobo Ploch, T. Wernicke, F. Mehnke, C. Kuhn, J. Enslin, M. Guttmann, C. Reich, A. Mogilatenko, J. Glaab, C. Stoelmacker, M. Lapeyrade, S. Einfeldt, M. Weyers, M. Kneissl, High power UV-B LEDs with long lifetime. Proc. SPIE Gall. Nitride Mater. Devices X **9363**, 93631K (2015). https://doi.org/10.1117/12.2077426
36. J. Glaab, C. Ploch, R. Kelz, C. Stölmacker, M. Lapeyrade, N. Lobo Ploch, J. Rass, T. Kolbe, S. Einfeldt, F. Mehnke, C. Kuhn, T. Wernicke, M. Weyers, M. Kneissl, Degradation of (InAlGa)N-based UV-B light emitting diodes stressed by current and temperature. J. Appl. Phys. **118**(9) (2015). https://doi.org/10.1063/1.4929656
37. J. Glaab, C. Ploch, R. Kelz, C. Stölmacker, M. Lapeyrade, N. Lobo Ploch, J. Rass, T. Kolbe, S. Einfeldt, F. Mehnke, C. Kuhn, T. Wernicke, M. Weyers, M. Kneissl, Temperature induced degradation of InAlGaN multiple-quantum well UV-B LEDs. MRS Proc. **1792** (2015). https://doi.org/10.1557/opl.2015.446
38. Q. Shan, D.S. Meyaard, Q. Dai, J. Cho, E. Fred Schubert, J. Kon Son, C. Sone, Transport-mechanism analysis of the reverse leakage current in GaInN light-emitting diodes. Appl. Phys. Lett. **99**(25), 253506 (2011). https://doi.org/10.1063/1.3668104
39. M.W. Moseley, A.A. Allerman, M.H. Crawford, J.J. Wierer, M.L. Smith, A.M. Armstrong, Detection and modeling of leakage current in AlGaN-based deep ultraviolet light-emitting diodes. J. Appl. Phys. **117**(9) (2015). https://doi.org/10.1063/1.4908543
40. K. Orita, S. Takigawa, M. Yuri, T. Tanaka, M. Meneghini, N. Trivellin, L.-R. Trevisanello, E. Zanoni, G. Meneghesso, Analysis of diffusion involved in degradation of InGaN-based laser diodes. 2009 IEEE International Reliability Physics Symposium (2009), pp. 736–740. https://doi.org/10.1109/IRPS.2009.5173340
41. M. Meneghini, L.-R. Trevisanello, S. Levada, G. Meneghesso, G. Tamiazzo, E. Zanoni, T. Zahner, U. Zehnder, V. Harle, U. Strauss, Failure mechanisms of gallium nitride leds related with passivation. IEEE International Electron Devices Meeting. IEDM Technical Digest (2005), pp. 1009–1012. https://doi.org/10.1109/IEDM.2005.1609534
42. J. Glaab, N. Lobo Ploch, J. Rass, T. Kolbe, T. Wernicke, F. Mehnke, C. Kuhn, J. Enslin, C. Stölmacker, V. Kueller, A. Knauer, S. Einfeldt, M. Weyers, M. Kneissl, Influence of the LED heterostructure on the degradation behavior of (InAlGa)N-based UV-B LEDs. SPIE Opto. **9748**, 97481O (2016). https://doi.org/10.1117/12.2208906

43. J.C. Zhang, Y.H. Zhu, T. Egawa, S. Sumiya, M. Miyoshi, M. Tanaka, Suppression of the subband parasitic peak by 1 nm i-AlN interlayer in AlGaN deep ultraviolet light-emitting diodes. Appl. Phys. Lett. **93**(13) (2008). https://doi.org/10.1063/1.2996580
44. T. Kolbe, J. Stellmach, F. Mehnke, M.A. Rothe, V. Kueller, A. Knauer, S. Einfeldt, T. Wernicke, M. Weyers, M. Kneissl, Efficient carrier-injection and electron-confinement in UV-B light-emitting diodes. Phys. Status Solidi Appl. Mater. Sci. **213**(1), 210–214 (2016). https://doi.org/10.1002/pssa.201532479
45. M.L. Nakarmi, N. Nepal, J.Y. Lin, H.X. Jiang, Photoluminescence studies of impurity transitions in Mg-doped AlGaN alloys. Appl. Phys. Lett. **94**(9), 91903 (2009). https://doi.org/10.1063/1.3094754
46. D. Monti, M. Meneghini, C. De Santi, G. Meneghesso, E. Zanoni, J. Glaab, J. Rass, S. Einfeldt, F. Mehnke, J. Enslin, T. Wernicke, M. Kneissl, Defect-related degradation of AlGaN-Based UV-V LEDs. IEEE Trans. Electron Devices **64**(1), 200–205 (2017). https://doi.org/10.1109/TED.2016.2631720
47. D. Monti, M. Meneghini, C. De Santi, G. Meneghesso, E. Zanoni, J. Glaab, J. Rass, S. Einfeldt, F. Mehnke, T. Wernicke, M. Kneissl, L. Institut, U. Berlin, I. Festkörperphysik, Defect generation in deep-UV AlGaN-based LEDs investigated by electrical and spectroscopic characterisation. Proc. SPIE **10124**, 1–9 (2017). https://doi.org/10.1117/12.2253843
48. C. De Santi, M. Meneghini, D. Monti, J. Glaab, M. Guttmann, J. Rass, S. Einfeldt, F. Mehnke, J. Enslin, T. Wernicke, M. Kneissl, G. Meneghesso, E. Zanoni, Recombination mechanisms and thermal droop in AlGaN-based UV-B LEDs. Photonics Res. **5**(2), 44–51 (2017). https://doi.org/10.1364/PRJ.5.000A44
49. C. De Santi, M. Meneghini, M. La Grassa, B. Galler, R. Zeisel, M. Goano, S. Dominici, M. Mandurrino, F. Bertazzi, D. Robidas, G. Meneghesso, E. Zanoni, Role of defects in the thermal droop of InGaN-based light emitting diodes. J. Appl. Phys. **119**(9), 94501 (2016). https://doi.org/10.1063/1.4942438
50. W.K. Wang, D.S. Wuu, S.H. Lin, P. Han, R.H. Horng, T.C. Hsu, D.T.C. Huo, M.J. Jou, Y.H. Yu, A. Lin, Efficiency improvement of near-ultraviolet InGaN LEDs using patterned sapphire substrates. IEEE J. Quantum Electron. **41**(11), 1403–1409 (2005). https://doi.org/10.1109/JQE.2005.857057
51. T. Mukai, D. Morita, M. Yamamoto, K. Akaishi, K. Matoba, K. Yasutomo, Y. Kasai, M. Sano, S.I. Nagahama, Investigation of optical-output-power degradation in 365-nm UV-LEDs. Phys. Status Solidi Curr. Top. Solid State Phys. **3**(6), 2211–2214 (2006). https://doi.org/10.1002/pssc.200565354
52. W.H. Liu, C.F. Chu, C.C. Cheng, K.H. Hsu, Y.T. Chung, Y.K. Wang, C.C. Li, J.Y. Chu, F.H. Fan, H.C. Cheng, Y.W. Chen, Y.H. Chang, L.W. Shan, T. Doan, C. Tran, Development of high-power UV LEDs for epoxy curing applications. Proc. SPIE **7602**, 76021K (2010). https://doi.org/10.1117/12.845472
53. W. Lin, T. Wang, S. Ou, J. Liang, D. Wuu, Improved performance of 365-nm LEDs by inserting an un-doped electron-blocking layer. IEEE Electron Device Lett. **35**(4), 467–469 (2014). https://doi.org/10.1109/LED.2014.2306711
54. F.J. Arques-Orobon, N. Nuñez, M. Vazquez, V. González-Posadas, UV LEDs reliability tests for fluoro-sensing sensor application. Microelectron. Reliab. **54**(9–10), 2154–2158 (2014). https://doi.org/10.1016/j.microrel.2014.07.059
55. H. Chen, H.Y. Shen, S.C. Shei, N.C. Kang, H.C. Lai, Y.C. Chu, H.W. Chang, Exploring failure mechanisms of near ultraviolet AlGaN/GaN light-emitting diodes by reverse-bias stress in water vapour. Int. J. Nanotechnol. **12**(1/2), 38 (2015). https://doi.org/10.1504/IJNT.2015.066192
56. D. Monti, M. Meneghini, C. De Santi, G. Meneghesso, E. Zanoni, Degradation of UV-A LEDs: physical origin and dependence on stress conditions. IEEE Trans. Device Mater. Reliab. **16**(2), 213–219 (2016). https://doi.org/10.1109/TDMR.2016.2558473
57. T. Li, J. Zhang, H. Wang, Z. Hu, Y. Yu, High-performance light-emitting diodes encapsulated with silica-filled epoxy materials. ACS Appl. Mater. Interfaces **5**(18), 8968–8981 (2013). https://doi.org/10.1021/am402035r

58. M. Yazdan Mehr, W.D. Van Driel, S. Koh, G.Q. Zhang, Reliability and optical properties of LED lens plates under high temperature stress. Microelectron. Reliab. **54**(11), 2440–2447 (2014). https://doi.org/10.1016/j.microrel.2014.05.003
59. J.Y. Bae, Y.H. Kim, H.Y. Kim, Y.B. Kim, J. Jin, B.S. Bae, Ultraviolet light stable and transparent sol-gel methyl siloxane hybrid material for UV light-emitting diode (UV LED) encapsulant. ACS Appl. Mater. Interfaces **7**(2), 1035–1039 (2015). https://doi.org/10.1021/am507132a
60. J.-Y. Bae, H.-Y. Kim, Y.-W. Lim, Y.-H. Kim, B.-S. Bae, Optically recoverable, deep ultraviolet (UV) stable and transparent sol–gel fluoro siloxane hybrid material for a UV LED encapsulant. RSC Adv. **6**(32), 26826–26834 (2016). https://doi.org/10.1039/C6RA01346E
61. Z. Chen, Z. Liu, G. Shen, R. Wen, J. Lv, J. Huo, Y. Yu, Effect of chain flexibility of epoxy encapsulants on the performance and reliability of light-emitting diodes. Ind. Eng. Chem. Res. **55**(28), 7635–7645 (2016). https://doi.org/10.1021/acs.iecr.6b01159
62. R. Wen, J. Huo, J. Lv, Z. Liu, Y. Yu, Effect of silicone resin modification on the performance of epoxy materials for LED encapsulation. J. Mater. Sci. Mater. Electron. **28**(14522), 1–14 (2017). https://doi.org/10.1007/s10854-017-7316-5
63. X. Qiu, J.C.C. Lo, A.W. Shang, S.W.R. Lee, Investigation of reliability of EMC and SMC on reflectance for UV LED applications. 17th International Conference on Thermal Mechanical Multi-Physics Simulation and Expriments in Microelectronics and Microsystems, EuroSimE 2016, vol. 2 (2016), pp. 1–7. https://doi.org/10.1109/EuroSimE.2016.7463398

Chapter 12
Nitride Nanowires for Light Emitting Diodes

Nan Guan, Xing Dai, François H. Julien, Joël Eymery, Christophe Durant, and Maria Tchernycheva

12.1 Introduction

Nitride-based light emitting diodes (LEDs) are of tremendous importance for future high-efficiency lighting technologies. More than 20 years have passed since the demonstration of the first InGaN/GaN LEDs [1]. Nitride LEDs represent today a huge market reaching $30.5 Billion in 2016. Their fabrication technology continuously progresses targeting higher efficiencies and lower production costs.

A standard nitride LED consists of functional thin films typically grown on a Sapphire substrate along the c-direction of the wurtzite crystal. It contains the n-doped GaN layer for electron injection, the InGaN/GaN quantum well active region followed by an electron blocking layer, and finally the p-doped GaN layer for hole injection. The whole structure is contacted and appropriately packaged. Despite the relative maturity of this technology, certain issues for nitride LEDs remain unsolved. The most important one is the efficiency droop at high injection. This is a major problem in high power LEDs, which operate beyond the optimal efficiency point. The principal physical phenomenon responsible for the efficiency droop is believed to be Auger recombinations [2]. These are three-body processes (mainly, interactions implying two electrons and one hole, but also processes mediated by

N. Guan · X. Dai · F. H. Julien · M. Tchernycheva (✉)
Centre de Nanosciences et de Nanotechnologies, UMR9001 CNRS, University Paris Sud, University Paris Saclay, Palaiseau, France
e-mail: maria.tchernycheva@u-psud.fr

J. Eymery
Univ. Grenoble Alpes, CEA, INAC, MEM, Grenoble, France

C. Durant
Univ. Grenoble Alpes, CEA, INAC, PHELIQS, "Nanophysique et Semiconducteurs", Grenoble, France

© Springer International Publishing AG, part of Springer Nature 2019

J. Li, G. Q. Zhang (eds.), *Light-Emitting Diodes*, Solid State Lighting Technology and Application Series 4, https://doi.org/10.1007/978-3-319-99211-2_12

interactions with phonons [3]). The losses due to Auger recombinations can only be reduced by reducing the carrier density. The second important problem is the so-called green gap, which transduces the decrease of efficiency in high indium content LEDs with emission wavelengths from green to red. This is due to the increased defect density in In-rich InGaN/GaN quantum wells, but also to the enhanced internal field spatially separating electrons and holes and increasing the radiative recombination time (quantum confined Stark effect).

The above-mentioned open issues of thin film LEDs have motivated a strong research effort on alternative LED architectures. Nanostructured LEDs have been proposed as a possible solution. The main-stream approach consists in nanostructuring of the substrate (for example, LED growth on a nanopatterned sapphire is today actively explored [4, 5]). It allows to reduce the dislocation density and to improve the light extraction while keeping a flat geometry for the active region and contact layers [5]. This approach is attractive for LED manufacturers since it requires only moderate modifications in the existing LED fabrication technology. Alternatively, one can further exploit the nanostructuring and fully change the device architecture from two-dimensional films to three-dimensional nanowires (NWs).

NWs can be obtained by either a top-down etching or a bottom-up growth. The top-down approach uses lithography and dry etching of a thin film LED to form either needles [6] or NWs [7] at well-controlled positions. It yields a NW LED with an axial architecture, i.e., an LED with the InGaN/GaN heterostructure along the wire axis sandwiched between the p-doped and n-doped GaN extremities as illustrated in Fig. 12.1 left. This approach benefits from the high degree of control over the layer thickness and doping profile achieved in thin film growth. Etching also allows to relax the strain and thus reduce the internal field in axial InGaN/GaN heterostructures, which is particularly important for green LEDs. Moreover, the light extraction is increased due to scattering in the array. As a drawback, for the axial geometry the active region intersects the NW surface, which increases the surface non-radiative recombination. In addition, dry etching induces surface damage, which, however, may be healed by wet etching and surface passivation [8].

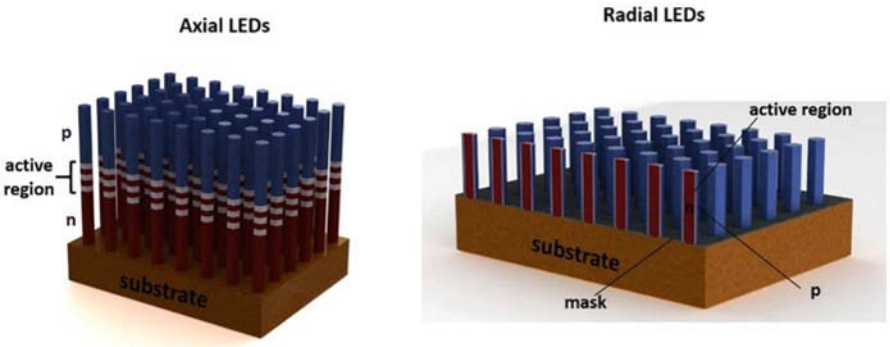

Fig. 12.1 Schematics of axial (left) and radial (right) LED architectures

Compared to the top-down etching, the bottom-up paradigm gives a larger design freedom since both axial and radial architectures can be implemented. Radial (also called core/shell) LEDs fully exploit the three-dimensionality of the NWs by forming the active region in the radial direction (Fig. 12.1 right). In this case, the InGaN/GaN cylindrical quantum wells are formed around an n-doped GaN core and are radially covered with a p-GaN shell. We note that a hybrid approach combining a top-down etching of the NWs with a subsequent radial overgrowth to form a core/shell active region has also been investigated [9–11].

Different types of functional nanostructures can be formed by a bottom-up approach such as pyramids, walls, or NWs. A common property of these nanostructures is the drastic reduction of the dislocation density compared to the planar case [12]. Micro- and nano-pyramids have been largely studied for LED application [13–16]. They have a hexagonal pyramidal shape defined by semipolar facets and can be obtained by selective area epitaxy. InGaN quantum wells deposited on their facets exhibit a lower internal electric field compared to c-plane and can incorporate more In, which is favorable for long wavelength emission [17]. The In content is reported to vary over the pyramid facets, which may yield a broad emission and can be used to realize phosphor-free white LEDs [18]. Other types of nanostructures such as vertical wall-shaped nanostructures [19] also called fins [20] or triangular nano-stripes [21] have been demonstrated and are quickly developing, however, light emitting devices based on these nanostructures remain today at an early stage [22].

NWs present a large number of advantages for three-dimensional LEDs. Thanks to their small footprint, NWs can accommodate the strain [23] arising from the lattice mismatch or from the thermal expansion mismatch and thus the defect density is reduced. The strain relaxation can take place not only at the NW/substrate interface, but also inside the active region (which is especially beneficial for axial In-rich heterostructures). This allows to avoid the dislocation formation in thin NWs with diameters of several tens of nanometers. For thicker NWs, dislocations can be formed at the NW/substrate interface, however, they bend to join the free lateral surface and can only be found in the immediate vicinity of the NW base [24]. The reduction of dislocations in NWs is predicted to lead to an enhancement of the quantum efficiency of NW devices compared to thin films.

Additional advantages for LEDs are provided by the core-shell geometry. This geometry can significantly increase the active area keeping the same device footprint as for a thin film LED [25]. This leads to a smaller carrier density in the quantum wells for a given injected current and thus to a droop reduction via lowering Auger effects. In addition, analyses of Auger coefficients in core/shell m-plane quantum wells revealed values two orders of magnitude lower than in c-plane thin film quantum wells [26]. These properties have motivated a strong research on core/shell NWs for high power high-efficiency LEDs. In addition, for core/shell LEDs the active region is usually grown on non-polar m-plane sidewalls, which allows to suppress the quantum confined Stark effect in InGaN/GaN quantum wells.

Finally, improved light extraction can be achieved in NW LEDs. Indeed, the three-dimensional geometry provides more escape passes for the light generated

inside the NWs than for the light generated in a thin film. However, care should be taken about the possible light reabsorption. In particular, in core/shell NWs having a several hundreds of nanometers diameter, the NW can efficiently guide light and it can be reabsorbed by the quantum wells. Depending on the quantum efficiency, the absorbed light can be either reemitted or lost via non-radiative mechanisms. For axial NW LEDs, reabsorption is less important and light extraction is reported to be improved with respect to thin films [27, 28].

Accounting for these advantages, NW arrays are today investigated as potential competitors to thin film LEDs for general lighting market. Many works focus on the white light emission either using phosphor downconversion [29] or by mixing red, green, and blue (RGB) colors [30]. Optimization of spectrally narrow nitride NW LEDs emitting blue, green, and red light [31] is also on going for the development of all-nitride RGB displays.

In addition to lighting and display applications, where NW LEDs compete with the standard thin film technology, bottom-up NWs also open the way for devices with new functionalities. For example, using selective area epitaxy one can exploit the dependence of the indium incorporation on the NW diameter to tune the emission color of nanowire LEDs grown in the same run from blue to red [32, 33]. Such tuning favorable for monolithic RGB integration is not possible in thin films devices. Thanks to their small footprint and mechanical flexibility, NWs can be reported on plastic or metal substrates in order to fabricate mechanically flexible LEDs [34–36]. Single NW LEDs also present a unique possibility to achieve bright sub-micrometer emitters that can be integrated into a functional photonic circuit [37, 38]. Vertical single NW LEDs can be used for optical stimulation in biomedical applications [39] or can be functionalized as a matrix of micro-pixels [40].

Bottom-up NWs can be formed using catalytic growth [41], self-assembled growth [42], or selective area epitaxy [43, 44]. Dominating growth techniques for their elaboration are MOVPE and MBE, however HVPE has also been used in early works [45]. MOVPE is better suited for core/shell LED geometry whereas MBE yields axial heterostructures. The NW LED performance critically depends on the wire-to-wire dispersion and intra-wire compositional variations. The complexity of the three-dimensional active region of NW LEDs makes the growth challenging. Selective area epitaxy allows to achieve a good control over the NW size distribution which in turn reduces the wire-to-wire fluctuations. However, the homogeneous indium incorporation within the NW remains an important issue even in organized NW arrays. Multicolor emission shifting with injection current has been observed not only in self-assembled NW LEDs [46] but also in organized NW LEDs [47–49]. In particular, in NWs with intrinsic compositional inhomogeneities the electroluminescence depends on the contact layout [50].

LEDs with a nanostructured active region bring new characterization challenges. Indeed, standard macroscopic characterization techniques provide only average values of important parameters, which is not sufficient for in-depth understanding of the device operation. First, electroluminescence of representative individual wires can be analyzed. This is performed using either single NWs detached from their substrate and electrically contacted in planar geometry [41, 46, 49] or vertical

NWs electrically contacted using nanoprobes in SEM [51] or with a nanoscale contact [50]. In addition, optical and electrical properties of individual NWs can be analyzed directly within an operational macroscopic LED using high-resolution techniques like cathodoluminescence (CL) and electron beam induced current (EBIC) microscopy [52].

In the following, different points highlighted in the introduction will be detailed. The main focus of this chapter will be on bottom-up NW LEDs. In the first part, we will describe the material growth. Next, the LED fabrication will be outlined and the early works on the NW LED fabrication will be enumerated. We will then review the present status of NW LEDs giving representative examples. Open issues of NW LEDs will be described. Finally, mechanically flexible LEDs based on nitride NWs will be presented.

12.2 NW Growth for LEDs

From the yearly reports of GaN NW synthesis [53, 54], intense efforts have been accomplished to control the NW growth in terms of length, size, density, doping, and heterostructure design. MBE and MOVPE are the two key growth techniques for the fabrication of nitride NW LEDs. These two approaches will be described separately to highlight the differences in NW morphologies and growth mechanisms.

12.2.1 Spontaneous Growth of GaN NWs by MBE

12.2.1.1 Growth Conditions

Compared to reactive MBE using NH_3 for N-precursor, the plasma-assisted MBE based on active N from RF plasma N_2 source is the most efficient method to grow GaN NWs. The MBE growth of self-assembled GaN NWs requires N-rich condition (i.e., V/III ratio > 1) and elevated growth temperature (730–850 °C). Figure 12.2 actually shows the domain (red area in panel c), where the NW growth (Fig. 12.2b) is obtained instead of a compact GaN layer (Fig. 12.2a) [55]. These conditions limit the nucleation site density and avoid the coalescence due to the reduction of the Ga adatom diffusion length [56].

The growth is usually performed on Si(111) substrates, even if the NW growth has also been reported on other substrates such as Si(001) [57], sapphire [54], or diamond [58]. The addition of an AlN layer on Si(111) that reduces the lattice mismatch is also commonly used to grow vertical GaN NWs. The thickness, crystalline granularity, and flatness of this AlN intermediate layer play a key role to control the orientation, diameter, density, and the polarity of GaN NWs [59–61]. The typical diameter of GaN NWs spontaneously grown by MBE is between 10 and 100 nm for lengths in the range of 0.5–3 μm depending on the growth

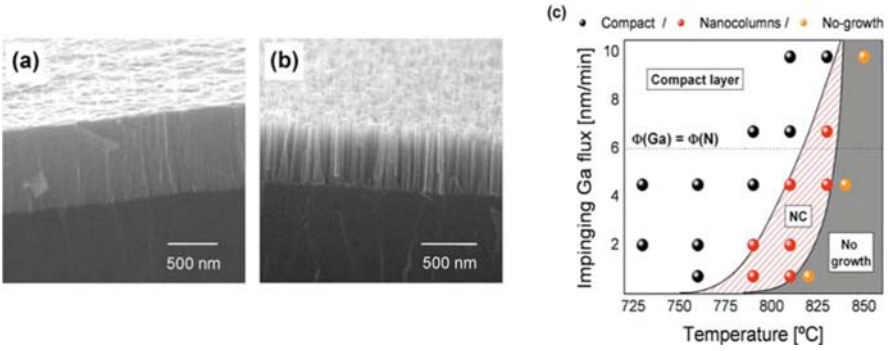

Fig. 12.2 Typical growth of GaN on Si(111) by MBE. (**a**, **b**) Bird-view SEM images of compact GaN layer and self-assembled GaN NWs. (**c**) Growth diagram showing different growth modes (layer, nanocolumns (NC), no growth) as a function of the growth temperature and V/III ratio (i.e., impinging Ga flux for a given impinging N flux of 6 nm/min). Adapted with permission from [55]

duration. Spontaneous growth by MBE produces high density of NWs (typically 10^9 to 10^{10} NWs/cm^2). For the direct growth on Si(111) substrate, the MBE GaN NWs polarity is mainly N-polar (i.e., with vertical chemical bonds pointing from N to Ga atoms along the $\bar{c}$ growth direction of the hexagonal lattice) [62, 63]. The growth conditions and morphology of an intermediate AlN layer have a direct impact on the wire polarity [64–66], but again by controlling its structural defect density, N-polar wires are preferentially grown [62, 67]. With the bending of misfit and threading dislocations to the sidewall surfaces, the GaN wire crystal is dislocation-free along most of its length. It results in excellent optical properties with a typical near band edge (NBE) emission broadening in the range of a meV or less. Moreover, no defect band emission is generally measured in these materials such as the yellow band (at ~550 nm) that can occur in planar materials [68, 69].

Recently, the use of alternative substrates such as glass [70], 2D materials as graphene [71], or metals [72] was reported for the GaN NW MBE growth. These emerging approaches are potentially promising for future flexible NW devices.

12.2.1.2 Growth Mechanisms Involved in MBE Growth

In general, growth mechanism highly depends on the surface properties: composition, amorphous or crystalline state, and morphology [73]. Actually, seed nucleation is strongly favored by the structural defects or morphological irregularities. On the contrary, if the nucleation surface is smooth with a low defect density, the nucleation is mainly related to specific growth mechanisms. It is, for example, the case for the growth performed on Si(111) substrate where an intermediate Si_xN_y layer is spontaneously formed on top of the Si substrate due to the reaction of the nitrogen plasma with the substrate surface [74].

More generally, the GaN NW growth on defect-free AlN or SiN_x surface can be decomposed into three subsequent phases: incubation, transition, and elongation. The incubation corresponds to the first moments of the nucleation where the nuclei are not completely stabilized [75]. The duration of this phase strongly depends on the growth conditions. At the end of the incubation period, the nucleation of stable "spherical" islands is observed both on AlN and SiN_x surfaces [75]. Then, a transition period occurs corresponding to a size increase of the nuclei associated with a shape modification that will lead to the NW formation. Two situations illustrated in Fig. 12.3 can be distinguished depending on the nature of the initial surfaces:

– For AlN nucleation surface, the elastic stress increases when the nucleus site rises due to the AlN/GaN lattice mismatch. Several modifications of the nucleus shape are observed and can be related to partial elastic relaxation: the spherical islands are converted into concatenated pyramids and then in full pyramidal islands. For nuclei having a size higher than the critical radius estimated to be 13 nm, a plastic relaxation happens with the formation of interfacial misfit dislocations [76]. The dislocation moves toward the nucleus center to relieve the residual strain, resulting in the last shape transition that corresponds to a NW-shaped nucleus. This mechanism shows that plastic relaxation plays a key role in the NW formation by the MBE method [60, 76, 77].

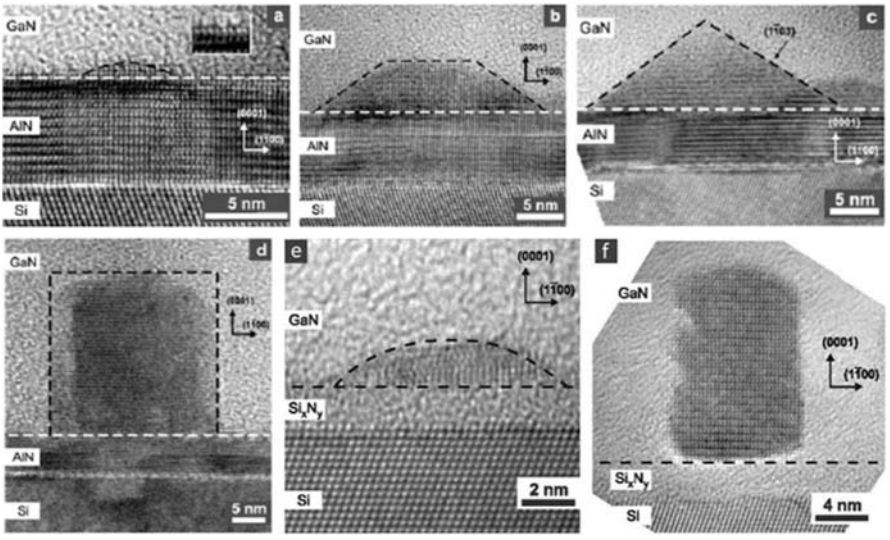

Fig. 12.3 Evolution of the GaN nucleus from spherical to NW shape during the transition phase based on a series of TEM images for two scenarios: GaN NW growth on Si(111) substrate with AlN buffer layer (**a–d**) (adapted with permission from [76]) and on Si(111) substrate with spontaneously formed SiN_x interlayer (**e**, **f**) (adapted with permission from [75])

– For SiN_x nucleation surface, epitaxial strain effects are not expected due to the amorphous nature of the SiN_x interlayer. Contrary to the AlN surface, the spherical islands keep the same shape when the size is increasing, until a critical value estimated at 5 nm is reached. Then, an abrupt shape transition (mainly driven by surface energy) is observed to reach directly the NW shape. An epitaxial relationship between GaN NWs and the Si substrate may be observed and depends on the conditions of SiN_x interlayer formation. The presence of crystalline domains in SiN_x interlayer could be a medium to drive substrate/NW epitaxial relationships [64, 74, 78].

The final NW shape of the nuclei on both AlN and SiN_x may be explained by the surface energy anisotropy, due to the lowest surface energy of m-plane surface (estimated to be ~118 meV/Å^2) compared to the c-plane surface (~123 meV/Å^2) [79, 80]. In addition, the edge energy can also be introduced to explain the final NW shape since it forms an energy barrier that increases with the facet angle of nucleus.

The last phase of the growth corresponds to the elongation of the NW nuclei. Direct adatom impinging and adatom diffusion on the substrate and along vertical NW sidewalls contribute to the NW elongation. Due to the high density of NWs grown by MBE, the elongation is also dependent on shadowing and collective effects [81]. The NW elongation is mainly governed by the Ga species flux coming from NW vertical sidewalls by surface diffusion. As a consequence, the NW length is rapidly increasing when the NW size is decreasing [82]. Moreover, the incorporation of Ga adatoms being likely more efficient on the c-plane surfaces than on the m-plane facets, the axial growth is significantly increased [83] and as the diffusion length of Ga adatoms is limited to about 50 nm on the NW sidewall [82, 84, 85], only the Ga adatoms impinging close to the NW top will participate to the NW elongation.

12.2.1.3 Selective Area Growth of GaN NWs in MBE

In MOVPE, selective area growth (SAG) is usually used to organize nanostructures using SiO_2 or SiN_x patterned mask deposited on GaN template. This technique has also been successfully developed in MBE growth using Ti patterned mask deposited on GaN templates by Kishino's group [86] and then followed by other groups [87, 88]. Realization of SAG by MBE is highly demanding because an excellent control of growth parameters and of the surface flatness of the patterned masks is needed. In contrast to self-assembled GaN NW growth, SAG mode requires a higher growth temperature (900–950 °C) [86, 89]. The increase of growth temperature favors both surface Ga adatoms diffusion allowing them to reach mask openings and desorption helping to limit the GaN overgrowth on the mask. Higher the temperature is, higher the Ga flux is required. Figure 12.4 shows that the reduction of N flux limits the formation of organized GaN NWs. A balance between the growth temperature and the N flux acting in opposite ways needs to be well controlled in order to obtain an effective selectivity [90].

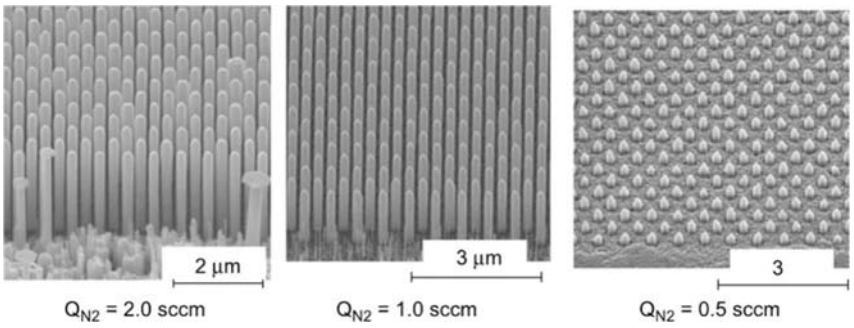

Fig. 12.4 SAG of GaN NWs grown by MBE using a Ti patterned mask on GaN/sapphire substrates. An increase of N flux promotes the NW growth and the mask selectivity at 900 °C. Adapted with permission from [86]

Other types of masks, for example, SiO_x [91, 92] and SiNx [59, 93], have also been employed for GaN NW SAG; however, the Ti mask remains the most frequent choice for NW LEDs. The SAG is usually performed on MOVPE-grown GaN template that imposes the Ga-polarity to GaN NWs. The SAG approach is an efficient way to control the LED emission color via the control of NW diameter and density as will be discussed later [32, 94].

12.2.1.4 Axial Growth of Heterostructures

As MBE is a physical deposition technique with sources positioned in front of the sample holder, the growth of heterostructures mainly results in axial geometry. Additionally, the high NW density prevents the radial growth by shadowing effect, even if a residual lateral growth can be present in some cases. Complex heterostructures with Al(Ga)N and In(Ga)N alloys can be axially grown by MBE for device fabrication. For Al(Ga)N/GaN heterostructures, sharp interfaces with a precise control of insertion thickness can be achieved. The realization of In(Ga)N/GaN heterostructures is more demanding in terms of interface and axial/radial geometry controls, nevertheless heterostructures with a high In composition can be achieved due to the strain relaxation in the NW geometry. Depending on the NW polarity, relatively flat InGaN insertions grown on the c-plane for N-polar NWs [95] or insertions of a complex shape following the semipolar planes in Ga-polar NW [94] were developed for LED fabrication. To enhance the quality of In-rich structures, growth of nano-umbrellas has been reported in view of fabricating red InGaN LEDs with improved efficiency [96, 97]. Note that the control of In(Ga)N/GaN heterostructures can be also improved by the SAG approach by mastering diffusion paths [32].

Regarding the heterostructures with different doping, we have to mention that the deposition of p-GaN is accompanied with a significant lateral growth that can be exploited to favor the coalescence of the high density NW layer.

12.2.2 MOVPE Growth of Catalyst-free Nitride NWs

Starting from 2005, the Lieber's group initiated a strong dynamic to study growth of nitride NWs with the first demonstrations of single NW photonic devices obtained by MOVPE growth assisted by nickel catalyst particles [98]. The catalyzed growth consists in using metallic nanoparticles to promote axial growth following the vapor-liquid-solid (VLS) process discovered in 1964 by Wagner and Ellis [99]. In the case of MOVPE-grown GaN NWs, catalyzed growth leads to triangular shaped nanoobjects with preferential growth directions along either a- or m-axes. Quantum wells deposited on such NWs (illustrated in Fig. 12.5) exhibit different properties depending on the facet orientation, which is undesirable for photonic applications. A better control over the NW shape can be achieved with a catalyst-free approach. The first demonstration of catalyst-free GaN NWs by MOVPE was achieved in 2003 based on organo-metallic azide precursors [100] and different methods have been developed later on.

12.2.2.1 Methods and Growth Conditions

Contrary to MBE where spontaneous growth of GaN NWs is easily achievable under N-rich condition, the conditions to spontaneously form NWs in MOVPE took a certain time to be determined and several ways have been opened. In general, a low V/III ratio (using trimethyl-gallium TMGa and ammonia) and high growth

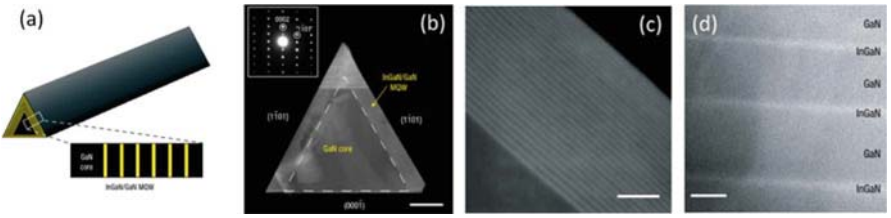

Fig. 12.5 Example of triangular Ni-catalyzed GaN NWs with core-shell InGaN/GaN multiple quantum wells (MQWs). (**a**) Schematic diagram of a GaN NW with a cross-sectional view showing InGaN/GaN core-shell MQWs (InGaN wells in yellow). (**b**) Dark-field cross-section STEM image along the [11–20] zone axis indicating the triangular GaN core with a shell composed of 26 MQWs (the scale bar is 100 nm). (**c**, **d**) Enlarged STEM images at the {1-101} facet corresponding to a detailed view of MQWs (the scale bar is equal to 20 and 2 nm, respectively). Adapted with permission from [41]

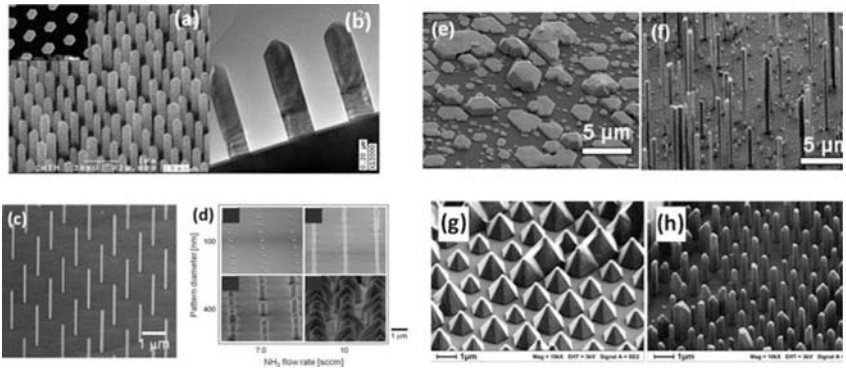

Fig. 12.6 Main MOVPE methods to grow catalyst-free GaN NWs. (**a**, **b**) SEM and TEM images of ordered GaN wire arrays grown by pulsed precursor mode (Adapted with permission from [101]). (**c**, **d**) SEM images of ordered GaN NW array grown by ultra-low precursor flux method as a function of the NH_3 flux and the pattern pitch (Adapted with permission from [102]). (**e**, **f**) SEM images of self-assembled GaN wires grown without (**e**) and with (**f**) silane flux addition. (**g**, **h**) SEM images of ordered GaN wire arrays grown without (**g**) and with (**h**) hydrogen dilution (2:1) of N_2 carrier gas (Adapted with permission from [103])

temperatures (>950 °C) are used to favor the vertical growth, but each method requires specific growth conditions including usually a preliminary seed nucleation stage followed by wire growth steps. The main MOVPE growth methods illustrated in Fig. 12.6 are detailed hereafter.

- *Growth based on pulsed precursor flows*: The Hersee's group was the first in 2006 to achieve the vertical growth of GaN wires along the c-axis without catalyst by introducing pulsed growth (see Fig. 12.6a, b) [101]. Beyond the absence of a catalyst, this pioneering work also demonstrated for the first time the use of SAG, opening the possibility to control the diameter, length, and density of the wire arrays. The growth is carried out in a pulsed manner, where the precursors III and V are injected alternately into the growth chamber. The principle is based on the discovery in the 2000s of the possibility to enhance vertical growth by injecting in a pulsed way the V precursor (NH_3) that also allows tuning the nanostructure shape [104]. The length of the wires is simply controlled by the number of cycles, leading to moderate growth rates in the order of 1–2 µm/h, corresponding to a growth of 3–6 nm of GaN by cycle. Such pulsed growth is performed on GaN templates on c-sapphire substrates leading to GaN NWs with Ga-polar crystal orientation imposed by the template polarity. The growth is usually performed at high temperature (>950 °C), low pressure (100–200 mbar), high V/III ratio (1500), and generally under H_2 carrier gas. The key point of this approach is the optimization of injection and waiting durations for elements III and V, which will depend on the reactor type, precursor fluxes, and growth temperature [30, 105, 106]. The pros and cons of this approach is the high growth control of complex NW arrays and the low growth rate, respectively. In addition, the optical and

structural properties reveal defects (including dislocations) mainly localized at the base of NWs [101].

- *Growth based on ultra-low precursor flux*: An effective approach to grow catalyst-free NWs consists in using an extremely low precursor flux and V/III ratio within a range of two orders of magnitude less compared to standard planar GaN growth (see Fig. 12.6c, d) [102, 107, 108]. These unusual growth conditions are opposite to the conditions conventionally used for the growth of the III–V semiconductors where the element V precursor is saturated in the gas phase to avoid the desorption of the V-elements, which are much more volatile than the III-elements. For the NW growth, the flux of TMGa is typically reduced to only 0.1–1.0 μmol/min and the NH_3 flux to 10–100 μmol/min (instead of 100 μmol/min for TMGa and 200 mmol/min for NH_3 for standard growth). Such a low precursor flux results in very low V/III ratio between 1 and 50, in comparison to the typical V/III ratio used for planar growth in the range of 1500–4000. The growth is usually performed at high temperature (950–1100 °C), low pressure (100 mbar), and generally under N_2 carrier gas with hydrogen dilution. As the ultra-low flux mode leads to Ga-polar NWs, this approach is achievable on surface favorable to Ga-polar growth, such as GaN templates grown on sapphire substrates [108]. The NW diameter in the range of 100 nm can be achieved with a low growth rate (typically 1–4 μm/h depending on the NW density) due to low precursor flux. This type of growth has been studied extensively by Arakawa's group, which has developed the selective growth of ordered NWs with a diameter of only 50 nm [102]. Excellent optical properties related to a high structural quality are reported, the near band edge emission width being similar to those of the wires obtained by MBE [108].
- *Growth based on silane flux addition*: In the case of a planar growth, it is known that Si doping using a high flux of silane favors vertical growth, whereas Mg doping favors lateral growth [109]. This idea has been used by the Eymery's group to grow NWs using a silane flux more than 10 times higher than the flux used for typical n doping (i.e., 10 nmol/min for standard n-doping at 10^{18} at./cm^2). Combining low V/III ratio (<50), high growth temperature (1050 °C), high pressure (800 mbar), and rich N_2 carrier gas, this approach is highly efficient with growth rate larger than 100 μm/h for silane flux of 200 nmol/min (see Fig. 12.6e, f) [110]. This approach is well suited to enhance the vertical growth of N-polar NWs. Such N-polar wires require N-polar GaN substrates or specific surface preparation of c-sapphire substrates to get, for example, AlN and SiN_x ultra-thin layers to promote N-polar growth. After a given wire length (>5 μm), it is possible to stop the silane flux keeping the NW morphology, but the growth rate is tremendously decreased as a function of length. The use of silane imposes n-type doping with a high doping level (>5 × 10^{19} at./cm^3) [110, 111]. The silane approach can also be employed on Ga-polar GaN NWs to enhance the vertical growth [20, 112]. The high doping level induces a broad emission peak of GaN accompanied by a blue shift due to band filling effect. These near band edge optical properties can be significantly

improved when a part of the NW is grown without silane, but we generally observe in parallel an increase of the yellow band related to deep defects [110].

- *Growth based on the mixing of H_2/N_2 carrier gas*: Another key approach that favors the occurrence of vertical m-plane facets for the formation of GaN NWs by MOVPE is the H_2/N_2 ratio of the carrier gas [103]. As shown by the Waag's group, selective growth on c-sapphire under N_2 results in a pyramid growth regime (Fig. 12.6g), whereas a progressive dilution of the carrier gas with hydrogen (H_2/N_2 ratio between 1:2 and 2:1) leads to the formation of m-facets associated with a strong limitation of lateral growth (Fig. 12.6h). For given growth conditions (V/III ratio <50 and growth temperature near 1050 °C), the control of the H_2/N_2 ratio carrier gas favors vertical planes and supports the formation of GaN NWs. This effect is very sensitive for Ga-polar NWs.

12.2.2.2 Growth Mechanisms Involved in MOVPE NW Formation

Three key mechanisms have been proposed to explain the GaN wire catalyst-free growth involved in the different MOVPE methods described before.

– *Preferential growth along the c-axis direction*: The enhanced elongation rate by pulsed growth can be understood by a larger adhesion coefficient of Ga adatoms to the c-plane than to the m-plane facets. Consequently, for a high enough temperature, the desorption rate of Ga adatoms from m-plane surfaces is much higher than from the c-plane surface. Therefore, when the Ga precursor is injected, the Ga adatoms first cover all the surfaces, but then preferentially desorb from the m-plane facets or diffuse toward the top c-plane surface during the waiting step, which causes an accumulation of adatoms on the upper c-plane facet. Then, the exposure to the ammonia flow forms GaN preferentially on the c-plane facet favoring the vertical growth [113, 114]. The same mechanism can also be proposed for the ultra-low precursor flux method, if the diffusion of Ga adatoms is considered faster than the GaN formation due to the low kinetic induced by the low precursor flux.
– *Self-passivation of NW sidewalls by SiN_x mask*: In the case of growth under a high silane flux, an accumulation of Si on wire sidewalls is observed related to the formation of an SiN_x passivation layer [22, 115, 116]. Once the SiN_x layer is formed spontaneously on the vertical facets, the lateral growth is blocked favoring the axial growth [115]. The formation of SiN_x is expected because the typical silane flux used for the in situ deposition of planar SiN_x is about 200 nmol/min, which is exactly the flux used in NW growths [117]. This mechanism is based on the fact that the SiN_x layer is formed preferentially on the m-plane surfaces compared to the c-plane surface. Consequently, Ga adatoms diffuse along the m-plane surfaces covered by an SiN_x shell until reaching the upper surface to contribute to the vertical growth. Since this surface passivation layer is formed continuously during the wire growth, this method is well suited to grow ultra-long GaN wires (>100 μm) just by increasing the growth time [118].

– *Surface hydrogen passivation*: It has been shown by the Waag's group that a flow of hydrogen has a passivation effect for the r-plane $(0\,1\,\bar{1}\,\bar{1})$semipolar surfaces in the case of Ga-polar crystals that significantly reduce the growth rate, leading to a pyramidal shape. On the contrary, the H-passivation mainly occurs on the c-plane surface compared to r-plane surfaces for the N-polarity revealing wire-shaped nanostructures [119]. In addition, hydrogen tends to preferentially etch the r-plane surfaces at the benefit of m-plan $(0\,1\,\bar{1}\,0)$ surfaces corresponding to non-polar vertical facets to spontaneously form wire nanostructures. This preferential etching most easily occurs with N-polar crystal. It is possible to form vertical m-plane facets on Ga-polar crystals if the r-plane H-passivated surfaces are exposed to a high Ga flux. In this case, the r-plane surfaces become unstable and promote the m-plane surface formation, resulting in wire-shaped nanostructure with a Ga-polarity. This phenomenon under high Ga flux can also explain the wire formation in the case of pulsed growths or low precursor flux methods that both allow growing Ga-polar wires.

The above-described three mechanisms are highly dependent on the polarity of the GaN crystal and can simultaneously play their role in GaN NW formation by MOVPE. Therefore, an accurate control of crystal polarity together with growth conditions is required to promote NW growth.

12.2.2.3 NW Growth by Selective Area Growth in MOVPE

SAG through regular hole array in a dielectric SiO_2 or Si_3N_4 mask is an effective way to control density, size, and height of the wires. This approach is largely used in MOVPE to manage the GaN wire growth with the benefit of high wire-to-wire uniformity. A preliminary nucleation step of GaN is usually required to get a perfect filling of all mask apertures [101, 120, 121]. Then, the growth conditions are switched to promote the vertical growth regime in order to achieve perfect ordered wire arrays. The selective growth is traditionally performed on a GaN surface, but can be also managed on c-sapphire or AlN/Si(111) substrates, however, with a lower selectivity. In the case of SAG, the Ga adatoms diffuse firstly on the mask and secondly along the wire sidewall to contribute to the wire growth (the diffusion is typically about 1–2 μm for the mask and 3–5 μm on sidewall) [43]. The control of the wire growth remains a key issue, because the SAG is highly dependent on the growth conditions (V/III ratio, flux of precursors, temperature, pressure, etc.) and also on the pattern design, as shown in Fig. 12.6d.

12.2.2.4 Radial Growth of Heterostructures

The principle of MOVPE growth is based on pyrolysis chemical reaction of precursors coming from the gas phase. Consequently, the growth occurs on all surfaces in contact with the gaseous species, which leads to a conformal coverage

of nanostructures. In the case of NWs, MOVPE growth of heterostructures results in a core-shell geometry. The radial growth is favored by reducing the growth temperature to limit the diffusion length of adatoms [122]. The radial growth is observed for InGaN/GaN multiple quantum wells under a low growth temperature for efficient In incorporation (700–800 °C) [110]. In the same way, the growth of GaN layer in core-shell structures is performed at a lower growth temperature (<1000 °C). The growth rate and the In incorporation of radial heterostructures are highly dependent on the facet crystalline orientation and also on the crystal polarity of GaN NWs. For pencil shaped Ga-polar NWs, the InGaN/GaN multiple quantum wells grow at a much higher rate with higher In incorporation on the horizontal c-plane facets localized on the NW summits compared to vertical m-plane facets corresponding to the NW sidewalls, with almost no growth on inclined r-plane facets of the NW upper part [48]. In the case of long NWs (>5 μm), a decrease of thickness and of In content can be observed along the NW from its top to its bottom leading to an emission wavelength shift, which has a negative effect on the LED performance as described later on in Sect. 12.9. The heterostructure growth conditions need to be carefully optimized in order to get an excellent uniformity of optical and electrical properties of NW ensembles.

12.2.3 Comparison of Catalyst-free Growth Method of Nitride NWs

A summary of the main methods to grow GaN NWs along the c-axis direction is proposed in Table 12.1 with a description of the related NW features. We stress that the morphology and properties of the produced NWs are different depending on the growth approach. On one hand, MBE allows getting high optical quality NWs with a diameter of few tens of nanometers. On the other hand, MOVPE produces larger NWs with the possibility to extend the NW length to several hundreds of micrometers by using silane flux.

Even if MBE is an efficient method to grow high quality GaN NWs with pioneer demonstrations of LED devices, MOVPE is a key growth technique used in the industry. The attempts of industrial development of NW devices are actually mostly based on MOVPE methods.

12.3 NW LED Fabrication

The architecture of NW array LEDs containing a large number of parallel-connected NWs is schematically shown in Fig. 12.7a. This schematic was elaborated following a typical morphology of organized core/shell NW arrays illustrated in the SEM image of Fig. 12.7b [49]. The growth substrate is normally used as a bottom

Table 12.1 Comparative table of GaN NW features as a function of the growth method

GaN NW growth methods	MBE	MOVPE			
		Pulsed precursor mode	Ultra-low precursor flux	Silane flux addition	Hydrogen dilution of carrier gas
NW diameter	10–100 nm	200–500 nm	30–200 nm	0.5–2 μm	0.2–1.5 μm
NW length	0.1–3 μm	0.3–2 μm	0.5–3 μm	5–500 μm	1–3 μm
NW density	$\sim 10^{10}$ cm^{-2}	$\sim 10^{8}$ cm^{-2} (SAG)	$\sim 10^{8}$ cm^{-2} (SAG)	10^{7}–10^{8} cm^{-2}	$\sim 10^{8}$ cm^{-2} (SAG)
Standard substrate and polarity	SiN/Si(111): ↓	GaN/c-sapphire: ↑	GaN/c-sapphire: ↑	c-sapphire: ↓ (↑)	c-sapphire: ↓ (↑)
↑: Ga-polarity	AlN/Si(111): ↑ ↓			AlN/Si(111): ↓ (↑)	AlN/Si(111): ↑
↓: N-polarity				GaN/c sapphire: ↑	GaN/c sapphire: ↑
Optical properties	Narrow NBE ∼1–10 meV	Large NBE ∼100 meV	Narrow NBE ∼1–25 meV	Large NBE ∼120 meV + band filling shift	Data not available
NBE: near band edge					
YB: yellow band	No YB	Presence of YB	No YB	Narrow YB	

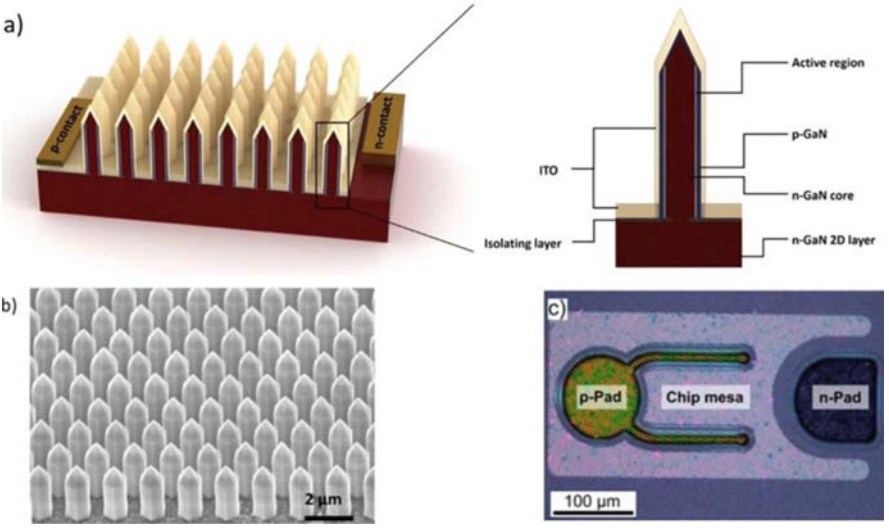

Fig. 12.7 (**a**) Schematic of a core/shell LED. (**b**) SEM image of as-grown organized core/shell NWs grown by GLO-AB. Adapted from [49]. (**c**) Blue NW LEDs fabricated by OSRAM. Reproduced with permission from [29]

contact (Fig. 12.7a). For axial LEDs, to ensure electrical insulation, the NWs are encapsulated into a polymer matrix (e.g., hydrogen silsesquioxane, BCB, polyimide, etc.) and the NW tips are exposed for contacting by etching the excess of the encapsulating material. For radial LEDs fabricated by a selective area growth using a dielectric mask (as exemplified in Fig. 12.7b), the encapsulation step can be omitted since the mask provides electrical insulation. In this case, a transparent contact can be deposited all around the NWs as shown in Fig. 12.7a. Lithography is used to define devices with a desired size, which may range from tens of microns to millimeters. If back contacting is not possible (e.g., when an insulating sapphire substrate is used), etching is used to access to the bottom contact layer as shown in the device schematic of Fig. 12.7a. A transparent conductive layer (typically indium tin oxide (ITO)) is deposed onto the LED front surface to form the upper contact suitable for light extraction. To reduce the series resistance, a metal current-spreading grid can be added. Fig. 12.7c shows a top-view optical microscopy image of a fully processed LED based on core/shell NWs, where the ITO layer and the top and bottom metal contacts are clearly visible [29].

12.4 Early Demonstrations of Nitride NW LEDs

First demonstrations of nitride NW LEDs have appeared at the beginning of years 2000. They were using self-assembled NWs. Kim et al. [123] reported

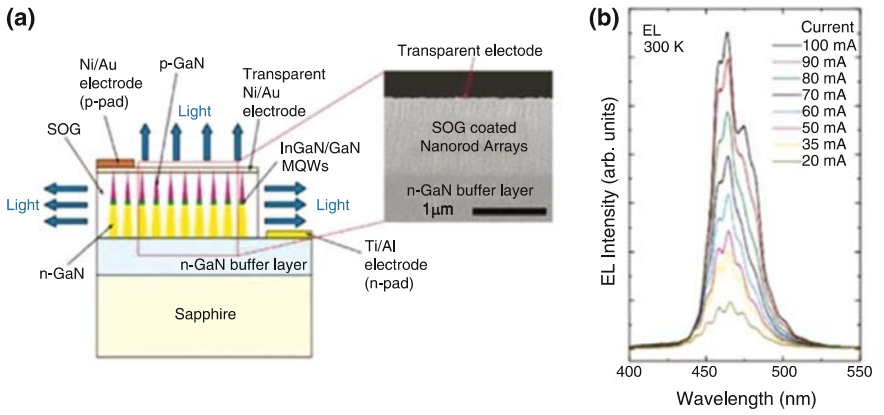

Fig. 12.8 (**a**) Cross-sectional schematic diagram (left) and SEM image (right) of InGaN/GaN multiple quantum well nanorod array LEDs. (**b**) Room temperature electroluminescence spectra of InGaN/GaN MQW nanorod array LEDs under different applied currents. Adapted with permission from [124]

the metalorganic-hydride vapor phase epitaxy (MO-HVPE) growth of axial GaN p–n junctions. Individual NWs were contacted using focused ion beam (FIB) lithography. They produced electroluminescence around 390 nm attributed to DAP recombination in the p-GaN segments. The same team reported one year later a demonstration of NW array LEDs containing quantum wells [124]. Axial InGaN/GaN nanoneedles with 6 $In_{0.25}Ga_{0.75}N$/GaN embedded axial quantum wells were grown by MO-HVPE. The structure was synthesized on a 2D n-GaN buffer layer on sapphire substrate used as a bottom contact. The empty space between the nanoneedles was filled with a spin-on glass and the p-GaN tips were contacted with a semi-transparent Ni/Au (20 nm/40 nm) electrode as illustrated in Fig. 12.8a. The device presented a broad blue electroluminescence peaked around 460 nm. The peak wavelength (Fig. 12.8b) was stable with injected current.

The same year Kikuchi et al. [125] have demonstrated an LED based on MBE-grown NWs [32, 126]. The structure illustrated in Fig. 12.9a contained 8 axial InGaN/GaN quantum wells grown on an n-doped GaN NW base. The growth of the p-doped GaN cap was performed at lower temperature under Mg flux, which led to the wire broadening and coalescence as seen in the SEM image of Fig. 12.9b. The coalesced top surface allowed to directly deposit a semi-transparent Ni/Au (2 nm/3 nm) contact without a planarization step. The emission wavelength was adjusted from green (530 nm) to red (645 nm) by changing the In content in the wells. Figure 12.9c shows optical microscopy images of the NW LEDs under operation. Due to wire-to-wire fluctuations the electroluminescence has a spotty nature with intensity and color variations within the array.

The group of C. Lieber has demonstrated in 2003 LEDs based on crossed p-GaN and n-GaN NWs synthesized by metal-catalyzed chemical vapor deposition

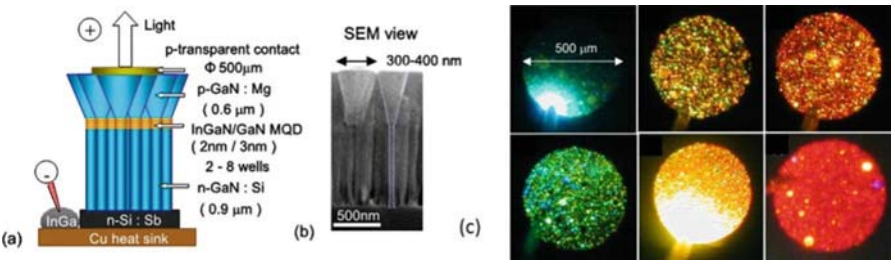

Fig. 12.9 (**a**) Schematic diagram of the MBE-grown InGaN/GaN NW LEDs, (**b**) their cross-sectional SEM image, and (**c**) their electroluminescence optical microscope images. Adapted with permission from [126]

[127]. During the following year, core/shell NW LEDs were realized by this team [41, 98]. The wires were synthesized by MOCVD using Ni particles as a catalyst. As mentioned in Sect. 12.2, this method yields NWs with the long axis aligned with a⟨11-20⟩direction and a triangular cross-section with one polar c-facet and two {1-10-1} semipolar facets. The GaN core was n-doped, then a radial single InGaN quantum well was deposited and capped with a p-doped GaN shell. Due to their different crystallographic orientation, the facets were non-equivalent and the InGaN layer was thicker on semipolar facets than on the (0001) facet. As illustrated in Fig. 12.10a, single NWs were contacted by the p-GaN shell and by the core, which was revealed by FIB etching of the shell on one of the NW extremities. Diodic current–voltage characteristics with a diode opening voltage around 3 V were achieved. The electroluminescence of single wires was imaged (Fig. 12.10b) and spectrally characterized (Fig. 12.10c). The emission wavelength was tuned by adjusting the In content in the quantum well (function of the growth temperature) from UV to yellow–green spectral range (namely, from 367 to 577 nm). The external quantum efficiency of single NW LED was estimated to be ∼5.8% at 440 nm and ∼3.9% at 540 nm.

12.5 NW LEDs With Emission Color in the Visible Spectral Range

Since the early demonstrations of NW LEDs, these nanostructures are believed to become serious competitors of thin films. A large number of research groups, but also start-ups and big industrial groups launched research activities on this topic exploring different designs and different growth techniques. In the following we present a non-extensive summary of the main achievements of the past ten years with a focus on the current progress.

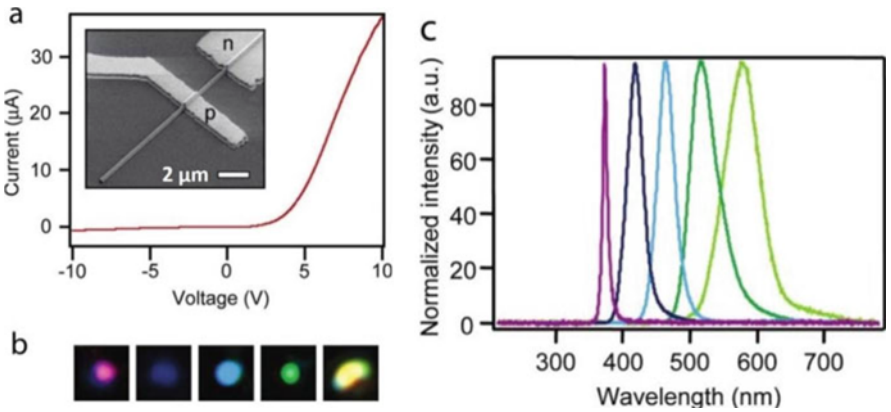

Fig. 12.10 (**a**) I–V curve of a core/multishell NW LED. Inset: SEM image of the device. (**b**) Optical microscopy images of electroluminescence emissions under forward bias, showing purple, blue, greenish-blue, green, and yellow emission, respectively. (**c**) Normalized electroluminescence spectra of five representative multicolor LEDs. Adapted with permission from [41]

12.5.1 MOVPE-grown NW LEDs

The potential advantages of the core/shell NW LEDs over the conventional planar technology were clearly highlighted by Waag et al. [128], the main one being the tremendous increase of the active surface. By taking a circular cylinder approximation for NWs and assuming that the radial quantum wells are close to the NW surface (i.e., neglecting the p-GaN shell), the increase of the active area in a NW LED with respect to the active area in a thin film LED of the same chip surface can be calculated as:

$$\frac{S_{\mathrm{NW}}}{S_{\mathrm{film}}} = \frac{2\pi \mathrm{RH}}{\pi R^2/F} = \frac{2H}{R}F,$$

where S_{NW} is the active area of a NW LED, S_{film} is the active area of a thin film LED with an equivalent chip surface, R is the NW radius, H is the NW height, and F is the fill factor, i.e., the ratio of the NW cumulated footprint to the total projected device surface. Thanks to the larger active area, the carrier concentration in the quantum wells of a core/shell NW LED is lower with respect to a thin film device. Therefore, NW emitters will show efficiency droop at a higher current [25].

Early works on MOVPE-grown core/shell NW LEDs mainly employed self-assembled catalyzed [129] or non-catalyzed [110] growth; however, organized growth on sapphire [128] and on GaN templates [48] was also reported.

Non-catalyzed GaN NWs with core/shell InGaN/GaN quantum wells (Fig. 12.11a) were used to fabricate single NW LEDs [46, 110]. In these devices, five radial InGaN/GaN quantum wells were grown around the upper part of the GaN NW stems. It was shown that quantum wells are formed not only on the lateral m-planes,

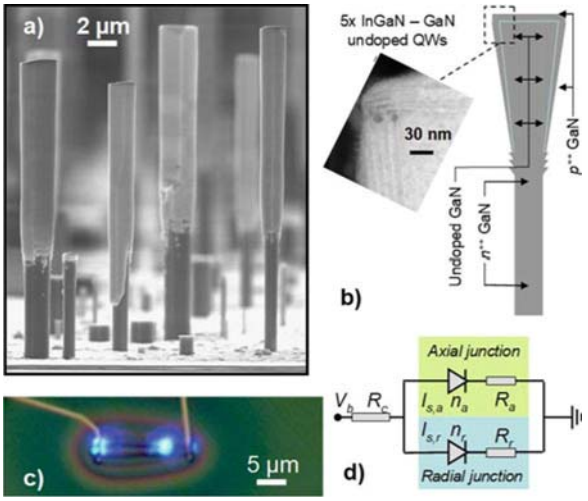

Fig. 12.11 (**a**) SEM image of MOVPE-grown core/shell NWs. (**b**) Schematic of the wire internal structure and a TEM image of the top region of a wire, evidencing the presence of radial and axial quantum wells. (**c**) Optical microscopic image of a single NW LED in operation. (**d**) Equivalent electrical circuit of the LED representing the axial and radial junctions. Adapted with permission from [46]

but also on the top-c plane as can be seen in the schematic and in the TEM image of Fig. 12.11b. Line defects propagating perpendicular to quantum well planes with an enriched In composition were evidenced in these type of wires [130]. The NWs were dispersed on SiO_2 on Si substrates and contacted using e-beam lithography as illustrated in Fig. 12.11c. The In content and the well thickness were different on the non-polar (radial) and on the polar (axial) planes. This structural dissimilarity, but also the difference in the internal field in the axial and radial quantum wells, resulted in different luminescence wavelengths as evidenced by cathodoluminescence [46]. The competition of the carrier injection in the axial and radial quantum wells caused the change of the electroluminescence color as a function of the injected current and as a function of temperature [46]. An electrical model describing the axial and radial junctions as parallel-connected diodes with different parameters (Fig. 12.11d) allowed to explain the observed electroluminescence color change.

Using self-assembled NWs of a similar geometry, Koester et al. [131] demonstrated LEDs based on NW arrays with an emission wavelength around 410 nm. In particular, the authors have characterized the device bandwidth as described later in Sect. 12.7.

The group at Chonbuk National University employed Au + Ga catalyst assisted MOCVD to demonstrate blue NW LEDs with an axial InGaN/GaN active region [129]. We note that this is one of the rare reports on purely axial NW LEDs grown by MOCVD. Dense mostly vertical 2 µm long NWs were formed. At the end of the growth, Au catalyst was no longer observed at the top of the NWs, which allowed to deposit quantum wells with well-defined interfaces. Pulsed-flow precursor method was used to grow axial multiple quantum wells at a reduced growth temperature. The quantum well emission wavelength was varied from 415 to 520 nm by adjusting the In content. A p-doped GaN cap segment was deposited on top of the quantum wells. To fabricate LED devices, polyimide encapsulation of the NWs and an ITO

top contact were used. Devices showed diodic behavior with an opening voltage around 2.75 V and exhibited blue electroluminescence varying linearly with the injected current up to an emitted power of 88 μW for 35 mA. Several months later the same group has applied a similar growth technique using Au catalyst to form LEDs with radial quantum wells on the non-polar and on the semipolar planes [132]. To obtain coaxial NWs the growth pressure was reduced during the quantum well deposition. A coalesced p-doped GaN layer was deposited under an increased Ga precursor flow. A p-GaN layer covered mainly the NW tops and the upper part of the m-plane sidewalls; however, the dominant electroluminescence originated from the m-planes. An external quantum efficiency (EQE) value of 27.9% was reported for an LED emitting at 440 nm wavelength under 50 mA injection; however, the details of the EQE estimation were not provided.

Self-assembled NWs suffer from geometrical and compositional fluctuations which have a dramatic impact on the electroluminescence. To improve the wire-to-wire homogeneity, SAG was applied. Hong et al. [48] demonstrated color-tunable LEDs using SAG of GaN NWs by MOVPE with a nanopatterned SiO_2 layer on GaN-on-sapphire templates. After the growth of the NW cores, InGaN/GaN quantum wells were deposited on the NW template yielding a complex axial and radial heterostructure with thick In-rich (In content ≈0.6) quantum wells on the top polar plane, thinner quantum wells with a lower In content (≈0.15) on the m-planes, and in addition a curved thick InGaN layer beneath the axial quantum wells. The NW structure was buried into a continuous p-doped GaN layer forming a nanorod-embedded thin film as seen in the SEM image of Fig. 12.12d. The LEDs were fabricated using a semi-transparent Ni/Au layer applied to a coalesced p-GaN surface for the top contact (Fig. 12.12c). The LED color changed with applied bias from a single broad peak around 690 nm under 3 V to a blue-shifted double peak (at 500 nm and 440 nm) under 10 V as shown in Fig. 12.12a, b. The authors explained the electroluminescence color change with a field distribution model. The equipotential surface in the highly resistive p-GaN layer was initially flat corresponding to the injection in the NW tops and then changed to a curved shape along the NWs promoting the injection in the m-plane quantum wells. The internal quantum efficiency (IQE) of the quantum well was estimated by temperature-dependent photoluminescence to be around 32%.

The variation of the emission color with bias [48] may be regarded as an advantage and used for LED color tuning; however, for standard narrow-band LEDs this phenomenon is undesirable. Chen et al. [133] demonstrated a NW LED with a stable emission color. Organized NWs were selectively grown by pulsed MOCVD on GaN on sapphire templates (Fig. 12.13a). Similar to the work of Hong et al. [48], quantum wells were deposited on the m-plane facets and on the c-plane in the tapered NW top part; however, the structural quality of the top wells was quite poor. Instead of a coalesced p-GaN layer, a conformal p-GaN shell was grown around the NWs. An original approach for the p-contacting was developed based on a deposition of a transparent conductive GaZnO by molecular beam epitaxy, which first formed a conformal shell but then coalesced at the NW tops as illustrated in the schematic of Fig. 12.13b. The LED turn-on voltage was around 6 V with

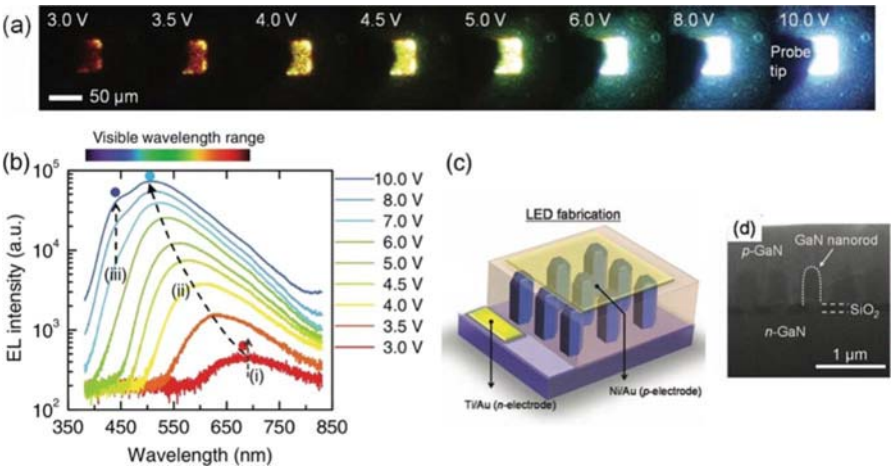

Fig. 12.12 (**a**) Optical microscopy images of LEDs operating under different applied biases. (**b**) Electroluminescence spectra for biases from 3 to 10 V. (**c**) Schematic of the LED showing core/shell NWs, the planarizing p-GaN layer, and the contacts. (**d**) Cross-sectional SEM image of a p-doped GaN layer burying GaN NWs. Adapted with permission from [48]

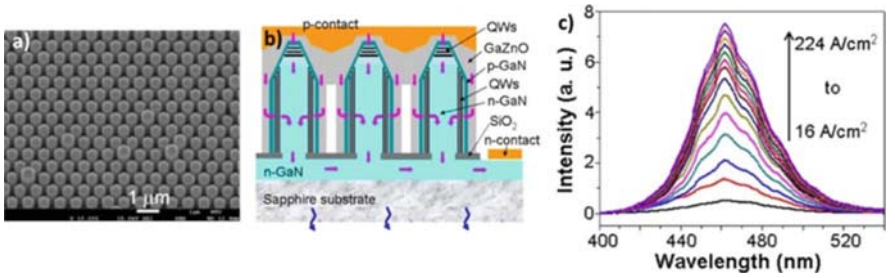

Fig. 12.13 (**a**) Tilted SEM image of a NW array. (**b**) Schematic of the NW structure and contact geometry. Pink arrows indicate the possible current flow directions. (**c**) Electroluminescence spectra when the injected current density increases from 16 to 224 A/cm^2. The insert shows the photograph of the LED in operation. Adapted with permission from [133]

a broad electroluminescence spectrum centered at 463 nm. Contrary to [48], the emission wavelength was remarkably stable with increasing injection (Fig. 12.13c), no redistribution of the injected current in the quantum wells along the wire axis was taking place.

Wang et al. [43] also developed NW SAG on GaN on sapphire templates covered with SiO_x mask patterned by nanoimprint lithography. Fixed 400 nm mask openings were chosen to define the NW diameter and growth positions. The statistical evaluation of the geometry of the GaN wire arrays after the growth showed that the standard deviation of the NW height is in the range of 4–8% and for the diameter it is close to 3% depending on the NW aspect ratio (higher standard deviations are observed for higher aspect ratio SAG wires).

The OSRAM group [29] extensively described the fabrication and properties of core/shell LEDs based on organized NWs (SAG is described in detail in [122]). A core/shell NW design was adopted to demonstrate both blue and white NW LEDs. Homogenous NW arrays with a height around 3 μm and a diameter close to 2 μm were synthesized by MOVPE. The wires had a hexagonal shape with m-plane facets and their tips were delimited by semipolar {10-12} facets. A single InGaN quantum well grown on both m- and semipolar-facets exhibited an increase of the In content on the semipolar planes as revealed by cathodoluminescence mapping. The IQE of the wires derived from optical experiments was close to 10%. Array LEDs with a 150 × 250 μm^2 projected surface were fabricated. Prior to the transparent contact deposition, an additional SiO_x insulating layer was deposited on the NW base part to avoid leakage through eventual defects of the SiO_x growth mask. The device morphology is illustrated in Fig. 12.13b in Sect. 12.3. The electroluminescence spectra evolved with the injection current showing first a green emission attributed to In-rich semipolar quantum wells and then turning quickly to the blue emission from the m-plan quantum wells. A further blue shift of the electroluminescence was observed, attributed to an In gradient in the m-plane quantum wells. The LEDs demonstrated an EQE of 3% for 400 mA/mm^2 and a maximum wall-plug efficiency of 1.5% at 300 mA/mm^2.

Core/shell NW LEDs were also developed by Glo-AB company using SAG on GaN-on-sapphire templates with an SiN_x mask patterned by nanoimprint [50, 52, 134]. The NW morphology is exemplified in Fig. 12.13b of Sect. 12.3. The NWs contained a single InGaN quantum well on the m-planes. Contrary to [29], no InGaN layer was observed on the semipolar top facets. However, an In-rich region located in the quantum well at the m-plane/semipolar plane junction was evidenced. Electroluminescence color switching shown in Fig. 12.14a was reported in these NWs both for single NW LEDs [49] and for NW array LEDs [50]. This color switching was explained within a simple electrical model [49]. A core/shell NW was represented by a network of parallel-connected diodes and the current distribution in this network was calculated for different applied biases and different contact layouts. To account for the compositional inhomogeneities, a different saturation current was ascribed to the diodes, corresponding to the top-most In-rich part of the core/shell quantum well. The saturation current depends on the quantum well bandgap energy following the equation [49]:

$$J_{\text{sat}} = \int_{\text{QW}} \mathrm{d}z \left(B \times {n_i}^2 \right) = wBN_cN_v \exp\left(\frac{E_g}{k_B T} \right)$$

and therefore increases in the In-rich regions, where the bandgap is smaller. For an electrical circuit shown in Fig. 12.14c, the current distribution in the individual diodes (Fig. 12.14d) showed that at low bias first the In-rich segment was injected. For higher biases, parallel and radial shell resistances started to play an important role and the current concentrated in the m-plane quantum well under the injecting p-contact, which resulted in the electroluminescence color switching. Similar effect was predicted for an extended contact covering the entire m-plane [49].

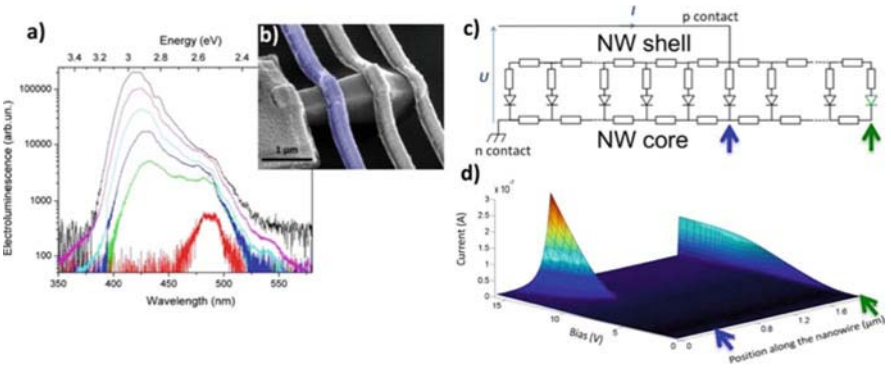

Fig. 12.14 (**a**) Electroluminescence spectra of a single NW LED with a metal contact on the m-plane. (**b**) SEM image of a single wire LED with the injecting contact highlighted in violet. (**c**) Equivalent electrical circuit of a core/shell NW LED. (**d**) Current distribution in a diode network as a function of the applied bias and diode position in the wire. Adapted with permission from [49]

Zhang et al. [50] showed that the emission color of NW LEDs exhibiting a compositional inhomogeneity could be controlled by modifying the contact layout. Core/shell NW LEDs with an In-rich region in the top part of the m-plane quantum well were examined. By removing the ITO contact from the top part of the NWs and by inhibiting the conductivity of the exposed p-GaN shell by CHF_3 plasma treatment, the undesired long wavelength emission could be suppressed. Figure 12.15 shows the electroluminescence spectra of a nominally blue NW LEDs for three different processing schemes: conformal ITO contact, ITO contact etched away from the NW top part, and the NW top part removed by ICP etching. Electroluminescence spectra for the same injected electrical power were compared. Two distinct emission peaks were observed for the conformal contact. The long wavelength peak was strongly suppressed after partial ITO removal and CHF_3 plasma exposure while the intensity of the blue emission was increased. ICP etching of the NW top part completely removed the undesired long wavelength peak, which proved that it originated from the top region.

12.5.2 MBE-grown NW LEDs

Thanks to its low growth temperature, MBE is a technique well suited to fabricate In-rich alloys. Therefore, a strong effort was committed to demonstrate and optimize MBE-grown NW LEDs emitting in the long wavelength spectral range (from the green to the near infrared (IR)).

The pioneer of the MBE NW LEDs is the group of Kishino. Various electroluminescence emission colors from green to red were achieved with axial InGaN/GaN multiple quantum discs grown in self-assembled GaN NWs on Si

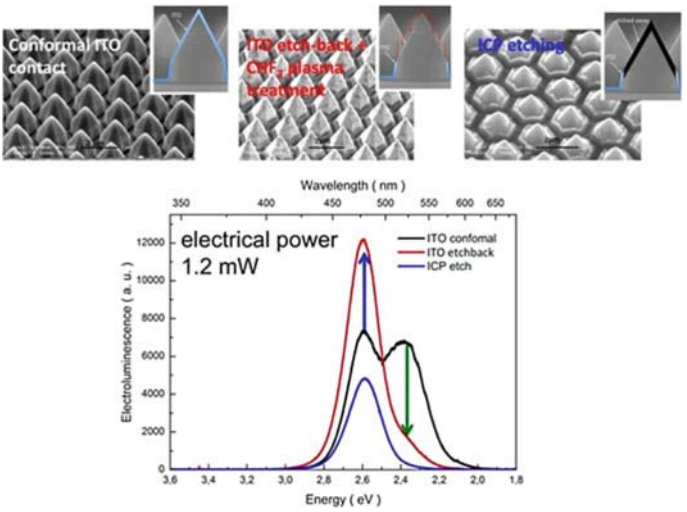

Fig. 12.15 Comparison of the electroluminescence spectra under the same electrical injected power of core/shell NW array LEDs processed with a conformal ITO contact, with a partially etched ITO contact and with the NW top part removed by ICP etching. The top row shows SEM images of the corresponding LEDs with a schematical drawing of the contact

substrates illustrated in Fig. 12.16a, b [125]. Later on, their research interests moved to SAG, which brings new functionalities for monolithic integration owing to the more precise control of the NW morphology and of the In composition [32]. We note that the SAG NWs have a different morphology with respect to self-assembled NWs. As illustrated in Fig. 12.16c, d, SAG NWs due to their Ga-polarity exhibit a pyramidal top. The multiple quantum wells grown on SAG wires are deposited on the sixfold side faces of the pyramidal top, which are semipolar planes with a low internal field. For self-assembled NWs, axial multiple quantum wells grow on the polar c-plane as shown in Fig. 12.16a, b.

By changing the NW diameter by SAG, InGaN quantum wells with different In composition were demonstrated within the same growth run [32]. With NW diameters ranging from 143 to 270 nm, these monolithically integrated NWs emitted light from blue to red. In 2013, a monolithic integration of 544, 583, and 597 nm emitting InGaN-based NW LEDs was demonstrated on the same Ti-masked GaN substrate in a single growth [136]. In 2015, a monolithic integration of four-color InGaN-based NW LEDs was achieved [33]. Figure 12.17 illustrates this spectacular realization. The Ti-mask was processed with different diameters of nano-holes in each region. The NWs were encapsulated into a spin-on glass and contacted with a transparent ITO layer on top as shown in Fig. 12.17a. Four electroluminescence colors (465, 489, 510, and 579 nm) were emitted from the NWs of different diameters as shown in Fig. 12.17b. A red LED with 670 nm emission wavelength was also fabricated using a larger pitch. It is noteworthy that this color control method can also be performed using SAG MOVPE growth, although the underlying

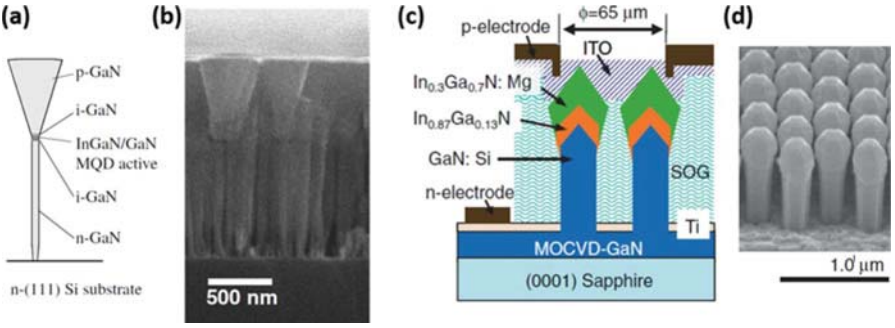

Fig. 12.16 (**a**) Schematic and (**b**) SEM image of self-assembled InGaN/GaN NW LEDs grown on Si substrate. Adapted with permission from [125]. (**c**) Schematic and (**d**) SEM image of SAG InGaN/GaN NW LEDs grown on Ti masked GaN substrate. Adapted with permission from [135]

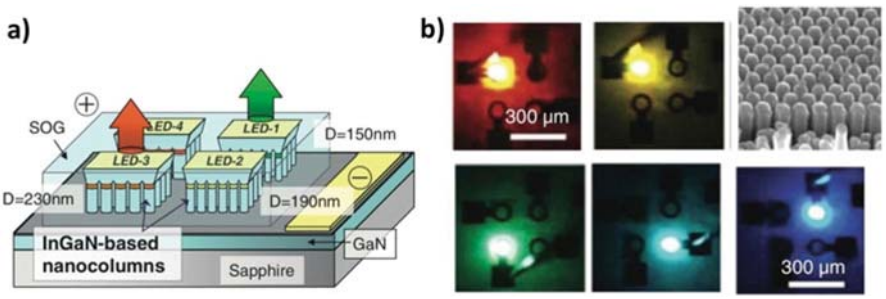

Fig. 12.17 (**a**) Schematic of the NW LED with SAG NW of different emission color. (**b**) Photographs of the NW LEDs in operation and an SEM image of the green LED. Reproduced by permission of the Institution of Engineering and Technology from [33]

mechanisms are different and the wavelength tunability range (440–520 nm) is smaller [137].

Angular profiles of the emission from the MBE SAG NW LEDs with NWs arranged into a photonic crystal were studied on the example of a yellow device [138]. The LED exhibited a high directionality with a radiation angle of ±20° due to the light diffraction at the photonic band edge. Flip-chip structure NW array LEDs were demonstrated [139]. This configuration showed an improvement of the thermal management of NW devices.

Many other groups have investigated green–yellow NW LEDs using MBE growth. Limbach et al. [140] demonstrated a self-assembled InGaN/GaN NW LED grown on an Si substrate. The electroluminescence was peaked at 540 nm. Bavencove et al. [141] demonstrated an MBE axial InGaN/GaN NW LED showing a spotty polychromatic emission from 566 nm to 585 nm under different injection currents. The EQE for a current density of the order of 50 kA cm^{-2} was 2.7%.

There are also several reports on red and near-IR MEB-grown NW LEDs. Jahangir et al. [142] demonstrated a red NW LED with InGaN/GaN discs on

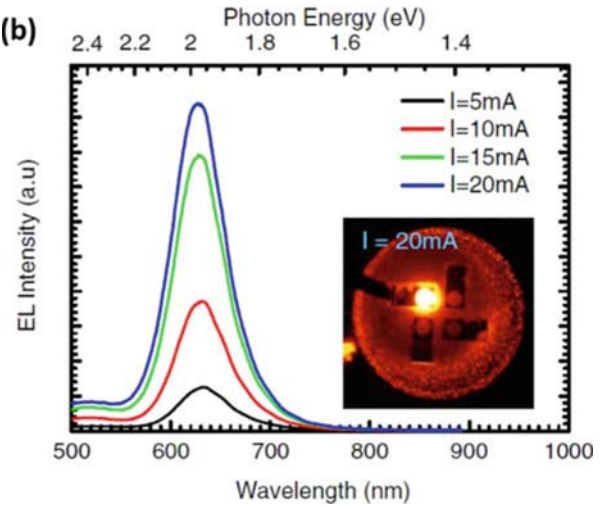

Fig. 12.18 Electroluminescence spectra under different injection currents of a red NW SAG LED. Inset: photograph of the LED in operation for 20 mA injected current. Adapted with permission from [136]

a silicon substrate. The authors found that the post-growth passivation of the NW surface with parylene and SiN_x can improve the carrier lifetime, leading to a significant improvement of the IQE from 10% to 52%. Kishino's group demonstrated red [136] and IR [135] InGaN/GaN NW LEDs by SAG on GaN templates. The red LED showed an emission at 633 nm with an output power of 16 μW at 20 mA injected current (see Fig. 12.18). The IR LED produced a weak electroluminescence at 1.46 μm at room temperature. The In concentration in the active region was 86%. Recently, following previous studies of Eu doped quantum dots [143], an alternative approach for the red-emitting NW LEDs was reported using Eu doped GaN NWs grown on Si substrate by MBE [144]. A GaN:Eu segment was grown axially between p-GaN and n-GaN extremities. This LED showed two main peaks at 620.3 and 633.8 nm, originating from the Eu ions.

A strong effort for wavelength tuning was performed by the group of Mi, who proposed a number of original approaches. The growth of quaternary AlInGaN insertions in GaN NWs was investigated [145] showing that a spontaneous Al-rich shell is formed during the growth, which protects the carriers from recombination on surface states. These core/shell structures were embedded into axial p–n GaN NWs to demonstrate LEDs with a color tunable from blue to red. Lateral integration of RGB LEDs was demonstrated using a three-step approach in which a protective SiO_2 mask was deposited allowing to form first the blue-emitting NWs, then another area was opened to deposit green-emitting NWs and finally red-emitting wires were grown during the third growth run [146]. Nguyen et al. [147] demonstrated that a high energy AlGaN barrier shell around the active InGaN/AlGaN quantum discs can eliminate the non-radiative surface recombinations and electron overflow. Recently, Philip et al. [148] also showed the enhancement of the carrier lifetime and photoluminescence intensity of a white NW LED by using this core-shell structure.

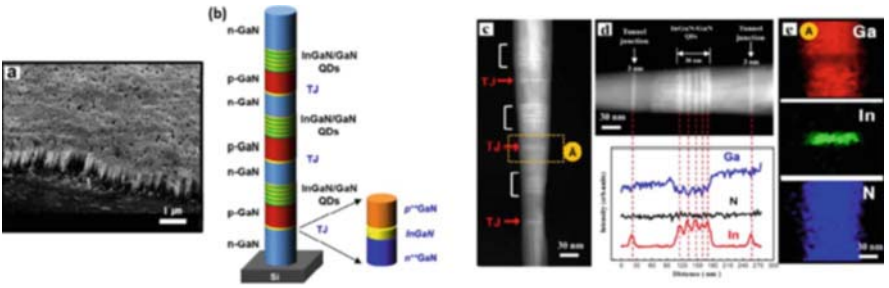

Fig. 12.19 AC multi-active-region tunnel junction InGaN/GaN NW LED (**a**) SEM image, (**b**) schematic, (**c**) HR-TEM of tunnel junction dot-in-a-wire LED structure, (**d**) top: high angle annular dark field (HAADF) image, bottom: EDXS line profile, and (**e**) EDXS elemental mapping image of tunnel junction region showing the In, Ga, and N variations. Adapted with permission from [150]

The Shockley–Read–Hall non-radiative recombinations in NW LEDs can be also reduced by octadecylthiol surface passivation [149].

An alternating current (AC) powered multi-active-region InGaN/GaN NW LED [150] was reported. Figure 12.19 shows the NW morphology, internal structure, and electron microscopy images revealing the internal structure. The NWs contained three emitting stages connected by tunnel junction. The tunnel junction design followed the strategy developed for thin films. In nitride thin film devices, a tunnel junction is typically based on polarization induced electric field of an AlN [151] or InGaN [152] insertion, which enhances tunneling in a GaN p–n junction. One advantage of the tunnel junction for LEDs is the possibility to take an ohmic contact for hole injection on n-GaN instead of a high-resistive p-GaN. In addition, it enables stacking of multiple LEDs [153] in series to produce a higher emission power for a given current. Sadaf et al. [150] have transferred this approach to NW LEDs. This realization is further described in Sect. 12.5.3.2.

MBE growth of nitride NWs was also demonstrated on metal substrates. Nitride visible NW LEDs were grown on Ti [154] and Mo [155, 156] films, showing a comparable opto-electronic performance to those grown on Si substrates. These approaches bring a new pathway not only for large-scale fabrication of NW devices with improved thermal management, but also for mechanically flexible devices. Further description of flexible LEDs grown on metal foils [157] is given in Sect. 12.10.

12.5.3 White NW LEDs

One of the envisioned applications of NW LEDs is general lighting. Two main routes for white NW LEDs are today explored: a conventional approach using phosphor down conversion and a direct mixing of red, green, and blue emissions from NWs of different composition.

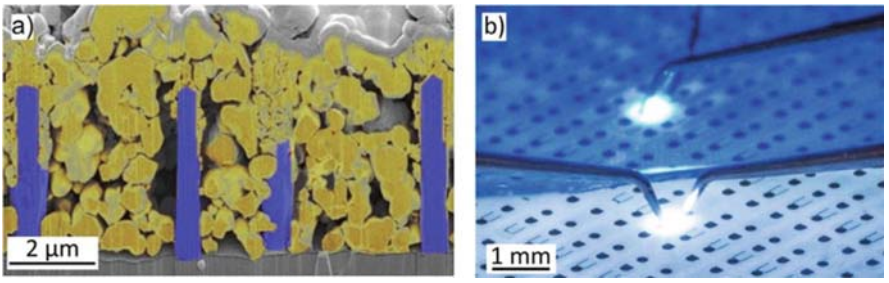

Fig. 12.20 (**a**) SEM image in artificial colors of phosphor particles filling the space between NWs. (**b**) Photograph of white NW LEDs in operation. Adapted with permission from [29]

12.5.3.1 Phosphor Converted White LEDs

The first approach consists in mimicking the well-developed technology of thin film LEDs, where an efficient blue LED is covered with a phosphor, which absorbs a part of the blue light end reemits a yellow light. By adjusting the relative intensities of the remaining blue emission and of the yellow luminescence of the phosphor one can obtain white light from the two-color mixture [158]. A white light of better quality can be obtained by using two different phosphors of two colors, e.g., yellow and red [159]. The OSRAM team has transferred this technology to NW LEDs [29]. In conventional thin film white LEDs, the phosphor is typically embedded in a silicone matrix with a bad thermal conductivity, which leads to phosphor heating. For NW white LEDs, the phosphor particles were integrated in contact with the active NWs. A special procedure was developed to form a phosphor material with a submicron grain size, which can be fitted into the space between the NWs. As illustrated in Fig. 12.20a, the phosphor particles fill the space between the NWs, which guaranties an efficient light conversion and also a more efficient phosphor cooling. By using red nitrido-silicate and yellow YAG:Ce phosphors, white emission (Fig. 12.20b) close to the Planckian locus with a coordinated color temperature of 6600 K and a color rendering index of 73 was achieved. Similar approach employing microscale phosphors for downconversion has been applied to demonstrate mechanically flexible white NW LEDs as will be discussed in Sect. 12.10.

12.5.3.2 Phosphor-free White LEDs by RGB Color Mixing

The energy down conversion process has a fundamental drawback: the difference in energy between the pump and the phosphor emission is lost as heat. This reduces the overall efficiency of phosphor-converted devices. Additional losses appear from the light backscattering in the phosphor layer and from the sub-100% efficiency of the phosphor converters. These drawbacks motivate a continuous search for converter-free white emitters based on mixing red, green, and blue colors. In principle, thanks

to the bandgap tuning over the whole visible range, the InGaN alloy with different compositions is well suited for fabricating monolithic white LEDs. A large number of investigations aiming on white all-InGaN LEDs by RGB color mixing were performed using thin film devices with both quantum wells and quantum dots in the active region [160–163]. However, high indium content InGaN layers suffer from a poor crystal quality due to a strong lattice mismatch. Therefore, the radiative efficiency of the green and red emitters is much weaker compared to the blue ones. Theoretical analyses of a monolithic InGaN RGB white source show that to be competitive with the standard phosphor-converted LEDs, a significant improvement of the efficiency of the green and red emitters beyond the state of the art is required [164]. Recently, the topic of monolithic RGB integration has gained a renewed interest with development of NW LEDs. Thanks to the efficient strain relaxation leading not only to a lower defect density but also to a lower internal field in NWs, these nanostructures are expected to improve the quantum efficiency for red and green InGaN LEDs. Many efforts are focused toward this objective.

The growth technique well suited for In-rich alloy formation is MBE, therefore most of the investigations of monolithic white LEDs make use of this growth method. Lin et al. [30] used spontaneous NW growth by MBE on an Si(111) substrate to form axial InGaN/GaN quantum discs embedded in a GaN p–n junction (Fig. 12.21a). The In content in the discs was varied within the same NW by changing the growth temperature to achieve blue, yellow, and red emission. As seen in Fig. 12.21b, the spatially averaged emission had a white color with a correlated color temperature close to 6000 K. However, the spontaneous NW growth resulted in compositional variations from wire to wire, therefore a significant fluctuation of the emission wavelength was observed at the microscale (Fig. 12.21c).

Guo et al. [165] followed the approach of Lin et al. [30], while transferring the growth to Si(001) substrate. Three groups of axial quantum discs with different In content were grown along the wire axis within an axial p–n junction. The structure

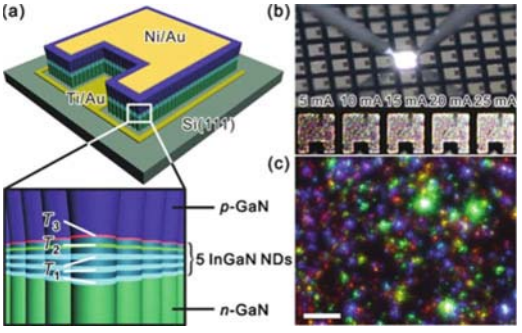

Fig. 12.21 (**a**) Schematic of NW white LED with axial InGaN/GaN quantum discs grown at different temperatures. (**b**) Photograph of a NW array LED emitting white light at 20 mA injection current. (**c**) Micro-electroluminescence image at 20 mA revealing wire-to-wire color variations. The scale bar is 10 μm. Adapted with permission from [30]

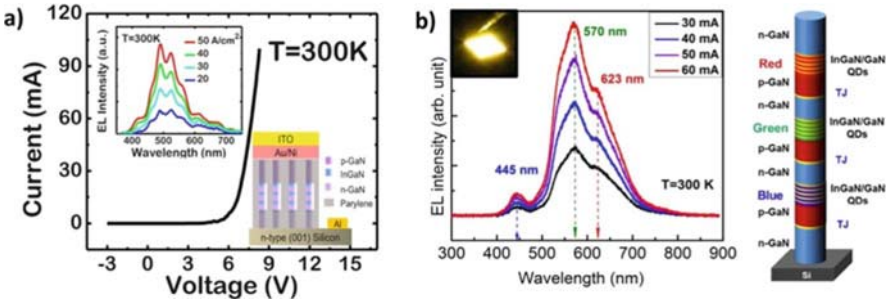

Fig. 12.22 (**a**) I–V characteristics of a white NW LED. The insets show the electroluminescence spectra for increasing injection current and the LED schematics. Adapted with permission from [165]. (**b**) Electroluminescence spectra of a white NW LED composed of axially stacked RGB stages and a schematic of the device showing the RGB stages connected with tunnel junctions. Inset shows the photograph of operating LED. Adapted with permission from [150]

was planarized using parylene, which is reported also to provide surface passivation [165], and contacted with a Ni/Au/ITO semi-transparent electrode (see inset of Fig. 12.22a). The LED showed a diodic behavior with a rather large opening voltage around 6 V (Fig. 12.22a) and a broad visible emission with a correlated color temperature ranging from 5500 to 6500 K. The electroluminescence spectra for increasing injection current shown in inset of Fig. 12.22a demonstrated a stable spectral shape with no spectral shift when varying the injection. The EQE analyses under pulsed injection with 1% duty cycle showed that the efficiency droop appeared at higher current densities (around 400 A/cm^2) compared to thin film LEDs; however, no absolute values of the EQE were reported.

Armitage and Tsubaki [95] demonstrated white NW LEDs by mixing emissions from axially and radially grown InGaN insertions in MBE-grown NWs. Similar to Sekiguchi et al. [32], the authors analyzed the In incorporation in InGaN/GaN quantum wells in GaN NWs; however, their analyses were based on self-assembled NWs. The authors controlled the average wire diameters by varying the Ga/N flux ratio and substrate temperature and they controlled the NW density by varying the GaN buffer layer growth temperature. Similar to [32], spontaneously grown NWs also showed diameter-dependent In incorporation with a trend toward shorter emission wavelengths for smaller wire diameters [95]. For low density NWs, two distinct emission peaks were observed, attributed to a combination of self-shadowing effects and different In incorporation efficiencies on the top and sidewall planes of the NWs. By adjusting the wavelength and relative intensity of these two peaks, Armitage and Tsubaki demonstrated white NW LEDs.

A strong effort toward optimization of white NW LEDs was performed in the group of Mi. Following thin film LED architecture, an AlGaN electron blocking layer was introduced in NW LEDs to prevent electron overflow into the p-GaN segment [166]. Surface recombination was identified as the main source of losses and the growth of a protective AlGaN shell around the active InGaN/GaN

region was optimized [167, 168]. The replacement of InGaN/GaN active region by InGaN/AlGaN quantum discs allows to form this AlGaN shell in a spontaneous way, and it can also act as a distributed electron blocking layer reducing the carrier overflow into the p-GaN top segment [147]. Finally, a complex design using tunnel junctions to connect red, green, and blue emitters was proposed [150]. The LED architecture is illustrated in Fig. 12.22b. The tunnel junction design follows the strategy developed for thin films [152]. The authors used a tunnel junction with an InGaN interlayer, which is placed in the bottom part of the LED to connect n-GaN to p-GaN segments and also between individual blue, green, and red LED sections (Fig. 12.22b). The multi-junction LED showed a light-up voltage approx. equal to three times value for a single junction LED (around 16 V). Electroluminescence spectra for different injection currents and a device photograph are shown in Fig. 12.22b. The LED produced a nearly white-light with a correlated color temperature ~3000 K.

12.6 Ultraviolet NW LEDs

For applications like water purification, phototherapy, or medical diagnostics, nitride UV LEDs are an appealing alternative for replacing mercury lamps. However, the efficiency of deep-UV nitride emitters remains low due to a high density of dislocations lowering the IQE to poor electrical injection issues because of the difficulty to dope AlGaN and fabricate ohmic contacts. In addition, the light extraction is impeded by the absorption in the contact and the predominant TM light polarization [169]. AlGaN NWs can potentially improve the IQE of UV emitters by improving the crystalline quality. Another advantage of NWs is the predicted improvement of light extraction efficiency [170, 171].

The light extraction efficiency (LEE) of AlGaN NW UV LED was investigated by finite-difference time-domain simulations [170, 171]. These numerical studies show that the LEE strongly depends on the geometrical parameters of the NWs, e.g., diameter, height. With an optimized structure, the theoretical LEE can be higher than 40%, both for transverse-magnetic and for transverse-electric modes.

Regarding experimental realizations, Sekiguchi et al. [172] demonstrated a GaN/AlGaN NW near-UV LED on Si substrate with a continuous planar p-GaN top layer by MBE. GaN/AlGaN multiple quantum discs were grown along the axial direction, emitting UVA light at 354 nm under an electrical injection of 50 mA. To explore UVB and UVC bands, growth of ternary AlGaN NWs on top of a GaN base segment was analyzed by different authors (e.g., [173]). Carrier localization in AlGaN composition inhomogeneities was observed and an optical (room temperature over low temperature) IQE of 50% was reported for emission from deep localized states in AlGaN alloys with a peak energy of 4.3 eV [173]. We note, however, that the IQE of the near band edge peak of these structures was much lower [173]. Himwas et al. [174] compared optical IQE for long AlGaN NW segments and for AlGaN/AlN quantum discs in NWs: 5% optical IQE was

reported for near band edge emission of AlGaN segments with 50% Al content and 30% IQE was achieved for quantum discs, thanks to 3D carrier confinement [174]. These undoped NWs were developed in view of deep-UV emission using electron beam pumping to avoid the problems of p-conductivity and contacting of AlGaN. Core/shell GaN/AlGaN [175] and GaN/InAlN [176] NWs were also investigated for UV emission.

The group of Mi reported a series of spectacular results on the NW deep UV emitters, which however have not yet been reproduced by other groups. Highly conductive Mg-doped AlN NWs grown by MBE on GaN NW templates were reported and used for realization of electrically injected near-vacuum-UV NW LEDs [177]. Electroluminescence at ~205 nm with a turn-on voltage of ~5.5 V was reported [177]. Electrically injected UV-B band NW lasers based on Anderson localization were reported [178, 179]. Electrically injected room temperature lasing was observed at 289 nm, with a small threshold of 300 A/cm^2 [178]. Recently, the same group also reported a NW UV-C LED with a tunnel junction between n-GaN and p-AlGaN sections inserting a metallic Al layer, which allowed to avoid p-AlGaN contacting [180]. This LED showed an optical IQE of ~80% and a wall plug efficiency of ~0.3%. Finally, Laleyan et al. [181] reported Mg dopant-free Al(Ga)N/h-BN NW UV-C LED exploiting strong p-type conductivity of h-BN in the presence of B vacancies, which allowed to avoid the AlGaN p-doping. These impressive results remain to be confirmed by other research teams.

12.7 Operation Speed of NW LEDs

Widespread application of LEDs to general lighting creates new functionalities, one of them being data transfer with visible light. High speed visible light communications (VLC) such as light fidelity (Li-Fi) are today a topic of intense research. VLC allows a simultaneous data transfer and lighting and it shows a good data safety. One main obstacle is that the theoretical maximal bandwidth for an LED transmitter is limited by the carrier lifetime in the active region, which is slowed down in c-plane LEDs due to the internal field. NW core/shell LEDs are considered as an alternative to thin film LEDs enabling ultra-fast operation. Indeed, in core/shell structures the active quantum wells are grown on the non-polar m-planes avoiding the internal electrical fields from the spontaneous and piezoelectric polarization.

In 2015, Koester et al. [131] demonstrated a high-speed m-planar core-shell InGaN/GaN NW LEDs grown on Si substrate by catalyst-free MOVPE. The NW morphology is illustrated in Fig. 12.23a. Carrier dynamics in core/shell InGaN/GaN quantum wells grown around the top part of the n-GaN wires was probed by time-resolved photoluminescence. Low-temperature carrier lifetime of 110 ps and room temperature value of 20 ps were reported. The devices were processed by partially encapsulating NWs into a spin-on-glass and depositing a Ni/Au contact on one side of the NWs (using a tilted deposition method (Fig. 12.23b, c). The devices showed an electroluminescence around 410 nm. For time-resolved electroluminescence

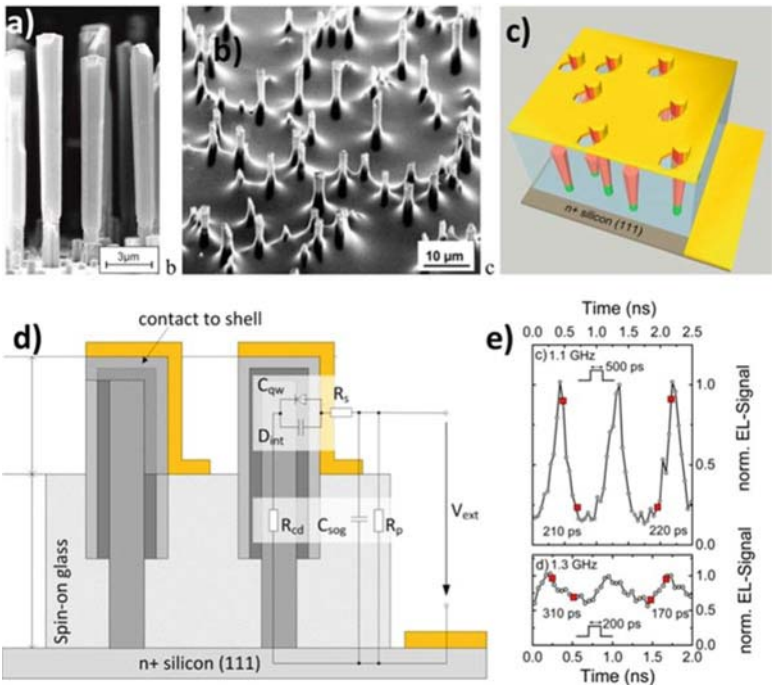

Fig. 12.23 SEM images of (**a**) as-grown core-shell InGaN/GaN NWs and (**b**) of NW encapsulated into spin-on-glass. (**c**) LEDs schematic. (**b**) Electroluminescence spectrum at 300 K of the nanowire array LED. (**d**) Device electrical circuit. (**e**) Time-resolved electroluminescence signal recorded for $V_{DC} = 8$ V and $V_{Pulse} = 6$ V square pulses for a frequency of 1.1 GHz (top) and for a frequency of 1.3 GHz (bottom). Adapted with permission from [131]

measurements the device was subjected to a DC bias superimposed with an RF input from a pulse pattern generator. An on/off modulation was achieved at room temperature at 1.1 GHz with an on/off ratio of ∼5. Ten ninety per cent rise- and fall-times close to 200 ps were recorded. For a modulation frequency increased to 1.3 GHz, the modulation depth strongly decreased down to about 1.6 (Fig. 12.23e). The electrical scheme of the NW LED was proposed (Fig. 12.23d). The authors showed that the RC low-pass behavior limiting the operation frequency originated not from the capacitance of the top/bottom contacts, but from the series resistance and the junction capacitance of the core/shell NW p–n junctions.

Different approaches can be implemented to increase the modulation bandwidth of NW LEDs. Zhu et al. [182] used top-down NWs etched from a c-plane LED (i.e., presenting an internal field in the quantum wells) to evidence the effect of carrier coupling with surface plasmons as a way to enhance the bandwidth. Deposition of Ag nanoparticles was shown to increase the -3dB cut-off frequency by a factor of ∼2 (going up to 30 MHz, which still remains rather low).

12.8 NW Photonic Platforms

Thanks to the nanoscale size and bright electroluminescence, single NW LEDs are considered as promising building blocks of the compact integrated platforms. Hybrid integrated platforms [183] with photonic and non-photonic elements are highly demanded for various applications in bio-detection, in optogenetics, or in optoelectromechanical systems. For example, NWs can play the role of active elements to generate and detect the visible light on a microfluidic chip. Alternatively, NW emitters can be used for optical communication systems not only in free space, but also on chip. III-nitride NWs represent an ideal solution for optical components in the visible spectral range.

An important technological step is the integration of NW emitters with waveguides. Park et al. [184] demonstrated coupling between an optically pumped CdS NW and a 2D photonic-crystal waveguide. Moreover, two colors of light emitted from the CdS/CdSe core/shell NW were split into two directions, showing the possibilities for on-chip light manipulation. Next, electrically pumped single InGaN/GaN NW LEDs were fabricated by dispersing NWs on top of the SiN_x membrane photonic crystal and depositing electrical contacts. Fig. 12.24a shows an SEM image of a fully processed NW LEDs coupled to a photonic-crystal waveguide. NW LEDs showed rectifying behavior (Fig. 12.24b) and visible emission peaked at 480 nm similar to single wire LEDs previously demonstrated in the group [41]. Electroluminescence from the NW was efficiently guided by the photonic-crystal waveguide over about 20 μm as shown in Fig. 12.24c, which superimposes an optical and an SEM image.

Brubaker et al. [37] realized an on-chip optical coupling between an LED and a photoconductive detector both based on GaN NWs. Axial p–n junction NWs were grown by MBE. The NWs were dispersed and closely lying pairs of wires were contacted to fabricate an LED (contacts on the p- and n-doped segments) and a photoconductive detector (both contacts on the n-doped segment). The communication took place in free space as schematized in Fig. 12.25a, b. GaN p–n junction NW (without quantum wells) presented a near sub-bandgap emission under electrical injection for biases above 20 V as illustrated in Fig. 12.25c. The NW detector showed a high photoconductive gain with the sensitivity down to $\sim 10^{-7}$ W/cm^2 but suffered from a slow switching speed (several tens of seconds). Figure 12.25d shows the detector current traces when the LED is consecutively switched on and off with a different injected current. The correlation between the photodetector signal and the LED switching was demonstrated; however, a continuously increasing baseline was observed due to a slow return to equilibrium in NW photoconductive detectors.

In [37] the LED-detector communication was taking place in free space. A waveguide for light channeling is expected to improve the LED-detector coupling efficiency. In addition, a fast photodetector with no persistent photoconductivity effects is also desirable to achieve high speed communication. In 2014, an integrated photonic platform consisting of an InGaN/GaN NW LED and a p–n NW photodiode

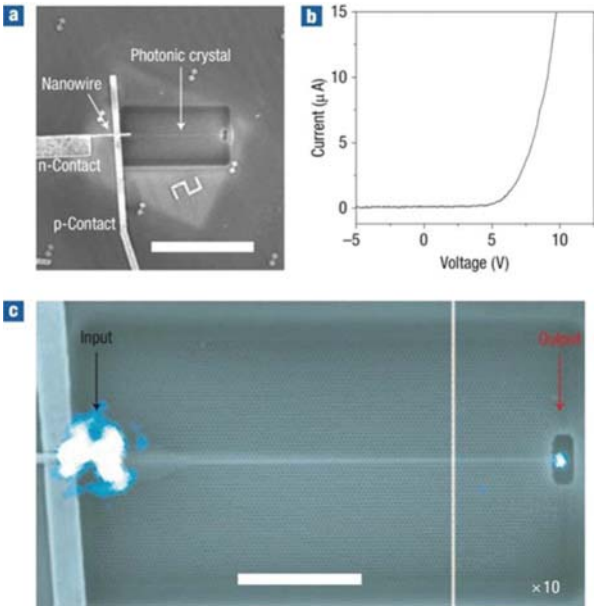

Fig. 12.24 (**a**) SEM image of single NW LED coupled to an SiN photonic-crystal waveguide (scale bar 20 μm). (**b**) I–V characteristic of the LED. (**c**) Electroluminescence image superimposed to the SEM image for photonic platform in operation (scale bar 5 μm). Adapted with permission from [184]

interconnected with an SiN_x waveguide was demonstrated [38]. MOVPE-grown core/shell InGaN/GaN NWs were used to fabricate the LED and the photodiode. As illustrated in Fig. 12.26a, the LED wires contained InGaN/GaN quantum wells whereas the photodiode wires were composed of a thick InGaN layer with an increased In composition in order to achieve a good spectral matching between the LED and the detector. The emitter and detector NWs were dispersed on an SiO_2 on Si templates, electrically contacted and connected with a multimode SiN_x waveguide, which was designed as a function of the wire positions, deposited by PECVD, and then structured using e-beam lithography. Figure 12.26a displays an SEM image of the resulting photonic platform. Observation of the platform in operation (Fig. 12.26b) demonstrated that the emitted light from the NW LED was coupled into an SiN_x multimode waveguide as evidenced by the light diffraction at the opposite end of the waveguide. At the end of the SiN_x waveguide, a NW photodetector realized light collection and optical-electrical signal conversion. Calculations of the LED to photodiode coupling efficiency estimated that only ~8.7% of the light intensity is coupled into the detecting NW. Despite this low coupling efficiency, the current trace of the NW photodiode under zero bias shown in Fig. 12.26c demonstrated a clear correlation with the LED on/off switching. Contrary to [37], no baseline due to slow photoconductive effects was observed in the current trace.

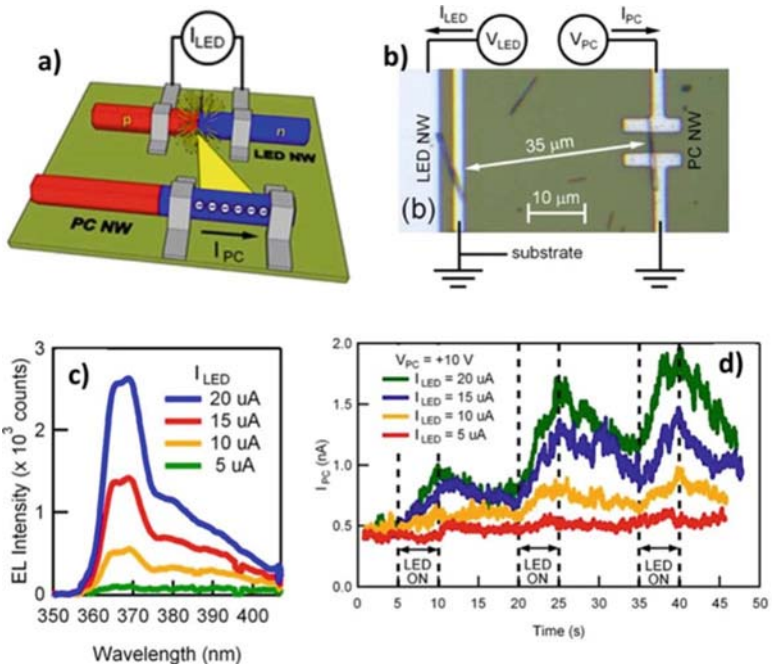

Fig. 12.25 (**a**) Schematic illustration of a free space coupled NW LED/photodetector platform. (**b**) Optical microscopy image of the LED-detector couple illustrating the electrical connections. (**c**) Electroluminescence spectra of the NW LED for increasing injection current. (**d**) Photodetector current trace for LED on/off switching for different LED currents. Adapted with permission from [37]

12.9 Open Issues of NW LEDs

Despite more than 10 years passed since the demonstration of the first NW LEDs and the constant efforts toward optimization of their performance, NW LEDs have not yet been commercialized and their performance remains behind the thin film values. Due to the complexity of the 3D architecture, nanoscale characterization of the NWs is necessary to point out the origin of existing problems of this new technology and to propose solutions. In this section, we consider the present open issues of NW LEDs together with the characterization techniques enabling their analyses.

12.9.1 Low IQE Values

One important problem of NW LEDs is the relatively low value of the IQE reported for core/shell InGaN/GaN quantum wells. Based on the temperature and

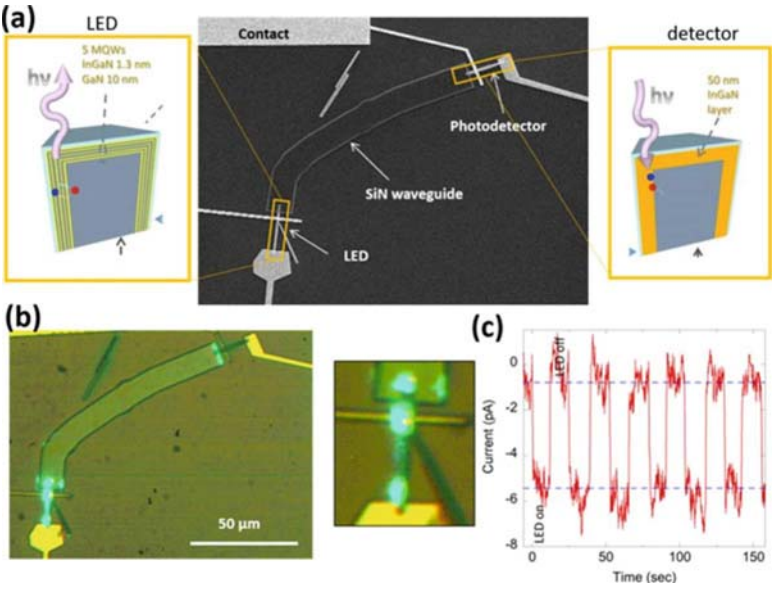

Fig. 12.26 (**a**) SEM images of the integrated photonic platform consisting of a waveguide-coupled NW LED and photodetector with the schematics of the internal structures of the constituting elements. (**b**) Photograph of the full system in operation and a close-up on the NW LED. (**c**) Current temporal trace of the detector when the LED is repeatedly switched on and off. Adapted with permission from [38]

power dependent photoluminescence with a resonant excitation of the quantum wells, Li et al. reported an IQE of 28% [119]. Hong et al. [48] reported an IQE of 32%; Schimpke et al. [29] reported 10%; Mounir et al. [185] used confocal photoluminescence to probe the IQE at different locations and reported local IQEs between 15 ± 1% near the NW tip and 44 ± 5% near the NW base. For comparison, IQE of m-plane quantum wells on a bulk m-GaN substrate can reach 80% [186] and for c-plane blue-emitting quantum wells it exceeds 90% [187]. It is not fully clear, why the IQE of core/shell NW quantum wells is below that of thin films. Mounir et al. [185] concluded that the radiative coefficient B is the main limiting factor for the efficiency and suggested that growing thinner multiple quantum wells instead of a single thick quantum well might improve the efficiency.

12.9.2 Reabsorption in Core/Shell LEDs

It is generally believed in the NW community that the NW geometry is good for light extraction properties. However, low IQE is a problem for light extraction from core/shell LEDs. For wire diameters D larger than 0.35λ, where λ is the emitted wavelength, GaN NWs sustain guided modes. Part of the emitted light is guided

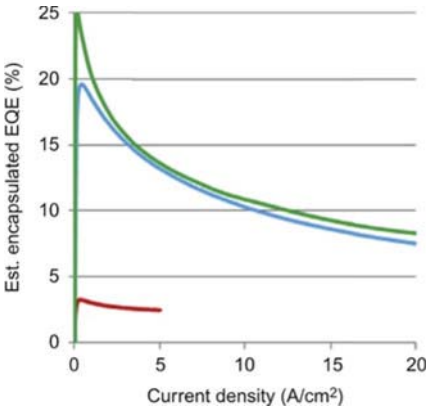

Fig. 12.27 EQE for encapsulated green (520 nm), blue (465 nm), and red (600 nm) nanowire LEDs. Adapted with permission from [31]

along the wire axis, the mode overlaps with the quantum wells and light can be reabsorbed during propagation [188]. The presently reported IQE values are rather low to allow for efficient photon recycling, so that a significant part of reabsorbed light is not reemitted. These reabsorption losses contribute to lower the external quantum efficiency.

12.9.3 Low EQE Values

The reported EQE values remain also lower than for thin film devices. An EQE of 3% was measured for the emission wavelength of 450 nm at a current density of 400 mA/mm^2 for highly homogeneous arrays of core/shell NWs [29]. Monemar et al. [31] reported the EQE of nitride NW core/shell LEDs as a function of current density (Fig. 12.27). The efficiency of the blue LED was quite poor, whereas the green LED showed an improved performance with a maximal EQE of 25%. However, a rather strong efficiency droop was observed: at 20 A/cm^2 the efficiency already dropped by a factor of 3. This fast decrease could have been related to thermal management in NW LEDs, since heat dissipation may be more difficult than in thin films. However, the authors suggested a different origin of the droop, which is attributed to an inhomogeneous incorporation of indium along the length of the wire resulting in inhomogeneous electron-hole injection.

12.9.4 Wavelength Control

Compositional homogeneity is of great importance for NW LEDs. It is generally accepted that SAG is the best way to reduce the wire-to-wire size and compositional fluctuations and therefore to control the NW LEDs wavelength. Indeed, in

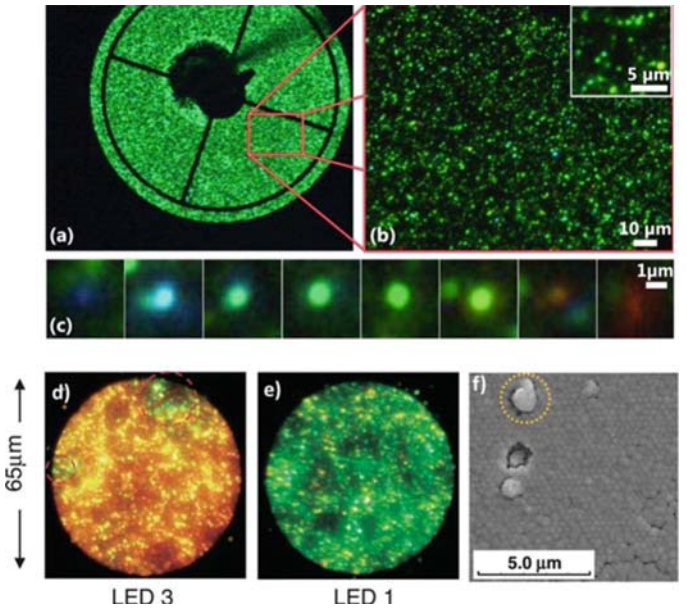

Fig. 12.28 Electroluminescence maps of an axial NW LED under 10 V forward bias imaged through a microscope at (**a**) 200× and (**b**) 500× magnification. The inset in (**b**) shows an enlarged part of the image. Panel (**c**) shows close-ups of individual luminescence spots taken from the image with 500× magnification. Adapted with permission from [140]. (**d**, **e**) Optical microscopy images of SAG MBE NW orange and green LEDs. (**f**) Top-view SEM image. Adapted with permission from [94]

spontaneously grown NWs, optical microscopy images evidence wire-to-wire color fluctuations [140] while a more homogeneous color is observed in SAG NW LED [29, 33]. Figure 12.28 compares MBE grown In-rich NW LEDs composed of self-assembled (Fig. 12.28a–c) and organized (Fig. 12.28d–f) NWs. Strong wire-to-wire fluctuations as well as a large percentage of dark NWs were observed in the self-assembled sample [140]. In addition, for MBE-grown LEDs with multiple axial quantum discs the disc shape and composition (and thus the emission wavelength) change within the stack, which increases the electroluminescence broadening [189]. Growth imperfections can still be present in SAG NWs leading to local color changes of the electroluminescence as illustrated in Fig. 12.28d–f [94]; however, a reduction of the spectral broadening and a higher yield of NWs producing electroluminescence were observed for SAG NWs.

Even for a perfectly homogenous array of core/shell NWs with no apparent growth imperfections obtained either by SAG or by top-down etching and regrowth, intra-wire gradients are still present in the quantum wells [10, 29, 49]. The presence of compositional inhomogeneity was evidenced by different groups by structural analyses (such as energy dispersive X-ray spectroscopy in STEM [52], atomic probe

tomography [10], nanofocus X-ray diffraction [190], and by optical techniques (confocal photoluminescence [185, 191], cathodoluminescence [10, 52, 190], time-resolved cathodoluminescence [192]).

In-rich regions locally change the parameters of the p–n junction and favor current injection in these locations [49]. Because of the current redistribution, the emission wavelength shifts with increasing injection [29, 49]. Therefore, the usual assumption of a homogeneous injection made in core/shell NW LED modelling [188, 193] is not fulfilled in the experiments. An inhomogeneous current density with a high carrier concentration in the In-rich regions results in an early onset of Auger recombinations and thus in efficiency droop. In addition, the emission wavelength of these regions is red shifted with respect to the wavelength for which the LED was designed. As described earlier, it was experimentally demonstrated that by inhibiting the injection in In-rich regions responsible for long wavelength emission it is possible to increase the intensity of the blue electroluminescence [50].

12.9.5 Electrical Injection Inhomogeneities

The problem of injection homogeneity (both intra-wire and wire-to-wire) is considered as a key challenge of NW LEDs.

12.9.5.1 Intra-wire Injection Inhomogeneities

Regarding intra-wire homogeneity, the top NW region where m-plane facets meet semipolar facets or the top c-plane may present injection singularities [50]. In addition to In-content variations in the quantum wells discussed in the previous section, electrical homogeneity of the core and the shell is important. It is a challenging task to analyze doping at the nanoscale. Micro-Raman [194] analyses were applied to access doping in the n-doped GaN cores, which can reach high values (10^{20} cm^{-3}) without degrading material quality. For these high doping values, the core resistance should not be a limiting factor for homogeneous electrical injection even in tens of micron long NWs. However, electrical activity at the interface between the axially grown n-GaN core and a radially grown n-GaN underlayer was reported [52], which may create a parasitic barrier for electron injection from the core to the active region. A good control of thickness and p-doping of the GaN shell along the wire axis is also important for homogeneous injection. It is more difficult to assess the doping of the shell compared to the core. Optical methods like cathodoluminescence [195] can be applied, however, it is difficult to achieve quantitative results. SIMS analyses are very challenging for NWs [110]. EBIC mapping of the NW cross-section was used to probe the p-GaN shell conductivity (Fig. 12.29a, b, d, e) [52, 196]. As illustrated in Fig. 12.29c, doping

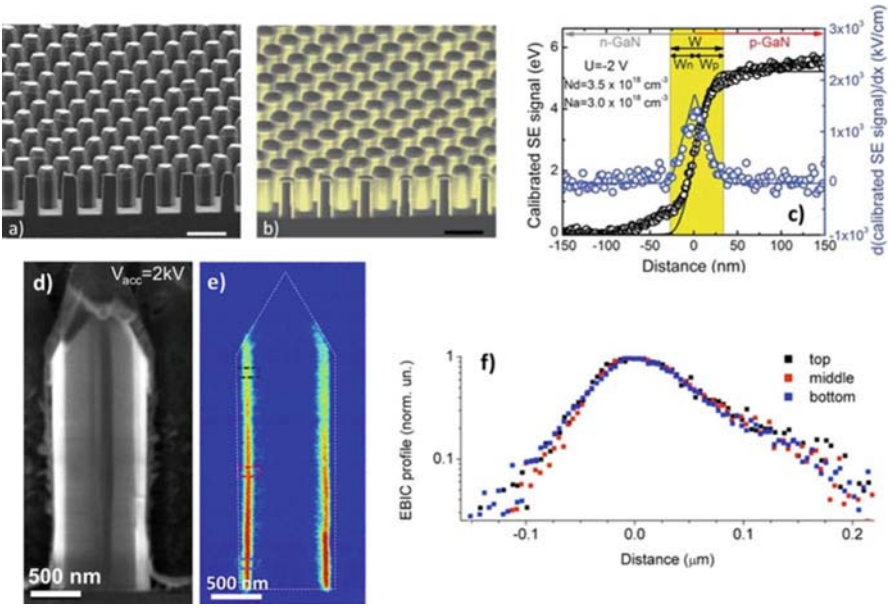

Fig. 12.29 (**a**) SEM image and (**b**) EBIC map at 10 keV of a cleaved processed array of core/shell n-p GaN NWs. (**c**) Secondary electron contrast profile and its derivative under reverse bias. Good agreement with an abrupt p–n junction theory is obtained for Na = 3.0 × 10^{18} cm^{-3} and Nd = 3.5 × 10^{18} cm^{-3}. Reproduced with permission from [196]. (**d**) SEM image and (**e**) EBIC map at 2 keV of an industrial-grade LED grown by GLO-AB based on InGaN/GaN core-shell NWs. (**f**) EBIC profiles at the top, middle and bottom part of the NWs. Adapted with permission from [52]

values in the 10^{18} cm^{-3} range were reported for core/shell p–n junction GaN wires using EBIC and secondary electron contrast profiles [196]. Figure 12.29f compares the EBIC profiles at different positions along the axis of a core/shell LED wire. It was concluded that in these LEDs the p-shell doping was homogeneous over the 2 μm NW length [52].

12.9.5.2 Wire-to-wire Injection Inhomogeneities

Fluctuations of the In composition and of the electrical parameters from wire to wire lead to a non-uniform current distribution in the NW array.

Limbach et al. [140] analyzed axial NW LEDs based on self-assembled MBE grown NWs by EBIC, CL, and electroluminescence techniques. The authors found that only 1% of NWs produced electroluminescence whereas a much larger amount of NWs yielded a CL signal. Higher CL homogeneity compared to electroluminescence shows that the limiting factor is not the fluctuation of IQE of individual

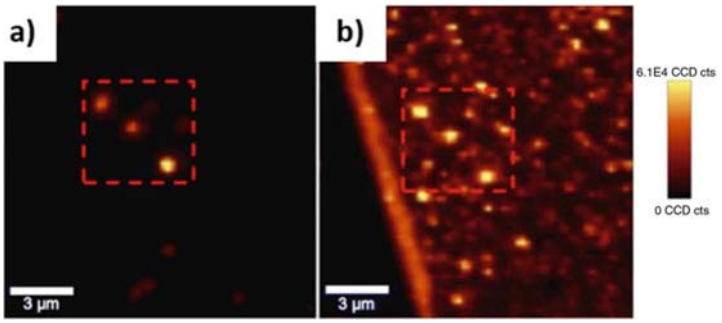

Fig. 12.30 Nanoscale mapping of MBE-grown axial NW LEDs. (**a**) Top-view micro-electroluminescence confocal mapping ($I = 50$ mA, $V = 9.3$ V) without laser excitation and (**b**) micro-electroluminescence–PL confocal mapping under laser excitation (excitation wavelength = 407 nm). Adapted with permission from [141]

wires, but the electrical injection. EBIC maps revealed that all NWs were correctly contacted. Therefore, the absence of electroluminescence in 99% of NWs was attributed to the differences in the individual currents in the NWs connected in parallel, which are due to fluctuations of individual series resistances and turn-on voltages. Similar conclusion was reached by Bavencove et al. [141] by analyzing micro-photoluminescence and micro-electroluminescence confocal maps. Figure 12.30a represents the micro-electroluminescence mapping, carried out solely under electrical injection compared with a map collected under a simultaneous electrical and laser excitations (Fig. 12.30b). The number of NWs producing intense photo-luminescence is much larger than that producing electroluminescence spots. This result clearly evidences that the electrical injection issue is the main factor of losses in these LEDs: despite a good IQE most of the wires remain inactive under electrical excitation.

The wire-to-wire injection homogeneity improves in SAG NW arrays, however, electroluminescence intensity fluctuations can still be observed (e.g., from [140] and [29]).

12.10 Flexible NW LEDs

Despite a certain number of challenges described in the previous section, NW LEDs are very attractive in particular, thanks to new functionalities that they can offer. In this section, we highlight one of them, namely fabrication of mechanically flexible light sources.

12.10.1 Motivation

Mechanically flexible LEDs are today a topic of intense research since they can provide novel functionalities and have the potential to open up a new branch of industry. Their applications include rollable displays, wearable intelligent electronics, deformable light sources, biomedical devices, e.g., lighting systems that can be ultimately integrated on a soft surface for biological and optogenetic purposes, etc. "Photonics Multiannual Strategic Roadmap 2014–2020" mentions flexible electronics, flexible light sources, displays, and solar cells as key emerging technologies with high expected growth of the market share. It is noteworthy that in the above-mentioned roadmap the notion of a "flexible device" is inseparable from an "organic device." Indeed, flexible devices mainly use organic materials integrated on lightweight and flexible plastic substrates. Thanks to the flexibility, relative ease of processing, compatibility with various flexible substrates, low cost, and their potential for large-scale manufacture, organic LEDs (OLEDs) are today the key technology for flexible displays [197]. However, organic devices are facing instabilities caused by oxidation, recrystallization, and temperature variations, which degrade the electrical conductivity of organic layers and interfaces in the active regions [198]. Moreover, organic LEDs present limitations in the short visible wavelength range [199]. They have a much lower luminance and a shorter lifetime in comparison to the LEDs based on inorganic semiconductors.

It is therefore advantageous to use inorganic semiconductors as the active material in flexible LEDs. However, the inorganic semiconductor devices are mechanically rigid. The fabrication of flexible devices from conventional thin film structures is challenging and requires additional processing steps to micro-structure the active layer. Moreover, the emission wavelengths of transferred thin film devices are shifting with the bending radii due to the strain induced shifts in the bandgap [200].

To avoid the micro-structuring step, it is advantageous to shrink the active element dimensions and to use bottom-up nanostructures, such as NWs, instead of two-dimensional films [201]. Polymer-embedded NWs offer an elegant solution to create flexible opto-electronic devices, which combine the high efficiency and the long lifetime of inorganic semiconductor materials with the high flexibility of polymers. NW arrays embedded in a flexible film and lifted-off from their native substrate can sustain large deformations, thanks to the high flexibility of individual NWs and to their footprint much smaller than the typical bending radius of the device [202–205]. Moreover, the lift-off and transfer procedure enables the assembly of free-standing layers of NW materials with different bandgaps without any constraint related to lattice-matching or growth conditions compatibility. This novel concept therefore allows for a large design freedom and modularity since it enables combination of materials with very different physical and chemical properties, which cannot be achieved by monolithic growth.

12.10.2 Fabrication Approaches

12.10.2.1 Direct Growth

A straightforward method for flexible LED fabrication would be a direct growth of NWs on flexible substrates. This method can readily be applied to some semiconductor materials such as ZnO. ZnO NW can be grown in solution on plastic substrates covered with a conductive layer at low temperature [206]. ZnO NW arrays grown directly on a flexible substrate have been used to demonstrate LEDs with a broad visible emission band. In 2008, Nadarajah et al. [207] reported single-crystalline ZnO NWs grown on flexible polymer-based indium-tin-oxide (ITO) substrates.

The direct growth of NWs on flexible materials eases the process of integration; however, it is limited to few kinds of semiconductors. As far as nitride NWs are concerned, the main limitation arises from the high growth temperature, which excludes the use of any plastic substrates. However, nitride NWs can be directly grown on metal foils. For example, MBE-grown GaN and AlGaN NWs were demonstrated on refractory metal foils like Ti and Ta foils [72, 157] and InN NWs were grown on brass [208]. The first LED from NWs grown on metal was demonstrated by May et al. in 2016 [157]. Self-assembled AlGaN NWs were grown on Ta and Ti foils by MBE. Within one metal grain, the NWs stand straight along the surface normal and have a good radius and height uniformity, as shown in Fig. 12.31. With an electroluminescence peak emission at around 350 nm, this LED showed a comparable opto-electronic performance to the NW LEDs grown on monocrystalline silicon substrate.

12.10.2.2 In-plane Transfer

As an alternative to a direct growth, one can transfer NWs to an exotic substrate to form an in-plane device.

Furthermore, the advances in the alignment of dispersed NWs with the assistance of electric field [209], magnetic field, fluid flow, capillary force, and so on offer new opportunities for the bottom-up approach to nanoelectronics. Lieber et al. [210] demonstrated a crossed-NW ultraviolet LED assembled from n-type GaN NWs and p-type Si NWs, which are sequentially dispersed on a plastic substrate through the orthogonal fluid-directed assembly. This NW LED maintained its emissive property upon multiple bending/unbending cycles [210]. However, the complexity of positioning single NWs and integrating with nonconventional substrates restricts their widespread applications.

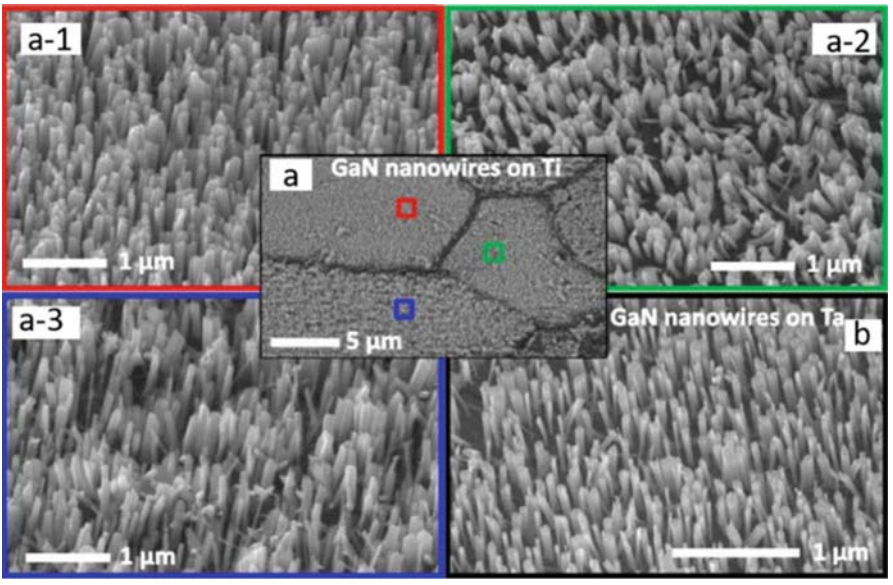

Fig. 12.31 SEM images of GaN NWs on flexible (**a**) Ti foil within different grains of the Ti foil and on (**b**) Ta foil. Adapted with permission from [157]

12.10.2.3 Vertical Transfer

NW arrays can also be transferred to flexible substrates preserving their vertical orientation. There have been several reports on light emitters based on polymer-embedded NW arrays, where active NW components are first embedded in a flexible film and then lifted-off from their native substrate [34–36, 201, 211]. First realizations used GaN micro-rods [35] and GaN/ZnO coaxial nanorod heterostructures [34] synthesized on graphene films. As shown in Fig. 12.32, active nanorods grown on graphene-covered Si/SiO_2 substrate were encapsulated in an insulating polymer layer. Then a lift-off process of the nanorods embedded in a polymer layer was realized by wet etching of the SiO_2 layer. Finally, the whole layer was transferred onto a metal coated flexible substrate [34]. In these realizations, a Ni/Au semi-transparent conductive layer was used as a top electrode; however, this semi-transparent contact can induce losses due to its non-ideal transmittance.

The transparency of the top contact can be improved by replacing Ni/Au layer by a conductive material presenting lower absorption such as Ag nanowire network. Blue and green flexible LEDs with Ag nanowire contact were elaborated using the following process flow [36]. First, the NW array was embedded into a polymer layer (e.g., PDMS). Plasma etching was used to expose and clean the top of the NWs. Then, the whole layer was peeled off to form a composite membrane with NWs maintaining their orientation and positions as illustrated in Fig. 12.33a. Two types of devices can be fabricated following this protocol: semi-transparent

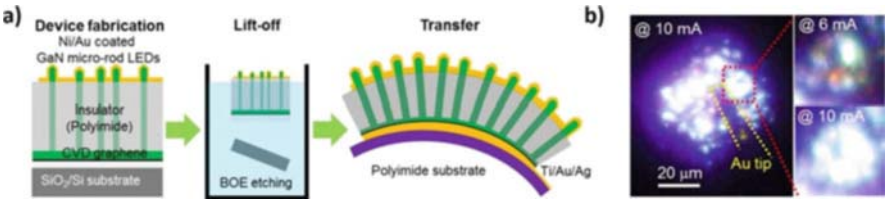

Fig. 12.32 (**a**) Fabrication process of flexible micro-rod LEDs grown on graphene substrate. (**b**) Photos of working LED under different injected currents. Adapted with permission from [35]

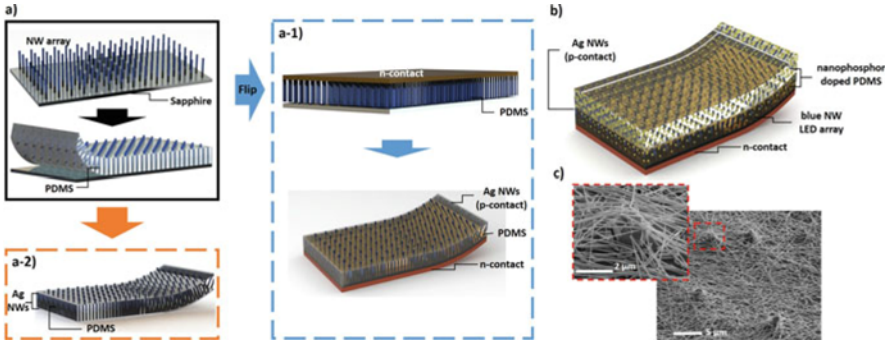

Fig. 12.33 (**a**) Process flows of flexible (**a-1**) semi-transparent NW LED and (**a-2**) fully transparent NW LED. (**b**) Schematic of the flexible NW white LED. (**c**) SEM images of Ag nanowire mesh spin-coated on PDMS layer with embedded NW LEDs. Tip of a core/shell NW protruding from the PDMS is shown by the red dashed rectangle. Adapted with permission from [36]

LEDs (Fig. 12.33a-1) and fully transparent LEDs (Fig. 12.33a-2). In the case of a semi-transparent device, the membrane is flipped onto an arbitrary receiver for the metallization of the NW bottom part. After that, a flexible substrate (e.g., PET or metal foil) is brought in contact with the backside metal layer which is mounted using silver epoxy. Next, Ag nanowires are spin-coated on the top side of the LED. In the case of a fully transparent device, considering the opacity of the backside metal layer, it is replaced by the Ag nanowires. Figure 12.33a-2 shows a schematic drawing of a fully transparent flexible NW LED with Ag nanowires as both the top and bottom transparent electrodes. The morphology of the transparent contact is illustrated in Fig. 12.33c, which presents an SEM image of the LED surface. Large objects correspond to protruding InGaN/GaN NWs, which are contacted by a large number of Ag nanowires.

MOVPE-grown core-shell InGaN/GaN NWs with different In concentration in the quantum wells were used as the active materials to generate light in the blue or green spectral range. As shown in Fig. 12.34a, these LEDs showed a good flexibility with a bending curvature less than 1 cm without showing any observable degradation of current and electroluminescence. The electroluminescence spectra of the blue and green LEDs are shown in Fig. 12.34b peaked at 425 nm and 530 nm, respectively.

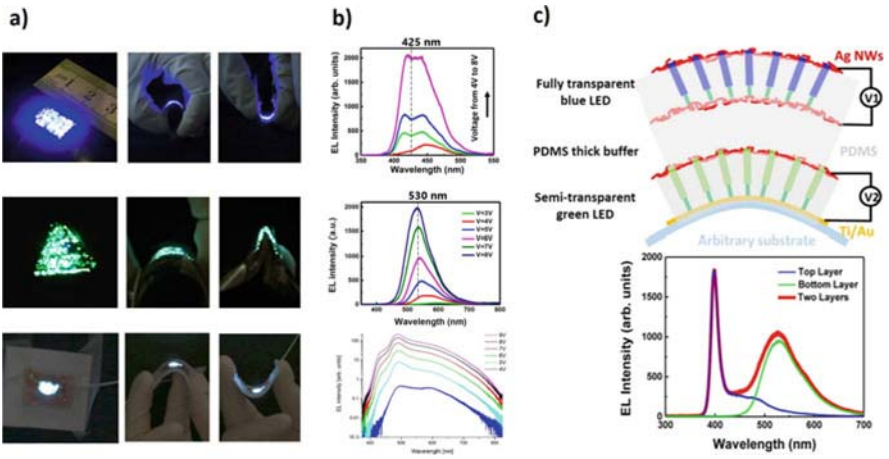

Fig. 12.34 (**a**) Photos of electroluminescence emissions and (**b**) electroluminescence spectra under different biases of blue, green, and white flexible NW LEDs. (**c**) Schematic (top) and electroluminescence spectra (bottom) of flexible bi-color LED. Adapted with permission from [36]

By assembling NW membranes with different In-content in the core/shell quantum wells, a blue–green two-color flexible LED was realized by mounting a fully transparent blue LED on top of a semi-transparent green LED. The electroluminescence spectra of the two-color LED are shown in Fig. 12.34c, corresponding to a superposition of the blue and green emissions of individual layers.

Similar method was applied to demonstrate a flexible phosphor converted white LED [211]. The nano-phosphor particles were mixed in the PDMS to fill the gaps between the blue LED NWs. An additional phosphor-doped PDMS cap layer was deposited on the top surface of the LED to increase the downconversion. The emission of the white LED presented in Fig. 12.34b covered a broad spectral range from 400 nm to 800 nm (i.e., almost the whole visible spectrum). The correlated color temperature of 6306 K and a color rendering index (CRI) of 54 were reported.

12.11 Summary

In summary, NW LEDs represent a promising approach for lighting and display applications. The addition of a third dimension to the device allows for complex architectures, namely core/shell, axial, or mixed geometries. Nitride NW LEDs covering UV to near IR spectral range as well as white emitters were demonstrated. Selective area epitaxy was shown to improve the NW LED performance by reducing wire-to-wire dispersion. However, it is still difficult for NW devices to compete with the main-stream thin film LED technology. Today, only prototypes of NW LEDs exist showing a lower efficiency compared to mature thin film emitters. For general

lighting applications, a strong boost of efficiency is necessary to become competitive with thin films. For niche applications in challenging spectral domains (e.g., green-red nitride LEDs or deep-UV LEDs) it should be easier for NWs to become competitive, still an efficiency improvement is desirable for large-scale deployment of NW devices. Despite the existing challenges, NW LEDs bring new functionalities inaccessible with thin film devices. One example of such a functionality is the elaboration of blue to red NW emitters in a single growth run for RGB all-nitride displays. Another attractive opportunity offered by NW LEDs is the realization of flexible inorganic light sources with a high luminance and long lifetime for lighting of displays.

Acknowledgements The authors acknowledge fruitful discussions with V. Consonni and A. V. Maslov.

This work has been partially financially supported by ANR "Investissement d'Avenir" programmes "GaNeX" (ANR-11-LABX-2014) and "NanoSaclay" (ANR-10-LABX-0035), by ANR-14-CE26-0020-01 project "PLATOFIL,", by EU ERC project "NanoHarvest" (grant no. 639052), and FP7 ITN Marie Curie project "INDEED" (grant no. 722176).

References

1. S. Nakamura, T. Mukai, M. Senoh, Candela- class high- brightness InGaN/AlGaN double-heterostructure blue- light- emitting diodes. Appl. Phys. Lett. **64**, 1687 (1994)
2. J. Iveland, L. Martinelli, J. Peretti, J.S. Speck, C. Weisbuch, Direct measurement of Auger electrons emitted from a semiconductor light-emitting diode under electrical injection: identification of the dominant mechanism for efficiency droop. Phys. Rev. Lett. **110**, 177406 (2013)
3. E. Kioupakis, P. Rinke, K.T. Delaney, C.G. Van de Walle, Indirect Auger recombination as a cause of efficiency droop in nitride light-emitting diodes. Appl. Phys. Lett. **98**, 161107 (2011)
4. C.I. Ashby, C.C. Mitchell, J. Han, N.A. Missert, P.P. Provencio, D.M. Follstaedt, G.M. Peake, L. Griego, Low-dislocation-density GaN from a single growth on a textured substrate. Appl. Phys. Lett. **77**, 3233 (2000)
5. Z. Li-Xia, Y. Zhi-Guo, S. Bo, Z. Shi-Chao, A. Ping-Bo, Y. Chao, L. Lei, W. Jun-Xi, L. Jin-Min, Progress and prospects of GaN-based LEDs using nanostructures. Chin. Phys. B **24**, 068506 (2015)
6. L.-W. Jang et al., Enhanced light output of InGaN/GaN blue light emitting diodes with Ag nanoparticles embedded in nano-needle layer. Opt. Express **20**, 6036 (2012)
7. Q. Li et al., Optical performance of top-down fabricated InGaN/GaN nanorod light emitting diode arrays. Opt. Express **19**, 25528 (2011)
8. M. Latzel, P. Büttner, G. Sarau, K. Höflich, M. Heilmann, W. Chen, X. Wen, G. Conibeer, S. Christiansen, Significant performance enhancement of InGaN/GaN nanorod LEDs with multilayer graphene transparent electrodes by alumina surface passivation. Nanotechnology **28**, 055201 (2016)
9. J.-H. Park, U. Chatterjee, S. Kang, K. Lee, J.-S. Kim, C.-R. Lee, Synthesis of hybrid nanowires comprising uniaxial and coaxial InGaN/GaN MQWs with a nano-cap. J. Mater. Chem. C **4**, 10005 (2016)
10. J.R. Riley, S. Padalkar, Q. Li, P. Lu, D.D. Koleske, J.J. Wierer, G.T. Wang, L.J. Lauhon, Three-dimensional mapping of quantum wells in a GaN/InGaN core–shell nanowire light-emitting diode array. Nano Lett. **13**, 4317 (2013)

11. Y.-J. Li, J.-R. Chang, S.-P. Chang, B.-W. Lin, Y.-H. Yeh, H.-C. Kuo, Y.-J. Cheng, C.-Y. Chang, Multifacet microrod light-emitting diode with full visible spectrum emission. J. Disp. Technol. **12**, 951 (2016)
12. S.D. Hersee, A.K. Rishinaramangalam, M.N. Fairchild, L. Zhang, P. Varangis, Threading defect elimination in GaN nanowires. J. Mater. Res. **26**, 2293 (2011)
13. Y.H. Ko, J.H. Kim, L.H. Jin, S.M. Ko, B.J. Kwon, J. Kim, T. Kim, Y.H. Cho, Electrically driven quantum dot/wire/well hybrid light- emitting diodes. Adv. Mater. **23**, 5364 (2011)
14. J. Kang, Z. Li, H. Li, Z. Liu, X. Li, X. Yi, P. Ma, H. Zhu, G. Wang, Pyramid array InGaN/GaN core–shell light emitting diodes with homogeneous multilayer graphene electrodes. Appl. Phys. Express **6**, 072102 (2013)
15. W. Chen et al., High-performance, single-pyramid micro light-emitting diode with leakage current confinement layer. Appl. Phys. Express **8**, 032102 (2015)
16. T. Kim, J. Kim, M.-S. Yang, S. Lee, Y. Park, U.-I. Chung, Y. Cho, Highly efficient yellow photoluminescence from {11–22} InGaN multiquantum-well grown on nanoscale pyramid structure. Appl. Phys. Lett. **97**, 241111 (2010)
17. T. Wernicke et al., Indium incorporation and emission wavelength of polar, nonpolar and semipolar InGaN quantum wells. Semicond. Sci. Technol. **27**, 024014 (2012)
18. K. Wu et al., Fabrication and optical characteristics of phosphor-free InGaN nanopyramid white light emitting diodes by nanospherical-lens photolithography. J. Appl. Phys. **115**, 123101 (2014)
19. K. Kishino, A. Kikuchi. III nitride structure and method for manufacturing III nitride semiconductor fine columnar crystal, (Google Patents, 2014).
20. J. Hartmann et al., High aspect ratio GaN fin microstructures with nonpolar sidewalls by continuous mode metalorganic vapor phase epitaxy. Cryst. Growth Des. **16**, 1458 (2016)
21. A.K. Rishinaramangalam, M. Nami, M.N. Fairchild, D.M. Shima, G. Balakrishnan, S. Brueck, D.F. Feezell, Semipolar InGaN/GaN nanostructure light-emitting diodes on c-plane sapphire. Appl. Phys. Express **9**, 032101 (2016)
22. J. Hartmann et al., Study of 3D-growth conditions for selective area MOVPE of high aspect ratio GaN fins with non-polar vertical sidewalls. J. Cryst. Growth **476**, 90 (2017)
23. F. Glas, Critical dimensions for the plastic relaxation of strained axial heterostructures in freestanding nanowires. Phys. Rev. B **74**, 121302 (2006)
24. P. Coulon, M. Mexis, M. Teisseire, M. Jublot, P. Vennéguès, M. Leroux, J. Zuniga-Perez, Dual-polarity GaN micropillars grown by metalorganic vapour phase epitaxy: Cross-correlation between structural and optical properties. J. Appl. Phys. **115**, 153504 (2014)
25. S. Li, A. Waag, GaN based nanorods for solid state lighting. J. Appl. Phys. **111**, 5 (2012)
26. S. Boubanga-Tombet, J.B. Wright, P. Lu, M.R. Williams, C. Li, G.T. Wang, R.P. Prasankumar, Ultrafast carrier capture and Auger recombination in single GaN/InGaN multiple quantum well nanowires. ACS Photon. **3**, 2237 (2016)
27. M. Djavid, Z. Mi, Enhancing the light extraction efficiency of AlGaN deep ultraviolet light emitting diodes by using nanowire structures. Appl. Phys. Lett. **108**, 051102 (2016)
28. Y.-H. Hsiao, M.-L. Tsai, J.-H. He, GaN-based multiple-quantum-well light-emitting diodes employing nanotechnology for photon management. IEEE Trans. Ind. Appl. **51**, 1277 (2015)
29. T. Schimpke et al., Phosphor- converted white light from blue- emitting InGaN microrod LEDs. Phys. Status Solidi A **213**, 1577 (2016)
30. H.-W. Lin et al., InGaN/GaN nanorod array white light-emitting diode. Appl. Phys. Lett. **97**, 073101 (2010)
31. B. Monemar, B.J. Ohlsson, N.F. Gardner, L. Samuelson, Chapter seven-nanowire-based visible light emitters, present status and outlook. Semicond. Semimetals **94**, 227 (2016)
32. H. Sekiguchi, K. Kishino, A. Kikuchi, Emission color control from blue to red with nanocolumn diameter of InGaN/GaN nanocolumn arrays grown on same substrate. Appl. Phys. Lett. **96**, 231104 (2010)
33. K. Kishino, A. Yanagihara, K. Ikeda, K. Yamano, Monolithic integration of four-colour InGaN-based nanocolumn LEDs. Electron. Lett. **51**, 852 (2015)

34. C.H. Lee, Y.J. Kim, Y.J. Hong, S.R. Jeon, S. Bae, B.H. Hong, G.C. Yi, Flexible inorganic nanostructure light- emitting diodes fabricated on graphene films. Adv. Mater. **23**, 4614 (2011)
35. K. Chung, H. Beak, Y. Tchoe, H. Oh, H. Yoo, M. Kim, G.-C. Yi, Growth and characterizations of GaN micro-rods on graphene films for flexible light emitting diodes. Appl. Mater. **2**, 092512 (2014)
36. X. Dai, A. Messanvi, H. Zhang, C. Durand, J. Eymery, C. Bougerol, F.H. Julien, M. Tchernycheva, Flexible light-emitting diodes based on vertical nitride nanowires. Nano Lett. **15**, 6958 (2015)
37. M.D. Brubaker et al., On-chip optical interconnects made with gallium nitride nanowires. Nano Lett. **13**, 374 (2013)
38. M. Tchernycheva et al., Integrated photonic platform based on InGaN/GaN nanowire emitters and detectors. Nano Lett. **14**, 3515 (2014)
39. C. Goßler et al., GaN-based micro-LED arrays on flexible substrates for optical cochlear implants. J. Phys. D. Appl. Phys. **47**, 205401 (2014)
40. D. Massoubre, E. Xie, B. Guilhabert, J. Herrnsdorf, E. Gu, I.M. Watson, M.D. Dawson, Micro-structured light emission from planar InGaN light-emitting diodes. Semicond. Sci. Technol. **29**, 015005 (2013)
41. F. Qian, S. Gradecak, Y. Li, C.-Y. Wen, C.M. Lieber, Core/multishell nanowire heterostructures as multicolor, high-efficiency light-emitting diodes. Nano Lett. **5**, 2287 (2005)
42. R. Köster, J.-S. Hwang, C. Durand, D.L.S. Dang, J. Eymery, Self-assembled growth of catalyst-free GaN wires by metal–organic vapour phaseepitaxy. Nanotechnology **21**, 015602 (2009)
43. X. Wang et al., Continuous-flow MOVPE of Ga-polar GaN column arrays and core–shell LED structures. Cryst. Growth Des. **13**, 3475 (2013)
44. Y.T. Lin, T.W. Yeh, Y. Nakajima, P.D. Dapkus, Catalyst- free GaN nanorods synthesized by selective area growth. Adv. Funct. Mater. **24**, 3162 (2014)
45. H.-M. Kim, D.S. Kim, Y.S. Park, D.Y. Kim, T.W. Kang, K.S. Chung, Growth of GaN nanorods by a hydride vapor phase epitaxy method. Adv. Mater. **14**, 991 (2002)
46. G. Jacopin et al., Single-wire light-emitting diodes based on GaN wires containing both polar and nonpolar InGaN/GaN quantum wells. Appl. Phys. Express **5**, 014101 (2011)
47. J.-R. Chang, S.-P. Chang, Y.-J. Li, Y.-J. Cheng, K.-P. Sou, J.-K. Huang, H.-C. Kuo, C.-Y. Chang, Fabrication and luminescent properties of core-shell InGaN/GaN multiple quantum wells on GaN nanopillars. Appl. Phys. Lett. **100**, 261103 (2012)
48. Y.J. Hong, C.H. Lee, A. Yoon, M. Kim, H.K. Seong, H.J. Chung, C. Sone, Y.J. Park, G.C. Yi, Inorganic optoelectronics: Visible- color- tunable light- emitting diodes (Adv. Mater. 29/2011). Adv. Mater. **23**, 3224 (2011)
49. M. Tchernycheva et al., InGaN/GaN core–shell single nanowire light emitting diodes with graphene-based p-contact. Nano Lett. **14**, 2456 (2014)
50. H. Zhang, G. Jacopin, V. Neplokh, L. Largeau, F.H. Julien, O. Kryliouk, M. Tchernycheva, Color control of nanowire InGaN/GaN light emitting diodes by post-growth treatment. Nanotechnology **26**, 465203 (2015)
51. J. Ledig, X. Wang, S. Fündling, H. Schuhmann, M. Seibt, U. Jahn, H.H. Wehmann, A. Waag, Characterization of the internal properties of InGaN/GaN core–shell LEDs. Phys. Status Solidi A **213**, 11 (2016)
52. M. Tchernycheva et al., Core–shell InGaN/GaN nanowire light emitting diodes analyzed by electron beam induced current microscopy and cathodoluminescence mapping. Nanoscale **7**, 11692 (2015)
53. M. Sanchez-Garcia, E. Calleja, E. Monroy, F. Sanchez, F. Calle, E. Munoz, R. Beresford, The effect of the III/V ratio and substrate temperature on the morphology and properties of GaNand AlN-layers grown by molecular beam epitaxy on Si (1 1 1). J. Cryst. Growth **183**, 23 (1998)

54. M. Yoshizawa, A. Kikuchi, M. Mori, N. Fujita, K. Kishino, Growth of self-organized GaN nanostructures on Al2O3 (0001) by RF-radical source molecular beam epitaxy. Jpn. J. Appl. Phys. **36**, L459 (1997)
55. S. Fernández-Garrido, J. Grandal, E. Calleja, M. Sánchez-García, D. López-Romero, A growth diagram for plasma-assisted molecular beam epitaxy of GaN nanocolumns on Si (111). J. Appl. Phys. **106**, 126102 (2009)
56. J. Ristić, E. Calleja, S. Fernández-Garrido, L. Cerutti, A. Trampert, U. Jahn, K.H. Ploog, On the mechanisms of spontaneous growth of III-nitride nanocolumns by plasma-assisted molecular beam epitaxy. J. Cryst. Growth **310**, 4035 (2008)
57. L. Cerutti, J. Ristić, S. Fernández-Garrido, E. Calleja, A. Trampert, K. Ploog, S. Lazic, J. Calleja, Wurtzite GaN nanocolumns grown on Si (001) by molecular beam epitaxy. Appl. Phys. Lett. **88**, 213114 (2006)
58. M. Hetzl, F. Schuster, A. Winnerl, S. Weiszer, M. Stutzmann, GaN nanowires on diamond. Mater. Sci. Semicond. Process. **48**, 65 (2016)
59. K.A. Bertness, A.W. Sanders, D.M. Rourke, T.E. Harvey, A. Roshko, J.B. Schlager, N.A. Sanford, Controlled nucleation of GaN nanowires grown with molecular beam epitaxy. Adv. Funct. Mater. **20**, 2911 (2010)
60. O. Landré, C. Bougerol, H. Renevier, B. Daudin, Nucleation mechanism of GaN nanowires grown on (111) Si by molecular beam epitaxy. Nanotechnology **20**, 415602 (2009)
61. R. Songmuang, O. Landré, B. Daudin, From nucleation to growth of catalyst-free GaN nanowires on thin AlN buffer layer. Appl. Phys. Lett. **91**, 251902 (2007)
62. J. Zúñiga-Pérez et al., Polarity in GaN and ZnO: Theory, measurement, growth, and devices. Appl. Phys. Rev. **3**, 041303 (2016)
63. K. Hestroffer, C. Leclere, C. Bougerol, H. Renevier, B. Daudin, Polarity of GaN nanowires grown by plasma-assisted molecular beam epitaxy on Si (111). Phys. Rev. B **84**, 245302 (2011)
64. K. Hestroffer, C. Leclere, V. Cantelli, C. Bougerol, H. Renevier, B. Daudin, In situ study of self-assembled GaN nanowires nucleation on Si (111) by plasma-assisted molecular beam epitaxy. Appl. Phys. Lett. **100**, 212107 (2012)
65. L. Largeau, E. Galopin, N. Gogneau, L. Travers, F. Glas, J.-C. Harmand, N-polar GaN nanowires seeded by Al droplets on Si (111). Cryst. Growth Des. **12**, 2724 (2012)
66. T. Auzelle, B. Haas, A. Minj, C. Bougerol, J.-L. Rouvière, A. Cros, J. Colchero, B. Daudin, The influence of AlN buffer over the polarity and the nucleation of self-organized GaN nanowires. J. Appl. Phys. **117**, 245303 (2015)
67. S. Fernández-Garrido, X. Kong, T. Gotschke, R. Calarco, L. Geelhaar, A. Trampert, O. Brandt, Spontaneous nucleation and growth of GaN nanowires: The fundamental role of crystal polarity. Nano Lett. **12**, 6119 (2012)
68. C. Chèze et al., Direct comparison of catalyst-free and catalyst-induced GaN nanowires. Nano Res. **3**, 528 (2010)
69. O. Brandt, C. Pfüller, C. Chèze, L. Geelhaar, H. Riechert, Sub-meV linewidth of excitonic luminescence in single GaN nanowires: Direct evidence for surface excitons. Phys. Rev. B **81**, 045302 (2010)
70. V. Kumaresan, L. Largeau, F. Oehler, H. Zhang, O. Mauguin, F. Glas, N. Gogneau, M. Tchernycheva, J.-C. Harmand, Self-induced growth of vertical GaN nanowires on silica. Nanotechnology **27**(13), 135602 (2016)
71. V. Kumaresan, L. Largeau, A. Madouri, F. Glas, H. Zhang, F. Oehler, A. Cavanna, A. Babichev, L. Travers, N. Gogneau, M. Tchernycheva, J.-C. Harmand, Epitaxy of GaN nanowires on graphene. Nano Lett. **16**(8), 4895 (2016)
72. G. Calabrese, P. Corfdir, G. Gao, C. Pfüller, A. Trampert, O. Brandt, L. Geelhaar, S. Fernández-Garrido, Molecular beam epitaxy of single crystalline GaN nanowires on a flexible Ti foil. Appl. Phys. Lett. **108**, 202101 (2016)
73. V. Consonni, A. Trampert, L. Geelhaar, H. Riechert, Physical origin of the incubation time of self-induced GaN nanowires. Appl. Phys. Lett. **99**, 033102 (2011)

74. C. Chèze, L. Geelhaar, A. Trampert, H. Riechert, In situ investigation of self-induced GaN nanowire nucleation on Si. Appl. Phys. Lett. **97**, 043101 (2010)
75. V. Consonni, M. Hanke, M. Knelangen, L. Geelhaar, A. Trampert, H. Riechert, Nucleation mechanisms of self-induced GaN nanowires grown on an amorphous interlayer. Phys. Rev. B **83**, 035310 (2011)
76. V. Consonni, M. Knelangen, L. Geelhaar, A. Trampert, H. Riechert, Nucleation mechanisms of epitaxial GaN nanowires: Origin of their self-induced formation and initial radius. Phys. Rev. B **81**, 085310 (2010)
77. M. Knelangen, V. Consonni, A. Trampert, H. Riechert, In situ analysis of strain relaxation during catalyst-free nucleation and growth of GaN nanowires. Nanotechnology **21**, 245705 (2010)
78. A. Wierzbicka et al., Influence of substrate nitridation temperature on epitaxial alignment of GaN nanowires to Si (111) substrate. Nanotechnology **24**, 035703 (2013)
79. J.E. Northrup, J. Neugebauer, Theory of GaN (10 1^{-} 0) and (11 2^{-} 0) surfaces. Phys. Rev. B **53**, R10477 (1996)
80. V.G. Dubrovskii, V. Consonni, A. Trampert, L. Geelhaar, H. Riechert, Scaling thermodynamic model for the self-induced nucleation of GaN nanowires. Phys. Rev. B **85**, 165317 (2012)
81. N.V. Sibirev, M. Tchernycheva, M.A. Timofeeva, J.-C. Harmand, G.E. Cirlin, V.G. Dubrovskii, Influence of shadow effect on the growth and shape of InAs nanowires. J. Appl. Phys. **111**, 104317 (2012)
82. R. Debnath, R. Meijers, T. Richter, T. Stoica, R. Calarco, H. Lüth, Mechanism of molecular beam epitaxy growth of GaN nanowires on Si (111). Appl. Phys. Lett. **90**, 123117 (2007)
83. L. Lymperakis, J. Neugebauer, Large anisotropic adatom kinetics on nonpolar GaN surfaces: Consequences for surface morphologies and nanowire growth. Phys. Rev. B **79**, 241308 (2009)
84. E. Galopin, L. Largeau, G. Patriarche, L. Travers, F. Glas, J. Harmand, Morphology of self-catalyzed GaN nanowires and chronology of their formation by molecular beam epitaxy. Nanotechnology **22**, 245606 (2011)
85. V. Consonni, V. Dubrovskii, A. Trampert, L. Geelhaar, H. Riechert, Quantitative description for the growth rate of self-induced GaN nanowires. Phys. Rev. B **85**, 155313 (2012)
86. K. Kishino, H. Sekiguchi, A. Kikuchi, Improved Ti-mask selective-area growth (SAG) by rf-plasma-assisted molecular beam epitaxy demonstrating extremely uniform GaN nanocolumn arrays. J. Cryst. Growth **311**, 2063 (2009)
87. Z.A. Gačević, D. Gomez Sanchez, E. Calleja, Formation mechanisms of GaN nanowires grown by selective area growth homoepitaxy. Nano Lett. **15**, 1117 (2015)
88. F. Schuster, M. Hetzl, S. Weiszer, J.A. Garrido, M. de la Mata, C. Magen, J. Arbiol, M. Stutzmann, Position-controlled growth of GaN nanowires and nanotubes on diamond by molecular beam epitaxy. Nano Lett. **15**, 1773 (2015)
89. H. Sekiguchi, K. Kishino, A. Kikuchi, Ti-mask selective-area growth of GaN by RFplasma-assisted molecular-beam epitaxy for fabricating regularly arranged InGaN/GaN nanocolumns. Appl. Phys. Express **1**, 124002 (2008)
90. A. Bengoechea-Encabo et al., Understanding the selective area growth of GaN nanocolumns by MBE using Ti nanomasks. J. Cryst. Growth **325**, 89 (2011)
91. T. Schumann, T. Gotschke, F. Limbach, T. Stoica, R. Calarco, Selective-area catalyst-free MBE growth of GaN nanowires using a patterned oxide layer. Nanotechnology **22**, 095603 (2011)
92. J. Kruse et al., Selective-area growth of GaN nanowires on SiO2-masked Si (111) substrates by molecular beam epitaxy. J. Appl. Phys. **119**, 224305 (2016)
93. M.D. Brubaker, S.M. Duff, T.E. Harvey, P.T. Blanchard, A. Roshko, A.W. Sanders, N.A. Sanford, K.A. Bertness, Polarity-controlled GaN/AlN nucleation layers for selective-area growth of GaN nanowire arrays on Si (111) substrates by molecular beam epitaxy. Cryst. Growth Des. **16**, 596 (2015)
94. K. Kishino, K. Nagashima, K. Yamano, Monolithic integration of InGaN-based nanocolumn light-emitting diodes with different emission colors. Appl. Phys. Express **6**, 012101 (2012)

95. R. Armitage, K. Tsubaki, Multicolour luminescence from InGaN quantum wells grown over GaN nanowire arrays by molecular-beam epitaxy. Nanotechnology **21**, 195202 (2010)
96. T. Kouno, K. Kishino, Well-arranged novel InGaN hexagonal nanoplates at the tops of nitrogen-polarity GaN nanocolumn arrays. AIP Adv. **2**, 012140 (2012)
97. X. Zhang, B. Haas, J.-L. Rouvière, E. Robin, B. Daudin, Growth mechanism of InGaN nano-umbrellas. Nanotechnology **27**, 455603 (2016)
98. F. Qian, Y. Li, S. Gradecak, D. Wang, C.J. Barrelet, C.M. Lieber, Gallium nitride-based nanowire radial heterostructures for nanophotonics. Nano Lett. **4**, 1975 (2004)
99. R. Wagner, W. Ellis, Vapor- liquid- solid mechanism of single crystal growth. Appl. Phys. Lett. **4**, 89 (1964)
100. J. Khanderi, A. Wohlfart, H. Parala, A. Devi, J. Hambrock, A. Birkner, R.A. Fischer, MOCVD of gallium nitride nanostructures using (N 3) 2 Ga {(CH 2) 3 NR 2}, R= Me, Et, as a single molecule precursor: morphology control and materials characterization. J. Mater. Chem. **13**, 1438 (2003)
101. S.D. Hersee, X. Sun, X. Wang, The controlled growth of GaN nanowires. Nano Lett. **6**, 1808 (2006)
102. K. Choi, M. Arita, Y. Arakawa, Selective-area growth of thin GaN nanowires by MOCVD. J. Cryst. Growth **357**, 58 (2012)
103. W. Bergbauer et al., Continuous-flux MOVPE growth of position-controlled N-face GaN nanorods andembedded InGaN quantum wells. Nanotechnology **21**, 305201 (2010)
104. R. Qhalid Fareed, J. Yang, J. Zhang, V. Adivarahan, V. Chaturvedi, M. Asif Khan, Vertically faceted lateral overgrowth of GaN on SiC with conducting buffer layers using pulsed metalorganic chemical vapor deposition. Appl. Phys. Lett. **77**, 2343 (2000)
105. Y.-S. Chen et al., Threading dislocation evolution in patterned GaN nanocolumn growth and coalescence overgrowth. J. Appl. Phys. **106**, 023521 (2009)
106. S.-Y. Bae, J.-Y. Lee, J.-H. Min, D.-S. Lee, Morphology evolution of pulsed-flux Ga- polar GaN nanorod growth by metal organic vapor phase epitaxy and its nucleation dependence. Appl. Phys. Express **6**, 075501 (2013)
107. W. Seifert, D. Asoli, Z. Bi, Nitride nanowires and method of producing such, (Google Patents, 2010).
108. X. Chen, B. Gayral, D. Sam-Giao, C. Bougerol, C. Durand, J. Eymery, Catalyst-free growth of high-optical quality GaN nanowires by metal-organic vapour phase epitaxy. Appl. Phys. Lett. **99**, 251910 (2011)
109. S. Haffouz, B. Beaumont, P. Gibart, Effect of magnesium and silicon on the lateral overgrowth of GaN patterned substrates by metal organic vapor phase epitaxy. MRS Internet J. Nitride Semicond. Res. **3**, e8 (1998)
110. R. Koester et al., M-plane core–shell InGaN/GaN multiple-quantum-wells on GaN wires for electroluminescent devices. Nano Lett. **11**, 4839 (2011)
111. P. Tchoulfian, F. Donatini, F. Levy, B. Amstatt, A. Amstatt, P. Dussaigne, E.B. Ferret, J. Pernot, Thermoelectric and micro-Raman measurements of carrier density and mobility in heavily Si-doped GaN wires. Appl. Phys. Lett. **103**, 202101 (2013)
112. B. Foltynski, N. Garro, M. Vallo, M. Finken, C. Giesen, H. Kalisch, A. Vescan, A. Cantarero, M. Heuken, The controlled growth of GaN microrods on Si (111) substrates by MOCVD. J. Cryst. Growth **414**, 200 (2015)
113. Y.-T. Lin, T.-W. Yeh, P.D. Dapkus, Mechanism of selective area growth of GaN nanorods by pulsed mode metalorganic chemical vapor deposition. Nanotechnology **23**, 465601 (2012)
114. B.O. Jung, S.-Y. Bae, Y. Kato, M. Imura, D.-S. Lee, Y. Honda, H. Amano, Morphology development of GaN nanowires using a pulsed-mode MOCVD growth technique. Cryst. Eng. Commun. **16**, 2273 (2014)
115. J. Eymery, D. Salomon, X. Chen, C. Durand, Method of selective growth without catalyst on a semiconducting structure, (Google Patents, 2015)
116. C. Tessarek, M. Heilmann, E. Butzen, A. Haab, H. Hardtdegen, C. Dieker, E. Spiecker, S. Christiansen, The role of Si during the growth of GaN micro-and nanorods. Cryst. Growth Des. **14**, 1486 (2014)

117. S. Haffouz, H. Lahreche, P. Vennéguès, P. De Mierry, B. Beaumont, F. Omnes, P. Gibart, The effect of the Si/N treatment of a nitridated sapphire surface on the growth mode of GaN in low-pressure metalorganic vapor phase epitaxy. Appl. Phys. Lett. **73**, 1278 (1998)
118. S. Salomon, J. Eymery, E. Pauliac-Vaujour, GaN wire-based Langmuir–Blodgett films for self-powered flexible strain sensors. Nanotechnology **25**, 375502 (2014)
119. S. Li et al., Nitrogen-polar core-shell GaN light-emitting diodes grown by selective area metalorganic vapor phase epitaxy. Appl. Phys. Lett. **101**, 032103 (2012)
120. X. Wang, J. Hartmann, M. Mandl, M. Sadat Mohajerani, H.-H. Wehmann, M. Strassburg, A. Waag, Growth kinetics and mass transport mechanisms of GaN columns by selective area metal organic vapor phase epitaxy. J. Appl. Phys. **115**, 163104 (2014)
121. X.J. Chen, J.-S. Hwang, G. Perillat-Merceroz, S. Landis, B. Martin, D.L.S. Dang, J. Eymery, C. Durand, Wafer-scale selective area growth of GaN hexagonal prismatic nanostructures on c-sapphire substrate. J. Cryst. Growth **322**, 15 (2011)
122. T. Schimpke, A. Avramescu, A. Koller, A. Fernando-Saavedra, J. Hartmann, J. Ledig, A. Waag, M. Strassburg, H.-J. Lugauer, The influence of MOVPE growth conditions on the shell of core-shell GaN microrod structures. J. Cryst. Growth **465**, 34 (2017)
123. H.M. Kim, T.W. Kang, K.S. Chung, Nanoscale ultraviolet- light- emitting diodes using wide-bandgap gallium nitride nanorods. Adv. Mater. **15**, 567 (2003)
124. H.-M. Kim, Y.-H. Cho, H. Lee, S.I. Kim, S.R. Ryu, D.Y. Kim, T.W. Kang, K.S. Chung, High-brightness light emitting diodes using dislocation-free indium gallium nitride/gallium nitride multiquantum-well nanorod arrays. Nano Lett. **4**, 1059 (2004)
125. A. Kikuchi, M. Kawai, M. Tada, K. Kishino, InGaN/GaN multiple quantum disk nanocolumn light-emitting diodes grown on (111) Si substrate. Jpn. J. Appl. Phys. **43**, L1524 (2004)
126. K. Kishino, A. Kikuchi, H. Sekiguchi, S. Ishizawa, InGaN/GaN nanocolumn LEDs emitting from blue to red. Proc. SPIE **2017**, 64730T (2007)
127. Z. Zhong, F. Qian, D. Wang, C.M. Lieber, Synthesis of p-type gallium nitride nanowires for electronic and photonic nanodevices. Nano Lett. **3**, 343 (2003)
128. A. Waag et al., The nanorod approach: GaN NanoLEDs for solid state lighting. Phys. Status Solidi C **8**, 2296 (2011)
129. Y.-H. Ra, R. Navamathavan, J.-H. Park, C.-R. Lee, High-quality uniaxial in x Ga1–x N/GaN multiple quantum well (MQW) nanowires (NWs) on Si (111) grown by metal-organic chemical vapor deposition (MOCVD) and light-emitting diode (LED) fabrication. ACS Appl. Mater. Interfaces **5**, 2111 (2013)
130. L. Rigutti et al., Correlation of microphotoluminescence spectroscopy, scanning transmission electron microscopy, and atom probe tomography on a single nano-object containing an InGaN/GaN multiquantum well system. Nano Lett. **14**, 107 (2013)
131. R. Koester et al., High-speed GaN/GaInN nanowire array light-emitting diode on silicon (111). Nano Lett. **15**, 2318 (2015)
132. Y.-H. Ra, R. Navamathavan, J.-H. Park, C.-R. Lee, Coaxial In x Ga1–x N/GaN multiple quantum well nanowire arrays on Si (111) substrate for high-performance light-emitting diodes. Nano Lett. **13**, 3506 (2013)
133. H.-S. Chen, Y.-F. Yao, C.-H. Liao, C.-G. Tu, C.-Y. Su, W.-M. Chang, Y.-W. Kiang, C. Yang, Light-emitting device with regularly patterned growth of an InGaN/GaN quantum-well nanorod light-emitting diode array. Opt. Lett. **38**, 3370 (2013)
134. N. Anttu, Modifying the emission of light from a semiconductor nanowire array. J. Appl. Phys. **120**, 043108 (2016)
135. K. Kishino, J. Kamimura, K. Kamiyama, Near-infrared InGaN nanocolumn lightemitting diodes operated at 1.46 μm. Appl. Phys. Express **5**, 031001 (2012)
136. R. Vadivelu, Y. Igawa, K. Kishino, 633 nm red emissions from InGaN nanocolumn lightemitting diode by radio frequency plasma assisted molecular beam epitaxy. Jpn. J. Appl. Phys. **52**, 08JE18 (2013)
137. M. Nami, R.F. Eller, S. Okur, A.K. Rishinaramangalam, S. Liu, I. Brener, D.F. Feezell, Tailoring the morphology and luminescence of GaN/InGaN core–shell nanowires using bottomup selective-area epitaxy. Nanotechnology **28**, 025202 (2016)

138. A. Yanagihara, S. Ishizawa, K. Kishino, Directional radiation beam from yellow-emitting InGaN-based nanocolumn LEDs with ordered bottom-up nanocolumn array. Appl. Phys. Express **7**, 112102 (2014)
139. H. Hayashi, D. Fukushima, T. Noma, D. Tomimatsu, Y. Konno, M. Mizuno, K. Kishino, Thermally engineered flip-chip InGaN/GaN well-ordered nanocolumn array LEDs. IEEE Photon. Technol. Lett. **27**, 2343 (2015)
140. F. Limbach et al., Current path in light emitting diodes based on nanowire ensembles. Nanotechnology **23**, 465301 (2012)
141. A. Bavencove et al., Submicrometre resolved optical characterization of green nanowirebased light emitting diodes. Nanotechnology **22**, 345705 (2011)
142. S. Jahangir, M. Mandl, M. Strassburg, P. Bhattacharya, Molecular beam epitaxial growth and optical properties of red-emitting (λ= 650 nm) InGaN/GaN disks-in-nanowires on silicon. Appl. Phys. Lett. **102**, 071101 (2013)
143. T. Andreev, E. Monroy, B. Gayral, B. Daudin, N.Q. Liem, Y. Hori, M. Tanaka, O. Oda, L. Si Dang, Eu locations in Eu-doped In Ga N/ Ga N quantum dots. Appl. Phys. Lett. **87**(2), 021906 (2005)
144. H. Sekiguchi, T. Imanishi, R. Matsuzaki, K. Ozaki, K. Yamane, H. Okada, K. Kishino, A. Wakahara, Stable-wavelength operation of europium-doped GaN nanocolumn light-emitting diodes grown by rf-plasma-assisted molecular beam epitaxy. Electron. Lett. **53**, 666 (2017)
145. R. Wang, X. Liu, I. Shih, Z. Mi, High efficiency, full-color AlInGaN quaternary nanowire light emitting diodes with spontaneous core-shell structures on Si. Appl. Phys. Lett. **106**, 261104 (2015)
146. R. Wang, H.P. Nguyen, A.T. Connie, J. Lee, I. Shih, Z. Mi, Color-tunable, phosphorfree InGaN nanowire light-emitting diode arrays monolithically integrated on silicon. Opt. Express **22**, A1768 (2014)
147. H.P.T. Nguyen et al., Engineering the carrier dynamics of InGaN nanowire white lightemitting diodes by distributed p-AlGaN electron blocking layers. Sci. Rep. **5**, 14745 (2015)
148. M.R. Philip, D.D. Choudhary, M. Djavid, M.N. Bhuyian, J. Piao, T.T. Pham, D. Misra, H.P. Nguyen, Controlling color emission of InGaN/AlGaN nanowire light-emitting diodes grown by molecular beam epitaxy. J. Vac. Sci. Technol. B: Nanotechnol. Microelectron. Mater. Process. Meas. Phenom. **35**, 02B108 (2017)
149. C. Zhao et al., An enhanced surface passivation effect in InGaN/GaN disk-in-nanowire light emitting diodes for mitigating Shockley–Read–Hall recombination. Nanoscale **7**, 16658 (2015)
150. S. Sadaf, Y.-H. Ra, H. Nguyen, M. Djavid, Z. Mi, Alternating-current InGaN/GaN tunnel junction nanowire white-light emitting diodes. Nano Lett. **15**, 6696 (2015)
151. J. Simon, Z. Zhang, K. Goodman, H. Xing, T. Kosel, P. Fay, D. Jena, Polarizationinduced Zener tunnel junctions in wide-band-gap heterostructures. Phys. Rev. Lett. **103**, 026801 (2009)
152. S. Krishnamoorthy, D.N. Nath, F. Akyol, P.S. Park, M. Esposto, S. Rajan, Polarizationengineered GaN/InGaN/GaN tunnel diodes. Appl. Phys. Lett. **97**, 203502 (2010)
153. M.J. Grundmann, U.K. Mishra, Multi- color light emitting diode using polarizationinduced tunnel junctions. Phys. Status Solidi C **4**, 2830 (2007)
154. A. Sarwar, S.D. Carnevale, F. Yang, T.F. Kent, J.J. Jamison, D.W. McComb, R.C. Myers, Semiconductor nanowire light- emitting diodes grown on metal: A direction toward large-scale fabrication of nanowire devices. Small **11**, 5402 (2015)
155. C. Zhao et al., Droop-free, reliable, and high-power InGaN/GaN nanowire light-emitting diodes for monolithic metal-optoelectronics. Nano Lett. **16**, 4616 (2016)
156. C. Zhao, T.K. Ng, N. Wei, A. Prabaswara, M.S. Alias, B. Janjua, C. Shen, B.S. Ooi, Facile formation of high-quality InGaN/GaN quantum-disks-in-nanowires on bulk-metal substrates for high-power light-emitters. Nano Lett. **16**, 1056 (2016)
157. B.J. May, A.G. Sarwar, R.C. Myers, Nanowire LEDs grown directly on flexible metal foil. Appl. Phys. Lett. **108**, 141103 (2016)

158. K. Bando, K. Sakano, Y. Noguchi, Y. Shimizu, Development of high-bright and purewhite LED lamps. J. Light. Vis. Environ. **22**, 1_2 (1998)
159. Y. Hu, W. Zhuang, H. Ye, D. Wang, S. Zhang, X. Huang, A novel red phosphor for white light emitting diodes. J. Alloys Compd. **390**, 226 (2005)
160. M. Yamada, Y. Narukawa, T. Mukai, Phosphor free high-luminous-efficiency white light-emitting diodes composed of InGaN multi-quantum well. Jpn. J. Appl. Phys. **41**, L246 (2002)
161. B. Damilano, N. Grandjean, C. Pernot, J. Massies, Monolithic white light emitting diodes based on InGaN/GaN multiple-quantum wells. Jpn. J. Appl. Phys. **40**, L918 (2001)
162. D. Yang, L. Wang, W.-B. Lv, Z.-B. Hao, Y. Luo, Growth and characterization of phosphor-free white light-emitting diodes based on InGaN blue quantum wells and green–yellow quantum dots. Superlattice. Microst. **82**, 26 (2015)
163. B. Damilano, B. Gil, Yellow–red emission from (Ga, In) N heterostructures. J. Phys. D. Appl. Phys. **48**, 403001 (2015)
164. D. Schiavon, M. Binder, A. Loeffler, M. Peter, Optically pumped GaInN/GaN multiple quantum wells for the realization of efficient green light-emitting devices. Appl. Phys. Lett. **102**, 113509 (2013)
165. W. Guo, A. Banerjee, P. Bhattacharya, B.S. Ooi, InGaN/GaN disk-in-nanowire white light emitting diodes on (001) silicon. Appl. Phys. Lett. **98**, 193102 (2011)
166. H.P.T. Nguyen, K. Cui, S. Zhang, M. Djavid, A. Korinek, G.A. Botton, Z. Mi, Controlling electron overflow in phosphor-free InGaN/GaN nanowire white light-emitting diodes. Nano Lett. **12**, 1317 (2012)
167. H.P.T. Nguyen, S. Zhang, A.T. Connie, M.G. Kibria, Q. Wang, I. Shih, Z. Mi, Breaking the carrier injection bottleneck of phosphor-free nanowire white light-emitting diodes. Nano Lett. **13**, 5437 (2013)
168. Z. Mi, H. Nguyen, M. Djavid, S. Zhang, A. Connie, S. Sadaf, Q. Wang, S. Zhao, I. Shih, High power phosphor-free InGaN/GaN/AlGaN core-shell nanowire white light emitting diodes on Si substrates. ECS Trans. **61**, 9 (2014)
169. S.-I. Inoue, T. Naoki, T. Kinoshita, T. Obata, H. Yanagi, Light extraction enhancement of 265 nm deep-ultraviolet light-emitting diodes with over 90 mW output power via an AlN hybrid nanostructure. Appl. Phys. Lett. **106**, 131104 (2015)
170. Y.K. Ooi, C. Liu, J. Zhang, Analysis on polarization-dependent light extraction and effect of passivation layer for 230 nm AlGaN nanowire light-emitting diodes. IEEE Photon. J. **9**, 1–12 (2017)
171. H.-Y. Ryu, Large enhancement of light extraction efficiency in AlGaN-based nanorod ultraviolet light-emitting diode structures. Nanoscale Res. Lett. **9**, 58 (2014)
172. H. Sekiguchi, K. Kato, J. Tanaka, A. Kikuchi, K. Kishino, Ultraviolet GaN- based nanocolumn light- emitting diodes grown on n- (111) Si substrates by rf- plasma- assisted molecular beam epitaxy. Phys. Status Solidi A **205**, 1067 (2008)
173. A. Pierret, C. Bougerol, S. Murcia-Mascaros, A. Cros, H. Renevier, B. Gayral, B. Daudin, Growth, structural and optical properties of AlGaN nanowires in the whole composition range. Nanotechnology **24**, 115704 (2013)
174. C. Himwas, M. Den Hertog, L.S. Dang, E. Monroy, R. Songmuang, Alloy inhomogeneity and carrier localization in AlGaN sections and AlGaN/AlN nanodisks in nanowires with 240–350 nm emission. Appl. Phys. Lett. **105**, 241908 (2014)
175. G. Jacopin et al., Photoluminescence polarization in strained GaN/AlGaN core/shell nanowires. Nanotechnology **23**, 325701 (2012)
176. C. Durand et al., M-Plane GaN/InAlN multiple quantum wells in core–shell wire structure for UV emission. ACS Photon. **1**, 38 (2013)
177. S. Zhao, M. Djavid, Z. Mi, Surface emitting, high efficiency near-vacuum ultraviolet light source with aluminum nitride nanowires monolithically grown on silicon. Nano Lett. **15**, 7006 (2015)
178. S. Zhao, S. Woo, M. Bugnet, X. Liu, J. Kang, G. Botton, Z. Mi, Three-dimensional quantum confinement of charge carriers in self-organized AlGaN nanowires: A viable route to electrically injected deep ultraviolet lasers. Nano Lett. **15**, 7801 (2015)

179. Z. Mi et al., Molecular beam epitaxial growth and characterization of Al (Ga) N nanowire deep ultraviolet light emitting diodes and lasers. J. Phys. D. Appl. Phys. **49**, 364006 (2016)
180. S. Sadaf, S. Zhao, Y. Wu, Y.-H. Ra, X. Liu, S. Vanka, Z. Mi, An AlGaN core–shell tunnel junction nanowire light-emitting diode operating in the ultraviolet-C band. Nano Lett. **17**, 1212 (2017)
181. D.A. Laleyan, S. Zhao, S.Y.-M. Woo, H.N. Tran, H.B. Le, T. Szkopek, H. Guo, G.A. Botton, Z. Mi, AlN/h-BN heterostructures for Mg dopant-free deep ultraviolet photonics. Nano Lett. **17**, 3738–3743 (2017)
182. S.-C. Zhu et al., Enhancement of the modulation bandwidth for GaN-based light-emitting diode by surface plasmons. Opt. Express **23**(11), 13752 (2015)
183. W. Pfaff, A. Vos, R. Hanson, Top-down fabrication of plasmonic nanostructures for deterministic coupling to single quantum emitters. J. Appl. Phys. **113**, 024310 (2013)
184. F. Qian, Y. Li, S. Gradečak, H.-G. Park, Y. Dong, Y. Ding, Z.L. Wang, C.M. Lieber, Multi-quantum-well nanowire heterostructures for wavelength-controlled lasers. Nat. Mater. **7**, 701 (2008)
185. C. Mounir, T. Schimpke, G. Rossbach, A. Avramescu, M. Strassburg, U.T. Schwarz, Optical properties and internal quantum efficiency of InGaN/GaN core-shell microrods for solid state lighting. J. Appl. Phys. **120**, 155702 (2016)
186. J. Lee, X. Li, X. Ni, Ü. Özgür, H. Morkoç, T. Paskova, G. Mulholland, K. Evans, On carrier spillover in c-and m-plane InGaN light emitting diodes. Appl. Phys. Lett. **95**, 201113 (2009)
187. T. Sano, T. Doi, S.A. Inada, T. Sugiyama, Y. Honda, H. Amano, T. Yoshino, High internal quantum efficiency blue-green light-emitting diode with small efficiency droop fabricated on low dislocation density GaN substrate. Jpn. J. Appl. Phys. **52**, 08JK09 (2013)
188. C. Kölper, M. Sabathil, F. Römer, M. Mandl, M. Strassburg, B. Witzigmann, Core–shell InGaN nanorod light emitting diodes: Electronic and optical device properties. Phys. Status Solidi A **209**, 2304 (2012)
189. G. Tourbot et al., Growth mechanism and properties of InGaN insertions in GaN nanowires. Nanotechnology **23**, 135703 (2012)
190. T. Krause et al., Nanofocus x-ray diffraction and cathodoluminescence investigations into individual core–shell (In, Ga) N/GaN rod light-emitting diodes. Nanotechnology **27**, 325707 (2016)
191. C. Mounir, T. Schimpke, G. Rossbach, A. Avramescu, M. Strassburg, U.T. Schwarz, Polarization-resolved micro-photoluminescence investigation of InGaN/GaN core-shell microrods. J. Appl. Phys. **121**, 025701 (2017)
192. M. Shahmohammadi, J.-D. Ganière, H. Zhang, R. Ciechonski, G. Vescovi, O. Kryliouk, M. Tchernycheva, G. Jacopin, Excitonic diffusion in InGaN/GaN core–shell nanowires. Nano Lett. **16**, 243 (2015)
193. C.-K. Li, H.-C. Yang, T.-C. Hsu, Y.-J. Shen, A.-S. Liu, Y.-R. Wu, Three dimensional numerical study on the efficiency of a core-shell InGaN/GaN multiple quantum well nanowire light-emitting diodes. J. Appl. Phys. **113**, 183104 (2013)
194. M. Mohajerani et al., Evaluation of local free carrier concentrations in individual heavily-doped GaN: Si micro-rods by micro-Raman spectroscopy. Appl. Phys. Lett. **108**, 091112 (2016)
195. V. Hortelano, O. Martínez, R. Cuscó, L. Artús, J. Jiménez, Cathodoluminescence study of Mg activation in non-polar and semi-polar faces of undoped/Mg-doped GaN core–shell nanorods. Nanotechnology **27**, 095706 (2016)
196. P. Tchoulfian, F. Donatini, F. Levy, A. Dussaigne, P. Ferret, J. Pernot, Direct imaging of p–n junction in core–shell GaN wires. Nano Lett. **14**, 3491 (2014)
197. A. Sugimoto, H. Ochi, S. Fujimura, A. Yoshida, T. Miyadera, M. Tsuchida, Flexible OLED displays using plastic substrates. IEEE J. Sel. Top. Quant. Electron. **10**, 107 (2004)
198. D. Kondakov, W. Lenhart, W. Nichols, Operational degradation of organic light-emitting diodes: Mechanism and identification of chemical products. J. Appl. Phys. **101**, 024512 (2007)

199. A. Fallahi, F.A. Taromi, A. Mohebbi, J.D. Yuen, M. Shahinpoor, A novel ambipolar polymer: from organic thin-film transistors to enhanced air-stable blue light emitting diodes. J. Mater. Chem. C **2**, 6491 (2014)
200. S.I. Park, A.P. Le, J. Wu, Y. Huang, X. Li, J.A. Rogers, Light emission characteristics and mechanics of foldable inorganic light- emitting diodes. Adv. Mater. **22**, 3062 (2010)
201. N. Guan, X. Dai, A. Babichev, F.H. Julien, M. Tchernycheva, Flexible inorganic light emitting diodes based on semiconductor nanowires. Chem. Sci. **8**, 7904–7911 (2017)
202. Z. Fan et al., Three-dimensional nanopillar-array photovoltaics on low-cost and flexible substrates. Nat. Mater. **8**, 648 (2009)
203. J.M. Spurgeon, S.W. Boettcher, M.D. Kelzenberg, B.S. Brunschwig, H.A. Atwater, N.S. Lewis, Flexible, polymer- supported, Si wire array photoelectrodes. Adv. Mater. **22**, 3277 (2010)
204. K.E. Plass, M.A. Filler, J.M. Spurgeon, B.M. Kayes, S. Maldonado, B.S. Brunschwig, H.A. Atwater, N.S. Lewis, Flexible polymer- embedded Si wire arrays. Adv. Mater. **21**, 325 (2009)
205. M.E. Reimer, G. Bulgarini, N. Akopian, M. Hocevar, M.B. Bavinck, M.A. Verheijen, E.P. Bakkers, L.P. Kouwenhoven, V. Zwiller, Bright single-photon sources in bottom-up tailored nanowires. Nat. Commun. **3**, 737 (2012)
206. M. Willander, O. Nur, Q.X. Zhao, L.L. Yang, M. Lorenz, B.Q. Cao, J.Z. Pérez, C. Czekalla, G. Zimmermann, M. Grundmann, A. Bakin, A. Behrends, M. Al-Suleiman, A. El-Shaer, A.C. Mofor, B. Postels, A. Waag, N. Boukos, A. Travlos, H.S. Kwack, J. Guinard, D.L.S. Dang, Zinc oxide nanorod based photonic devices: recent progress in growth, light emitting diodes and lasers. Nanotechnology **20**, 332001 (2009)
207. A. Nadarajah, R.C. Word, J. Meiss, R. Könenkamp, Flexible inorganic nanowire lightemitting diode. Nano Lett. **8**, 534 (2008)
208. H. Li, G. Zhao, L. Wang, Z. Chen, S. Yang, Morphology controlled fabrication of InN nanowires on brass substrates. Nanomaterials **6**, 195 (2016)
209. H.K. Park, S.W. Yoon, Y.J. Eo, W.W. Chung, G.Y. Yoo, J.H. Oh, K.N. Lee, W. Kim, Y.R. Do, Horizontally assembled green InGaN nanorod LEDs: scalable polarized surface emitting LEDs using electric-field assisted assembly. Sci. Rep. **6**, 28312 (2016)
210. M.C. McAlpine, R.S. Friedman, S. Jin, K.-H. Lin, W.U. Wang, C.M. Lieber, Highperformance nanowire electronics and photonics on glass and plastic substrates. Nano Lett. **3**, 1531 (2003)
211. N. Guan et al., Flexible white light emitting diodes based on nitride nanowires and nanophosphors. ACS Photon. **3**, 597 (2016)

Chapter 13
Light-Emitting Diodes for Healthcare and Well-being

Ying Gu, Haixia Qiu, Ying Wang, Naiyan Huang, and Timon Cheng-Yi Liu

13.1 Basic Theories and Mechanisms of LED Phototherapy

13.1.1 Basic Theories and Mechanisms of Low-Level Light Therapy

13.1.1.1 Development History of LED for Low-Level Light Therapy

In 1903, the Danish scientist Finsen pioneered in treating skin tuberculosis with ultraviolet light, which turned over a new chapter for modern phototherapy. With the advancement of science and technology, the light source of phototherapy has experienced the development from sunlight, wide spectrum artificial light source to single spectral line laser light source, which makes the treatment more effective. At present, due to its high light intensity and better monochromaticity and coherence, laser has become the best source of monochromatic light, which in recent years has made remarkable breakthroughs in the fields of treatment. Nevertheless, the available laser wavelengths for clinical use are still limited at present.

In recent years, with the rapid progress of LED production, especially in the aspects of lighting intensity, wavelength, and price, LED now has more advantages than laser. The LED lighting efficiency has been improved markedly. For instance, the lighting efficiency of an orange red LED of a wavelength of 620 mn reaches 100 lm/W with a luminous flux amounting to that of 4mW helium–neon gas laser, which can meet the ordinary clinical demands.In respects of wavelength,

Y. Gu (✉) · H. Qiu · Y. Wang · N. Huang
Chinese PLA General Hospital, Beijing, China

T. C.-Y. Liu
South China Normal University, Guangzhou, China

© Springer International Publishing AG, part of Springer Nature 2019

J. Li, G. Q. Zhang (eds.), *Light-Emitting Diodes*, Solid State Lighting Technology and Application Series 4, https://doi.org/10.1007/978-3-319-99211-2_13

practicability, and price, the LED far outperforms laser. Laser can only emit the light of a few different wavelengths, but LED spans nearly the whole visible light region. With regard to practicability, due to its simple structure, small power, lower consumption, long lifetime, reliability, and easy promotion, the price of LED is much less than that of any kind of laser in the market. For these reasons, LED has promising prospects and the higher practicability in the fields of medical treatment. With the further development of LED chip technology, the increasing light intensity of LED units, extension of the LED spectrum range from ultraviolet to infrared, the appearance of more LED wavelengths, and LED phototherapy will certainly play a more and more important role in the area of low-intensity phototherapy.

The application of LED in the field of medical treatment can be traced back to the treatment of neonatal jaundice. In 1968, Lucy made use of light to cure the jaundice of premature infants for the first time, but the limitation of light source resulted in a low treatment efficiency. Since 2000, blue LED has been utilized in the treatment of neonatal jaundice, and gradually replaced the traditional method of soft laser therapy. At present, blue LED has been recommended by the American Academy of Pediatrics as the best light source for the treatment of neonatal unconjugated hyperbilirubinemia. In 2001, in the process of curing leukemia pediatric patients by Whelan H. T. and some people, prior to the bone marrow implantation matched with their cell antigen, the patients had to accept radiotherapy and chemotherapy for the maximum dose to kill the neoplastic bone marrow in the bodies. However, the drugs used in the chemotherapy and radiotherapy will indiscriminately kill rapidly dividing cells, such as oral cavity membrane cells and gastrointestinal tract cells, which will cause serious negative gastrointestinal effects. As a result, the patients given the chemotherapy usually suffered acute oral ulcer and food dysphagia. On the other hand, once these patients were given the last chemotherapy and 688mn LED 4 J/cm^2 per day, 47% of them were relieved of oral pain, and the healing rate of oral ulcers was better than expected. In 2012, it was reported that some Japanese scholars discovered that LED light can assuage bone metabolism disorder in children with cerebral palsy. Subsequently, in 2014, it was reported by the Korean University in South Korea that 635 nm LED could reduce the resorption induced by osteoclasts, and mediate the homeostasis of bones. In 2013, Park KY used 830 nm LED light source to treat acute herpes zoster ophthalmicus, confirming that LED phototherapy can promote wound healing and reduce pain and discovering that LED phototherapy can reduce pigmentation and scars in the wake of inflammation, and LED light source also has regulatory effect on the inflammatory immune system. In 2016, Sohn, H. and M. and others found that 635 nm red light LED can inhibit osteoclast activity and bone resorption and delay the progress of osteoporosis.

13.1.1.2 Interactivity Between Light and Human Tissues

When shining on the tissues of a human body, most of the light will be absorbed by the tissues except some being reflected or penetrating the tissues. Following the absorption of the photons in human tissues, the light energy will be transformed into

other forms of energy, such as thermal energy, mechanical energy, and chemical energy. A series of biological effects will be induced, such as thermal effect, mechanical effect, and photochemical reaction. The absorption of photons in human tissues can also cause photon re-emission. The photons haven't undergone energy exchange with human tissues remain constant regarding frequency, and the spatial distribution of these photons is also closely related to the structure and function of the tissues.

13.1.1.3 Light Dosiology for LED Used in Low-Level Light Therapy

The main parameters of LED mediated low-level light therapy are wavelength, average output, power density, irradiance or treatment time, energy density, accumulated energy, output mode, etc. In terms of the wavelengths, nanometer (nm) is the main unit. The available wavelengths for LED cover the visible lights and parts of the invisible lights. The power of LED is usually between 1 and 1000 mW. For LLLT, a few or dozens of mW is usually used. The main unit for power density is mW/cm^2, which can also be called irradiance. The output modes include continuous wave and pulsed wave. If the light beam is pulsed wave, the reported power should be average power. The calculation is as follows: peak power (W) $\times$ pulse width (s) $\times$ pulse frequency (Hz) $=$ average power (mW). Talking about dose–effect relationship, there is a two-way stoichiometric reaction between irradiation time and energy density. If the light does not have enough energy density or the irradiation time is too short, no effect will appear. On the other hand, should the energy density be too high or the irradiation time too long, the response may be suppressed. Nevertheless, there is always a best combination of energy density and irradiation time in certain place, which will produce the best effect. This two track reaction can be traced back into an article published in 1887 by Hugo Schultz, after which Rudolf introduced his own theory that lower dose of light irradiation will bring in stimulating effect and higher dose inhibiting effect [1]. The division of high and low doses hinges on the change of biological structure and function.

13.1.1.4 Mechanisms of Low-Level Light Therapy

According to current researches, it is known that low-level light therapy mainly leads to functional changes at cellular, subcellular, and molecular levels. Its role is complex due to the diversity of parameters and observational indicators and the lack of consistency in the results of studies on the dose–effect relationship. In terms of mechanism researches, since the cellular signals and pathways involved in low-level light therapy have not yet been fully explored, non-invasive detection techniques that can accurately detect functional changes at cellular and molecular levels are very limited, which restricts the exploration of the mechanisms of low-level light therapy. Currently, despite the existence of some hypotheses, the exact mechanisms have not yet been fully elucidated.

13.1.1.4.1 Photobiomodulation

Low-level light therapy is also called photobiomodulation therapy. The mechanism of photobiomodulation (PBM) lies in the fact that non-ionizing optical radiation in the visible and near-infrared spectral range can be absorbed by endogenous chromophores to elicit photophysical and photochemical events at various biological scales.

Firstly, there is a set of parameters (wavelength, irradiance, energy density, pulsed vs continuous wave, exposure time, duty cycle–on time/dark period, frequency of exposure, time interval between exposures, etc.) that determine the types of the cellular effects as well as the relative intensity and duration of these effects.

Secondly, PBM modulates the activities of cells by stimulating/inhibiting or activating/deactivating natural cellular processes. There are multiple mechanisms of action for photobiomodulation of living cells. Mitochondrial mechanism is the most recognized mechanism, which will be introduced in the following part.

Thirdly, different cell types may respond differently to the same photomodulation parameters. Homeostasis is one of the most remarkable and typical properties of a highly complex open biosystem [2]. It is a negative-feedback response of a biosystem to maintain constant conditions inside the biosystem. It has been extended to be function-specific homeostasis (FSH) by Liu et al. [3–5]. An FSH is a negative-feedback response of a biosystem to maintain the function-specific conditions inside the biosystem so that the function is perfectly performed. The functions are finely categorized into two types: the normal and dysfunctional. The transformation of a function from a dysfunctional one to a normal one is called the normalization of the dysfunctional function. It has been found that PBM can promote the normalization of a dysfunctional function [6]. The FSH has been quantitatively represented with quantitative difference (QD) by Liu et al. [7–9].

13.1.1.4.2 Mitochondrial Mechanism

There were many theories on the precise molecular mechanism of PBM. Among them, the cytochrome c oxidase (COX) theory was very popular [1, 10–13]. Cytochrome c and COX represent the terminal step of the electron transport chain in mitochondria, the proposed rate-limiting reaction in mammals. Cytochrome c and COX show unique regulatory features including allosteric regulation, isoform expression, and regulation through cell signaling pathways [14]. The COX theory [11] suggested that COX in mitochondria was the primary photoacceptor upon LLLT exposure of cells, and PBM was mediated by LLLT increased COX activities. The LLLT increased COX activity may be mediated by low-level mitochondrial reactive oxygen species (ROS). It was demonstrated by Wu et al. [15] that the initial reaction after photon absorption of moderate intensity monochromatic light was the photosensitization of COX, which would inhibit enzymatic activity of COX in situ and cause respiratory chain ROS burst.

On the other hand, low-level mitochondrial ROS has been found with the ability to keep cells alive under stressful conditions [16, 17]. High level mitochondrial ROS may induce apoptosis through the intrinsic pathway to protect from severely damaged cells as being observed by Wu et al. [15]. However, Yee et al. [17] demonstrated that sensing of low-level mitochondrial ROS with apoptotic pathway would, independently of apoptosis, elicit the protective mechanism that keeps the nematode alive under stressful conditions and extend the nematode longevity. De Haes et al. [16] showed that metformin extended life span through the process of mitohormesis and proposed a signaling cascade in which metformin-induced production of ROS increased overall life expectancy of nematodes. They also revealed that this beneficial signal of the mitohormetic pathway was propagated by the peroxiredoxin PRDX-2. Because of its evolutionary conservation, peroxiredoxin signaling might underlie a general principle of prolongevity signaling.

In summary, COX-induced low-level ROS production in mitochondria under LLLT may promote the normalization of a dysfunctional function.

13.1.1.4.3 Phototransduction

The COX theory on PBM does not universally hold. There are strong evidences suggesting that LLLT acts on mitochondria will promote adenosine triphosphate (ATP) production. It was shown by Drew et al. [18] that an age-associated decline in ATP content and rate of ATP production was tissue specific as it occurred in skeletal muscles but not heart, and mitochondrial ATP production was not altered by caloric restriction in both tissues. The observation that nitric oxide (NO) was released from cells during LLLT irradiation has led to a speculation that COX and NO release are linked. Montoro et al. [19] found lipopolysaccharide (LPS)-induced stress resulted in significant increase in NO production by human dental pulp cells without causing damage to cell respiratory metabolism and NO production was significantly reduced when LPS-stressed cells were irradiated with infrared light-emitting diode irradiation irrespective of energy dose delivered. Moreover, the COX theory cannot explain the PBM on erythrocytes [20]. In view of this background, the phototransduction mechanism of PBM was introduced.

Phototransduction is the process by which a photon of light captured by a molecule of visual pigment generates an electrical response in a photoreceptor cell [21]. In this way, the photoreceptor-specific G protein mediates between the membrane visual pigment, rhodopsin, and the effector enzyme, cGMP phosphodiesterase. The possibility of extraocular phototransduction (EPT) was put forward by Campbell and Murphy [22] in their report, according to which 3 h of bright light exposure to the area behind the knee caused phase shifts of the circadian rhythms of both body temperature and saliva melatonin in humans. However, as early as in 1996, Liu et al. [23] have put forward the quasi-hormone model of laser biostimulation from the viewpoint of EPT, which was developed as BIMP [24]. The first EPT phenomenon was observed in low-intensity He–Ne laser irradiation induced respiratory burst of polymorphonuclear neutrophils in our

laboratory in 2001 [25]. Since then, many LLLT induced EPT phenomena have been observed [26]. Moreover, BIMP has held for the EPT phenomena. It may be further understood with FSH [5]. A cellular normal function in its FSH can resist not only external perturbations under its threshold but also the activation of other signal transduction pathways so that there should be normal function-specific signal transduction pathways (NSPs). For a cellular function, there are many redundant genes and redundant NSPs. The full expression of one redundant gene may fully activate its redundant NSP to maintain its normal cellular function. The full activation of one redundant NSP maintains the first-order normal function. The synergistic activation of n redundant NSPs maintains the *n*th-order normal function. The more the fully activated redundant NSPs, the higher the fitness of the normal function. A cellular PBM can promote the activation of a partially activated NSP, and can be classified into direct and indirect PBM (dPBM and iPBM). For a cellular dysfunctional function, dense signal transduction pathways are partially activated, but there is no fully activated redundant NPS. A cellular dPBM can promote the activation of one partially activated redundant NSP until it is fully activated and then the dysfunctional function becomes a normal one. For an *n*th-order normal function, n redundant NSPs have been fully and synergistically activated. A cellular iPBM may promote the activation of the partially activated $(n + 1)$th redundant NSP until it is fully activated and then the *n*th-order normal function is transformed into its $(n + 1)$th-order one.

13.1.2 Basic Theories and Mechanisms of LED Mediated Photodynamic Therapy

13.1.2.1 Basic Theories of LED-Mediated Photodynamic Therapy

Photodynamic therapy (PDT) is a promising targeting treatment for both malignant and benign diseases. Its function is based on the reactive oxygen species (ROS) generated through a series of photochemical reaction, which is mediated through the interaction of photosensitizing agents, light and oxygen. Currently, PDT is performed on body surface or via endoscopic and interstitial methods in clinic. The clinical application and basic research mainly focus on anti-tumor PDT, vascular targeted PDT, and anti-microbial PDT.

13.1.2.1.1 Light Sources for Photodynamic Therapy

So far, laser, filtered xenon arc, metal halogen lamp, fluorescent lamp and LED, and even sun light have been used as light sources for PDT. The question which light source is the best for PDT has always been a topic of debate. Laser is the most commonly used PDT light source as it may greatly increase the penetration depth in tissues because of its high intensity and collimation. At the same time,

the monochromaticity of laser will enable a concentration of energy during the absorption peak of photosensitizers. Laser may also be transferred to digestive tracts and respiratory tracts via fibers. For these reasons, laser is undoubtedly the most suitable light source for endoscopic and interstitial PDT. In recent years, LED has been used in the PDT for superficial skin mucosal lesion. For example, the combination of LED and tropical applied 5-ALA or MAL (Metvix; Galderma) to treat actinic keratosis (AKs) is effective, which is much less painful than laser guided PDT [27].

LED is more cost-effective than laser because of its low manufacture cost and long service life. Moreover, a LED array usually has a big shiny surface. Its curvature, size, and shape can be designed according to the geometry characteristics of targeted body surface. Lots of portable and battery-equipped wearable LEDs have been applied in clinical PDT or undergoing clinical trials.

13.1.2.1.2 Dosimetry of Photodynamic Therapy

The dosimetry of PDT is more complicated than that of photothermal treatment. Not only light but also photosensitizer, oxygen, and target lesion play important roles in the process of PDT. Single factor (for example, light and photosensitizer) doesn't show linear relationship with the therapeutic effect. Studies have indicated that only when all the above factors match well can PDT achieve the best therapeutic effect. At present, only light dose and photosensitizer dose are adjustable in clinical practice. The dose of a photosensitizer includes the type of the photosensitizer, dosage (concentration) applied, time interval between drug administration and light delivery. The dose of light involves wavelength, power density or irradiance, irradiation time or treatment time, and continuous wave or pulsed mode. As light sources for PDT, the main difference between LED and laser is the penetration depth [28]. It is mainly caused by the different collimation of LED and laser. The collimation of laser enables it to illuminate the lesion surface vertically and generate a large number of forward scattering in the tissue, indicating a deeper penetration. To the contrary, light generated from LED is not collimated. The photons of LED irradiate the lesion surface from various directions, and more backscatter is induced within the tissue. As a result, most of the photons deposit only in the shallow part of the tissue.

The absorption peak of photosensitizer and the depth of target lesion are the main factors guiding the choice of light wavelength. From UV to infrared band, the penetration depth of light in tissue grows with the increase of wavelength. Lights with longer wavelength such as red and infrared are more suitable for tumor targeted PDT. For vascular target PDT, green light and blue light are widely used in clinic and red light is selected sometimes. The selection of light wavelength should be mainly based on the depth of the targeted vessel. The effect of the hemoglobin absorption on light penetration depth and the excitation effect on photosensitizer should also be taken into consideration. In general, the effect of light dose on efficacy/side effect is more significant for PDT with photosensitizer intravenously injected than for the

topical PDT. As to topical PDT, the main factor affecting the therapeutic effect is the diffusion depth and concentration gradient of photosensitizer in target tissues.

The comparison between pulsed laser and continuous laser guided PDT in therapeutic efficiency has been controversial. Current clinical experience and experimental results in solution suggest that under the same fluence rate, the PDT effect of pulsed laser of nanosecond pulse is lower than that of continuous laser. For the pulsed laser of microseconds pulse, no obvious difference is observed [29].

In conclusion, the dose–response relationship of PDT is complex. Real-time monitoring is an important mean to improve the effectiveness and accuracy of PDT. Many studies have been carried out with a view to establish non-invasive monitoring platform for the detection of fluence rate, photosensitizer fluorescence intensity, oxygen content, and the signals of single oxygen yield during PDT.

13.1.2.2 Mechanisms of LED-Mediated Photodynamic Therapy

Theoretically, both LED and laser are electromagnetic waves although they are different in collimation and monochromaticity. The mechanisms of PDT reactions are consistent. The following is a brief introduction on the mechanisms of PDT for different biological effects.

13.1.2.2.1 Anti-Tumor Photodynamic Therapy

At present, the mechanism of anti-tumor effect mainly includes: direct killing of tumor cells, tumor vascular damage, inflammatory response, and subsequent anti-tumor immune response. The latter three functions play important roles for a sustainable tumor destruction and long-term control of tumor.

13.1.2.2.1.1 Direct Killing of Tumor Cells

PDT-induced direct killing of tumor cells is mainly divided into three types: necrosis, apoptosis, and autophagy related cell death. The direct damage is confined to the locations where photosensitizers are localized because of the limited oxygen lifetime (approximately 10–320 ns) and the limited diffusion distance (10–55 nm in cells) [30]. For most photosensitizers, cell membrane, mitochondria, and lysosome are the most sensitive subcellular structure of PDT, and other organelles, such as endoplasmic reticulum, microtubules, ribosomes, and nucleuses might also be damaged. In general, the photosensitizers located in mitochondria and endoplasmic reticulum will induce apoptosis, and the photosensitizers located in the cell membrane and lysosomes may induce necrosis. Nevertheless, it is not absolute as mitochondrial damage or high doses of PDT can also lead to necrosis.

13.1.2.2.1.2 Vascular Closure Effect

In the 1960s, scientists discovered the vascular effect of PDT. It was observed that PDT can damage tumor cells as well as cause slowing-down of microvascular blood flow, aggregation of platelet, and shutdown of lumen [31]. Further studies have shown that PDT can damage endothelial cells and shut down microvascular.

13.1.2.2.1.3 Inflammatory Response and Anti-Tumor Immunity

PDT-induced inflammation is initiated from the increase of tumor vascular permeability, which leads to the gathering of circulating neutrophil and a large release of inflammatory mediators, affects inflammatory cells (neutrophils, mast cells, macrophages, etc.) and expands the inflammatory response [32]. Despite the fact that the photosensitizers are mainly located in tumor cells, PDT still have the same effect. Its inflammatory response is mainly activated by the photooxidation damage around the blood vessels, and it also reaches the vascular endothelium through the gradient of chemotaxis. Local tissue edema after PDT is an expression of inflammatory response. Inflammatory cells will quickly gather in large quantities in tumor tissues when the damaged tumor cells are removed. The role of neutrophils is particularly important. Neutrophils can release a large number of oxygen free radicals, peroxidase, and lysosomal enzyme in tumor tissues, which are directly involved in the destruction of tumor tissues. It can also release cell chemotactic agent to raise more inflammatory cells and immune cells to enhance anti-tumor immune inflammatory response and induce the follow-up reactions. The anti-tumor immune response induced by PDT is based on the inflammatory response. There are two types of immunity: innate immunity and acquired immunity.

13.1.2.2.2 Vascular Targeted Photodynamic Therapy

The mechanism of the selective microvascular effect of PDT is based on the difference of the concentration of photosensitizers inside and outside the vessel. The difference will appear in a period of time after intravenous injection of photosensitizers. When light irradiation is initiated, photosensitizers in normal tissues surrounding the vessels will be rapidly photobleached while intravascular photosensitizers being constantly supplied with the blood flow. Then, a large amount of reactive oxygen will be generated only in the vessel. Vascular targeted PDT is applied in the treatment of Port Wine Stains [33] age-related macular degeneration [34] and vascular lesions in gastrointestinal mucous [35].

13.1.2.2.3 Anti-Microbial Photodynamic Therapy

At present, most of the researches on anti-microbial PDT are to explore the anti-microbial effect of various novel photosensitizers. Few studies focus on the

mechanisms of anti-microbial effect. It is generally believed that the anti-microbial effect of PDT is mainly induced by the oxidative damage of biological macromolecular (such as protein and lecithin) or functional unit within the microbial cells. The photophysical and photochemical properties of photosensitizers and their targeting towards certain microbial cells are key factors for excellent anti-microbial effect.

13.2 Clinical Application of LED Light

13.2.1 LED Light in Low Level Light Therapy

Low level light therapy (LLLT) makes use of a relative low power density of light to treat diseases with the biological stimulation of light, which will not produce any irreversible damage. Being non-invasive, safe and painless, and, among other things, having no adverse reactions, LLLT has a wide range of clinical applications due to its anti-inflammatory, pain-relieving and detumescent functions and its role in promoting wound healing.

The most commonly used therapeutic light source for LLLT is laser light source, such as semiconductor lasers and He–Ne lasers. Therefore, LLLT is also called low level laser therapy. In recent years, some non-laser light sources like LED have also gradually been used clinically as LLLT light sources. LLLT is a physical therapy highly dependent on irradiation parameters (wavelength, power, power density, energy density, time, etc.) and more clinical evidences are needed to prove whether the efficacy of LED-based LLLT is comparable to that of laser-based LLLT. At present, LED-based LLLT is often used in the areas given below.

13.2.1.1 Neonatal Jaundice

Neonatal jaundice is attributed to abnormal metabolism of bilirubin that improves the neonatal blood bilirubin level, leading to typical emergence of yellow staining of skin, mucous membrane, and sclera. Blue LED is most effective in degrading bilirubin (28%), which is followed by cyan LED (18%), white LED (14%), and green LED (11%) in a decreasing order.

Kumar et al. evaluated whether LED light therapy is superior to conventional light therapy in reducing serum total bilirubin level of postoperative and preterm neonates (wavelength 430–490 nm, power density $\geq$30mW/cm^2) [36]. The result indicated that LED therapy had better therapeutic effect. Mohammadizadeh M compared LEDs with fluorescent phototherapy in the treatment of preterm infants with neonatal jaundice. The duration of phototherapy was the same. The results showed no significant difference was found in the rate of fall of bilirubin between these two methods. However, in terms of side effects, energy saving, service life, and cost, LED phototherapy was better and more promising than conventional phototherapy [37].

13.2.1.2 Emotion Cognitive Impairment

Recent studies highlight that human circadian rhythm systems are LED-sensitive [38]. The efficacy of LED phototherapy to treat seasonal affective disorder (SAD) was tested in a randomized, double-blind, and placebo-controlled multicenter trial. Subjects were 18–65 years old and randomly isolated for a week, The patients were placed 20 in. apart from the LED (1350 Lux visible white with a spectral peak of 464 nm and 564 nm). They were wakened up before 8 am every morning for 30 min' treatment. The observation was conducted 1, 2, 3, and 4 weeks, respectively, after the treatment. The results revealed that the subjects' symptoms were remarkably relieved.

There are evidences proving that three major types of brain diseases, namely traumatic events (stroke, traumatic brain injury, and global ischemia), degenerative diseases (dementia, Alzheimer's disease, and Parkinson's disease), and mental disorders (depression, anxiety, post-traumatic stress disorder) may benefit from the photobiomodulation (PBM) produced by skull illumination. PBM can be used even for cognitive enhancement in healthy people [10]. Schiffer et al. applied LED to patients with major depressive disorder and anxiety by having LED light on their forefronts (wavelength 810 nm, output power 1 W, power density 250 mW/cm^2, 4 min, energy density 60 J/cm^2) [39]. It was found that their Hamilton depression rating scale (HAM-D) and Hamilton anxiety rating scale (HAM-A) improved 2 weeks after a single treatment. According to a study report, the transcranial posterior LED therapy for chronic and mild traumatic brain injury (mTBI) would lead to a significant improvement of cognitive performance [40].

The details on the application of blue narrow-band LED phototherapy to treat SAD by Gena Glickman et al. were as follows: blue LED light, 468 nm, 607 mW/cm^2; red LED, 654 nm, 34 mW/cm^2; 45 min' treatment each morning for 3 week [41]. SIGH-SAD assessment and scoring was performed weekly. The result of the mixed-effect analysis showed that the SIGH-SAD score of the blue short-wavelength light treatment was remarkably higher than that of the red light treatment, and the depressive symptoms of the patients would be reversed when the light intensity was 607 mW/cm^2.The efficacy of the LED treatment may be related to increased cerebral blood flow [42, 43].

13.2.1.3 Wound Healing

Currently, the application of LED in wound healing is gradually increasing, including diabetic foot, refractory ulcer, adjuvant therapy after laser treatment, and surgery. Dixit et al. successfully cured a refractory ulcer about 3.6 cm × 3.8 cm of a 69-year-old male with Klippel-Trenaunay syndrome by using He–Ne laser in combination with LED [44]. The treatment parameters were as follows: LED 660 nm, power density 50 mW/cm^2, 6 min, energy density 22.8 J/cm^2; He–Ne laser 632.8 nm, 15 min, energy density 1.58 J/cm^2; twice a week; shift application of LED and He–Ne laser at an interval of 10 min. After about 7 months' treatment,

the ulcers completely healed and no recurrence was found, which was followed up for 8 months. Sutterfield reported that Charcot, a 66-year-old diabetic patient, was treated with LED (4.9 J/cm^2, 1.44 min) and his plantar ulcers was cured completely within 8 weeks after the treatment [45].

LED can effectively promote post-laser and post-operative wound healing. Trelles MA performed LED (633 nm, 20 min, 96 J/cm^2) adjuvant treatment for 5 metatarsophalangeal patients given Er: YAG laser therapy immediately and 2, 6, and 10 days after the laser treatment, respectively. On the sixth day after the operation, the wounds were significantly reduced and granulation tissues formed [46].

13.2.1.4 Acne

Acne is a common sebaceous gland disease with a prevalence of up to 80% in adolescents. In recent years, LED has been widely used in the treatment of acne. The combination of 415 nm blue and 633 nm red is the most commonly used LED group. Lee et al. treated 24 patients with mild to moderate and severe facial acne with 415 nm blue light (40 mW/cm^2, 48 J/cm^2) and 633 nm red light (80 mW/cm^2, 96 J/cm^2), which was given twice a week for 4 weeks, 20 min each time with one of the LED lights in shifts [47]. The final mean percentages of improvement in non-inflammatory and inflammatory lesions were 34.28% and 77.93%, respectively. In another study [48], subjects were given 8 alternating treatments with LED 415 nm blue light (20 min/time, 48 J/cm^2) and 633 nm red light (20 min/time, 96 J/cm^2), 3 times a week at an interval of 3 days. At week 4 and 12 after the treatment, the average number of lesions was reduced by 46% and 81%, respectively, and no apparent side effect was found. Sadick evaluated the efficacy of a combination of 415 nm blue and 830 nm near-infrared LEDs in the treatment of moderate acne [49]. The blue light (40 mW/cm^2) was applied for 20 min firstly and near-infrared light (55 mW/cm^2) was used for 20 min after an interval of 2–3 days, which lasted for 4 weeks. The results showed that the IR/blue LED combination did not improve the inflammatory lesions better than the red–blue LED combination, but had better efficacy on non-inflammatory lesions.

Compared with drugs and other treatments, LED has unique advantages in acne treatment. de Arruda et al. evaluated the safety and efficacy of blue light therapy and topical 5% benzoyl peroxide on grade II and grade III acne patients in a prospective, randomized, open, and comparative study [50]. The treatment parameters of the therapy were: 407–420 nm, 40 mW/cm^2, twice a week for a total of 8 treatments. The results showed that both the treatments were effective for grade II and III acne, but the adverse effects of light therapy were smaller. Another randomized trial of patients with acne vulgaris in China compared the efficacy of three light treatments for moderate to severe acne vulgaris [51]. Totally 150 patients were randomly divided into three groups and given PDT, IPL, or red–blue LED phototherapy on their right half faces, respectively. The patients were examined 1 and 3 months after the treatment. It was found that LEDs did not behave better than the other two phototherapy methods in terms of lesion clearance, treating course required, and

relapse rate. The PDT group had the highest rate of lesion clearance or the highest improvement of moderate acne vulgaris and the shortest average course of treatment a month after the treatment. In the PDT group, only 4 cases developed papules and pustules and no nodular pustular recurred 3 months after the treatment.

13.2.1.5 Facial Rejuvenation

Weiss et al. observed the effect of LEDs on photoaging of skin in a prospective study. A total of 90 patients were included in the study [52]. The parameters were set at: LED wavelength 590 nm, energy density 0.1 J/cm^2, continuous treatment of 8 times for 4 weeks in total. The follow-up was performed 4, 8, 12, and 18 weeks and 6 and 12 months after the treatment, respectively. The digital imaging data showed that 90% of the subjects had reduced signs of photoaging, periorbital wrinkles, erythema, and pigmentation as well as smoother skin texture. The results of optical profilometry revealed a 10% increase in surface topography measurements. Histological data also showed a significant increase in collagen in the papillary dermis of all treated skin specimens.

In a spilt-face single-blind study, Barolet et al. evaluated the efficacy of 660 nm LEDs on 40 patients with skin photoaging [53]. The treatment was given 3 times a week, 4 weeks in total. The results showed that the wrinkle depth and surface roughness decreased in more than 90% of the patients, and the results of blinded assessment also revealed a decrease in severity Fitzpatrick wrinkle score in 87% of the patients.

In a prospective, randomized, placebo-controlled, double-blind clinical study, Lee et al. divided 76 patients with facial wrinkles randomly into four groups, of which the patients were given respectively 830 nm, 633 nm, 830 nm plus 633 nm light treatment and pseudo light treatment twice a week for 4 weeks [54]. The follow-up period was 3 months, during which the efficacy was evaluated via continuous photography, contour determination, and skin elasticity and objective measurement of melanin. The results showed a significant reduction of wrinkles (up to 36%) and increase of skin elasticity (up to 19%) in the three treatment groups based on a comparison to the baselines.

13.2.1.6 Scars

In Barolet's study, prophylactic low-level LED at the wavelength of 805 nm was used to treat keloids and hypertrophic scars or such scars left after carbon dioxide laser ablation. After the initial treatment, each scar of each patient was treated with LED for 15 min a day for 30 days (805 nm, 30 mW/cm^2). The therapeutic effect was determined with VSS score, measurement of scar height, and quantitative assessment of skin morphology photographs, and the result was satisfactory [55]. Park et al. used 830/590 nm LED-LLLT to treat 35 patients with scars attributing to thyroidectomy [56]. From the first day after the surgery, the

patients were given 60 J/cm^2 (11 min) treatment per day for 1 week and then 3 times a week for 3 weeks. Colorimetric assessments were performed with tristimulus colorimeter and an assessment on scar formation was performed 1 and 3 months after the thyroidectomy, respectively. The results indicated that LED-LLLT was a safe method to inhibit scar formation after thyroidectomy.

13.2.1.7 Motor Functions

Leal-Junior et al. performed a systematic review with meta-analysis to investigate the effects of low-level laser therapy (LLLT) or narrow-band light-emitting diode therapy (LEDT) in modulating the activity-induced skeletal muscle fatigue or subsequently protecting against muscle injury [57]. Totally 13 randomized controlled trials (RCTs) (4 trials had the LED as light source) were included. Based on a comparison with the placebo, the time until exhaustion increased significantly by 4.12 s (95% CI 1.21–7.02, $p < 0.005$) and number of repetitions by 5.47 (95% CI 2.35–8.59, $p < 0.0006$) after the phototherapy. The most significant and consistent results were found with the application of red or infrared phototherapy before exercises with a power output of 50–200 mW and dose of 5–6 J per point (spot). Foley et al. assessed the effect of 830 nm light-emitting diode (LED) phototherapy on injured university athletes in a pilot study [58]. A total of 395 injuries were treated with 1669 sessions of 830 nm LED phototherapy (mean of 4.3 treatments per injury, range 2–6). The result showed that the average LED-mediated return to play (RTP) in the 65 subjects was 9.6 days, significantly shorter than the mean anticipated RTP of 19.23 days. Eighty-eight patients (78.5%) were either very satisfied or satisfied, and only 8 patients (7.2%) were dissatisfied. One limitation of the present study was the subjective nature of the assessments and the lack of control groups. Further controlled studies are expected to enable the confirmation and generalization of the desirable results from the present studies.

13.2.1.8 Pains

Leal-Junior et al. investigated the effects of the phototherapy combining the light sources of laser (905 nm) and LEDs (875 nm and 640 nm) in treating nonspecific knee pain [57]. Eighty-six patients rated 30 or greater on the pain VAS were recruited and included in the study. The patients in the LLLT group were given 12 treatments of active phototherapy (with 905 nm super-pulsed laser and 875 and 640 nm LEDs) and conventional treatment (physical therapy or chiropractic care), and those in the placebo group were treated in the same way but with placebo phototherapy devices. Pain assessments (VAS) were performed respectively at baseline and the fourth, seventh, and tenth treatments, after the completion of the treatments and at 1-month's follow-up. The results demonstrated that the combination of super-pulsed laser, red, and infrared LEDs was effective to decrease the knee pain of the patients and improve their quality of life.

13.2.2 Application of LED Light Sources in Photodynamic Therapy

The light source to be used for PDT has to meet these demands: (1) the wavelength of the light source should correspond well with the photosensitizer selected to achieve maximum excitation efficiency; (2) it has certain output power to meet the needs of PDT; and (3) it has accurate and convenient method of measurement. Besides a wide range of wavelength and large output powers, LED has such advantages as low cost and flexible structure. It can be predicted that LED will be more and more widely used in PDT.

13.2.2.1 Actinic Keratosis

Actinic keratosis (AK) is a kind of pre-cancerous damage caused by long-term sun exposure and damages to skin. Boasting excellent cosmetic effects, PDT is a first-line method currently recommended for treating actinic keratosis. PDT treatment of AK is an early use of LED as a source of light for PDT.

Pariser et al. evaluated the efficacy of the MAL (methyl-aminolevulinic acid) mediated PDT using red LED light [59]. Totally 49 patients with 363 AK lesions were given the illumination (630 nm, light dose 37 J/cm^2) at a distance of 5–8 cm from the skin for an average period of 8 min after MAL was applied at least 3 h. Repeated treatment was conducted 1 week later. At 3 months after the last treatment, the complete response of MAL-PDT of the lesions and patient were 86.2% and 59.2%, respectively.

In another study, the combined application of 633 nm LED and ALA was used to treat head and facial multiple non-hypertrophic AK. The lesions were exposed to the LED light of an irradiance of 1.3 mW/cm^2 for 45 min with a total fluence of 3.5 J/cm^2. All the 15 patients were improved after the first PDT session and only 2 patients required a second session to obtain satisfactory remission. None of the patients relapsed during the 3 months' follow-up period [60].

13.2.2.2 Acne

PDT is mainly used to treat severe acne at grade III–IV. The combination of 633 nm LED (50–70 J/cm^2, 66 mW/cm^2) and 10% ALA cream is the most commonly used PDT regimen for acne. Twenty-two percent of the patients had excellent effect on their first treatment, 34% on the second treatment, and some patients required more treatments. The treatment had trivial side effects, neither ulcer scar nor other obvious side effects were observed, the symptoms of recurrent patients were mild and the routine local treatment had a good response [61, 62].

In addition, the combination of LED (633 $\pm$ 3 nm, 126 J/cm^2, 66 mw/cm^2) and low concentration of ALA (3.6%) was also quite effective in treating acne. ALA

was locally applied for 1.5 h, and the irradiation was given for 20 min at an interval of 2 weeks, 3 times in total. The results showed no difference between the acne of different degrees in therapeutic effect, and the therapy was applicable to moderate to severe acne with mild side effects [63, 64].

The combination of LED with chlorophyll for acne has also been reported. After topical application of chlorophyll for 30 min, blue light (430 ± 10 nm, 600 mW/cm^2, 1170 J/cm^2) combined with red light (660 ± 10 nm, 650 mW/cm^2, 1080 J/cm^2) was used to Illuminate the face for 30 min twice a week for 8 times. The results showed that the acne lesion count, severity grade, and sebum level were significantly lower in the PDT group than in the LED group and the side effects were tolerable [65].

13.2.2.3 Basal Cell Carcinoma

Basal cell carcinoma is a type of low-grade basal cell malignancy. Boasting good curative and cosmetic effect, PDT is the recommended first-line therapy for low-risk multi-focal superficial basal cell carcinoma.

The LED parameters used for the routine treatment include: 630 nm, 37 J/cm^2; illumination for 7–9 min; 20% ALA or MAL as the photosensitizer and partially encapsulated for 3 h; twice of treatment at an interval of 1 week [66]. There is a study on the comparison between the LED-based PDT (630 nm, 30 mW/cm^2, 150 J/cm^2) and 585 nm PDL-based PDT (spot diameter 7 mm, 10 J/cm^2, 10% overlap, 3 scans) in the treating effect on basal cell carcinoma. The parameters adopted in the study include: topical application of 20% 5-ALA; PDL-PDT treatment of 3–5 min; LED-PDT treatment of 65 min. The treating effect of the two methods is similar. Basal cell carcinoma completely disappeared 3 or 12 months after the treatment. Despite a slightly higher pain index and longer treating duration, LED-PDT had a lower recurrence rate than PDL-PDT [67].

For nodular basal cell carcinoma, certain physical methods are needed as supplementary treatment. There were studies on combined application of LED-PDT and skin grinding to treat nodular basal cell carcinoma of nose. Firstly, tumor lesions were removed via skin grafting, and then 20% aminolevulinic acid was locally applied for 3–4 h. Finally, the site of the treatment was irradiation with LED (630 ± 10 nm, 100 J/cm^2) for 20 min. The treatment was given once a week for 3 weeks. One year later, the tumor recurrence and scar formation were evaluated. The results showed that the wound healed quickly, the postoperative recurrence rate was low, and patient satisfaction was high.

13.2.2.4 Oral Antibacterial Therapy

In a study, a combination of LED and curcumin as a photosensitizer was adopted for oral antibacterial treatment. The subjects were divided into three groups: LED plus curcumin group, LED group, and curcumin group. The LED parameters were:

455 ± 30 nm, 600 mW/cm^2, 200 J/cm^2; irradiation area: 0.6 cm^2; irradiation time: 5 min; curcumin concentration: 30 mg/l. The patients in the PDT group were asked to gargle with curcumin firstly and given LED irradiation 5 min later. The colony forming units in saliva samples were counted respectively before the treatment, immediately after the treatment, and 1 and 2 h later. Compared with that before the treatment, the count of the colony forming units of the PDT group immediately and 1 and 2 h after the treatment was significantly smaller. No effect was observed in the LED group. As to the curcumin group, the unit count of the colony formation increased rather than decreased 1 h after the treatment and dropped to the baseline level after 2 h. The results showed that the combined application of LED and curcumin was effective for oral disinfection [68].

There is a study on a combined usage of LED and curcumin for the antibacterial treatment of children given orthodontic tooth treatment. The subjects were divided into three groups: 2% chlorhexidine group, placebo group, and LED plus curcumin (1.5 mg/ml) group (LED parameters: 450 nm, 165 mW/cm^2, 96 J/cm^2). The patients were given the treatment weekly for 4 weeks. A follow-up was performed 1 and 3 months after the treatment, respectively, the plaque accumulation was evaluated with plaque index (PI), and gingival conditions were evaluated with gingival bleeding index (GBI). The results showed that there was no significant difference in dental plaque index between the LED plus curcumin group and the other two groups at month 1 follow-up, but the plaque index was significantly higher than the other two groups at month 3 follow-up. The result of gingival bleeding index evaluation showed that the gingival bleeding level of the LED plus curcumin group and the chlorhexidine group at month 1 follow-up was significantly lower than the basic level of bleeding gums, but no significant difference existed at month 3 follow-up. In conclusion, with a main function of reducing gum bleeding, the anti-microbial treatment of LED in combination with curcumin has short-term effect for children given orthodontic treatment.

13.2.2.5 Bactericidal Treatment for Deep Caries

Deep dental caries sterilization is rather difficult. There is a study on the combined application of LED and toluidine blue to kill bacteria caused by dental caries. In the experiment, the subjects were divided into two groups: LED plus toluidine blue group and LED plus saline group as the control group. After the infiltration of 10 μl toluidine blue (100 μg/ml) or 10 μl saline in the cavities for 5 min, irradiation of LED (parameter: 630 nm, output power 150 mW, 94 J/cm^2) was given 2 mm away from the cavities. The amount of live bacteria, Streptococcus mutans, and lactic acid bacteria colonies were counted immediately before and after the treatment. The results showed that, compared with the control group, the amount of live bacteria and counts of colony forming units of Streptococcus mutans and Streptococcus lactis significantly decreased in the LED plus toluidine blue group. It was proven via the research that the combination of LED and toluidine blue was effective in

killing caries-caused bacteria [69]. However, a long-term study is needed to find out whether the method may prevent the further development of dental caries and even avoid the removal of dental caries.

13.2.2.6 Periodontitis

Periodontitis often leads to gingival recession and bleeding. Treating periodontitis with PDT is a clinical exploration. There is a study on treating periodontitis jointly with LED and methylaniline blue. In the experiment, the subjects were divided into two groups: LED plus toluidine blue group and LED group. The LED parameters used in the treatment were: 628 nm; 2000 mW/cm^2; 10 s per exposure; 40 s in total. The therapeutic effect was evaluated with the detection results of the periodontal bag depth and the bleeding and microorganism under the gums before the treatment and 1 week after the treatment. The results showed that the treatment of both the two groups improved significantly the depth of pocket and probe bleeding 1 week after the treatment, but the therapeutic effect of the PDT group was better. While both the methods being able to reduce the amount of a large variety of microorganisms, the effect of the PDT and red LED group was more obvious [70].

13.2.2.7 Denture Stomatitis

Denture use often induces denture stomatitis and is difficult to cure. In some studies, PDT was adopted to treat denture stomatitis, which had achieved good results via local fungal killing. One of the researches was carried out with LED and porphyrin derivatives. In the experiment, the subjects were divided into two groups: LED plus Photogem (500 mg/l) group and mycostatin group. The LED parameters were 455 nm and 102 mW/cm^2. The energy density of the denture irradiation was 37.5 J/cm^2 and that of the maxillary irradiation 122 J/cm^2. The treatment was given 3 times a week for 2 weeks. Nystatin (100,000 IU) was topically applied, 1 min at a time, 4 times per day for 2 weeks. To evaluate the therapeutic effect, caries and maxillary fungal culture and standard photographic treatment of the upper jaw were performed before the treatment and 15, 30, 60, and 90 days after the treatment, respectively. For both groups, the number of fungal colonies at the end of treatment was reduced significantly and the reduction was most pronounced 30 days after the treatment, and the comparison via pictures showed that the success rates of the two groups were similar. It was proven that PDT was as effective as topical application of nystatin in treating denture stomatitis, but the operating process of PDT was relatively cumbersome [71].

13.3 LED Medical Equipment

13.3.1 Application of LED Equipment in Medical Field

LED is currently the most efficient and energy-saving artificial light source, its light efficiency can reach 254 lm/W, the light spectrum of LED is relatively pure, and the half-wave width is only 10 nm or even more less. LED is also characterized by good direction, monochrome performance, fast response, little flicker, easy adjustment of color temperature, high reliability, long life, and so on, making it suitable for medical application as a light source. After decades of development, the medical application of LED focuses mainly in the following areas.

13.3.1.1 Lighting

Lighting includes indoor and outdoor lighting in hospital buildings, lesion observation lighting, and surgical procedure lighting. Lighting is the most common function of LED at present, but, compared with general lighting, medical lighting is somewhat particular in terms of market demand and access. For example, when a lesion is illuminated, the light source used has to be healthy and easy to adjust and control for the sake of preventing the damage from ultraviolet and infrared light. For operation process lighting, the requirements include good illumination, no shadow, high uniformity, easy adjustment of color temperature, and light intensity and low heat.

13.3.1.2 Disinfection and Sterilization

The reason to use LED for disinfection and sterilization lies mainly in the fact that the ultraviolet light passing through microbial cell membrane and nucleus may damage their DNA or RNA molecular chains, making them lose their ability to copy and other functions.

13.3.1.3 Phototherapy

As a new type of light source, LED, with its biological effects gradually recognized by people, is playing an active role in medical treatment. Phototherapy achieves therapeutic effects via a series of chemical reactions caused by the thermal and photochemical effects that appear as a result of the absorption of the energy of lights of different wavelengths by biological tissues.

13.3.2 LED Phototherapy Device

In recent years, with the rapid development of the third-generation semiconductor materials and technologies, new types of LED are introduced continuously. While the luminous intensity of LED being increasing, the peak wavelength is more and more stable, the half-wave bandwidth more and more narrow, and the monochromatic performance and direction function better and better.

LED also has a wide coverage of wavelength from UV to infrared, covering basically the full spectrum of visible light. At the same time, two-color light, three-color light, and white LED with excellent performance have also been developed. According to the different needs of phototherapy, single wavelength light source such as blue light, green light, red light and infrared light, or the combination of multi-wavelength light source are designed to treat the target diseases. It provides a solid hardware foundation for the wide application of LED device in phototherapy.

At the same time, LED can be used to form complicated geometric shapes, including but not limited to point, line, and plate, and can even be made into flexible soft light sources so as to change shape according to the shape of the treatment site, making the light irradiation more evenly. There are now three common LED-based phototherapy modes: top projection, LED bed, and LED blanket based on patched LED [72].

At present, LED phototherapy equipment mainly includes low-lever light therapy devices and photodynamic therapy devices. The main difference between them is that photodynamic therapy devices have to be used jointly with photosensitizers. Moreover, they need higher power, and their wavelength should match with the photosensitizer selected.

13.3.2.1 Low-Level Light Therapy (LLLT) Devices

13.3.2.1.1 Single Wavelength LED LLLT Devices

13.3.2.1.1.1 Blue LED Phototherapy Devices

Treating neonatal jaundice is a typical application of blue light device. Currently, there are many companies producing LED phototherapy systems, which are designed in diversified types such as blanket, projection, and bed type. The LED phototherapy systems designed in blanket type include the Bilisoft LED phototherapy system manufactured by the US GE Corporation and the neoBLUE blanket by the US Natus Company. The Bilisoft LED phototherapy system contains two sizes of blanket LED cold light source, their power densities are 35 and 50 $\mu W/cm^2/nm$, and their wavelengths range from 440 to 460 nm. Thanks to the soft carpet design and fiber conduction mode, phototherapy can be performed from a position close to children's skin (http://www3.gehealthcare.co.uk/en-gb/products/categories/perinatal_care/phototherapy/bilisoft_phototherapy_system). The neoBLUE blanket has a wavelength ranging from 450 to 475 nm and

a power density of 30–35 μW/cm^2/nm at the factory, which can be adjusted to more than 50 μW/cm^2/nm (http://www.natus.com/index.cfm?page=products_1&crid=583&contentid=657).

Projection design is currently used in most Blu-ray phototherapy devices, such as the Lullaby LED Phototherapy System of GE, which has a wavelength of 450–465 nm and a power density of 22–45 μW/cm^2/nm. The irradiation is in the range of 50 × 30 cm when the projection distance is 35 cm (http://www.natus.com/index.cfm?page=products_1&crid=189&contentid=90). Other projection phototherapeutic devices include Bilitron (wavelength: 400–550 nm) produced by Fanem, Select BiliBee (wavelength: 430–490 nm) by Medical Company, BiliLED (wavelength: 453–487 nm) by Controles Company, and so on.

Bilitron™ Bed 4006 produced by Fanem Company uses 17 Super LEDs with a wavelength of 450 nm and a power density of 47.5 ± 5 μW/cm^2/nm (http://www.ssemmthembu.co.za/index.php/product-ranges/phototherapy-led/fanem-bilitron-bed-4006). Bilitron 3006, another device designed by the company, is an ultra-compact portable phototherapy device using 5 Super LEDs with a wavelength of 460 nm. Bilitron 3006 can be used alone or be fixed on an adjustable bracket, which makes it highly adaptable (http://www3.gehealthcare.co.uk/en-GB/Products/Categories/Perinatal_Care/Phototherapy/Lullaby_LED_Phototherapy_System#tabs/tabD7FF1A1F7C8A425DB477CD6C8AC4FCAE). The neoBLUE® cozy LED phototherapy system produced by Natus is a typical LED bed device, which has a wavelength of 450–470 nm and a power density greater than 30 μW/cm^2/nm (http://www.ssemmthembu.co.za/index.php/product-ranges/phototherapy-led/bilitron-3006-the-super-led-phototherapy).

In addition to the treatment of neonatal jaundice, blue LEDs are also used for patients with psoriasis such as the LED based on rechargeable battery array developed by Philips company in the Netherlands, which consists of 40 high-intensity array LED light source of a wavelength of 453 ± 5 nm and a power density up to 50 mW/cm^2. The device was inserted into the hole in the middle of the textile fixing belt and bound through the fixing belt on the surface of the lesion skin to be irradiated [73].

13.3.2.1.1.2 Red LED Phototherapy Devices

Red light has a wavelength ranging from 600 nm to 760 nm, and the LEDs of this wavelength are used to treat various diseases. For example, the FDA has approved the use of Omnilux Revive™ at 633 nm for skin rejuvenation, which has an output power density of 105 mW/cm^2. Having been actively committed to the development of non-invasive LED phototherapy equipment since the late nineteenth century, the laser medicine department of the PLA General Hospital developed a wearable red LED phototherapy device in 2000, and a series of red band LED wearable products on this basis, such as the flexible and wearable hair-growing and sleeping-assisting head phototherapy system (Patent Application number 201610697781.3), the flexible and wearable phototherapy device (Patent Application No. 201610694853.9)

for lumbar muscle injury, the flexible and wearable phototherapy device (Patent Application No. 201610694879.3) for osteoarthrotic diseases, and the flexible and wearable phototherapy device (Patent Application No. 201610695946.3) for elbow joint injuries.

13.3.2.1.1.3 Infrared LED Phototherapy Devices

At present, there are few independent infrared LED phototherapy devices, which are usually used jointly with lights of other wavelengths. The 980 nm near-infrared MIRE (monochromatic infrared energy) treatment system (Anodyne® Therapy/MIRE™) produced by Anodyne® Therapy was approved for clinical use by the FDA in 1994. Being the first near-infrared therapeutic apparatus approved by FDA, it is widely used in the USA. Anodyne® Therapy/MIRE™ contains multiple flexible touch pads. The device is mainly used to improve circulation and relieve pain, stiffness, and muscle spasm.

Moreover, Omnilux Plus™ (830 nm, power 55 mW/cm^2), one of the near-infrared phototherapy equipment, is used for rejuvenation and promoted wound healing. The Omnilux Rehabilitation System (Photo Therapeutics, Limited, Altrincham, UK) with a wavelength of 830 nm ± 8 nm is used in clinical studies on various sports injuries, including tendons, muscle tears and injuries, back pain, and joint pain.

13.3.2.1.2 Multi-Wavelength LED Phototherapy Devices

With the progress of science and technology, multiple LED chips with different wavelengths can integrate into one LED device, which can meet the needs of different combinations of phototherapy.

For example, Lutronic's Healite II uses 1800 LEDs having the wavelengths of 830/590 nm, 633 nm, and 415 nm, which is supported with the patented optical lens array technology (OLAT) to collimate the light output from the LED and improve the optical transmission efficiency. In addition, the photo-sequencing technology (PST) of the wavelength of 830/590 nm is also used. The working principle of the PST is to sequentially treat the cells with 590 nm light and continuously irradiate them with 830 nm after 1960s, which can be used for wound healing, pain relief, arthritis, hair regeneration, and other treatment (http://www.international.lutronic.com/healiteii) [74]. Dermalux's Dermalux® LED Phototherapy comprises 8 LED arrays, each having multiple 415 nm, 633 nm, and 830 nm LEDs. The main feature of the device is that the three wavelengths can be used independently or jointly depending on clinical purposes (http://www.dermaluxled.com/led-phototherapy.php).

The Omnilux (TM) System, a product of the USA, comprises 2000 LED arrays that provide 415 nm blue light, 633 nm red light, and 830 nm near-infrared light. It can be used to treat severe acnes based on a combined application of 415 nm

blue light and 633 nm red light, and skin photoaging by combining 830 nm near-infrared and 633 nm red light. Delphia Del SolTM manufactured by Edge Systems LLC of the USA is also a triple therapy system providing 430 nm blue light, 600–700 nm red light, and 700–1000 nm near-infrared light in a continuous manner, which can be used to treat skin photoaging. In addition, LIGHTWAVE Professional of the USA, consisting of the LED of 417 nm blue light, 630 nm red light, and 880 nm near-infrared light and providing the light in a pulsed manner, is also used for treating skin photoaging. Furthermore, devices of more wavelength composites have been developed such as Max7 (Flip4, Inc., Quebec, Canada), which is based on the visible light of 7 wavelengths ranging from 420 nm to 700 nm and also used for facial photoaging.

The Litebook® LED Phototherapy Instrument (The Litebook Company Ltd., Alberta, Canada) consists of 60 LEDs, having a wavelength ranging from 400 nm to 700 nm, a peak wavelength at 464 nm, and a sub-peak wavelength at 564 nm, is mainly used for the treatment of seasonal affective disorder (SAD) [38].

13.3.2.2 LED Photodynamic Therapeutic Devices

13.3.2.2.1 LED Photodynamic Therapeutic Devices of Single Wavelength

At present, the most common light source of PDT is laser due to desirable monochromaticity and the excitation wavelength of the absorption peak of suitable photosensitizers that may guarantee a high efficiency of the photosensitizers. In addition, for endoscopic and inter-organizational PDT, laser is undoubtedly the most suitable light source because it can be transferred to digestive tracts, respiratory tracts, and so on. For body surface irradiation, in addition to laser, LED is more and more used in the PDT for superficial skin-mucosal lesions.

13.3.2.2.1.1 Blue LED Photodynamic Therapeutic Devices

The Omnilux blue™ (Photo Therapeutics, Limited, Altrincham, UK) has a wavelength of 415 nm with the output intensity of 40 mW/cm^2 and dose range from 1 to 150 J/cm^2, which has been approved by the FDA for the treatment of superficial actinic keratosis based on 5-ALA-PDT [75, 76].

13.3.2.2.2 Red LED Photodynamic Therapeutic Devices

Red LED is mainly used in the photodynamic therapy of cancer. For example, in the USA, Omnilux PDT™ (633 nm) is to be approved for the treatment of nonmelanoma skin cancer (NMSC). Recently, Ambicare Health Ltd. has developed a portable adhesive PDT device for nonmelanoma skin cancer [77].

13.3.2.2.3 Hybrid Multi-Wavelength LED Photodynamic Therapeutic Devices

The BS-LED3E LED treatment instrument developed by Sincery International Limited may provide 940 nm infrared light, 630 nm red light, 590 nm yellow light, and 460 nm blue light with a maximum power density of 90 J/cm^2. The output light energy is divided into 10 levels and can be adjusted. The instrument has two independent treatment arms that allow simultaneous treatment of two different regions of the same patient or two patients, each having LEDs of 4 independent wavelengths (http://www.sincery.com/productdetails/beauty/44.html). The BS-LED2, a product of single-arm dual-wavelength design, provides both 630 nm and 470 nm light with an energy density of 64 J/cm^2 and 48 J/cm^2, respectively, and works for a set period of 1–90 min (http://www.sincery.com/productdetails/beauty/30.html). In addition, the LED-IA (Yage Optic and Electronic Technique, Wuhan, China) adopts a half-arc projection mode and uses lever-type electric control to adjust its height. It may provide the lights of 633 nm, 590 nm, and 417 nm with a power of 20–100 mW/cm^2, 10–40 mW/cm^2, and 25–120 mW/cm^2, respectively (http://www.yagelaser.com/content/?91.html).

References

1. H. Chung et al., The nuts and bolts of low-level laser (light) therapy. Ann. Biomed. Eng. **40**(2), 516–533 (2012)
2. W. Cannon, *The Wisdom of the Body* (W. W. Norton, New York, 1932)
3. T.C.Y. Liu et al., Homeostatic photobiomodulation. Front. Optoelectron. China **2**(1), 1–8 (2009)
4. T.C.Y. Liu et al., Photobiomodulation on stress. Int. J. Photoenergy **2012**, 628649 (2012). https://doi.org/10.1155/2012/628649
5. T.C.Y. Liu et al., Microenvironment dependent photobiomodulation on function-specific signal transduction pathways. Int. J. Photoenergy **2014**, 904304 (2014). https://doi.org/10.1155/2014/904304
6. T.C.Y. Liu, Y.Y. Kang, Functional photobiomodulation. Photomed. Laser Surg. **32**(9), 479–480 (2014)
7. T.C.Y. Liu et al., The mitochondrial $Na^+/Ca2^+$ exchanger is necessary but not sufficient for $Ca2^+$ homeostasis and viability. Adv. Exp. Med. Biol. **1072**, 281–285 (2018)
8. T.C.Y. Liu et al., Quantitative biology of exercise-induced signal transduction pathways. Adv. Exp. Med. Biol. **977**, 419–424 (2017)
9. C.Y. Liu et al., Self-similarity constant and quantitative difference and their applications in sports science. J. Phys. Educ. **24**(6), 72–78 (2017). in Chinese
10. M.R. Hamblin, Shining light on the head: photobiomodulation for brain disorders. BBA Clin. **6**, 113–124 (2016)
11. T. Karu, *The Science of Low-Power Laser Therapy* (Gordon and Breach Science, Amsterdam, 1998)
12. N. Lane, Cell biology - power games. Nature **443**(7114), 901–903 (2006)
13. X.L. Wang et al., Interplay between up-regulation of cytochrome-c-oxidase and hemoglobin oxygenation induced by near-infrared laser. Sci. Rep. **6**, 30540 (2016)

14. M. Huttemann et al., Phosphorylation of mammalian cytochrome c and cytochrome c oxidase in the regulation of cell destiny: respiration, apoptosis, and human disease, in *Mitochondrial Oxidative Phosphorylation: Nuclear-Encoded Genes, Enzyme Regulation, and Pathophysiology*, vol. 748, (Springer, New York, 2012), pp. 237–264
15. S.A. Wu et al., Cancer phototherapy via selective photoinactivation of respiratory chain oxidase to trigger a fatal superoxide anion burst. Antioxid. Redox Signal. **20**(5), 733–746 (2014)
16. W. De Haes et al., Metformin promotes lifespan through mitohormesis via the peroxiredoxin PRDX-2. Proc. Natl. Acad. Sci. U. S. A. **111**(24), E2501–E2509 (2014)
17. C. Yee, W. Yang, S. Hekimi, The intrinsic apoptosis pathway mediates the pro-longevity response to mitochondrial ROS in C. elegans. Cell **157**(4), 897–909 (2014)
18. B. Drew et al., Effects of aging and caloric restriction on mitochondrial energy production in gastrocnemius muscle and heart. Am. J. Physiol. Regul. Integr. Comp. Physiol. **284**(2), R474–R480 (2003)
19. L.A. Montoro et al., Infrared LED irradiation photobiomodulation of oxidative stress in human dental pulp cells. Int. Endod. J. **47**(8), 747–755 (2014)
20. G.Y. Luo et al., The effects of low-intensity He-Ne laser irradiation on erythrocyte metabolism. Lasers Med. Sci. **30**(9), 2313–2318 (2015)
21. V.Y. Arshavsky, T.D. Lamb, E.N. Pugh, G proteins and phototransduction. Annu. Rev. Physiol. **64**, 153–187 (2002)
22. S.S. Campbell, P.J. Murphy, Extraocular circadian phototransduction in humans. Science **279**(5349), 396–399 (1998)
23. T.C.Y. Liu, Y.Q. Gao, S.H. Liu, Light-cell interaction: quasi-hormone model and time theory. Proc. SPIE **2887** (1996). https://doi.org/10.1117/12.251944
24. Liu, T. C. Y., et al., Membrane mechanism of low intensity laser biostimulation on a cell. Simunovic Z. Lasers in Medicine, Surgery and Dentistry. Zagreb: European Medical Laser Association. 2003: p. 83–105
25. R. Duan et al., Signal transduction pathways involved in low intensity He-Ne laser-induced respiratory burst in bovine neutrophils: a potential mechanism of low intensity laser biostimulation. Lasers Surg. Med. **29**(2), 174–178 (2001)
26. S.N. Wu, D. Xing, Intracellular signaling cascades following light irradiation. Laser Photonics Rev. **8**(1), 115–130 (2014)
27. L.R. Braathen et al., Guidelines on the use of photodynamic therapy for nonmelanoma skin cancer: an international consensus. International Society for Photodynamic Therapy in Dermatology, 2005. J. Am. Acad. Dermatol. **56**(1), 125–143 (2007)
28. M.H. Abdel-Kader, *Photodynamic Therapy. From Theory to Application* (Springer, New York, 2014), pp. 102–103
29. D.F. Chen et al., Effects of pulse width and repetition rate of pulsed laser on kinetics and production of singlet oxygen luminescence. J. Innov. Opt. Health Sci. **9**(6), 1650019 (2016)
30. J.S. Dysart, M.S. Patterson, Characterization of Photofrin photobleaching for singlet oxygen dose estimation during photodynamic therapy of MLL cells in vitro. Phys. Med. Biol. **50**(11), 2597–2616 (2005)
31. V.H. Fingar et al., The role of microvascular damage in photodynamic therapy: the effect of treatment on vessel constriction, permeability, and leukocyte adhesion. Cancer Res. **52**(18), 4914–4921 (1992)
32. M. Firczuk, D. Nowis, J. Golab, PDT-induced inflammatory and host responses. Photochem. Photobiol. Sci. **10**(5), 653–663 (2011)
33. H.X. Qiu et al., Twenty years of clinical experience with a new modality of vascular-targeted photodynamic therapy for port wine stains. Dermatol. Surg. **37**(11), 1603–1610 (2011)
34. U. Schmidt-Erfurth, T. Hasan, Mechanisms of action of photodynamic therapy with verteporfin for the treatment of age-related macular degeneration. Surv. Ophthalmol. **45**(3), 195–214 (2000)
35. H.X. Qiu et al., Vascular targeted photodynamic therapy for bleeding gastrointestinal mucosal vascular lesions: a preliminary study. Photodiagn. Photodyn. Ther. **9**(2), 109–117 (2012)

36. P. Kumar, D. Chawla, A. Deorari, Light-emitting diode phototherapy for unconjugated hyperbilirubinaemia in neonates. Cochrane Database Syst. Rev. (12), CD007969 (2011). https://doi.org/10.1002/14651858.CD007969.pub2
37. M. Mohammadizadeh, F.K. Eliadarani, Z. Badiei, Is the light-emitting diode a better light source than fluorescent tube for phototherapy of neonatal jaundice in preterm infants? Adv. Biomed. Res. **1**(1), 51 (2012)
38. P.H. Desan et al., A controlled trial of the litebook light-emitting diode (LED) light therapy device for treatment of seasonal affective disorder (SAD). BMC Psychiatry **7**(1), 38 (2007)
39. F. Schiffer et al., Psychological benefits 2 and 4 weeks after a single treatment with near infrared light to the forehead: a pilot study of 10 patients with major depression and anxiety. Behav. Brain Funct. **5**(1), 46 (2009)
40. M.A. Naeser et al., Significant improvements in cognitive performance post-transcranial, red/near-infrared light-emitting diode treatments in chronic, mild traumatic brain injury: open-protocol study. J. Neurotrauma **31**(11), 1008–1017 (2014)
41. G. Glickman, B. Byrne, C. Pineda, et al., Light therapy for seasonal affective disorder with blue narrow-band light-emitting diodes (LEDs). Biol. Psychiatry **59**(6), 502–507 (2006)
42. A.S. Salgado et al., The effects of transcranial LED therapy (TCLT) on cerebral blood flow in the elderly women. Lasers Med. Sci. **30**(1), 339–346 (2015)
43. H. Nawashiro, K. Wada, K. Nakai, et al., Focal increase in cerebral blood flow after treatment with near-infrared light to the forehead in a patient in a persistent vegetative state. Photomed. Laser Surg. **30**(4), 231–233 (2012)
44. S. Dixit et al., Closure of non-healing chronic ulcer in Klippel–Trenaunay syndrome using low-level laser therapy. BMJ Case Rep. **2012**, bcr2012006226 (2012). https://doi.org/10.1136/bcr-2012-006226
45. R. Sutterfield, Light therapy and advanced wound care for a neuropathic plantar ulcer on a Charcot foot. J. Wound Ostomy Continence Nurs. **35**(1), 113–115 (2008)
46. M.A. Trelles, I. Allones, E. Mayo, Er:YAG laser ablation of plantar verrucae with red LED therapy-assisted healing. Photomed. Laser Surg. **24**(4), 494–498 (2006)
47. S.Y. Lee, C.E. You, M.Y. Park, Blue and red light combination LED phototherapy for acne vulgaris in patients with skin phototype IV. Lasers Surg. Med. **39**(2), 180–188 (2007)
48. D.J. Goldberg, B.A. Russell, Combination blue (415 nm) and red (633 nm) led phototherapy in the treatment of mild to severe acne vulgaris. J. Cosmet. Laser Ther. **8**(2), 71–75 (2006)
49. N. Sadick, A study to determine the effect of combination blue (415 nm) and near-infrared (830 nm) light-emitting diode (led) therapy for moderate acne vulgaris. J. Cosmet. Laser Ther. **11**(2), 125–128 (2009)
50. L.H. de Arruda et al., A prospective, randomized, open and comparative study to evaluate the safety and efficacy of blue light treatment versus a topical benzoyl peroxide 5% formulation in patients with acne grade II and III. An. Bras. Dermatol. **84**(5), 463–468 (2009)
51. L.H. Liu et al., Randomized trial of three phototherapy methods for the treatment of acne vulgaris in Chinese patients. Photodermatol. Photoimmunol. Photomed. **30**(5), 246–353 (2014)
52. R.A. Weiss et al., Clinical trial of a novel non-thermal led array for reversal of photoaging: clinical, histologic, and surface profilometric results. Lasers Surg. Med. **36**(2), 85–91 (2005)
53. D. Barolet et al., Regulation of skin collagen metabolism in vitro using a pulsed 660 nm led light source: clinical correlation with a single-blinded study. J. Invest. Dermatol. **129**(12), 2751–2759 (2009)
54. S.Y. Lee et al., A prospective, randomized, placebo-controlled, double-blinded, and split-face clinical study on led phototherapy for skin rejuvenation: clinical, profilometric, histologic, ultrastructural, and biochemical evaluations and comparison of three different treatment settings. J. Photochem. Photobiol. B **88**(1), 51–67 (2007)
55. D. Barolet, A. Boucher, Prophylactic low-level light therapy for the treatment of hypertrophic scars and keloids: a case series. Lasers Surg. Med. **42**(6), 597–601 (2010)
56. Y.J. Park et al., Prevention of thyroidectomy scars in Asian adults with low-level light therapy. Dermatol. Surg. **42**(4), 526–534 (2016)

57. E.C. Leal-Junior et al., Adjunctive use of combination of super-pulsed laser and light-emitting diodes phototherapy on nonspecific knee pain: double-blinded randomized placebo-controlled trial. Lasers Med. Sci. **29**(6), 1839–1847 (2014)
58. J. Foley et al., 830 nm light-emitting diode (led) phototherapy significantly reduced return-to-play in injured university athletes: a pilot study. Laser Ther. **25**(1), 35 (2016)
59. D. Pariser et al., Topical methyl-aminolevulinate photodynamic therapy using red light-emitting diode light for treatment of multiple actinic keratoses: a randomized, double-blind, placebo-controlled study. J. Am. Acad. Dermatol. **59**(4), 569–576 (2008)
60. C.D. Enk, A. Levi, Low-irradiance red LED traffic lamps as light source in PDT for actinic keratoses. Photodermatol. Photoimmunol. Photomed. **28**(6), 332–334 (2012)
61. X.L. Wang et al., Topical ALA PDT for the treatment of severe acne vulgaris. Photodiagn. Photodyn. Ther. **7**(1), 33–38 (2010)
62. L. Ma et al., Low-dose topical 5-aminolevulinic acid photodynamic therapy in the treatment of different severity of acne vulgaris. Photodiagn. Photodyn. Ther. **10**(4), 583 (2013)
63. S.Q. Tao et al., Low-dose topical 5-aminolevulinic acid photodynamic therapy in the treatment of different severity of acne vulgaris. Cell Biochem. Biophys. **73**(3), 701–706 (2015)
64. S.Q. Tao et al., Efficacy of 3.6% topical ALA-PDT for the treatment of severe acne vulgaris. Eur. Rev. Med. Pharmacol. Sci **20**(2), 225–231 (2016)
65. B.H. Song et al., Photodynamic therapy using chlorophyll-a in the treatment of acne vulgaris: a randomized, single-blind, split-face study. J. Am. Acad. Dermatol. **71**(4), 764–771 (2014)
66. E. Christensen et al., Guidelines for practical use of MAL-PDT in non-melanoma skin cancer. J. Eur. Acad. Dermatol. Venereol. **24**(5), 505–512 (2010)
67. A. Čarija et al., Single treatment of low-risk basal cell carcinomas with pulsed dye laser-mediated photodynamic therapy (PDL-PDT) compared with photodynamic therapy (PDT): a controlled, investigator-blinded, intra-individual prospective study. Photodiagn. Photodyn. Ther. **16**, 60–65 (2016)
68. D.P. Leite et al., Effects of photodynamic therapy with blue light and curcumin as mouth rinse for oral disinfection: a randomized controlled trial. Photomed. Laser Surg. **32**(11), 627–632 (2014)
69. M.A. Melo et al., Photodynamic antimicrobial chemotherapy and ultraconservative caries removal linked for management of deep caries lesions. Photodiagn. Photodyn. Ther. **12**(4), 581–586 (2015)
70. C. Mongardini, G.L. Di Tanna, A. Pilloni, Light-activated disinfection using a light-emitting diode lamp in the red spectrum: clinical and microbiological short-term findings on periodontitis patients in maintenance. A randomized controlled split-mouth clinical trial. Lasers Med. Sci. **29**(1), 1–8 (2014)
71. E.G. Mima et al., Comparison of photodynamic therapy versus conventional antifungal therapy for the treatment of denture stomatitis: a randomized clinical trial. Clin. Microbiol. Infect. **18**(10), E380–E388 (2012)
72. H.J. Vreman, R.J. Wong, D.K. Stevenson, Phototherapy: current methods and future directions. Semin. Perinatol. **28**(5), 326–333 (2004)
73. S. Pfaff et al., Prospective randomized long-term study on the efficacy and safety of UV-free blue light for treating mild psoriasis vulgaris. Dermatology **231**(1), 24–34 (2015)
74. W.S. Kim, R.G. Calderhead, Is light-emitting diode phototherapy (LED-LLLT) really effective? Laser Ther. **20**(3), 205–215 (2011)
75. H.S. Xiang et al., Led is applied to the development of light therapy. Beijing Biomed. Eng. **24**(4), 311–315 (2005)
76. T. Yan, LED light source is in the application of skin medicine. China Illuminating Society light biology, photochemical application research forum and ecological lighting forum (2013)
77. S.K. Attili, An open pilot study of ambulatory photodynamic therapy using a wearable low-irradiance organic light-emitting diode light source in the treatment of nonmelanoma skin cancer. Br. J. Dermatol. **161**(1), 170–173 (2009)

Chapter 14
Light-Emitting Diodes for Horticulture

Dongxian He, Toyoki Kozai, Genhua Niu, and Xin Zhang

14.1 Fundamentals and Challenges of LED Lighting Technology for Horticulture

Applications of light-emitting diodes (LEDs) in agriculture, horticulture, and fishery have been expanding since around 2010. Especially, its applications in greenhouse horticulture as supplemental light source to solar light and in plant factories with artificial lighting (PFAL) or indoor vertical farms as sole light source have been becoming more and more popular since around 2015.

In this section, fundamental concepts, methodology, challenges, and opportunities of LED applications in the PFAL are discussed. Useful information on LED lighting in the greenhouse horticulture can be obtained from a comprehensive and informative review paper consisting of 87 pages by Mitchel et al. [1] and from a book by Kozai et al. [2]. This section is a kind of concept article and a summary of recently published books by Kozai et al. [3] and Kozai [4].

D. He (✉)
Key Laboratory of Agricultural Engineering in Structure and Environment of Ministry of Agriculture and Rural Affairs, China Agricultural University, Haidian, Beijing, China
e-mail: hedx@cau.edu.cn

T. Kozai
Japan Plant Factory Association, c/o FC Center of Chiba University, Kashiwa, Chiba, Japan
e-mail: kozai@faculty.chiba-u.jp

G. Niu
Texas A&M AgriLife Research at El Paso, Texas A&M University System, El Paso, TX, USA
e-mail: gniu@ag.tamu.edu

X. Zhang
Beijing Research Center for Information Technology in Agriculture, Haidian, Beijing, China
e-mail: zhangx@nercita.org.cn

© Springer International Publishing AG, part of Springer Nature 2019

J. Li, G. Q. Zhang (eds.), *Light-Emitting Diodes*, Solid State Lighting Technology and Application Series 4, https://doi.org/10.1007/978-3-319-99211-2_14

14.1.1 Role of Light and Major Light Environmental Factors

In the greenhouse horticulture and the PFAL, light is provided to plants for controlling the growth and development, for protecting plants from pest insects and harmful small animals, and for providing comfortable working environments for humans. Role of light for plants can be categorized into 2 groups: energy source and signal source. Light as energy source is primarily provided for photosynthesis of plants where the light energy is converted to chemical energy of carbohydrates in plants. While, light as a signal source is provided to stimulate photoreceptors for photomorphogenesis, photoperiodism, phototropism, secondary metabolite production, and stomatal functioning, etc. Light signals captured by the photoreceptors initiate various kinds of biochemical metabolisms.

In the energy conversion phase, less than 10% of light energy captured by chlorophylls and carotenoids is converted into chemical energy in leaves. In other words, more than 90% of light energy absorbed by plants is converted to sensible or latent heat. In addition, a significant portion of light energy incident to the plant canopy is not absorbed by leaves, but absorbed by its surroundings. Thus, in the PFAL, improving the ratio of light energy received by leaves to the light energy emitted by the light source is of primary importance as well as the ratio of light energy fixed by leaves to the light energy absorbed by leaves. The former ratio is influenced by the plant canopy architecture and the design of cultivation space. The latter ratio is influenced by the environments and genetic traits of plants.

Major light environmental factors include:

1. Photosynthetic photon flux density (PPFD, μmol m^{-2} s^{-1}) with waveband from 400 nm to 700 nm;
2. Spectral distribution in the range between 300 nm and 800 nm;
3. Lighting cycle (photoperiod/dark periods);
4. Lighting direction (downward, sideward, and upward lighting).

In the PFAL, these light environmental factors at the plant canopy surface can be controlled fairly well. However, PPFD and its spectral distribution in the plant canopy are significantly influenced by the plant canopy structure and its optical characteristics [2].

14.1.2 Dry Mass Increase and Value-Addition of Plant by Lighting

Amount of light energy required in the energy conversion phase for photosynthesis to increase the dry mass or amount of carbohydrates of plants is roughly 100 times greater than that required as light signals for morphogenesis, etc. After receiving the light signals, plants switch on or off a biochemical pathway and affect the economic value of the produce.

In the plant production process, the energy conversion phase and signal transmission phase often occur concurrently. A basic strategy for LED lighting in plant production is to maximize the economic value of total produce, which is expressed by a product of unit economic value of produce and volume of salable (marketable) produce. Unit economic value of produce is influenced by, for example, the contents of particular secondary metabolites in the produce. The secondary metabolite content often increases under stressful environment for improving quality formation. While, the content of secondary metabolite such as hypericin in St John's wort (*Hypericum perforatum*), a medicinal plant, increases with the increasing temperature stress [5].

Only 30% of electric energy is reported to be converted by current LEDs for horticultural lighting to photosynthetic radiation (from 400 nm to 700 nm) in practice, although the percentage will be improved to around 40% in the near future. Furthermore, only a portion of photosynthetic radiation is received and absorbed by leaves of plants in the cultivation space [2]. As a result, the electricity cost in the PFAL accounts for about 25% of the total production cost [3]. Thus, there is much space to improve the electric and light energy use efficiencies in the PFAL and the greenhouse.

14.1.3 Basic Properties of LEDs Necessary for Design and Operation of PFAL

Basic properties of LED lamp and LED lighting system (consisting of LED lamps and luminaire) for the PFAL to be released by LED manufacturing companies as product label to the customers are listed in Table 14.1. The data on these properties are minimum requirements for lighting system design of the PFAL. A similar product label but with a wider view has been proposed for horticultural lamps including high pressure sodium, fluorescent, incandescent, and LED lamps by Both et al. [6].

The data on LEDs necessary for plant lighting but unnecessary for office/home lighting include: photosynthetic photon flux (μmol s^{-1}), photosynthetic radiation flux (W), photosynthetic photon number efficacy (μmol J^{-1}), and photosynthetic radiation energy efficiency (J J^{-1}). The photon-related data are necessary because photosynthesis, photomorphogenesis, etc. respond to photons, while energy-related data are necessary for energy management of the PFAL.

Table 14.1 Characteristics of LED lamp or LED lighting system (consisting of lamps and luminaire), to be released by LED manufacturing companies as product label, which are required for lighting design of PFAL (revised after Goto [7]). The figure in the right-hand column is strictly an example, and does not imply a representative or standard value

Item	Unit	Example
Temperature of ambient air	°C	25
Power characteristics		
Voltage	V (voltage)	200
Current	A (ampere)	0.16
Effective power consumption	W (watt)	32.0
Light characteristics		
Spectral distribution (300–800 nm) as a dataset	μmol m^{-2} s^{-1} nm^{-1}	In excel file
Percentages of UV (300–399 nm), blue (400–499), green (500–599), red (600–699), far-red (700–799), and near-infrared (800–1500)	–	0.25, 20, 40, 35, 4.5, 0.25
Angular distribution curves perpendicular to and parallel to LED tube[a], as a dataset	mol s^{-1} rad^{-1} (see note 1 for rad.)	In excel file
Photosynthetic photon flux (PPF)	μmol s^{-1}	48.0
Photosynthetic radiation energy (radiant) flux	W (=J s^{-1})	8.0
Luminous flux[b]	lm	450
Correlated color temperature (CCT)[c]	K	3000
Color rendering index (CRI or Ra)[c]	–	87.0
Efficiency/Efficacy		
Photosynthetic radiation energy efficiency (also called PAR energy efficiency)	J J^{-1}	0.35
Photosynthetic photon number efficacy	μmol J^{-1}	3.2
Luminous efficacy	lm W^{-1}	200
Maintainability: Product age (life time) (h) of 10% decrease in PPF, product age of malfunction (h), and waterproof and dust-proof characteristics		
Thermal characteristics: Lamp or package surface temperature—PPF curve		
Luminaire: The entire electrical light fitting, including all the components needed to mount, operate, and use		
Size, shape, and weight: Drawing and weight of package, and drawing of LED lamp		

[a]Radian: SI unit of plane angle; 1 rad (1 radian) = 57.3° = 180/π = 180/3.14
[b]lm: Lumen
[c]CCT and CRI are omissible for monochromatic LEDs

Table 14.2 Factors affecting the economic value of vegetables

	Factor	Example
1	Weight, size	Fresh/dry weight of salable and unsalable parts of plants
2	Shape, color, and texture	Plant height, leaf shape, stem/internode length, leaf area index, leaf thickness, pigment formation, color, and appearance
3	Functional components	Vitamin C (ascorbic acid), antioxidant substances such as polyphenols, carotenoids, polysaccharides, and minerals such as Fe and Mn
4	Physiological disorder	Edema (intumescence), white/black spots due to micronutrient deficiencies
5	Taste, flavor	Sugar (glucose, fructose, and sucrose), polysaccharides, aromas, amino acids, proteins, lipids, NO_3^-, K^+, and bitterness
6	Mouth feeling	Percent water (turgor pressure), cell wall thickness, and smoothness
7	Shelf life	Colony formation unit per gram

14.1.4 Complexity of Light Environmental Control

14.1.4.1 Purpose of Environmental Control

Purpose of environmental control of the PFAL is to obtain a maximum yield of produce sustainably with highest quality using minimum resources, resulting in minimum emission of wastes and minimum costs. In other words, its purpose is to achieve a maximum cost performance (CP) over a long time period. The CP is expressed by the equation:

$$\mathrm{CP} = \text{total sales/total costs} = \Sigma\,(\mathrm{UV}\,(i) \times \mathrm{AP}\,(i))\,/\,\Sigma\,(\mathrm{UC}\,(j) \times \mathrm{ARS}\,(j))$$

where UV (i) and AP (i) are, respectively, unit economic value of produce (i) and amount of salable produce (i) ($i = 1, 2, \ldots$), and UC (j) and ARS (j) are, respectively, unit cost of resource (j) and amount of resource (j) supplied to the PFAL ($j = 1, 2, 3, \ldots$). Thus, environmental control for maximum yield alone and/or highest quality alone do not bring about the highest CP. The unit economic value of produce and unit costs of resources affect the CP considerably, both of which change with time. Unit economic values of vegetables are affected positively or negatively by, for example, factors shown in Table 14.2.

14.1.4.2 Optimal PPFD as Affected by Other Environmental Factors

Net photosynthetic rate generally increases with increasing PPFD but is gradually saturated at a high PPFD, so that 80–90% of saturated PPFD is often considered to be optimal to obtain the highest CP. This optimal PPFD changes with other

environmental factors such as air temperature, vapor pressure deficit (relative humidity), CO_2 concentration, air current speed, and nutrient solution composition.

The optimal PPFD changes also with other light environmental factors (light quality, photoperiod, and lighting direction). Furthermore, the optimal PPFD changes significantly with growth stage, plant canopy architecture (leaf area, leaf angle, planting density, etc.), physiological status, and genetic characteristics (cultivar) of plants, etc.

As discussed above, the relationships among the environment, plant growth, quality of produce, and the CP are complicated, so that it is necessary to conduct a series of experiments with minimum labor hours to find an optimal combination of environmental factors (the number of factors is as many as 16 or more). In order to conduct a factorial experiment for 16 factors each with 3 levels, we need an experiment with $3^{\wedge}16$ (=43 millions) treatments. On the other hand, in the current LED lighting system, the electricity cost is significantly high, and light energy use efficiency is considerably low. Thus, developing a smart LED lighting system for the next-generation PFAL is crucial.

14.1.5 Challenges for Smart LED Lighting Systems

14.1.5.1 Starting Points

Some starting points to develop smart LED lighting systems are given as examples below:

1. The traditional idea of providing the light downward from the top to the plants is discarded. We may find unexpected plant responses useful for humans under controlled environments which have never occurred in nature. For examples, upward lighting, upward air current from underneath, monochromatic light lighting, dark period temperature much higher than photoperiod temperature, fluctuating CO_2 concentrations between 500 μmol mol^{-1} and 2000 μmol mol^{-1}, etc.
2. A large-scale experiment to reveal the environmental effects on plant traits is conducted during commercial production in a PFAL. This is possible by using an automated phenotyping system described later to measure the plant traits under unintentional or unavoidable fluctuations of environments and/or faint genomic variations.
3. During the above experiment, light quality, lighting cycle, lighting direction, and other environmental factors in a limited cultivation space are dynamically changed, and their time-series data on spatial fluctuations are recorded, and the plant responses are measured.
4. For the big data analysis, artificial intelligence (AI), multivariate statistical and mechanistic models are all used.
5. The database is connected with Internet, and the big data are shared with other groups.

14.1.5.2 Basic Ideas

As the first step, we assume that our objective of plant production in the PFAL is to maximize the dry weight of produce multiplied by its unit economic value per unit production cost. Then, basic ideas for the LED lighting system would be as follows:

1. Light energy be absorbed by plant leaves only;
2. Light energy be absorbed by all parts of all leaves equally even at high planting density with high LAI;
3. Environmental factors except light environmental factors be controlled to maximize the light energy use efficiency;
4. Time-dependent set points of light environmental factors (PPFD, light quality, lighting cycle, and lighting direction) be optimized to meet the objective of PFAL operation mentioned above.

When LEDs are installed at the ceiling of cultivation space, and the light is provided downward to the plant canopy with high LAI, most light energy is absorbed by upper leaves. In this case, total net photosynthetic rate or dry mass increase of plant canopy should be significantly lower compared to that of the plant canopy which receives the light equally by all parts of all leaves as mentioned in the above paragraph.

14.1.5.3 Simple Examples

A simple example of LED lighting system based on the basic ideas described above is a soft and movable plastic string with many LEDs at 1–2 cm intervals used for upward lighting in the PFAL. This LED lamp placed on the culture panel for upward lighting from underneath increased the dry and fresh weights of marketable portion of cos lettuce (*Lactuca sativa* L.) plants by retarding the senescence of lower leaves [8]. A similar but rigid bar-type LED lamp has been used for sideward (interplant) supplemental lighting in the greenhouse [9].

A small LED lamp with a small battery or fixed at one end of thin string can be placed at the central part of the crisp head lettuce or cabbage seedlings or young plants. Then, the LED illuminates the plant from the bottom center of head to all. With this inside-out lighting, the color of whole head will become green due to the production of chlorophylls in inner leaves. A similar effect can be expected by illuminating the head downward using green LED which penetrates the head (transmittance of a green leaf for green light is 30–40%) (Lunatic Asylumz et al., unpublished).

14.1.5.4 Smart LED Lighting System

Recent advancement of information and communication technology (ICT) are remarkable, which includes AI, big data mining, Internet of Things (IoT), virtual reality, camera/laser image capturing, and processing for intact measurement of plant architecture and physiological status. Advancement of omics (metabolomics, proteomics, transcriptomics, and genomics) is also remarkable. By introducing the abovementioned ICT and omics, we can challenge for developing a smart LED lighting system to search the time-dependent set points of environmental factors to maximize the CP under given constraints.

The smart LED lighting system for the PFAL is considered to be advantageous over the current LED lighting system, because the environmental factors, resource (electricity, light energy, CO_2, nutrient solution, and labor) supply rates and their use efficiencies, and plant responses can be measured continuously. These data are relatively accurate and can be used for big data mining using AI, multivariate analysis, and mechanistic models. Recent advancement of phenotyping technology is making it possible to get the time-series data of plant traits.

Plant phenotyping is defined as application of methodologies and protocols to measure a plant-specific trait noninvasively, ranging from the cellular level to canopy level, related to plant structure and function [10]. Plant traits include contents of water, nitrogen, chlorophyll, photosynthetic efficiency (PSII), leaf area, canopy structure, etc. These traits are often measured using image sensors including visible camera, spectroradiometry, light detection and ranging (LiDAR) device, visible to far-red hyperspectral camera, thermal camera, fluorescence, and 3D laser scanning, trichromatic (RGB) sensors.

The data on phenome (whole sets of expressions of the genome) obtained by phenotyping are related to the environmental data, and the related results can be used for improving the set points of environmental factors. The analyzed results can also be related with genome data to find a specific gene or a group of genes which are expressed under the specific environment. Then, we can use the gene or a gene group as a gene marker or gene markers for breeding and selection of a plant having a special trait.

Spatial variations of plant growth and other traits will become measurable by plant phenotyping as described above. Spatial variations of environmental factors in the PFAL are measurable already using relatively inexpensive sensors. On the other hand, it is costly to make the spatial variations of environments and resulting plant traits being negligibly small. Under the above conditions, we may discriminate the variations of plant traits due to environmental variations from those due to genetic variations. Then, the former information can be used to find the environmental effects on plant traits, which can be used for improving the set points of environmental factors. The latter information can be used for selecting plants with elite traits for breeding and genomic analysis.

14.2 Case Study: LED Lighting for Lettuce Seedlings in PFAL

In PFAL, seedling stage is often produced in an area separate from production area due to the differences in planting intensity and environmental conditions [11–14]. High-quality seedlings should be compact, with short internodes and firm stems, dark green leaves, and large white roots. Lighting environment (PPFD, quality, and photoperiod) influences seedling growth and quality, which affects subsequent growth and yield after transplanting. Effect of light quality on plant morphology and physiology is more complex compared with that of PPFD and photoperiod [15]. Lettuces have different morphological and physiological responses to specific spectrum, and they are more sensitive to red and blue lights than the other wavelengths [16]. However, monochromatic red or blue lights could not satisfy the requirement of normal plant growth. Leaf length, leaf width of the maximum leaf blade, stem length, and hypocotyl length were decreased with an increase of blue photon flux in lettuce seedlings, and the pattern is likely attributed to blue photon flux which simulated cryptochrome photoreceptor [17, 18]. Cucumber seedlings under red light had unexpected greater plant height, hypocotyl, and epicotyl length than seedlings under the combination of red and blue light [13]. Red light at seedling stage also decreased leaf thickness, palisade tissue, and inhibited chloroplast development and delayed flowering time of female flower of cucumber plant [19]. The combination of red and blue lights had been investigated by many researchers in lettuce [16, 20, 21]; as a general trend, the biomass accumulation of lettuce was decreased with the increase of blue photon flux. Nevertheless, many researchers focus on the light environment at vegetative stage of lettuce, and different PPFDs, photoperiods, or light qualities were used at seedling stage [16, 21–23]. However, little is known about different PPFDs and photoperiods at seedling stage of hydroponic lettuce with its subsequent growth and nutritional values under LEDs with different light spectra.

In this and next sections, we are presenting two case studies, which are parts of a master graduate research project [24] and a doctoral dissertation [25]. The objectives were to investigate the effects of PPFD, photoperiod, and light quality on seedling quality and growth and the residual effects after transplanting on growth and nutritional values of hydroponic lettuce.

14.2.1 Plant Materials and Experiment Design

14.2.1.1 Plant Materials and Growth Conditions

Seeds of lettuce (*Lactuca sativa* L. cv. Frill ice) were sown in sponge cube (23 mm × 23 mm × 23 mm) filled with water in plastic containers (52 cm × 36 cm × 9 cm). After sowing, lettuce seedlings were randomly divided into nine treatments (Table 14.3 as Expt. 1) or 12 treatments (Table 14.4 as Expt. 2)

Table 14.3 Details of treatments: nine combinations of three photosynthetic photon flux density (P) and three photoperiods (H) for hydroponic lettuce seedlings grown under LED with R:B ratio of 1.2

Photosynthetic photon flux density	Photoperiod	DLI	
μmol m^{-2} s^{-1}	h day^{-1}	mol m^{-2} day^{-1}	Treatment symbol
150	12	6.48	P150-H12
200	12	8.64	P200-H12
250	12	10.80	P250-H12
150	14	7.56	P150-H14
200	14	10.08	P200-H14
250	14	12.60	P250-H14
150	16	8.64	P150-H16
200	16	11.52	P200-H16
250	16	14.40	P250-H16

Note: DLI (daily light integral, mol m^{-2} day^{-1}) = Photosynthetic photon flux density (μmol m^{-2} s^{-1}) $\times$ photoperiod (h day^{-1}) $\times$ 3600 (s h^{-1}) $\times$ 10^{-6}

Table 14.4 Details of treatments: photosynthetic photon flux density (PPFD), photoperiod (H), and light quality (light source with R:B ratio) for hydroponic lettuce at seedling stage

		PPFD	Photoperiod	DLI	
Lighting source	R:B ratio	μmol m^{-2} s^{-1}	h day^{-1}	mol m^{-2} day^{-1}	Treatment symbol
Fluorescent lamp	1.8	200	14	10.08	F1.8-P200-H14
		200	16	11.52	F1.8-P200-H16
		250	14	12.60	F1.8-P250-H14
		250	16	14.40	F1.8-P250-H16
LED	1.2	200	14	10.08	L1.2-P200-H14
		200	16	11.52	L1.2-P200-H16
		250	14	12.60	L1.2-P250-H14
		250	16	14.40	L1.2-P250-H16
LED	2.2	200	14	10.08	L2.2-P200-H14
		200	16	11.52	L2.2-P200-H16
		250	14	12.60	L2.2-P250-H14
		250	16	14.40	L2.2-P250-H16

for 20 days in a walk-in growth chamber (China Agricultural University, Beijing, China). One hundred lettuce seedlings were grown in each treatment. When the cotyledons were fully expanded, lettuce seedlings were transplanted to 128-cell trays, and they were placed in plastic containers (52 cm $\times$ 36 cm $\times$ 9 cm) containing nutrient solution. After 20 days of treatments, 35 uniform seedlings were transplanted from 128-cell trays to hydroponic cultivation beds with a planting density of 32 plants m^{-2}, and grown under PPFD of 250 μmol m^{-2} s^{-1} with photoperiod of 16 h day^{-1} provided by LEDs with R:B ratio of 1.2 (WR-LED-16W, Beijing Lighting Valley Technology Co., Ltd., China) for 20 days.

The air temperature and relative humidity at photoperiod and dark period were maintained at 22 ± 1 °C/18 ± 1 °C and 70 ± 5%/65 ± 5%, respectively, and CO_2 concentration was controlled at 800 ± 50 μmol mol^{-1} from seeding to harvest. A Yamasaki lettuce nutrient solution in pH of 6.0–6.5 and EC of 1.0–1.2 mS cm^{-1} was utilized as a standard solution. Pure water was used for the first 2 days after seeding. Then, a quarter strength of standard nutrient solution was used for the cotyledon stage, and one third strength was used for the 1–2 true leaves stage. When lettuce had 2–3 true leaves, half strength nutrient solution was used. After transplanting, a full strength nutrient solution was applied, and the nutrient solution was replaced every 10 days.

14.2.1.2 Treatment and Experiment Design

In Expt. 1, lettuce seedlings were grown under nine combination of three levels of PPFD at 150, 200, or 250 μmol m^{-2} s^{-1} and three photoperiods of 12, 14, or 16 h day^{-1} provided by LED lamps with R:B ratio of 1.2 (WR-LED-16W, Beijing Lighting Valley Technology Co., Ltd., China) for 20 days, a total of nine treatments (Table 14.3). In Expt. 2, lettuce seedlings were grown under combination of two levels of PPFD at 200 and 250 μmol m^{-2} s^{-1} and two photoperiods of 14 and 16 h day^{-1} under three kinds of artificial light with different R:B ratios for 20 days, a total of 12 treatments (Table 14.4). The three light sources are fluorescent lamp (T5-28W, Shanghai Flower and Biology Lighting Co., Ltd., China) with R:B ratio of 1.8 and two LED lamps with R:B ratios of 1.2 and 2.2 (WR-16W, Beijing Lighting Valley Technology Co., Ltd., China), respectively. Figure 14.1 shows the spectral distribution of different lamps determined for light wavebands ranging from 300 nm to 800 nm at 15 cm below the lamps with a PPFD of 250 μmol m^{-2} s^{-1} by using fiber spectrometer (AvaField-2, Avantes Inc., Apeldoorn, the Netherlands). The PPFDs were measured at 15 cm above the bench top which is the same to 15 cm below the lamps using a quantum sensor (LI-190SA, LI-COR Inc., Lincoln, NE, USA) connected to a data-logger (LI-1400, LI-COR Inc., Lincoln, NE, USA). Daily light integral (DLI) was calculated as follows:

$$\mathrm{DLI}\left(\mathrm{mol\ m^{-2}\ day^{-1}}\right) = \mathrm{PPFD}\left(\mathrm{\mu mol\ m^{-2}\ s^{-1}}\right) \times \mathrm{photoperiod}\left(\mathrm{h\ day^{-1}}\right) \times 3600\left(\mathrm{s\ h^{-1}}\right)/10^{6}.$$

14.2.1.3 Measurements for Lettuce Growth and Quality

Leaf length (LL) and leaf width (LW) of maximum leaf blade, leaf dry weight, and root dry weight were measured for 6 plants selected from each treatment at 20 days after sowing (DAS). Leaf fresh and dry weights, root fresh and dry weights, and contents of nitrate N, vitamin C, and soluble protein were determined for 6 lettuce

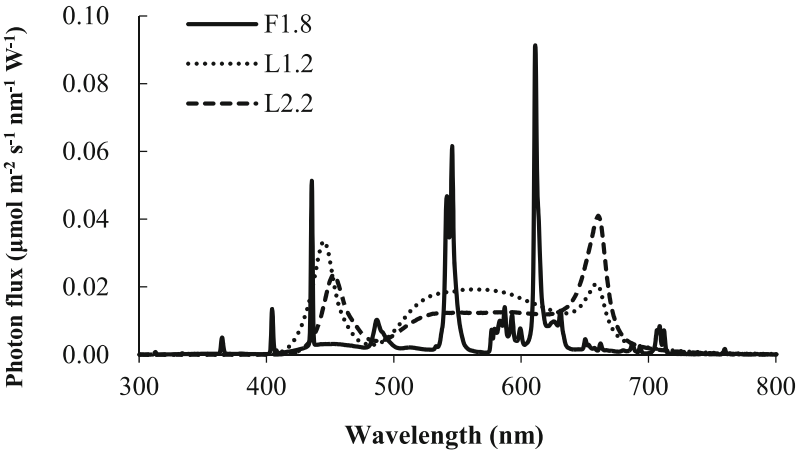

Fig. 14.1 Spectral distribution of fluorescent lamp with R:B ratio of 1.8 (F1.8), and two LED lamps with R:B ratios of 1.2 and 2.2, respectively (L1.2 and L2.2)

plants selected from each treatment at 40 DAS in Expt. 1. Lettuce quality indicators such as nitrate N, vitamin C, soluble sugar, soluble protein, and anthocyanin contents were determined for all treatments, six replicates per treatment, sampled on the seventeenth day after transplanting in Expt. 2. Nitrate N content was determined at wavelength of 410 nm by using a spectrophotometer (UV3150, Shimadzu Productions Co., Japan) based on coloration method of sulfosalicylic acid [26]. Vitamin C content was determined by the 2,6-dichlorophenol indophenol titration method [26]. Soluble sugar content was determined at wavelength of 630 nm by using the same spectrophotometer based on anthrone-sulfuric acid colorimetry method [26]. Coomassie Brilliant Blue G-250 dye method [26] was used to measure soluble protein content at wavelength of 595 nm by using the same spectrophotometer.

14.2.2 Effect of Lighting Environment at Seedling Stage on Leaf Morphology and Growth of Lettuce Seedlings

In Expt. 1, PPFD and photoperiod significantly affected morphology and growth of lettuce seedlings (Fig. 14.2). Leaf length was longest and ratio of leaf length to leaf width was greatest in the treatment of P150-H12, and they decreased with the increase of PPFD or photoperiod. LL and LL/LW decreased with the increase of DLI in a logarithmic fashion. LL and LL/LW at initial DLI of 6.48 mol m^{-2} day^{-1} were 46.5% and 70.2% higher than those under DLI of 14.4 mol m^{-2} day^{-1}, which was in treatment of P250-H16, the highest DLI among all treatments. Leaf and root dry weights at 20 DAS in Expt. 1 were highest in treatment of P250-H16 and lowest

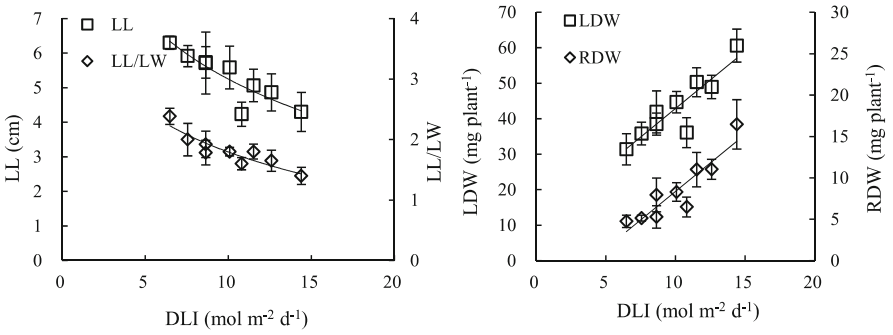

Fig. 14.2 Relationships between daily light integral (DLI) and leaf length (LL), ratio of leaf length to leaf width (LL/LW), and leaf dry weight (LDW) and root dry weight (RDW) of hydroponic lettuce transplants at 20 days after sowing. Regression equations are: LL = −2.53 * ln(DLI) + 11.07 (R^2 = 0.79), and LL/LW = −ln(DLI) + 4.09 (R^2 = 0.84), LDW = 3.22 × DLI + 10.65 (R^2 = 0.81), and RDW = 1.38 × DLI-5.41 (R^2 = 0.83)

in treatment of P150-H12. Both leaf and root dry weights increased linearly with DLI. Leaf and root dry weights at DLI of 14.4 mol m^{-2} day^{-1} were 93% and 244% higher than those grown at DLI of 6.48 mol m^{-2} day^{-1}, respectively.

In Expt. 2, light quality significantly influenced LL and LW but not LL/LW (Table 14.5). Generally, lettuce seedlings grown under FL were bigger regarding leaf size and accumulated more dry weight in both leaves and roots compared to those grown under LEDs. Higher PPFD led to a lower LL with the same photoperiod under FL and LEDs with R:B ratio of 2.2, and no significant difference was found in LL under LEDs with R:B ratio of 1.2. Under LED with R:B ratio of 1.2, higher PPFD led to lower LL/LW with the same photoperiod. Under FL and LED at R:B ratio of 1.2, no significant differences in LW were found among treatments. At LEDs with R:B ratio of 2.2, LW was smallest in the treatment of L2.2-P200-H16, followed by L2.2-P250-H16. Generally, higher PPFD resulted in lower LL/LW, regardless of light source. Leaf dry weight was higher in the treatment of F1.8-P200-H16, followed by F1.8-P250-H14 and F1.8-P250-H16. Root dry weight was highest in the treatment of F1.8-P200-H16 among all treatments. Higher PPFD led to higher root dry weight under LEDs with R:B ratio of 1.2.

Seedlings with high quality should have a higher dry mass and lower LL/LW. Our results showed that leaf and root dry weight increased linearly with the increase of DLI, and LL and LL/LW decreased with DLI in a logarithmic fashion, which agreed with the study reported by Kitaya et al. [27]. PPFD plays an important role for seedling morphology and growth. Low PPFD inhibits plant growth and productivity, whereas excess PPFD has detrimental effects on the photosynthetic apparatus, and plants have developed sophisticated biochemical and physiological mechanisms in order to adapt to the light environment [28–30]. Health index, dry weight, and fresh weight of young tomato plants increased with the increase of PPFD, and they were superior in plants grown under 300, 450, and 500 μmol m^{-2} s^{-1} than those under

Table 14.5 Effects of photosynthetic photon flux density (PPFD), photoperiod (H), and light quality (LQ) during seedling stage on leaf morphology and dry weight of hydroponic lettuce transplants at 20 days after sowing

Treatment	Leaf length cm	Leaf width cm	LL/LW	Leaf dry weight mg plant^{-1}	Root dry weight mg plant^{-1}
F1.8-P200-H14	7.75 ± 0.63 a	6.12 ± 0.67 a	1.28 ± 0.14 ab	242.0 ± 44.3 c	31.7 ± 7.4 c
F1.8-P200-H16	7.55 ± 0.33 ab	6.50 ± 0.42 a	1.16 ± 0.11 bc	317.7 ± 34.3 a	42.5 ± 6.9 a
F1.8-P250-H14	7.07 ± 0.41 b	6.42 ± 0.47 a	1.13 ± 0.10 cd	274.5 ± 41.1 b	40.5 ± 10.0 a
F1.8-P250-H16	6.73 ± 0.69 c	6.44 ± 0.74 a	1.02 ± 0.05 d	267.2 ± 50.3 bc	34.1 ± 10.3 b
L1.2-P200-H14	6.78 ± 0.25 c	5.30 ± 0.22 d	1.27 ± 0.12 ab	177.2 ± 25.7 e	23.1 ± 5.4 d
L1.2-P200-H16	6.70 ± 0.28 cd	5.00 ± 0.52 d	1.34 ± 0.08 a	222.1 ± 34.4 cd	27.4 ± 3.5 cd
L1.2-P250-H14	6.40 ± 0.29 d	5.33 ± 0.25 d	1.14 ± 0.05 c	192.9 ± 21.7 de	31.9 ± 4.0 c
L1.2-P250-H16	6.38 ± 0.41 d	5.36 ± 0.24 cd	1.16 ± 0.04 bc	255.4 ± 32.6 bc	34.8 ± 5.1 ab
L2.2-P200-H14	7.73 ± 0.28 a	6.00 ± 0.43 ab	1.29 ± 0.08 ab	197.1 ± 13.4 de	23.1 ± 5.1 d
L2.2-P200-H16	6.82 ± 1.02 c	5.33 ± 0.73 d	1.29 ± 0.21 ab	224.3 ± 24.7 cd	30.9 ± 5.1 c
L2.2-P250-H14	7.03 ± 0.50 b	5.94 ± 0.26 b	1.17 ± 0.07 b	233.8 ± 34.6 cd	31.6 ± 6.5 c
L2.2-P250-H16	5.98 ± 0.25 e	5.50 ± 0.37 c	1.09 ± 0.09 cd	208.7 ± 14.7 d	30.8 ± 11.2 c
ANOVA					
PPFD	*	NS	*	NS	*
H	*	NS	NS	*	NS
LQ	*	*	NS	*	*
PPFD × H	NS	NS	NS	*	*
PPFD × LQ	NS	NS	NS	NS	NS
H × LQ	*	*	NS	NS	NS
PPFD×H × LQ	NS	NS	NS	NS	NS

Note: Means with different letters in the same columns were significantly different tested by LSD's multiple comparison at $P \leq 0.05$. NS, * represent no significant and significant difference at $P \leq 0.05$, respectively

50, 150, 200 μmol m^{-2} s^{-1} [31]. Our study showed that lettuce seedlings grown at PPFD of 150 μmol m^{-2} s^{-1} with photoperiod of 12 h day^{-1} resulted in longest LL and greatest LL/LW, an undesirable trait for seedlings. These adaptations maximized the capture of available light to meet the demand for photosynthesis [32]. Kitaya et al. [27] found that dry mass, percent dry mass, and leaf number increased linearly as DLI increased at 21 DAS. In addition to lettuce, linear relationships between shoot dry weight and DLI were also found in petunia seedlings and pansy seedlings [33].

14.2.3 Effects of PPFD and Photoperiod at Seedling Stage on Mature Lettuce Growth and Quality

Leaf and root fresh weights at 40 DAS were significantly affected by PPFD and photoperiod during seedling stage (Table 14.6). Leaf and root fresh weights were greatest in treatment of P200-H16. Leaf fresh weight reached to 96 g $plant^{-1}$ in treatment of P200-H16, which was 26.8% and 17.3% higher compared with those grown in treatments of P150-H16 and P250-H16, respectively. The PPFD levels during seedling stage did not affect the leaf and root dry weights of mature lettuce plants at 40 DAS. However, photoperiod of 16 h day^{-1} resulted in higher leaf and root dry weights compared to that at photoperiod of 12 and 14 h day^{-1}.

PPFD and photoperiod during seedling stage affected vitamin C content significantly but not nitrate content. Lettuce seedlings grown under a photoperiod of 12 h day^{-1} had lower vitamin C content compared to those under a photoperiod of 16 h day^{-1}. No differences in vitamin C content were found among those under a photoperiod of 16 h day^{-1}. For soluble protein content, generally lower PPFD led to lower content, and photoperiod had no significant effect.

14.2.4 Effects of PPFD, Photoperiod, and Light Quality at Seedling Stage on Mature Lettuce Growth and Quality

PPFD during seedling stage affected leaf and root weights of mature lettuce at 40 DAS (Table 14.7). Among the three light sources, FL generally led to higher leaf fresh weight, followed by LEDs with R:B ratio of 2.2. Leaf fresh weights were biggest in treatments of L2.2-P200-H16, L2.2-P250-H14, and F1.8-P200-H16 and smallest in treatments of L1.2-P200-H14, L1.2-P250-H16, and L2.2-P250-H16. Lettuce seedlings grown at PPFD of 200 μmol m^{-2} s^{-1} with photoperiod of 16 h day^{-1} had higher leaf fresh weight than those grown at 250 μmol m^{-2} s^{-1} with photoperiod of 16 h day^{-1} at 40 DAS regardless of light quality. Root fresh weight grown under FL and LEDs with R:B ratio of 1.2 was higher than those under

Table 14.6 Effects of photosynthetic photon flux density (PPFD) and photoperiod (H) during seedling stage on subsequent growth and nutritional qualities of hydroponic lettuce at 40 days after sowing

Treatment	Leaf fresh weight g plant^{-1}	Root fresh weight g plant^{-1}	Leaf dry weight g plant^{-1}	Root dry weight g plant^{-1}	Nitrate content mg kg^{-1}	Vitamin C content mg 100 g^{-1}	Soluble protein content mg g^{-1}
P150-H12	59.59 ± 7.88 d	5.52 ± 0.52 d	1.74 ± 0.48 c	0.19 ± 0.04 bc	3066 ± 514 a	23.75 ± 1.64 d	4.48 ± 0.70 c
P200-H12	65.97 ± 3.81 cd	6.54 ± 0.70 d	1.95 ± 0.35 bc	0.20 ± 0.03 b	2594 ± 295 ab	26.86 ± 3.64 c	5.13 ± 1.04 b
P250-H12	65.98 ± 3.46 cd	7.60 ± 0.82 c	1.73 ± 0.18 cd	0.21 ± 0.03 b	2398 ± 398 b	28.77 ± 2.80 bc	5.35 ± 0.34 ab
P150-H14	56.51 ± 1.70 d	5.43 ± 0.38 d	1.86 ± 0.15 c	0.16 ± 0.02 c	2225 ± 353 b	24.61 ± 1.32 d	4.88 ± 0.56 bc
P200-H14	74.09 ± 9.73 bc	6.67 ± 0.69 cd	2.03 ± 0.59 bc	0.22 ± 0.04 b	2553 ± 372 b	30.63 ± 3.75 ab	5.23 ± 0.78 ab
P250-H14	68.88 ± 7.00 c	6.26 ± 0.48 d	1.36 ± 0.06 d	0.23 ± 0.03 b	2443 ± 322 b	32.95 ± 1.61 a	5.22 ± 0.70 ab
P150-H16	75.69 ± 8.42 bc	7.90 ± 0.89 bc	2.04 ± 0.44 b	0.34 ± 0.04 a	2517 ± 433 b	29.27 ± 2.32 b	4.92 ± 0.66 bc
P200-H16	95.99 ± 13.31 a	9.93 ± 0.62 a	2.63 ± 0.64 a	0.36 ± 0.03 a	2679 ± 792 ab	32.03 ± 5.13 a	5.69 ± 0.90 ab
P250-H16	81.86 ± 14.00 b	8.28 ± 1.84 b	2.56 ± 0.62 a	0.38 ± 0.10 a	2539 ± 243 b	29.46 ± 1.17 ab	6.21 ± 1.40 a
ANOVA							
PPFD	*	*	NS	NS	NS	*	*
H	*	*	*	*	NS	*	NS
PPFD × H	NS	*	NS	NS	NS	NS	NS

Note: Means with different letters in the same columns were significantly different tested by LSD's multiple comparison at $P \leq 0.05$. NS, * represent no significant and significant difference at $P \leq 0.05$, respectively

Table 14.7 Effects of photosynthetic photon flux density (PPFD), photoperiod (H), and light quality (LQ) during seedling stage on subsequent growth and nutritional qualities of hydroponic lettuce at 40 days after sowing

Treatment	Leaf fresh weight g plant^{-1}	Root fresh weight g plant^{-1}	Leaf dry weight g plant^{-1}	Root dry weight g plant^{-1}	Nitrate content mg kg^{-1}	Vitamin C content mg 100 g^{-1}	Soluble protein content mg g^{-1}
F1.8-P200-H14	79.85 ± 8.52 bc	12.82 ± 3.00 a	3.39 ± 0.45 b	0.33 ± 0.04 de	4030 ± 270 ab	20.32 ± 2.91 cd	5.48 ± 0.75 c
F1.8-P200-H16	92.85 ± 13.02 a	12.91 ± 2.49 a	3.52 ± 0.36 ab	0.40 ± 0.04 c	4265 ± 186 a	30.52 ± 2.59 a	7.45 ± 0.70 a
F1.8-P250-H14	78.16 ± 5.51 bc	10.01 ± 0.52 bc	3.23 ± 0.28 c	0.39 ± 0.03 cd	3507 ± 239 ab	29.19 ± 4.59 ab	6.97 ± 1.17 ab
F1.8-P250-H16	80.52 ± 9.25 bc	11.89 ± 1.70 ab	3.37 ± 0.12 bc	0.53 ± 0.08 b	3414 ± 359 ab	31.25 ± 6.87 a	7.30 ± 1.02 ab
L1.2-P200-H14	70.09 ± 2.39 d	11.13 ± 2.18 ab	2.99 ± 0.33 d	0.35 ± 0.01 d	3290 ± 447 b	18.54 ± 3.40 cd	6.42 ± 0.63 b
L1.2-P200-H16	82.79 ± 10.76 b	12.98 ± 2.40 a	3.90 ± 0.23 a	0.51 ± 0.07 b	3618 ± 399 ab	21.37 ± 6.49 cd	6.35 ± 0.55 b
L1.2-P250-H14	75.34 ± 10.56 c	10.63 ± 1.26 b	3.16 ± 0.35 cd	0.35 ± 0.04 d	3375 ± 337 b	18.32 ± 3.73 d	6.15 ± 0.92 bc
L1.2-P250-H16	72.47 ± 12.28 cd	11.29 ± 1.05 ab	3.24 ± 0.22 bc	0.63 ± 0.07 a	3003 ± 244 b	18.30 ± 1.93 d	5.57 ± 1.08 bc
L2.2-P200-H14	76.25 ± 4.71 c	7.77 ± 1.20 d	3.05 ± 0.27 cd	0.31 ± 0.05 e	4008 ± 806 a	22.93 ± 1.52 c	5.36 ± 1.02 c
L2.2-P200-H16	93.20 ± 13.15 a	9.19 ± 0.75 c	3.65 ± 0.44 ab	0.40 ± 0.02 c	3547 ± 239 ab	27.19 ± 6.04 ab	5.48 ± 0.76 c
L2.2-P250-H14	84.36 ± 7.96 b	7.97 ± 1.03 d	3.33 ± 0.43 bc	0.30 ± 0.04 e	3822 ± 1067 ab	23.98 ± 3.48 b	5.88 ± 1.33 bc
L2.2-P250-H16	70.29 ± 7.44 cd	8.65 ± 1.26 cd	3.00 ± 0.28 cd	0.41 ± 0.04 c	3450 ± 531 ab	26.46 ± 3.61 ab	7.69 ± 1.12 a
ANOVA							
PPFD	*	*	*	*	*	NS	*
H	NS	*	*	*	NS	*	*
LQ	*	*	NS	*	NS	*	*
PPFD × H	*	NS	*	*	NS	NS	NS
PPFD × LQ	NS	NS	NS	*	*	NS	*
H × LQ	NS	NS	NS	*	NS	NS	*
PPFD×H × LQ	NS	NS	*	NS	NS	NS	*

Note: Means with different letters in the same columns were significantly different tested by LSD's multiple comparison at $P \leq 0.05$. NS, * represent no significant and significant difference at $P \leq 0.05$, respectively

LEDs with R:B ratio of 2.2, and no significant difference was found between FL and LEDs with R:B ratio of 1.2 at the same DLI. Lettuce grown under PPFD at 200 μmol m^{-2} s^{-1} with a photoperiod of 16 h day^{-1} had higher leaf dry weight than other treatments regardless of light quality, and no significant difference was found in leaf dry weight between two kinds of LEDs at the same DLI; however, lettuce grown under LEDs with R:B ratio of 1.2 had higher root dry weight than those under LEDs with R:B ratio of 2.2 at the same DLI.

Under each light source, there was no significant difference in nitrate content among treatment, that is, no significant difference between the two PPFDs and two photoperiods. Photoperiod and light quality affected vitamin C and soluble protein contents significantly. Similar to Expt. 1, no significant differences were found as the photoperiod extended from 14 h day^{-1} to 16 h day^{-1} in vitamin C and soluble protein contents under LEDs with R:B ratio of 1.2. Lettuce grown under FL or LEDs with R:B ratio of 2.2 had higher vitamin C content than those under LEDs with R:B ratio of 1.2. Generally, FL led to higher vitamin C and soluble protein content than those under LEDs.

Light quality shows much more complex effects on plant morphology and physiology compared with PPFD and photoperiod [16]. Continuous red light can elicit photomorphogenic seedling development, and led to robust cotyledon expansion in wild-type *Arabidopsis* seedlings [34]. Blue light is a very effective inhibitor of hypocotyl elongation and inducer of cotyledon expansion because blue light stimulates the phytochromes and the blue light photoreceptors [35, 36]. In the present study, lettuce seedlings had shorter LL under LEDs with R:B ratio of 1.2 compared with those under LEDs with R:B ratio of 2.2 with a fixed photoperiod of 14 h day^{-1}, which indicated that elongation of lettuce leaf was inhibited by LEDs containing more blue photon flux under shorter photoperiod (Table 14.7).

The optimal R:B ratio differed in the plants species, growth periods, and the targeted qualities. Shoot fresh weight and dry weight decreased with the increased blue photon flux under the combination of red and blue photon flux in cucumber seedlings [13]. Shoot and root dry weights of pepper seedlings grown under R:B ratio of 7.0 were higher compared with those under R:B ratio of 1.0, which indicated that a high proportion of red light positively affected the morphology and biomass accumulation of pepper seedlings [36]. Dry weight of lettuce seedlings was higher under the R:B ratio of 4.0 than those under R:B ratio of 9.0, 2.3, and 1.5, suggesting that lettuce seedlings was in favor of red light compared with blue light, and dry weight was inhibited by excessively high ratio of red to blue photon flux [37].

Leaf vegetables accumulate nitrate excessively, and nitrate can be converted to nitrite in human body, which is considered as a potential threat to human health [38]. Nitrate levels in leafy vegetables can be controlled by light conditions during seedling stage. Chang et al. investigated the effects of multiple wavelength-band LED lighting during different growth stages on nitrate content of lettuce, and their results indicated that a reduction of nitrate content was attributed to UV-A lighting during seedling stage [39]. In our study, no significant difference was found

in nitrate content of mature lettuce in both experiments, suggesting that lettuce plants might have adjusted by the environment after transplanting. Johkan et al. reported that significant difference was found in total phenols and anthocyanin during seedling stage, while the differences diminished at the final cultivation [11].

Soluble proteins provide essential proteins for human body and are considered as an important nutrient in vegetables [40]. An increase in soluble protein content is important for improving the nutritional quality of vegetables for human consumption. PPFD at 250 μmol m^{-2} s^{-1} led to higher soluble protein content in lettuce than those grown under PPFD at 150 μmol m^{-2} s^{-1} (Table 14.6). The soluble protein content was higher under LEDs with R:B ratio of 1.2 than those under LEDs with R:B ratio of 2.2 with a fixed PPFD at 200 μmol m^{-2} s^{-1} (Table 14.7). Zhang et al. found that the soluble protein content of pea seedling grown under blue light was the highest compared with red light, white light, or mixture of red and blue lights [41].

Vitamin C must be supplemented by food because it cannot be synthesized and accumulated in human body [42]. Therefore, vitamin C content is an important index for evaluating vegetable nutritional quality [43]. In the present study, higher vitamin C content was obtained in lettuce grown under a higher PPFD or longer photoperiod. No significant differences were found in vitamin C content between those grown under FL and LEDs with R:B ratio of 2.2 with photoperiod of 16 h day^{-1}. Qian et al. reported that no significant difference was observed in vitamin C content of lettuce grown under FL and LEDs with R:B ratio of 0.9 [44]. Vitamin C content of mature lettuce grown under LEDs with R:B ratio of 2.2 was higher than those under LEDs with R:B ratio of 1.2 (Table 14.7), which indicated that a high proportion of red light positively affected the vitamin C accumulation. This conclusion agreed with the findings of study reported by Qian et al. [44] that red light enhanced the vitamin C content compared with blue light in Chinese kale sprout. However, Pinho et al. found that there was no significant difference in vitamin C content in lettuce grown under white-red LEDs with W:R ratio of 1.0 or 4.0 [43]. Ohashi et al. found that vitamin C contents were higher in lettuce grown under blue FL and the combination of red and blue FL with R:B ratio of 2.0 than those under red FL under PPFD at 300 μmol m^{-2} s^{-1} with a photoperiod of 12 h day^{-1} [45]. These studies indicated that nutritional response to light quality is dependent on the species or experimental conditions.

Nutritional values of lettuce can be enhanced by employing different spectra strategically, and the administration of a combination of LEDs at seedling stage led to favorable plant growth [22, 39, 46]. Based on seedling quality and its subsequent growth and nutritional values, PPFD at 200 μmol m^{-2} s^{-1} with photoperiod of 16 h day^{-1} provided by FLs or LEDs with R:B ratio of 2.2 was recommended for seedling production of hydroponic lettuce under controlled environment. Our results can be used as basic information for future studies using LEDs with different R:B ratios at seedling stage. Furthermore, studies on effects of supplemental light quality, including ultraviolet A or far-red under LEDs as the main light source at seedling stage on growth and its late nutritional qualities of hydroponic lettuce may be required.

14.3 Case Study: LED Lighting for Hydroponic Lettuce in PFAL

In this section, which is part of a doctoral dissertation [25], effects of light intensity, photoperiod, and light quality on growth and quality of hydroponic lettuce were investigated to find out the optimal LED lighting condition for commercial lettuce production in PFAL. In addition, the photosynthetic property was examined continuously for 2 days under a combination of light intensity and photoperiod.

14.3.1 Plant Materials and Experiment Design

14.3.1.1 Plant Materials and Growth Conditions

Seeds of purple leaf lettuce (*Lactuca sativa* L. cv. "Ziwei") were sown in sponge cube (23 mm × 23 mm × 23 mm) in a hydroponic system. After germination, seedlings were grown for 18 days in a closed plant factory system (China Agricultural University, Beijing, China) under PPFD of 200 μmol m^{-2} s^{-1} provided by LEDs with R:B ratio of 1.2 (WR-LED-16W, Beijing Lighting Valley Technology Co., Ltd. China) with photoperiod of 16 h day^{-1}. When the seedlings had 5 true leaves, they were transplanted to the hydroponic cultivation bed under different lighting environment for 17 days. The air temperature and relative humidity at photoperiod and dark period were maintained at 22 ± 1 °C/18 ± 1 °C and 70 ± 5%/65 ± 5%, respectively, and CO_2 concentration was controlled at 800 ± 50 μmol mol^{-1} from seeding to harvest. The Yamasaki lettuce nutrient solution in pH of 6.0–6.5 and EC of 1.0–1.2 mS cm^{-1} was utilized to cultivate hydroponic lettuce as shown above in Sect. 14.2.1.

14.3.1.2 Treatment and Experiment Design

Twenty-four treatments were created by a combination of four levels of PPFD at 150, 200, 250, and 300 μmol m^{-2} s^{-1} and two photoperiods of 12 and 16 h day^{-1} (factorial design) under three kinds of artificial light with different R:B ratios as shown in Table 14.8. Fluorescent lamps (FLs) with an R:B ratio of 1.8 (T5-28W, Shanghai Flower and Biology Lighting Co., Ltd., China) and LED lamps with R:B ratios of 1.2 and 2.2 (WR-LED-16W, Beijing Lighting Valley Technology Co., Ltd. China) were placed at 35 cm above the cultivation bed. The spectral distribution of different lamps is shown above in Fig. 14.1.

Table 14.8 A list of treatments created by combinations of different photosynthetic photon flux density (PPFD), photoperiod (H), and three different lamps with different R:B ratios

Lighting source	R:B ratio	PPFD (μmol m^{-2} s^{-1})	Photoperiod (h day^{-1})	DLI (mol m^{-2} day^{-1})	Treatment symbol
Fluorescent lamp	1.8	150	12	6.48	F1.8-P150-H12
		200	12	8.64	F1.8-P200-H12
		250	12	10.80	F1.8-P250-H12
		300	12	12.96	F1.8-P300-H12
		150	16	8.64	F1.8-P150-H16
		200	16	11.52	F1.8-P200-H16
		250	16	14.40	F1.8-P250-H16
		300	16	17.28	F1.8-P300-H16
LED	1.2	150	12	6.48	L1.2-P150-H12
		200	12	8.64	L1.2-P200-H12
		250	12	10.80	L1.2-P250-H12
		300	12	12.96	L1.2-P300-H12
		150	16	8.64	L1.2-P150-H16
		200	16	11.52	L1.2-P200-H16
		250	16	14.40	L1.2-P250-H16
		300	16	17.28	L1.2-P300-H16
LED	2.2	150	12	6.48	L2.2-P150-H12
		200	12	8.64	L2.2-P200-H12
		250	12	10.80	L2.2-P250-H12
		300	12	12.96	L2.2-P300-H12
		150	16	8.64	L2.2-P150-H16
		200	16	11.52	L2.2-P200-H16
		250	16	14.40	L2.2-P250-H16
		300	16	17.28	L2.2-P300-H16

The three lamps are fluorescent lamp with R:B ratio of 1.8 (F1.8) and two LEDs with R:B ratio of 1.2 and 2.2 (L1.2 and L2.2), respectively. Daily light integral (DLI) is a product of PPFD and photoperiod

14.3.1.3 Growth Quality and Photosynthetic Measurements

In each treatment, one layer of cultivation shelves with a total of 18 plants was employed in experiments. At the end of the treatment, six plants were selected randomly in each treatment for evaluating growth and quality properties. The fresh weights (FW) of leaves and roots were recorded by an electronic analytical balance with accuracy of 0.1 mg (FA1204B, Shanghai Jingke Electr. Inc., Shanghai, China). The leaves and roots were dried in an oven at 105 °C for 3 h and subsequently set to 80 °C and dried for 72 h, and dry weight (DW) of leaves and roots was recorded. The third vigorously growing leaf from the top of the lettuce was used to determine the quality indicators.

Lettuce quality indicators such as nitrate N, vitamin C, soluble sugar, soluble protein, and anthocyanin contents were determined for all treatments, six replicates per treatment, sampled on the seventeenth day after transplanting. The measurement methods of nitrate N content, vitamin C, soluble sugar, and soluble protein were described above in Sect. 14.2.1. The anthocyanin content was measured at 530 nm and 600 nm by using the spectrometric method [46].

Net photosynthetic rates of lettuce leaves were measured continuously for 2 days in treatments of F1.8-P250-H12, F1.8-P250-H16, F1.8-P300-H12, and F1.8-P300-H16, one leaf per treatment, during the last 2 days before harvest by using two open path dynamic photosynthetic systems with four leaf chambers (MD-100A, Yizongqi Technology Co., Beijing, China). In this continuous photosynthesis measurement system, the differential CO_2 concentrations of the inlet and outlet were measured automatically by an infrared gas analyzer (LI-7000, LI-COR Inc., Lincoln, NE, USA) for calculating and recording the net photosynthetic rate every 8 min [47]. The light environment, CO_2 concentration, and temperature in the leaf cuvette were the same as those in the above same cultivation environment. The net photosynthetic rate and light response curve were measured by using two portable photosynthesis systems (LI-6400XT, LI-COR Inc., Lincoln, NE, USA).

Smart electronic metering (TP-9004, Shenzhen Northmeter Co., Ltd., Shenzhen, China) was used to monitor the total power consumption for each treatment. The recorded power consumption was divided by the value of 100 g fresh weight or 1 g dry weight of lettuce leaves. Light energy use efficiency (LEU) was determined as follows:

$$\mathrm{LEU} = (k \times D) / \mathrm{PAR}$$

where k is the conversion coefficient from dry weight to chemical energy (about 20 MJ kg^{-1}), D is the increase of dry weight in specific growth time per unit area (kg m^{-2}), and PAR is photosynthetically active radiation (W m^{-2}).

The electric energy use efficiency (EUE) was defined as:

$$\mathrm{EUE} = h \times \mathrm{LEU}$$

where h is the conversion factor from electric energy to PAR energy, which is around 0.195 for FLs (R:B ratio of 1.8), 0.382 for LEDs with R:B ratio of 1.2, and 0.326 for LED lamps with R:B ratio of 2.2 [48].

14.3.2 LED Lighting Affects Growth of Hydroponic Lettuce

The growth of hydroponic lettuce was significantly influenced by PPFD, photoperiod, and light quality (Table 14.9). Leaf fresh weights were highest in the treatments of F1.8-P250-H16 and F1.8-P300-H16. However, there were no differences in leaf fresh weight between the two LED lamps, regardless of PPFD and photoperiod.

Table 14.9 Effects of different photosynthetic photon flux density (PPFD), photoperiod (H), and light quality (LQ) on fresh weight (FW) and dry weight (DW) of leaves and roots of hydroponic lettuce at day 18 after transplanting ($n = 6$)

Treatment	Leaf FW ($g \cdot plant^{-1}$)	Root FW	Leaf DW	Root DW
F1.8-P150-H12	28.1 ± 1.1 de	3.06 ± 0.30 f	0.91 ± 0.06 e	0.14 ± 0.01 e
F1.8-P200-H12	34.5 ± 1.0 cd	3.90 ± 0.25 e	1.34 ± 0.04 d	0.17 ± 0.01 de
F1.8-P250-H12	40.3 ± 2.8 b	4.61 ± 0.45 cd	1.66 ± 0.13 c	0.19 ± 0.02 d
F1.8-P300-H12	36.2 ± 1.1 c	5.18 ± 0.18 c	1.48 ± 0.07 cd	0.23 ± 0.01 c
F1.8-P150-H16	37.7 ± 2.3 bc	3.82 ± 0.13 e	1.27 ± 0.08 d	0.16 ± 0.01 e
F1.8-P200-H16	47.3 ± 0.1 ab	5.32 ± 0.25 c	1.69 ± 0.20 bc	0.19 ± 0.01 d
F1.8-P250-H16	50.1 ± 2.9 a	6.01 ± 0.34 b	1.85 ± 0.09 bc	0.28 ± 0.02 b
F1.8-P300-H16	49.3 ± 6.5 a	6.41 ± 0.40 b	2.00 ± 0.08 ab	0.30 ± 0.02 b
L1.2-P150-H12	23.2 ± 1.9 e	2.94 ± 0.28 f	1.04 ± 0.09 e	0.11 ± 0.03 f
L1.2-P200-H12	28.4 ± 2.5 de	3.61 ± 0.35 ef	1.35 ± 0.01 d	0.15 ± 0.02 e
L1.2-P250-H12	31.1 ± 3.0 d	3.73 ± 0.23 e	1.44 ± 0.05 d	0.17 ± 0.01 de
L1.2-P300-H12	30.6 ± 3.6 d	5.14 ± 0.52 c	1.54 ± 0.16 cd	0.23 ± 0.02 c
L1.2-P150-H16	28.3 ± 2.9 de	4.23 ± 0.30 d	1.37 ± 0.13 d	0.21 ± 0.02 cd
L1.2-P200-H16	32.8 ± 2.8 cd	4.80 ± 0.40 cd	1.64 ± 0.12 cd	0.26 ± 0.04 bc
L1.2-P250-H16	39.9 ± 2.1 b	5.95 ± 0.41 b	1.94 ± 0.18 b	0.28 ± 0.02 b
L1.2-P300-H16	38.2 ± 1.8 bc	5.50 ± 0.49 bc	2.18 ± 0.17 a	0.27 ± 0.04 b
L2.2-P150-H12	25.7 ± 2.3 e	3.51 ± 0.20 ef	1.26 ± 0.09 d	0.14 ± 0.01 e
L2.2-P200-H12	34.9 ± 2.4 cd	4.64 ± 0.11 cd	1.60 ± 0.13 cd	0.22 ± 0.02 cd
L2.2-P250-H12	37.3 ± 2.2 bc	6.01 ± 0.51 b	1.89 ± 0.10 b	0.25 ± 0.01 bc
L2.2-P300-H12	31.4 ± 3.3 d	6.35 ± 0.67 b	1.80 ± 0.10 bc	0.25 ± 0.02 bc
L2.2-P150-H16	30.7 ± 2.3 d	5.02 ± 0.64 c	1.38 ± 0.13 d	0.16 ± 0.02 e
L2.2-P200-H16	37.0 ± 3.7 bc	5.93 ± 0.60 b	1.88 ± 0.11 b	0.18 ± 0.01 de
L2.2-P250-H16	42.7 ± 2.2 b	7.34 ± 0.62 a	2.03 ± 0.31 ab	0.29 ± 0.04 b
L2.2-P300-H16	40.0 ± 5.0 b	6.60 ± 0.94 b	2.28 ± 0.26 a	0.35 ± 0.04 a
ANOVA				
PPFD	*	*	*	*
H	*	*	*	*
LQ	*	*	*	*
LQ × PPFD	NS	*	NS	*
LQ × H	*	NS	*	*
PPFD × H	NS	*	*	*
PPFD × H × LQ	NS	*	NS	*

Note: Different letters in the same columns were significantly different tested by LSD's multiple comparison at $P \leq 0.05$. NS, * represent no significant and significant difference at $P \leq 0.05$, respectively

With photoperiod of 12 h day^{-1}, leaf fresh weights were higher under FL than LED at PPFD of 250 and 300 μmol m^{-2} s^{-1}. Root fresh weight was highest in treatment of L2.2-P250-H16, while there were no differences between FL and LED with R:B ratio of 1.2. No substantial differences were found in leaf fresh weight between FL

and LED with R:B ratio of 1.2, while some treatments in LED with R:B ratio of 2.2 had higher leaf dry weight compared to the other two lamps. Similar tendencies were observed for root dry weight among treatments.

Increasing light intensity generally increases photosynthesis and hence plant growth [16, 18], as shown in this experiment. The biomass of lettuce was higher under longer photoperiod at the same PPFD. Longer photoperiod led to more carbohydrates used for physiological metabolism and growth. Longer photoperiod could stimulate the photosensitive pigments to induce gene expression in lettuce growth, quality, and nutrition uptake [49, 50]. Based on the growth parameters, plants performed better in treatments of P250-H16 and P300-H16 than other treatments regardless of light quality. Our results were slightly different from other studies. For example, Jeong et al. reported no differences in lettuce growth among PPFDs of 200, 230, and 260 μmol m^{-2} s^{-1}, but PPFD of 290 μmol m^{-2} s^{-1} resulted in better growth and development of lettuce [51]. No differences in fresh weight of romaine lettuce were found between PPFD of 400 and 200 μmol m^{-2} s^{-1} [35]. These differences may be due to the different types or cultivars of lettuce used in these studies. Based on our results of biomass, light intensity between 250 and 300 μmol m^{-2} s^{-1} was reasonable for lettuce production in PFAL.

In treatments with both photoperiods, fresh and dry weights were higher at PPFD of 200 μmol m^{-2} s^{-1} than that at 150 μmol m^{-2} s^{-1}. With photoperiod of 16 h day^{-1}, PPFD at 250 μmol m^{-2} s^{-1} resulted in similar or even higher fresh and dry weights compared to that at 300 μmol m^{-2} s^{-1}, except for leaf dry weight in L1.2 treatments and root dry weight in L2.2 treatments. Based on the relationships between DLI and leaf fresh and dry weights, it was obvious that as DLI increased, leaf fresh and dry weights increased linearly (Fig. 14.3). Significant interactions were observed between PPFD and photoperiod on root fresh weight, leaf dry weight, and root dry weights; PPFD and light quality on root fresh and dry weights; light quality and photoperiod on leaf fresh and dry weights and root dry weight; and PPFD, photoperiod, and light quality on root fresh and dry weights.

Dry mass accumulation was proportional to DLI which is the product of light intensity and photoperiod. The linear relationships between DLI and leaf fresh and dry weights were obtained in this study, which were consistent with other report in lettuce greenhouse production [52]. DLI has been used to manage light environment in greenhouse production for many years. The growth and quality of lettuce are closely related to DLI. Longer photoperiod could compensate for a low PPFD at the same DLI [28]. In commercial lettuce production, Both suggested that a daily light integral of 17 mol m^{-2} day^{-1} should be maintained in the greenhouse [53]. Our experiments showed a lower DLI (14.4 mol m^{-2} day^{-1}) that was sufficient. The DLI of 14.4 mol m^{-2} day^{-1} (P250-H16) had similar growth and quality compared with P300-H16, DLI of 17.28 mol m^{-2} day^{-1}.

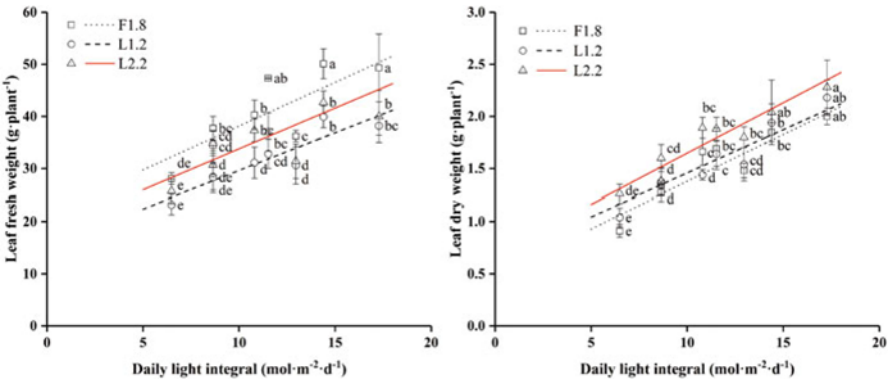

Fig. 14.3 Relationships between daily light integral and leaf fresh and dry weights of hydroponic lettuce. The vertical bars represent the standard deviation. Data points with different letters above the bar were significantly different tested by LSD's multiple comparison at $P \leq 0.05$

14.3.3 LED Lighting Affects Hydroponic Lettuce Quality

PPFD, photoperiod, and light quality had significant effects on the contents of nitrate N, vitamin C, soluble sugar, soluble protein, and anthocyanin (Table 14.10). Nitrate N content was lower at higher PPFD and longer photoperiod, while vitamin C, soluble sugar, soluble protein, and anthocyanin contents were higher. The nitrate N content was lowest in plants grown under higher PPFD at 250 and 300 μmol m^{-2} s^{-1} and longer photoperiod. No differences in the contents of nitrate N, vitamin C, and soluble sugar were found between treatments of P250-H16 and P300-H16, regardless of light quality. Vitamin C, soluble protein, and soluble sugar contents were lower in F1.8 treatments than those in L2.2 treatment. There were no differences in anthocyanin content between PPFD at 250 and 300 μmol m^{-2} s^{-1} with a photoperiod of 16 h day^{-1} except for the treatment of F1.8-P300-H16 which had the highest anthocyanin content. Generally, the differences in anthocyanin among different light quality were small compared to vitamin C, soluble sugar, and protein contents. PPFD and photoperiod interactively affected nitrate N, vitamin C, and anthocyanin contents. PPFD, photoperiod, and light quality interactively affected soluble protein content but not for other quality parameters.

Higher PPFD and longer photoperiod could achieve higher vitamin C, soluble sugar, and soluble protein contents while reducing nitrate N content, which agreed with other reports [54, 55]. The activity of nitrate reductase was higher under high PPFD, which could decrease the nitrate accumulation. High PPFD would increase the photosynthetic production (sucrose concentration), which promoted assimilation of nitrate ion [56]. Genetics, temperature, and light environment affected the anthocyanin content [57]. Our results on anthocyanin was similar to other researches which indicated that PPFD, photoperiod, and light quality significantly affected anthocyanin content [58, 59]. Plants in treatments of P300-H16 had the best quality,

Table 14.10 Effects of different photosynthetic photon flux density (PPFD), photoperiod (H), and light quality (LQ) on contents of nitrate N, vitamin C, soluble sugar, soluble protein, and anthocyanin of hydroponic lettuce at 18 days after transplanting ($n = 6$)

Treatments	Nitrate N content mg kg^{-1}	Vitamin C content mg 100 g^{-1}	Soluble sugar content %	Soluble protein content mg g^{-1}	Anthocyanin content $\triangle OD \cdot g^{-1}$ FW
F1.8-P150-H12	783.1 ± 45.0 a	21.0 ± 2.2 d	1.01 ± 0.06 e	9.9 ± 0.7 de	0.62 ± 0.14 d
F1.8-P200-H12	697.5 ± 182.9 bc	22.4 ± 2.2 d	1.11 ± 0.36 de	10.4 ± 1.5 de	0.87 ± 0.11 cd
F1.8-P250-H12	565.6 ± 89.6 cd	22.1 ± 3.8 d	1.48 ± 0.13 d	9.3 ± 1.3 e	0.95 ± 0.18 c
F1.8-P300-H12	470.0 ± 75.5 de	23.5 ± 2.0 d	1.47 ± 0.16 d	11.8 ± 1.1 cd	1.31 ± 0.28 bc
F1.8-P150-H16	756.2 ± 104.0 bc	21.6 ± 2.3 d	0.90 ± 0.47 e	10.3 ± 0.9 de	0.96 ± 0.26 c
F1.8-P200-H16	563.2 ± 79.1 cd	23.4 ± 4.7 d	1.50 ± 0.40 cd	11.6 ± 0.7 d	1.09 ± 0.30 bc
F1.8-P250-H16	292.5 ± 43.1 e	30.3 ± 2.0 cd	2.11 ± 0.55 c	13.7 ± 2.0 bc	1.35 ± 0.09 b
F1.8-P300-H16	339.5 ± 72.0 e	34.7 ± 3.9 bc	2.16 ± 0.66 c	11.6 ± 1.1 d	2.30 ± 0.61 a
L1.2-P150-H12	667.5 ± 121.7 ab	24.4 ± 3.7 cd	1.04 ± 0.44 e	9.5 ± 1.8 e	0.33 ± 0.05 e
L1.2-P200-H12	626.6 ± 99.0 bc	26.9 ± 3.0 cd	0.94 ± 0.15 e	11.9 ± 0.9 cd	0.59 ± 0.15 de
L1.2-P250-H12	589.7 ± 121.7 bc	29.3 ± 7.4 cd	1.28 ± 0.45 de	12.4 ± 1.6 cd	0.61 ± 0.25 d
L1.2-P300-H12	546.3 ± 73.7 cd	29.5 ± 4.3 cd	1.88 ± 0.64 cd	12.7 ± 1.4 c	0.78 ± 0.18 cd
L1.2-P150-H16	654.8 ± 27.4 b	25.7 ± 4.4 cd	1.08 ± 0.33 de	12.8 ± 1.8 c	0.57 ± 0.17 de
L1.2-P200-H16	539.2 ± 65.3 cd	32.0 ± 3.8 c	1.55 ± 0.28 cd	11.9 ± 1.4 cd	0.73 ± 0.13 cd
L1.2-P250-H16	528.4 ± 20.1 cd	41.7 ± 8.8 ab	1.92 ± 0.17 cd	14.3 ± 2.1 b	1.12 ± 0.18 bc
L1.2-P300-H16	506.7 ± 38.2 d	43.3 ± 3.0 a	2.02 ± 0.24 c	13.3 ± 1.3 bc	1.50 ± 0.58 b
L2.2-P150-H12	810.4 ± 78.4 a	33.5 ± 3.2 bc	1.55 ± 0.31 cd	10.0 ± 1.8 de	0.33 ± 0.07 e

(continued)

Table 14.10 (continued)

Treatments	Nitrate N content mg kg^{-1}	Vitamin C content mg 100 g^{-1}	Soluble sugar content %	Soluble protein content mg g^{-1}	Anthocyanin content $\bigtriangleup$OD·g^{-1} FW
L2.2-P200-H12	797.8 ± 119.7 a	34.1 ± 6.9 bc	2.98 ± 0.29 b	12.9 ± 1.2 c	0.51 ± 0.12 de
L2.2-P250-H12	779.3 ± 39.6 ab	35.4 ± 4.0 b	3.09 ± 0.78 b	13.4 ± 1.1 bc	0.83 ± 0.09 cd
L2.2-P300-H12	520.8 ± 90.1 cd	35.8 ± 4.9 bc	3.96 ± 0.72 a	14.3 ± 1.4 b	0.82 ± 0.07 cd
L2.2-P150-H16	624.7 ± 70.0 bc	31.2 ± 2.7 c	2.56 ± 0.59 bc	13.3 ± 0.8 bc	0.60 ± 0.08 de
L2.2-P200-H16	590.7 ± 110.0 c	35.6 ± 6.2 b	4.01 ± 1.24 a	14.1 ± 2.1 bc	0.86 ± 0.18 cd
L2.2-P250-H16	479.2 ± 43.3 de	38.4 ± 3.7 ab	4.27 ± 0.60 a	15.6 ± 1.2 b	1.47 ± 0.30 b
L2.2-P300-H16	456.8 ± 59.5 de	40.1 ± 4.9 ab	4.26 ± 0.44 a	18.9 ± 1.7 a	1.34 ± 0.26 b
PPFD	*[y]	*	*	*	*
H	*	*	*	*	*
LQ	*	*	*	*	*
PPFD×H	*	*	NS	NS	*
PPFD×LQ	*	NS	*	*	*
H × LQ	NS	*	NS	NS	NS
PPFD×H × LQ	NS	NS	NS	*	NS

Note: Means with different letters in the same columns were significantly different tested by LSD's multiple comparison at $P \leq 0.05$. NS, * represent no significant and significant difference at $P \leq 0.05$, respectively

and those in P250-H16 had similar contents of soluble sugar, vitamin C, and nitrate N. Considering the higher power consumption, in treatments of P300-H16 and P250-H16, LED lighting at PPFD of 250 μmol m^{-2} s^{-1} with photoperiod of 16 h day^{-1} was recommended for commercial lettuce production in PFAL.

Effect of light quality on lettuce growth, development, and quality has been investigated using monochromatic LED lights, a combination of red and blue LED lights, and other light sources such as white LED and fluorescent lamp [22, 60]. Many reports have concluded that combination of red and blue lights could effectively promote the lettuce growth and development than monochromatic light. For example, Lin et al. reported that combined red, blue, and white LEDs were better than red and blue LEDs and FL based on growth, nutrition, appearance, and the edible quality of lettuce plants grown in a growth chamber at PPFD of 210 μmol m^{-2} s^{-1} [22]. Continuous light exposure at pre-harvest could effectively reduce nitrate accumulation and increase phytochemical concentrations in lettuce plants [61]. In this experiment, LEDs with R:B ratios of 1.2 and 2.2 using white and red chips had higher quality and lower power consumption than fluorescent lamps.

14.3.4 Continuous Photosynthesis and Light Responses of Hydroponic Lettuce

The two-day continuous measurement of photosynthesis indicated that highest net photosynthetic rates of lettuce leaves were observed in treatments of F1.8-P250-H16 and F1.8-P300-H16 (Fig. 14.4). The differences between the two PPFD with a shorter photoperiod (F1.8-P250-H12 and F1.8-P300-H12) were smaller compared to those with a longer photoperiod. Although the treatment of F1.8-P250-H16 had the greatest net photosynthetic rate, no statistical differences in either leaf fresh or

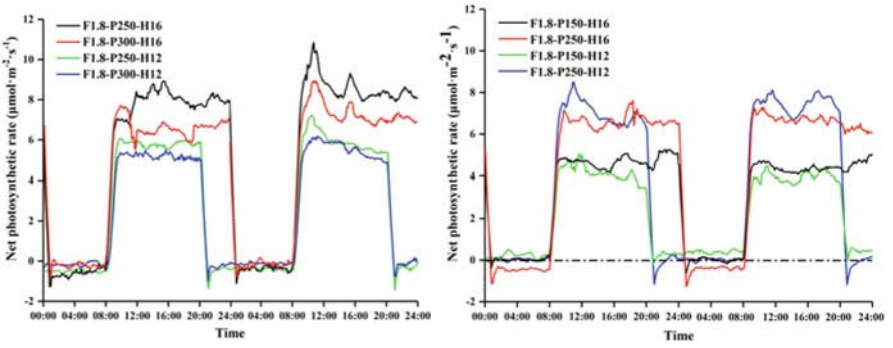

Fig. 14.4 Continuous measurement of net photosynthetic rate of hydroponic lettuces for 2 days before harvest under fluorescent lamps with R:B ratio of 1.8 at PPFD of 150–300 μmol m^{-2} s^{-1} with photoperiod of 12 and 16 h day^{-1}

Table 14.11 Effect of lighting environment at PPFD from 150 μmol m^{-2} s^{-1} to 300 μmol m^{-2} s^{-1} with a photoperiod of 12 and 16 h day^{-1} using fluorescent lamps with R:B ratio of 1.8 on daily CO_2 assimilation of the hydroponic lettuces

Treatments	Daily CO_2 assimilation at 16 days after transplanting	Daily CO_2 assimilation at 17 days after transplanting
	mmol m^{-2} day^{-1}	
F1.8-P250-H12	**219.1 (100%)**	**229.6 (100%)**
F1.8-P300-H12	205.5 (−6%)	221.5 (−4%)
F1.8-P250-H16	429.3 (+96%)	472.2 (+106%)
F1.8-P300-H16	374.0 (+71%)	402.4 (+75%)
F1.8-P150-H12	**183.3 (100%)**	**180.4 (100%)**
F1.8-P250-H12	295.1 (+61%)	310.6 (+72%)
F1.8-P150-H16	269.6 (+47%)	248.6 (+38%)
F1.8-P250-H16	357.9 (+95%)	355.0 (+97%)

Note: Bold identification in the table are references for comparison for treatments of same light quality. Percentage of positive and negative showed above was compared with the treatment of F1.8-P250-H12 or F1.8-P150-H12 at the same day

dry weights were observed at PPDF from 250 μmol m^{-2} s^{-1} to 300 μmol m^{-2} s^{-1}. The photosynthetic data in last two days do not necessarily reflect the whole production period; however, the daily CO_2 assimilation in treatments of F1.8-P250-H16 and F1.8-P300-H16 calculated based on the two-day continuous measurement of photosynthesis was greater in 71–106% increasing than treatment of F1.8-P250-H12 at 16 days and 17 days after transplanting (Table 14.11). The daily CO_2 assimilation at 16 days and 17 days after transplanting at PPFD of 250 μmol m^{-2} s^{-1} with photoperiod of 16 h day^{-1} were higher 60–97% compared with that at 150 μmol m^{-2} s^{-1} with photoperiod of 12 h day^{-1}, respectively, but long photoperiod in 16 h day^{-1} has improved by 30–40% increasing only at the same PPFD.

Figure 14.5 shows the light response curves of hydroponic lettuce at 17 days after transplanting at temperature of 22 °C and CO_2 concentration of 800 μmol mol^{-1} in treatments of L1.2-P250-H16 and L1.2-P300-H16. The fitting curves of rectangular hyperbola model and exponential model are diffusive progressive line, and the difference between the fitting value and measured value increases gradually when the light intensity is larger than 1200 μmol m^{-2} s^{-1}. The coefficient of determination of the non-rectangular hyperbola model is highest in all model simulations, but it is difficult to fit the photo-inhibition phenomenon. The photo-inhibition and photo-saturation phenomena were well explained by the modified rectangular hyperbola model by Ye et al. [62].

The modified rectangular hyperbola model was used to fit the net photosynthetic rate in treatment of L1.2-P250-H16 at 8 days and 17 days after transplanting (Fig. 14.6). The results showed that the maximum net photosynthetic rate, initial quantum efficiency, and saturated light intensity of the hydroponic lettuce were in decreasing trends over time, but the dark respiration rate and light compensation

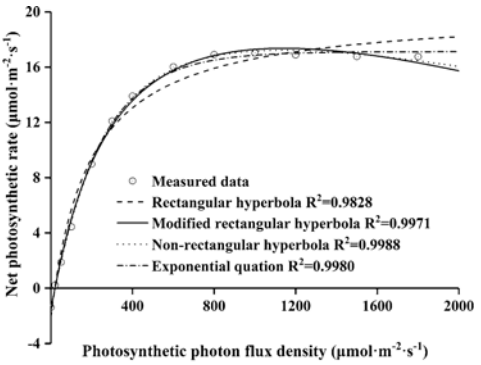

Fig. 14.5 Net photosynthetic rate of hydroponic lettuce response to photosynthetic photon flux density and fitted by rectangular hyperbola, modified rectangular hyperbola, non-rectangular hyperbola, and exponential models compared with the measured data

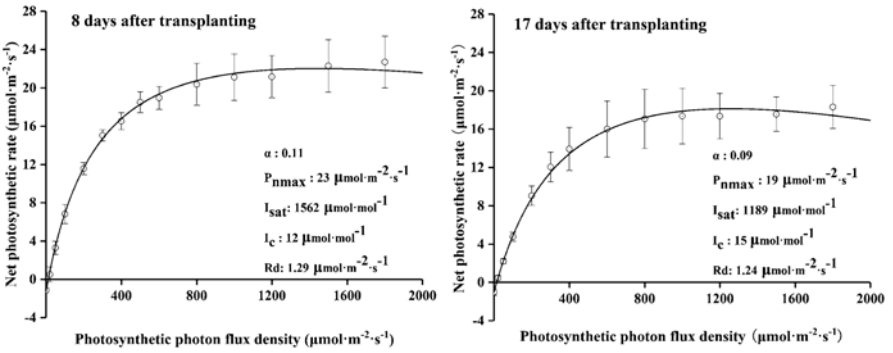

Fig. 14.6 Light response curves of hydroponic lettuce at 8 days and 17 days after transplanting under PPFD of 250 μmol m^{-2} s^{-1} with photoperiod of 16 h day^{-1}, using LED lamps with R:B ratio of 1.2. α means initial slope in the light response curve, P_{nmax} means maximal net photosynthetic rate, I_{sat} means saturation of light intensity, and Rd means rate of dark respiration

point were not changed which agreed with a practical measurement in single leaf. The net photosynthetic rates of lettuce leaves were rapidly increased with increasing photosynthetic photon flux density from 0 to 400 μmol m^{-2} s^{-1} because of the effective light qualitum efficiency. Therefore, high lettuce growth rate could be obtained with less light energy consumption when light intensity was less than 400 μmol m^{-2} s^{-1} under controlled environment.

14.3.5 Energy Use Efficiency of Artificial Light for Lettuce Production

Power consumption per 100 g leaf fresh weight and 1 g leaf dry weight of the lettuce were highest under fluorescent lamps (Table 14.12). LEDs had the advantage of higher LEU and EUE than fluorescent lamps. The EUE of LEDs was lower at higher PPFDs and longer photoperiod. The LEU for LEDs did not change substantially in

Table 14.12 Energy utilization efficiency of the fluorescent lamps and LEDs of the hydroponic lettuces produced in the closed plant factory system

Treatment	Power consumption per 100 g leaf fresh mass (kW h 100 g^{-1} FW)	Power consumption per 1 g leaf dry mass (kW h g^{-1} DW)	Light energy use efficiency (LEU)	Electric energy use efficiency (EUE)
F1.8-P150-H12	4.35	1.32	0.019	0.0038
F1.8-P200-H12	4.60	1.18	0.021	0.0041
F1.8-P250-H12	4.82	1.18	0.021	0.0041
F1.8-P300-H12	6.28	1.53	0.016	0.0031
F1.8-P150-H16	4.30	1.27	0.020	0.0039
F1.8-P200-H16	4.43	1.25	0.020	0.0039
F1.8-P250-H16	5.11	1.36	0.018	0.0036
F1.8-P300-H16	6.17	1.50	0.016	0.0032
L1.2-P150-H12	2.46	0.56	0.025	0.0096
L1.2-P200-H12	2.78	0.59	0.025	0.0091
L1.2-P250-H12	2.90	0.63	0.021	0.0086
L1.2-P300-H12	3.54	0.72	0.020	0.0076
L1.2-P150-H16	2.60	0.54	0.026	0.0101
L1.2-P200-H16	3.13	0.62	0.024	0.0087
L1.2-P250-H16	2.91	0.60	0.022	0.0090
L1.2-P300-H16	3.83	0.68	0.021	0.0079
L2.2-P150-H12	2.47	0.52	0.031	0.0099
L2.2-P200-H12	2.40	0.52	0.030	0.0097
L2.2-P250-H12	2.74	0.56	0.029	0.0092
L2.2-P300-H12	3.48	0.64	0.023	0.0080
L2.2-P150-H16	2.67	0.62	0.026	0.0082
L2.2-P200-H16	2.94	0.61	0.026	0.0083
L2.2-P250-H16	3.15	0.68	0.024	0.0075
L2.2-P300-H16	3.74	0.66	0.022	0.0078

Note: FW means fresh weight of leaves and DM means dry weight of leaves

the PPFD range from 150 μmol m^{-2} s^{-1} to 300 μmol m^{-2} s^{-1} with a photoperiod from 12 h day^{-1} to 16 h day^{-1}. For commercial lettuce production in a closed plant factory system, light intensity, photoperiod, and light quality are controlled collectively in consideration of plant growth or yield, energy consumption, and initial and operational costs. Although many researchers have studied the effect of single factor (PPFD or photoperiod) or two factors (PPFD and photoperiod) on growth and quality of lettuce, limited attention has been paid on the effects of multiple factors as shown in this experiment.

Acknowledgments The research was supported by NEDO (New Energy and Industrial Technology Development Organization) project of Preliminary Study on Plant Phonemics and its Application by Artificial Intelligence, Japan (2017–2019), National High Technology Research and Development Program of China (2013AA103005), and National Key Research and Development Program of China (2017YFB0403901), respectively.

References

1. C.A. Mitchell, M.P. Dzakovich, C. Gomez, R. Lopez, J.F. Burr, R. Hernandez, C. Kubota, C.J. Currey, Q. Meng, E.S. Runkle, C.M. Bourget, R.C. Morrow, A.J. Both, Light-emitting diodes in horticulture. Hortic. Rev. **42**, 1–87 (2015)
2. T. Kozai, K. Fujiwara, E. S. Runkle (eds.), *LED Lighting for Urban Agriculture* (Springer, Singapore, 2016), pp. 3–448
3. T. Kozai, G. H. Niu, M. Takagaki (eds.), *Plant Factory: An Indoor Vertical Farming System for Efficient Quality Food Production* (Academic, Amsterdam, 2015), pp. 3–399
4. T. Kozai (ed.), *Smart Plant Factory: Next-Generation Indoor Vertical Farms* (Springer, Singapore, 2018)
5. S.M.A. Zobayed, F. Afreen, T. Kozai, Temperature stress can alter the photosynthetic efficiency and secondary metabolites concentrations in St. John's wort. Plant Physiol. Biochem. **43**, 977–984 (2005)
6. A.J. Both, B. Bugbee, C. Kubota, R.G. Lopez, C. Mitchell, E.S. Runkle, C. Wallace, Proposed product label for electric lumps used in the plant sciences. HortTechnology **27**(4), 544–549 (2017)
7. Goto E (2016) Measurement of photonmetric and radiometric characteristics of LEDs for plant cultivation. In: Kozai T, Fujiwara K, Runkle ES. LED Lighting for Urban Agriculture. Springer, Singapore, pp 395-402
8. G. Zhang, S. Shen, M. Takagaki, T. Kozai, W. Yamamoto, Supplemental upward lighting from underneath to obtain higher marketable lettuce (*Lactuca sativa*) leaf fresh weight by retarding senescence of outer leaves. Front. Plant Sci. **6**, 1–9 (2015)
9. Lu N, Mitchell CA (2016) Supplemental lighting for greenhouse grown fruiting vegetables. In: Kozai T, Fujiwara K, Runkle ES. LED Lighting for Urban Agriculture. Springer, Singapore, pp 219-232
10. M.E. Ghanem, H. Marrou, T.R. Sinclair, Physiological phenotyping of plants for crop improvement. Trends Plant Sci. **20**(3), 139–144 (2015)
11. M. Johkan, K. Shoji, F. Goto, Blue light-emitting diode light irradiation of seedlings improves seedling quality and growth after transplanting in red leaf lettuce. HortScience **45**(12), 414–415 (2010)
12. X.Y. Liu, T.T. Chang, S.R. Guo, Z.G. Xu, J. Li, Effect of different light quality of LED on growth and photosynthetic character in cherry tomato seedling. Acta Hortic. (907), 325–330 (2011). https://doi.org/10.17660/ActaHortic.2011.907.53
13. R. Hernández, C. Kubota, Physiological responses of cucumber seedlings under different blue and red photon flux ratios using LEDs. Environ. Exp. Bot. **121**(1), 66–74 (2016)
14. J. Song, Q. Meng, W. Du, D. He, Effects of light quality on growth and development of cucumber seedlings in controlled environment. Int. J. Agric. Biol. Eng. **10**(3), 312–318 (2017)
15. X.L. Chen, Q.C. Yang, W.P. Song, Growth and nutritional properties of lettuce affected by different alternating intervals of red and blue LED irradiation. Sci. Hortic. **223**, 44–52 (2017)
16. J. Wang, W. Lu, Y.X. Tong, Q.C. Yang, Leaf morphology, photosynthetic performance, chlorophyll fluorescence, stomatal development of lettuce (*Lactuca sativa* L.) exposed to different ratios of red light to blue light. Front. Plant Sci. **7**, 250 (2016)

17. K. Okamoto, T. Yanagi, S. Kondo, Growth and morphogenesis of lettuce seedlings raised under different combinations of red and blue light. Acta Hortic. (435), 149–158 (1997). https://doi.org/10.17660/actahortic.1997.435.14
18. M.E. Hoenecke, R.J. Bula, T.W. Tibbitts, Importance of 'blue' photon levels for lettuce seedlings grown under red-light-emitting diodes. HortScience **127**(5), 427 (1992)
19. Y.X. Miao, Physiological response mechanism of cucumber seedlings to red and blue light, Ph.D. Thesis of China Agriculture University, 2015, pp. 17–25
20. K.H. Son, M.M. Oh, Leaf shape, growth, and antioxidant phenolic compounds of two lettuce cultivars grown under various combinations of blue and red light-emitting diodes. HortScience **48**(8), 988–995 (2013)
21. W.H. Kang, J.S. Park, K.S. Park, Leaf photosynthetic rate, growth, and morphology of lettuce under different fractions of red, blue, and green light from light-emitting diodes (LEDs). Hortic. Environ. Biotechnol. **57**(6), 573–579 (2016)
22. K.H. Lin, M.Y. Huang, W.D. Huang, The effects of red, blue, and white light-emitting diodes on the growth, development, and edible quality of hydroponically grown lettuce (*Lactuca sativa* L. var. capitata). Sci. Hortic. **150**(2), 86–91 (2013)
23. M. Johkan, K. Shoji, F. Goto, Effect of green light wavelength and intensity on photomorphogenesis and photosynthesis in *Lactuca sativa*. Environ. Exp. Bot. **75**, 128–133 (2012)
24. H. Zhai, Effect of lighting environment at seedling stage on growth of hydroponic lettuce transplant and its late harvest, Master Thesis of China Agricultural University, 2017, pp. 10–43
25. X. Zhang, Technical foundation of environmental feedback control of hydroponic lettuce based on photosynthesis simulation, Ph.D Thesis of China Agricultural University, 2017, pp. 12–28, 58–82
26. H.S. Li, *Experimental Principle and Technology of Plant Physiology and Biochemistry* (High Education Press, Beijing, 2000), pp. 122–123, 190–192, 202–204, 267–268
27. Y. Kitaya, G.H. Niu, T. Kozai, M. Ohashi, Photosynthetic photon flux, photoperiod, and CO_2 concentration affect growth and morphology of lettuce plug transplants. HortScience **33**(6), 988–991 (1998)
28. L. Gaudreau, J. Charbonneau, L.P. Vézina, Photoperiod and photosynthetic photon flux influence growth and quality of greenhouse-grown lettuce. HortScience **29**(11), 1285–1289 (1994)
29. J.A. Zavala, D.A. Ravetta, Allocation of photoassimilates to biomass, resin and carbohydrates in *Grindelia chiloensis* as affected by light intensity. Field Crop Res. **69**(2), 143–149 (2001)
30. H.K. Lichtenthaler, A. Alexander, M.V. Marek, Differences in pigment composition, photosynthetic rates and chlorophyll fluorescence images of sun and shade leaves of four tree species. Plant Physiol. Biochem. **45**(8), 577–588 (2007)
31. X.X. Fan, Z.G. Xu, X.Y. Liu, Effects of light intensity on the growth and leaf development of young tomato plants grown under a combination of red and blue light. Sci. Hortic. **153**, 50–55 (2013)
32. T. Steinger, B.A. Roy, M.L. Stanton, Evolution in stressful environments II: adaptive value and costs of plasticity in response to low light in *Sinapis arvensis*. J. Evol. Biol. **16**(2), 313–323 (2003)
33. W. Oh, E.S. Runkle, R.M. Warner, Timing and duration of supplemental lighting during the seedling stage influence quality and flowering in petunia and pansy. HortScience **45**(9), 1332–1337 (2010)
34. T.W. McNellis, X.W. Deng, Light control of seedling morphogenetic pattern. Plant Cell **7**(11), 1749 (1995)
35. W. Fu, P.P. Li, Y. Wu, J. Tang, Effects of different light intensities on anti-oxidative enzyme activity, quality and biomass in lettuce. Hortic. Sci. **39**, 129–134 (2012)
36. Z. Yang, W. He, S. Mou, X. Wang, D. Chen, X. Hu, L. Chen, J. Bai, Plant growth and development of pepper seedlings under different photoperiods and photon flux ratios of red and blue LEDs. Trans. Chin. Soc. Agric. Eng. **33**(17), 173–180 (2017)

37. R. Wojciechowska, O. Długosz-Grochowska, A. Kołton, M. Zupnik, Effects of LED supplemental lighting on field and some quality parameters of lamb's lettuce grown in two winter cycles. Sci. Hortic. **187**, 80–86 (2015)
38. C.T. Della Valle, C.R. Daniel, B. Aschebrook-Kilfoy, A.R. Hollenbeck, A.J. Cross, R. Sinha, M.H. Ward, Dietary intake of nitrate and nitrite and risk of renal cell carcinoma in the NIH-AARP Diet and Health Study. Br. J. Cancer **108**, 205–212 (2013)
39. C.L. Chang, K.P. Chang, The growth response of leaf lettuce at different stages to multiple wavelength-band light-emitting diode lighting. Sci. Hortic. **179**, 78–84 (2014)
40. R. Breessani, J.E. Braham, L.G. Elias, All vegetable protein mixtures for human feeding. Can. J. Biochem. **42**(4), 631 (1964)
41. L.W. Zhang, S.Q. Liu, Z.K. Zhang, Dynamic effects of different light qualities on pea sprouts quality. North. Hortic. **8**, 4–7 (2010)
42. S. Nobile, J. M. Woodhill (eds.), *Vitamin C in the Human Body* (Springer, Dordrecht, 1981), pp. 57–75
43. P. Pinho, K. Jokinen, L. Halonen, The influence of the LED light spectrum on the growth and nutrient uptake of hydroponically grown lettuce. Light. Res. Technol. **49**(7), 866–881 (2017)
44. H.M. Qian, T.Y. Liu, M.D. Deng, Effects of light quality on main health-promoting compounds and antioxidant capacity of Chinese kale sprouts. Food Chem. **196**, 1232–1238 (2015)
45. K. Ohashi, M. Takase, N. Kon, Effect of light quality on growth and vegetable quality in leaf lettuce, spinach and komatsuna. Environ. Control. Biol. **45**(3), 189–198 (2007)
46. J. K. Cao, W. B. Jiang, Y. M. Zhao (eds.), *Physiological and Biochemical Experimental Guidance of Fruits and Vegetables* (China Light Industry Press, Beijing, 2007), pp. 49–50
47. Z.J. Zhang, D.X. He, G.H. Niu, R.F. Gao, Concomitant CAM and C3 photosynthetic pathways in *Dendrobium officinale* plants. J. Am. Soc. Hortic. Sci. **139**(3), 290–298 (2014)
48. T. Kozai, Resource use efficiency of closed plant production system with artificial light: concept, estimation and application to plant factory. Proc. Jpn. Acad. Ser. B Phys. Biol. Sci. **89**(10), 447–461 (2013)
49. N.N. Cometti, M.Q. Martins, C.A. Bremen Kamp, J.A. Nunes, Nitrate concentration in lettuce leaves depending on photosynthetic photon flux and nitrate concentration in the nutrient solution. Hortic. Bras. **29**, 548–553 (2011)
50. J.Z. Mao, Q. Qiu, F. Zhang, N. Li, Y.G. Hu, X.Z. Xue, Impact of different photoperiods on the morphological index, quality and absorptive amount to ions of lettuce in fluorescent light source. North. Hortic. **15**, 24–28 (2013). in Chinese
51. H.K. Jeong, K.K. Sugumaran, L.S.A. Sarah, B.R. Jeong, J.H. Seung, Light intensity and photoperiod Influence the growth and development of hydroponically grown leaf lettuce in a closed-type plant factory system. Hortic. Environ. Biotechnol. **54**(6), 501–509 (2013)
52. L.D. Albright, A.J. Both, A. Chiu, Controlling greenhouse light to a constant daily integral. Trans. ASAE **43**(2), 421–431 (2000)
53. A.J. Both, Ten years of hydroponic lettuce research. Knowledgecenter, illumitex.com, 2001, pp. 1–14
54. A. Scaife, S. Schloemer, The diurnal pattern of nitrate uptake and reduction by spinach (Spinacia oleracea L.). Ann. Bot. **73**(3), 337–343 (1994)
55. N. Gruda, Impact of environmental variables on product quality of greenhouse vegetables for fresh consumption. Crit. Rev. Plant Sci. **24**, 227–247 (2005)
56. D. McCall, J. Willumsen, Effects of nitrogen availability and supplementary light on the nitrate content of soil-grown lettuce. J. Hortic. Sci. Biotechnol. **174**(4), 458–463 (1999)
57. G. Aparna, M.D. Kleinhenz, J.C. Scheerens, P.P. Ling, Anthocyanin levels in nine lettuce (*Lactuca sativa*) cultivars: influence of planting data and relations among analytic, instrumented, and visual assessments of color. HortScience **42**(2), 232–238 (2007)

58. J. Zhong, T. Seki, S. Kinoshita, T. Yoshida, Effect of light irradiation on anthocyanin production by suspended culture of *Perilla frutecens*. Biotechnol. Bioeng. **38**, 653–658 (1991)
59. J.E. Park, Y.G. Park, B.R. Jeong, S.J. Hwang, Growth and anthocyanin content of lettuce as affected by artificial light source and photoperiod in a closed-type plant production system. Korean J. Hortic. Sci. Technol. **30**(6), 673–679 (2012)
60. X.L. Chen, W.Z. Guo, X.Z. Xue, L.C. Wang, Growth and quality response of 'Green Oak Leaf' lettuce as affected by monochromic or mixed radiation provided by fluorescent lamp (FL) and light-emitting diode (LED). Sci. Hortic. **172**, 168–175 (2014)
61. W. Zhou, W. Liu, Q. Yang, Reducing nitrate concentration in lettuce by elongated lighting delivered by red and blue LEDs before harvest. J. Plant Nutr. **36**, 481–490 (2013)
62. Z.P. Ye, J.D. Suggett, P. Robakowski, A mechanistic model for the photosynthesis-light response based on the photosynthetic electron transport of PS II in C3 and C4 species. New Phytol. **152**, 1251–1262 (2013)

Chapter 15
The Effect and Mechanism of Light on the Growth, Food Intake, and Gonad Development of Atlantic Salmon (*Salmo salar*) Reared in RAS

Ying Liu, Xiaolong Gao, and Liang Chi

15.1 Photoperiod Regulate Gonad Development via Kisspeptin/Kissr in Hypothalamus and Saccus Vasculosus of *Salmo salar*

15.1.1 Introduction

Kisspeptin and its receptor GPR54 (kissr) have been identified as key factors in controlling the reproductive cycle by stimulating gonadotropin-releasing hormone (GnRH) secretion in mammals. Loss of functional mutations in mouse and human GPR54 shows that GPR54 is absolutely required for reproduction in mammals [1–3]. In teleost, the study of kisspeptin and its receptor is still in its infancy. Parhar and co-workers were the first to report the importance of kissr and GnRH in fish reproduction and found that kissr was involved in the sexual development of a cichlid fish [4]. Since then, kisspeptin and kissr have become the subject of active research in fish reproduction. It is believed that kisspeptin and kissr perform similar roles in fish to kisspeptin/GPR54 reported in mammals. Kisspeptin has been reportedly associated with the onset of puberty in some fish species [5–7] and has GnRH regulatory functions in several others [8]. In addition, Martinez-Chavez et al. found that a long photoperiod could delay the onset of puberty and suppress GPR54 expression in Nile tilapia by reducing the expression of kisspeptin. This was the first study of teleost to suggest a possible connection between photoperiod

Y. Liu (✉) · X. Gao
Dalian Ocean University, Dalian, China
e-mail: yingliu@dlou.edu.cn

L. Chi
Qingdao Agricultural University, Qingdao, China

© Springer International Publishing AG, part of Springer Nature 2019

J. Li, G. Q. Zhang (eds.), *Light-Emitting Diodes*, Solid State Lighting Technology and Application Series 4, https://doi.org/10.1007/978-3-319-99211-2_15

and kisspeptin. Similar results have also been found in other fish species [9–11]. Furthermore, most research into photoperiods and GnRH have focused on the stage of puberty. Furthermore, there is very limited reference to the effects of kisspeptin/kissr on other stages of gonad development [12, 13].

Atlantic salmon (*Salmo salar* L.), are native to the North Atlantic and its surrounding rivers, and were introduced into Chinese using Recirculating Aquaculture Systems (RAS). Atlantic salmon are short-day seasonal breeders and are very sensitive to the photoperiod [14]. Furthermore, salmonids are characterized by their direct sensitivity to daylight and lack of endogenous rhythms found in other fish [15, 16]. In a previous study, we found that photoperiod can significantly affect the gonadal development of Atlantic salmon reared in RAS. In order to enrich our knowledge of the functions of the SV in teleost fish, we set out to clarify the relationship between kissr and GnRH in the hypothalamus and SV of Atlantic salmon under the different photoperiod regimes.

15.1.2 Materials and Methods

Atlantic salmon with an average body mass of 1071.70 ± 155.54 g were purchased from the Shandong Oriental Ocean Sci-Tech Co., Ltd., Shandong province, China. The fish were then allowed to acclimate for 4 weeks in an RAS under 24L:0D photoperiod, after which they were distributed between the experimental RAS tanks (130 cm height ×200 cm diameter). Each experimental group contained 60 fish. During the experimental period, the water temperature was maintained at 16.27 ± 0.54 °C, pH 7.2 ± 7.5, total ammonia-nitrogen <0.25 mg/L, and salinity 24–26 over the course of the experiment.

The fish were divided into six photoperiod treatment groups. Four of the photoperiod treatments remained constant throughout the experiment 24L:0D, 18L:6D, 12L:12D, and 16L:8D. The remaining two photoperiod groups had varying photoperiods during the experiment. In the first treatment, the photoperiod changed from 24L:0D to 8L:16D (the LL-SL treatment), and in the second the photoperiod changed from 8L:16D to 24L:0D (the SL-LL treatment), the photoperiod being changed by 5 min per day in both cases. There were three replicate tanks (initially $n = 60$ fish/tank). The experiment was performed over a 7-month period from September to the following March, a period spanning the first reproductive period. Fish were sampled every month. Nine female fish were anesthetized until death in seawater with 0.05% MS-222 (3-aminobenzoic acid ethyl ester methanesulfonate). Body weight, length, and gonad weight were recorded, and the brains were immediately weighed, frozen in liquid nitrogen, and stored at −80 °C. The gonads and brains were placed in Bouin's solution for 24 h and then stored in 70% ethanol for later histological examination. Blood was centrifuged, and plasma was stored at −80 °C.

Furthermore, the gonadal development in this paper was determined based on GSI, external morphological and histology observation as follows: stage II

(beginning of vitellogenesis with primary yolk vesicles, GSI = 0.15% ± 0.05%), stage III (secondary yolk stage, GSI = 0.31% ±0.18%), stage IV (accumulation of yolk happened, GSI = 11.87% ± 8.85%), and stage V (cytoplasm of oocyte was filled with yolk granules, GSI = 17.57% ± 3.01%). All of the procedures described in this study were reviewed and approved by the ethical committee of the Institute of Oceanology, Chinese Academy of Sciences.

Antisense digoxigenin (DIG) probes and antisense fluorescein isothiocyanate (FITC) were transcribed for salmon sGnRH gene and skissr gene by using a DIG and FITC-Labeling Kit (Roche, USA). Sense probe for salmon sGnRH and skissr was transcribed as negative control. The brains from Atlantic salmon reared in the different photoperiod treatments were fixed in 4% paraformaldehyde in 0.1 M PBS (phosphate buffered saline, pH 7.4) at 4 °C overnight. The samples were then dehydrated using a graded methanol series. After that, the samples were mixed with warm paraffin to embed. Sections of paraffin-embedded brains were prepared on 5-μM glass slides coated with 0.1% poly-L-lysine solution. The partial CDS of sGnRH3 and skissr were cloned into pGEM-T vectors for preparing sense and antisense RNA probes from a T7 or SP6 promoter using a FITC or digoxigenin (DIG) RNA-Labeling Kit (Roche). The sections were hybridized with the sense or antisense probes at 66 °C for 18 h. After hybridization, the samples were incubated overnight at 4 °C with horseradish peroxidase (POD)-conjugated anti-FITC antibody (Roche) at a 1:2000 dilution in the blocking solution to detect the FITC signal. After three washes in PBST, the samples were incubated for 1 h in TSA-Fluorescein at a 1:150 dilution in TSA Amplification Buffer. The samples were then subjected to detect the DIG signal. They were incubated overnight at 4 °C with POD-conjugated anti-DIG antibody (Roche) at a 1:2000 dilution in blocking buffer with 1% H_2O_2. Following three PBST washes, the samples were incubated in TSA-plus tetramethylrhodamine for 1 h. Double-color fluorescence in situ hybridization was performed using tyramide signal amplification (TSA™) plus fluorescein and tetramethylrhodamine (TMR), according to the manufacturer's instructions (NEL756, PerkinElmer). The nuclei were stained using 4′-6-diamidino-2-phenylindole (DAPI) and embedded in ProLong1 Gold Antifade reagent (Invitrogen). The slides were then mounted and photographed using a Nikon Eclipse 50i fluorescence microscope. In this procedure, two antisense RNA probes were co-incubated in a single sample during the hybridization step, and developed red and green fluorescence.

15.1.3 Results

15.1.3.1 The Location of Skissr and sGnRH3 in the Brain of Atlantic Salmon

First, the mRNA expressions of skissr and sGnRH3 were detected in the different regions of the Atlantic salmon brain using qPCR (quantitative real-time PCR) with

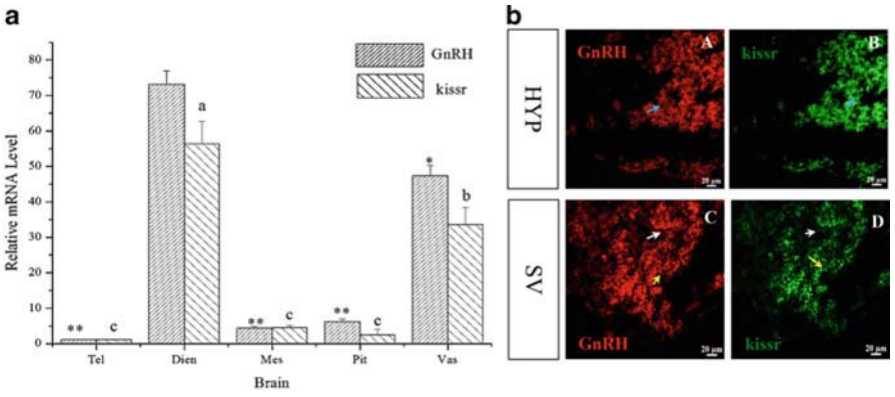

Fig. 15.1 (**a**) The distribution of sGnRH3 and skissr in the Atlantic salmon brain. *Tel* telencephalon, *Dien* diencephalon, *Mes* mesencephalon, *Pit* pituitary gland, *SV* saccus vasculosus. (**b**) The expression of sGnRH3 and skissr in the hypothalamus (A, B) and SV (C, D). The cells which express sGnRH3 mRNA are indicated by blue arrows; the white arrows indicate the supporting cells of the SV; and the yellow arrows indicate the coronet cells of the SV. The results show that skissr is mainly expressed in the cerebrospinal fluid-contacting (CSF-c) cells of the SV. Hyp: hypothalamus; SV: saccus vasculosus; Results are presented as mean ± SD. Significant differences were found at $p \leqq 0.5$* and $p \leqq 0.1$**; and different letters indicate statistical significance at $p < 0.05$

β-actin mRNA as a reference gene. The results showed that both sGnRH3 and skissr transcripts were primarily expressed in the diencephalon. The transcription levels of sGnRH3 and skissr were higher in the SV than in other parts of the brain except the diencephalon (Fig. 15.1a). Second, the diencephalon and SV of Atlantic salmon were isolated and used to perform in situ hybridization in order to confirm the precise location of sGnRH3 and skissr transcripts. The results showed that sGnRH3 and skissr transcripts were mainly expressed in the Hyp of the diencephalon. In the SV, the sGnRH3 and skissr also showed the same expression pattern. Both sGnRH3 and skissr were found in the cells close to the ventricles (Fig. 15.1b).

15.1.3.2 Changes in Skissr in the Hyp and SV During Gonad Development

The experiment ran throughout virtually every stage of development of the Atlantic salmon, from stage II to maturity. The expression levels of kissr were taken as the mean value in each photoperiod treatment. In the early and late stages of gonad development, when the ovaries were at stage II and stage V, the expression levels of kissr transcripts were significantly higher than at stage III and stage IV (Fig. 15.2a and c). A similar phenomenon was also observed in the SV (Fig. 15.2b and c).

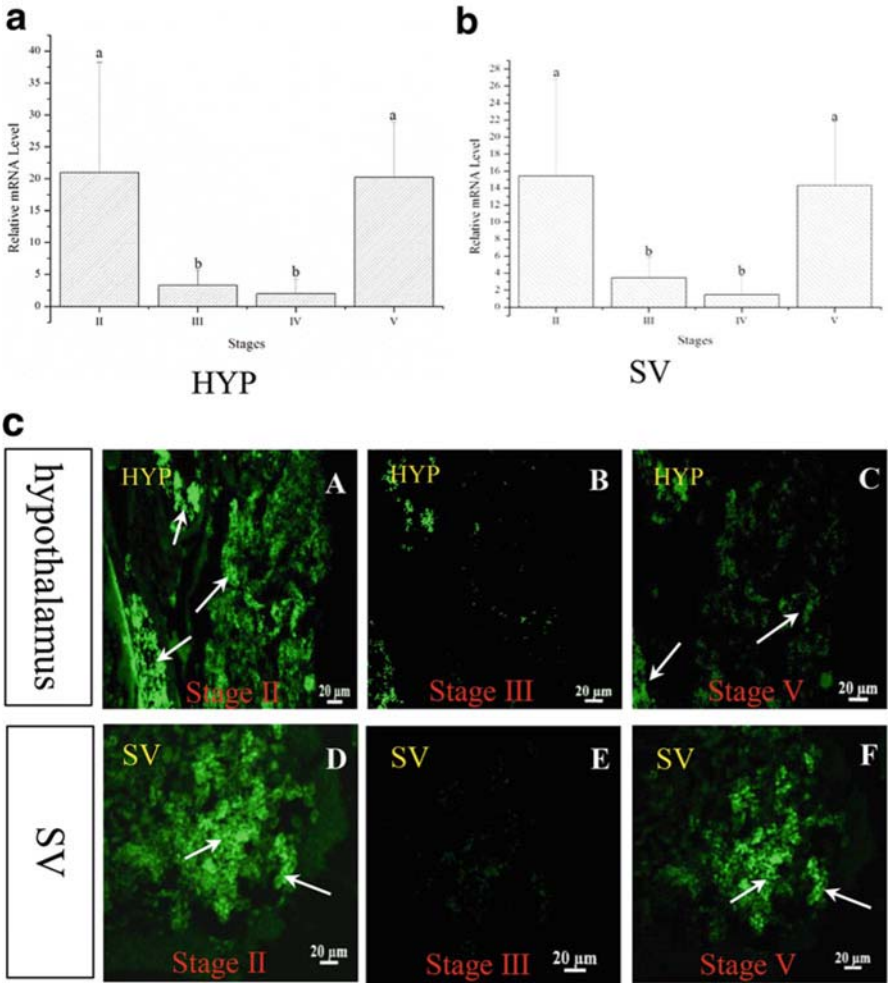

Fig. 15.2 The expression pattern of skissr in the hypothalamus (**a**) and SV (**b**) during the development process of Atlantic salmon. II: the gonad at stage II; III: the gonad at stage III; IV: the gonad at stage IV; and V: the gonad at stage V. (**c**) The expression of kissr in the Atlantic salmon hypothalamus (A, B, and C) and SV (D, E, and F) when fish with different stages of gonad development are assayed using in situ hybridization. *SV* saccus vasculosus. The kissr was mainly expressed in the early and late stages of gonad development in Atlantic salmon both in the hypothalamus and the SV. Data are shown as mean ± SD. One-way ANOVA is performed to determine the significant differences between means. Columns sharing different letters show significant difference ($p < 0.05$)

15.1.3.3 Changes in sGnRH3 in the Hyp and SV During Gonadal Development

The expression of sGnRH3 in the Hyp and SV increased as the gonads developed. The expression of sGnRH3 transcripts was lowest when the ovaries were at stage II. The expression of sGnRH3 mRNA was relatively stable when the ovaries were at stage III and stage IV. The mRNA level of sGnRH3 increased to its highest when the ovaries were at stage V (Fig. 15.3a). The level of sGnRH3 transcripts in the SV showed the same expression pattern as in the Hyp, while the expression level of sGnRH3 in the SV was lower than in the Hyp (Fig. 15.3b).

15.2 Photoperiod May Regulate Growth via a Leptin Receptor in the Hypothalamus and Saccus Vasculosus of *Salmo salar*

Photoperiod is believed to regulate growth in fish, although the mechanism involved is still unclear. In this paper, we report a relationship between leptin-receptor (AsLR), melatonin-receptor (AsMR), and photoperiod in Atlantic salmon. Atlantic salmon (mean weight 1071.70 ± 155.54 g) were reared under six photoperiod regimes, four constant light regimes 24L:0D, 18L:6D, 12L:12D, and 8L:16D, hours of light (L) and dark (D) and two varying light regimes, LL-SL = 24L:0D–8L:16D, and SL-LL = 8L:16D–24L:0D over a period of 7 months. The results showed that AsLR transcripts were mainly existed in the hypothalamus and saccus vasculosus (SV), while AsMR was mainly expressed in the hypothalamus. Long photoperiod inhibited the expression of AsLR and AsMR transcripts in the Atlantic salmon brain. The expression pattern of AsLR was similar to the expression pattern of AsMR in the hypothalamus. Food intake was higher in fish with lower AsLR transcript levels. This demonstrated that photoperiod influenced somatic growth by changing expression of AsLR in the hypothalamus and SV to affect appetite. In addition, the SV appears to act as a seasonal sensor regulating reproduction in a similar way to the hypothalamus.

15.2.1 Introduction

Leptin is secreted by adipose tissue and has an important role in regulating appetite, adiposity, food intake, and energy expenditure in mammals [17]. Leptin interacts with several neuropeptides to regulate food intake in the hypothalamus [18]. The physiological functions of leptin are mediated the leptin receptor (LR) in mammals [19]. In fish, leptin or LRs have been identified in many species including zebrafish, medaka, Arctic charr, rainbow trout, and Atlantic salmon [20, 21]. The functions

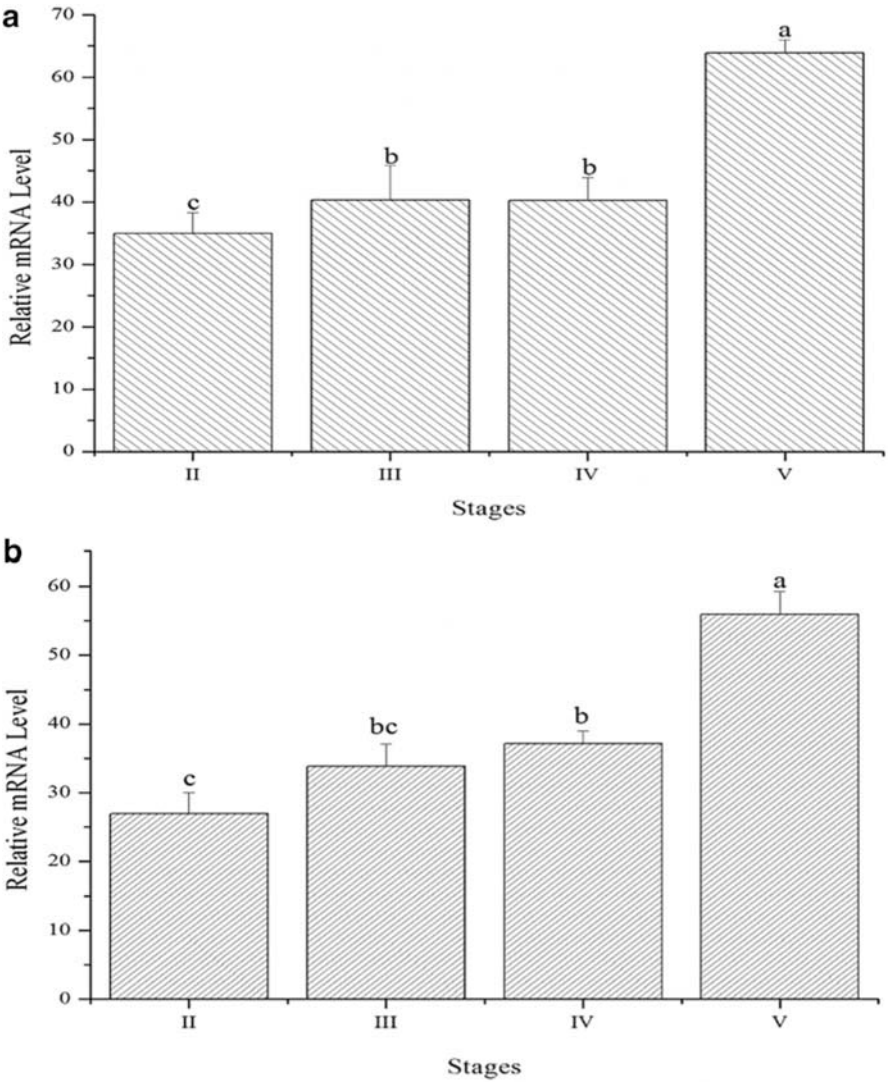

Fig. 15.3 The expression pattern of sGnRH3 in the hypothalamus (**a**) and saccus vasculosus (**b**) during the development of Atlantic salmon. II: the gonad at stage II; III: the gonad at stage III; IV: the gonad at stage IV; and V: the gonad at stage V

of leptin and LRs in fish are similar to those in mammals. The action of leptin is mediated through LRs expressed on appetite-related neurons and circuits in the hypothalamus [22]. Studies in mammals have found that the expression of leptin is rhythmic, which is related to the pineal melatonin axis in ruminants [23]. In fish, the rhythm of leptin/LRs is mainly focused on the feeding regime. Daily changes in leptin mRNA were first studied in Atlantic salmon, in which changes

were seen in white muscle, belly flap, visceral adipose tissue, and liver, when fish are exposed to short-term feeding restrictions [24]. Meanwhile, in goldfish, hepatic leptin expression peaks appear at 9 h post-feeding [25]. These results suggest that leptin/LRs could be affected by environmental factors. Up to now, however, our understanding of the relationship of leptin/LRs and photoperiod is still limited.

Photoperiod could regulate growth in fish and growth is related to leptin and LRs, thus we hypothesized that there may be some relationship between photoperiod and leptin/LRs. Atlantic salmon are native to the north Atlantic and its surrounding rivers, and were introduced into China using Recirculating Aquaculture Systems (RAS). In our previous study, we found that photoperiod significantly affected growth of Atlantic salmon reared in an RAS. In this paper, the relationship between photoperiod and leptin/LRs of Atlantic salmon was investigated using an RAS. In addition, the regulation center for photoperiod is mainly located in the brain, and therefore, this study focused on Atlantic salmon LRs, which are also mainly expressed in the brain.

15.2.2 Materials and Methods

Atlantic salmon (weight: 1071.70 ± 155.54 g) were collected from Shandong Oriental Ocean Sci-Tech Co. Ltd., Shandong province, China. The fish were randomly distributed into experimental RAS tanks (130 cm high × 200 cm diameter) and reared by satiation feeding with a commercial salmon diet (Skretting, Norway) containing 48% protein and 18% fat twice daily during the period of light manipulation, and the total food consumption of each tank was recorded. Each experimental tank contained 60 fish. The water temperature was maintained at 16.27 ± 0.54 °C, total ammonia-nitrogen <0.25 mg/L, salinity 24–26, and a pH between 7.2 and 7.5.

Six photoperiod treatment groups were designed. Four of the photoperiods were constant throughout the experiment 24L:0D, 18L:6D, 12L:12D, and 16L:8D [hours of light (L) and dark (D)]. The other two photoperiods varied. In the first, the photoperiod changed from 24L:0D to 8L:16D (LL-SL treatment), and in the second changed from 8L:16D to 24L:0D (SL-LL treatment), with the lighting period changing 5 min per day in both cases. Each group contained three replicate tanks (60 fish/tank). The experiment was performed from September to the following March, a period almost spanning the first reproductive period. First, all fish in each tank were anesthetized using 0.05% MS-222 and measured for body weight and body length every month individually. Then, fish were sampled, and three fish in each tank were anesthetized to death in seawater using 0.05% MS-222. Body mass and length were recorded, and the brain were frozen in liquid nitrogen, and immediately stored at −80 °C. The gonads were stored in Bouin's fixative for 24 h and then in 70% ethanol for histological examination to confirm the specific stage of the

experimental fish. All of the procedures described in this study were reviewed and approved by the ethical committee of the Institute of Oceanology, Chinese Academy of Sciences.

The feeding ratio (FR) was calculated as FR (%) = 100 × F/[0.5 × (BW2 + BW1) × (T2 − T1)], where BW1 and BW2 were the average individual weights at days T1 and T2. F was total food consumption.

The brains of Atlantic salmon were fixed in 4% paraformaldehyde in 0.1 M PBS (phosphate buffered saline, pH 7.4) overnight at 4 °C. The samples were dehydrated in a graded series of methanol. Sections of paraffin-embedded brains were prepared on 5-μM glass slides coated with 0.1% 164 poly-L-lysine solution. The partial CDS of AsMR and AsLR were cloned into pGEM-T vectors for preparing sense and antisense RNA probes from a T7 or SP6 promoter by using FITC or digoxigenin (DIG) RNA-Labeling Kit (Roche), respectively. The sections were hybridized with the sense or antisense probes at 66 °C for 18 h. After hybridization, the samples were incubated overnight at 4 °C with horseradish peroxidase (HRP)-conjugated anti-FITC antibody (Roche) at a 1:2000 dilution in blocking solution to detect the FITC signal. After three washes in PBST, the samples were incubated 1 h in tyramide signal amplification (TSA)-fluorescein at a 1:150 dilution in TSA buffer. The DIG signal was detected in samples. They were incubated overnight at 4 °C with HRP-conjugated anti-DIG antibody (Roche) at a 1:2000 dilution in blocking buffer with 1% H_2O_2. Following three PBST washes, the samples were incubated in TSA-plus tetramethylrhodamine (TMR) for 1 h. Double-color fluorescence in situ hybridization was performed using TSA plus fluorescein and TMR according to the manufacturer's instruction (NEL756, PerkinElmer). The nuclei were stained using 4′-6-diamidino-2-phenylindole (DAPI) and embedded in ProLong Gold Antifade reagent (Invitrogen, Carlsbad, CA, USA). The slides were then mounted and photographed by Nikon Eclipse 50i fluorescence microscope (Tokyo, Japan). In this procedure, two antisense RNA probes were co-incubated in a single sample during the hybridization step, to develop red and green fluorescence.

The Atlantic salmon brain was fixed in Bouin's fixative for 24 h and preserved in 70% ethanol. The samples were stained using hematoxylin 186 and eosin (H&E), and sections were observed by a light microscope (NikonYS-100, Japan). Photographs were taken with a digital camera (Nikon coolpix-4500, Japan).

15.2.3 Results

15.2.3.1 Location of AsMR and AsLR in the Brain of Atlantic Salmon

The location of AsMR and AsLR were examined by quantitative real-time PCR with β-actin mRNA as a loading control. The results showed that AsLR was primarily expressed in the diencephalon, pituitary gland, and SV, and AsMR were mainly

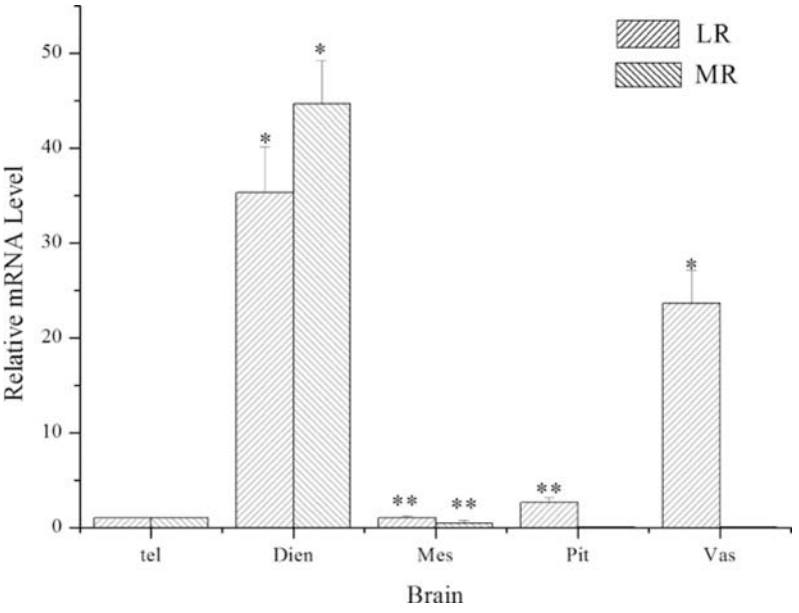

Fig. 15.4 Distribution of AsLR and AsMR in the Atlantic salmon brain. *Tel* telencephalon, *Dien* diencephalon, *Mes* mesencephalon, *Pit* pituitary gland, *Vas* saccus vasculosus

expressed in the diencephalon in the Atlantic salmon brain (Fig. 15.4). To confirm the precise location of AsLR, the diencephalon and SV were isolated to perform in situ hybridization. The results showed that both AsLR and AsMR transcripts were mainly expressed in the hypothalamus of the diencephalon (Fig. 15.5g–i). In the SV, the LR transcripts mainly appeared in the cerebrospinal fluid-contacting (CSF-c) cells (Fig. 15.5d–f). Besides the brain, the LR transcripts were mainly expressed in the gills, gut muscle, and ovaries (Fig. 15.6).

15.2.3.2 Expression Pattern of AsMR in the Different Photoperiod in the Hypothalamus of Atlantic Salmon

Expression of AsMR in the hypothalamus could be influenced by photoperiod. At the beginning of the experiment, the AsMR transcripts levels were lowest in the 24L:0D group, followed by the LL-SL group. The expression level of AsMR transcripts was highest in the 8L:16D group followed by the SL-LL group (Fig. 15.7a). At the end of the experiment, the lowest level of AsMR transcripts appeared in the 24L:0D and SL-LL groups and the highest level in the 8L:16D and LL-SL groups (Fig. 15.7b).

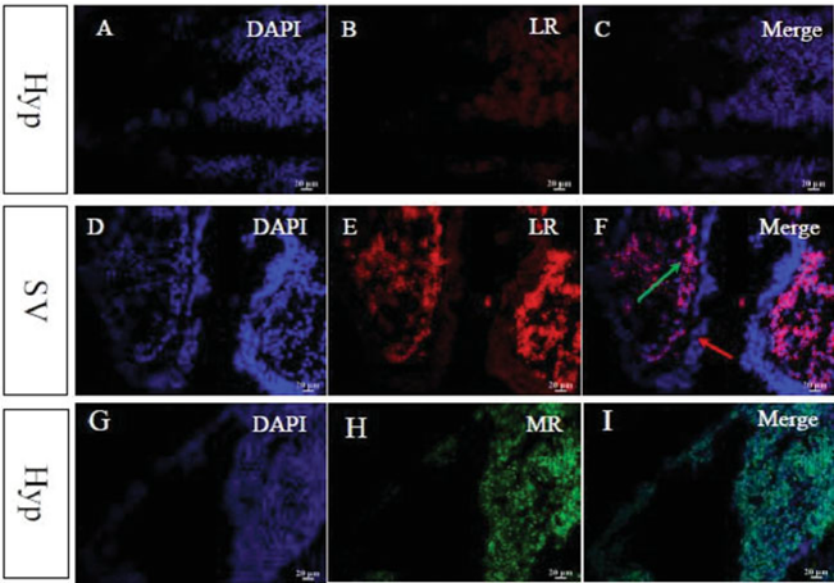

Fig. 15.5 Expression of AsLR and AsMR in the hypothalamus and saccus vasculosus. (**a–c**) Expression pattern of AsLR in the hypothalamus of Atlantic salmon brain; (**d–e**) expression pattern of AsLR in the saccus vasculosus of Atlantic salmon brain; and (**g–i**) location of AsMR mRNA in the hypothalamus using in situ hybridization. The green arrow indicates the cerebrospinal fluid-contacting cells; and the red arrow indicates the coronet cells. *SV* saccus vasculosus, *Hyp* hypothalamus

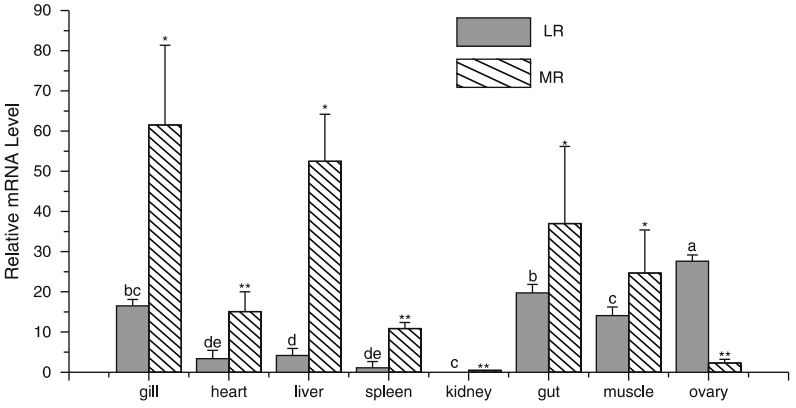

Fig. 15.6 Distribution of AsLR and AsMR transcripts of adult Atlantic salmon. Results are presented as mean ± SD. Significant differences were found at $p < 0.5$* and $p < 0.1$**; and different letters indicate statistical significance at $p < 0.05$

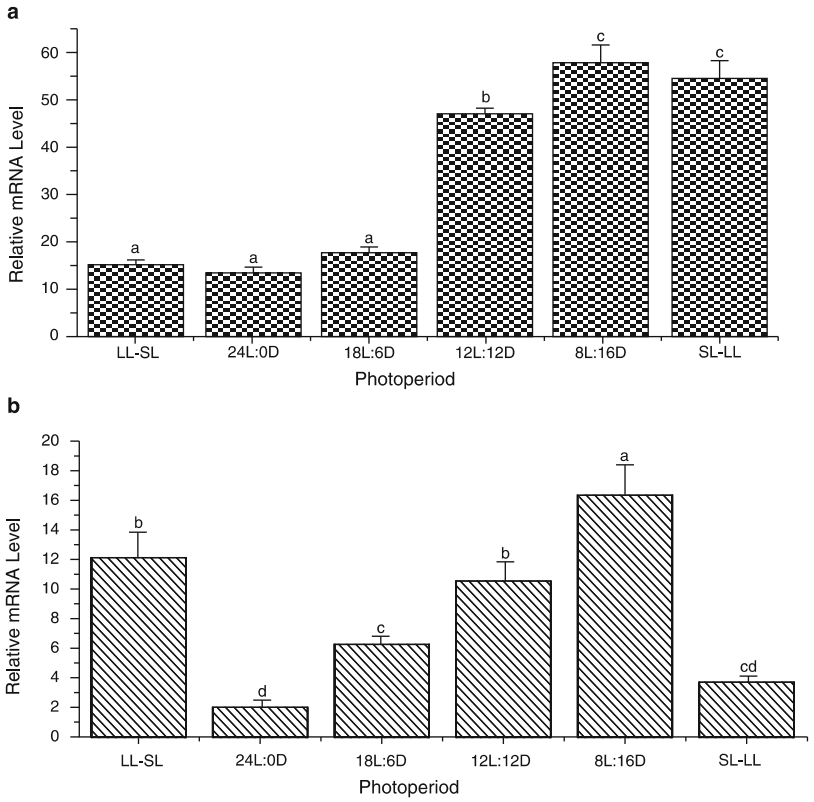

Fig. 15.7 Expression pattern of AsMR transcripts in different photoperiods. (**a**) Expression pattern of AsMR transcripts in different photoperiods at the early stage of the experiment; (**b**) expression pattern of AsMR transcripts in different photoperiods at the end of the experiment. Different letters indicate statistical significance at $p < 0.05$

15.2.3.3 Expression Pattern of AsLR in Different Photoperiods in the Hypothalamus and SV of Atlantic Salmon

Since AsLR was mainly expressed in the hypothalamus and SV, we examined the expression of AsLR in the hypothalamus and SV under different photoperiods. The results showed that photoperiod affected the expression of AsLR in the hypothalamus and SV. In the hypothalamus, AsLR transcripts were lowest in the 24L:0D and the LL-SL photoperiod groups (Fig. 15.8a) at the early stage of the experiment. At this time, these two treatments had the longest photoperiod. At the end time of the experiment, the lowest AsLR transcripts levels were in the 24L:0D group followed by the SL-LL group (Fig. 15.8b). The expression pattern of AsLR in the SV is similar to the hypothalamus. However, the expression level of AsLR in the SV is lower than that in the hypothalamus (Fig. 15.9a and b).

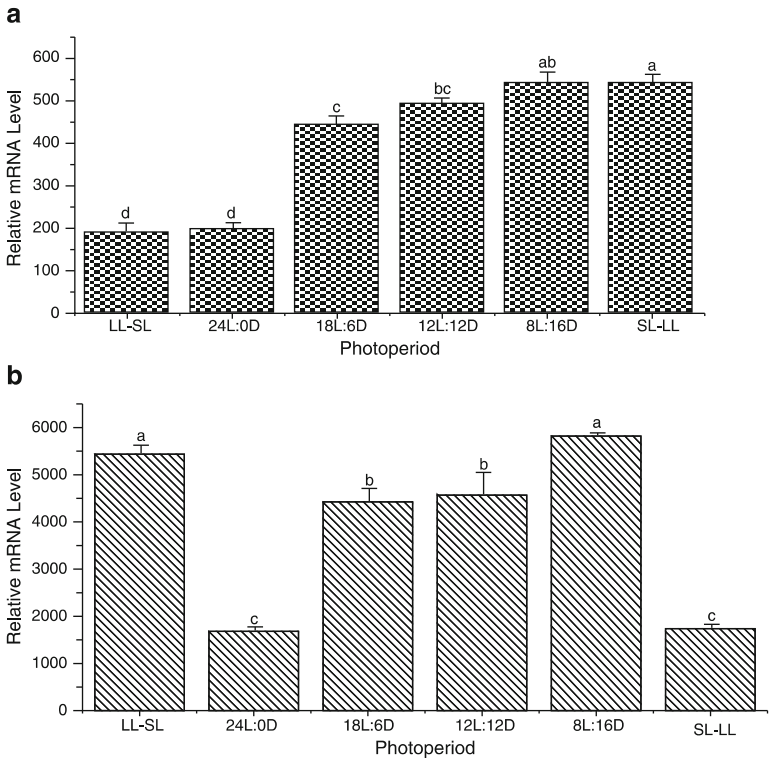

Fig. 15.8 Expression pattern of AsLR transcripts in the Atlantic salmon hypothalamus in different photoperiods. (**a**) Expression pattern of AsLR transcripts in different photoperiods at the early stage of the experiment; and (**b**) expression pattern of AsLR transcripts in different photoperiods at the end of the experiment. Different letters indicate statistical significance at $p < 0.05$

15.3 The Effect and Mechanism of Light on the Growth, Food Intake, and Energy Budget of Abalone (*Haliotis discus hannai Ino*)

Light is one of the key environmental factors influencing the growth, development, and survival of aquatic organisms, which have evolved to be able to change their physiology and behavior to adapt to changes in light conditions. In this study, a bioenergetics approach was used to examine the effects of different LED light qualities (red, orange, blue, green light, natural light, and a dark setting) on the growth and survival of the abalone *Haliotis discus discus*, and its physiological response mechanism under different light qualities. The results suggest that under blue or green light, the survival rate, specific growth rate, food intake, and food conversion efficiency of *H. d. discus* were significantly lower than in those groups under red or orange light ($P < 0.05$). Under red or orange light, the protein content,

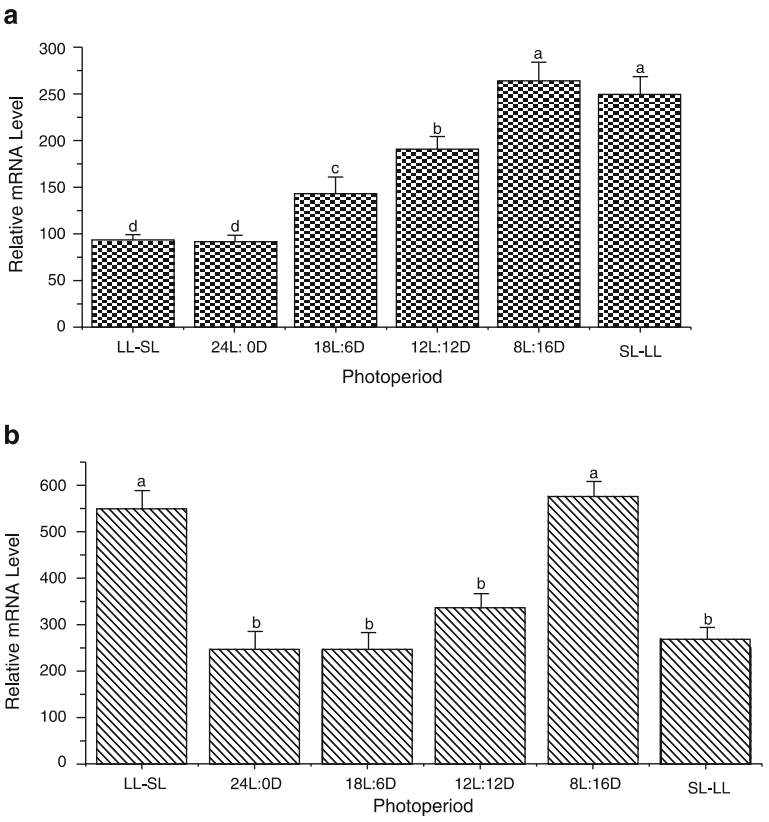

Fig. 15.9 Expression pattern of AsLR transcripts in the Atlantic salmon SV in different photoperiods. (**a**) Expression pattern of AsLR transcripts in different photoperiods at the early stage of the experiment; and (**b**) expression pattern of AsLR transcripts in different photoperiods at the end of the experiment. Different letters indicate statistical significance at $p < 0.05$

ash, and tissue:shell ratio of *H. d. discus* were significantly higher than in those groups under other light qualities ($P < 0.05$). Under red or orange light, pepsin, amylase, and cellulose activity was significantly higher than those in any other light quality group ($P < 0.05$), whereas lipase activity exhibited no significant difference among the light quality groups ($P > 0.05$). Under blue or green light, hexokinase and pyruvate kinase activity was higher than in any other group ($P < 0.05$). Under red or orange light, or in dark setting, succinate dehydrogenase activity was significantly higher than in any other group ($P < 0.05$), indicating the enhanced aerobic metabolism that was conductive to the continuous crawling of *H. d. discus*. Under blue or green light, lactate dehydrogenase activity and lactic acid content were higher ($P < 0.05$), suggesting enhanced anaerobic metabolism. Under blue or green light, *H. d. discus* lost more energy via excretion, feces, and respiration than was acquired from its food; as a consequence, there was no energy available for its

growth. Under red or orange light, *H. d. discus* acquired more energy from its food and lost less energy via excretion and feces; as a result, its assimilation efficiency (K1) and net growth efficiency (K2) were significantly higher than those of any other group ($P < 0.05$). Therefore, we suggest that red or orange light should be used as a light source for the aquaculture of *H. d. discus* to reduce costs, increase the yield per water body, and improve the welfare culture of this and other species of abalone.

15.3.1 Introduction

The disc abalone *Haliotis discus discus* is an economically important shellfish in China, with demand growing for this high-protein and low-fat seafood. In 2012, 90,694 tons of *H. d. discus* were harvested from aquacultural sources, but supply cannot currently meet consumer demand. In recent years, the natural habitat of *H. d. discus* has declined as a result of overfishing, marine reclamation, and water pollution, among others, leading to a sharp decrease in the numbers of *H. d. discus* in the wild [26]. Thus, the development of an aquacultural system for farming *H. d. discus*, as well as for its protection in the wild, is the focus of current research. As a result, there is a need to identify the tolerance limits of *H. d. discus* seedlings to different environmental factors and how it responds physiologically to such stress factors. Currently, most studies on the growth and survival of abalone have focused on the effects of temperature [27], salinity [28], flow velocity [29], ammoniacal nitrogen [30], and dissolved oxygen [31], whereas only a few studies [32] have considered the effects of light on the growth and physiology of *H. d. discus*.

In this study, light-emitting diode (LED) lights were used as a light source instead of traditional fluorescent lamps; LEDs have become a mainstay in many research areas and are known to be safe to use, with few, if any, detrimental environmental impacts. LEDs produce less heat, have longer life, more precise wavelength emission, and more precise control of light level [33] making them more efficient sources of light. In addition, LED lights have been shown to not only increase the growth rate of aquatic organisms but also produce high-quality pollution-free food. Therefore, we adopted a bioenergetic approach to examine the effects of different light qualities on the growth and survival of *H. d. discus*, and its physiological response mechanism under different light qualities. Our results will provide a reference on which to base the development of the rapid and biologically friendly aquaculture of *H. d. discus*.

15.3.2 Materials and Methods

LED lights were purchased from the Hangzhou YD Illumination Co. Ltd., China. Four treatment groups under different light qualities and one fully dark setting were established. Light qualities included blue (450 nm), green (565 nm), red (620 nm),

and orange light (600 nm). In addition, abalones were reared in natural light ("NL") as a control group, following the natural photoperiod of 14:10 light:dark. Light cycle was controlled by fully masking the sunlight using the blackout cloth in the control group. The LED light was hung above the aquarium, and the light intensity in the different light-quality treatment groups was kept as constant as possible by adjusting the distance from the LED light to the water surface. A spectroradiometer (JETI LiVal Spectroradiometer Model Specbos 1xx1, Jena, Germany) was used to measure the wave peak of light quality and light intensity, and five different points inside the aquarium were selected and then averaged to ensure that the wave peak of each light quality was within the required range. During this experiment, the light cycle was 14:10 light:dark, and lights were turned on at 06.00 h and off at 20.00 h via a clock controller.

Four repetitions of each treatment group per light quality were set up, with a total of 24 39-L plastic aquariums (45 cm × 25 cm × 35 cm). Ten individuals were placed in each aquarium, and a blackout cloth was used to separate the treatment groups of different light qualities, creating six separate square small chambers (1.5 m × 0.8 m × 0.5 m) to avoid light pollution. The approximate extent of light intensity was 1.82 ± 0.34 $\mu mol/m^2/s$ in the different chambers. In the chamber under a dark setting, the abalones were exposed to no light except briefly during water exchange, feeding, or feces collection. The water temperature was kept at 17 °C with the same salinity and pH as described above. Aeration was almost continuously provided in each aquarium to keep the concentration of dissolved oxygen >6 mg/L; it was stopped for 30 min before collecting the food residues and feces, during which time the ammonia and nitrogen concentrations were < 0.1 mg/L.

All abalones were starved for 24 h before starting the experiment; 240 juvenile abalones (shell length: 42.51 ± 3.66 mm, body weight: 14.72 ± 2.39 g) were randomly divided into treatment groups under different light qualities. In total, 20 abalone samples were randomly selected for pre-treatment analysis to determine their initial weight, energy, and crude protein content before the experiment. As mentioned above, the abalones were fed daily at 17.00 h; at 07.00 h, food residue and feces were siphoned out, dried in the oven at 70 °C until a constant weight was achieved, and then stored in the refrigerator at −20 °C for the determination of energy and nitrogen values following the study. Simultaneously, *Lonicera japonica* (quantity equivalent to 6% of the wet body weight of abalone) were placed in another three aquariums without abalone to determine any possible effects that this food source may have on the experimental setup (e.g., nutrient damage, changes in chemical composition, etc.). The following morning, the food residue were collected, weighed, and dried to determine the value of food intake. During this experiment, two-thirds of the water volume was exchanged daily. After the experiment had finished, four abalones were collected from each aquarium and dried in the oven at 75 °C until a constant weight was achieved, to determine the energy content of the abalones. In addition, three abalones were collected from each aquarium to analyze and determine the enzyme activity and body composition.

Moisture on the surface of the abalones was removed using absorbent paper, and the abalones were then rapidly dissected on an ice tray. After shelling, the

hepatopancreas was put into a 1.5-mL centrifuge tube, quickly placed in liquid nitrogen, and later moved to the refrigerator at −80 °C to be tested. Then, 0.2–0.4 g tissues were suspended in 1.8 mL 0.86% normal saline and fully ground in an ice-water bath. The tissue suspension was centrifuged at 3500 r/min for 10 min, until a 10% tissue homogenate were produced for further investigations. The activity of hexokinase (HK), pyruvate kinase (PK), succinic dehydrogenase (SDH), and lactic dehydrogenase (LDH), and the protein content of each sample were determined via kits supplied by Nanjing Jiancheng Bioengineering Institute (Nanjing, PR China), as per the manufacturer's instructions. PK activity was defined as: tissue protein per g converting 1 μmol phosphoenolpyruvate to pyruvic acid at 37 °C, pH 7.6 every 1 min (i.e., 1 activity unit). HK activity was defined as: at 37 °C, pH 7.6, the amount of issue protein per g generating 1 mmol NADPH every 1 min (i.e., 1 enzyme activity unit). SDH activity was defined as: the amount of protein per mg reducing the absorbency of the reaction medium (comprising 0.1 mol/L sodium succinate, 0.01% methylene blue, 0.04 mol/L disodium malonate, and pH 7.0 phosphate buffer) at 37 °C every 1 min by 0.01 (i.e., 1 specific activity unit). LDH activity was defined as: the amount of tissue protein per g reacting with the substrate (4 mol/L NaOH, 2,4-dinitrophenylhydrazine, 2 mmol/L sodium pyruvate, and coenzyme I) at 37 °C for 15 min to produce 1 μmol pyruvic acid (i.e., 1 activity unit). The SDH activity unit was expressed in U/mg prot, whereas those for PK, HK, and LDH were in U/g prot. Meanwhile, the activity of pepsin (PES), lipase (LPS), cellulase (CL), and amylase (AMS) and the protein content of the sample were also determined via kits supplied by Nanjing Jiancheng Bioengineering Institute (Nanjing, PR China). For the determination of PES, CL, and AMS, 0.2–0.4 g tissue was fully ground with 1.8 mL 0.86% normal saline in an ice-water bath. The suspended tissues were then centrifuged at 2500 r/min, 8000 r/min, and 2500 r/min at 4 °C for 15 min, until a 10% tissue homogenate was produced for further investigations. PES activity was defined as: the amount of tissue protein per mg decomposed into 1 μg amino acid at 37 °C in 1 min (i.e., 1 enzyme activity unit). CL activity was defined as: the amount of tissue per g catalyzed to 1 μg glucose in 1 min (i.e., 1 enzyme activity unit). AMS activity was defined as: the amount of protein per mg in the tissues reacted with the substrate at 37 °C for 30 min to hydrolyze 10 mg amylon (i.e., 1 AMS activity unit). To determine LPS activity, 0.2–0.4 g tissue was fully ground with 1.8 mL 0.86% normal saline in an ice-water bath. The tissues were then mechanically homogenized at 2500 r/min, centrifuged for 10 min, and the supernatant then used to determine LPS activity. This was defined as the amount of tissue protein per g reacted with the substrate in this response system at 37 °C for 1 min to consume 1 μmol substrate (i.e., 1 enzyme activity unit). AMS and PES activity units were expressed in U/mg prot, whereas those of CL and LPS were expressed in U/g prot.

Abalones and *L. japonica* were dried at 105 °C to a constant weight to determine their moisture content. An elemental analyzer (Vario EL III, Germany) was used to determine the nitrogen content. The Soxhlet method was used to determine the fat content. Food and abalone were put in a muffle furnace (SX2-5-12, Shanghai, China) at 550 °C for 12 h to determine the resulting ash content [34]. An oxygen bomb calorimeter (Parr 1281, USA) was used to determine the energy value of food,

feces, and abalone body. Each sample was analyzed at least three times. The content of lactic acid was determined via kits supplied by Nanjing Jiancheng Bioengineering Institute (Nanjing, PR China), when NAD was used as hydrogen acceptor, LDH catalyzed the dehydration of lactic acid to pyruvic acid and converted NAD^+ into NADH. PMS transferred hydrogen to reduce nitrotetrazolium blue chloride (NBT) to a purple chromogenic substrate. When the absorbency of the chromogenic substrate equaled 530 nm, it correlated linearly with the content of lactic acid, thus enabling us to determine the lactic acid content of the sample.

Energy budgets were based on the model proposed by Carfoot [35]: $C = F + U + R + G$ was converted to $G = C - F - U - R$, where C was the energy contained in the food intake, G was the energy accumulated for growth, F was the energy lost in feces, U was the excretion energy, and R was the energy lost through respiration. The energy values of C, G, and F were determined using an oxygen bomb calorimeter (Parr 1281, USA) after tissue samples had been dried at 70 °C until they had reached a constant weight.

The energy of excretion was calculated as: $U = U_N \times 24{,}830 = (C_N - G_N - F_N) \times 24{,}830$ [36], where U_N was the excreted nitrogen, C_N was the nitrogen contained in the food intake, G_N was the nitrogen stored in the abalone, and F_N was the nitrogen excreted in feces; the factor 24,830 represents the energy value contained in ammonia nitrogen per g (J g^{-1}). Given that most shellfish are ammonotelic, NH_4^+–N is the major form of excreted nitrogen, with only a low amount carbamide; thus, the latter was deemed negligible in this study. An elemental analyzer (Vario EL III, Germany) was used to determine the nitrogen content, and the energy of respiration was expressed as: $R = C - G - F - U$.

The assimilation efficiency (K_1) and net growth efficiency (K_2) were calculated using the following equations: $K_1\ (\%) = 100 \times (G + R)/(G + R + U)$ and $K_2\ (\%) = 100 \times G/(G + R)$.

During the study, the survival rate (S%), shell length/body weight-specific growth rate (SGR, %day^{-1}), food intake (FI, % body weight day^{-1}), and food conversion efficiency (FCE, %) of abalone were calculated every other month, as follows:

$$S\ (\%) = [(N_1 - N_2)/N_1] \times 100$$

$$\text{SGR}\ \left(\%\text{day}^{-1}\right) = (\ln W_2 - \ln W_1)/T \times 100 \text{ and}$$

$$\text{FI}\ \left(\%\text{body weight day}^{-1}\right) = F/[T \times (W_2 + W_1)/2] \times 100$$

$$\text{FCE}\ (\%) = (W_2 - W_1)/\text{F} \times 100,$$

where N_1 and N_2 were the number of abalones at the beginning and end of the experiment, respectively, W_1 and W_2 were the wet weight (g) of abalones at the beginning and end of the experiment, respectively, L_1 and L_2 were the shell length

at the beginning and end of the experiment, respectively, T was the length of the experiment in days, and F was the weight of food intake during the experimental process (dry weight, g).

15.3.3 Results

15.3.3.1 Specific Growth Rate

Different light qualities had significant effects on the body weight and shell length of SGR of *H. d. discus*. Under orange or red light, the body-weight SGR of *H. d. discus* was significantly higher than that of the treatment group under any other light quality (Fig. 15.10, $F = 124.27$, $P < 0.001$). Under natural light or in a dark setting, the body-weight SGR was >0.2 mg day^{-1}. Under blue or green light, *H. d. discus* lost weight, resulting in body-weight SGRs that were significantly lower than the treatment group under any other light quality ($F = 163.29$, $P < 0.001$). Under orange light, the shell-length SGR was also significantly longer compared with that of the treatment group under any other light quality ($F = 85.33$, $P < 0.001$). Under natural or red light, or in dark setting, the shell-length SGR showed no significant difference ($F = 3.07$, $P = 0.114$), whereas under green or blue light, it was the lowest recording at <0.05 μm day^{-1}.

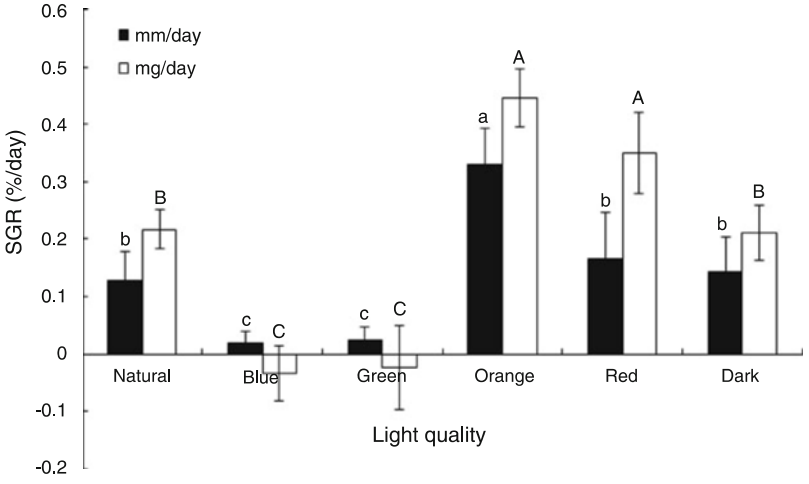

Fig. 15.10 Effect of LED light quality on the specific growth rate of juvenile abalone (*H. d. discus*). Capital letters indicate the difference among the mean body-weight-specific growth rate, whereas lowercase letters indicate the difference among the mean shell length specific growth rate. There was no significant difference between bars with the same letter, whereas significant differences occurred between bars with different letters

15.3.3.2 Biochemical Composition

Under natural, green, or blue light, or in dark setting, the moisture content of *H. d. discus* was significantly higher than that of the treatment group under red light ($F = 15.38$, $P = 0.013$), but no significant difference in moisture content occurred in *H. d. discus* under natural, green, or blue light (Table 15.1, $F = 2.71$, $P = 0.121$). Under orange light, the moisture content of *H. d. discus* was also low (mean 81.87%). The protein content of *H. d. discus* under natural or orange light was significantly higher than that of any other treatment group ($F = 32.58$, $P < 0.001$). The protein content under blue or green light was the lowest and significant differently compared with that under red light or in dark setting ($F = 28.57$, $P = 0.001$). The amount of ash of *H. d. discus* under orange light or in dark setting was significant greater than under any other light quality ($F = 11.82$, $P = 0.017$), but there was no difference in the ash content from treatment groups under any other light quality ($F = 2.02$, $P = 0.145$). Under orange or red light or in dark setting, the fat content of *H. d. discus* was significantly higher compared with that of treatment groups under any other light quality ($F = 18.95$, $P = 0.003$). Under natural, green, or blue light, the amount of lactic acid accumulated in *H. d. discus* was significantly higher than under any other light quality ($F = 49.26$, $P < 0.001$). Under orange or red light or in dark setting, the lactic acid content was lower, but with no significant difference ($F = 1.64$, $P = 0.173$) compared with the other groups. Under green or blue light, the tissue:shell ratio of abalone was significantly less than that of any other treatment group (Table 15.1, $F = 30.17$, $P < 0.001$).

15.3.3.3 Determination of Energy Parameters

As shown in Table 15.2, under different light qualities, there were significant differences in the energy parameters of *H. d. discus*. Under orange or red light or in a dark setting, energy acquired from food was significantly higher than that of the treatment groups under any other light quality ($F = 169.22$, $P < 0.001$). Under green or blue light, energy acquired from food was the lowest with a significant difference compared with any other treatment group ($F = 94.37$, $P < 0.001$). In a dark setting, energy lost in feces was significantly higher than that in any other treatment group ($F = 61.29$, $P < 0.001$). Under blue or green light, energy lost in feces was the lowest with a significant difference compared with any other treatment group ($F = 45.12$, $P < 0.001$). Under orange light, energy accumulated for growth was significantly higher than that in any other treatment group, followed by red light, a dark setting, and natural light ($F = 39.28$, $P < 0.001$). Under blue or green light, abalones exhibited negative growth. In a dark setting, energy lost via excretion was the highest ($F = 19.36$, $P = 0.003$). However, under orange light, energy lost via excretion was significantly less than that of the treatment group under any other light quality ($F = 40.16$, $P < 0.001$). Under orange light, energy lost via respiration was significantly higher than in any other treatment group ($F = 28.08$, $P = 0.001$). Under natural or red light, energy lost via respiration was higher than under any other

Table 15.1 Mean biochemical content (± standard error) and the tissue:shell ratio of juvenile *H. d. discus*, reared under six different light qualities[a]

	Light quality					
Variable	Natural	Blue	Green	Orange	Red	Dark
Tissue moisture (%)	84.63 ± 1.51^{ab}	88.12 ± 2.65^{a}	88.71 ± 0.82^{a}	81.87 ± 1.47^{b}	75.42 ± 2.24^{c}	84.06 ± 1.71^{ab}
Protein (%DTW)	28.31 ± 2.84^{a}	15.35 ± 1.57^{c}	17.72 ± 1.55^{c}	32.92 ± 0.97^{a}	24.76 ± 1.12^{b}	21.31 ± 2.44^{b}
Ash	23.82 ± 2.24^{b}	24.62 ± 1.38^{b}	22.75 ± 1.62^{b}	27.70 ± 2.14^{a}	22.83 ± 1.06^{b}	29.91 ± 1.15^{a}
Lipid	2.01 ± 0.10^{b}	1.77 ± 0.14^{bc}	1.42 ± 0.13^{c}	2.91 ± 0.32^{a}	2.79 ± 0.21^{a}	3.09 ± 0.26^{a}
Lactic acid content (mmol/g prot)	0.38 ± 0.02^{a}	0.47 ± 0.03^{a}	0.49 ± 0.06^{a}	0.19 ± 0.02^{b}	0.22 ± 0.03^{b}	0.17 ± 0.06^{b}
Tissue:shell ratio	0.44 ± 0.01^{a}	0.31 ± 0.04^{b}	0.28 ± 0.02^{b}	0.44 ± 0.04^{a}	0.46 ± 0.07^{a}	0.42 ± 0.02^{a}

[a]The same superscript means that the difference between biochemical content and tissue:shell ratio was not significant, whereas different superscripts means that the differences were significant

Table 15.2 Energy parameters in juvenile abalone, *H. d. discus*, under different light qualities[a]

	Energy parameters				
Light quality	C (J g^{-1} day^{-1})	F (J g^{-1} day^{-1})	G (J g^{-1} day^{-1})	U (J g^{-1} day^{-1})	R (J g^{-1} day^{-1})
Natural	827.61 ± 92.74^{b}	411.36 ± 65.42^{c}	87.52 ± 64.34^{c}	72.21 ± 15.64^{bc}	256.64 ± 72.10^{bc}
Blue	389.38 ± 85.74^{c}	206.42 ± 94.54^{d}	-65.74 ± 28.62^{e}	85.93 ± 10.24^{b}	162.72 ± 64.47^{d}
Green	293.57 ± 102.82^{c}	195.97 ± 61.16^{d}	-104.87 ± 69.50^{d}	57.93 ± 14.23^{c}	144.55 ± 83.27^{d}
Orange	1247.62 ± 139.51^{a}	606.53 ± 122.31^{b}	271.67 ± 72.92^{a}	38.77 ± 9.82^{d}	327.82 ± 89.19^{a}
Red	1032.12 ± 127.37^{ab}	471.27 ± 96.55^{c}	204.57 ± 92.15^{b}	69.16 ± 8.75^{bc}	289.37 ± 80.51^{b}
Dark	1451.74 ± 158.62^{a}	1002.50 ± 106.72^{a}	107.65 ± 47.21^{c}	117.59 ± 12.64^{a}	224.13 ± 54.90^{c}

[a]Values were expressed as mean ± SE; $n = 4$; C feeding energy, F energy loss in feces discharge, G energy deposit for growth, U energy loss in excretion, R energy loss in respiration. The same superscript means that the differences were not significant, whereas different superscripts mean that the differences were significant

treatment except for orange light, and was the lowest among blue or green light, although there was no significant difference among groups ($F = 1.39$, $P = 0.187$).

15.4 Effects of Light Quality and Photoperiod on the Growth and Energy Metabolism of *H. discus hannai*

The goal of this experiment was to examine the effects of different light qualities (red, white, and blue) and cycles (12L:12D, 8L:16D, 4L:20D, 0L:24D, and 16L:8D) on the survival, growth, metabolism, and antioxidant defense system of *Haliotis discus hannai Ino*. Under red and white light at 4L:20D, the body-weight-specific growth rate of abalones was significantly higher than that of the 0L:24D group ($P < 0.05$). At 16L:8D, succinate dehydrogenase activity decreased and lactate dehydrogenase and alanine aminotransferase activity and the lactic acid content significantly rose ($P < 0.05$) in the red and white light groups. Under blue light, reactive oxygen species and malondialdehyde content for each light cycle were significantly higher than those of the red and white groups ($P < 0.05$). Under blue, white, and red light, total antioxidant capacity (T-AOC), superoxide dismutase (SOD) activity, glutathione peroxidase (GPX) activity, and reduced glutathione (GSH) content gradually rose with increased duration of light exposure. Under red light, significant differences in these parameters were detected between the 4L:20D and 16L:8D groups ($P < 0.05$). Under blue and white light at 16L:8D, values of T-AOC, SOD, GPX activity, and GSH content were significantly lower than those of the 12L:12D group ($P < 0.05$). Overall, these results indicate that red light at light cycles of 4L:20D and 8L:16D is optimal for the culture and production of *H. discus hannai*, as these conditions promoted food intake, growth, and health maintenance as well as normal physiological metabolism of the organism.

15.4.1 Introduction

Most of the natural rhythmicity (day and night or seasonal) observed in aquatic organisms is closely related to the light cycle. For example, abalone adjust their physiological activities by hiding in cracks in the rocks during the day and feeding at night [37]. García-Esquivel et al. [38] reported that the growth rate of *Haliotis fulgens* was highest under the 00:24 Light:Dark (L:D) light cycle. Gorrostieta-Hurtado et al. [39] found that the survival and food intake rates of *Haliotis corrugata* larvae were significantly higher in the dark setting than under constant lighting. In addition, the oxygen consumption rate and ammonia excretion rate of *Haliotis discus discus* were found to be significantly higher under light than in a dark setting [32]. Day et al. [40] reported that the growth rate of *Haliotis rubra* was 15.65% faster in a lightproof water tank than that in the light. Gao et al. [41] found that

Haliotis discus hannai exhibited significant tropism to red and orange light and a significant escape behavior under blue, green, and purple light. Under blue light, the energy appropriated for the growth of *Litopenaeus vannamei* was low and that for excretion was high, thus the specific growth rate (SGR) under blue light was significantly lower than that of groups under any other light quality [42]. The growth of *Salmo salar* larvae can be promoted if the duration of light application increases after food intake begins [43]. Thorpe et al. [44] found that *S. salar* had the fastest growth rate in summer, which is characterized by a long period of light each day. Other researchers have noted that a gradual increase in the light cycle is more effective at influencing the development of the fish gonad compared to a gradual decrease in the light cycle [45].

To date, little is known about the effects of the interaction between light quality and cycle on the food intake, growth, metabolism, and other physiological activities of *H. discus hannai*. *H. discus hannai* is an economically important shellfish species in China, but culture of this species has been experiencing numerous problems as the aquaculture industry develops and expands (e.g., incomplete seed development, worsening summer mortality, and rise of feeding costs). In traditional Chinese aquaculture, producers often use sunshade nets in aquaculture hatcheries to provide a dark for abalone. However, in the abalone's natural environment, the light quality and cycle are subject to the seasonal rhythm and variations in concentration of suspended particles, zooplankton, and phytoplankton. Abalones are able to survive, grow, and reproduce in the ever-changing natural environment, and light may have important regulatory effects on growth and development in this setting.

In this study, the food intake, growth, metabolism, and antioxidant defense system of *H. discus hannai* under different light qualities and cycles were examined. The results should provide a theoretical basis for the optimization of aquaculture conditions to produce healthy and productive *H. discus hannai* in a sustainable aquaculture setting.

15.4.2 Materials and Methods

This experiment was carried out using LED lights supplied by the Institute of Semiconductors CAS (Beijing, China). The lights were suspended above each aquarium. The following three light quality treatments were used: blue, at 450 nm, light intensity 1.81 ± 0.02 μmol m^{-2} s^{-1}; red, at 620 nm, intensity 1.80 ± 0.03 μmol m^{-2} s^{-1}; and white, main peak at 460 nm, intensity 1.78 ± 0.03 μmol m^{-2} s^{-1}. White light was set using the full spectrum to simulate natural light. The light intensity in different light quality groups was kept as constant as possible by adjusting the distance between the light and the water surface. A spectroradiometer (JETI LiVal Spectroradiometer Model Specbos 1xx1, Jena, Germany) was used to measure the wave peak of light quality and light intensity, and five different points inside the aquarium were selected and then averaged to ensure that the wave peak of each light quality was within the required range. Five

different light cycle groups (12L:12D, 8L:16D, 4L:20D, 0L:24D, and 16L:8D) were set up, and the lights were controlled using a timer. In total, 60 aquariums (45 cm × 25 cm × 35 cm, water volume: 39 L) were used in this experiment, with four replicates for each of the light quality–cycle combinations.

Twelve abalones were placed in each aquarium. Blackout cloths were used to separate the different light quality and cycle groups to avoid interference. Water exchange, feeding, and collection of residual food were performed during the dark period. During this experiment, the room temperature was kept at 18 °C, and the salinity and pH were the same as those used during acclimation. The water was kept clean by sand filtration, ultraviolet radiation disinfection, a protein-foam separator, and biofiltration using the circulating aquaculture system. One-third of the water volume was exchanged each day, and each aquarium was scrubbed every 7 days. In addition, each aquarium was provided with continuous aeration to maintain a dissolved oxygen concentration >6 mg/L. However, aeration was stopped 20 min before the collection of residual food. The ammonia concentration was always <0.1 mg/L in this experiment. The experiment lasted for 100 days.

All experimental abalones were sourced from the same batch after artificial hatching. They were starved for 24 h before the start of the experiment. Thirty abalones not used in the experiment were randomly selected for the analysis of crude protein content, and 720 abalones (shell length: 3.62 ± 0.13 cm, body weight: 6.85 ± 0.19 g) were randomly divided into the different treatments (12 individuals in each of 60 tanks). During the experiment, these abalones were fed with *L. japonica* at 5% of their wet body weight each day at 17:00H. The food residue was collected and weighed the following morning at 8:00. Samples of the fresh *L. japonica* used to feed these abalones were weighed and then placed in another three aquariums to determine the quantity that might be lost due to disintegration and dissolution rather than consumption. The next morning, the samples were collected and weighed, and the quantity lost was calculated and used to correct the food intake values. After the completion of the experiment, three abalones were randomly collected from each aquarium for the analyses described below.

The water on the body surface of each abalone was removed using absorbent paper, and the specimen then was rapidly dissected on ice. After shelling, the hepatopancreas was removed and placed in a 1.5-mL centrifuge tube, which was quickly placed in liquid nitrogen and later moved to a −80 °C freezer. The hepatopancreas was used for the enzyme activity and biochemical composition analyses.

For enzyme activity analysis, 0.2–0.4 g of hepatopancreas was mixed with 1.8 mL 0.86% normal saline and the sample was fully ground in an ice-water bath. The tissues were centrifuged at 3500 r/min for 10 min until a 10% tissue homogenate was produced. The activities of succinate dehydrogenase (SDH), lactic dehydrogenase (LDH), superoxide dismutase (SOD), and lactic acid content in the homogenate were determined following the method described by Gao et al. [46]. The protein content in the homogenate was determined using Coomassie Blue Staining as described by Bradford [47], and bovine serum albumin was used as the protein marker.

Alanine aminotransferase (GPT) activity, reactive oxygen species (ROS) content, total antioxidant capacity (T-AOC), reduced glutathione (GSH) content, glutathione peroxidase (GP_X) activity, and malondialdehyde (MDA) content were determined using kits purchased from Nanjing Jiancheng Bioengineering Institute (Nanjing, Jiangsu, China). Contents and activities were determined as follows:

- GPT activity: At 37 °C and pH = 7.4, GPT reacts with a substance composed of alanine and α-ketoglutaric acid in the homogenate, generating pyruvic acid and glutamic acid. After 30 min, 2,4-dinitrophenylhydrazinehydrochloric acid is used to terminate the reaction. 2,4-Dinitrophenylhydrazine reacts with the carbonyl group of ketonic acid and generates pyruvic acid phenylhydrazone. Phenylhydrazone appears red-brown in color under the alkaline condition, and the absorbance is tested at 505 nm using a spectrophotometer (721G-100, INESA.CC, Shanghai, China). Absorbance data then are used to calculate the enzyme activity, according to the standard curve shown in the kit instructions. The activity of GPT (U/g prot) in tissue = the activity of GPT in the homogenate, which was obtained from the standard curve divided by the concentration of protein (g prot/L) in the homogenate.
- ROS content: The tissue homogenate was centrifuged at 1000 r/min for 10 min, and then 1 mmol/L DCFH-DA (2′,7′-dichlorofluorescin diacetate) was added to the supernatant. The mixture was incubated at 37 °C for 30 min after being fully and evenly mixed. A fluorescence spectrophotometer (960MC, INESA.CC) was used to determine the fluorescence intensity at the optimum excitation wavelength of 500 nm and at the optimum emission wavelength of 525 nm, and the results were expressed as fluorescence arbitrary units (A.U.)
- T-AOC: T-AOC was determined using the ferric reducing ability of plasma method. The antioxidant substances in an organism can reduce Fe^{3+} to Fe^{2+}, which can form a stable complex with phenanthroline-like substances. The level of T-AOC of a sample was determined using the colorimetric method. At 37 °C, a unit (U/mg) of total antioxidant capacity (T-AOC) was defined as the increase of 0.01 of optical density of all chemical reaction substances by 1 mg of tissue protein per minute.
- GSH content: Following the method described by Anderson [48], one yellow compound can be generated when DTNB (5,5′-dithiobis-(2-nitrobenzoic acid)) reacts with sulfhydryl compounds. The colorimetric method then was used to measure the absorbance of the yellow compound.
- GP_X activity: The DTNB method described by Li et al. [49] was used to measure GPx activity. GPx was assayed spectrophotometrically using glutathione (GSS) as the substrate and measuring the decrease of GSH at 412 nm. One unit (U) of GPx activity was defined as the amount needed to reduce 1 μmol/L of GSH in the reaction system (minus any nonenzymatic reaction) by 1 mg of tissue protein/min.
- MDA content: MDA was determined by measuring the amount of red product produced by MDA and TBA, which has a maximum absorption peak at 532 nm. The absorbance was measured in nmol/mg protein using the spectrophotometer (721G-100, INESA.CC, Shanghai, China).

In addition, the activities of pepsin (PES), cellulase (CL), and amylase (AMS) and the protein content of each sample were determined following the methods described by Gao et al. [46]. In brief, 0.2–0.4 g of tissue was added to 1.8 mL 0.86% normal saline and fully ground in an ice-water bath. The tissues then were centrifuged at 2500 r/min, 8000 r/min, and 2500 r/min at 4 °C for 15 min until 10% tissue homogenates were produced. These homogenates then were used for the assays.

15.4.3 Results

15.4.3.1 Food Conversion Efficiency

The food conversion efficiency (FCE) of abalones in the blue group was significantly lower than that in the white and red groups for all light cycles except 0L:24D (Fig. 15.11, $F = 67.43$, $P < 0.001$), and no significant difference among light cycles was identified for the blue light group ($F = 1.59$, $P = 0.141$). Under red and white light, the FCE at 4L:20D was significantly higher than that of any other light cycle ($F = 12.71$, $P = 0.005$). The FCE in the red and white groups differed significantly under each light cycle except 8L:16D and 0L:24D ($F = 16.04$, $P = 0.002$).

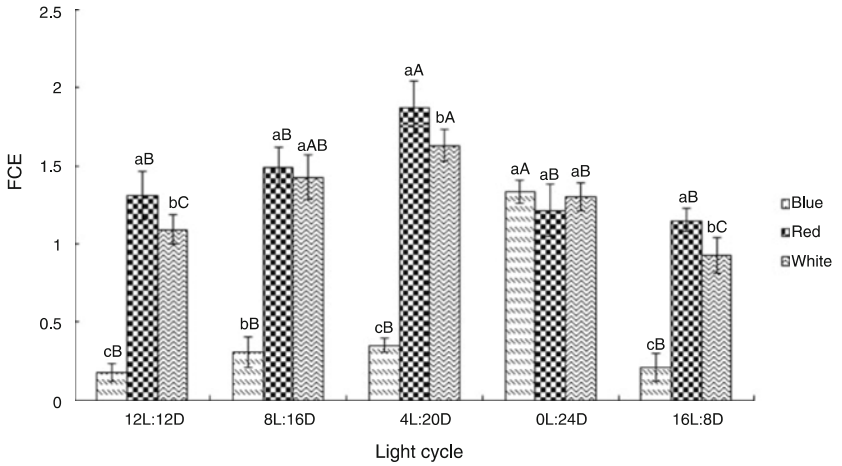

Fig. 15.11 Effects of light qualities and light cycles on the food conversion efficiency of juvenile abalone (*H. discus hannai*). Values are expressed as mean ± s.e. ($n = 4$). The same small letters indicate similar food conversion efficiency, and different small letters indicate significantly different ($P < 0.05$) food conversion efficiency in relation to light quality. The same capital letters indicate similar food conversion efficiency, and different capital letters indicate significantly different ($P < 0.05$) food conversion efficiency in relation to light cycle

15.4.3.2 Digestive Enzyme Activity

Under blue light, the PES activity of abalones in each light cycle group decreased with increased duration of light exposure, but no significant differences were identified (Table 15.3, $F = 1.34$, $P = 0.157$). Under red light, the PES activity was significantly higher at 4L:20D and 8L:16D than at 0L:24D ($F = 23.25$, $P = 0.001$). Under white light, the activity of PES was highest at 4L:20D, and it differed significantly from the activities at 8L:16D and 16L:8D ($F = 15.15$, $P = 0.004$). The interaction between light quality and light cycle also had a significant effect on the PES activity (light quality × light cycle, $F = 17.39$, $P = 0.002$). Under red and white light at 4L:20D, 16L:8D, and12L:12D, the PES activity of abalones was significantly higher than that under blue light ($F = 28.87$, $P = 0.001$).

Under red light, the CL activity of abalones was significantly higher at 8L:16D than at any other light cycle ($F = 11.97$, $P = 0.008$). Under white light, the CL activity was significantly higher at 4L:20D than at any light cycle ($F = 7.81$, $P = 0.015$). Under blue light, no significant differences in CL activity were detected among any of the light cycles ($F = 1.28$, $P = 0.163$) except 0L:24D. At 4L:20D, 16L:8D, and 12L:12D, the CL activity in the red and white groups was significantly higher than that in the blue group ($F = 50.45$, $P < 0.001$). At 8L:16D, the CL activity in the red group was significantly higher than that in the white group ($F = 17.94$, $P = 0.002$).

Light quality and light cycle also had a significant effect on the AMS activity of abalones. Under blue light, the AMS activity at 4L:20D was significantly higher than at 16L:8D, 12L:12D, and 8L:16D (Table 15.3, $F = 15.48$, $P = 0.004$). Under red and white light, the AMS activity at 4L:20D was also significantly higher than at 16L:8D and12L:12D ($F = 24.71$, $P = 0.001$); however, no significant difference between 16L:8D and 12L:12D under red light was detected ($F = 2.04$, $P = 0.117$). The AMS activity under red and white light was significantly higher than that under blue light for all light cycles ($F = 31.64$, $P < 0.001$) except 0L:24D.

15.4.3.3 Antioxidant Enzyme Activity

The ROS content increased as duration of light exposure increased. Under blue and red light, the ROS content was significantly higher at 16L:8D than that at any other light cycle (Table 15.4, $F = 85.27$, $P < 0.001$), but no significant difference between the 8L:16D and 12L:12D groups was detected ($F = 2.94$, $P = 0.092$). Under white light, the ROS content did not differ significantly between the 16L:8D and12L:12D groups ($F = 2.11$, $P = 0.108$), but the contents in these two groups were significantly higher than that at any other light cycle ($F = 71.08$, $P < 0.001$). The ROS content in the blue light group was significantly higher than that in red and white light groups for all light cycles except 0L:24D ($F = 97.39$, $P < 0.001$).

Light quality and light cycle also had a significant effect on the T-AOC of abalones. Under blue and white light, the T-AOC was significantly higher at 12L:12D than at any other light cycle ($F = 41.28$, $P < 0.001$); however, the T-AOC

Table 15.3 Effects of light qualities and light cycles on the activity of digestive enzyme of juvenile abalone (*H. discus hannai*)

Light quality	Light cycle	Variable		
		Pepsase (PES) (U mg^{-1} prot)	Cellulase (CL) (U g^{-1} prot)	Amylase (AMS) (U mg^{-1} prot)
Blue	16L:8D	2.11 ± 0.33^{bB}	2.33 ± 0.19^{bB}	1.85 ± 0.22^{cC}
	12L:12D	1.97 ± 0.15^{bB}	3.01 ± 0.41^{bB}	2.46 ± 0.46^{cB}
	8L:16D	2.46 ± 0.28^{bB}	4.51 ± 0.29^{bC}	2.05 ± 0.16^{cB}
	4L:20D	3.15 ± 0.24^{bB}	3.64 ± 0.57^{bB}	5.91 ± 0.81^{bB}
	0L:24D	5.52 ± 0.39^{aA}	10.29 ± 1.31^{aA}	14.17 ± 1.28^{aA}
Red	16L:8D	5.98 ± 0.66^{abA}	9.45 ± 1.35^{bA}	9.31 ± 1.65^{bA}
	12L:12D	6.22 ± 0.75^{abA}	8.79 ± 1.62^{bA}	9.04 ± 1.44^{bA}
	8L:16D	7.41 ± 0.49^{aA}	12.37 ± 1.25^{aA}	12.41 ± 1.69^{abA}
	4L:20D	7.09 ± 0.28^{aA}	9.02 ± 1.08^{bA}	14.22 ± 1.50^{aA}
	0L:24D	4.59 ± 0.42^{bA}	10.55 ± 1.94^{bA}	12.58 ± 1.11^{abA}
White	16L:8D	4.25 ± 0.87^{bA}	7.86 ± 0.92^{bA}	4.33 ± 0.83^{cB}
	12L:12D	6.85 ± 0.93^{aA}	7.59 ± 0.84^{bA}	8.62 ± 1.34^{bA}
	8L:16D	4.11 ± 0.34^{bB}	8.92 ± 1.03^{bB}	11.74 ± 0.79^{abA}
	4L:20D	6.47 ± 0.51^{aA}	11.79 ± 1.65^{aA}	16.29 ± 1.67^{aA}
	0L:24D	5.36 ± 0.27^{abA}	11.28 ± 1.77^{aA}	12.95 ± 1.41^{abA}

Values are expressed as mean ± s.e. ($n = 4$). Different small letters indicate significant differences in activity of digestive enzyme for the same light cycle at different light qualities, $P < 0.05$. Different capital letters indicate significant differences in activity of digestive enzyme for the same light quality with different light cycles, $P < 0.05$

Table 15.4 Effects of light qualities and light cycles on the T-ACO, contents of ROS, GSH and MDA, and activities of SOD and GPX in juvenile abalones (H. discus hannai)

Light quality	Light cycle	Variable					
		Reactive oxygen species (ROS) (A.U.)	Total antioxidant capacity (T-AOC) (U/mg prot)	Superoxide dismutase (SOD) (U/mg prot)	Glutathione peroxidase (GPx) (U/mg prot)	Glutathione (GSH) (mg/g prot)	Malondialdehyde (MDA) (nmol/mg prot)
Blue	16L:8D	562.16 ± 32.19^{aA}	0.69 ± 0.05^{bA}	9.38 ± 1.17^{bA}	24.15 ± 4.11^{bB}	3.73 ± 0.25^{bA}	14.75 ± 2.02^{aA}
	12L:12D	344.81 ± 25.88^{bA}	0.93 ± 0.08^{aA}	17.29 ± 1.26^{aA}	55.64 ± 2.09^{aA}	6.54 ± 0.81^{aA}	10.01 ± 1.51^{aA}
	8L:16D	261.42 ± 15.97^{bA}	0.51 ± 0.05^{bA}	15.76 ± 1.52^{aA}	49.51 ± 6.14^{aA}	5.38 ± 0.55^{aA}	6.22 ± 0.47^{abA}
	4L:20D	159.03 ± 14.21^{cA}	0.45 ± 0.04^{bA}	8.43 ± 1.13^{bA}	27.38 ± 3.34^{bA}	3.95 ± 0.24^{bA}	3.40 ± 0.65^{bA}
	0L:24D	50.77 ± 8.03^{dA}	0.21 ± 0.01^{cA}	6.27 ± 0.94^{bA}	14.22 ± 1.37^{cA}	2.17 ± 0.32^{bA}	2.96 ± 0.14^{bA}
	16L:8D	109.72 ± 14.76^{aB}	0.56 ± 0.03^{aB}	9.22 ± 1.20^{aA}	30.56 ± 3.72^{aA}	4.02 ± 0.69^{aA}	5.26 ± 1.44^{aB}
	12L:12D	84.13 ± 7.33^{bB}	0.42 ± 0.03^{abC}	6.04 ± 0.85^{bC}	24.77 ± 2.08^{abB}	3.79 ± 0.48^{aB}	4.13 ± 0.23^{abB}
Red	8L:16D	75.94 ± 11.25^{bB}	0.34 ± 0.01^{bB}	6.35 ± 0.61^{bB}	26.48 ± 1.55^{aB}	2.88 ± 0.36^{bB}	3.72 ± 0.19^{abB}
	4L:20D	50.09 ± 5.79^{cB}	0.20 ± 0.02^{cB}	5.92 ± 0.72^{bB}	19.05 ± 2.67^{bB}	2.31 ± 0.22^{bB}	2.61 ± 0.33^{bB}
	0L:24D	54.26 ± 10.08^{cA}	0.25 ± 0.01^{cA}	6.14 ± 0.88^{bA}	16.17 ± 1.83^{bA}	2.05 ± 0.16^{bA}	2.48 ± 0.18^{bA}
	16L:8D	131.27 ± 10.75^{aB}	0.53 ± 0.06^{bB}	9.97 ± 1.09^{aA}	32.95 ± 3.95^{bA}	3.19 ± 0.40^{bB}	7.62 ± 0.85^{aB}
	12L:12D	125.39 ± 16.08^{aB}	0.75 ± 0.02^{aB}	10.69 ± 1.38^{aB}	47.28 ± 5.94^{aA}	4.84 ± 0.47^{aB}	5.74 ± 0.77^{abB}
White	8L:16D	60.88 ± 5.21^{bB}	0.47 ± 0.07^{bA}	7.49 ± 1.02^{bB}	28.39 ± 4.26^{bB}	2.47 ± 0.34^{bB}	4.25 ± 0.26^{abB}
	4L:20D	48.17 ± 4.30^{bB}	0.29 ± 0.02^{cB}	6.52 ± 0.84^{bB}	20.55 ± 3.18^{cB}	2.59 ± 0.19^{bB}	3.58 ± 0.34^{bA}
	0L:24D	42.38 ± 8.16^{bA}	0.25 ± 0.04^{cA}	6.83 ± 1.21^{bA}	13.98 ± 2.67^{cA}	2.33 ± 0.20^{bA}	2.21 ± 0.56^{bA}

value in the red and white groups was significantly lower at 4L:20D than at any other light cycle ($F = 29.61$, $P < 0.001$). Under red light, the T-AOC was significantly higher at 16L:8D and 12L:12D than at any other light cycle, and no significant difference between these two light cycles was detected ($F = 1.15$, $P = 0.195$). The T-AOC under blue light was significantly higher than that in the red and white light groups at 4L:20D and 16L:8D ($F = 24.46$, $P = 0.001$). No significant difference in the T-AOC was detected between the blue and white groups at 8L:16D, but the values were significantly higher than that in red light group ($F = 18.47$, $P = 0.002$).

Under blue light, the SOD activity of abalones was significantly higher at 12L:12D and 8L:16D than at any other light cycle ($F = 23.27$, $P = 0.001$), and it decreased significantly at 16L:8D ($F = 20.35$, $P = 0.002$). Under red light, the SOD activity was significantly higher at 16L:8D than at any other light cycle ($F = 15.49$, $P = 0.004$). Under white light, the SOD activity was significantly higher at 12L:12D and 16L:8D than at any other light cycle ($F = 14.68$, $P = 0.005$). At 8L:16D and 4L:20D, the SOD activity in the blue group was significantly higher than that in the red and white light groups, but no significant difference between the red and white groups was detected ($F = 1.37$, $P = 0.155$). At 16L:8D, the SOD activity in the red and white light groups was significantly higher than at the other light cycles, and no significant difference among these two light qualities was detected ($F = 2.79$, $P = 0.096$).

Under white light, the GP_X activity and GSH content were significantly higher at 12L:12D than that at any other light cycle ($F = 17.36$, $P = 0.002$); however, as duration of light exposure increased to 16 h, the GP_X activity and GSH content decreased significantly ($F = 8.27$, $P = 0.013$). Under red light at 16L:8D, the GP_X activity and GSH content significantly increased ($F = 16.43$, $P = 0.002$), but the values did not differ significantly from those of the 12L:12D group. The GP_X activity and GSH content in the blue group were significantly higher than those in the red and white groups at 4L:20D and 8L:16D ($F = 30.57$, $P < 0.001$). At 12L:12D, the GP_X activity in the blue and white groups was significantly higher than that in the red group ($F = 26.85$, $P = 0.001$).

For each light quality, the MDA content was higher at 16L:8D and 12L:12D than at the other light cycles, and no significant difference between these two groups was detected ($F = 1.90$, $P = 0.128$). The MDA content for each light quality was lower at 0L:24D and 4L:20D than at the other light cycles, and no significant difference between these two groups was detected ($F = 1.52$, $P = 0.147$). The interaction between light quality and light cycle also had a significant effect on the MDA content (light quality $\times$ light cycle, $F = 19.35$, $P = 0.002$). At 4L:20D, the MDA content in the blue and white groups was significantly higher than that in the red group ($F = 12.73$, $P = 0.006$). However, the MDA content in the blue group was higher than that in the red and white groups at 8L:16D, 12L:12D, and16L:8D ($F = 39.46$, $P < 0.001$).

References

1. S.B. Seminara, S. Messager, E.E. Chatzidaki, R.R. Thresher, J.S. Acierno Jr., J.K. Shagoury, et al., The GPR54 gene as a regulator of puberty. N. Engl. J. Med. **349**(17), 1614–1627 (2003)
2. S. Messager, E.E. Chatzidaki, D. Ma, A.G. Hendrick, D. Zahn, J. Dixon, et al., Kisspeptin directly stimulates gonadotropin-releasing hormone release via G protein-coupled receptor 54. Proc. Natl. Acad. Sci. U. S. A. **102**(5), 1761–1766 (2005)
3. S. Funes, J.A. Hedrick, G. Vassileva, L. Markowitz, S. Abbondanzo, A. Golovko, et al., The KiSS-1 receptor GPR54 is essential for the development of the murine reproductive system. Biochem. Biophys. Res. Commun. **312**(4), 1357–1363 (2003)
4. I.S. Parhar, S. Ogawa, Y. Sakuma, Laser-captured single digoxigenin-labeled neurons of gonadotropinreleasing hormone types reveal a novel G protein-coupled receptor (Gpr54) during maturation in cichlid fish. Endocrinology **145**(8), 3613–3618 (2004)
5. C.C. Martinez-Chavez, M. Minghetti, H. Migaud, GPR54 and rGnRH I gene expression during the onset of puberty in Nile tilapia. Gen. Comp. Endocrinol. **156**(2), 224–233 (2008)
6. B.H. Beck, S.A. Fuller, E. Peatman, M.E. McEntire, A. Darwish, D.W. Freeman, Chronic exogenous kisspeptin administration accelerates gonadal development in basses of the genus Morone. Comp. Biochem. Physiol. A Mol. Integr. Physiol. **162**(3), 265–273 (2012)
7. N. Zmora, J. Stubblefield, Z. Zulperi, J. Biran, B. Levavi-Sivan, J.-A. Muñoz-Cueto, et al., Differential and gonad stage-dependent roles of kisspeptin1 and kisspeptin2 in reproduction in the modern teleosts, morone species. Biol. Reprod. **86**, 177 (2012)
8. A. Elizur, The KiSS1/GPR54 system in fish. Peptides **30**(1), 164–170 (2009)
9. S. Kanda, T. Karigo, Y. Oka, Steroid sensitive kiss2 neurones in the goldfish: evolutionary insights into the duplicate kisspeptin gene-expressing neurones. J. Neuroendocrinol. **24**(6), 897–906 (2012)
10. A. Servili, Y. Le Page, J. Leprince, A. Caraty, S. Escobar, I.S. Parhar, et al., Organization of two independent kisspeptin systems derived from evolutionary-ancient kiss genes in the brain of zebrafish. Endocrinology **152**(4), 1527–1540 (2011)
11. M. Tena-Sempere, A. Felip, A. GoÂmez, S. Zanuy, M. Carrillo, Comparative insights of the kisspeptin/kisspeptin receptor system: lessons from non-mammalian vertebrates. Gen. Comp. Endocrinol. **175**(2), 234–243 (2012)
12. A.S. Mechaly, J. Viñas, F. Piferrer, Identification of two isoforms of the kisspeptin-1 receptor (kiss1r) generated by alternative splicing in a modern teleost, the Senegalese sole (Solea senegalensis). Biol. Reprod. **80**(1), 60–69 (2009)
13. S. Selvaraj, H. Kitano, Y. Fujinaga, H. Ohga, M. Yoneda, A. Yamaguchi, et al., Molecular characterization, tissue distribution, and mRNA expression profiles of two kiss genes in the adult male and female chub mackerel (Scomber japonicus) during different gonadal stages. Gen. Comp. Endocrinol. **169**(1), 28–38 (2010)
14. G.L. Taranger, C. Haux, S.O. Stefansson, B.T. BjoÈrnsson, B.T. Walther, T. Hansen, Abrupt changes in photoperiod affect age at maturity, timing of ovulation and plasma testosterone and oestradiol-17β profiles in Atlantic salmon, Salmo salar. Aquaculture **162**(1), 85–98 (1998)
15. M. Iigo, T. Abe, S. Kambayashi, K. Oikawa, T. Masuda, K. Mizusawa, et al., Lack of circadian regulation of in vitro melatonin release from the pineal organ of salmonid teleosts. Gen. Comp. Endocrinol. **154**(1-3), 91–97 (2007a)
16. M. Iigo, T. Azuma, M. Iwata, Lack of circadian regulation of melatonin rhythms in the sockeye salmon (Oncorhynchus nerka) in vivo and in vitro. Zool. Sci. **24**(1), 67–70 (2007b)
17. E.N. Fuentes, D. Safian, I.E. Einarsdottir, J.A. Valdes, A.A. Elorza, A. Molina, B.T. Bjornsson, Nutritional status modulates plasma leptin, AMPK and TOR activation, and mitochondrial biogenesis: implications for cell metabolism and growth in skeletal muscle of the fine flounder. Gen. Comp. Endocrinol. **186**, 172–180 (2013)
18. Y. Minokoshi, B.B. Kahn, Role of AMP-activated protein kinase in leptin-induced fatty acid oxidation in muscle. Biochem. Soc. Trans. **31**, 196–201 (2003)

19. S.H. Bates, R.N. Kulkarni, M. Seifert, M.G. Myers, Roles for leptin receptor/STAT3-dependent and -independent signals in the regulation of glucose homeostasis. Cell Metab. **1**, 169–178 (2005)
20. M. Gorissen, N.J. Bernier, S.B. Nabuurs, G. Flik, M.O. Huising, Two divergent leptin paralogues in zebrafish (Danio rerio) that originate early in teleostean evolution. J. Endocrinol. **201**, 329–339 (2009)
21. E. Froiland, K. Murashita, E.H. Jorgensen, T. Kurokawa, Leptin and ghrelin in anadromous Arctic charr: cloning and change in expressions during a seasonal feeding cycle. Gen. Comp. Endocrinol. **165**, 136–143 (2010)
22. Q. Liu, Y. Chen, D. Copeland, H. Ball, R.J. Duff, B. Rockich, R.L. Londraville, Expression of leptin receptor gene in developing and adult zebrafish. Gen. Comp. Endocrinol. **166**, 346–355 (2010)
23. D.A. Zieba, M. Szczesna, R. Klocek-Gorka, E. Molik, T. Misztal, G.L. Williams, K. Romanowicz, E. Stepien, D.H. Keisler, M. Murawski, Seasonal effects of central leptin infusion on secretion of melatonin and prolactin and on SOCS-3 gene expression in ewes. J. Endocrinol. **198**, 147–155 (2008)
24. A.G.G. Moen, R.N. Finn, Short-term, but not long-term feed restriction causes differential expression of leptins in Atlantic salmon. Gen. Comp. Endocrinol. **183**, 83–88 (2013)
25. A.B. Tinoco, L.G. Nisembaum, E. Isorna, M.J. Delgado, N. de Pedro, Leptins and leptin receptor expression in the goldfish (Carassius auratus). Regulation by food intake and fasting/overfeeding conditions. Peptides **34**, 329–335 (2012)
26. J.K. Wang, Z.L. Yan, Current status and development trend on abalone culture. Fish. Sci. **31**(12), 749–753 (2012). in Chinese
27. Z.M. Romo, A.D. Re, F. Díaz, A. Mena, Physiological responses of pink abalone Haliotis corrugata (Gray, 1828) exposed to different combinations of temperature and salinity. Aquac. Res. **41**, 953–960 (2010)
28. W. Cheng, S.P. Yeh, C.S. Wang, J.C. Chen, Osmotic and ionic changes in Taiwan abalone Haliotis diversicolor supertexta at different salinity levels. Aquaculture **203**, 349–357 (2002)
29. M. Wassnig, R.D. Roberts, A. Krsinich, R.W. Day, Effects of water flow rate on growth rate, mortality biomass return of abalone in slab tanks. Aquac. Res. **41**, 839–846 (2010)
30. M.A. Naylor, H. Kaiser, C.L.W. Jones, The effect of free ammonia nitrogen, pH and supplementation with oxygen on the growth of south African abalone, Haliotis midae L. in an abalone serial-use raceway with three passes. Aquac. Res. **45**, 213–224 (2014)
31. J.O. Harris, G.B. Maguire, S.J. Edwards, D.R. Johns, Low dissolved oxygen reduces growth rate and oxygen consumption rate of juvenile greenlip abalone, Haliotis laevigata Donovan. Aquaculture **174**, 265–278 (1999)
32. F. Ahmed, S. Segawa, M. Yokota, S. Watanabe, Effect of light on oxygen consumption and ammonia excretion in Haliotis discus discus, H. gigantea, H. Madaka and their hybrids. Aquaculture **279**, 160–165 (2008)
33. J.K. Kim, Y.X. Mao, G. Kraemer, C. Yarish, Growth and pigment content of Gracilaria tikvahiae McLachlan under fluorescent and LED lighting. Aquaculture **436**, 52–57 (2015)
34. Y.W. Dong, S.L. Dong, X.L. Tian, F. Wang, M.Z. Zhang, Effects of diel temperature fluctuations on growth, oxygen consumption and proximate body composition in the sea cucumber Apostichopus japonicus Selenka. Aquaculture **255**, 514–521 (2006)
35. T.H. Carfoot, *Animal energetics* (Academic Press, New York, 1987), pp. 407–515
36. D. Lemos, V.N. Phan, Energy partitioning into growth, respiration, excretion and exuvia during larval development of the shrimp Farfantepenaeus paulensis. Aquaculture **199**, 131–143 (2001)
37. R. Jan, K. Shao, K. Chang, A study of diurnal periodicity in oxygen consumption of the small abalone Haliotis diversicolor supertexta Lischke. Bull. Inst. Zool. Acad. Sin. **20**, 1–8 (1981)
38. Z. García-Esquivel, S. Montes-Magallon, M.A. Gonzalez-Gomez, Effect of temperature and photoperiod on the growth, feed consumption, and biochemical content of juvenile green abalone, Haliotis fulgens, fed on a balanced diet. Aquaculture **262**, 129–141 (2007)

39. E. Gorrostieta-Hurtado, R. Searcy-Bernal, C. Anguiano-Beltrán, Z. García-Esquivel, E. Valenzuela-Espinoza, Effect of darkness on the early postlarval development of Haliotis corrugata abalone fed different diatom densities. Cienc. Mar. **35**, 113–122 (2009)
40. R. Day, P. Gilmour, S. Huchette, Effects of density and food supply on postlarval abalone: behaviour, growth and mortality. J. Shellfish Res. **23**, 1009–1018 (2004)
41. X.L. Gao, M. Zhang, J.M. Zheng, X. Li, L. Chi, C.B. Song, Y. Liu, Effect of LED light quality on the phototaxis and locomotion behaviour of Haliotis discus hannai. Aquac. Res. **47**, 3376–3389 (2016)
42. B. Guo, F. Wang, S.L. Dong, Q.F. Gao, The effect of rhythmic light color fluctuation on the molting and growth of Litopenaeus vannamei. Aquaculture **314**, 210–214 (2011)
43. A. Berg, T. Hansen, S. Stefansson, First feeding of Atlantic salmon (Salmo salar L.) under different photoperiods. J. Appl. Ichthyol. **8**, 251–256 (1992)
44. J.E. Thorpe, C.E. Adams, M.S. Miles, D.S. Keay, Some influences of photoperiod and temperature on opportunity for growth in juvenile Atlantic salmon, Salmo salar L. Aquaculture **82**, 119–126 (1989)
45. M. Carrillo, S. Zanuy, A. Felip, M. Bayarri, G. Molés, A. Gómez, Hormonal and environmental control of puberty in perciform fish. Ann. N. Y. Acad. Sci. **1163**, 49–59 (2009)
46. X.L. Gao, M. Zhang, X. Li, C. Shi, C.B. Song, Y. Liu, Effects of LED light quality on the growth, metabolism, and energy budgets of Haliotis discus discus. Aquaculture **453**, 31–39 (2016)
47. M. Bradford, A rapid and sensitive method for the quantitation of microgram quantities of protein utilizing the principle of protein-dye binding. Anal. Biochem. **72**, 248–254 (1976)
48. M.E. Anderson, Determination of glutathione and glutathione disulfide in biological samples. Methods Enzymol. **113**, 548–555 (1985)
49. L.J. Li, F. Zhang, X.M. Liu, Y.P. Guo, E.B. Ma, Oxidative stress related enzymes in response to chromium (VI) toxicity in Oxya chinensis (Orthoptera: Acridoidae). J. Environ. Sci. (China) **17**, 823–826 (2005)

Index

A
Abalone (*Haliotis discus hannai Ino*)
acclimation, 573
antioxidant enzyme activity, 576, 578–579
artificial hatching, 573
assimilation efficiency, 566
biochemical composition, 568–569
bioenergetics approach, 561–562
blackout cloths, 573
collection of residual food, 573
contents and activities, 574–575
digestive enzyme activity, 576–577
elemental analyzer, 565
energy budgets, 566
energy of excretion, 566
energy parameters, 568, 570–571
FCE, 566–567, 575
feeding, 573
food intake, 566–567
growth rate of, 571–572
hepatopancreas, 573
Institute of Semiconductors CAS, 572
light qualities, 563–564, 571
light quality treatments, 572
Lonicera japonica, 564
oxygen bomb calorimeter, 565–566
PK, HK, and LDH, 565
PMS transferred hydrogen, 566
SDH, 565
seasonal rhythm and variations, 572
shell length/body weight-specific growth, 566–567
Soxhlet method, 565
spectroradiometer, 564, 572–573
stress factors, 563
survival rate, 566–567
treatment groups, 564
water exchange, 573
Absolute quantum efficiency (AQE), 298
Actinic keratosis (AK), 491, 499
Acute herpes zoster ophthalmicus, 486
Adenosine triphosphate (ATP), 489
ALA, 499–500
Alanine aminotransferase (GPT) activity, 574
AlGaInP/AlGaAs material system
direct-indirect transition in, 173
epitaxy by MOCVD, 173–175
lattice and bandgap energy, 171–173
LED structure design and manufacture
Bragg reflector, 175–178
flip-chip structure, 185, 186
textured chip surfaces, 178–179
thin-film structure (*see* Thin-film structure, AlGaInP/AlGaAs LED)
transparent substrate, 179–181
p-type and n-type doping, 174
AlGaInP/AlGaAs red/yellow LED application
in communication, 191–193
in display, 190–191
in solid-state lighting
architectures, 185, 186
green gap, 187–189
hy-LED, 185, 189
LER and CRI, 187
light source efficacy, YAG:Ce^{3+} phosphor, 187, 188
optical power spectra, 185, 186
pc-LED, 185–187, 190

© Springer International Publishing AG, part of Springer Nature 2019

J. Li, G. Q. Zhang (eds.), *Light-Emitting Diodes*, Solid State Lighting Technology and Application Series 4, https://doi.org/10.1007/978-3-319-99211-2

AlGaInP/AlGaAs red/yellow LED application (*cont.*)
red LED efficiency, 189–190
relative white light luminous efficacy, 189, 190
AlGaInP-based LEDs, VLC, 192
AlGaInP GSSFC-LEDs structure, 186
AlGaInP zinc blende structure, 171, 172
AlGaN-based ultraviolet light-emitting diodes
AFM scans, 398
aging test, 399
AlN molar fraction, 402
apparent charge profile, 400, 401
catastrophic degradation, 398
C–V measurements, 405
degradation mode, 409, 410
DLTS analysis, 411
electro-optical characteristics, 408
EL spectra, 400, 401, 406
emission intensity, 403
emission wavelength, 407, 411
external quantum efficiency, 397
high III/V molar ratio, 411
I–V characteristics, 407, 409
L-I characteristics, 405
lifetime measurements, 400
long-term reliability, 400
low efficiency problem, 400
low-frequency noise, 402
MELEO technique, 401
Mg-doped AlN interlayer, 410
near-field spectra, 404
non-radiative recombination processes, 404
operating current and temperature, 397
optical power, 398, 399, 405, 406, 408, 409
output power, 399, 400
performance and reliability measurements, 407
photocurrent spectroscopy, 411, 412
QW peak and parasitic peak, 410, 411
spectral noise density, 402
TEM images, 407
wall-plug efficiency, 397
AlGaN UV-C LEDs, 337
AlInGaP-based red LED, 189–190
AlN MOVPE
adduct reactions
as functions of temperature, 248–249
initial process of, 247–248
surface reaction, 249–251
Al metal-organic precursors and ammonia, 245
chemical equation, AlN growth, 245
parasitic reactions, 245, 252–254
reaction mechanism, 246–247
surface morphology and quality, 246
TMAl, decomposition processes, 250–252
Al-rich III-nitride materials
DUV LEDs, structural design (*see* Deep ultraviolet light-emitting diodes)
epitaxy on sapphire, defects and stress control
Al atomic surface mobility, 254
buffer-assisted technique, 256–257
ELOG, 255, 256
interlayers, 257–258
parasitic reactions, 254
special growth process control, 258–259
two-step method, 255
wafer bowling, 255
heteroepitaxy by MOVPE (*see* AlN MOVPE)
Al-rich-induced optical polarization effect, 268–270
Ammonothermal growth
mineralizer, 11–12
solvothermal process, 10–11
Ammonothermal method, 93, 298
Artificial intelligence (AI), 518, 520
As-prepared wafer, 158
Atlantic salmon (*Salmo salar* L.)
AsLR, 554
appetite-related neurons and circuits, 555
DIG, 557
expression pattern, 560–562
feeding ratio, 557
FITC, 557
location of, 557–559
RAS, 556
treatment groups, 556–557
AsMR, 554
appetite-related neurons and circuits, 555
DIG, 557
expression pattern, 558, 560
feeding ratio, 557
FITC, 557
location of, 557–559
RAS, 556
treatment groups, 556–557
GnRH
antisense DIG probes and FITC, 551
expression levels, 554–555
external morphological and histology observation, 550–551
location of, 551–552
loss of functional mutations, 549

photoperiod treatment groups, 550
RAS, 550
kissr
antisense DIG probes and FITC, 551
expression levels, 552–553
GSI, 550–551
location of, 551–552
loss of functional mutations, 549
photoperiod treatment groups, 550
RAS, 550
Atomic layered growth (ALD) process, 210–211
Auger non-radiative recombination, 296

B

Band-filling, 304
Bandgap renormalization (BGR), 301
Bethe–Salpeter equation (BSE) method, 349
Big data analysis, 518, 520
Bimolecular radiative recombination, 295
Bottom window (BW), 176–178
Bragg reflector
AlGaInP LED, 176, 177
bottom window, 176–178
DBRs, 176–178
DH-LED structure with, 176
high-brightness LED, 175, 176
MOCVD-based AlGaAs, 176, 177
Brilliant Mix concept, 187
Buffer technology
GPSS, thin AlN buffer on
AFM morphology, 141, 142
buffer layers, 137
ELOG process, 139, 140
Ga melt-back defects, 137, 138
GaN island-like nucleation layer, 139–140
mismatch dislocation density, 138–139
MMELOG, 140, 141
NH_3 reaction, 137, 138
polished and wet-cleaned Si (111) substrate surface, AFM images, 136, 137
schematic view, 136, 137
selective area growth, 136
TEM image, 140, 141
threading dislocation, 139
X-ray diffractometer, substrate orientation by, 135
graded AlGaN buffer on bare Si substrate
$Al_{0.17}Ga_{0.83}N/Al_{0.35}Ga_{0.65}N/AlN$ buffer, 145, 146
as-grown GaN film, crystalline quality of, 146
as-grown GaN-on-Si template, 147
CTE, 142, 143, 145
dark-field two-beam cross-sectional TEM images, 143, 144
double-crystal x-ray rocking curves, 146–147
five-step-graded AlGaN/AlN buffer, 144, 145
panchromatic cathodoluminescence image, 147
stress evolution, 142, 143
XRCs FWHMs, 143
Bulk GaN substrates
high-pressure high-temperature growth method, 93
homoepitaxial GaInN/GaN light-emitting diode growth (*see* Homoepitaxial GaInN/GaN light-emitting diode growth)
HVPE (*see* Hydride vapor-phase epitaxy)
hydrogen-thermal method, 93
light efficiency extraction
chip shaping method, 122–124
EQE, 120
photonic crystal method, 124–127
surface treatment methods, 121, 122
total device efficiency, 120
nonpolar and semipolar orientations GaN LED growth (*see* Nonpolar and semipolar orientations GaN LED)

C

Cathodoluminescence (CL) image, as-grown GaN-on-Si film, 147
Charge asymmetric resonance tunneling (CART) structure, 290
Chemo-mechanical polishing (CMP)
AFM image, SiC wafer surface, 87, 88
AlN substrate surfaces, 262, 263
chemical equation, 87
FWHM of (0004) reflection rocking curves, 89
machining processes, 90
SiO_2, 86
surface after KOH etching, 89
surface roughness, 87
Chip fabrication process, 155
Chip-scale packaging (CSP), 218
CMP, *see* Chemo-mechanical polishing
Coefficient of thermal expansion (CTE), 142, 143, 145

Color rendering index (CRI), 187, 192
Complementary contact, 157
Cone-shaped patterned sapphire substrate (CPSS), 324
Contact potential difference (CPD), 101
Conventional flip-chip bulk-GaN LEDs, 123
Conventional transparent-substrate chip, 180
Convergent beam electron diffraction (CEBD) patterns, 108
Coomassie Brilliant Blue G-250 dye method, 524
Cost performance (CP), 517
Cytochrome c oxidase (COX) theory, 488–489

D
Daily light integral (DLI), 523, 525, 536
DBR, *see* Distributed Bragg reflector
Deep-level transient spectroscopy (DLTS) analysis, 411
Deep ultraviolet light-emitting diodes (DUV-LEDs), 291, 295
  AlGaN
    epitaxial structure, 259
    epitaxy technology, 260
    n, p, and active regions, 259
    n-type doping, 260
    p-type doping, 260–261
  on AlN substrate
    homoepitaxy, 262–263
    pseudomorphic AlGaN, 264–265
    pseudomorphic DUV LEDs, 265–268
  applications, 337
  cryogenic operation
    carrier freeze-out effect, 386
    doping concentrations, 383
    energy band diagram, 383, 384
    flux-time diagram, 382
    J-V and EL *vs*. J measurements, 385
    J-V characteristics, 383
    L-I characteristics, 384, 385
    NDR phenomena, 381, 384
    schematic diagram, 381, 382
    temperature-dependent EL measurements, 386
  EQE, 338–339
  with GaN/AlN quantum structures (*see* GaN/AlN quantum structures)
  injection efficiency, 343–344
  IQE
    ABC model, 340
    definition, 339
    ELO method, 341
    energy band diagram, 340, 341
    non-radiative recombination, 340
    QCSE, 342–343
    radiative lifetime, 340
    recombination rates, 340
    SRH recombination process, 340
    TDD, 341–342
  light exaction issues
    Al-rich-induced optical polarization effect, 268–270
    high reflective techniques, 272
    surface patterning, 270–272
    TE mode LEE, 268
    TM mode LEE, 268
    total internal reflection, 268
  light extraction efficiency, 344–346
  loss mechanisms, 339
  performance metric, 338
  polarization property, 338
  UV LED structure, quantum efficiency, 261
  wall-plug efficiency, 343–344
Density-activated defect recombination (DADR), 301
Dermalux's Dermalux® LED Phototherapy, 506
Device passivation, 162
Digoxigenin (DIG), 551, 557
Dislocation elimination by the epitaxial growth with inverse-pyramidal pits (DEEP), 96
Distributed Bragg reflector (DBR), 176–178, 216, 313–314
Double hetero-structure (DH), 286
Dry weight (DW), 533
DUV-LEDs, *see* Deep ultraviolet light-emitting diodes

E
e-beam evaporation technique, 379
Efficiency droop, IQE, 282
  Auger coefficient, 299
  band-filling, 301
  BGR effect, 301
  carrier delocalization, 300–301
  defect-assisted tunneling, 301
  density-activated defect recombination, 301
  dislocation density, 302
  internal losses and carrier leakage, 299, 300
  mechanism classification, 299, 300
  Mg doping, 301
  p-GaN and AlGaN EBL layers, 301
  polarization-induced carrier leakage, 301

polarization-matched AlGaInN quantum barriers and EBL, 300
remedies
classification, 302
EQE, 303
finished and assembled III–nitride, 303, 304
freestanding GaN substrate, 304
light output power dependence, 304, 305
μ–LEDs, 304
polarization match, 303
pulsed, room temperature EQE *vs.* current density, 303, 304
QW number, 302
SP-QW coupling process, 305
Shockley-Read-Hall recombination, 302
S-shape dependence, 301
temperature-dependent droops, 302
Electric energy use efficiency (EUE), 534, 542–543
Electroluminescence (EL), 104
GaN NW, 443–444
MOVPE, 446–447, 449–450
spectra, 296
Electron-beam-induced current (EBIC) method, 100
Electron-blocking layer (EBL), 286, 290
Electron paramagnetic resonance (EPR) spectrum, 82
Electron reservoir layer (ERL), 286
ELOG, *see* Epitaxial lateral overgrowth
Epitaxial GaN/sapphire interface, 285
Epitaxial lateral overgrowth (ELOG), 18, 204–205, 284, 327, 341
AlN epitaxy on sapphire, 255, 256
dislocation reduction and strain control, 96
heterogeneous epitaxial growth, 25
HVPE LEO a-plane growth, 26
morphology, 26
pendeo-epitaxial regrowth, 27
plasma-enhanced chemical vapor deposition, 25
V/III ratio, 26
Epitaxial lift-off (ELO) process, 184
EQE, *see* External quantum efficiency
Etch-pit density (EPD) measurements, 205
External quantum efficiency (EQE), 119–120, 211–212, 338–339, 464
of AlGaInP/AlGaAs LED, 175
in conventional transparent-substrate chip, 180
semipolar LED, 287, 288
Extraocular phototransduction (EPT), 489

F

Fe-doped bulk SI GaN (SI-GaN:Fe), 99
Flat sapphire substrate (FSS), 260
Flip-chip structure, AlGaInP/AlGaAs LED, 185, 186
Fluorescein isothiocyanate (FITC), 551, 557
Fluorescence, 520
Fluorescent lamps (FLs), 532–533
Food conversion efficiency (FCE), 566–567, 575
Food dysphagia, 486
Food intake (FI), 566–567
Fresh weight (FW), 533
Full width at half maximum (FWHM), 372, 380, 402
of DCXRCs, 146, 147
EL spectrum, 193
of GaN (0002), 110, 143, 146, 209
linewidth, 189, 190
PL spectra, 370
of (0004) reflection rocking curve
SiC surface etched by KOH, 86, 88
SiC wafer surface, 89
XRD values, 206–207
XRD ω-scan FWHMs, 293, 294
Function-specific homeostasis (FSH), 488
FWHM, *see* Full width at half maximum

G

Gallium nitride (GaN) NW
blue LEDs
aligned nanowires, 223
c-plane devices, 213
electron cooler, 214
electron overflow, 214
EQE, 211–212
flip-chip LED, 217–219
graphene, 209–210
GSL layer, 213
heteroepitaxial growth, 208
high-power, 214
internal quantum efficiency, 211
lateral LED, 215–217
lattice constant mismatch, 204
LEE, 211–212
light-emitting triodes, 212–213
MLBs, 214
morphological evolution, 205–206
nanocolumns, 223–224
nanorods, 223
plasma treatment, 209
radial nanowire heterostructures, 224
sapphire, 204–205

Gallium nitride (GaN) NW (*cont.*)
SiC substrates, 209
single-crystal aluminum oxide, 204
substrate patterning, 214–215
surface roughening, 214–215
synthesis, 221–223, 234
TDDS, 207–208
3D-2D growth process, 205–206
vdWE, 208–209
VLED, 219–221
WS_2 and MoS_2 interlayers, 211–212
wurtzite structure, 203
XRD FWHM, 206–207
ZnO nanowalls, 209
diodic current–voltage characteristics, 443–444
electroluminescence, 443–444
elongation phase, 431
green LEDs
Auger recombination efficiency, 233
effective dopant doping, 226–227
energy-band engineering, 228
Ga-face multiple quantum wells, 226
GEBL, 231
In-rich quantum wells, 228, 232
LET, 229
light extraction efficiency, 233–235
nitride material, 227–228
p-GaN layer, 229–230
polarization fields, 224–225
polarized sheet charges, 229
pre-strained superlattice structure, 226–227
quantum dots, 232–233
reverse fields, 226
simulation results, 229–230
SL-EBL, 229, 231
growth conditions, 429–430
heterostructures, 433–434
incubation phase, 431
p-doped shell, 443–444
plastic relaxation, 431
seed nucleation, 430
selective area growth, 432–433
surface energy anisotropy, 432
surface properties, 430
transition phase, 431
GaN/AlN quantum structures
BSE method, 349
enhanced carrier injection
cryogenic operation, 381–387
polarization-induced doping, 374–376
structural design, 376, 377
tunable deep-UV emission, 377–381
GW method, 349
HR-XRD, 349, 350
light extraction enhancement, 387–390
material-based challenges, 346
MBE-grown samples
condition markers, 357–360
experimental data, 350, 351
growth modes, 357
in situ RHEED-based characterization, 353, 355–356
parameter optimization, 362–364
quantum wells/quantum dots/disks, 360–362
schematic diagram, 354
single and double monolayer δ-GaN quantum wells, 364–367
structure, 354–355
optical and electronic gap calculation, 349, 350
photoluminescence measurements, 349
physical challenges, 346
PL spectra broadening, 350, 352
SvR equation, 353
TE-polarized spontaneous emission rate, 347
transverse-magnetic-polarized emission, 347
ultrathin AlN/GaN/AlN heterostructures, 347–349
GaN-based LEDs, 2
GaN LED on Si substrate
buffer technology (*see* Buffer technology)
device processing
chip fabrication process, 155
complementary contact, 157
device passivation, 161–163
film transferring, 158–159
n-polar n-type GaN, surface roughening, 159–162
ohmic contact on n-polar n-GaN, 159–161
reflective p-type ohmic contact, 155–156
epitaxy
dislocation density, 134–135
film-cracking problem, 134
lattice and thermal mismatch, 133–134
quantum well strain engineering, 148–150
vertical thin film LEDs, device characterization
emission intensity *vs.* current density, 165
features, 162
"flip chip" structure, 165

junction temperature, 165, 166
thermal conductivity, 164
vertical and lateral structure, 163, 164
V-I characteristics, 163–164
white LEDs, spectra of, 166, 167
white light projection, 166, 167
V-pits
area ratio of pits, 154
EL spectra, 151, 152
hole injection into c-plane QW process, 153
InGaN/GaN MQW LEDs, 151
IQE dependence, 154
luminescence intensity, 151
photoluminescence intensity, 151
schematic structure, 150, 151
TD densities, 151
"V pits enhancing hole injection" model, 152–155
"V pits screening TD" model, 152
GaN substrates
bulk GaN substrates, 5
GaN laser diodes
applications, 4
vs. sapphire-based approaches, 5
gas-phase growth
gas-phase transport method, 16–17
HVPE (*see* Hydride vapor-phase epitaxy)
hetero-epitaxy, 8
homogeneous epitaxial GaN films, 3
laser stripping process, 2
LED chip structure, 2, 3
liquid-phase growth
ammonothermal growth, 10–12
HPNSG, 9–10
Na-flux method (*see* Na-flux method)
sapphire, 2
technical routes
GaN liftoff substrate wafers, 6–7
GaN templates, 7–8
native GaN substrates, 5–7
TIE GaN wafer forecast, 4
wafer bonding process, 2
Glow discharge mass spectroscopy (GDMS) measurements, 90
Glutathione (GSH) content, 574, 579
Glutathione peroxidase (GP_X) activity, 574, 579
Gonadotropin-releasing hormone (GnRH)
antisense DIG probes and FITC, 551
expression levels, 554–555
external morphological and histology observation, 550–551
location of, 551–552
loss of functional mutations, 549
photoperiod treatment groups, 550
RAS, 550
Graded AlGaN buffer on bare Si substrate
$Al_{0.17}Ga_{0.83}N/Al_{0.35}Ga_{0.65}N/AlN$ buffer, 145, 146
as-grown GaN film, crystalline quality of, 146
as-grown GaN-on-Si template, 147
CTE, 142, 143, 145
dark-field two-beam cross-sectional TEM images, 143, 144
double-crystal x-ray rocking curves, 146–147
five-step-graded AlGaN/AlN buffer, 144, 145
panchromatic cathodoluminescence image, 147
stress evolution, 142, 143
XRCs FWHMs, 143
Graded-composition electron-blocking layer (GEBL), 231
Graded superlattice (GSL) layer, 213
Green-gap LEDs, 188–189
Grid-patterned Si substrate (GPSS), thin AlN buffer on
AFM morphology, 141, 142
buffer layers, 137
ELOG process, 139, 140
Ga melt-back defects, 137, 138
GaN island-like nucleation layer, 139–140
mismatch dislocation density, 138–139
MMELOG, 140, 141
NH_3 reaction, 137, 138
polished and wet-cleaned Si (111) substrate surface, AFM images, 136, 137
schematic view, 136, 137
selective area growth, 136
TEM image, 140, 141
threading dislocation, 139
X-ray diffractometer, substrate orientation by, 135

H

Hamilton anxiety rating scale (HAM-A), 495
Hamilton depression rating scale (HAM-D), 495
Hexagonal pyramids array vertical-injection light-emitting diodes (HPA V-LEDs), 318–319
Hexokinase (HK), 565
High-brightness AlGaInP thin-film LED, 183

High-brightness p-side-up thin-film AlGaInP-based LEDs
fabrication process for, 184, 185
wafer-transfer technique, 184
High-pressure nitrogen solution growth (HPNSG), 9–10
High purity semi-insulating (HPSI) SiC, 79
High reflective techniques, DUV LEDs, 272
High-resolution X-ray diffraction (HRXRD), 83, 89, 110, 263, 363
High-temperature chemical vapor deposition (HTCVD) method, 45–46
Homoepitaxial GaInN/GaN light-emitting diode growth
AIX-200RF MOCVD reactor, 102
efficiency droop and efficiency enhancement, 118–120
electrical characterization and optical characterization
defect density, 111
electrical characteristics, 112
forward voltages, distribution of, 112, 113
HRXRD rocking curves, 110
InGaN/GaN MQW LEDs, 109
low-pressure metal-organic chemical vapor deposition, 109
reverse-bias current, 111
reverse currents, distribution of, 112
SIMS measurements, 110
temperature-dependent *I–V* characteristics, 110–111
electroluminescence, 104
freestanding HVPE GaN, 102
GaN templates, 102
LED on GaN, 104
LED on sapphire, 104
nonpolar and semipolar LEDs performance, 102, 103
photoluminescence spectra, 104
threading dislocation density
CBED patterns, 108
hexagonal pits, SEM, 105, 106
inversion domains, 108
inverted pyramids, 107–109
LED on GaN at 79 K, 105, 106
QWs, cross-sectional TEM micrograph, 106, 107
reduction, 101
V-defects, 102
Homoepitaxy on AlN substrate, 262–263
Horticultural lighting, *see* Plant factories with artificial lighting (PFAL)
HVPE, *see* Hydride vapor-phase epitaxy
Hybrid LED (hy-LED), 185–186, 189–190
Hydride vapor-phase epitaxy (HVPE)
advantage, 93
arsenic and phosphide semiconductor materials, 17
chemical reaction, 18–20
combined GaN crystal growth
ammonothermal growth, 34, 35
bulk GaN wafers, 34
dislocation density, 34
Na-flux growth, 34
platelet and needle GaN single crystal, 31–32
post-processing technology, 32, 33
difficulties
ammonium chloride powder, 24–25
brittle quartz reactor, 25
liquid gallium source consumption, 24
space parasitic reaction, 24
dislocation reduction and strain control
DEEP, 96
ELOG, 95–96
GaN NW array, 96, 97
nano-mask, 96
panchromatic CL images, 96, 97
ELO, 18
epitaxial lateral overgrowth
heterogeneous epitaxial growth, 25
HVPE LEO a-plane growth, 26
morphology, 26
pendeo-epitaxial regrowth, 27
plasma-enhanced chemical vapor deposition, 25
V/III ratio, 26
Fe-doping, high-resistivity GaN substrate, 98–100
freestanding HVPE-GaN substrate
chemical etching, 28
laser liftoff process, 28–30
quasi homo-substrates, 27
self-separation methods (*see* Self-separation methods)
thermal expansion coefficients, 28
GaN boule, 34–36
growth mechanism, 94–95
hydride gas-phase epitaxial growth system, 20–21
laser lift-off technique, 93
low-cost HVPE-GaN templates on sapphire, 37
minority diffusion lengths, bulk GaN, 99–101
MOVPE, 18
nitrides growth and doping

AlN-AlGaN, 22–24
cubic GaN, 22
heterogeneous nucleation, 21
InN-InGaN, 24
Mg doping, 22
pretreatment, 21
Zn doping, 22
nonpolar GaN substrate, 36
sapphire substrate, 17
self-separation, 93
Si-doping, *n*-GaN substrate, 98
Hydroponic lettuce
Lactuca sativa L. cv. Frill ice
cucumber seedlings, 521
effects of growth and quality, 527–531
growth and quality measurement, 523–524
high-quality, 521
leaf morphology and growth, 524–527
morphological and physiological responses, 521
plant materials and growth conditions, 521–523
treatment and experiment design, 522–523
Lactuca sativa L. cv. "Ziwei"
continuous photosynthesis and light responses, 540–542
effect of light quality, 537–540
effects of growth, 534–537
EUE, 542–543
growth and quality properties, 533–534
photosynthesis measurement, 534
plant materials and growth condition, 532
treatment and experiment design, 524, 532–533
Hypothalamus, *Salmo salar*, *see* Atlantic salmon (*Salmo salar* L.)

I

InAs quantum dots, 290
Indoor vertical farms, 513
Information and communication technology (ICT), 520
InGaN/AlInGaN MQW LED structures, 286, 287
InGaN-based ultraviolet light-emitting diodes, 412–413
InGaN/GaN MQW, 195
InGaN quantum dot-based LED, 197
Injection efficiency (INJ), 343–344
Internal quantum efficiency (IQE), 118, 462–463
ABC model, 340
blue LED, 281
conventional LED, 286, 287
double hetero-structure, 286
ELOG technique, 284
epitaxial GaN/sapphire interface, 285
InGaN/AlInGaN MQW LED structures, band diagram, 286, 287
LLO process, 283
MQW, 286
nonpolar/semipolar LEDs, 287–288
NPSS, 284–285
polarization, 286, 287
PSS technology, 284
quasi-homoepitaxial LED, 283
SAE, 284
sandwiched LED, 286, 287
sapphire substrate, 283–284
siliane, 285
SQW, 286
strain-controlled substrate, 285
TDD, 282–283, 285
trapezoid QW, 286
VSLED, 283
characterization
carrier recombination mechanisms, 295–296
EL spectra, 296, 297
fitting process and quantum efficiencies, 297
generation rate, 296
integrated PL intensity, InGaN UL, 295, 296
PL and ODPL spectra, 298, 299
PL and PA signals, 297–298
recombination rate, 296
TDPL, 295
definition, 281, 339
of DUV LEDs, 254
efficiency droop (*see* Efficiency droop, IQE)
ELO method, 341
energy band diagram, 340, 341
GaN/AlGaN MQWs, 282
green gap, 281
green LED
Ag arrayed LED, 291, 292
Ag NPs array, 291
AlGaN/AlN SL buffer layers, 293–294
AlGaN-based DUV-LEDs, 292, 295
AlInGaN layers, 290

Internal quantum efficiency (IQE) (*cont.*)
CART structure, 290
core-shell LED, 288, 289
crystalline quality, 288
electron-blocking layer, 290
InGaN QDs, 290
LT-GaN layer, 291, 294
Mg-doped AlGaN, 294
micro-rod GaN template, 288, 289
m-plane n-GaN core, 288
n-AlGaN bottom-cladding layer, 294
nanorod array, 289–290
on nonpolar and semipolar GaN substrate, 288
NPSS, 293
PALE-AlN buffer, 292
polarization field, 288
polarization-matched barriers, 290
pulsed-flow growth method, 290
QDs structures, 290
sandwiched QWs structure, 290
SP mode, 291
tapered AlGaN EBL, 290
V-pits, 291
whole-composition-range AlGaN MQWs, 292
non-radiative recombination, 340
PL intensity, 282
QCSE, 342–343
radiative lifetime, 340
recombination rates, 340
single and double monolayer δ-GaN quantum wells
SK quantum dots/disks, 366–373
temperature-dependent PL measurement, 364
SRH recombination process, 340
TDD, 341–342
III-nitride-based light-emitting diodes, 311
in III-nitride materials, 282
wave function overlapping, 281
Internet of Things (IoT), 520
IQE, *see* Internal quantum efficiency
IQE DUV-LEDs, 295
Irradiance, 487

J
Jahn-Teller coupling, 99

K
Kelvin probe force microscopy (KPFM), 100
Kisspeptin and receptor GPR54 (kissr)
antisense DIG probes and FITC, 551
expression levels, 552–553
GSI, 550–551
location of, 551–552
loss of functional mutations, 549
photoperiod treatment groups, 550
RAS, 550
KOH etching, 83

L
Lactic dehydrogenase (LDH), 565, 573
Laser lift-off (LLO) process, 28–30, 283
Leaf length (LL), 521, 523, 525
Leaf width (LW), 521, 523, 525
LEE, *see* Light extraction efficiency
Lely method, 42
Leptin-receptor (AsLR), 554
appetite-related neurons and circuits, 555
DIG, 557
expression pattern, 560–562
feeding ratio, 557
FITC, 557
location of, 557–559
RAS, 556
treatment groups, 556–557
Light detection and ranging (LiDAR) device, 520
Light efficiency extraction
chip shaping method, 122–124
EQE, 120
photonic crystal method
air-gap embedded PhCs, 124
embedded and double SiO_2 PhC LEDs, 125
embedded PhC of SiO_2 nanodisks, 125–126
far-field emission patterns, 126
freestanding substrates, 126–127
surface treatment methods, 121, 122
Light-emitting triode (LET), 229
Light energy use efficiency (LEU), 534
Light extraction efficiency (LEE), 281, 344–346
blue LEDs, 211–212
pseudomorphic DUV LEDs on AlN substrates, 266–268
Light extraction techniques, 180
Light output power (LOP) dependence, 304, 305
Light quality (LQ), *see* Hydroponic lettuce
Liquid-phase epitaxy (LPE), 12, 14, 173
Litebook® LED Phototherapy Instrument, 507

LLLT, *see* Low-level light therapy
Localized SP (LSP), 291
Low-level light therapy (LLLT)
  acne, 496–497
  continuous wave, 487
  development history, 485–486
  emotion cognitive impairment, 495
  energy density, 487
  facial rejuvenation, 497
  He–Ne lasers, 494
  high and low doses hinges, 487
  irradiation time, 487
  light and human tissues, 486–487
  mitochondrial mechanism, 488–489
  motor functions, 498
  neonatal jaundice, 494
  pain assessments, 498
  parameters and observational indicators, 487
  PDT (*see* Photodynamic therapy)
  photobiomodulation therapy, 488
  phototherapy devices
    Blu-ray phototherapy devices, 505–506
    infrared LED, 506
    multi-wavelength LED, 507
    photosensitizers, 504
    red light, 506
    thermal and photochemical effects, 503
  phototransduction, 489–490
  pulsed wave, 487
  scars, 497–498
  semiconductor lasers, 494
  wavelengths for, 487
  wound healing, 495–496
Low-pressure solution growth (LPSG), 16
Low-temperature GaN (LT-GaN) layers, 286, 291
Luminous efficacy of radiation (LER), 187, 189
Luminous efficiency
  green LED, 291
  white LED, 281

M
Malondialdehyde (MDA) content, 574, 579
MBE, *see* Molecular beam epitaxy
Mechanical polishing (MP)
  AFM micrograph, 85, 87
  AlN substrate surfaces, 262, 263
  FWHM of (0004) reflection rocking curve, 86, 88
  KOH etching, 86
  surface geometry, 85
  surface roughness, 85
  surface unflatness, SiC wafer, 85, 86
Mechanistic models, 518
Medical equipment
  disinfection and sterilization, 504
  lighting, 503
  phototherapy device (*see* Low-level light therapy (LLLT))
Melatonin-receptor (AsMR), 554
  appetite-related neurons and circuits, 555
  DIG, 557
  expression pattern, 558, 560
  feeding ratio, 557
  FITC, 557
  location of, 557–559
  RAS, 556
  treatment groups, 556–557
Metal-organic chemical vapor deposition (MOCVD), 173–176, 204, 219
Metal-organic-hydride vapor phase epitaxy (MO-HVPE) growth, 442
Metal-organic vapor-phase epitaxy (MOVPE), 18, 102
  catalyst-free nitride NWs, 440
    growth along c-axis direction, 437
    growth conditions, 434–437
    radial growth of heterostructures, 438–439
    selective area growth, 438
    SiN_x passivation, 437
    surface hydrogen passivation, 438
    VLS process, 434
  electroluminescence spectrum, 446–447, 449–450
  MBE
    AC multi-active-region, 453
    angular profiles, 451
    core-shell structure, 452–453
    green–yellow NW, 451
    red and near-IR MEB-grown NW, 451–452
    self-assembled growth, 449–451
    spectacular realization, 450–451
    thermal management, 453
    wire broadening and coalescence, 442–443
  m-plane/semipolar plane junction, 448–449
  non-catalyzed growth, 444–445
  OSRAM group, 447–448
  p-doped GaN cap segment, 445–446
  pulsed-flow precursor method, 445
  radial quantum wells, 444
  sapphire templates, 446–447
  self-assembled catalyzed growth, 445–446

Methyl-aminolevulinic acid (MAL), 499
Micro-patterned sapphire substrates (MPSS), 325
Migration-enhanced lateral epitaxial overgrowth (MELEO) technique, 401
Migration-enhanced MOCVD technology (MEMOCVD) technology, 260
Mild traumatic brain injury (mTBI), 495
MOCVD, *see* Metal-organic chemical vapor deposition
Modified Lely method, 43–44
Modified physical vapor transport (M-PVT), 73–74
Modified rectangular hyperbola model, 541–542
Modulated precursor flow epitaxial growth (MPEG), 263
Molecular beam epitaxy (MBE), 18
  AC multi-active-region, 453
  angular profiles, 451
  core-shell structure, 452–453
  green–yellow NW, 451
  red and near-IR MEB-grown NW, 451–452
  self-assembled growth, 449–451
  spectacular realization, 450–451
  thermal management, 453
  wire broadening and coalescence, 442–443
Monochromatic infrared energy (MIRE) treatment system, 506
MOVPE, *see* Metal-organic vapor-phase epitaxy
MP, *see* Mechanical polishing
MQWs, *see* Multiple quantum wells
"Multi-chip" approach, 192
Multilayer QBs (MLBs), 214
Multiple quantum wells (MQWs), 281, 286
  InGaN/GaN MQW, 195
  whole-composition-range AlGaN MQWs, 292
Multivariate statistical model, 518

N

Na-flux method
  advantages, 12, 15–16
  coalescence growth, 15
  crystal nucleation position, 12
  dislocation density, 14, 16
  epitaxial growth, 13
  growth mechanism, 12, 13
  growth rate, 16
  HVPE-GaN substrate, 13
  LPE, 12, 14
  LPSG, 16
  modified Na-flux method, 13, 14
  necking technique, 14, 15
Nano-mask, 96
Nano-patterned sapphire substrate (NPSS), 260, 270, 284–285, 293, 325
Negative-differential-resistance (NDR) phenomena, 381, 384
Neonatal jaundice
  bilirubin, 494
  treatment of, 486
"Ni sacrifice" process, 157
Nitric oxide (NO), 489
Nitride nanowires
  advantages, 427–428
  bottom-up approach, 427–429
  dry etching, 426
  efficiency droop, 425
  fabrication, 425, 439, 441
  flexible light sources, 468
    applications, 469
    direct growth, 470
    inorganic semiconductors, 469
    in-plane transfer, 470–471
    organic devices, 469
    polymer-embedded NWs, 469
    vertical transfer, 471–473
  GaN NW growth
    diodic current–voltage characteristics, 443–444
    electroluminescence, 443–444
    elongation phase, 431
    growth conditions, 429–430
    heterostructures, 433–434
    incubation phase, 431
    p-doped shell, 443–444
    plastic relaxation, 431
    seed nucleation, 430
    selective area growth, 432–433
    surface energy anisotropy, 432
    surface properties, 430
    transition phase, 431
  green gap, 426
  injection inhomogeneity
    intra-wire injection, 466–467
    wire-to-wire injection, 467–468
  low EQE values, 464
  low IQE values, 462–463
  MO-HVPE growth, 441–442
  MOVPE (*see* Metal-organic vapor-phase epitaxy)
  operation speed, 458–459
  p-doped and n-doped GaN extremities, 426
  phosphor converted white LEDs, 454

phosphor-free white, RGB color mixing
AlGaN shell, 456–457
axial InGaN/GaN quantum discs, 455
diodic behavior, 456
drawbacks, 454
In incorporation efficiencies, 456
parylene, 456
Si(001) substrate, 455
strain relaxation, 455
photonic platforms
LED-detector communication, 460–461, 463
on-chip optical coupling, 460, 462
photonic-crystal waveguide, 460–461
principal physical phenomenon, 425
reabsorption losses, 463–464
top-down etching, 427
ultraviolet, 457–458
wavelength control, 464–466
Nonmelanoma skin cancer (NMSC), 507
Nonpolar and semipolar orientations GaN LED
conventional c-plane LEDs and motivation, 113–114
crystallography and piezoelectricity, 115–117
homoepitaxial substrates, 117–118
Nonpolar GaN substrate, 36
Nonpolar/semipolar LEDs, 287
Normal function-specific signal transduction pathways (NSPs), 490
NPSS, *see* Nano-patterned sapphire substrate
n-side-up AlGaInP-based light-emitting diode, 179

O

ODR-LED structure, 183
Omnidirectional photoluminescence (ODPL) spectra, 298, 299
Omnidirectional reflector (ODR), 216
Omnilux blue™, 508
Omnilux Rehabilitation System, 506
Omnilux (TM) System, 507
Optical admittance spectroscopy (OAS), 81
Optical lens array technology (OLAT), 506
Oral ulcer, 486
Organic LEDs (OLEDs), 469

P

PALE-AlN buffer, 292
Patterned sapphire substrate (PSS), 234–235, 284, 285, 293, 324–328
PDT, *see* Photodynamic therapy
PFAL, *see* Plant factories with artificial lighting
PhC method, *see* Photonic crystal method
Phosphate buffered saline (PBS), 551
Phosphor-converted LED (pc-LED), 185–190, 192
Photo-acoustic (PA) signals, 297
Photobiomodulation (PBM), 488
Photocurrent (PC) spectroscopy, 411, 412
Photodynamic therapy (PDT)
acne, 499–500
actinic keratosis, 499
anti-microbial effect, 493–494
anti-tumor effect
acquired immunity, 493
direct killing of tumor cells, 492
inflammatory response, 493
innate immunity, 493
vascular effect, 493
basal cell carcinoma, 500
deep dental caries, 501
denture stomatitis, 503
dosimetry of, 491–492
light sources, 490–491
oral antibacterial therapy, 500–501
periodontitis, 502
PWS, 501
single wavelength
blue LED, 508
excitation wavelength, 507
green LED, 508
hybrid multi-wavelength LED, 508
red LED, 508
vascular targeted PDT, 493
Photoluminescence (PL) intensity, 282
Photonic crystal (PhC) method
air-gap embedded PhCs, 124
embedded and double SiO_2 PhC LEDs, 125
embedded PhC of SiO_2 nanodisks, 125–126
far-field emission patterns, 126
freestanding substrates, 126–127
p-GaN, PhCs holes of, 291
Photoperiod, *see* Hydroponic lettuce
Photo-sequencing technology (PST), 507
Photosynthetic photon flux density (PPFD)
Lactuca sativa L. cv. Frill ice cucumber seedlings, 521
effects of growth and quality, 527–531
growth and quality measurement, 523–524
high-quality, 521
leaf morphology and growth, 524–527
morphological and physiological responses, 521

Photosynthetic photon flux density (PPFD) (*cont.*)
plant materials and growth conditions, 521–523
treatment and experiment design, 522–523
Lactuca sativa L. cv. "Ziwei"
continuous photosynthesis and light responses, 540–542
effect of light quality, 537–540
effects of growth, 534–537
EUE, 542–543
growth and quality properties, 533–534
photosynthesis measurement, 534
plant materials and growth condition, 532
treatment and experiment design, 524, 532–533
Physical vapor transport (PVT) method, 43–44
congruent melt method, 48
crucible and induction coil, 50, 51
crystal growth procedure
high-temperature and high-pressure stage, 52
low-temperature and high-vacuum stage, 52
pressure decreasing and crystal growth stage, 52, 54
pressure increasing and cooling stage, 54
SiC nucleation stage, 52
stable crystal growth stage, 54
4H-SiC single crystal, 50, 52
longitudinal cut slice, 51, 54
principle and growth furnace, 48
radial growth rate distributions, 50, 54
Si, Si_2C, and SiC_2 partial pressures, 48, 49
source graphitization, 48
temperature distribution and growth front, 50, 53
thermal field, 49–51
Piezoelectric polarization, 116
Plant factories with artificial lighting (PFAL), 513
characteristics of, 515–516
dry mass/amount of carbohydrates, 514
environmental factors, 514
lettuce seedlings (*see* Hydroponic lettuce)
light environmental control, 517–518
photosynthetic radiation, 515
smart lighting system, 518–520
unit economic value, 515
POD-conjugated anti-DIG antibody, 551
Polarization field effects, 116, 117
Port wine stains (PWS), 493
PPFD, *see* Photosynthetic photon flux density
Printed circuit board (PCB), 218
Pseudomorphic AlGaN on AlN substrate, 264–265
Pseudomorphic DUV LEDs on AlN substrates
cross-sectional TEM image, 265, 266
dislocation density, 265, 266
light extraction efficiency, 266–268
PSS, *see* Patterned sapphire substrate
Pulsed atomic-layer epitaxy (PALE) approach, 292
PVT method, *see* Physical vapor transport method
Pyruvate kinase (PK), 565

Q
Quantitative difference (QD), 488
Quantum-confined stark effect (QCSE), 113–114, 261, 281, 325, 337, 342–343
Quantum dots (QD), 232–233
Quantum well intermixing (QWIM), 290
Quasi-homoepitaxial LED, 283

R
Reactive oxygen species (ROS) content, 488–489, 574
Recirculating Aquaculture Systems (RAS), 550, 556
Reflective p-type ohmic contact, 155–156
Root-mean-square (RMS) roughness, 262

S
Saccus vasculosus (SV), *Salmo salar*, *see* Atlantic salmon (*Salmo salar* L.)
Schottky barrier, 100
Seasonal affective disorder (SAD), 495
Second ion mass spectrometry (SIMS) measurements, 110
Seed sublimation method, 43–44
Selective area epitaxy (SAE), 284
Selective area growth (SAG), 136
Self-separation methods, 28
epitaxial procedure, 30
sapphire substrates, 30
substrate structure with GaN seeds, 30, 31
TiN voids, 30–31
VAS-GaN wafer, 30, 32
VAS technology, 30–31
Serial resistance, 281

Shockley-Read-Hall non-radiative recombination, 295
Shockley van Roosbroeck (SvR) equation, 353
Short period superlattice (SPSL) technique, 374–376
SiC LED, 42
Silane flux addition, 436
SiLENSe simulations, 369, 378, 379
Silicon (Si), 199
Silicon carbide (SiC), 199
Silicon carbide (SiC) single crystal
  Acheson process, 41
  growth
    by PVT method (*see* Physical vapor transport (PVT) method)
    by sublimation growth (*see* Sublimation growth, SiC single crystal)
  4H-SiC, 41
  6H-SiC, 41
  HTCVD method, 45–46
  large-diameter SiC wafer processing
    As-grown SiC single crystal boules, 83
    CMP (*see* Chemo-mechanical polishing)
    crystal boule slicing, 84
    epitaxial growth, 4H-SiC, 83
    ingot to wafer, 82
    KOH etching and HRXRD, 83
    lapping, 84–85
    mechanical polishing (*see* Mechanical polishing)
  LED, 42
  polytypism, 41, 46
  solution growth method, 44–45
  structural defects (*see* Structural defects, SiC single crystals)
  structure and physical properties
    bilayer stacking, 47
    cubic sites, 47
    electronic devices, advantages, 47–48
    hexagonal sites, 47
    polytypes, 46
    semiconductor materials, 47
  vapor growth method
    4H and 15R-SiC polytype, 43
    Lely method, 42
    modified Lely method, 43–44
    porous graphite, 42
Single and double monolayer δ-GaN quantum wells
  IQE (*see* Internal quantum efficiency (IQE))
  optical properties, 364
    PL and absorption spectra, 364, 366
    schematic structure, 364, 365
Single quantum well (SQW), 286
Smart electronic metering, 534
Sodium flux growth method, 93
Solid-state lighting
  architectures, 185, 186
  green gap, 187–189
  hy-LED, 185, 189
  LER and CRI, 187
  light source efficacy, YAG:Ce^{3+} phosphor, 187, 188
  optical power spectra, 185, 186
  pc-LED, 185–187, 190
  red LED efficiency, 189–190
  relative white light luminous efficacy, 189, 190
Solid-state lighting is redefined by bandgap engineering techniques (SORBET), 290
Solution growth method, SiC single crystal, 44–45
Specific growth rate (SGR), 566–567
Spectroradiometry, 520
Spin-orbit coupling, 99
SP polaritons (SPP), 291
Stacking faults (SFs), 71
Stranski–Krastanov (SK) quantum dots/disks
  HAADF-STEM image, 367, 368
  modified SK growth scheme, 370–373
  optical properties, 368, 369
  schematic structure, 367, 368
  SiLENSe simulations, 369
  structural characterization, 367
Structural defects, SiC single crystals
  dislocations
    BPDs, 66
    categories, 65, 66
    elimination process, 68
    "repeated a-face" growth process, 67
    surface morphology, oxidation pits, 66
    synchrotron monochromatic beam X-ray topographs, 68, 69
    TED, 66
    TSD, 66
  foreign polytypes
    empirical observation, 63, 64
    4H, 6H, and 15R polytypes, scanning image, 62, 63
    nucleation energy, 65
    supersaturation, 65
    surface morphology, 6H-SiC crystal, 65
    2D nucleation theory, 63, 64

Structural defects, SiC single crystals (*cont.*)
micropipe defects
AFM image, 6H-SiC single crystal, 55, 56
back-reflection synchrotron topograph, 55–57
back-reflection X-ray topographs, 56, 59
Burgers vectors, 55, 56
foreign polytype, 58
graphite particle, 58, 61
4H-SiC and 3C-SiC unit cell, 60, 62
longitudinal cut 4H-SiC crystal, 57–58, 60
propagation, 60, 62
radius of hollow core, 55
seed face, 61
sources, 59
super-screw dislocation, 55, 56, 58
surface morphology, 4H-SiC, 60, 63
void and micropipe formation process, 57, 60
Sublimation growth, SiC single crystal
n-type doping
Al-N co-doping 4H-SiC crystal growth, 71, 72
etching morphologies, longitudinal cut SiC crystals, 71, 72
nitrogen doping, 69
N_2 partial pressure dependence, 70–71
stacking faults, 71
p-type doping
Al and N concentrations, 75, 76
aluminum doping, 73–74
charge carrier mobility *vs.* concentration, 75
longitudinal cut 6H-SiC crystal, optical transmission image, 73, 74
M-PVT using TMA, 74
SIMS, Raman spectroscopy, and resistivity measurement, 75
semi-insulating
admittance *vs.* photon energy, 81
EPR spectrum, 4H-SiC HPSI sample, 82
Fermi level, compensation ratio, 77
GDMS measurements, 90
Hall effect measurements, 79
high-resolution resistivity map, 90
HPSI SiC, 79
inner crucible, 78
longitudinal cut 6H-SiC, scanning image, 77, 78
nitrogen and boron, 79–80
OAS, 81
temperature-dependent resistivities, HPSI samples, 80–82
vanadium compensation, 76–77, 79
vanadium evaporation rate, 78
V-doped and V-B co-doped 6H-SiC crystals, 79
V-doped semi-insulating 6H-SiC bulk single crystals, 77
vertical devices fabrication, 68
Succinate dehydrogenase (SDH), 565, 573
Superlattice electron-blocking layer (SL-EBL), 229, 231
Superoxide dismutase (SOD), 573
Surface patterning, DUV LEDs, 270–272
Surface photovoltage spectroscopy (SPS) method, 100
Surface plasmon-enhanced LEDs, 328–331
Surface plasmon (SP) modes, 291
Surface-structured OSRAM chips, 178
Surface texturing
anisotropic wet etching process, 318
dangling bond density, 318
dry etching, 318
dual-layer ITO electrode, 320
ITO nanoballs, 320, 321
nitride-based HPA V-LEDs, 318–319
normalized average light optical power, 320, 322
N-polar wet etching technique, 318
p-GaN surface, 319, 320

T

TDD, *see* Threading dislocation density
Temperature-dependent PL (TDPL), 295
Textured chip surfaces, AlGaInP/AlGaAs LED
n-side roughened-surface AlGaInP LED, 179
surface-structured OSRAM chips, 178
Thermal camera, 520
Thin-film flip-chip LED (TFFC LED), 218–219
Thin-film LEDs (TF-LEDs), 181–182
Thin-film structure, AlGaInP/AlGaAs LED
with buried microreflectors, 181–182
epitaxial lift-off process, 184
hexagonal and Archimedean lattices, 183
ODR-LED structure, 183
p-side-up thin-film AlGaInP LED, 184, 185
stability factors, 184
vs. TS-LEDs, 181
wafer-bonding processing, 182

Threading dislocation density (TDD), 204–205, 207–208, 254, 341–342
CBED patterns, 108
hexagonal pits, SEM, 105, 106
inversion domains, 108
inverted pyramids, 107–109
LED on GaN at 79 K, 105, 106
QWs, cross-sectional TEM micrograph, 106, 107
reduction, 101
3D laser scanning, 520
III-nitride-based light-emitting diodes
applications, 311
chip structure engineering, 312–313
external quantum efficiency, 311
IQE, 311
material alloy, 311
micro-/nanostructure engineering
patterned sapphire substrates, 324–328
photonic crystal, 321–323
surface texturing, 318–322
optical reflections
current–voltage characteristics, 316
distributed Bragg reflectors, 313–314
metal reflectors, 313, 314
MgF_2/Al ODR mirror, 317
micro-reflectors, 316–317
oblique-angle deposition, 315
omnidirectional reflectors, 313–315
optical power, 316
reflective mirror, 315
schematic device architecture, 316
truncated cone AlGaN structure, 317
surface plasmon-enhanced LEDs, 328–331
III-nitrides red/yellow LED
GaN-based yellow LED
efficiency drop, 194
green gap, 194, 195
InGaN/GaN MQW, 195
research of, 195–196
semipolarized/nonpolarized GaN, 196–197
using quantum dot/quantum wire, 197
substrate technique, 198–199
Total antioxidant capacity (T-AOC), 574, 579
Total internal reflection (TIR), 268
Transparent substrate (TS), AlGaInP/AlGaAs LED, 179–181
Transverse electric (TE) mode LEE, 268
Trichromatic (RGB) sensors, 520
Truncated cone (TC) AlGaN structure, 317
Truncated-inverted-pyramid (TIP) chip geometry, 180–181
Truncated pyramidal-shaped flip-chip bulk-GaN LEDs, 123–124
TSA-plus tetramethylrhodamine (TMR), 551, 557
Two-step growth method, 283

U
Ultraviolet light-emitting diodes
AlGaN-based ultraviolet light-emitting diodes, 397–412
InGaN-based ultraviolet light-emitting diodes, 412–413
reliability of packages, 414–419

V
van der Waals epitaxy (vdWE), 208–209
Vapor growth method, SiC single crystal
4H and 15R-SiC polytype, 43
Lely method, 42
modified Lely method, 43–44
porous graphite, 42
Vapor-liquid-solid (VLS) process, 434
Vertical structure LED (VSLED), 219–221, 283
Vertical thin film LEDs, device characterization
emission intensity *vs*. current density, 165
features, 162
“flip chip” structure, 165
junction temperature, 165, 166
thermal conductivity, 164
vertical and lateral structure, 163, 164
V-I characteristics, 163–164
white LEDs, spectra of, 166, 167
white light projection, 166, 167
Visible camera, 520
Visible light communication (VLC), 192
Visible to far-red hyperspectral camera, 520
Void-assisted separation (VAS) technology, 30–31
Volcano-shaped patterned sapphire substrate (VPSS), 324–325
V-pits
area ratio of pits, 154
EL spectra, 151, 152
hole injection into c-plane QW process, 153
InGaN/GaN MQW LEDs, 151
IQE dependence, 154
LT-GaN, 291
luminescence intensity, 151
photoluminescence intensity, 151

V-pits (*cont.*)
schematic structure, 150, 151
TD densities, 151
"V pits enhancing hole injection" model, 152–155
"V pits screening TD" model, 152

W
Wafer-bonding processing, thin-film LEDs, 182
Wafer-transfer technique, 184
Wall-plug efficiency (WPE), 343–344
Wide bandgap semiconductor
GaN substrates (*see* GaN substrates)
III-N materials, 1
marketization, 1
properties, 1
Wurtzite lattice structure

X
X-ray rocking curves (XRCs), 143
XRCs FWHMs, 143
XRD FWHM, 206–207

Y
YAG:Ce^{3+} phosphor, 188

Z
Zero-phonon line (ZPL), 99, 100